minerals

Mineralogy of Noble Metals and “Invisible” Speciations of These Elements in Natural Systems, Volume II

Edited by
Galina Palyanova

Printed Edition of the Special Issue Published in *Minerals*

www.mdpi.com/journal/minerals

MDPI

Mineralogy of Noble Metals and "Invisible" Speciations of These Elements in Natural Systems, Volume II

Mineralogy of Noble Metals and "Invisible" Speciations of These Elements in Natural Systems, Volume II

Editor

Galina Palyanova

MDPI • Basel • Beijing • Wuhan • Barcelona • Belgrade • Manchester • Tokyo • Cluj • Tianjin

Editor
Galina Palyanova
Siberian Branch of the Russian
Academy of Sciences
Novosibirsk State University
Russia

Editorial Office
MDPI
St. Alban-Anlage 66
4052 Basel, Switzerland

This is a reprint of articles from the Special Issue published online in the open access journal *Minerals* (ISSN 2075-163X) (available at: https://www.mdpi.com/journal/minerals/special_issues/noble_metals_volume_ii).

For citation purposes, cite each article independently as indicated on the article page online and as indicated below:

LastName, A.A.; LastName, B.B.; LastName, C.C. Article Title. *Journal Name* **Year**, *Volume Number*, Page Range.

ISBN 978-3-0365-2526-6 (Hbk)
ISBN 978-3-0365-2527-3 (PDF)

Cover image courtesy of Galina Palyanova

Contents

About the Editor

Galina Palyanova Ph.D., is a leading scientist at the V.S. Sobolev Institute of Geology and Mineralogy of the Siberian Branch of the Russian Academy of Sciences and a lecturer at the Department of Mineralogy and Geochemistry of Novosibirsk State University. She graduated from Novosibirsk State University with a degree in geochemistry. Her main areas of research are ore mineralogy and thermodynamic and experimental modeling of ore-forming processes. She has published over 90 research articles in international journals. Her monograph, "Physical and chemical features of the behavior of gold and silver in the processes of hydrothermal ore formation", was awarded a medal and a diploma from the Russian Mineralogical Society. She was awarded medals of the Russian Ministry of Higher Education and the Russian Academy of Sciences and an honorary diploma by the Ministry of Natural Resources and Energy Resources for her great contribution to the development of the Mineral Resource Base of Russia.

minerals

MDPI

Editorial

Editorial for Special Issue "Mineralogy of Noble Metals and 'Invisible' Speciations of These Elements in Natural Systems, Volume II"

Galina Palyanova

Sobolev Institute of Geology and Mineralogy, Siberian Branch of Russian Academy of Sciences, 630090 Novosibirsk, Russia; palyan@igm.nsc.ru

The articles published in the 2019 Special Issue "Mineralogy of Noble Metals and 'Invisible' Speciations of These Elements in Natural Systems" [1] do not cover all the stated problems of the specified topic, and hence, a second volume is being released. At present, a significant part of the reserves of gold and other noble metals consists of deposits of sulphide ores. Many sulphide ores are referred to as refractory ores by technologists. Knowledge of the mineralogy of these ores, including micro and nano minerals of noble metals, is a key factor in developing rational processing and enrichment schemes. The aim of this Special Issue is to facilitate new knowledge for solving fundamental and applied tasks.

The second volume Special Issue consists of one review on noble metal speciation in sulphide ores and eleven research articles on various other topics.

Vikentyev et al. [2] reviewed the distribution and speciation of noble metals in contrasting types of mineralisation from the Urals, one of the largest ore belts in the world. They describe the distribution and structural-chemical state of Au and Ag in sulphides from the late-magmatic to low-temperature hydrothermal, regarded as the indicators of the conditions of mineralisation and metamorphism of ores, with emphasis on the economically significant genetic types of ore deposits. This article is based on a large amount of new and existing information: mineralogical, electron microprobe, mass-spectrometric, and neutron activation. The ratio of forms of free and invisible gold in sulphides is discussed. Admixtures of metals and metalloids provide the increased crystal structure defects for the entry of noble metal impurities into sulphides by the mechanism of heterovalent isomorphism. The invisible gold is enlarged and passes into the visible state as native gold, Au-Ag tellurides, Au-Ag sulphides, and other minerals.

A number of articles [3–11] are devoted to the study of gold mineralization at different deposits and the characterization of the physicochemical conditions of its formation.

Jin and Sui [3] presented major and trace element analyses by electron microprobe and laser ablation inductively coupled plasma mass spectrometry on two types of tourmalines from the newly recognized intrusion-related Laodou gold deposit in the West Qinling Orogen of central China. Both tourmaline types fall into the alkali group and are classified under the schorl-dravite solid solution series. Chemical compositions and changes in tourmaline textures may provide evidence for changes in the processes related to the evolution of the hydrothermal system. In the Laodou gold deposit, type 1 tourmaline is a product of the late crystallization of the quartz diorite porphyry, whereas type 2 tourmaline coexists with Au-bearing arsenopyrite and is crystallized from the ore-forming fluids. The composition of tourmaline is largely controlled by fluid/rock ratios and chemical equilibria with coexisting phases in the hydrothermal system [3].

Kalinin and Kudryashov [4] investigated the Pellapahk Cu-Mo and Oleninskoe Au-Ag deposits in the western segment of the Russian Arctic in the Kolmozero–Voronya greenstone belt (Kola Peninsula). They regard these deposits as two parts of an Archean (2.83–2.82 Ga) porphyry-epithermal system, probably the oldest such deposit in the Fennoscan-

Citation: Palyanova, G. Editorial for Special Issue "Mineralogy of Noble Metals and 'Invisible' Speciations of These Elements in Natural Systems, Volume II". *Minerals* **2021**, *11*, 817. https://doi.org/10.3390/min11080817

Received: 1 July 2021
Accepted: 27 July 2021
Published: 28 July 2021

dian Shield. The formation of the Oleninskoe Au-Ag deposit at the epithermal stage of the system is indicated by the spatial and genetic relationships with the sills of granite porphyry. The geological and structural characteristics of the Oleninskoe and the Pellapahk deposits, i.e., their location in a shear zone, the morphology and size of ore bodies, the scale of the deposits, and the intensity and zoning of rock alteration, are consistent with this model.

Kudrin et al. [5] studied disseminated gold–sulphide mineralization in metasomatites of the Khangalas deposit, Yana–Kolyma Metallogenic Belt (Northeast Russia). The textural and mineralogical-geochemical features, isotope-geochemical characteristics of gold-bearing sulphides from proximal metasomatites, and possible forms of Au in pyrite and arsenopyrite were investigated using electron microprobe, atomic absorption, LA-ICPMS trace element, isotope analysis, and computed microtomography. The gold content of sulphides and proximal metasomatites indicates that the Khangalas deposit has higher commercial potential than was previously indicated. Khangalas provides an exploration model useful in targeting similar gold deposits from the local to the regional scale.

Kondratieva et al. [6] studied tellurium mineralization from gold deposits of the Aldan shield (Southern Yakutia, Russia). Twenty-nine tellurium minerals, including 16 tellurides, 5 sulfotellurides, and 8 tellurates, have been identified from new results of this study and previously published results. The analysis of the composition of Te minerals in these gold deposits allowed identification of three mineral types: Au-Ag-Te, Au-Bi-Te, and mixed Au-Ag-Bi-Te. Tellurium minerals are developed in all known types of metasomatic formations represented by sericite-microcline metasomatites, beresites, gumbaites, jasperoids, and argillizites. The Au-Ag-Bi-Te minerals are the important sources of gold reserves in this district.

Sidorov et al. [7] studied fluid inclusions from different types of quartz vein associations at the Maletoyvayam Deposit (Koryak Highland, Russia). This epithermal gold deposit contains unique ore mineralization with native gold, tellurides, selenides, and sulphoselenotellurides of Au, including maletoyvayamite, unnamed phases (AuSe, Au(Te,Se)), and oxidation products of Au-tellurides. The maletoyvayamite has not been reported anywhere else.

Fluid inclusions in quartz have salinities from 0.2 to 4.3 wt.% NaCl eq. (NaCl + KCl). The indicated temperature variations for quartz crystallization were 295–135 °C with pressures from 79 to 4 bar. These physicochemical characteristics of the Maletoyvayam ore deposit coincide with other high-sulphidation (HS)-type epithermal deposits. It can be speculated that Au–Cu–porphyry mineralization may be found at deeper horizons in the Maletoyvayam area.

Kolova et al. [8] investigated the features of Au-Ag-S-Se-Cl-Br mineralization at the epithermal Au-Ag Corrida deposit (Chukchi Peninsula, Russia) and estimated the physicochemical conditions of its formation on the basis of the study of fluid inclusions and thermodynamic modelling. This deposit is a new example of an epithermal deposit with significant quantities of Au–Ag chalcogenides (Se-acanthite, uytenbogaardtite, fischesserite, S-naumannite, and others) and Ag halides of the chlorargyrite-embolite-bromargyrite series. Fluid inclusions indicate that the ore-bearing quartz was formed at temperatures of 340 to 160 °C; from low salinity (3.55 to 0.18 wt. % NaCl eq.) fluids. Thermodynamic modelling suggests that mineralization formed under the following conditions: sulphur (log $fS2$ from -6 to -27), selenium (log $fSe2$ from -14 to -35), and oxygen (log $fO2$ from -36 to -62).

Palyanova et al. [9] reported results of studies of the composition of native gold and minerals in intergrowth with it in two ore zones of the Chudnoe Au-Pd-REE deposit (Subpolar Urals, Russia). This deposit and some other Ural deposits (Baronskoe, Volkovskoe, Nesterovskoe, Ozernoe) are unique in the set of impurity elements in native gold (Ag, Cu, Pd, Hg) and variability of their concentrations. Despite the numerous results, the reasons for compositional changes in native gold and the presence of a wide set of impurity elements are not clear yet. The formation of native gold is probably related to fuchsitization and allanitization of rhyolites as well as to Na-, Si-, and K-metasomatism.

The absence of carbonates and sulphides and the presence of palladium minerals, Cu and Pd in native gold, and Cr in fuchsite indicate a relationship between ore formation and mafic-ultramafic magmatism.

Silyanov et al. [10] studied the oxidized ores from the Olympiada deposit (Eastern Siberia, Russia). They obtained new data on the morphology and chemical composition of native gold and proposed a model of supergene redistribution of noble metals and other elements in the oxidation zone. They found that the supergene gold crystals (~1 μm), their aggregates, and their globules (100 nm to 1 μm) predominate in the upper oxidized zones, and spongiform gold occurs in the lower zone at the boundary with the bedrock.

Stepanov et al. [11] described the morphological features and composition of native gold and its relation to minerals in ore-bearing breccias with realgar-orpiment cement from the Vorontsovskoe gold deposit (Northern Urals, Russia). Despite a comprehensive study of this deposit, its genesis remains controversial. The general geological and geochemical patterns of the Turyinsk-Auerbakh metallogenic province [12] and the presence of small non-economic porphyry copper deposits suggest that the Vorontsovskoe deposit is an integral part of a large ore-magmatic system genetically associated with the formation of the Auerbakh intrusion.

Nikiforova [13] studied the typomorphism of placer gold and the mechanisms of its distribution in the east of the Siberian Platform. She developed a method for diagnosing the genotype of placer gold from its morphological characteristics (alluvial, aeolian, pseudo-ore). The diagnostic method and morphogenetic criteria for identifying the genesis of placers and different sources in the platform areas developed by Nikiforova [13] can be successfully used by production geological organizations for the exploration of placer gold deposits.

Simakin et al. [14] performed an experimental study of Pt solubility in a CO-CO2 rich fluid at PT conditions close to the subsolidus conditions of upper crust ultramafic–mafic intrusions. They demonstrated that the solubility of Pt in a CO-CO2 fluid at 50–200 MPa and 950 °C is 15–150 ppm, presumably in the form of Pt3(CO)62−. Their results demonstrate that the formation of carbonyl itself can be an important mechanism for the transport of Pt by fluid at the post-magmatic stage of layered ultramafic–mafic intrusions.

These studies contribute to our understanding of the behaviour of noble metals and the forms of occurrence in natural ore-forming systems.

Funding: This editorial was supported by the state assignment of the V.S. Sobolev Institute of Geology and Mineralogy of the Siberian Branch of the Russian Academy of Sciences financed by the Ministry of Science and Higher Education of the Russian Federation.

Acknowledgments: I thank the authors of the articles and the organizations that have financially supported the research in the areas related to this topic. I would like to give my special thanks to the Editor-in-Chief, the Section Editor-in-Chief, the editorial board, and the reviewers for their work on this issue.

Conflicts of Interest: The author declares no conflict of interest.

References

1. Palyanova, G. Editorial for Special Issue: "Mineralogy of Noble Metals and "Invisible" Speciations of These Elements in Natural Systems". *Minerals* **2020**, *10*, 210. [CrossRef]
2. Vikentyev, I.; Vikent'eva, O.; Tyukova, E.; Nikolsky, M.; Ivanova, J.; Sidorova, N.; Tonkacheev, D.; Abramova, V.; Blokov, V.; Spirina, A.; et al. Noble metal speciations in sulphides. *Minerals* **2021**, *11*, 488. [CrossRef]
3. Jin, X.; Sui, J. Geochemistry of Tourmaline from the Laodou Gold Deposit in the West Qinling Orogen, Central China: Implications for the Ore-Forming Process. *Minerals* **2020**, *10*, 647. [CrossRef]
4. Kalinin, A.A.; Kudryashov, N.M. Porphyry-Related Metamorphosed Au-Ag and Cu-Mo Deposits in the Precambrian of the Fennoscandian Shield. *Minerals* **2021**, *11*, 139. [CrossRef]
5. Kudrin, M.; Fridovsky, V.; Polufuntikova, L.; Kryuchkova, L. Disseminated Gold-Sulfide Mineralization in Metasomatites of the Khangalas Deposit, Yana–Kolyma Metallogenic Belt (Northeast Russia): Analysis of the Texture, Geochemistry, and S Isotopic Composition of Pyrite and Arsenopyrite. *Minerals* **2021**, *11*, 403. [CrossRef]

6. Kondratieva, L.A.; Anisimova, G.S.; Kardashevskaia, V.N. Types of Tellurium Mineralization of Gold Deposits of the Aldan Shield (Southern Yakutia, Russia). *Minerals* **2021**, *11*, 698. [CrossRef]
7. Sidorov, E.G.; Borovikov, A.A.; Tolstykh, N.D.; Bukhanova, D.S.; Palyanova, G.A.; Chubarov, V.M. Gold Mineralization at the Maletoyvayam Deposit (Koryak Highland, Russia) and Physicochemical Conditions of Its Formation. *Minerals* **2020**, *10*, 1093. [CrossRef]
8. Kolova, E.E.; Savva, N.E.; Zhuravkova, T.V.; Glukhov, A.N.; Palyanova, G.A. Au-Ag-S-Se-Cl-Br Mineralization at the Corrida Deposit (Russia) and Physicochemical Conditions of Ore Formation. *Minerals* **2021**, *11*, 144. [CrossRef]
9. Palyanova, G.; Murzin, V.; Kuznetsov, S.; Karmanov, N. Native gold of the Au-Pd-REE Chudnoye deposit (Subpolar Ural, Russia): Composition, mineral associations, genesis. *Minerals* **2021**, *11*, 451. [CrossRef]
10. Silyanov, S.A.; Sazonov, A.M.; Zvyagina, Y.A.; Savichev, A.A.; Lobastov, B.M. Gold in the Oxidized Ores of the Olympiada Deposit (Eastern Siberia, Russia). *Minerals* **2021**, *11*, 190. [CrossRef]
11. Stepanov, S.Y.; Palamarchuk, R.S.; Varlamov, D.A.; Kiseleva, D.V.; Sharpyonok, L.N.; Škoda, R.; Kasatkin, A.V. The Features of Native Gold in Ore-bearing Breccias with Realgar-orpiment Cement of the Vorontsovskoe Deposit (Northern Urals, Russia). *Minerals* **2021**, *11*, 541. [CrossRef]
12. Minina, O.V. Auerbakh complex ore-magmatic system in the Middle Urals. *Natl. Geol.* **1994**, *7*, 17–23. (In Russian)
13. Nikiforova, Z. Criteria for Determining the Genesis of Placers and TheirDifferent Sources Based on the Morphological Features of Placer Gold. *Minerals* **2021**, *11*, 381. [CrossRef]
14. Simakin, A.; Salova, T.; Borisova, A.Y.; Pokrovski, G.S.; Shaposhnikova, O.; Tyutyunnik, O.; Bondarenko, G.; Nekrasov, A.; Isaenko, S.I. Experimental Study of Pt Solubility in the CO-CO_2 Fluid at Low fO_2 and Subsolidus Conditions of the Ultramafic-Mafic Intrusions. *Minerals* **2021**, *11*, 225. [CrossRef]

minerals

MDPI

Review

Noble Metal Speciations in Hydrothermal Sulphides

Ilya Vikentyev [1,2,*], Olga Vikent'eva [1], Eugenia Tyukova [1,3], Maximilian Nikolsky [1], Julia Ivanova [1,2], Nina Sidorova [1], Dmitry Tonkacheev [1], Vera Abramova [1], Vyacheslav Blokov [1,4], Adelina Spirina [1,2], Diana Borisova [1,5] and Galina Palyanova [6,7]

[1] Institute of Geology of Ore Deposits, Petrography, Mineralogy, and Geochemistry, Russian Academy of Sciences, 119017 Moscow, Russia; ovikenteva@rambler.ru (O.V.); evgtyuk@mail.ru (E.T.); mnickolsky@gmail.com (M.N.); jnivanova@yandex.ru (J.I.); nsidorova181189@gmail.com (N.S.); tonkacheev@mineralog.com (D.T.); winterrain@rambler.ru (V.A.); blok_off@mail.ru (V.B.); shakhtiyarova@bk.ru (A.S.); bda.96@mail.ru (D.B.)
[2] Department of Geology, Mining and Oil&Gas Engineering, Academy of Engineering, Peoples' Friendship University of Russia (RUDN University), 117198 Moscow, Russia
[3] Scientific Geoinformation Centre, Russian Academy of Sciences, 119019 Moscow, Russia
[4] Institute of Mineralogy, Geochemistry and Crystal Chemistry of Rare Elements, 121357 Moscow, Russia
[5] Department of Geology, Lomonosov Moscow State University, 119992 Moscow, Russia
[6] Sobolev Institute of Geology and Mineralogy, Siberian Branch of the Russian Academy of Sciences, 630090 Novosibirsk, Russia; palyan@igm.nsc.ru
[7] Department of Geology and Geophysics, Novosibirsk State University, 630090 Novosibirsk, Russia
* Correspondence: viken@igem.ru; Tel.: +7-499-230-82-26

Abstract: A significant part of the primary gold reserves in the world is contained in sulphide ores, many types of which are refractory in gold processing. The deposits of refractory sulphide ores will be the main potential source of gold production in the future. The refractory gold and silver in sulphide ores can be associated with micro- and nano-sized inclusions of Au and Ag minerals as well as isomorphous, adsorbed and other species of noble metals (NM) not thoroughly investigated. For gold and gold-bearing deposits of the Urals, distribution and forms of NM were studied in base metal sulphides by laser ablation-inductively coupled plasma mass spectrometry and by neutron activation analysis. Composition of arsenopyrite and As-pyrite, proper Au and Ag minerals were identified using electron probe microanalysis. The ratio of various forms of invisible gold—which includes nanoparticles and chemically bound gold—in sulphides is discussed. Observations were also performed on about 120 synthetic crystals of NM-doped sphalerite and greenockite. In VMS ores with increasing metamorphism, C_{Au} and C_{Ag} in the major sulphides (sphalerite, chalcopyrite, pyrite) generally decrease. A portion of invisible gold also decreases—from ~65–85% to ~35–60% of the total Au. As a result of recrystallisation of ores, the invisible gold is enlarged and passes into the visible state as native gold, Au-Ag tellurides and sulphides. In the gold deposits of the Urals, the portion of invisible gold is usually <30% of the bulk Au.

Keywords: invisible gold; sulphides; LA-ICPMS; synthesis; gold deposits; VMS deposits; Urals

Citation: Vikentyev, I.; Vikent'eva, O.; Tyukova, E.; Nikolsky, M.; Ivanova, J.; Sidorova, N.; Tonkacheev, D.; Abramova, V.; Blokov, V.; Spirina, A.; et al. Noble Metal Speciations in Hydrothermal Sulphides. *Minerals* **2021**, *11*, 488. https://doi.org/10.3390/min11050488

Academic Editor: Liqiang Yang

Received: 28 February 2021
Accepted: 28 April 2021
Published: 3 May 2021

1. Introduction

Considering the "visible" gold occurrence in gold deposits, it has long been noted that the association of native gold with sulphides is the most sustainable (e.g., [1,2]). However, gold invisible to optical methods also commonly associates with sulphides, notably pyrite [3–5]. The presence of invisible gold is established by chemical and assay analyses of bulk samples as well as by sensitive and relatively local LA-ICPMS analysis (e.g., [6–8]). Such invisible gold can be extracted from sulphides by repeated heating (up to 850 °C; cf. during metamorphism of sulphide ore [9]), resulting in enlargement of gold particles [3,10]. The mechanism of this process was unclear, and Bürg [11] introduced the concept of "self-cleaning of the crystal lattice" of pyrite.

The form in which gold occurs in sulphides of the Fe-As-S system, which are key minerals within the deposits of Au, Cu ± Au, Fe, Mo, U, Zn attracted enormous attention in the last quarter of the 20th century. From an experimental point of view, the limits of invisible gold in sulphides are defined over a wide temperature range [6,8,12–18]. It is also determined experimentally that sulphide heating, as an analogue of metamorphic transformation, leads to release of chemically bound gold from the crystal lattice of host minerals (such as pyrite, arsenopyrite) and to the formation of elemental microparticles (for example, see the review of the problem in [15] and also the experimental data review in [19]).

The behaviour of gold is most representatively characterised for high-temperature sulphide systems: gold-copper-porphyry and gold-copper (and Fe-Cu-Au, Fe-Au, subtypes) skarn deposits. Deposits of the copper–porphyry family represent some of the greatest gold concentrations in the Earth crust. In addition, these deposits are possibly the sources of gold for epithermal and other related deposits. Experimental data show that bornite and chalcopyrite, formed under high-temperature conditions (about 600–700 °C) typical for deep zones of copper–porphyry deposits, may contain about 1000 ppm of gold. Saturation of these minerals with gold, however, occurs only at much lower (200–300 °C) temperatures, corresponding to low-temperature minerlisation stages [20]. Thus, these deposits reveal a wide range of sulphides with different contents of gold, varying from its disseminated form to the larger "visible" native gold [20,21]. In addition, during the formation of these deposits, the processes of extraction and redistribution of gold and copper occur within immiscible sulphide melt and gas fluid at different levels (or alteration zones) of the unified systems, resulting in different Cu/Au ratios both in the gold-copper-porphyry and skarn systems.

In other high-temperature sulphide systems—magmatic (or orthomagmatic) ones—the behaviour of platinum-group elements (PGE) is important because of their high cost and scarcity on the global metal market. The authors partially summarised information about PGE in sulphides of magmatic and hydrothermal systems in papers (for pyrite [22] and pyrrhotite [23]). For hydrothermal deposits of the Urals, data were published in [24–28]. A much more complete review of the data is given in [29], devoted to magmatic sulphides.

In the ores of gold and gold-bearing deposits, Au occurs as: (1) own Au-Ag solid solution (rarer with Cu, Pd and Hg), i.e., native gold (with Ag content up to 50 wt% and fineness of 500–1000‰ in mole fractions $Au_{1–0.35}Ag_{0–0.65}$) and native silver (with an Ag content higher than 50 wt% and fineness of 0–500‰, in mole fractions $Ag_{1–0.65}Au_{0–0.35}$), compounds with Te or with other chalcogens (S, Se) and metalloids (As, Sb, Bi), and (2) the invisible (or fine dispersed) state. Invisible Au cannot be identified by conventional optical microscopes or scanning electronic techniques, being scattered in the host sulphides as nanoscale particles ("nanoparticles") and/or in chemically bound state. Visible segregations of native gold (called "nuggets" when becoming millimetre-sized and larger) and as discrete Au minerals can be effectively extracted from the ore. In fairly common cases, where Au is present in invisible form, processing results in the loss of most gold to tailings. In many gold-bearing volcanogenic massive sulphide (VMS) deposits, the proportion of invisible gold can be very high. For example, in the Uchaly VMS deposit in the South Urals, it reaches 85% [15].

The mineral balance of the NM forms in ore sulphides is essential for evaluating the NM recovery, i.e., their output into technological products and concentrates and, as for Au, the possibility of its leaching by the cyanide solution (the most cheap and effective method for extraction of fine-grained gold).

In many cases, the direct correlation between the concentrations of As and invisible Au in hydrothermal pyrite is observed (e.g., [30]; see [15] for discussion). However, As-poor pyrites can also demonstrate high gold concentrations. For example, the colloform pyrites in the large Agua Rica Cu (+Mo, Au) porphyry deposit, Argentina, are As-poor (<30 ppm) but rich in Au (up to 6.7 ppm) and Ag (up to 136 ppm) ([31]). No correlation between Au and As in pyrite occurs in the ores of the shear-hosted gold-vein system of the Fairview

mine, South Africa [32], VMS La Zarza, Migollas and Sotiel deposits, the Iberian Pyrite Belt [33], multistage sedimentary-metamorphic (orogenic) sediment-hosted Sukhoi Log gold deposit, South Siberia ([6]), "orogenic" gold deposits of the northern margin of the North China Craton, China [8], intrusion-related lode gold deposits of the Xiaoqinling–Dabie Orogenic Belt, China [34], and sediment-hosted (siltstone, shale and limestone) Qiuling gold deposit in the West Qinling orogenic belt, China ([35]). There is no correlation between As and Au in pyrites from most of the Au-bearing deposits of the Urals: the VMS deposits [15,36,37], the Novogodnee-Monto Fe-Au-skarn deposit [38], the Petropavlovsk gold-porphyry deposit [39,40] and the Svetlinsk Au-Te deposit [41,42]. Binary diagrams show the low correlation between Au and As for pyrite of the Zn-Pb-Se-Bi-Au-rich VMS Falun deposit, Sweden ([43]).

Understanding of the chemical state of Au in sulphide ores reached a new level when it became possible to study Au-bearing minerals synthesised at the contrasting TP conditions using different experimental techniques [13,44,45] and analytical methods [12,16,17,46–52]. The chemical state of Au in sulphides, i.e., its position in the host mineral structure, valence state and local atomic environment, can be determined using spectroscopic methods [19]. The spectroscopic studies of the sulphides rich in Au were performed using X-ray photoelectron spectroscopy (XPS, see [16,46,47] and references cited), Mössbauer spectroscopy [12,48,49] and X-ray absorption near-edge structure (XANES) spectroscopy [16,17,50–52].

The main problems preventing the determination of the chemical state of Au are: (1) relatively low concentrations of Au in natural sulphides, and hence the inability to use the mentioned physical (spectroscopic) methods for gold identification, and (2) limitations existing for the synthesis methods: (i) it is difficult to recreate the entire T/f S_2 range of natural sulphide formation, (ii) the variability of the composition and thin zoning of sulphide grains with respect to the main components, especially for arsenopyrite and As-pyrite, and (iii) the presence of a large number of other trace elements in addition to gold in the natural sulphides, which partly calls into question the complete analogy of synthetic and natural mineral grains.

In comparison with other precious metals in hydrothermal deposits, gold is the most important, so it is the focus of this study. Gold is among the rarest elements in the Earth's crust [53] and reserves of its largest deposits do not exceed first thousands of tons, however, the high economic and social-political significance of this metal requires sustainable reproduction and increase of gold natural resources. The increase in metal prices during the last 20 years favours the growth of gold supply and exploration in the world, but, taking into account an exhaustion of brown field resources and traditionally mined types of mineralisation, the further development of the resource base needs to be supported with new ideas based on a comprehensive level of knowledge. A forecasting geological model is one of the major requirements of successful exploration [54].

The purpose of this paper is to review the distribution and forms of NM in contrasting types of mineralisation on the example of one of the largest ore belts in the world. Distribution and structural-chemical state of Au and Ag in sulphides through the ore deposits from late-magmatic to low-temperature hydrothermal are considered as indicators of the conditions of mineralisation and metamorphism of ores (e.g., [9,15]). Thus, NM forms are regarded as one of the key aspects of the general model of the evolution of ore-forming systems related to fluid activity (from high- to low-temperature).

The research results contribute to fundamental knowledge on NM forms of occurrence in ores and minerals, and concentration levels of NM in sulphides. Our data can be useful in the analysis of the distribution of NM in the Earth's crust and will add data into the experimental database to support the thermodynamic models. Moreover, the data obtained on the contents and forms of NM accumulation in base metal sulphides are an important practical result of the work. They will help to develop ore processing.

The present research is based on studies of NM distribution and speciation in gold and gold-bearing deposits of the Urals. The gold deposits include Au-sulphide-quartz

(mesothermal intrusion-related, "traditional" type for the Urals) Berezovsk, Au-telluride mesothermal Svetlinsk and Au-sulphide-realgar Carlin-style Vorontsovka (both are large but are seen as unconventional for the Urals types [55]) (Table 1). Other types include VMS deposits (Cu-dominated Gai and Zn-dominated Uchaly, Uzelga, Galka) and the skarn-porphyry family (Novogodnee-Monto Au-magnetite-skarn and Petropavlovsk Au-porphyry deposits). The mentioned gold and gold-bearing deposits together provide about 95% of the production of Au of the Urals. The paper proposes an application of the modern achievements in the field of the analytical techniques for advancing the theoretical basis of the NM behaviour in hydrothermal ore mineralising systems with emphasises on economically significant genetic types of ore deposits.

Table 1. Main endogenous Au- and Cu-bearing deposits of the Urals.

Geodynamic Environments		Ore Deposit Type	Ore-Bearing Magmatic Complexes	Main Ore Elements	Examples of Ore Deposits
Oceanic spreading $O_{1–2}$		Co-Ni-sulphide	Ultramafic, tholeiite-basalt	Co, Ni (As, Au)	Ivanovka, Dergamysh
Island arc (O_3-D_1)	primitive	Cu VMS (Dombarovsk)	Tholeiite-basalt	Cu (Zn, Co)	Mauk, Letnee, Buribai, Koktau
		Cu-Zn VMS (Uralian)	Sodium rhyolite-basalt	Cu, Zn (Au)	**Gai**, Safyanovka, Yubileynoe, Priorskoe
			Sodium basalt-rhyolite	Zn, Cu (Au, Ag, Se, Te)	**Uchaly**, **Novo-Uchaly**, Sibai, **Uzelga**, Degtyarsk, Podolsk
		Cu-barite-Cu-Zn VMS (Baimak)	Potassium-sodium andesite-dacite	Cu, Zn, Au, Ba (Pb, Ag)	Bakr-Tau, Balta-Tau, Maiskoe, Tash-Tau, Uvarjazh, **Galka**
		Cu-titanomagnetite-apatite	Gabbro-norite	Cu, Fe (Au, Pd, Pt, Ti, V, P)	Volkovskoe
	mature	Cu-porphyry	Andesite-diorite	Cu	Tominskoe
		Au-porphyry	Plagiogranite	Au, Cu	Yubileinoe (Au)
		Au-epithermal	Andesite-diorite	Au, Cu (Pb, Zn, Se, Te)	Bereznyakovskoe
		Cu-skarn (porphyry)	Rhyolite-basalt, gabbro-diorite	Cu, Fe (Au)	Gumeshki
		Au-polymetallic	Andesite-dacite	Au, Ag (Pb, Zn)	Murtykty
Arc-continent collision and active margin of continent (D_3-C_1)		Skarn-magnetite	Sodium andesite-basalt, gabbro-diorite	Fe (Cu, Au)	Sokolovskoe, Sarbay
			Potassium-sodium andesite-basalt, gabbro-diorite-granite	Fe (Cu, Co, Au)	Vysokogorsk, Goroblagodat
		Cu-magnetite skarn		Cu, Fe (Au, Co)	Tur'insk group
		Au-sulphide-realgar		Au, Ag (Hg, Sb,Tl)	**Vorontsovka**
		Au-magnetite-skarn	Potassium-sodium andesite-basalt, gabbro-diorite	Fe, Au (Cu, Mo, Co, Ag)	**Novogodnee-Monto**
		Au-porphyry		Au (Ag, Te, W)	**Petropavlovsk**
		Au-skarn (porhyry)	Diorite-granodiorite	Au, Cu	Varvarinskoe
		Cu-porphyry (Mo)		Cu (Mo, Au, Re)	Mikheevskoe
		Cu-porphyry		Cu (Mo, Au)	Benkala

Table 1. *Cont.*

Geodynamic Environments	Ore Deposit Type	Ore-Bearing Magmatic Complexes	Main Ore Elements	Examples of Ore Deposits
The main collision (C/P)	Au-sulphide-quartz	Tonalite-granodiorite	Au(Cu,Pb,Zn,Ag)	**Berezovsk**
			Au (As)	Kochkar′
	Au-telluride	Gabbro-diabase, plagiogranite	Au (Te, Ag)	**Svetlinsk**

Bold—deposits under consideration.

2. Geological Framework

The Urals is the largest single ore belt in the world, and it contains 5.0 Bt non-ferrous metal ore (80 Mt of Cu + Zn), 4,900 t Au and 41,000 t Ag reserves in endogenous ore deposits. The bulk of Uralian gold is produced from sulphide ores containing large gold deposits (Berezovsk, Kochkar, Svetlinsk, etc., [55]) and giant Cu-Zn-Au-Ag VMS deposits [56,57], with reserves of 50–500 t Au for each deposit of both types. Most gold-bearing (VMS, etc.) deposits and some gold deposits are located on the eastern slope of the Urals (Figure 1), within the Main Greenstone Belt of the Urals—the Tagil-Magnitogorsk synclinorium zone [56,58,59]. Major large gold deposits occur inside of the East Uralian anticlinorium zone [55,60].

The Urals is the oldest (275 years, from 1745) gold-mining province of Russia [55]. The four largest gold deposits and nine gold-bearing deposits of the Urals contribute about 45% (2220 t Au) of proven gold reserves, adding to the past production of this province (4900 t Au).

2.1. Gold Deposits

The objects of this study are the large gold deposits of different genetic types [59]: Vorontsovka (Au-As-Sb-Hg-Tl, Carlin-style), Berezovsk (Au, mesothermal intrusion-related), Svetlinsk (Au-telluride mesothermal) and Petropavlovsk (Au-porphyry) (Tables 1 and 2). The Vorontsovka deposit (101 t Au) is located in the Tagil zone, while the Berezovsk (~490 t Au) and Svetlinsk (~135 t Au) deposits are located in the East Uralian zone (Figure 1).

Specific features of the Vorontsovka deposit [62,63] are as follows: thinly disseminated sulphide mineralisation in carbonate-clastic sequence; quartz-sericite, argillic (clay-quartz-carbonate) and jasperoid types of alteration; abundance of As and Fe sulphides (pyrite, arsenopyrite, realgar); correlation of Au ($r > 0.5$) with Ag, As, Hg, Co, Ni, Pb and Ba in the ores; geochemical types of mineralisation: As-Hg-Tl-Sb (the early stage) and Ag-Pb-Zn-Cu-Sb (the late stage); Au/Ag ratio ≥ 1 in ore. Our genetic model for the Vorontsovka gold deposit suggests that the gold mineralisation is coeval with the formation of the Auerbakh volcano-plutonic complex. Low-sulphide gold-bearing assemblages were deposited at lower temperatures on the periphery of the skarn zones (Tables 1 and 3).

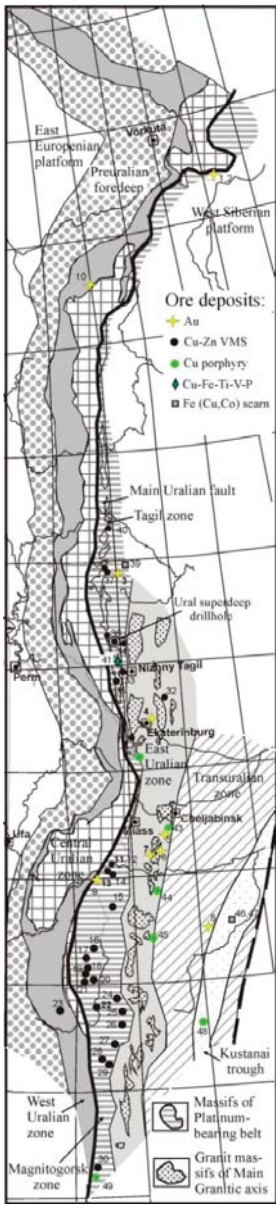

Figure 1. Structural zones of the Urals and the position of Au- and Cu-bearing deposits (on the tectonic base of [61]). Ore deposits: 1 **Novogodnee-Monto**, 2 **Pervopavlovsk**, 3 **Vorontsovka**, 4 **Berezovsk**, 5 Bereznyakovsk, 6 Kochkar, 7 Svetlinsk, 8 Varvarinskoe, 9 Murtikty, 10 Chudnoe, 11 **Uchaly**, 12 **Novo-Uchaly**, 13 **Uzelga**, 14 Molodeznoe, 15 Aleksandrinskoe, 16 Sibai, 17 Bakr-Tau, Balta-Tau, Uvarjazh, Tash-Tau, 18 Maiskoe, 19 Yubileynoye, 20 Podolskoe, 21 Oktyabrskoe, 22 **Gai**, 23 Bl'ava, Komsomolskoe, Yaman-Kasy, 24 Dzhusa, 25 Barsytchiy Log, 26 Letnee, Osenee, Levobereznoe, 27 Vesenee, 28 Priorsk, 29 50-let Oktjabrja, 30 Kundizdi, 31 Degtyarsk, 32 Safyanovsk, 33 San-Donato, 34 Krasnogvardeysk, 35 Levikha, 36 Kaban, 37 **Galka**, 38 Valentorskoe, 39 Tur'a, 40 Tarnjer, 41 Volkovskoe, 42 Gumeshevskoe, 43 Tominskoe, Kalinovskoe, 44 Tarutinskoe, 45 Mikheevskoe, 46 Sokolovskoe, 47 Sarbai, 48 Benkala, 49 Yubileinoe (Au). Bold—deposits under consideration.

Table 2. Characteristics of studied gold deposits.

Deposit, Region	Svetlinsk, South Urals	Berezovsk, Middle Urals	Vorontsovka, North Urals	Petropavlovsk, Polar Urals
Host rocks	Metamorphosed volcaniclastic (D-C)	Volcaniclastic (O-S), gabbro, serpentinite, granite	Volcaniclastic (S_2-D_1)	Volcaniclastic (S_2-D_1)
Geochemical type	Au-Te	Au, Ag (W, Bi)	Au-As-Sb-Hg-Tl	Au (Ag, Te, Bi, W)
Ore bodies	Vein-disseminated zones; veins	Suits of veins usually occurred inside of dykes	Vein-disseminated zones; rare veinlets	Stockwork, vein-disseminated zones
Wall rock alteration	Quartz-biotite (with amphibole), quartz ± biotite-sericite	Beresite, listvenite	Propylitic, quartz-sericite, argillic, jasperoid	Silicification, albitisation, chloritisation, sericitisation
Stage of mineral formation	Quartz-pyrite→ Au-Te-polymetalic→ Quartz-carbonate-sulphide	Ankerite-quartz → Pyrite-quartz → Polymetalic → Carbonate	Arsenopyrite-pyrite → Pyrite-realgar → Sulphosalt-polymetalic → Polymetalic	Pyrite-magnetite → Pyrite (± chalcopyrite, sphalerite, pyrrhotite) → Gold–telluride → Quartz–carbonate
Au reserves (C_{Au})	~135 t (1.8–2.8 g/t)	490 t (2.4 g/t)	~101 t (2.8 g/t)	26 t (1.4 g/t)

Table 3. Arsenopyrite-bearing mineral assemblages of the Vorontsovka gold deposit.

№	Mineral Ore Type	Ore Mineral Assemblage	t, °C	P, kbar	log *f* S_2
I	impregnated gold-polymetallic	arsenopyrite-sulphosalts-polymetallic	400–270	0.6–0.2	−7 to −9
II	finely disseminated gold-pyrite-realgar	arsenic-löllingite-arsenopyrite	370–250	0.2–0.15	−12 to −17

Quartz-sulphide veins of the Berezovsk deposit (about 55% of total gold reserves) contain 90–95 vol% of quartz, 5–10 vol% of sulphides and average 18–20 g/t Au [64]. Impregnated sulphide ores—hydrothermal-altered granitoid dykes ("beresite")—contain 1–2 vol% of pyrite and 0.1–5 g/t Au (commonly 0.2–1.3 g/t) (Tables 1 and 2).

The Svetlinsk deposit is represented by the system of sulphide-quartz veins, veinlets and large lens-shaped vein-disseminated zones of quartz-pyrite (± pyrrhotite) mineralisation. The deposit is located within the strongly metamorphosed (up to amphibolitic facies) volcano-sedimentary series: metabasite, terrigenous/volcaniclastic sediments and marble (D-C). The average gold content is not high (2–3 g/t). Native gold in sulphide-quartz veins is closely associated with tellurides [65,66].

The Petropavlovsk deposit is located in the Silurian-Devonian island-arc volcanic complexes of the Polar Urals [40]. It tends to the apical part of a large polyphase (with dominating diorite) pluton and is closely related to porphyritic diorite. The ore body is a large isometric stockwork composed of gold-sulphide (low-sulphide) stringer-disseminated ore associated with albitisation zones, intersected by moderately Au-rich, late quartz veins [39,40]. Gold, finely dispersed in pyrite (<0.1 mm), predominates in the ore bodies and is associated with Ag, W, Mo, Cu, As, Te and Bi in geochemical haloes. The Novogodnee-Monto iron-gold-skarn deposit (7 t by-product Au reserves) is located on the east flank of the Petropavlovsk deposit, 0.5 km away. They both probably represent a single ore-magmatic system of porphyry type [40], and their features are compiled in Tables 1, 2 and 4.

Table 4. Mineral assemblages and physicochemical parameters of mineral-forming fluids of the Petropavlovsk gold field.

Ore Deposit	Mineral Assemblage (and Gold Mineralisation)	T_{hom}, °C	Salt Composition	C_{salt}, wt%-eq. NaCl
Novogodnee-Monto Fe-Au-skarn	Chalcopyrite-pyrite-quartz, early stage	430–300	(Na, Mg)Cl	10–12.9
	Pyrite-chalcopyrite-quartz (with Au)	315–270	(Na, K)Cl	4.5–12.2
	Chalcopyrite-pyrite-magnetite (with Co and Au)	230–215	NaCl	3.4–9.2
	Pyrite-chalcopyrite-telluride (with Au)	210–180	NaCl	10.5–13.9
	Polysulphide-quartz-carbonate	170–140	(Na, K)Cl	6.0–8.0
Petropavlovsk Au-porphyry	Chalcopyrite-pyrite-magnetite (with Au)	250 *	no data	
	Polysulphide-quartz (with Au)	260–245	no phase transitions were observed	
	Pyrite-chalcopyrite-telluride (with Au)	200	(Na, K)Cl	11
	Polysulphide-quartz-carbonate (with Au)	160–150	(Na, K)Cl	14

* Co geothermometer (coexisting pyrite and chalcopyrite).

2.2. VMS Deposits

VMS deposits of the Urals began to play a major role in its gold industry in the middle of the 20th Century. The VMS deposits belong to Uralian (or Cu-Zn-pyritic) type (the major one for the Urals), which can be divided into two subtypes: Cu>>Zn and Zn>>Cu, and two minor types: copper (Dombarovsk type) and gold-barite-copper-zinc or Au-polymetallic (Baimak type). Among the Uralian type, ten deposits contain >100 t Au and/or >1000 t Ag—the largest, Gai, Uchaly, Novo-Uchaly and Uzelga, together amount to 1000 t Au and ~13,200 t Ag [57,67,68]. According to the modern genetic model, the formation of these deposits was related to a shallow chamber of acidic magma formed as a result of the differentiation of mantle-derived basalt [69,70].

The study of modes in which gold occurs in sulphides (including invisible gold) covers two large, slightly metamorphosed volcanogenic massive sulphide deposits: Uchaly and Uzelga, as well as the giant intensively deformed Gai VMS deposit (Figures 1–3; Tables 1 and 5). Massive sulphide ores predominate in these deposits with a subordinate contribution of disseminated ores (commonly 5–15 vol%). Au and Ag are relatively uniformly distributed in massive sulphide ores (av. values are 0.5–1.5 g/t Au, 5–50 g/t Ag), but local enrichment occurs (up to 10–90 g/t Au and up to 1000–3000 g/t Ag). The specific feature of Uchaly and Uzelga deposits (Zn-dominated subtype) is the uplifted levels of Au, Ag, Pb, Se, Te, Sb, As, Sn and Cd comparing to most of the other VMS districts of the Urals [71,72].

Table 5. Characteristics of the studied VMS deposits.

Deposit, Region	Gai	Uchaly, Novo-Uchaly	Uzelga	Galka, North Urals
	South Urals			
Host rocks	Bimodal-mafic (with minor chert)	Bimodal-felsic (with minor chert)	Bimodal-felsic (with minor chert, limestone, andesite and dacite)	Bimodal-felsic (with minor andesite and dacite)
Geological age	Emsian	Mid-Eifelian	Late Eifelian–Early Givetian	Late Ordovician–Early Llandoverian
Geochemical type	Zn-Cu (Au, Ag)	Cu-Zn (Au, Ag)	Cu-Zn (Au, Ag)	Zn-(Cu-Pb-Ag-Au)
Metamorphic grade (t, °C)	Greenschist, 250–450	Prehnite-pumpellyite, 150–350 (locally up to 400)	Prehnite-pumpellyite, 180–350 (locally up to 450)	Zeolite, 100–200
Dominant ore-host structures	Steeply dipping to vertical, pseudomonoclinal shear-related structures	Steeply dipping to vertical; limb of large anticlinal fold	Gentle doms and trenchs	Gentle doms and trenchs
Ore bodies	Platelike, podiform	Lensoid, antiform	Lensoid	Stockwork, vein-disseminated zones; (minor lensoid)
Wall rock alteration	Albitisation, silicification, chloritisation, sericitisation (±pyrophyllite)	Silicification, sericitisation, albitisation, chloritisation	Silicification, sericitisation, carbonation, albitisation, chloritisation	Argillic, silicification, sericitisation
Ore reserves	450 Mt *	230.4 (116 + 114.4) Mt *	80.7 Mt *	4.3 Mt
Cu + Pb + Zn, wt%	2.2	4.3 (4.8 and 3.6)	4.2	3.3
Au reserves	520 t *	344 (180 + 164) t *	136.6 t *	6 t
C_{Au}, g/t	1.2	1.5	1.7	1.35
Ag reserves	6,300 t *	4,381 t *	2,495 t *	200 t
C_{Ag}, g/t	14	19	31	46.5

* including past production.

During 60 years, two hundred million tonnes of ore have been mined from the Gai deposit (Cu-dominated subtype), and ~45% of initial reserves contained about 10 million tonnes of non-ferrous metals (Cu:Pb:Zn = 1:0.03:0.49), 520 t Au and 6300 t Ag (Au/Ag = 0.08). The annual output of the underground mine reached 5 Mt of Cu and Cu-Zn ore (>70 Kt Cu) [9,73,74]. The deposit consists of a package of steeply dipping sheet-like bodies, from 40 up to 1300 m down the dip, with a thickness of the large lodes up to 150 m in bulges. Together, the ore bodies comprise a lineal mineral zone (thickness ~300 m, up to 800 m). The ore zone extends for 3.7 km along the strike and more than 1.7 km down the dip, remaining not contoured at a depth. The deposit was affected by regional metamorphism (greenschist facies), strike-slip deformations and folding. Therefore, ore structures and textures observed are mostly epigenetic (e.g., [9,74,75]). Massive, breccia-like, impregnated and stringer-impregnated structures are dominant. Gneissose, foliated and banded structures often occur in the outer parts of massive sulphide lodes and are found within narrow zones controlled by later steeply dipping normal and strike-slip faults [57,74].

The Uchaly deposit also demonstrates one of the largest potentials if the Novo-Uchaly deposit located directly to the south of the Uchaly deposit is considered as its separate ore body. Therefore, the total reserves of metals contained in the two ore bodies—the northern one, Uchaly, and the southern one, Novo-Uchaly—will amount to 9.96 million tonnes Cu + Pb + Zn, with Cu:Pb:Zn = 1:0.17:3.12, 344 t Au and 4381 t Ag (Au/Ag = 0.08) [15,36,76]. The Uchaly lode comprises a single subvertical thick (up to 180 m in bulges) lens of solid Cu–Zn ore, approximately 1.2 km in the lateral direction and 1.3 km along the dip. The Novo-Uchaly lode (1250 m × 900 m) reaches 186 m thick and comprises a steeply dipping VMS lens, crumpled into an anticlinal fold. The deposit was affected by regional metamorphism (subgreenschist facies). The ore body reveals complex

lenticular contours complicated by pinch and swell areas. The primary ores—brecciated and rhythmically foliated—are preserved only as relics. Gneissose and folded varieties of ore occur along the contacts of the ore body and in zones of postmineral faults.

The total reserves of the Uzelga deposit range 81 million tonnes of ore, containing 3.43 million tonnes Cu + Pb + Zn (Cu:Pb:Zn = 1:0.22:1.90), 137 t Au and 2495 t Ag (Au/Ag = 0.05) [9,67,68]. Paleovolcanic structures are mostly gentle and weakly deformed [69,76]. Bodies of VMS solid ores occur at two hypsometric levels, 130–380 m from day surface (body Nos. 1, 5, 6, 9) and 420–640 m (body Nos. 2–4, 7, 8), with ~300 m between the levels [25,77]. Ore bodies are represented by thick lenses, sometimes by irregular ellipsoidal and isometric ones with obtuse terminations (ore body 4) or ball-shaped ones (ore body 3). Ores are commonly slightly recrystallised: cryptograined and hypidiomorphic-granular textures predominate in ores [78,79]. There are spherolitic and radial fabrics in kidney aggregates. Rhythmic zonality of pyrite is often marked by bands or fine inclusions of chalcopyrite, sphalerite, tennantite, tetrahedrite or a member of the tetrahedrite-tennantite series (further "fahlore"). Cataclastic texture often occurs in pyrite grains. Framboidal, metaglobular pyrite is sometimes found.

The Galka deposit is small (Table 5) and comprises gentle VMS lenses (max. 2000 m × 350 m; thickness up to 30 m) of veinlet-impregnated Au–pyrite–polymetal ores [80,81]. Locally semi-massive and massive sulphide ore forms thin (up to 1 m) lenses in interlayers of carboniferous fineclastic sedimentary rocks. The abundant veinlet-impregnated ores are hosted by argillic (illite/smectite–sericite–quartz and kaolinite) alteration, formed after cement of rhyodacitic breccia [82]. The ores are almost unaffected by any metamorphism, so colloform structures, and fine-grained textures of ores, are widespread, and sulphides carry a high proportion of invisible gold [15].

During processing, most of the total amount of trace elements is not extracted (Au, Ag, Pt, Pd, Pb, Se, Te, Sb, As, Bi, Sn, Co, Ni and Hg), and many of them (Pb, Se, Te, Sb, As, Co, Ni and Hg) become pollutants (together with sulphur dioxide and Fe) [72,83]. The increasing volume of processed VMS ores has aggravated the problem of gold recovery: while copper and zinc are taken in concentrates almost completely (75–85%), integrated gold recovery into the copper and zinc concentrates ranges from 20% (Uchaly) up to 50% (Gai). The loss of gold into the pyritic concentrate and tailings exceeds 15 tonnes (up to 20 t) annually, which is three times more than Au recovery from massive sulphide ores of the Urals. Therefore, tailing dumps of ore-processing plants can be compared with large gold deposits: for example, the Gai (110 t Au in the tailing dump) and Uchaly (90 t Au) concentrating mills.

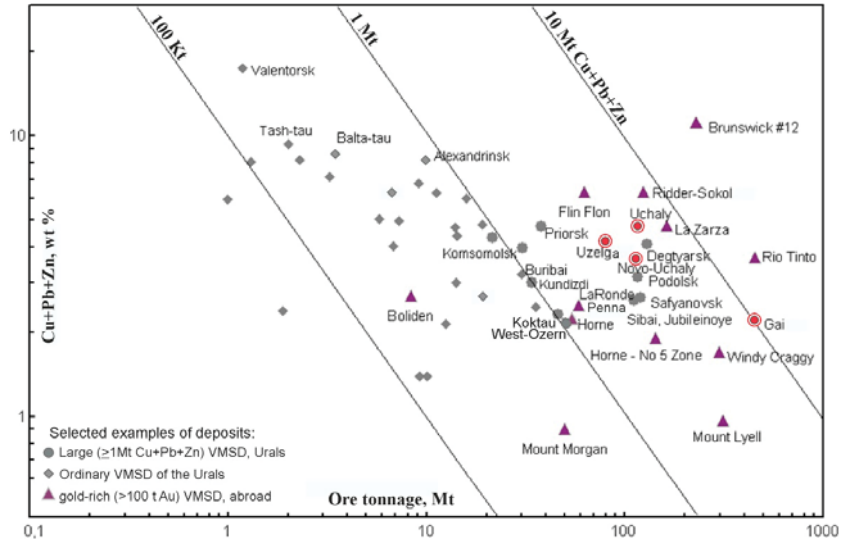

Figure 2. Parameters of VMS deposits of the Urals in terms of ore and base metal tonnage and their comparison with large, Au-rich VMS deposits of the world (>100 t Au); red circles—deposits under consideration. Parameters for other deposits were selected from the review in [84].

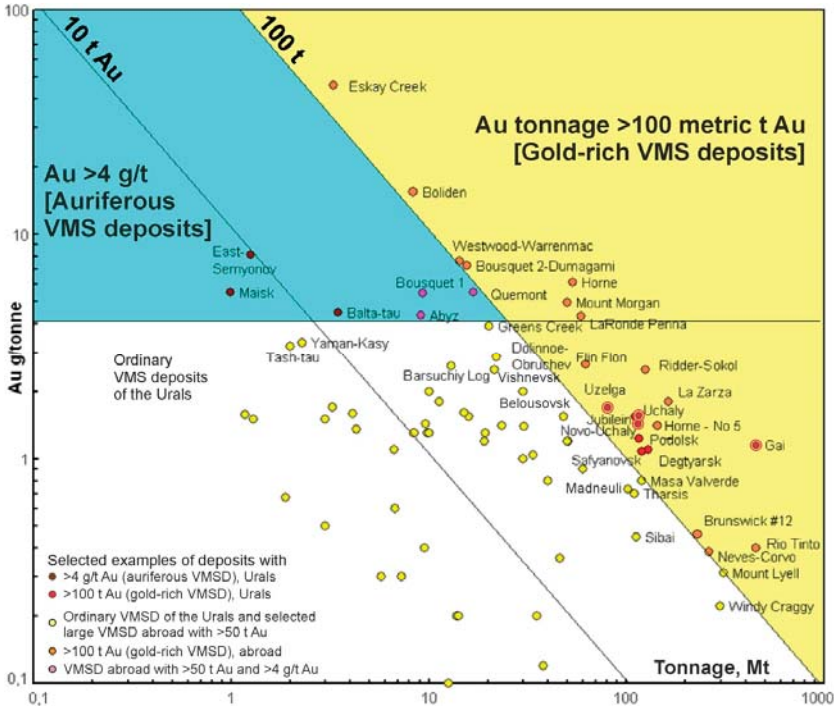

Figure 3. Parameters of VMS deposits of the Urals, in terms of ore and gold tonnage, and their comparison with major Au-bearing VMS deposits of the world; red circles with a red ring—deposits under consideration. Design and parameters for other deposits were adapted from the review in [84].

3. Materials and Methods

The study was based on mapping and sampling of drill core and open pits. Collections of ores include 100–300 samples for each deposit, and 150–500 polished sections were studied for each deposit. Mineralogical observations, electron probe microanalyses (EPMA) and a study using the scanning electron microscope (SEM) with an EDS were carried out for polished sections as well as for sulphide and heavy concentrates prepared from ores and, in some cases, from tailings. Manually selected sulphide monomineral fractions and sulphides from heavy concentrates by separating dozens of samples for each deposit were studied.

EPMA: The analyses were performed in IGEM RAS on the JXA-8200 Jeol, JEOL Ltd., Tokyo, Japan, electron microprobe equipped with five WD spectrometers and one ED spectrometer. The major constituents were determined at an accelerating voltage of 20 kV, current intensity on the Faraday cup of 20 nA, 10 s counting time and beam diameter of 1 μm. Conditions of analysis are provided in Appendix A Table A1. The Au$M\alpha$ line was chosen for Au analysis in arsenopyrite and pyrite (with 100–200 s counting time for PGE and Au) because it was established that the signal/background ratio of *M* series lines is better than that of *L* series lines [18]. These operating conditions and correctly selected background points made it possible to decrease the detection limit (3σ) down to 45 ppm for line Au$M\alpha$.

SEM/EDS: The JSM-5610LV electron microscope (JEOL Ltd., Tokyo, Japan) equipped with an X-Max 100 energy dispersive spectrometer (IGEM RAS) was used for the studies.

INAA: For instrumental neutron activation analysis, sulphide separates of 20 to 50 mg weight were handpicked under a binocular microscope. The purity of separation was tested with the help of the X-ray powder diffraction technique. The fraction of a sulphide examined in a sample analysed was more than 90%. The grains of sulphides selected for analysis were sealed in polyethylene film. For activation, the polyethylene packages were wrapped in filter paper and aluminium foil. Samples, standardised by the State Geological Survey of the USSR (State Standard Samples 3593–86; 3594; 3595; RUS 1 ÷ 4) and the United States (USGS: BHVO-1; Mag-1; QLO-1; RGM-1, SCo-1, SDC-1, SGR-1), were prepared for irradiation in the same manner. The samples were activated for 15 to 17 h in the IRT reactor at the Moscow Engineering Physical Institute with a neutron flux of 1×10^{13} s cm^{-2}. Measurements of induced activity were carried out in IGEM RAS with a gamma spectrometer: the analyser was the 919+GEM45190 ORTEC (AMETEK ORTEC, Oak Ridge, TN, USA)(HPGe coaxial detector; the range of energy measured was from 100 to 1800 KeV, with a resolution of 1.8 KeV at the line of 1332 KeV). The nuclide and the gamma line used for the analyses (KeV) were: ^{198}Au (412), ^{122}Sb (564), ^{124}Sb (602 and 1691), ^{60}Co (1332), ^{76}As (559), ^{110}MAg (657), ^{59}Fe (1099), ^{65}Zn (1115), ^{115}Cd (336 and 528). The measurements were conducted in two stages: in 7 to 10 days after activation, As, Cd and Au concentration were detected, and in 25 to 30 days after activation, Fe, Co, Zn, Ag and Sb were analysed (see details in [12]). INAA examined the contents of NM, base metals and some rare elements in the bulk samples, ultra-heavy concentrates and hand-made mineral concentrates.

LA-ICPMS: The high-sensitivity mass-spectrometer laser ablation method (LA-ICPMS, ThermoXSeries, NewWave 213 device, AMETEK, Berwyn, PA, USA) was chosen as a key analytical method for trace element analysis of sulphides, including determination of noble metals [39]. Primary determination of major components was carried out on EPMA. For the LA-ICPMS method, sulphide reference material MASS-1 [85] was used as an external calibration standard together with in-house pyrrhotite-based standard $Fe_{0.9}S$ (20 ppm PGE, gold and silver, synthesised at IGEM RAS using the method from [86]) and calibrated in the LabMaTer at the Université du Québec à Chicoutimi (Chicoutimi, QC, Canada) for to the concentration of Au against a standard prepared by J.H.G. Laflamme. The analysis of sulphide grains was realised using spot and profile ablation. The diameter of the laser beam was 30–60 μm. The laser pulse frequency was 10 Hz, and the energy at the sample surface was 7–8 J/cm^2. The detection limit for most elements was 0.02–0.05 ppm. Investigations

were carried out in IGEM RAS, and a part of LA-ICPMS control analyses was also done in the LabMaTer at the Université du Québec à Chicoutimi. We used the thermochemical method to determine the ionic form of gold according to [87–89].

To study the form of invisible Au in sulphides, we and our colleagues synthesised the Au-bearing chalcogenides using different methods (hydrothermal and gas transport methods and salt flux technique [44,45,90]) at contrasting $T/f\ S_2$ conditions and addressed the Au local environment using XAS [16,91,92]. High Au, Pt, Pd and other metals' contents intentionally introduced into the synthetic phases allowed using the spectroscopic methods to determine the structural-chemical state of the NM in sulphides using first-principles quantum chemical calculations and Bader charge analysis (e.g., [19]).

The microanalyses of natural sulphides for all deposits under consideration were accompanied by studies on conditions of ore formation based on fluid inclusion data and mineral geothermometry, and they are partly implied but not discussed in detail in this paper. The regime of volatiles was also briefly discussed.

4. Noble Metal Distribution and Speciations

4.1. Gold Deposits

4.1.1. The Vorontsovka Gold Deposit

The Vorontsovka deposit is mainly comprised of vein-disseminated zones with rare gold-quartz veinlets. Ore contains pyrite, arsenopyrite, chalcopyrite, sphalerite, galena, hessite Ag_2Te, coloradoite HgTe, alabandine MnS, native gold (fineness 910–998 for early and 680–690 for late generations) (Table 6; Figure 4) and various As-Sb mineralisation: native As, realgar AsS, orpiment As_2S_3, tennantite, tennantite-tetrahedrite, aktashite $Cu_6Hg_3As_4S_{12}$, cinnabar HgS, alabandine MnS, clerite $MnSb_2S_4$, routhierite $TlHgAsS_3$, pierrotite $Tl_2(Sb,As)_{10}S_{17}$, stibnite Sb_2S_3, zinkenite $Pb_9Sb_{22}S_{42}$, chalcostibite $CuSbS_2$, boulangerite $Pb_5Sb_4S_{11}$, jamesonite $Pb_4FeSb_6S_{14}$, bournonite $PbCuSbS_3$, plagionite $Pb_5Sb_8S_{17}$ and geocronite $Pb_{14}(Sb,As)_6S_{23}$ [63]. There are four groups of mineral assemblages in the ore bodies. The later assemblages often overprint the early ones: (1) VMS-like (with low Au content), (2) gold-pyrite-arsenopyrite (gold fineness 910–998), (3) magnetite and epidote-garnet skarn and skarnoid (with low gold content) and (4) gold-pyrite-realgar (gold fineness 680–690) [63].

Table 6. Mineral forms of Au and Ag in the large gold deposits of the Urals, modified after [93].

Vorontsovka	Berezovsk	Svetlinsk	Petropavlovsk
Hessite Ag_2Te, native gold, küstelite, Ag-tetrahedrite, freibergite $(Ag,Cu)_{12}Sb_4S_{13}$	Native silver, native gold, freibergite $(Ag,Cu)_{12}Sb_4S_{13}$, matildite $AgBiS_2$, hessite Ag_2Te, acanthite Ag_2S	Native gold, calaverite $AuTe_2$, aurostibite $AuSb_2$, montbrayite $(Au,Sb)_2Te_3$, krennerite $(Au,Ag)Te_2$, sylvanite $AuAgTe_4$, petzite Ag_3AuTe_2, volynskite $AgBiTe_2$, maldonite Au_2Bi, hessite Ag_2Te, γ-hessite $Ag_{1.9}Te$, acanthite Ag_2S	Native gold, hessite Ag_2Te, petzite Ag_3AuTe_2, calaverite $AuTe_2$, sylvanite $AuAgTe_4$

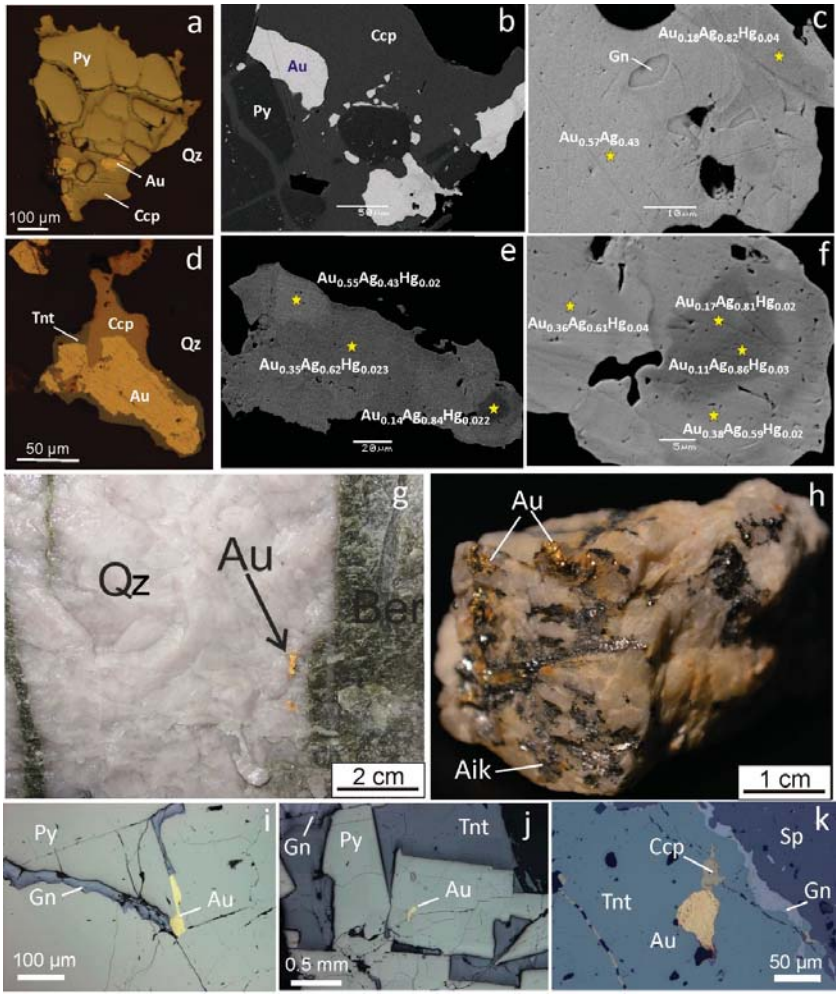

Figure 4. Native gold in the Vorontsovka (**a**–**f**) and Berezovsk deposits (**g**–**k**). (**a**–**f**) Inhomogeneous native gold in quartz veinlet (**c**—details of **b**, **f**—details of **e**). (**g**,**h**) Macroscopic native gold: (**g**) native gold 1.5 × 8 mm near the contact of quartz and beresite (Ber), (**h**) native gold 1–4 mm associated with aikinite in quartz-carbonate vein. (**i**–**k**) Native gold in pyrite (**i**,**j**) and tennantite (**k**). Ccp—chalcopyrite, Tnt—tennantite, Gn—galena, Sp—sphalerite, Aik—aikinite, Qz—quartz. (**b**,**c**,**e**,**f**) BSE images, (**d**,**e**) details of (**c**).

Invisible gold in arsenopyrite and As-pyrite: The study of gold modes in arsenopyrite is particularly important and relevant. This mineral is widespread in the dominant—in terms of gold reserves—black-shale-hosted gold deposits. This particular mineral demonstrates peak concentrations of invisible gold, as well as a exceptionally high resistance to endogenous and exogenous epigenetic processes. Simultaneously, arsenopyrite is "refractory" in hydrometallurgy processing ([51]; cf., [94]). One of the most relevant for the study of invisible gold is the Carlin deposit type [7,50,51,95–97], where gold-bearing arsenopyrite is the predominant host mineral for gold in the ore (i.e., Au-concentrator, along with As-pyrite) with up to sub-wt% level of Au content. In this paper, we conducted a comparative study of the distribution of gold in 'Carlin' and 'pre-Carlin' arsenopyrites on

the example of the Vorontsovka gold deposit in the Urals [18,63,80] (Figure 5). Studied arsenopyrite-bearing mineral assemblages were crystallised at the contrast TPX conditions (Table 3).

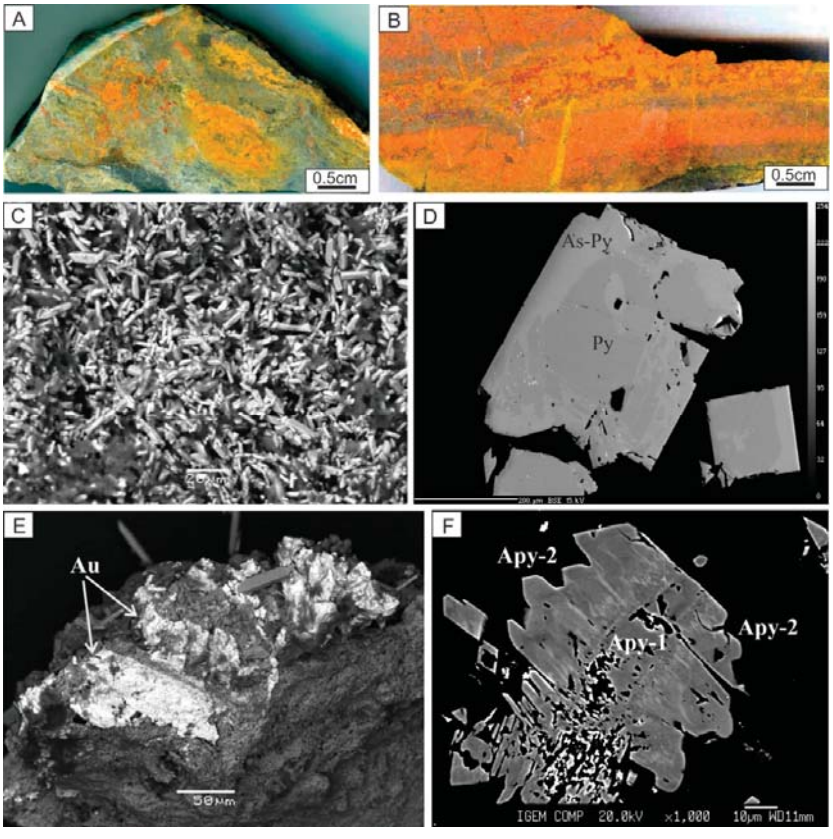

Figure 5. Carlin-style gold-bearing mineralisation, Vorontsovka gold deposit: (**A**) argillised volcaniclastic rock with "spots" and zonal veinlets: argillisite → quartz → carbonate → realgar, (**B**) carbonated layered volcano-sedimentary rock with thick impregnation of realgar (± orpiment), and disseminated pyrite, arsenopyrite and stibnite along layers. (**C**) Aggregate of small (less than 20 μm) needle-shaped crystals of arsenopyrite, (**D**) zonal pyrite crystals: pyrite without As admixture occurs in the central part, the next zone contains 1.8 wt% As. (**E,F**) Intergrowths of arsenopyrite of different composition and morphology in the gold-pyrite-realgar assemblage: (**E**) idiomorphic crystals of arsenopyrite and a felt-like aggregate of thin needle-like arsenopyrite and interstitial gold inclusions (Au), (**F**) aggregates of parallel elongated zonal crystals of As-rich arsenopyrite (Apy-2) overgrowing the prismatic crystal of the earlier S-rich arsenopyrite (Apy-1). (**C**–**F**) BSE images.

With more detail, we studied arsenopyrite from the arsenopyrite-sulphosalt-polymetallic assemblage of the skarn group (Apy-1) and arsenopyrite from the later As-löllingite-arsenopyrite assemblage (Apy-2) by INAA and EPMA [80]. Moreover, As-rich arsenopyrite (Apy-2) grows orthogonally on the elongated prismatic relics of the S-rich arsenopyrite (Apy-1) that appears to be the earlier arsenopyrite from the previous mineralisation stage (Figure 5d).

Both arsenopyrite generations are characterised by zonal structure (Figures 5–8). Apy-1 contains ~28.9 at% As and As/S is 0.89 ± 0.04, while C_{Au} varies from the detection limit to 0.25 wt%. C_{Au} increases to 170 ppm in the lighter zones of the S-rich arsenopyrite

(Figure 7). In contrast, the outer high-arsenic rim of this arsenopyrite crystal (the lightest in BSE zones on the Figure 7a,b) contains no gold (Au < 45 ppm, EPMA).

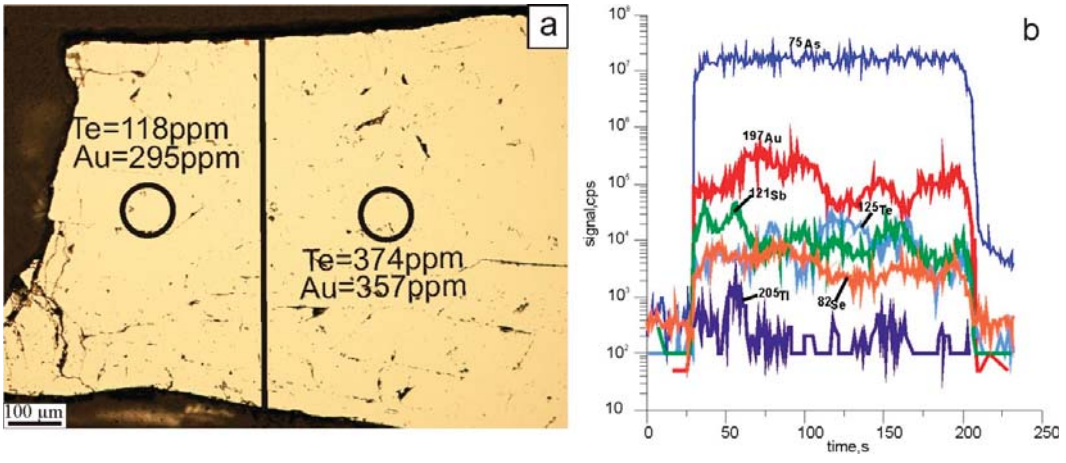

Figure 6. Arsenopyrite in skarnoid of the Vorontsovka deposit: (**a**) grain of Apy-1 from marble (skarnoid) with impregnation of arsenopyrite and sulphosalts in micro-veinlets, (**b**) LA-ICPMS profile; Co, Ni, Ag, Hg, Tl—not detected. Au is distributed zonally across the profile, as well as Sb and Te, but there is no correlation between the peaks of these element contents across the profile.

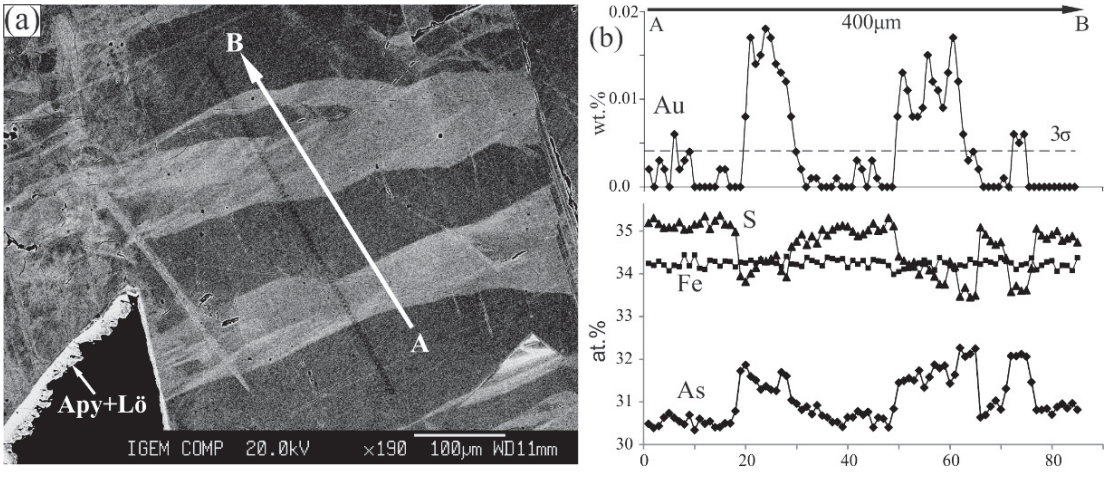

Figure 7. Compositional zoning of the S-rich arsenopyrite Apy-1, EPMA. (**a**) Zonal structure of arsenopyrite with the outer rim of As-rich arsenopyrite with microinclusions of löllingite, BSE image. (**b**) Distribution of C_{Au} (wt%) and S, Fe and As (at%) along the profile (A–B). C_{Au} was measured by precision microprobe analysis with detection limit 45 ppm.

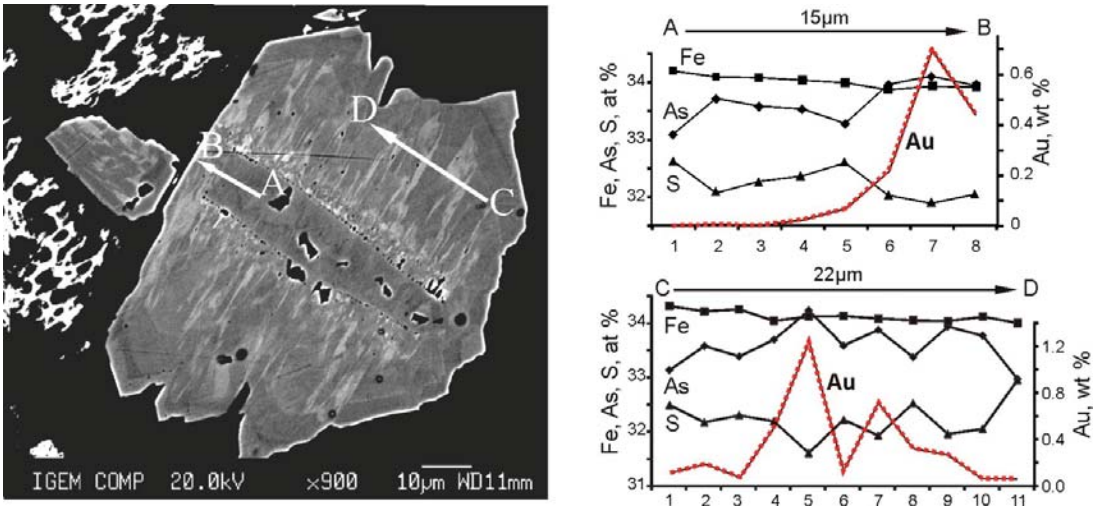

Figure 8. Variations of Fe, As, S (at%) and Au (wt%) in Apy-2, EPMA. **Left**—BSE image with an indication of the profiles A–B and C–D used to measure the composition of arsenopyrite. Note that profile A–B starts in Apy-2, replaced the relict Au-poor Apy-1, and finished in Au-rich Apy-2.

Apy-2 has the average ratio As/S = 1.04 ± 0.03, and the Au content in Apy-2 varies from the detection limit to 1.23 wt% (Figure 8). The average gold content is 5–6 ppm. Typomorphic impurities for this arsenopyrite are Te (up to 1.2 wt%, mainly 400–500 ppm) and Tl (up to 43 ppm), and the Au content fluctuations correlate with the thallium variations. Gold distribution in the late arsenopyrite demonstrates a absence of positive Au–As correlation (Figure 8).

Early ore assemblages of the Vorontsovka gold deposit were formed at 510–240 °C (including magnetite skarn and later arsenopyrite-sulphosalt-polymetallic assemblage), whereas late Carlin-style gold-(Fe, As, Hg)-sulphide-quartz mineralisation was deposited at decreasing temperatures from ~350 to 100 °C [63,80,98]. In general, crystallisation of the arsenopyrite-bearing mineral assemblages occurs as temperature and, especially, $f\,S_2$ (from 10^{-7} to 10^{-17}) decrease [63,80].

According to INAA data, pyrite from the sample Vr10–17 of the gold-skarn ore of the Vorontsovka deposit contains: As 4.3 wt%, Co 215 ppm, Sb 259 ppm, Ag 104 ppm and Au 2777 ppm. In this sample, a precision study of the relationship between the contents of Au and the main components of pyrite was performed by the EPMA method under conditions similar to those described in [18]. The correlation coefficient of As and Au in the pyrite crystal is 0.91 (N = 143). Figure 9 clearly shows two groups of impurity contents in the pyrite: one group has low As contents and close to Au detection limit (≤0.004 wt%). In contrast, the second group ranges from ~2 wt% As and with increasing its concentration, the Au impurity increases linearly to 0.036 wt%.

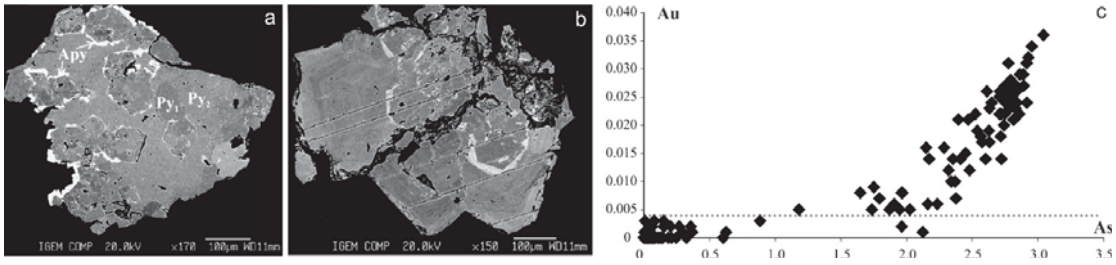

Figure 9. Pyrite from the gold-skarn ore of the Vorontsovka deposit. (**a**) A crystalline granular aggregate of pyrite of different generations (Py1 and Py2), and arsenopyrite crystallises in the intergranular space of these pyrite generations. (**a, b**) BSE images, Jeol JXA-8200. (**b**) An aggregate of zonal pyrite crystals: in bright zones, the As content is about 4 wt%. (**c**) Distribution of As and Au contents (EPMA, wt%) in pyrite; the dashed line is Au detection limit.

4.1.2. The Berezovsk Gold Deposit

The dominant opaque minerals commonly filling the fractures in quartz are pyrite, tetrahedrite, aikinite, galena and chalcopyrite. The sulphide contents range from 2 to 10 vol%. Major Au mineral is native gold (Table 3; Figure 4), bearing 85–100 wt% of its total balance. Early dust-like (<10 μm) gold-I grains are included in pyrite, and gold fineness ranges 863–984. The size of later gold-II grains is larger (commonly 0.05–0.5 mm, up to 1 mm, and rarely more). Gold fineness ranges 729–904 [64]. The contents of Au and Ag in sulphides are as follows: pyrite 0.18–73.5 ppm Au and <0.2–92 ppm Ag; galena 0.15–2.96 ppm Au, 0.1–2.51 ppm Ag, INAA; pyrite 0.01–21.8 ppm Au and galena 0.05–0.3 ppm Au, LA-ICPMS; chalcopyrite 0.06–0.32 wt% Au, 0.07–0.18 wt% Ag, EPMA.

In most pyrite crystals, the main impurity elements are Co (0.09–4180; geometric mean (geom. mean) 16 ppm), Ni (1.2–244; geom. mean 21 ppm) and As (14–1486; geom. mean 388 ppm), and their distribution is zonal with an increase in the amount of Co and Ni and a decrease of As from the margin to the centre of the grain (Figure 10). Less common impurities are: Cu (1–560; geom. mean 14 ppm), Zn (0.5–113; geom. mean 4.3 ppm), Pb (0.1–1090; geom. mean 2.4 ppm) and Bi (0.01–84; geom. mean 0.3 ppm). Rare impurities are Mn (0.7–14 ppm), Ga (0.06–0.2 ppm), Ge (0.3–1.2 ppm), Ag (0.03–40 ppm), Cd (0.01–1.8 ppm), Sn (0.05–0.7 ppm), Sb (0.03–15 ppm), Te (0.5–10 ppm) and Hg (0.4–6 ppm). In this pyrite, C_{Au} ranges 0.08–0.1 ppm and Au occurs as single peaks of the Ag-Pb-Cu-Sb group.

Au-bearing pyrite (C_{Au} varies from 1 to 22 ppm) was found in two adjacent ladder veins of the Pervopavlovsk dyke [99]. An inhomogeneity was revealed in the pyrite (Figure 11a,c) in the form of irregular dark areas on the BSE images, in which small (from less than 1 to 10 × 1 microns) inclusions of bright (in reflected electrons) Sn-containing mineral phases, presumably stannite, were detected.

Profile analysis of the pyrite grains (Figure 11) revealed that light in BSE parts of the grains are enriched in As and Au, and the dark ones in BSE—Sn, Cu, Zn, Pb, Cd, In, Ag, Ga, Ge. The high C_{Au} are only partially consistent with the regions of C_{As} peaks, since the invisible gold was found only in pyrite crystals containing sub-millimetre domains with small inclusions (from less than 1 to 10 × 1 microns) of stannite. These areas are Au-poor and rich in Sn, Ag, Bi, Cd, Cu, Ga, In, Pb and Zn (Figure 12). The Au-bearing variety of pyrite is characterised by a low content of Co (<0.16 ppm) and Ni (<0.3 ppm) and increased As (51–8277, geom. mean 1325 ppm). The point-like increased contents of Ni and Co on the element maps is probably associated with relict inclusions of the pyrite-2. The "synchronous" increased contents of impurity elements (Ag, Cu, Pb, Zn, Bi, Sb, Co, Ni) at the grain edges probably reflects the presence of thin film of their sulphides and sulphosalts on the surface of the pyrite grain.

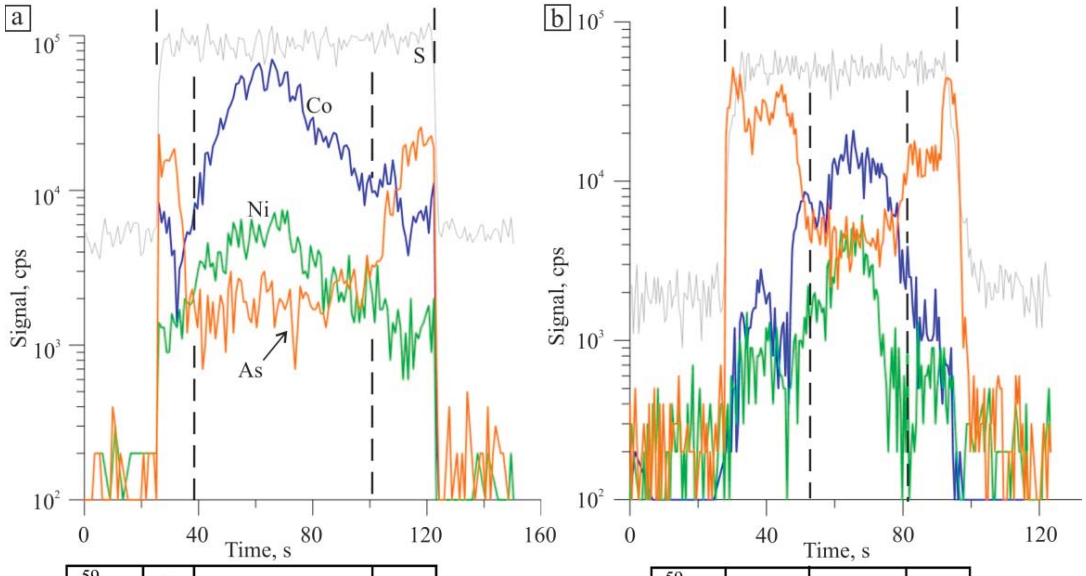

^{59}Co	10	132	17
^{61}Ni	17	78	19
^{75}As	158	22	183

^{59}Co	7	56	5
^{61}Ni	14	44	9
^{75}As	750	105	680

Figure 10. Graphic images of two probing profiles for the pyrite crystals from the sulphide-quartz veins of the Ilyinskaya dyke, the Berezovsk deposit. Here, and in the Figures 11 and 13, the y-axis is signal (counts per second) and x-axis is time (in seconds). Profiles length: (**a**) 482 μm, (**b**) 330 μm. Average content of elements (ppm) in the profile intervals in the table below each figure is indicated (here and in Figures 11 and 13).

The LA-ICPMS method revealed an inhomogeneous distribution of Au (0.01–0.04 ppm) in galena from the sulphide-quartz veins of the gumbeite alteration (quartz + orthoclase + dolomite-ankerite ± scheelite) of the Shartash granite massif, south of the Berezovsk deposit, with an increase in the crystal periphery to 0.59 ppm (Figure 13). Together with Au, the Cu (up to 241 ppm, geom. mean 22 ppm) and Sb (up to 680 ppm) contents increase to the grain edges, which may be due to fine inclusions of bournonite $CuPbSbS_3$, possibly Au-containing. This pattern is traced in all the grains of the mineral (the total number of ablation test points is 33). The distribution of other elements' impurities is homogeneous within single grain with arithmetic mean values (in ppm): Zn—2.5, As—11, Se—4.6, Ag—927, Cd—130, Sn—0.4, Te—150, Tl—2.8 and Bi—2154. Their contents have minor variations in galena from different veins.

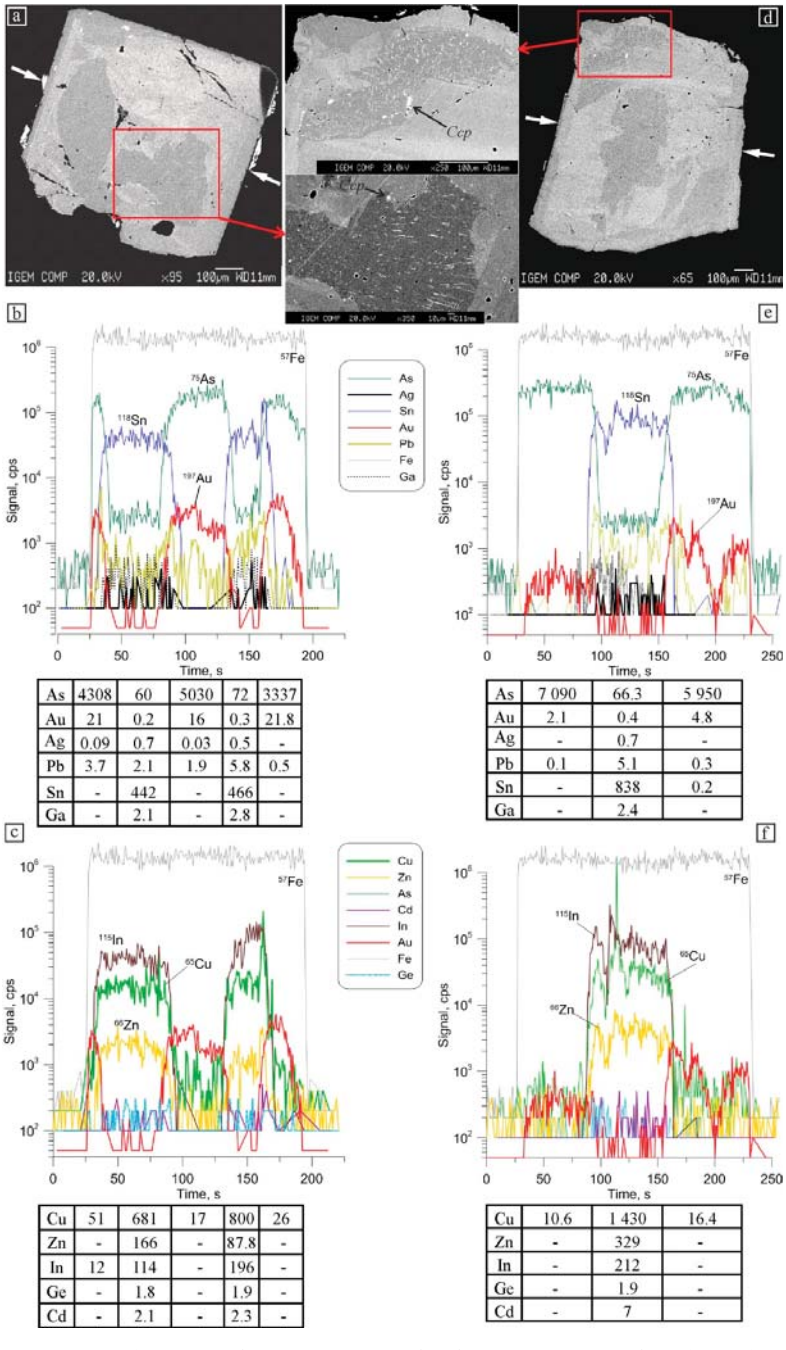

As	4308	60	5030	72	3337
Au	21	0.2	16	0.3	21.8
Ag	0.09	0.7	0.03	0.5	-
Pb	3.7	2.1	1.9	5.8	0.5
Sn	-	442	-	466	-
Ga	-	2.1	-	2.8	-

As	7 090	66.3	5 950
Au	2.1	0.4	4.8
Ag	-	0.7	-
Pb	0.1	5.1	0.3
Sn	-	838	0.2
Ga	-	2.4	-

Cu	51	681	17	800	26
Zn	-	166	-	87.8	-
In	12	114	-	196	-
Ge	-	1.8	-	1.9	-
Cd	-	2.1	-	2.3	-

Cu	10.6	1 430	16.4
Zn	-	329	-
In	-	212	-
Ge	-	1.9	-
Cd	-	7	-

Figure 11. Graphic images of the two probing profiles for the pyrite crystals from the sulphide-quarts veins of the Pervopavlovsk dyke, the Berezovsk deposit. BSE images (**a**,**c**), cursors indicate the location of the probing profiles, LA-ICPMS profile length (**b**,**d**–**f**): left—842 μm, right—330 μm. Frames in (**a**,**c**) indicate the areas with stannite (small, elongated) and chalcopyrite (Ccp) inclusions, see the insets.

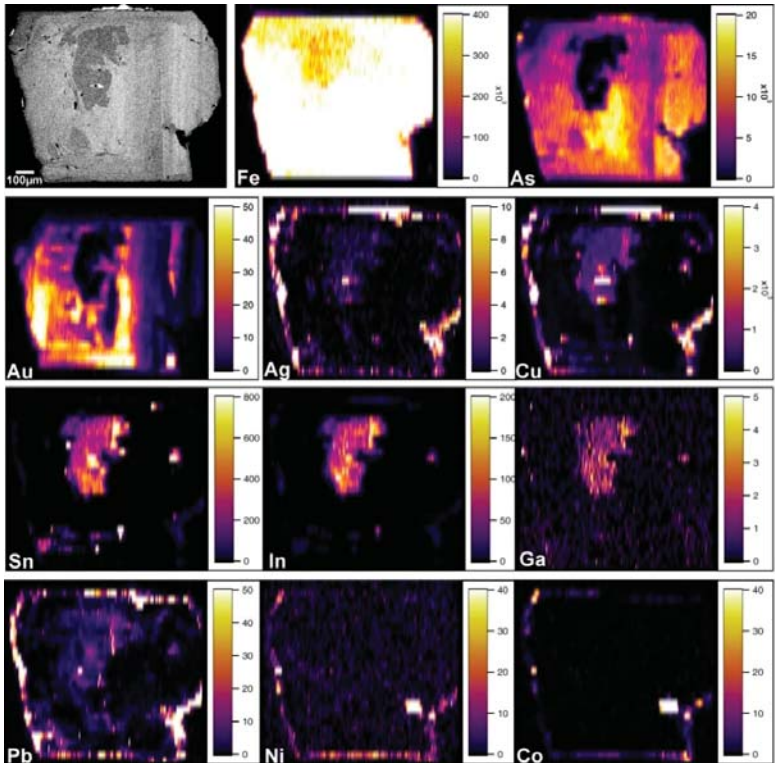

Figure 12. The pyrite crystal BSE image (top left) and the element distribution maps; semi-quantitative analysis, scales in ppm.

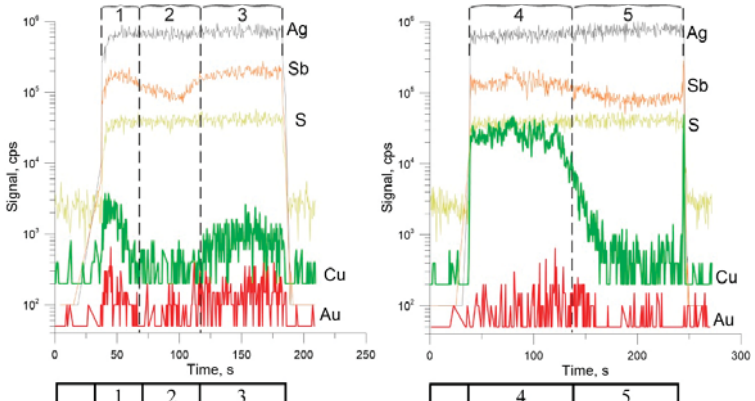

	1	2	3
Cu	15	1	6
Sb	314	178	310
Au	0.24	0.04	0.17

	4	5
Cu	190	2
Sb	235	131
Au	0.08	0.01

Figure 13. Graphic images of the two probing profiles for the galena crystals from quarts veins of the gumbeites from the Shartash massive, the Berezovsk ore field. Profile length: left—1031 μm, right—728 μm.

4.1.3. The Svetlinsk Gold-Telluride Deposit

The Svetlinsk gold-telluride deposit contains the gold ores, which can be divided into two types (except for ore in regolith): (1) disseminated pyrite-pyrrhotite in the host rocks (C_{Au} up to 1 g/t), and (2) sulphide-quartz veins and veinlets, superimposed on the disseminated mineralisation (average C_{Au} = 0.8–2.5 g/t). Sulphides are typically about 3–5 vol% (sometimes up to 20 vol%) of the bulk gold-bearing ore. Native gold (fineness 618–964; single value 485) in sulphide-quartz veins forms inclusions in pyrite, tetrahedrite and quartz, as well as is closely associated with tellurides: melonite $NiTe_2$, frohbergite $FeTe_2$, altaite PbTe, tellurantimony Sb_2Te_3, Ag- and Au-Ag-tellurides (Table 2, Figure 14) [41]. The bulk ore analyses revealed that vein-disseminated gold ores (Au~2–4 ppm) contained (in ppm) 5–17 Sb, 4–7.3 Te and 2.5–4 Se. For the Svetlinsk deposit, native ($Au_{0.48–0.96}Ag_{0.02–0.49}$) and telluride (calaverite $AuTe_2$, montbrayite ($(Au,Sb)_2Te_3$), sylvanite $AuAgTe_4$, krennerite $(Au,Ag)Te_2$, petzite Ag_3AuTe_2, hessite Ag_2Te and γ-hessite $Ag_{1,9}Te$) forms of manifestation prevail among the Au and Ag minerals (Table 3).

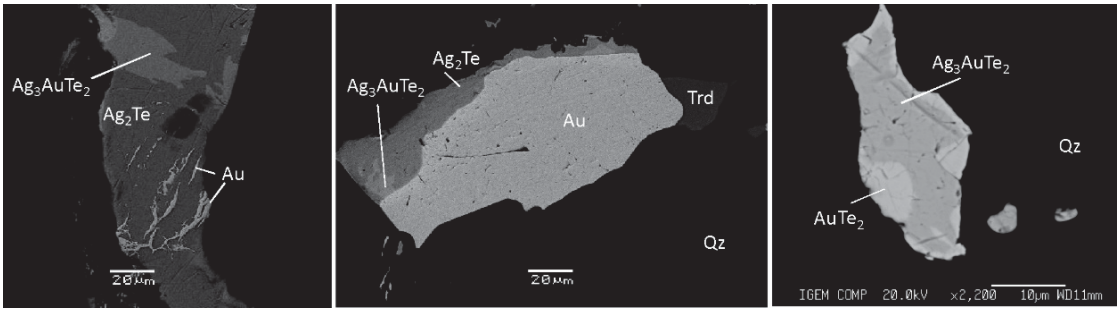

Figure 14. Au and Ag minerals in quartz veins of the Svetlinsk deposit. Qz—quartz, Trd—tetrahedrite.

Many Te minerals are important carriers of Au in sulphide-bearing ore [67,100]. The minerals found in the deposit contain up to 1 wt% Au (altaite—up to 0.6 wt%, tellurantimony—from 0.3 to 1 wt%, and tetradymite—up to 0.2 wt%, EPMA). EPMA revealed the presence of Ag in the sulphides of early associations of the quartz-sulphide veins (wt%): chalcopyrite 0.02–0.48, pyrite up to 0.05 and pyrrhotite up to 0.02.

The LA-ICPMS data have been obtained for pyrite and chalcopyrite from the disseminated pyrite-pyrrhotite mineralisation (*Py I*) and from the gold-sulphide-telluride-quartz veins (*Py II*). *Py I* is enriched in Au, Ag, Pd, Sb, Bi and Te and contains (ppm): Au 0.1–33.8, Ag 0.1–146, Pt 0.01–0.03, Pd up to 0.1, In up to 4.2, Te 2.2–192, Sb 0.1–50.8, Co 11.7–833 (for 1 sample—6088), Ni 2.5–648 (1 sample—2382), Ga 0.1–47, Ge 0.1–5.3, Se 2.2–71, Bi 0.1–5.3; *Py II:* Au 0.01–3.4, Ag 0.1–3.4, Pt 0.01–0.09, Pd up to 0.03, In is below the detection limit, Te 1.9–152, Sb 0.1–8.7, Co 0.05–1019 (2 samples—1.2 wt%), Ni 1.8–587.4 (2 samples—0.1 wt%), Ga 0.1–3.4, Ge 0.2–0.5, Se 3.5–52 and Bi up to 0.6 (Figure 15b). Vein-chalcopyrite contains (ppm): 0.1–0.2 Au, 0.9–441 Ag, 1.4–2.5 Pd, 11.8–41 In, 3.3–11 Te, 0.3–130 Sb, 0.6–1.0 Ga and 38–63 Se.

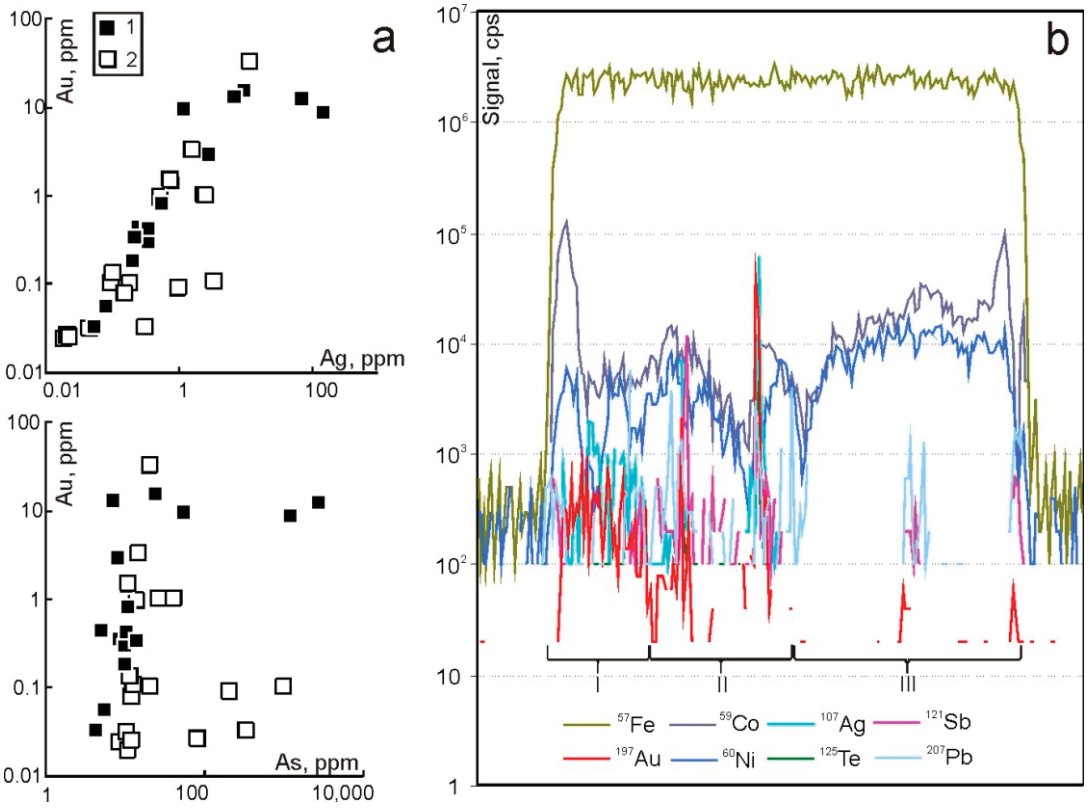

Figure 15. Trace element distribution in pyrite of the Svetlinsk gold deposit according to LA-ICPMS analyses. (**a**) Correlation of Au, Ag and As contents in the disseminated (1) and vein (2) pyrite, (**b**) nonuniform Au distribution in the pyrite crystal according to ablation profile data: I—zone with uniform distribution, probably indicating the entry of Au into the pyrite structure, II—zone with inclusions of Au-Ag-Sb-Te phases and III—zone with gold content below the detection limit.

At Au $\leq$ 10 ppm, the direct correlation between the contents of Au and Ag (Figure 15a), as well as that of Au and Ag with Te was found for early pyrite. This data may indicate the presence of nano-scale inclusions of petzite Ag_3AuTe_2 and hessite Ag_2Te in pyrite. At higher concentrations (Au > 10 ppm), the gold nanoparticles probably occur in both pyrite varieties. At Au from 0.01 to 0.1 ppm, Au–As correlation possibly suggests structurally bound Au in pyrite. The lower Au and Ag concentrations in the late pyrite are probably related to the deposition of their own mineral forms at this mineral formation stage. In contrast, for the early pyrite, an incorporation of Au into the pyrite structure can be suggested. Cu-rich pyrite (I and II) and Ni-rich Py II contain a detectable value of Pd.

4.1.4. The Petropavlovsk Gold-Porphyry Deposit

Pyrite from the skarn-magnetite assemblage contains peak concentrations of Co up to 17,141 ppm, Ni 3738 ppm and elevated As content of 1944 ppm according to LA-ICPMS data (see Tables 7 and 8). Pyrite from the gold-sulphide assemblage contains maximum Te up to 650 ppm, Au 80 ppm, Bi 116 ppm and elevated Ag 105 ppm and Pb (up to 838 ppm). The peak contents of Pb up to 4.80 wt%, Zn 8.6 wt%, 0.7 wt%, Ni 0.38 wt%, Se 223 ppm, Ag up to 111 ppm, Sb 10.5 ppm and Sn 4.4 ppm, as well as increased Te up to 137 ppm, Au 66 ppm and Bi 5 ppm are found in pyrite from the gold-telluride assemblage. The presence of high "spot" occurrences of Pb and Zn in some samples is commonly associated with

tiny inclusions of galena and sphalerite. The contents of most impurity elements (Au, Ag, Te, Sb, As, Co, Bi) decrease—usually an order of magnitude—in the pyrite of the latest quartz-carbonate assemblage.

Table 7. Contents of trace elements in pyrite (ppm) of different assemblages of the Petropavlovsk gold-porphyry deposit according to LA-ICPMS data.

n	Concentration	Co	Ni	As	Se	Ag	Au	Sn	Te	Bi
Pyrite-1 (skarn-magnetite assemblage)										
25	min	3.4	8	18	1.6	0.03	0.02	0.03	0.03	0.03
	max	17,141	3738	1944	42	16	13	0.4	66	3
	geom. mean	250	52	55	15	0.3	0.2	0.14	8	0.4
Pyrite-2 (gold-sulphide assemblage)										
15	min	2	4.5	11	2	14	2	0.03	65	0.03
	max	75	37	211	26	105	80	0.4	650	116
	geom. mean	18	10	40	11	47	18	0.1	120	0.34
Pyrite-3 (gold-telluride assemblage)										
70	min	0.2	0.02	9.6	3.2	0.02	0.03	0.02	0.02	0.03
	max	2234	3791	7048	223	111	66	4.4	137	5
	geom. mean	17	12	56	13	1.3	0.6	0.1	6	0.5
Pyrite-4 (quartz-carbonate assemblage)										
30	min	0.07	3	5	1.4	0.02	0.02	0.02	0.02	0.02
	max	737	70	417	40	4.2	1.7	1.6	28	2.3
	geom. mean	27	21	37	14	0.5	0.3	0.3	4	0.3

n—number of analysis points.

Table 8. Occurrence forms of main and trace elements and their mineral inclusions in pyrite of different assemblages at the Petropavlovsk gold-porphyry deposit.

Mineral	Main Trace Elements	Minor Elements (<50 ppm)	Mineral Inclusions		
			Common	Rare	Submicroscopic *
Py-1	Cu, Co, As, Ni, Zn, Te	Sn, Bi, Se, Ag, Au, Pb	*Sp, Mt*	*Hem, Rt*	
Py-2	Pb, Te, Bi, Au, Co, Zn, As, Ag	Se, Ni, Sn, Cu	*Ccp, Sp*	*Mt, Po*	*Au*
Py-3	Ni, As, Zn, Se, Ag, Sn, Cu, Au, Te, Pb	Bi	*Ccp, Gn, Hs, Pz, Alt, Cal, Syl, Au, Sp*	*Po*	*Ks, Cal, Pz, Hs*
Py-4	Co, Ni	Se, Ag, Au, Sn, Te, Bi, Zn, Pb, Cu	*Ccp*		

* Here and in Tables 11, 13, 15 and 17 minerals are indicated as probable forms of concentration of a group of chemical elements in submicroscopic and nano-scale inclusions, assumed by their co-occurrence of "synchronous" peaks of impurity elements in host base metal sulphide. Mineral abbreviations (italics) here and in Tables 11, 13, 15 and 17: *Ccp*—chalcopyrite, *Sp*—sphalerite, *Mt*—magnetite, *Gn*—galena, *Hs*—hessite, *Pz*—petzite, *Cal*—calaverite, *Syl*—sylvanite, *Au*—native gold, electrum, *Hem*—hematite, *Po*—pyrrhotite, *Rt*—rutile, *Alt*—altaite, *Ks*—küstelite, *Fhl*—fahlore, *Cbt*—cobaltite, *Em*—empressite.

According to LA-ICPMS data, a positive linear relationship between the Au and Ag contents in pyrite is observed for the gold-bearing ore: correlation coefficient (r) is 0.99 for the skarn-magnetite assemblage, for gold-sulphide, r = 0.89, for gold-telluride, r = 0.9, and for quartz-carbonate, r = 0.84 (Figure 16). Positive correlation of these elements corresponds to the occurrence of invisible gold, mainly represented by submicroscopic and nano-sized native gold (electrum).

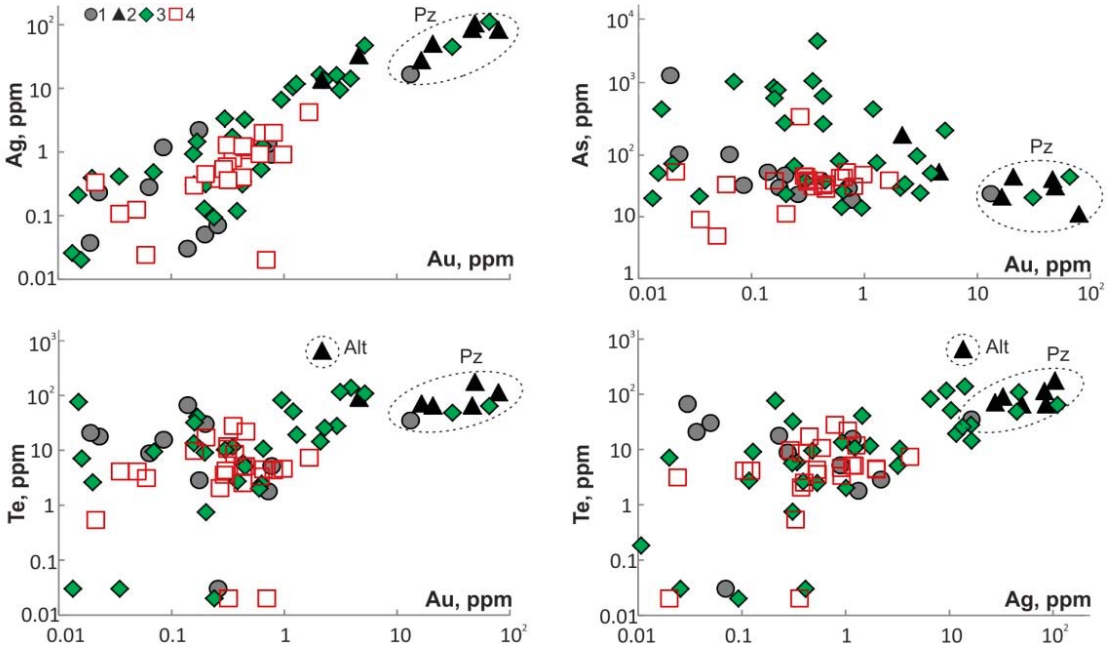

Figure 16. Binary diagrams of the contents of Au, Ag, Te and As in pyrite of the Petropavlovsk gold-porphyry deposit according to LA-ICPMS analyses. Mineral assemblages in ores: 1—skarn-magnetite; 2—gold-sulphide; 3—gold-telluride; 4—quartz-carbonate. The dashed line counters the probable submicroscopic inclusions of altaite (C_{Pb} = 104–838 ppm) and petzite.

A negative correlation is observed for Te with Au and Ag in pyrite for the gold-sulphide assemblage (−0.4 and −0.44, respectively) and a positive correlation for Ag/Te (0.46) and Au/Te (0.4) for the gold-telluride assemblage. The presence of a positive connection between Ag and Te can be explained by the occurrence of submicroscopic and nano-scale inclusions of Ag telluride (hessite) and Au-Ag telluride (petzite) in the pyrite of the last assemblage.

There is a correlation between Co and Ni for the gold-sulphide assemblage (r = 0.46). A positive correlation is also observed between Co and As for the following assemblages: skarn-magnetite (r = 0.98) and quartz-carbonate (r = 0.5), and it commonly corresponds to small cobaltite inclusions. A significant correlation between Au and As, but negative (r = –0.6), is observed for the pyrite of the gold-sulphide assemblage. Correlation Au/As is absent for other assemblages.

The examples of the spot analyses of two grains of anhedral and subhedral pyrites (gold-sulphide and gold-telluride assemblages, correspondingly) are demonstrated in Figure 17. Gold concentration ranges from 0.3 to 31 ppm (anhedral pyrite) and from 0.06 to 1 ppm for the subhedral pyrite crystal (profile ablation). The contents of silver and tellurium are from 0.6 to 45 ppm and from 0.3 to 8.3 ppm, respectively (sample PP 308/2). Nano-sized petzite inclusions probably occur in the pyrite from the gold-sulphide assemblage (Figure 17a).

Tiny isolations of petzite are often observed microscopically in close intergrowths with native gold, native silver and galena in this assemblage. Inclusions in another anhedral pyrite grain (from the gold-telluride assemblage, PP 309/5) are unevenly distributed. They are present in both areas and probably represented by küstelite, electrum and petzite (see Figure 17b).

An on-site study of the same pyrite grain ("mapping" mode of LA-ICPMS analysis) shows that increased concentration of Au, Ag and Te corresponds to one of its marginal parts. Dense clusters of bright points with their increased contents (Figure 18a) create an irregular, "fine-spotted" picture of their distribution, indicating the possible occurrence of nano-sized inclusions of Au-Ag tellurides (mainly petzite?) here. Elevated contents of Ni and Co belong to the edge zone of the pyrite crystal. Analysis reveals average contents (excluding peak areas): Au 0.6 ppm, Ag 2 ppm, Te 1.2 ppm, Co 3.4 ppm, Ni 16 ppm and As 23 ppm (Figure 18a).

Laser ablation of another pyrite grain (Figure 18b) demonstrates a different picture of the distribution of impurity elements with maxima, ppm: Au 0.43, Ag 0.34, Te 6, Co 118, Ni 117 and As 318. Gold contents do not correlate with Te and Ag, and Te and Ag peaks belong to only one of the crystal margins, which is possibly also associated with the abundance of nano-sized inclusions of silver tellurides (hessite?) here. Elevated Co contents belong to the entire edge zone, and Ni, on the contrary, belongs to the central part of the pyrite crystal. Figure 19 shows an example of a LA-ICPMS profile across an idiomorphic pyrite grain from the gold-sulphide assemblage (PP 309/10), which also showed a generally uneven distribution of impurity elements in pyrite. We divided the ablation time-profile into 5 areas: Au, Ag and Te are evenly distributed in all zones. The elements form peaks probably due to submicron inclusions of native gold, küstelite and hessite (Table 9).

Table 9. Average concentration of Au, Ag and Te (ppm) in the zones of the pyrite grain.

Chemical Element	Zones				
	1	**2**	**3**	**4**	**5**
^{197}Au	0.52	0.06	2.7	0.03	1
^{107}Ag	2.5	0.6	8.6	1.14	2.4
^{124}Te	0.88	0.7	0.23	0.19	0.3

Note: Peak concentrations are excluded from calculation of average values.

Chalcopyrite: Elevated concentrations of Co (143 ppm), Ni (242 ppm), As (80 ppm), Se (194 ppm), Sb (20.4 ppm) and Sn (4 ppm) are found in chalcopyrite-1 and Te (up to 4200 ppm), and those of Au (up to 25 ppm), Ag (up to 7600 ppm) and Bi (11 ppm) in chalcopyrite-2 (Tables 10 and 11). It is probably associated with the capture of nano-scale inclusions of cobaltite (Co, As, Ni), fahlore (Cu, Ag, As, Sb), altaite (Pb, Te), as well as petzite (Ag_3AuTe_2), calaverite ($AuTe_2$), native gold, native silver and hessite (Ag_2Te).

Galena: Elevated concentrations of Co (up to 1060 ppm), Ni (670 ppm), As (93 ppm), Se (407 ppm), Sb (8.6 ppm) and Sn (0.8 ppm) are recorded in galena-1, and those of Te (up to 1770 ppm), Au (980 ppm), Ag (2050 ppm) and Bi (62 ppm) in galena-2 (Tables 12 and 13).

Generally, the gold content in the sulphides of the deposit is maximum in galena (980 ppm), followed by pyrite (80 ppm) and chalcopyrite (25 ppm). According to the LA-ICPMS method, the pyrite of the early ore assemblages of the Petropavlovsk deposit is characterised by high contents of Co, Te, Au, Ag and Bi, increased Ni, As and Se and noticeable Sb and Sn. For the pyrite of later assemblages, elevated Zn, Pb, As, Ni, Se, Sb and Sn are found. The maximum Au was established in pyrite from the gold-telluride assemblage (up to 80 ppm). Minimal Au concentration was established in the pyrite of the latest quartz-carbonate assemblage (up to 1.7 ppm). Detectable admixtures of tellurium characterise the pyrite of all mineral assemblages. Proper mineral forms of the trace elements are presented, including Te compounds with Au (± Ag) in late mineral assemblages.

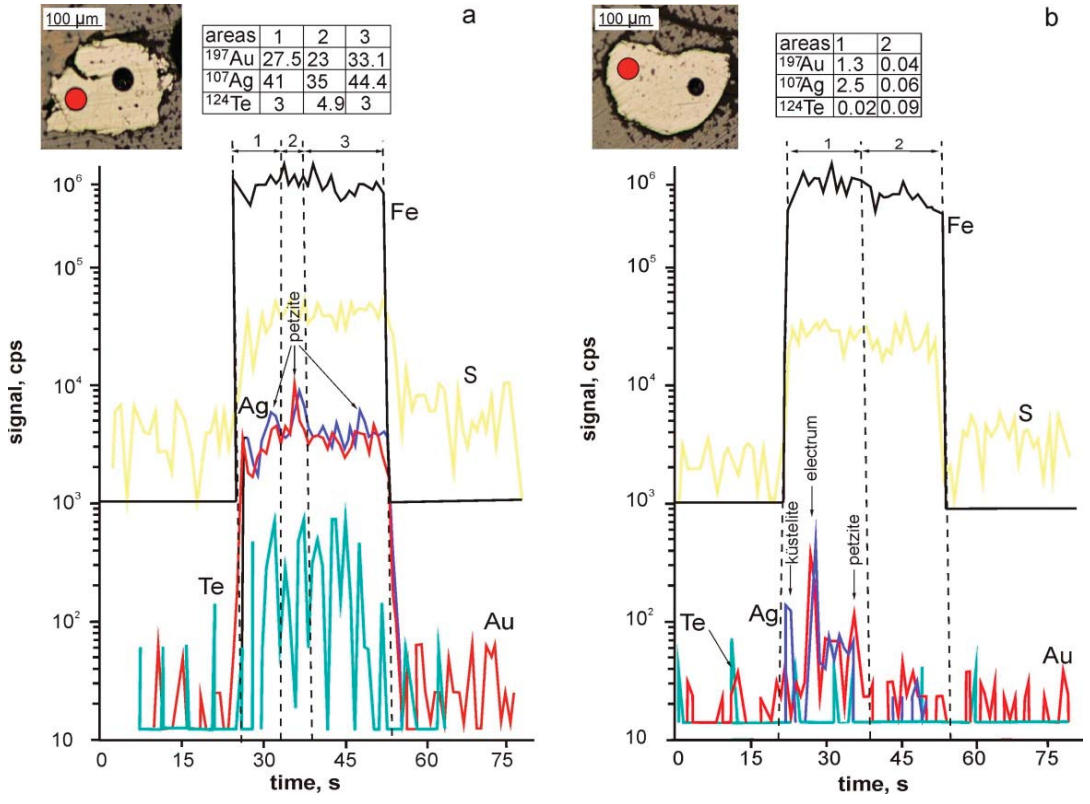

Figure 17. Composition of pyrite from the gold-telluride assemblage obtained by the LA-ICPMS method for the Petropavlovsk deposit: (**a**) tiny inclusions of native gold and petzite are evenly distributed, the gold-sulphide assemblage, sample PP 308/2. (**b**) A few peaks are probably related with inclusions of native gold or küstelite and petzite, the gold-telluride assemblage, sample PP 309/5. Note (here and in Figure 19): the graphs show the main (Fe, S) and some minor (Au, Ag, Te) elements in pyrite.

According to the LA-ICPMS analyses, gold in sulphides of the deposit is present mainly in the invisible form (from 0.02 to 80 ppm). It mainly associates with pyrite-2. At least part of such gold probably occurs as nano-scale inclusions of native gold (close in composition to *AuAg*) as well as Au- and Au-Ag-tellurides [39].

The data obtained suggest that the gold was evenly distributed in pyrite crystals in the early assemblages of the Petropavlovsk deposit. Gold was further enlarged and partly redeposited in pyrite defects at the final stages of mineralisation.

A close relationship is observed between Au and Ag (correlation coefficient $r > 0.7$), as well as between Ag and Te ($r = 0.46$) for the gold-telluride assemblage. It can be explained that these elements are present in the deposit in the form of tiny inclusions of native gold, hessite and petzite. Au–As correlation is not traced in pyrite. The uneven distribution of Au, Ag and Te over the area of pyrite grains with "spots" of their peak concentrations probably indicates the presence of clusters of nano-sized inclusions of Au-Ag tellurides.

The concentrations of trace elements in galena and chalcopyrite (as well as in pyrite) change with the evolution of ore formation. The contents of Ni, Co, As, Se and Sb are maximum in the main gold stage. The concentrations of Au, Ag, Te and Bi increase at the end of this stage. In general, the gold content in the sulphides of the deposit reaches highs in galena (up to 980 ppm). Next are pyrite (49 ppm) and chalcopyrite (25 ppm).

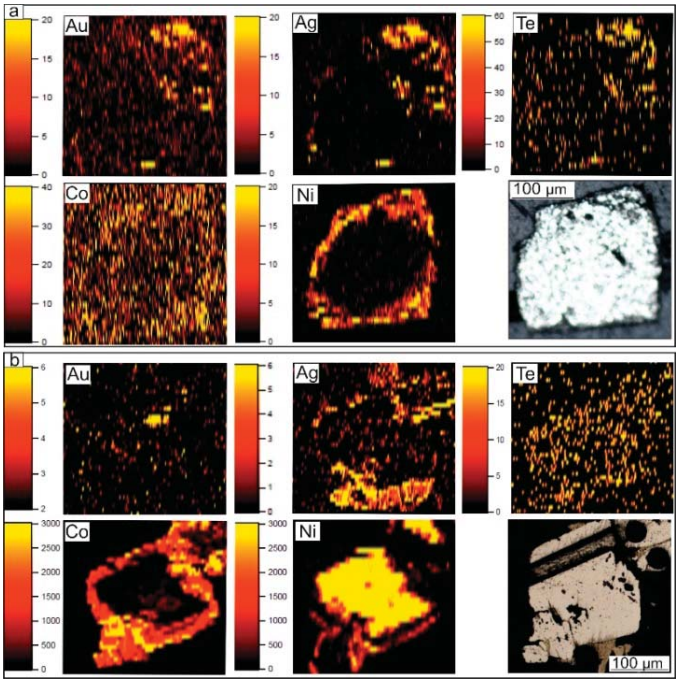

Figure 18. LA-ICPMS distribution maps of impurity elements in pyrite crystals from the gold-telluride assemblage of the Petropavlovsk gold-porphyry deposit: sample PP 309/5 (**a**) and sample PP 1444/71 (**b**), scales in ppm.

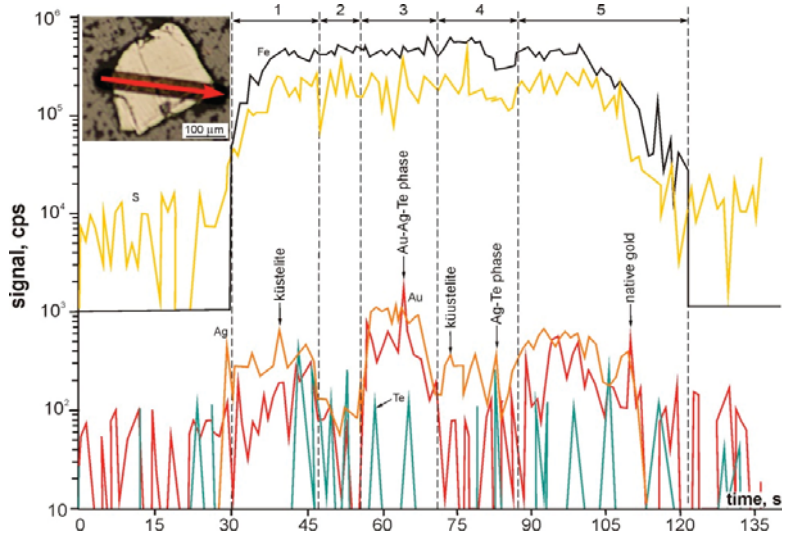

Figure 19. Composition of pyrite of the gold-sulphide assemblage from the Petropavlovsk deposit, LA-ICPMS profile (sample PP 309/10). Submicron inclusions of native gold, küstelite and hessite are probable. For average content of elements in the profile intervals, see Table 9.

Table 10. The limits and average values of the contents of trace elements (ppm) in chalcopyrite of different assemblages of the Petropavlovsk gold-porphyry deposit according to LA-ICPMS data.

n	Concentration	Co	Ni	As	Se	Ag	Au	Sn	Te	Bi
Chalcopyrite-1 (gold-sulphide assemblage)										
2	min	0.02	0.03	4	14	0.7	0.01	0.07	0.02	6
	max	143	272	80	194	63	2.5	4	68	8
	geom. mean	0.4	15	30	43	7	0.3	1	0.8	7
Chalcopyrite-2 (gold-telluride assemblage)										
21	min	0.08	0.03	26	28	870	6	1	870	0.05
	max	0.14	57	44	32	7600	25	1.8	4200	11
	geom. mean	0.11	1.3	33.8	30	2571	12.3	1.4	1912	0.3

Table 11. Occurrence forms of main and trace elements and their mineral inclusions in chalcopyrite of different assemblages of the Petropavlovsk gold-porphyry deposit.

Mineral	Main trace Elements	Minor Elements (<50 ppm)	Mineral Inclusions		
			Main	Rare	Submicroscopic
Ccp-1	Co, Ni, As, Se, Sn, Ag, Te	Bi, Au	*Sp, Py*		*Cbt, Fhl*
Ccp-2	Ag, Au, Te, Bi Ni	As, Se, Sn	*Sp*	*Hs, Au*	*Alt, Pz, Au, Hs, Cal*

Table 12. The limits and average values of the contents of trace elements in galena (ppm) of different assemblages of the Petropavlovsk gold-porphyry deposit according to LA-ICPMS data.

n	Concentration	Co	Ni	As	Se	Ag	Au	Sn	Te	Bi
Galena-1 (gold-sulphide assemblage)										
37	min	0.02	0.02	0.8	1.2	0.7	0.09	0.03	0.03	0.01
	max	1060	670	93	407	42	5	0.8	730	2.7
	geom. mean	0.6	3	10	19	7	0.6	0.3	11.4	0.2
Galena-2 (gold-telluride assemblage)										
6	min	0.13	3.1	2.5	2.4	23	13	0.13	56	0.01
	max	1030	252	73	58	2050	980	0.4	1770	62
	geom. mean	200	70	31	16	263	74	0.2	252	1

Table 13. Occurrence forms of main and trace elements and their mineral inclusions in galena of different assemblages of the Petropavlovsk gold-porphyry deposit.

Mineral	Main Trace Elements	Minor Elements (<50 ppm)	Mineral Inclusions		
			Common	Rare	Submicroscopic
Gn-1	Co, Ni, As, Se, Sn, Te	Ag, Au, Bi	*Sp, Py, Ccp*		*Hs, Em*
Gn-2	Ag, Au, Te, Bi, Co, Ni, As, Se	Sn	*Alt*	*Pz, Au, Hs*	

4.1.5. The Novogodnee-Monto Iron-Gold-Skarn Deposit

Pyrite of the magnetite-pyrite assemblage is characterised by impurity concentrations peaking in As (11,050 ppm), Co (up to 3530 ppm), Ni (774 ppm), Au (12 ppm) and elevated of Te (up to 89 ppm) (Table 14). Pyrite of the polymetallic assemblage contains the maximum concentrations of Zn (3130 ppm) and Sn (0.4 ppm). Pyrite from the gold-sulphide and gold-telluride assemblages is characterised by the highest values of Cu (4520 ppm), Ag (159 ppm), Te (141 ppm) and Bi (15 ppm). Pyrite from the quartz-carbonate assemblage contains the maxima of Sb (98 ppm) and Se (363 ppm). It is possible that high concentrations of some elements are associated with the capture of nano-scale inclusions of chalcopyrite,

sphalerite, hessite (Ag_2Te), petzite (Ag_3AuTe_2), empressite (AgTe) and cobaltite (Co, As, Ni) (Table 15). It is confirmed by synchronous peaks of individual chemical elements on the profiles of laser ablation or in the form of bright point "inclusions" on bitmaps during analysis in the mapping mode [39,101].

Table 14. The trace element contents (ppm) in pyrite of different assemblages of the Novogodnee-Monto deposit according to LA-ICPMS data.

n	Concentration	Co	Ni	As	Sb	Ag	Au	Sn	Te	Bi
Pyrite-1 (magnetite-pyrite assemblage)										
14	min	144	3.3	6	0.06	0.02	0.05	0.08	0.02	0.02
	max	3530	774	11,050	15	64	12	0.3	89	4.5
	geom. mean	1938	34	1625	0.7	0.8	0.6	0.2	7	0.15
Pyrite-2 (polymetallic assemblage)										
12	min	0.8	0.02	0.6	0.05	0.16	0.04	0.09	1.3	0.02
	max	922	2	5287	60	14	1.3	0.4	33	5
	geom. mean	288	79	735	13	6	0.44	0.2	11	0.8
Pyrite-3 (gold-sulphide-magnetite assemblage in skarns)										
7	min	14	5	53	0.05	0.2	0.16	0.13	0.5	0.03
	max	592	18	4168	0.3	2	1.2	0.3	12	0.6
	geom. mean	90	11	70	0.2	0.6	0.4	0.2	3.5	0.1
Pyrite-4 (gold-sulphide and gold-telluride assemblage)										
5	min	146	11	60	0.08	0.04	0.3	0.12	26	0.03
	max	707	416	455	0.65	159	2	0.3	141	15
	geom. mean	378	57	142	0.2	4	0.6	0.23	50	0.51
Pyrite-5 (quartz-carbonate assemblage)										
7	min	0.8	0.3	0.6	0.02	0.03	0.07	0.2	1.2	0.02
	max	920	251	3830	98	2.3	0.6	0.36	39	0.8
	geom. mean	177	14	284	0.4	0.3	0.3	0.2	7.7	0.1

Table 15. Occurrence forms of main and trace elements and their mineral inclusions in pyrite of different assemblages at the Novogodnee-Monto deposit.

Mineral	Main Trace Elements *		Minor Elements (<50 ppm)	Minerals Inclusions		
	Maximum, ppm	High Values, ppm		Main	Rare	Submicroscopic
Py-1	Co, Ni, As, Au, Zn, Cu	Ag, Te	Sb, Sn, Bi	*Mt, Ccp*	*Cbt*	*Cbt, As*
Py-2	Sb, Sn	Co, As, Cu	Ni, Ag, Au, Te, Bi, Zn	*Ccp, Sp, Gn*	*Hem, Cbt, Apy, Po*	
Py-3		Co, As	Ni, Sb, Sn, Au, Ag, Te, Bi, Cu, Zn	*Ccp*	*Cbt, Ag*	
Py-4	Ag, Te, Bi	Co, Ni, As, Cu	Au, Sb, Sn, Zn	*Pt, Hs, Alt*	*Au, Ag*	*Pz, Clc, Gt, Ccp, Dg*
Py-5	Sb	Co, Ni, As, Cu	Ag, Au, Sn, Te, Bi, Zn	*Bn, Cv, Clc, Gt, Dg, Cu*		

Designation here and in Table 17: *Apy*—arsenopyrite, *Ag*—native silver, *Bn*—bornite, *Cv*—covellite, *Clc*—chalcocite, *Gt*—goethite, *Dg*—digenite.

According to the LA-ICPMS data, a positive relationship occurs between Au and Ag in magnetite-pyrite (0.6) and gold-sulphide-magnetite (0.9) assemblages (Figure 20). A positive correlation is observed between Au and Te in pyrite of the magnetite-pyrite (0.8) and quartz-carbonate assemblages (0.6). A stronger correlation between Ag and Te is

found in pyrite of magnetite-pyrite (0.78) and gold-telluride (0.9) assemblages. A notable relationship between Au and As is observed only for the magnetite-pyrite assemblage (0.7). A positive correlation between the Co and Ni is revealed in pyrite for magnetite-pyrite (0.7) and polymetallic (0.7) assemblages. The negative correlation between the Co and Ni is observed in pyrite for the gold-sulphide-magnetite assemblage (−0.6). A positive correlation between Co and As is also found in pyrite for magnetite-pyrite (0.5) and gold-telluride (0.5) assemblages.

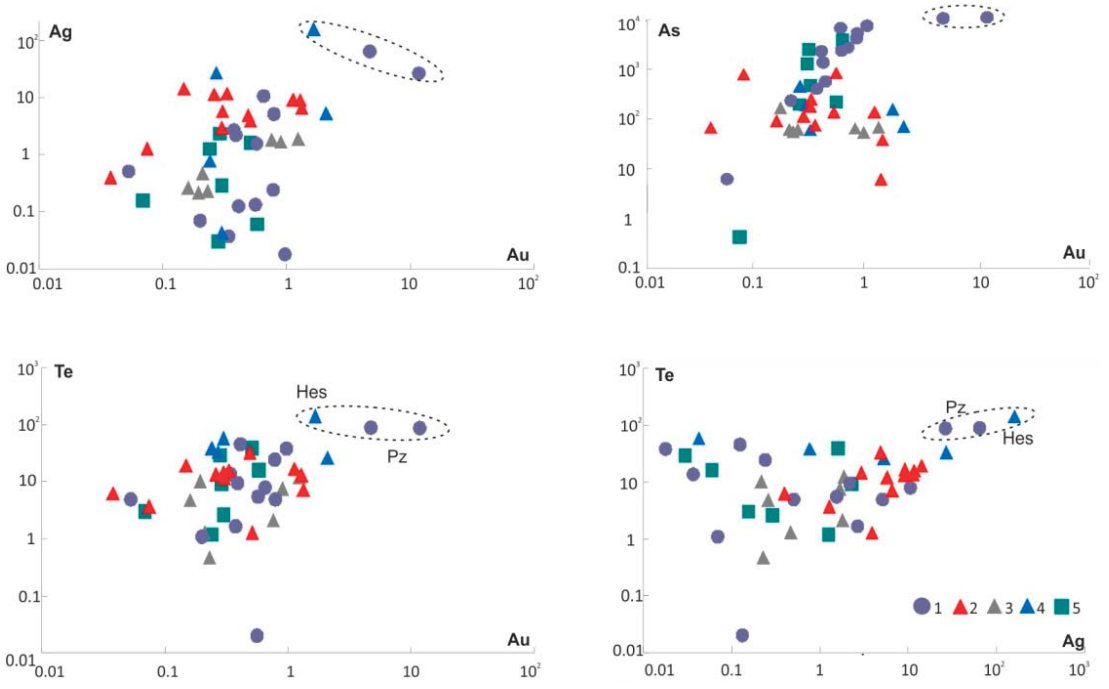

Figure 20. Binary diagrams of the contents of Au, Ag, Te and As (ppm) in pyrite of the Novogodnee-Monto Fe-Au-skarn deposit according to the LA-ICPMS data. Mineral assemblages in the ores: 1—magnetite-pyrite, 2—polymetallic, 3—gold-sulphide-magnetite in skarns, 4—gold-sulphide and gold-telluride, 5—quartz-carbonate. The dashed counter shows probable inclusions of petzite and hessite.

The profile ablation of pyrite grains from the polymetallic assemblage by the LA-ICPMS method showed an uneven distribution of the majority of impurity elements in pyrite, with average contents (geom. mean., excluding peak areas): 1.3 ppm Au, 9 ppm Ag, 13.1 ppm Te, 177 ppm Co, 132 ppm Ni and 6 ppm As (Figure 21). Confined to the marginal parts of the pyrite grain, high Au concentrations correlate with elevated Ag contents but do not correlate with Te. An on-site study of the same pyrite grain in mapping mode shows close for Au and Ag areas of the increased concentrations, gravitated to the edge parts of the pyrite grain, while Te-maxima are localised separately. The increased contents of As and Co belong to the marginal zones of the pyrite grain.

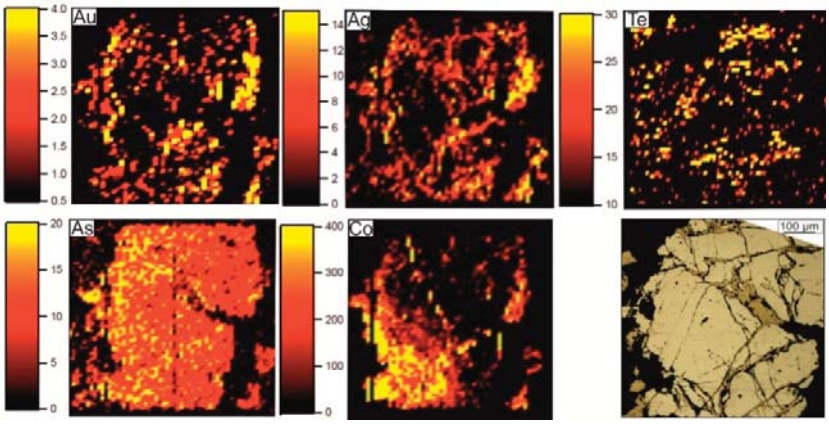

Figure 21. LA-ICPMS distribution map of impurity elements in pyrite grain from the polymetallic assemblage of the Novogodnee-Monto deposit (sample NM 46), scales in ppm.

Chalcopyrite: Peak concentrations of As (up to 3230 ppm), Pb (up to 1050 ppm), Co (up to 887 ppm), Se (up to 109 ppm), Ag (up to 88 ppm), Au (up to 13 ppm), Ni (up to 9 ppm) and Sn (up to 2 ppm) are found in chalcopyrite-1 (Tables 16 and 17). Maxima of Zn (up to 145 ppm), Sb (up to 37 ppm), Te (up to 15 ppm) and Bi (up to 3 ppm) occur in chalcopyrite-2. The peaks of Pb, As, Zn, Te, Ag and Au on the LA-ICPMS profiles are probably related to the capture of small inclusions of galena, arsenopyrite, sphalerite, altaite, calaverite, native gold, hessite and petzite, which were found microscopically.

Table 16. The trace element contents (ppm) in chalcopyrite of different assemblages of the Novogodnee-Monto deposit according to LA-ICPMS data.

n	Concentration	Co	Ni	As	Sb	Ag	Au	Sn	Te	Bi
		Chalcopyrite-1 (polymetallic assemblage)								
22	min	0.02	0.02	2.8	0.04	0.2	0.02	0.06	0.07	0.02
	max	887	8.8	3230	37	88	13	2.14	9.1	0.4
	geom. mean	1.3	0.31	73	0.8	2.34	0.22	0.15	0.5	0.04
		Chalcopyrite-2 (gold-sulphide-magnetite assemblage in skarns)								
4	min	0.02	0.1	0.9	0.03	0.03	0.06	0.2	5.7	1.03
	max	50	5.7	23	3.5	11.3	1	0.6	15	3
	geom. mean	1.3	2	5	0.75	1.7	0.4	0.4	9	1.8

Table 17. Occurrence forms of main and trace elements and their mineral inclusions in chalcopyrite of different assemblages at the Novogodnee-Monto deposit.

Mineral	Main Trace Elements		Minor Elements (<50 ppm)	Mineral Inclusions		
	Maximum, ppm	High Values, ppm		Main	Rare	Submicroscopic
Ccp-1	Co, Ni, As, Sb, Ag, Au, Sn		Te, Bi	*Po, Sp, Gn*		*Cal, Alt, Au, Hs, Pz*
Ccp-2	Te, Bi	Co	Ni, As, Sb, Ag, Au, Sn		*Au*	

Native gold in the ore is associated mainly with pyrite impregnations. It is characterised by high fineness (893) in the gold-sulphide-magnetite assemblage in skarns. The Au contents in pyrite are significantly reduced in the later gold-telluride assemblage. Native

gold from this assemblage has a size from 2–5 to 10–20 μm and fineness from 750 to 893. The size of the segregations and fineness of gold increase (up to 40–50 μm and up to 893, respectively) in contact with the late dyke. Pyrrhotite appears in the gold-pyrite-magnetite assemblage. The gold concentrations in pyrite of the early magnetite-pyrite assemblage belong to the limits of possible uniformly distributed gold (for a pyrite crystal with a size of 0.5 mm, the maximum value of uniformly distributed gold detected by the method in [102] is about 12.3 ppm). These researchers evaluated the structural gold contribution as 1–10% of the bulk uniformly distributed gold. The peak Te contents (up to 141 ppm) were established in the pyrite of the gold-telluride assemblage, in some cases probably due to submicron inclusions of calaverite $AuTe_2$.

In general, gold of the early assemblages was evenly distributed in pyrite crystals at the Novogodnee-Monto deposit, and that at the Petropavlovsk deposit. Later, at the final stages of mineral formation, invisible gold (submicron native gold isolations, nano-scale domains and isomorphic gold in pyrite) was enlarged and redeposited in pyrite defects.

It is possible that high concentrations of some elements are associated with the capture of nano-scale inclusions of chalcopyrite, sphalerite, hessite (Ag_2Te), petzite (Ag_3AuTe_2), muthmannite ($AuAgTe_2$), sylvanite ($(Au,Ag)_2Te_4$), krennerite (Au_3AgTe_8), empressite (AgTe) and cobaltite ((Co,Ni)AsS) during alalysis. It is confirmed by the appearance of synchronous peaks of individual chemical elements on the laser ablation profiles or in the form of bright dot-like "inclusions" on bitmaps during analysis in the mapping mode [40]. It is also confirmed by strong ($r > 0.7$) bonds between Au and Te (0.8), Au and As (0.7), Co and Ni (0.7) and Ag and Te (0.8) for the magnetite-pyrite, Ag and Te for the gold-telluride (0.9), Au and Ag (0.9) for the gold-sulphide-magnetite and Co and Ni (0.7) for the polymetallic assemblages. The uneven distribution of Au, Ag and Te over the pyrite grain area with "spots" of their peak concentrations probably indicates, as in the Petropavlovsk deposit, the presence of dense clusters of nano-scale inclusions of Au-Ag tellurides, as well as cobaltite. Moreover, the Novogodnee-Monto deposit is characterised by increased concentrations of Au and Ag. These concentrations are consistent with each other, while Te is localised separately.

Concentrations of trace elements in chalcopyrite also change along with the ore formation. The contents of Ni, Co, As, Se, Au and Bi reach their maximum values in the earlier polymetallic assemblages. The concentrations of Te, Sn, Ag, Zn, Sb and Pb increase for chalcopyrite of the gold-sulphide-magnetite assemblage in skarn. In general, the gold concentration in chalcopyrite is slightly lower (geom. mean 0.22 ppm) than in pyrite (geom. mean 0.6 ppm). The gold concentration in magnetite does not exceed tenths of a ppm (up to 0.2 ppm, geom. mean 0.11 ppm).

4.2. The VMS Deposits of the Urals

Pyrite is the dominant mineral of the VMS ores (40–90 vol%). Chalcopyrite and sphalerite are the major economic minerals (1–10, up to 30 vol%), and fahlore (mainly tennantite) is a common mineral (0.1–1 vol%). Occurrence of some minerals is locally significant: bornite for Gai, pyrrhotite (up to 20 vol%) and fahlore for Uzelga (up to 10 vol%), galena for Uchaly and Uzelga (up to 2 vol%), magnetite for Uchaly and arsenopyrite for Uchaly and Gai (up to 1 vol%) deposits. The ore samples which are anomalous in terms of gold concentration commonly contain Ag-bearing fahlore, Ag-bearing galena (±Ag-bearing bornite) with subordinated sulphosalts of silver (pyrargyrite, freibergite, stephanite, polybasite, pyrostilpnite, argentotetrahedrite, pearceite, proustite), tellurides (altaite, hessite, stützite, empressite, petzite, krennerite, sylvanite, montbrayite, muthmannite), sulphotellurides (tetradymite), Au-Ag-sulphides (petrovskaite, uytenbogaardtite, acanthite) and native elements (native gold, native silver, native tellurium) [9,15,71,103] (Table 18, Figure 22).

Table 18. Mineral forms of Au and Ag in the largest VMS deposits of the Urals, modified after [93].

Highly Metamorphosed	Weakly Metamorphosed		Non-Metamorphosed
Gai	**Uchaly**	**Uzelga**	**Galka**
Hessite Ag_2Te, native gold (710–980), native silver (100–0), calaverite $AuTe_2$, sylvanite $AuAgTe_4$, krennerite $(Au,Ag)Te_2$, petzite Ag_3AuTe_2, montbrayite $(Au,Sb)_2Te_3$, muthmannite $AuAgTe_2$, acanthite Ag_2S, Ag-betekhtenite $(Ag,Cu,Fe)_{21}Pb_2S_{15}$	Hessite Ag_2Te, empressite AgTe, electrum (340–690), freibergite $Ag_{12}Sb_4S_{13}$, petrovskaite AuAg(S,Se), acanthite Ag_2S, pearceite $[Ag_9CuS_4][(Ag,Cu)_6(As,Sb)_2S_7]$, polybasite $[(Ag,Cu)_6(Sb,As)_2S_7][Ag_9CuS_4]$, ytenbogaardtite $AuAg_3S_2$	Hessite Ag_2Te, stützite Ag_5Te_3, native gold (770–870), native silver, acanthite Ag_2S, sylvanite $AuAgTe_4$, petzite Ag_3AuTe_2	Native gold (700–1000), electrum (250–700), acanthite Ag_2S, freibergite $Ag_{12}Sb_4S_{13}$, argentotetrahedrite, pyrargyrite Ag_3SbS_3, stephanite Ag_5SbS_4, proustite Ag_3AsS_3, polybasite $[(Ag,Cu)_6(Sb,As)_2S_7][Ag_9CuS_4]$, petrovskaite AuAg(S,Se), ytenbogaardtite $AuAg_3S_2$, kurilite Ag_8Te_3Se

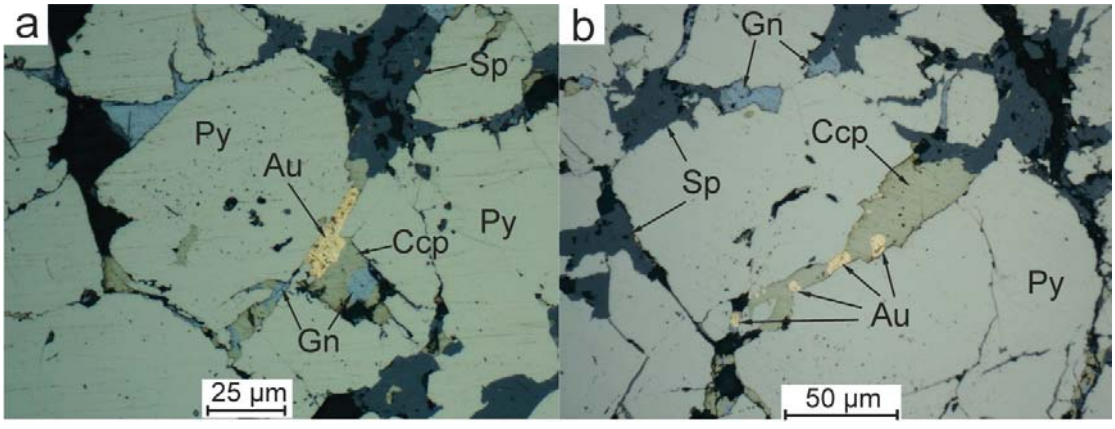

Figure 22. Solid Cu-Zn VMS ore with the late Au-polymetallic assamblege overprinted on the recrystallised early pyrite and native gold (Au) occurred in its interstices, the Novo-Uchaly lode, the Uchaly field: (**a**) Au + galena (Gn) + chalcopyrite (Ccp) + sphalerite (Sp), (**b**) Au + chalcopyrite + sphalerite.

We will consider the mineral composition of ores and the behaviour of precious metals in their minerals on the example of the largest deposits of the Urals: Gai (Cu-dominant subtype), Uchaly and Uzelga (Zn-dominant subtype).

4.2.1. The Gai Deposit

In the Gai deposit, pyrite is the dominant mineral of ores (50–95 vol%), and it contains ~3.8 ppm Au and ~8 ppm Ag (Tables 19 and 20; Figure 23). Chalcopyrite with ~0.06 ppm Au (Table 21; Figure 24) and low Fe (0.12–2.8 wt%) sphalerite, with ~0.02 ppm Au (Table 22; Figure 25), are the major economic minerals (1–10 vol%, up to 50 vol%). Tennantite-tetrahedrite and bornite are common ore minerals (0.1–1 vol%). Fahlore (low-iron tennantite is the dominant variety) contains up to (wt%, EPMA) Te 2.18, Hg 1.07, Bi 0.98, Se 0.33 and Pt 0.26. Bornite, usually pseudomorphically replacing chalcopyrite, is Ag-rich (0.16–3.53 wt%, in most analyses >0.4 wt%, EPMA), the Ag content in bornite is 2–3 times higher than in coexisting tennantite [73], however according to LA-ICPMS data, C_{Ag} in these minerals are lower: ~0.02 wt% in bornite and ~0.03 wt% in fahlore (Table 20). Galena, marcasite, digenite, magnetite and arsenopyrite are notable in some places. Altaite, tellurobismuthite, coloradoite, V-As-germanite, Ag-betekhtenite, mawsonite, Ge-stannoidite, native gold, acanthite, hessite and Au-Ag tellurides are rare [9,74,75]. Among Te minerals, altaite is the most abundant and forms the impregnation of about 20 microns within chalcopyrite and

tennantite in the late paragenesis, together with hessite, coloradoite and Au-Ag tellurides. Admixtures of up to (wt%, EPMA) Hg 0.76, Bi 0.69, Cu 0.47, Au 0.62 and Ag 0.07 were detected in altaite [9]. Hessite containing 0.26 wt% Au, 0.41 wt% Hg and 0.27 wt% Pb occurs as idiomorphic grains in intergrowth with native gold and galena. Coloradoite sometimes contains Ag (4.24 wt%). Sn-Ge sulphosalts, betekhtenite (0.95 wt% Ag) and digenite can be found only in bornite-bearing ores.

Table 19. Contents of Au, Ag and some impurities in pyrite of VMS deposits according to LA-ICP-MS data (ppm).

Deposit	n	C_i	Au	Ag	Se	Te	As
Gai	17	min	1.4	3.8 (8)	7	11 (8)	25
		max	31	47.5	267	115	1901
		geom. mean	3.8	8	61	24	226
k (Au)				0.27	−0.05	0.2	0.64
Uzelga	67	min	0.01	0.3	2 (66)	1 (19)	0.2 (66)
		max	20	204	657	197	5599
		geom. mean	0.5	15	83	22	114
k (Au)				0.57	0.02	0.96	−0.13
Galka	27	min	0.01	2.2	0.5 (13)	0.8 (10)	14 (26)
		max	9	934	32	392	15,486
		geom. mean	1.2	57	3.5	19	450
k (Au)				0.17	0.49	0.23	0.13
Uchaly	79	min	0.01	0.01	3	3 (42)	34
		max	29	326	1800	2500	5370
		geom. mean	1.6	13	54	54	1311
k (Au)				0.67	−0.26	−0.11	0.3

Here and in Tables 21 and 22, the number of values below the detection limit is shown in parentheses; k (Au)—pair correlation coefficient; n—number of analysis points.

Table 20. Summary data on contents of Au and Ag in ore minerals of VMS deposits according to LA-ICP-MS analysis.

Deposit	n	Minerals	Au, ppm			Ag, ppm		
			Min	Max	geom. mean	Min	Max	geom. mean
Gai	17	pyrite	1.4	31	3.8	3.8	47.5	8
	11	chalcopyrite	0.01	1.2	0.06	0.19	18	1.2
	4	sphalerite	0.01	0.03	0.016	2.4	5.5	3.2
	10	bornite	0.01	0.99	0.04	5.3	1250	223
	16	fahlore	0.01	1.4	0.05	132	432	285
Uzelga	67	pyrite	0.01	20	0.5	0.3	204	15
	17	chalcopyrite	0.01	19	0.2	0.3	511	7.4
	14	sphalerite	0.01	11	0.4	1.3	207	21.5
Galka	27	pyrite	0.01	9	1.2	2.2	934	57
	4	chalcopyrite	1.2	3.7	1.9	32	127	76
	21	sphalerite	0.01	32	0.64	1.2	167	51
	5	marcasite	0.02	5	0.6	7	60	22
	1	galena		0.05			153	
Uchaly	79	pyrite	0.01	29	1.6	0.01	326	13
	3	chalcopyrite	1	6	3	0.04	0.15	0.07

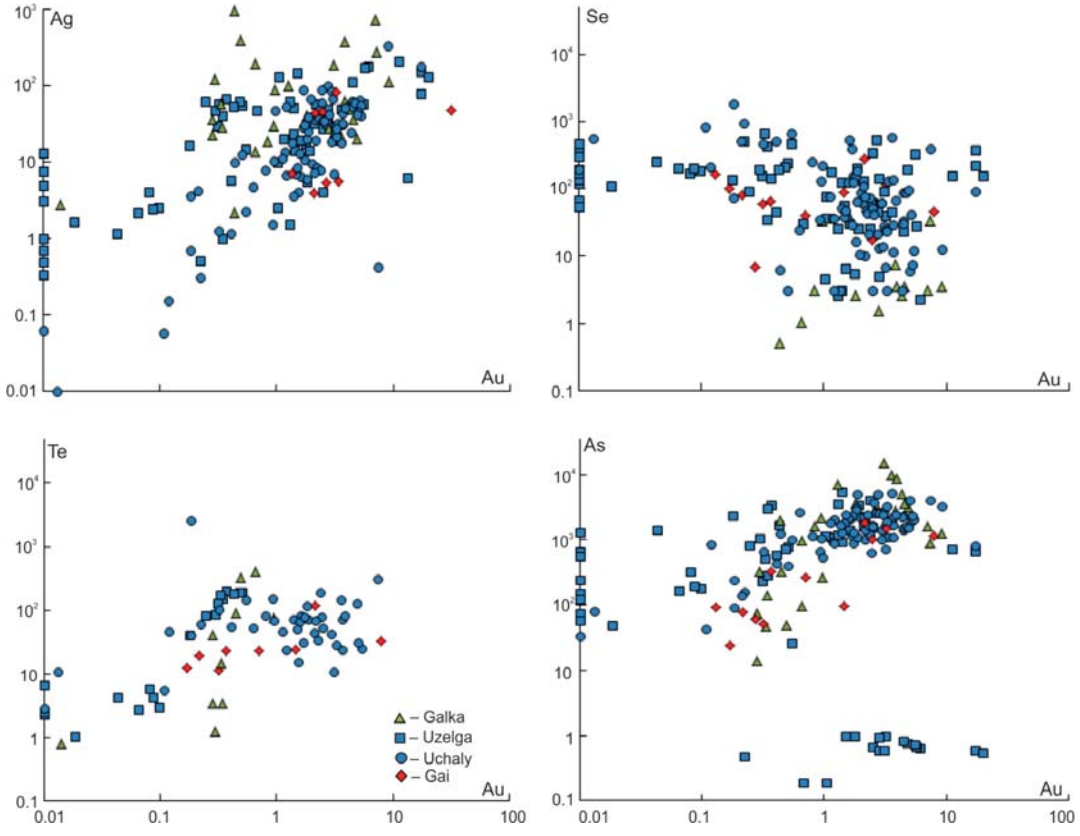

Figure 23. Binary diagrams of the contents of Au, Ag, Se, Te and As (ppm) in pyrite of the VMS deposits of the Urals according to the LA-ICPMS data.

Table 21. Contents of Au, Ag and some impurities in chalcopyrite of VMS deposits according to LA-ICP-MS data (ppm).

Deposit	n	C_i	Au	Ag	Se	Te	As
Gai	11	min	0.01	0.19	0.01 (10)	0.01 (10)	6
		max	1.2	18	167	22.05	312
		geom. mean	0.06	1.2	19	0.02	15
k (Au)				0.96	0.7	0.97	−0.05
Uzelga	17	min	0.01	0.3	39	0.01 (14)	9 (7)
		max	19	511	714	314	1530
		geom. mean	0.2	7.4	217	4.7	109
k (Au)				0.87	−0.52	0.9	−0.48
Galka	4	min	1.2	32	-	0.01	556
		max	3.7	127	-	326	4058
		geom. mean	1.9	76	-	5	1615
Uchaly	3	min	1	0.04	7	2	14
		max	6	0.15	73	4	45
		geom. mean	3	0.07	25	2.9	22

Dash—no data.

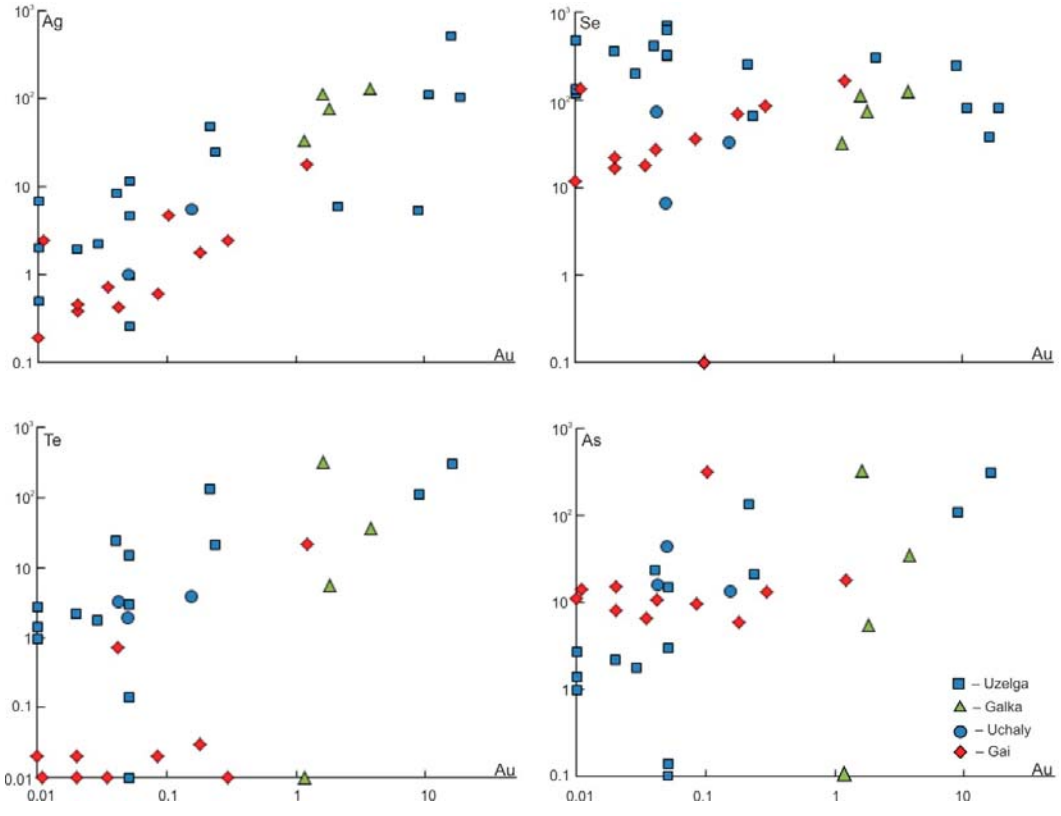

Figure 24. Binary diagrams of the contents of Au, Ag, Se, Te and As (ppm) in chalcopyrite of the VMS deposits of the Urals according to the LA-ICPMS data.

Table 22. Contents of Au, Ag and some impurities in sphalerite of VMS deposits according to LA-ICP-MS data (ppm).

Deposit	n	C_i	Au	Ag	Se	Te	As
Gai	4	min	0.01	2.4	0.01	0.01	2
		max	0.03	5.5	2.3	0.03	3.6
		geom. mean	0.016	3.2	0.4	0.19	2.8
Uzelga	14	min	0.01	1.3	0.01	1.1 (9)	2.8 (8)
		max	11	207	470	1367	1195
		geom. mean	0.4	21.5	13	47	81
k (Au)				0.8	0.1	0.99	0.7
Galka	21	min	0.01	1.2	0.3 (22)	0.4 (15)	1.2 (20)
		max	32	167	94	258	5426
		geom. mean	0.64	51	11	15	139
k (Au)				0.89	−0.6	0.38	0.1

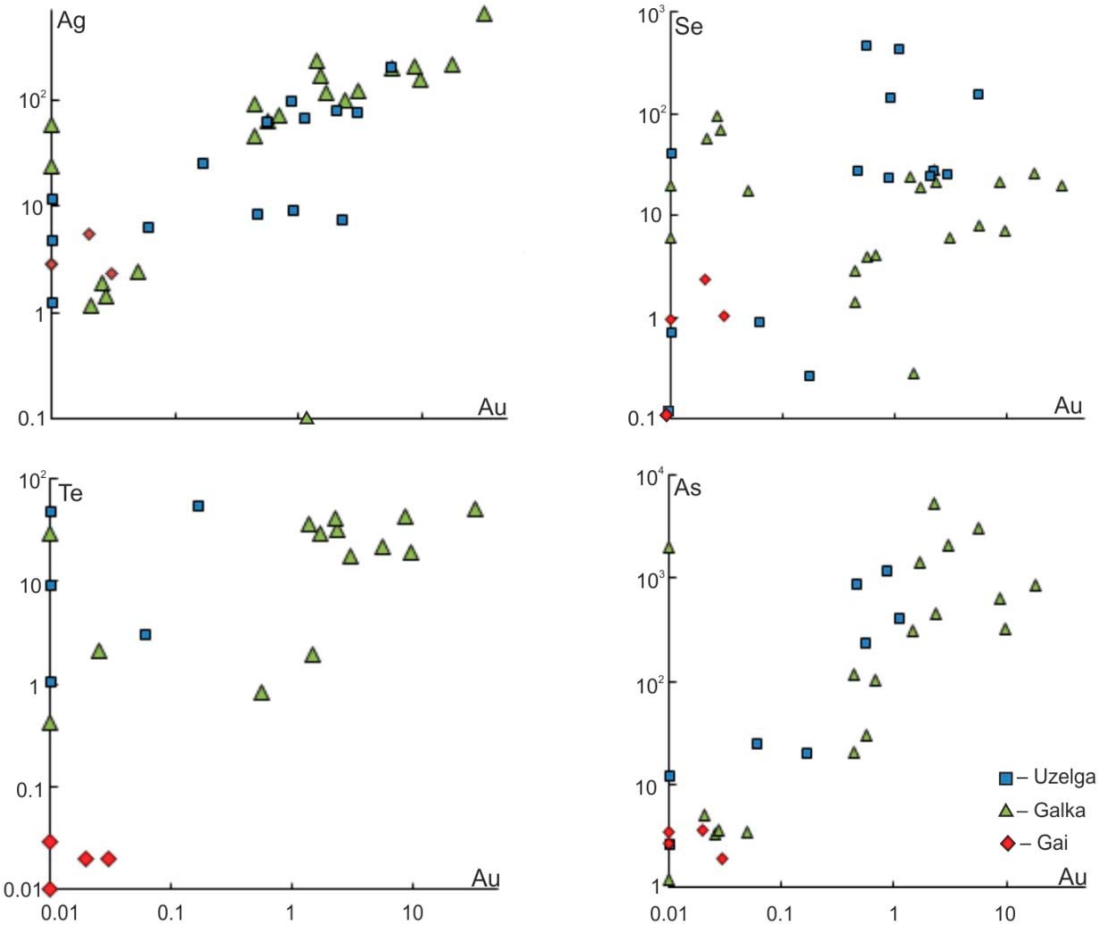

Figure 25. Binary diagrams of the contents of Au, Ag, Se, Te and As (ppm) in sphalerite of the VMS deposits of the Urals according to the LA-ICPMS data.

4.2.2. The Uzelga Deposit

Pyrite is the dominant mineral of the ores (40–90 vol%). Chalcopyrite and sphalerite are the major economic minerals (1–10, up to 15 vol% for chalcopyrite and up to 60 vol% for sphalerite). Fahlore (usually tennantite) is a common mineral in the lower-level ore bodies and is a widespread one (0.5–5 vol%) (Table 20) in the upper ore level predominating above chalcopyrite. Galena also occurs widely but in smaller quantities (up to 0.5 vol%). Pyrrhotite is abundant in the axial zone of the southern part of the largest ore body of the deposit (body 4, see [77]). Hessite, altaite, coloradoite and other Te minerals [25,78] are rare. Gold occurs predominantly in pyrite and chalcopyrite (0.1–20 ppm Au in the mode of "invisible" gold) (Tables 19 and 20; Figure 23). Au enrichment in reniform pyrite (5.5–19.6 ppm) also exists [25]. The euhedral pyrite associated with this variety is characterised by an order of magnitude lower concentrations of Au, Ag and As. Ag content in pyrite ranges 0.3–204 ppm. Gold contents in chalcopyrite average 1.5–3 ppm (total ranges 0.001–19 ppm Au and 0.5–511 ppm Ag) (Table 21; Figure 24).

Sphalerite that contains emulsion-like inclusions of chalcopyrite contains 1.8 to 11 ppm Au (Table 22; Figure 25). The gold content in pure grains of sphalerite is 0.02 to 5.5 ppm.

Therefore, gold-bearing chalcopyrite inclusions in sphalerite are considered to be responsible for an essential part of bulk gold. Galena contains various combinations of Au 0.05–0.41 wt%, Ag 0.01–0.34 wt%, Se 0.1–0.2 wt% and Te 0.1–0.14 wt% (EPMA). Additionally, Au is present as a trace element in some tellurides, such as altaite (0.02–5.2 wt%) and hessite (0.02–0.63 wt%).

Fahlore is the main concentrator of Ag. Its dominant variety is a tennantite-(Zn). Tetrahedrite grains are commonly inhomogeneous with internal mosaic texture or regular growth-zoning. The Ag content in tennantite from the upper-level ores ranges from 0.1 to 0.6 wt% (average 0.4 wt%), whereas tennantite from the lower ore level commonly contains <0.2 wt% Ag. The largest concentration of Ag (0.2–0.5 wt%) and Hg (up to 1–2 wt%) in fahlore of the lower ore bodies (bodies 3 and 4) was found near contacts with mafic dykes and near the obtuse east end of the ore body 4.

4.2.3. The Uchaly Deposit

In the Uchaly deposit, the bulk of Au and Ag occurs in pyrite (Figure 23), with average contents ~1.6 ppm Au and ~13 ppm Ag (Tables 19 and 20; Figure 23). Most of the gold (approximately 85%) is represented by dispersed and finely impregnated Au in pyrite, while free gold constitutes only 16% [15,88,89]. Gold occurs mainly in the zinc, copper and pyrite concentrates (4.0, 2.5 and 1.5 g/t, respectively). Contents of Au and trace elements in sulphides are the following (ppm): pyrite—Au 0.01–29.4, Ag 0.01–326, As 93–5370, Sb 1–990; chalcopyrite—Au 0.04–0.15, Ag < 2–5.7; tennantite—Au < 0.5, Ag 3000 (LA-ICPMS, Tables 19–22; Figures 23–25); sphalerite—Au 0.01–1.78, Ag 6–20 (INAA).

In the massive ores, visible gold was found in near-contact zones with a gabbro-diorite dyke (up to 20 m thick) or in areas that experienced local dynamometamorphism and tectonic flow. The gold aggregates (Figure 26a) have a fineness of 610–640 and 724–735 and are usually found in intergrowth with galena, chalcopyrite and tennantite-(Zn). As a rule, this mineral association cements recrystallised coarse-grained pyrite, often cataclased.

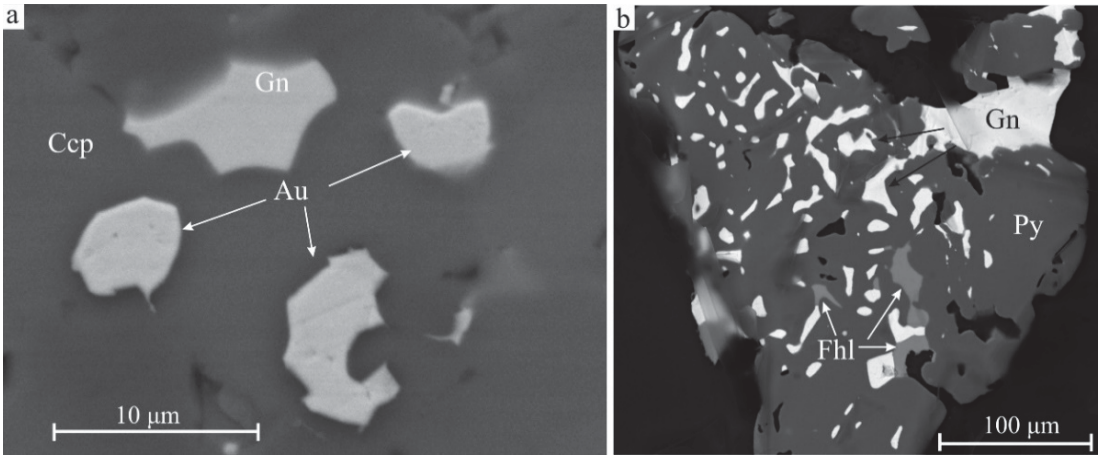

Figure 26. Gold and silver minerals in massive ore of the Novo-Uchaly lode. (**a**) Gold and galena inclusions in chalcopyrite, (**b**) Ag-bearing tetrahedrite and galena symplectites in pyrite.

The mineral forms of silver (Table 18) are represented by Ag-containing tetrahedrite and tennantite (Figure 26b), and rarer electrum, silver tellurides (hessite, empressite), sulphides (acanthite, uytenbogaardtite, petrovskaite) and sulphosalts (freibergite, polybasite and pearceite; Figure 27). Silver impurity in pyrite (up to 400 ppm, EPMA) was also recorded. A strong positive correlation of silver and antimony was found for the fahlore (Figure 27).

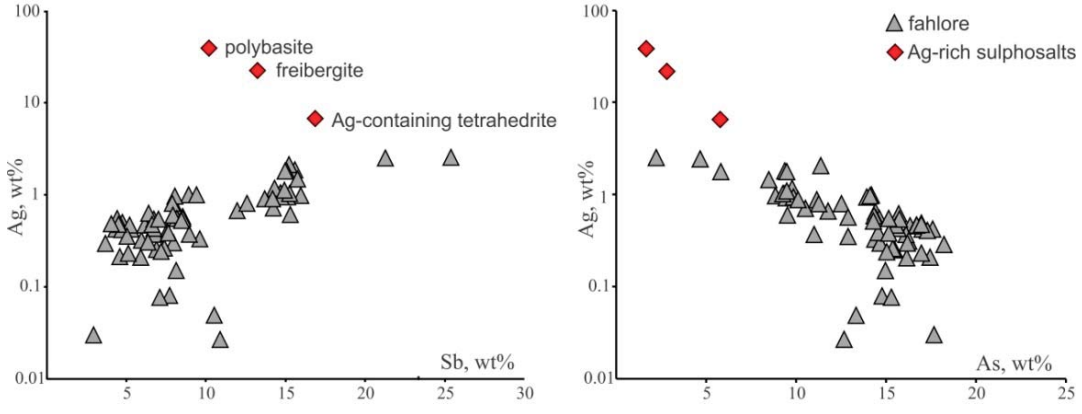

Figure 27. Dependence of the silver concentration on the arsenic and antimony contents in the fahlore and silver sulphosalts, the Novo-Uchaly lode.

4.2.4. The Galka Deposit

Along with the usually predominant pyrite, sphalerite, marcasite, chalcopyrite and less often galena, arsenopyrite, pyrrhotite, native gold, native silver, acanthite, freibergite, argentotetrahedrite, pyrargyrite, stephanite, proustite, polybasite and rare Au-Ag minerals petrovskaite, uytenbogaardtite and kurilite appear at the Galka deposit [15]. A special feature of pyrite of the Galka deposit is the increased content of As (0.027–0.878 wt%, avaverage 0.26 wt%, INAA; up to 1.5 wt%, average 0.05 wt%, LA-ICP-MS, Table 19) and Sb (7.4–873.4 ppm, average 184.2 ppm). The Sb content directly correlates with Au in pyrite (0.44–9.59 ppm, average 4.16 ppm), and Au is also directly related to Te (2.4–453.9 ppm, average 70.05 ppm) and Ag (2.15–711.7 ppm, average 137.0 ppm).

PGE shows extremely low concentrations in the sulphides of VMS ores (Table 23), although ores and industrial products contain a noticeable amount of PGE [24,25,28]. In the common VMS ores (Au 0.2–3 ppm) of the Urals, essential parts (47–87%, Figures 28a and 29) of gold are incorporated in the sulphides in the form of invisible gold. Thus, Au fails to tailings with pyrite and partly with other sulphides [15,72]. The fraction of native gold as an Au-concentrator ranges 13–90%, but this number decreases to 13–53% if the technological bulk probes enriched in Au (7.9–21.2 ppm) are excluded (Figure 28a). Native gold and other gold minerals occur in ore samples with bulk Au content higher than 3 g/t [37,67,104,105].

Table 23. Contents of PGE in ore minerals of VMS deposits, LA-ICP-MS data, ppm.

Deposit	Minerals	Pt	Pd	Rh	Ru	Os	Ir
Gai	fahlore	-	-	12.6	0.062	0.005	0.01–0.07
	sphalerite	0.016	-	-	-	-	-
Uchaly	pyrite	-	0.03–0.2	0.04–0.26	-	-	-

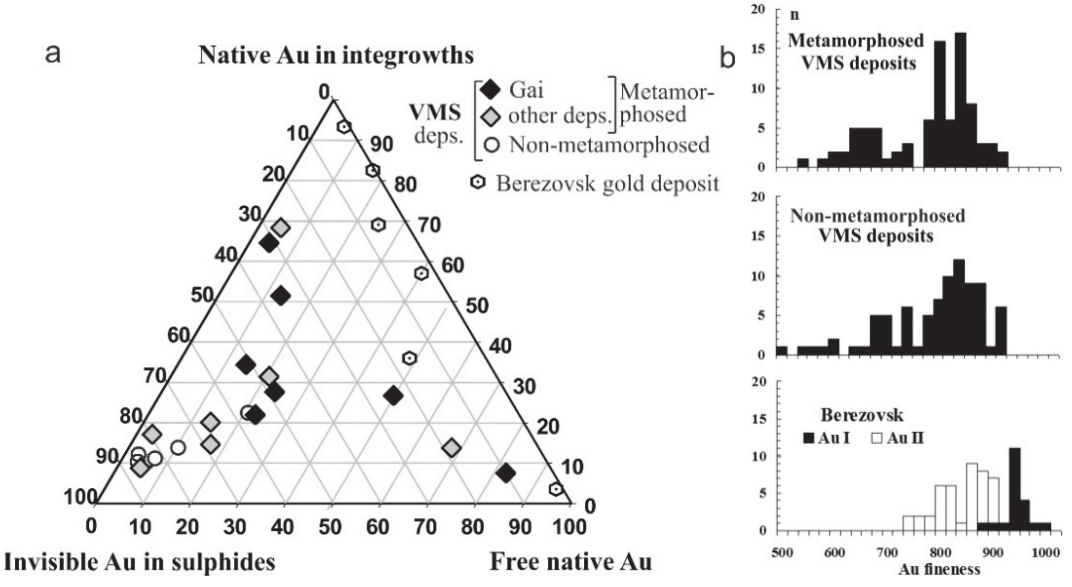

Figure 28. Gold in sulphide ores of the Berezovsk and VMS deposits of the Urals. (**a**) Gold occurrence forms in the ore, based on the results of step-by-step autoclave leaching of technological bulk probes; (**b**) gold fineness, microprobe data.

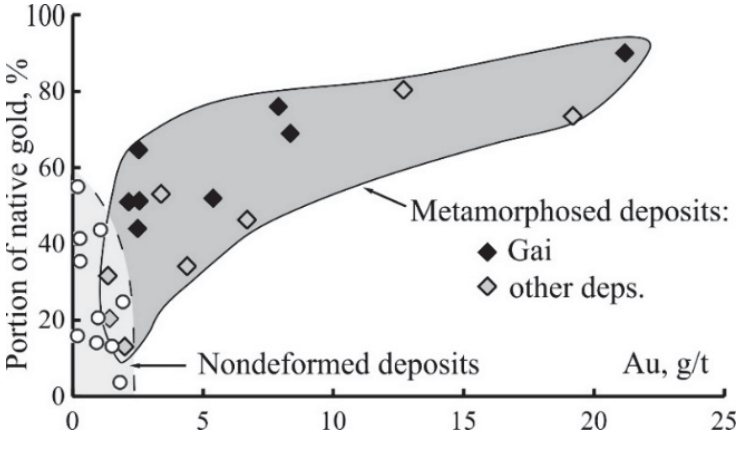

Figure 29. Correlation between the portion of native gold and the gold content in the ores of the highly and weakly metamorphosed VMS deposits of the Urals.

In the VMS deposits of the Urals, native gold forms grains and aggregates with size of about 1–50 μm and up to 150 μm. Larger grains are rare [103]. The fineness of gold ranges from 340 to 900 for slightly transformed deposits and from 500 to 980 for highly metamorphosed deposits (Figures 28b and 30). Ag content varies from 11.88 to 39.45 wt%, and admixtures (wt%) of Pt up to 2.23, Pd up to 0.85, Te up to 1.17, Hg up to 0.89, Fe up to 0.5 and Se up to 0.49 are found. Hg-bearing native gold (8–11 wt% Hg) rarely occurs. According to the high-resolution transmission electron microscopy (HR-TEM) data, nano-sized particles of native gold (1–50 nm) occur in pyrite of the VMS ores [15].

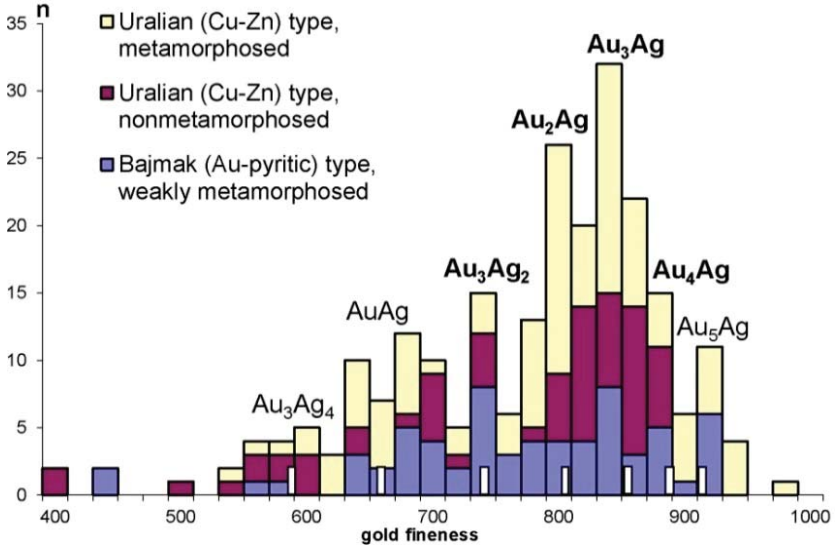

Figure 30. Composition range of native gold in massive sulphide ores of the Urals.

Characterising native Au-Ag solid solution, we adhere to the terminology adopted in early publications [106,107]: native silver, $Ag_{1.0}Au_{0.0}$–$Ag_{0.94}Au_{0.06}$ (0–100‰); küstelite, $Ag_{0.94}Au_{0.06}$–$Ag_{0.85}Au_{0.15}$ (100–250‰); electrum, $Ag_{0.85}Au_{0.15}$–$Ag_{0.44}Au_{0.56}$ (250–700‰); high-fineness gold, $Ag_{0.44}Au_{0.56}$–$Ag_{0.0}Au_{1.0}$ (700–1000‰). Native gold with fineness ~780–860 is commonly dominated in VMS deposits of the Urals (Figure 30), but more low-fineness gold is found in some VMS deposits of the Urals, the Galka, for example (fineness ~640–720).

4.3. Experimental Results

4.3.1. Geochemistry of Au in Sulphides

An experimental study of concentration mechanisms of NM in base metal sulphides was conducted in the frame of the Russian Scientific Foundation grant No. 14–17-00693 "Distribution and structural-chemical state of noble metals in sulphides through the ore deposits from magmatic to hydrothermal as an indicator of the conditions of mineralisation" (2014–2018), led by the first author. As a result of work on the sources of synchrotron radiation measurement, X-ray absorption spectra (XANES/EXAFS) and interpretation of the resulting data, and using X-ray photoelectron spectroscopy, the position of gold in the structure of sulphides was revealed. Main results were published in a series of papers devoted to Au in covellite CuS [16,17], in Fe-S and Fe-As-S minerals [19,52], in sphalerite (e.g., [92]), Au, Ag, Pt and Pd in pyrite and pyrrhotite [91], Pt in pyrite [22] and pyrrhotite [23].

Gold can form a solid solution with Fe-S and Cu-Fe-S minerals. When pyrite is heated, chemically bound Au, even in the presence of liquid sulphur, is released as a metal, while in copper minerals, heating, on the contrary, promotes the transition of the metal into a "chemically bound" form. In general, results [17,19,22,52,91,92] suggest that Au and other NM (PGE, Ag) can occur in the chemically bound state in the Cu-Fe and Cu-Zn-Fe sulphide ores.

Below, we will focus on zinc sulphide and its close crystal-chemical "relative" greenockite. Both minerals—unlike pyrite and arsenopyrite (see, e.g., [19,52,91] and references within)—are much less studied experimentally (e.g., [108]). Zinc sulphide occurs in nature in two polytypes—sphalerite and würtzite—or their mixture. These phases have different chemical elements' solubility limits. Both forms of ZnS are important in mineralogy as many minerals crystallise in the same structures. For example, there are würtzite and spha-

lerite forms of AgI (iodargyrite and miersite) and CdS (greenockite and hawleyite) [109]. Most of our gas vapour transport and salt flux experiments led to the formation of pure cubic sphalerite. The existence of minor amounts of würtzite in sphalerite crystals, probably arising due to the changes in the sulphur fugacity in the system, contributed to the formation of low-Au-saturated ZnS (<50 ppm Au) with inhomogeneity distribution of all the admixtures. However, we never obtained pure würtzite using the mentioned methods. To supplement missing data on Au solubility, we used synthetic crystals of greenockite as a model compound for the würtzite-type structure.

4.3.2. Noble Metal Speciations in Synthetic Sphalerite and Greenockite

For synthesis experiments, the starting mixtures were pure ZnS (würtzite) or CdS, and several milligrams of In_2S_3, FeS and MnS for sphalerite or greenockite. The initial phases were powdered in the agate mortar and then loaded into silica glass ampoules (10–11 mm outer diameter, 8 mm inner diameter and ~110 mm length) together with Au metal wire and transport agent or salt mixture. We used mainly the eutectic mixture of NaCl/KCl in the salt flux experiments, and the amount of salt flux melt was approximately 50–65% of the ampoule volume. We used both I_2 and NH_4Cl as transport agents in chemical vapour transport experiments. The total quantity of the obtained crystals was higher when we used NH_4Cl compared to I_2. It is important to note that we control the activity of gold by the presence of pure metal wire inside the ampoule. Therefore, the concentration of gold in sphalerite represents the maximum possible value for the given parameters. In one series of chemical vapour transport experiments, a tiny piece of sulphur was added before sealing. Then, we performed a synthesis without adding any additional sulphur. To understand the influence of $f\,S_2$ on the concentration of gold in the final crystals, different amounts (from 0 to 0.035 g) of sulphur were added to the ampoules of the chemical vapour transport suite. The loaded ampoules were evacuated up to 10^{-4} bar, sealed with an oxygen-gas burner and placed into a horizontal tube furnace that was then heated to the synthesis temperature over 2–3 h and then kept at this temperature during 16–30 days. The temperature gradient in the furnace was 50–100 °C, and the measured temperature at the hot end of the ampoules was 850 °C. At the end of the experiment, the ampoules were quenched in cold water. Sphalerite crystals were found in the cold end of the ampoules (Figures 31–33). It is important to note that the attempts to synthesise Au-bearing sphalerite at the lower temperatures using other salt mixtures (e.g., CsCl/NaCl/KCl mixture at 645 and 555 °C at the hot and cold end of the ampoule respectively, and LiCl/RbCl mixture at 470 and 340 °C, respectively) led to the formation of tiny crystals of sphalerite with the gold content < 5 ppm. These crystals cannot be used for the XAFS study due to the difficulties in measuring low amounts of the impurities. Therefore, we did not use these samples in our further observations. Only high-temperature synthesis (≥850 °C in the hot end of the ampoule) led to the crystallisation of Au-rich crystals.

Table 24. Concentration of In (C_{In}) and Au (C_{Au}) in the crystals grown at 850 °C using gas transport method and NH_4Cl as a transport agent (LA-ICPMS data, ppm ± 2σ).

Sample	2027	2032
C_{In}	86 ± 5	5400 ± 200
C_{Au}	5 ± 3	84 ± 10

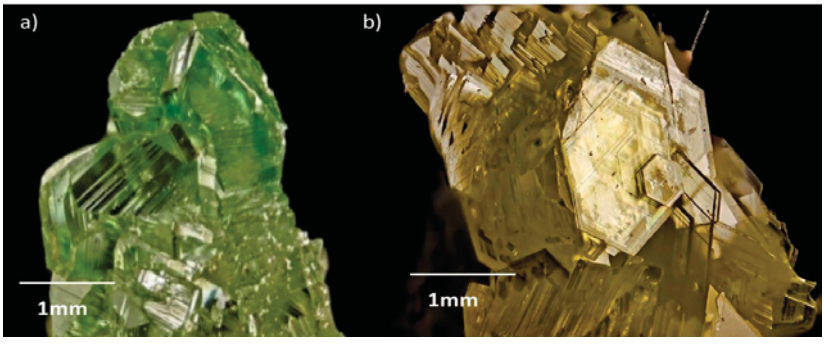

Figure 31. Microphotos of the light-green synthetic sphalerite with admixture of In and Au. (**a**) Sample 2027, (**b**) sample 2032; see Table 24 for details. Figure 31, Figure 32, Figure 33 and Figure 40—photos prepared by Timofey Pashko.

Table 25. Concentration of In and Au according to LA-ICPMS data (ppm ± 2σ) in the crystals grown using the gas transport method with various fugacity of sulphur at 850 °C.

Samples	2289	2290	2291	2292
C_{In}	64 ± 14	1913 ± 113	6914 ± 212	7012 ± 201
C_{Au}	6 ± 1	3314 ± 112	5142 ± 224	6033 ± 511
$f\ S_2$, bar	0.1 [1]	0.23	2.26	8.72

[1] Sulphur fugacity of this sample is conditionally calculated as minimal in this system.

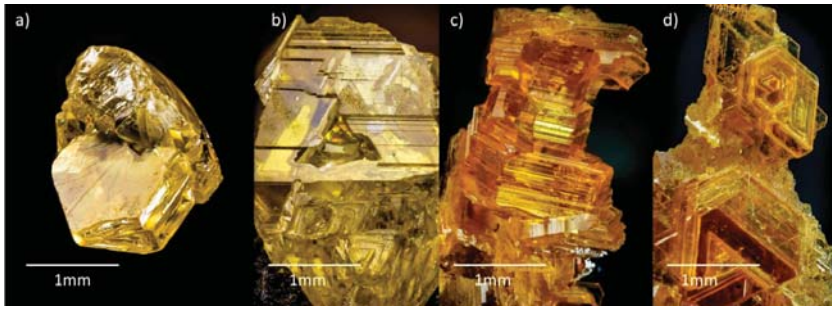

Figure 32. Microphotos of the yellowish sphalerite crystals with admixture of In and Au, synthesised at various $f\ S_2$, see Table 25 for details. (**a**) Sample 2289, (**b**) sample 2290, (**c**) sample 2291, (**d**) sample 2292.

The synthesis of Ag-bearing sphalerite using the gas transport method and silver wire led to the formation of Ag-bearing sphalerite with heterogeneous distribution of the dopant in some cases. We also tried to grow crystals of Ag-bearing sphalerite at low temperatures in an eutectic mixture of LiCl/RbCl at 550 and 460 °C at the hot and cold ends of the ampoule, respectively. The products of the synthesis contained the needles of Ag_2S. According to the phase diagram, the optimal way of Ag-bearing sphalerite synthesis is conducted by the calculated amount of Ag_2S as a dopant source instead of Ag wire for such experiments.

Figure 33. Microphotos of the synthetic sphalerite crystals with admixtures of Ag and In, synthesised using the gas transport method (sample 4197). According to EPMA [108], C_{Ag} = 4.74 ± 0.82 wt%, C_{In} = 5.15 ± 0.46 wt%. However, according to (N. Trofimov, pers. com.), $C_{Ag(min)}$ = 3.41 wt%; $C_{Ag(max)}$ = 75.99 wt%, because of the capture of the tiny Ag_2S inclusions in the analysis, and $C_{In(min)}$ = 0.64 wt%, $C_{In(max)}$ = 5.85 wt%.

The chemical composition of the final crystals was studied both by EPMA (for the major and minor elements) and by LA-ICPMS (for the trace elements). Experiments show that in simulated conditions, as in nature (e.g., [15]), sphalerite can incorporate more Au in the presence of admixtures of other elements. Natural sphalerite can contain Au, Ag, Cu, Tl, Hg, Fe, Mn, Cd, In, Ga, Ge, As, Bi, Pb, etc. [8]. Some of these chemical elements are presented in the form of mineral microinclusions (e.g., Pb, Bi, etc.), while others can substitute Zn^{2+} (e.g., Cd, Mn, Fe, etc.) in the crystal structure of sphalerite [8]. We prepared the sample with admixtures typical for the natural environments: Fe, Mn, Se, In and Cd, together with gold, which were added one by one, in pairs, or simultaneously. The elements are evenly distributed inside the sphalerite (Figures 34 and 35; [110]). In the resulting crystals, we observed an extremely high concentration of gold (up to 3000 ppm) in comparison with the sample of the Fe-bearing sphalerite with Au (up to 250 ppm) (Figures 35–39).

According to chemical analysis, the amount of Au increases instantly with the increase of the sulphur fugacity in cases when In was added to the system (Figures 36 and 37, shaded symbols). In some synthesis experiments, adding more than 2.28 wt% In leads to the formation of intergrowths of sphalerite and sulphospinel phase of the approximate composition $ZnIn_2S_4$ (Figure 38a). In the absence of indium, C_{Au} does not exceed 10 ppm (Figure 37, non-shaded symbols). In the synthesis experiments, the close coalescence of sphalerite crystals with native gold dendrites (Figure 40) indirectly confirms that we are probably dealing with the maximum values of Au impurity that can enter the composition of sphalerite under these conditions.

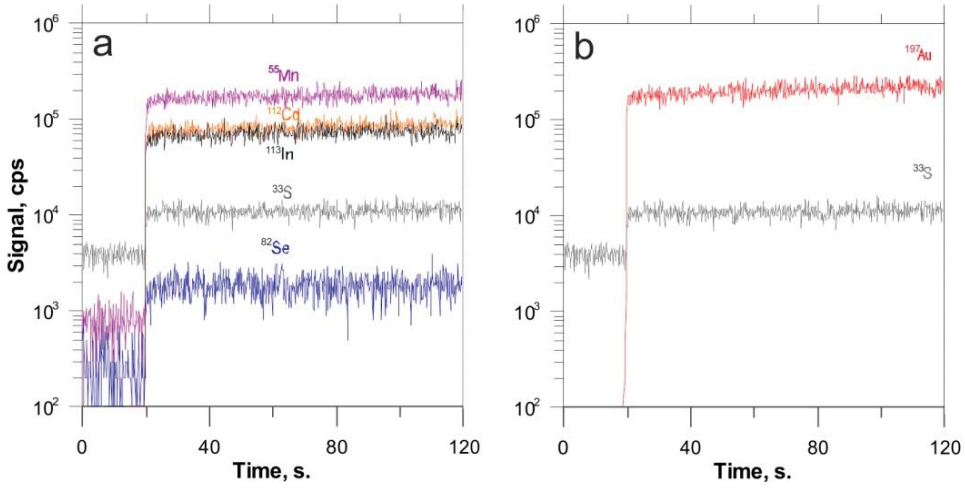

Figure 34. LA-ICPMS profile through sphalerite containing Fe, Mn, In, Cd, Se and Au. (**a**)—signals for Mn, Cd, In, S, Se; (**b**)—signals for Au, S. See Table 26 for details.

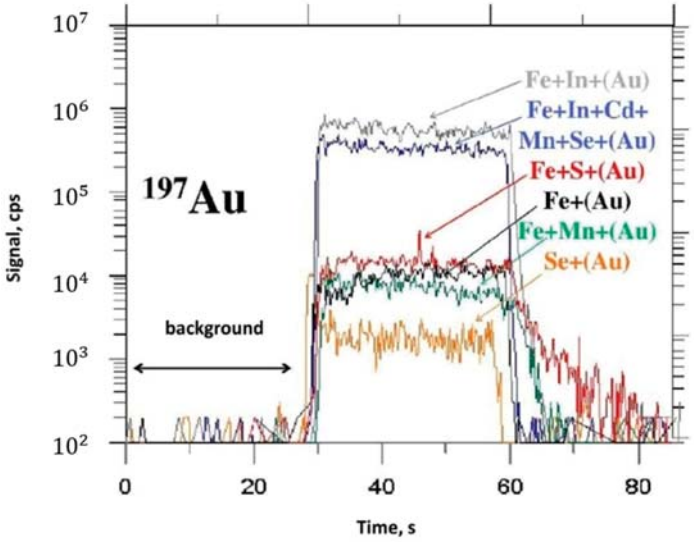

Figure 35. LA-ICPMS profile through sphalerite containing Au and different additional impurities. Salt flux synthesis at 850/750 °C, see Table 27 for details.

Table 26. Chemical composition of ZnS sample 1450 (EPMA) synthesised at 850 °C using the gas transport method with I_2 as a transport agent.

FeS, mol%	wt% ± 2σ								
	Zn	**S**	**Fe**	**Mn**	**Cd**	**Se**	**In**	**Au**	**Total**
2.80	63.95 ± 0.51	33.73 ± 0.32	1.62 ± 0.13	0.24 ± 0.05	0.48 ± 0.11	0.13 ± 0.07	0.32 ± 0.03	0.30 ± 0.05	100.77

Table 27. Concentration of Au in the samples of synthetic sphalerite doped by different admixtures, grown using the salt flux method (in eutectic melts of NaCl/KCl) at 850 °C.

Sample (color [1])	FeS, mol.%	EPMA, wt% ± 2σ								Total	Formula	LA-ICPMS, wt% ± 2σ
		Zn	**S**	**Fe**	**Mn**	**Cd**	**Se**	**In**	**Au**			
1660 (blue)	3.70	64.15 (0.50)	33.72 (0.11)	2.15 (0.07)	0.12 (0.02)	0.50 (0.04)	0.25 (0.03)	0.17 (0.02)	0.20 (0.01)	101.26	$Zn_{0.94}Fe_{0.04}S_{1.01}$	0.1892 (0.0112)
1661 (grey)	3.24	65.08 (0.43)	33.82 (0.49)	1.89 (0.06)	-	-	-	0.22 (0.03)	0.20 (0.01)	101.21	$Zn_{0.95}Fe_{0.03}S_{1.01}$	0.2092 (0.0082)
1662 (black)	1.67	64.77 (1.61)	33.37 (0.85)	0.96 (0.01)	-	-	-	-	-	99.66	$Zn_{0.96}Fe_{0.02}Cu_{0.02}S_{1.01}$	0.0077 (0.0046)
1663 (green)	4.20	64.17 (0.89)	33.51 (0.39)	2.44 (0.08)	0.50 (0.10)	-	-	-	-	100.62	$Zn_{0.94}Fe_{0.04}S_{1.01}$	0.0094 (0.0012)
1665 [2] (red)	4.33	63.29 (1.45)	33.33 (0.71)	2.48 (0.22)	-	-	-	-	-	99.10	$Zn_{0.94}Fe_{0.04}S_{1.01}$	0.0096 (0.0046)
1666 (yellow)	-	67.09 (0.64)	33.19 (0.23)	-	-	-	0.94 (0.06)	-	-	101.22	$Zn_{0.99}SSe_{0.01}$	0.0014 (0.0007)

[1] Colour on graph (Figure 35); [2] Synthesis with adding a few mg of additional sulphur in the ampoule.

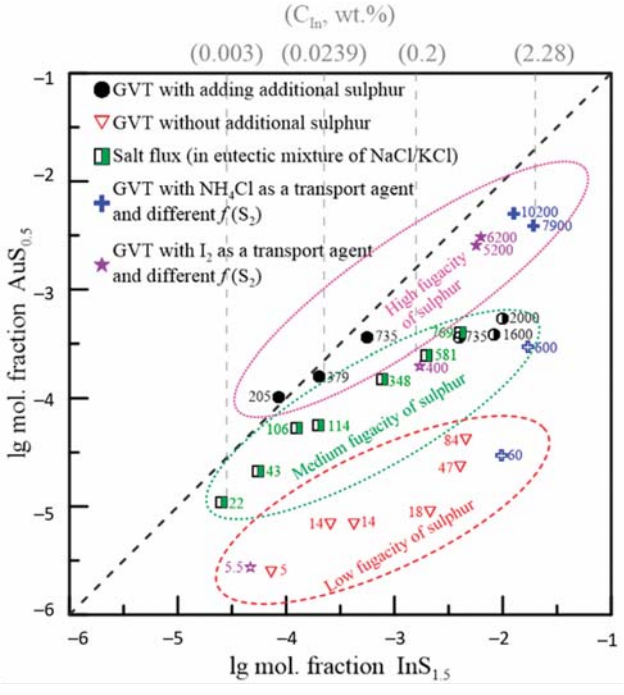

Figure 36. Graph showing the relation between the In and Au concentrations in the synthetic crystals of sphalerite. Numbers near the marks correspond to C_{Au}, ppm. GVT (gas vapour transport)—gas transport method. Synthesis procedure is described in [90].

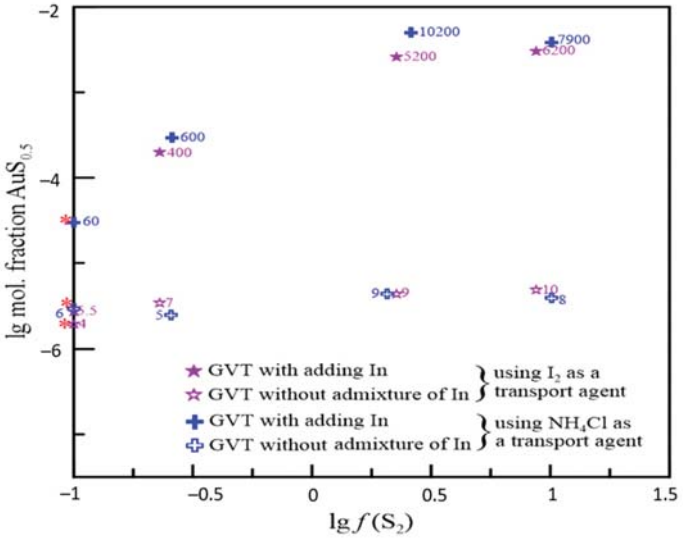

Figure 37. Chemical composition (in mol. fraction $AuS_{0.5}$) of sphalerite crystals doped in In and without admixture of In synthesised at various activity of sulphur f S_2. Here, and in Figure 39, numbers near the marks show the concentration of Au in ppm. Red asterisks (*) indicate samples whose fugacity is conditionally shown as minimal in these systems.

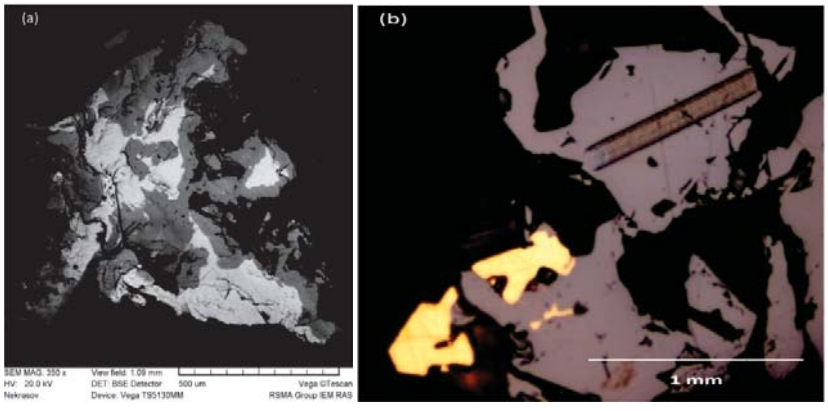

Figure 38. The internal structure of the synthesised crystals of sphalerite (polished sections). (**a**) Intergrowth of sphalerite (dark grey in BSE) with sulphospinel (light grey) with the approximate composition $ZnIn_2S_4$, (**b**) intergrowths of sphalerite with native gold, reflected light. There is also a LA-ICPMS pathway (width of the ablated zone is 60 μm) in the right corner of the image.

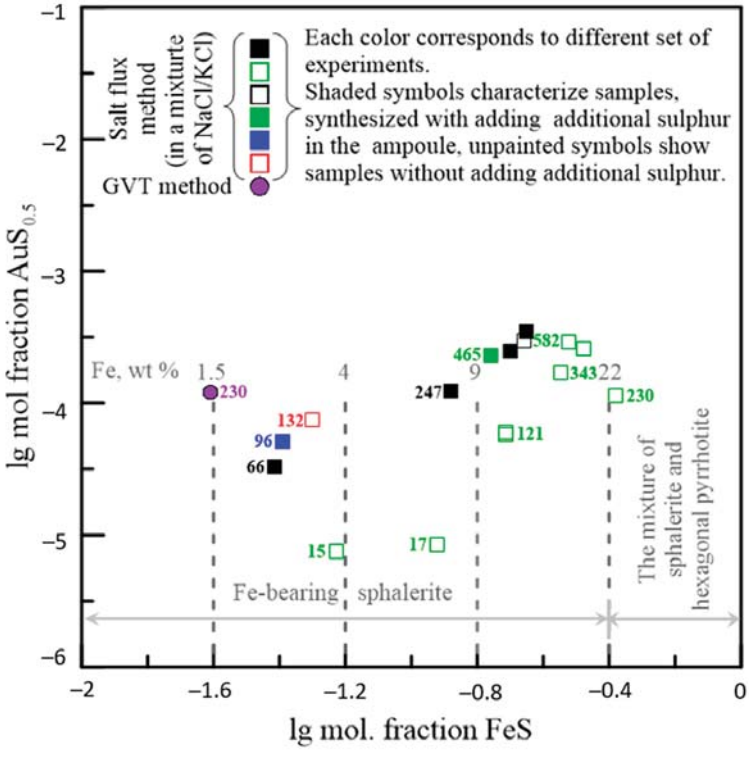

Figure 39. Relation between the Fe and Au concentrations in the synthetic crystals of sphalerite. Crystals were synthesised at ~850 °C at the hot and ~750 °C at the cold end of the ampoule. Grey lines show the concentration of Fe (wt%, EPMA) for some samples.

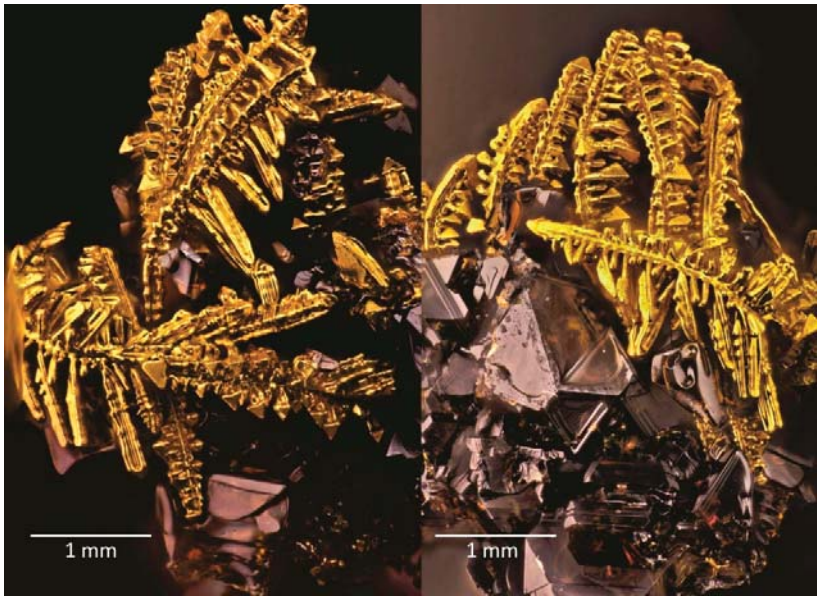

Figure 40. Microphotos of the synthetic sphalerite crystals with native gold dendrites, synthesised using the salt flux method (sample 1662).

Our experiments on solubility of Pt, Pd, Os and Ir in sphalerite show that these noble metals cannot penetrate into the structure of zinc sulphide, even in the low amounts.

The presence of In and/or Fe admixtures also affects the concentration of Au in synthetic crystals of greenockite (Table 28; Figure 41 [111]). The concentration of Au in In- and Fe-doped greenockite is ten-fold higher in comparison with pure CdS. The distribution of Au, Ag, In, Cd, Se, Fe and Mn in sphalerite and greenockite is homogeneous according to the LA-ICPMS line mode spectra (Figures 34, 35 and 41).

Table 28. Chemical composition of greenockite crystals with admixtures of Fe, In and Au, synthesised using the gas transport method at 850 °C.

Sample	EPMA, wt% (±2σ)						LA-ICPMS Au, wt% (±2σ)
	Cd	S	Fe	In	Au	Total	
5457	78.18 (0.07)	22.23 (0.17)	-	-	bdl	100.41 (0.24)	0.0015 (±0.0005)
5458	74.78 (0.22)	22.84 (0.29)	2.84 (0.04)	-	bdl	100.46 (0.55)	0.0410 (±0.0005)
5459	77.76 (0.62)	22.27 (0.23)	-	0.73 (0.03)	bdl	100.77 (0.88)	0.0311 (±0.0020)

bdl—below the detection limit.

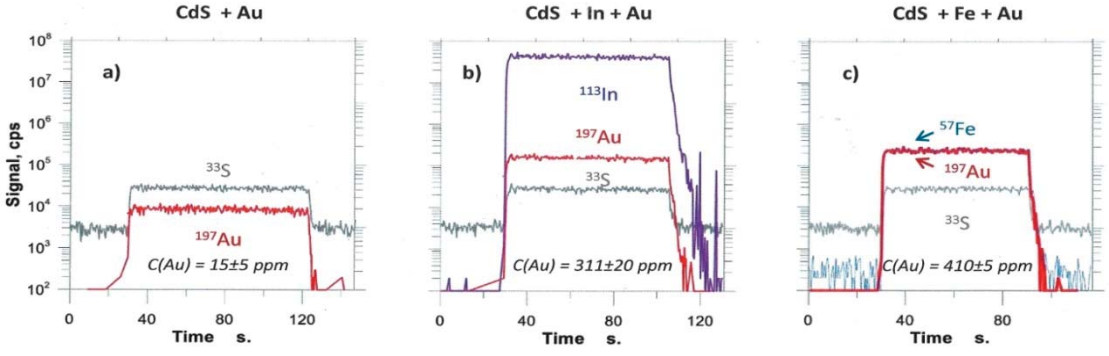

Figure 41. LA-ICPMS line mode spectra of the line ablated through the samples of CdS with admixtures of gold (**a**) sample 5457, indium and gold (**b**) sample 5459, iron and gold (**c**) sample 5458.

5. Discussion

A significant part of the primary gold reserves in Russia and the world are sulphide ores ([112–114] and references cited therein). Many sulphide ores are classified as refractory by technologists. It is the deposits of refractory sulphide ores that are the main potential source of gold production. The refractory gold and silver in sulphide ores can be associated with micro- and nanoinclusions of gold and silver minerals as well as isomorphous, colloidal, surface and adsorbed species of NM. However, the forms of invisible gold and other NM are still insufficiently investigated.

A series of authors' papers [9,15,24,25,39,63,67,80] were devoted to the problem of invisible and microscopic gold in sulphides. Based on the study of the VMS ores of the Urals (e.g., [15,25,67,115]), Rudny Altai [76,116] and modern hydrothermal systems of the ocean floor [76,117–119], it was concluded that gold was primarily manifested in an invisible form, mainly in iron and copper sulphides. Gold enlargement with its release in the form of its own minerals occurred during later epigenetic hydrothermal processes and metamorphism. Native gold and Au-Ag tellurides, sulphides and selenides are found as microinclusions in base metal sulphides, particularly in pyrite, marcasite, chalcopyrite, sphalerite and arsenopyrite sulphosalts [112]. The size and shape of gold particles and their 3D mineral associations within ore samples were established by X-ray tomography [120].

Invisible gold should include gold in the form of a solid solution or an isomorphous impurity that is part of the structure of the Au-Ag-bearing matrix minerals. Invisible gold also includes fullerenes, colloids, clusters and surface-bound gold < 1 nm [15,121,122].

In gold deposits of the Urals, the portion of invisible gold is usually small, for example, only 1–16% in the mesothermal Berezovsk deposit and ~20–30% of the bulk Au in the Vorontsovka Carlin-style gold deposit [9,63,105], but it can also be very high. The data of local analyses (LA-ICPMS, INAA, EPMA, SEM/EDS) allow us to estimate the portion of bound Au in pyrite ~60% of the bulk Au of ores from the Novogodnee-Monto gold-skarn deposit [40], and even more, ~80% of the bulk Au for the Petropavlovsk gold-porphyry deposit [39,40].

Based on the composition, pyrites of the Berezovsk deposit can be divided into two groups: (1) Au-bearing, and (2) virtually Au-free. Pyrite of the second group prevails; in this pyrite, Au occurs in the amount of 0.08–0.1 ppm in the mode of single peaks of the group of Ag-Pb-Cu-Sb, probably in the form of microinclusions of native gold in pyrite in intergrowths with galena and fahlore. The Au-bearing variety of pyrite of the first group may contain structurally bound Au (C_{Au} up to 73.5 ppm, INAA; 21.8 ppm, LA-ICPMS). It is generally accepted that all gold in the deposit is free, i.e., it is found exclusively in the form of native gold. The new data obtained indicate, although rarely, the presence of finely dispersed, possibly chemically bound gold in pyrite. Such pyrite could be formed

during late, relatively low-temperature processes, later than "ordinary" pyrite with a zonal distribution of Co, Ni and As, which carries gold only in the form of native gold inclusions.

In galena from the sulphide-quartz veins of the Shartash granite massif, Berezovsk gold field, there are correlations in the Ag-As-Se-Bi-Sn series (r = 0.8–0.9) and in the Bi-Te (r = 0.84) and Bi-Tl (r = 0.7) pairs. Since the distribution of the elements is uniform, we can assume that they enter the galena isomorphic according to the schemes: $(Ag,Tl,Cu)^{+} + (Bi,As,Sb,In)^{3+} \leftrightarrow 2Pb^{2+}$, $(Sn)^{4+} + 2(Ag,Tl,Cu)^{+} \leftrightarrow 3Pb^{2+}$, $(Se,Te)^{2-} \leftrightarrow S^{2-}$. A high degree of correlation is observed in the Cu-Sb (r = 0.87), Cu-Ag (r = 0.72) and Ag-Sb (r = 0.89) pairs. The inhomogeneous joint distribution of Au with Cu and Sb may be related to the finely dispersed inclusions of bournonite $CuPbSbS_3$ since the latter is a characteristic common humbeite mineral, and its presence could contribute to the deposition of submicroscopic native gold.

In the Urals, about 25 million tons of VMS ores are processed per year, only 15–40% (for various plants) of the total gold is extracted and losses with pyrite concentrate and in the tailings of enrichment amount to 13–15 tonnes of Au per year [77].

For weakly metamorphosed VMS deposits, the following sequence of decrease in the invisible gold concentration in sulphides is observed: galena (up to 122 ppm, geom. mean 90.5 ppm)–chalcopyrite (40/9.6)–pyrite (10/1)–marcasite (5/0.6)–sphalerite (6/0.4). For highly metamorphosed VMS objects: pyrite (31/2.3)–chalcopyrite (8/0.65)–sphalerite (0.7/0.4)–arsenopyrite (0.7/0.2)–fahlore (3.3/0.12)–bornite (3.2/0.06)–pyrrhotite (0.1/0.05)–galena (0.1/0.04), and, in general, $C_{invis.\ Au}$ is noticeably lower.

Estimates of the portion of invisible gold in VMS deposits in the Urals vary widely (within 30–90% of the total gold of ores) at a concentration of such fine gold from 0.8 to 5 g/t [9,72]. Higher values (~65–85% of the bulk Au of ores) are typical for the portion of invisible gold of weakly metamorphosed ores [15,36]. With increasing metamorphism [57], the contents of Au and Ag in the main ore-forming sulphides (sphalerite, chalcopyrite, pyrite) generally decrease [25,112]. In most cases, the portion of invisible gold also decreases (~35–60% of the total ore volume), so there is an inverse correlation between the proportion of invisible gold and the increase in the degree of metamorphism of ores [9,57,89]. As a result of the recrystallisation of ores, the invisible gold is enlarged and passes into the visible state [67,94].

For the VMS deposits of the Urals, the Z-shaped variation of native gold composition (Figure 30) probably reflects the continuous-discrete character of the Au-Ag solid solution. The presence of possible miscibility gaps in this binary system was discussed in [106,123,124]. Independent mineral phases with contrasting compositions were clearly recorded in the Ag-rich zone [123]. In [124], species with Ag < 25 wt% are referred to the zone of stable solid solutions, but at least two phases (Au_3Ag and AuAg) are believed to be present in the Ag-depleted zone. According to [106], the existence of the Au_2Ag compound is the most probable in nature. Our data obviously confirm these assumptions, although the occurrence frequency of electrum (AuAg) in the VMS deposits of the Urals is lower than that of Au_3Ag and Au_2Ag.

However, only in the last two decades, with the broad involvement of the LA-ICPMS method and other spectroscopic methods ([6,7,14,17,19,92,119–121,125–128], etc.), did a breakthrough in studying the forms of noble metal occurrence in sulphides become possible. LA-ICPMS or EPMA correlation analysis of the concentrations in a particular mineral usually gives uncertain conclusions. However, these methods predominate in ore geology (see, e.g., [129] or [130]). X-ray absorption fine structure spectroscopy allows getting more definite results, especially for synthesised sulphides [17,19,52,92], but the beam-time is more expensive and data processing is complicated by concentration levels of NM impurities in studied sulphides (see [15] for a discussion).

Below, we will focus on our data on the noble metal speciation in synthetic sphalerite and greenockite.

5.1. Conditions Conducive to the Formation of Au-Saturated Sphalerite

Sphalerite is not considered as a significant source of Au production during the mining and processing of ore deposits [8]. However, a noticeable amount of gold can enter sphalerite in an invisible form [15,25,117], especially in relatively high-temperature conditions realised in medium- and high-temperature types of deposits. The typical contents for natural sphalerite are in the range of 0.1–10 ppm Au [8,15,117,131]. It can contain micro-inclusions of native gold, especially at the deposits that have undergone syn-metamorphic remobilisation [25,71]. Pure sphalerite, in contrast to bornite and chalcopyrite, is one of the weakest Au absorbers [128]. Using the phase composition correlation principle, Lipko and co-authors calculated the solubility of Au in pure and Fe-bearing sphalerite, and the latter is 3.5 times higher than in pure mineral [128]. Thus, the goal of the first experimental study was to find suitable conditions for the formation of Au-bearing sphalerite. Thus, we also addressed the evaluation of the exact chemical form of Au in synthesised specimens.

In general, the results of our experiments ([110], this study) clearly show that the concentration of Au is higher in sphalerite containing different impurity components than in its pure crystals. A similar pattern is observed in ore deposits ([15,25,37], etc.) and modern hydrothermal fields on the oceanic floor ([118,131,132], etc.). The entry of Au into sphalerite is favoured not so much by the low-temperature conditions of its crystallisation but by the supersaturated nature of the evolved magmatic fluids and the co-deposition with Au of other chemical elements, especially In, Cu and Mn.

For sphalerite, after a few series of synthesis experiments, we conclude that the main element that favours gold to "intrude" in the crystal structure of ZnS is indium [92,108,110]. Iron also affects the concentration of Au but to a lesser degree. We infer that it may be related to the valence state of the elements. Indium is a trivalent element and some recent works of our colleagues suggest that a minor fraction of iron in sphalerite is also trivalent (e.g., [133]). We propose that the same mechanism of coupled substitution as in the case of Cu [134,135] occurs in the Au-bearing-sphalerite: $Au^{+} + In^{3+} \leftrightarrow 2Zn^{2+}$. Our recent XAFS results demonstrate that at high concentrations (0.03–0.2 wt% In), Au can exist in sphalerite in two forms: primarily as a nano-sized Au_2S (or $AuInS_2$) cluster and secondarly, in the form of a solid solution (e.g., $(Zn,Au)InS_2$); according to the spectroscopic study, all trivalent In in sphalerite substitutes Zn, without any Au-In clustering [92]. Unfortunately, we were not able to observe the Fe^{3+} in the sphalerite using synchrotron methods due to the extremely low concentration of this isotope.

The EPMA and LA-ICPMS data do not provide univocal information regarding the chemical state of Au and In in ZnS. However, the XAFS method is inadequate at concentrations below hundreds of ppm. Therefore, in contrast to arsenian pyrite and arsenopyrite, due to the low C_{Au} in natural sphalerite, it is generally impossible to study the chemical state of NM in the mineral by this method (cf., [134]). EPMA and LA-ICPMS data complement the existing results (Figures 38, 39 and 41; Tables 27 and 28) since they do not contradict the conclusion that at least part of the gold in sphalerite exists in the form of solid solution [136]. This form may predominate at low concentrations of gold in sphalerite, especially in nature.

According to chemical analysis, the amount of Au increases instantly with the increase of the sulphur fugacity in cases when In was added to the system (Figures 38 and 39). This fact proves the mechanism of vacancies formation in cation subcell leading to the accumulation of additional gold and the existence of the following isomorphous scheme: $3Zn^{2+} \leftrightarrow 2In^{3+} + \square$, described in [137]. In our synthesis experiments, adding more than 2.28 wt% indium leads to the formation of intergrowths of sphalerite and sulphospinel $ZnIn_2S_4$ phase (Figure 40. In the absence of indium or any other impurities, C_{Au} does not exceed 10 ppm (Figures 37 and 39).

Divalent elements (notably Fe, Cd and Mn) commonly enter the sphalerite structure by isomorphic substitution of Zn (e.g., [129,138]). Other elements, for example, In, Cu and Ag, replace Zn in heterovalent coupled and/or multiple substitutions, such as: $2Zn^{2+} \leftrightarrow Cu^{+} + In^{3+}$, $2Zn^{2+} \leftrightarrow Cu^{+} + Fe^{3+}$ and $4Zn^{2+} \leftrightarrow 2Cu^{+} + Fe^{3+} + (Sn,Ge)^{4+}$ [8,129,139,140]. The latter mech-

anism may have played a fundamental role in the crystallisation of Au-bearing sphalerite from fluids of postmagmatic volcanic-arc systems, usually enriched in Au, other metals and metalloids (e.g., [141]).

Like natural samples of more chemically pure sphalerite, usually with minimal C_{Au} (e.g., [15,25]), pure synthetic sphalerite is usually unsaturated by Au compared to the specimens with admixtures ([128], this study). Tauson and co-authors [142] linked this phenomenon to the variation of the chemical bonding parameters due to incorporating of the additional metals in the structure (cf., [128]).

For synthetic crystals of Ag-bearing sphalerite doped by In (or without In), the XAFS data revealed that Ag exists in sphalerite mainly in the form of a solid solution according to the scheme $2Zn^{2+} \leftrightarrow Ag^{+} + In^{3+}$, also suggested for natural sphalerite; however, a part of Ag (<5%) exist in the Ag-bearing sphalerite in the sulphide form Ag_2S ([108]; cf., [130]). In the absence of In, XANES spectra show Ag mainly in the native element mode (formal oxidation state 0) and sulphide forms. At high sulphur fugacity in the experimental system, sulphide form Ag_2S predominates [108]. Presence of submicron inclusions of laforêtite $AgInS_2$ in Ag-, In-bearing sphalerite is probable. This mineral has the same sphalerite structure and may form a solid solution series in ZnS-$AgInS_2$ system. Occurrence of $AuInS_2$ in Au-, In-bearing sphalerite can also be assumed. Solid solution ZnS–$AuInS_2$ is also possible in nature.

Thus, gold and silver both prefer accumulation in In-bearing sphalerite as a solid solution. However, in the absence of In, their dominant forms are Au_2S, native Ag and Ag_2S, respectively. This fact corresponds to the low solubility of Au and Ag in sphalerite solid solution [128].

5.2. Correlation of As and Au Contents in Pyrite

The positive correlation of the As and Au contents in As-pyrite is noteworthy (Figure 9), which can be considered as evidence of an isomorphic substitution of the Fe position in the As-pyrite lattice (cf., [143,144]). In recent years, this has been interpreted as Au sorption on the growing faces of pyrite crystals [143,145,146]. For example, at sediment-hosted Carlin-type ore, invisible gold in arsenic disulphides represents Au deposited from the metal-bearing fluid by chemisorption at As-rich, Fe-deficient growth surfaces and incorporated into the sulphide crystals in the mode of metastable solid solution [96]. It corresponds to our data for the Vorontsovka Carlin-style deposit (Figure 9).

However, in other cases, there is a weak negative correlation of Au with As according to LA-ICPMS data for pyrite of the Geita Hill, Kumtor and Witwatersrand Carbon Leader Reef giant gold deposits [127]. A similar situation (there is no positive Au/As correlation in pyrite or it is very feeble) is observed for many deposits everywhere [6,8,31–35,43], as well as for many sulphide deposits of the Urals [36–42].

When analysing As-pyrite, two aspects should be considered: As and Au impurities in pyrite and their relationship. Thus, the maximum solubility of As in pyrite at 600 °C according to the experimental data of Clark [147] is 0.53 wt%, and As content reaches 9.3 wt% in natural pyrites [96,148], and some researchers detected up to 14 wt% As in pyrite (e.g., [149]). Moreover, most researchers note that the sum of the S and As contents in pyrite remains ~66.7 at%, and they interpret low As concentrations (up to ~1.2 wt% As) as a solid solution with local clustering of As atoms. However, at higher concentrations of As in pyrite (6–9 wt%), arsenopyrite domains were detected on the HRTEM images [150,151]. Another feature of the As-pyrites that should be noted is the inhomogeneity and, more often, zoning in the distribution of As, which can be caused by changes in the crystallographic orientation of the phase (different interplanar distances and changing parameters of the solid solution) and fluctuations in the contents of not only sulphur but also iron [18,152] as well as other impurities (see [15] for discussion). Perhaps this is consistent with the inhomogeneous type of conductivity in a single crystal [153].

In many cases, there is a linear positive dependence of the increase in the gold content in pyrite on the level of arsenic concentrations (e.g., [143]). Simultaneously, there are

two clusters of Au content points in this dependence: in the range of 2–5 wt% As and 6 and above [149]. This fact, as well as in the case of the entry of only As impurities into pyrite [40], can probably be explained by a change in the structural form of the entry of Au into As-pyrite: at relatively low concentrations of As (2–5 wt%), gold enters the solid solution S_2^{2-}AsS AsS^{3-}, and at high concentrations of As, gold enters the pyrite and marcasite-structural (arsenopyrite) domains.

Unlike arsenic, the situation with tellurium in pyrite is quite different. Tellurium is also a common isomorphic impurity in pyrite, but its abnormally high contents are due to the occurrence of submicroscopic and nano-scale inclusions of Au-Ag tellurides (mainly hessite and petzite) in this mineral. For the Petropavlovsk gold-porphyry and Novogodnee-Monto Fe-Au-skarn deposits, similarly to in [143], a positive correlation of Au and Ag with Te in pyrite corresponds to the probable occurrence of tiny telluride grains in the smallest defects in the mineral (Figures 16 and 20). It is also proven by the presence of synchronous peaks of Te, Au and Ag on the graphs during laser ablation by the profile sampling mode (Figures 17 and 19) or bright points of their segregations on Te distribution pictures during mapping mode analysis (Figures 18a and 21).

5.3. Forms of Gold in Arsenopyrite

Intensive debates about the forms of gold in arsenopyrite of 1988–1989 ([95,154,155], etc.) remain unsettled (see reviews in [19,51], cf., [156,157]). Gold in the chemically bound, structural form commonly reaches its maximum values in this mineral (e.g., [12,128,155]). Simultaneously, there are opposite opinions on the peculiarities of the chemical composition of Au-rich arsenopyrite. In most studies, the ratio As/S>1 is noted in the composition of Au-bearing arsenopyrite [63,96,97,154,158]. However, in other papers, sulphuric (deficient in As) arsenopyrite is richer in Au [12,156,159–162]. Some authors reported about As- and S-rich arsenopyrites both rich in gold.

For the Vorontsovka deposit, the data obtained for arsenopyrite crystals in Carlin-style gold-sulphide assemblage indicate the presence of an inverse correlation between the Au and Fe contents and a direct correlation for Au/As (Figure 42; cf., [96]). Besides, this dependence is manifested not only at the local level within a single crystal, but also in the whole deposit, because more arsenic Apy-2, according to the point analysis by the LA-ICPMS method, contains more gold (4–315 ppm, mean geom. 24.3 ppm, [63]). The LA-ICPMS profiles for pyrite showed that high Au concentrations commonly correlate with higher contents of As, Ag, Sb, Se or Tl (Figures 6–8; cf., [63]).

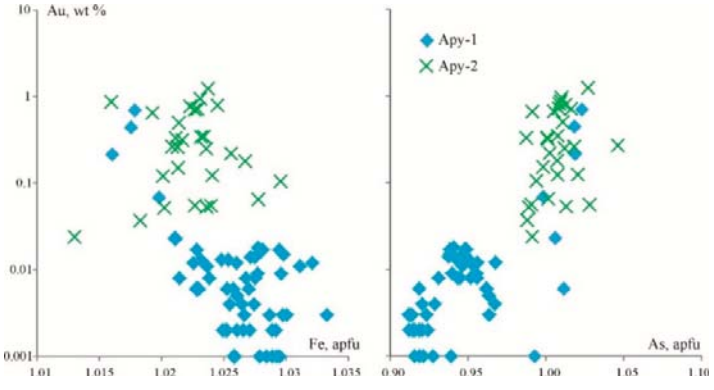

Figure 42. Relationship of Au content with the main elements (Fe and As) in the studied arsenopyrite samples of the Vorontsovka Carlin-style deposit. Blue diamonds—arsenopyrite from skarn complex (Apy-1); green crosses indicate highly arsenic arsenopyrite of the gold-pyrite-realgar assemblage (Apy-2).

In general, the set of data obtained for the samples of synthetic [18] and natural ([63], this study) arsenopyrites shows a weak positive correlation of Au contents with the As/S ratio and a clear negative correlation between Au and Fe. The higher Au contents are typical for the As-rich and close to stoichiometric late arsenopyrite generation, while in S-rich early arsenopyrite, the Au content normally does not exceed 0.02 wt%. However, overall, early generation arsenopyrite (Apy-1) also contains fairly high C_{Au}. Gold is mainly concentrated in the As-rich, low-thickness zones of its prismatic crystals (Figures 7 and 8).

The incorporation of lattice-bound Au into arsenopyrite is resulted from the substitution of Fe by Au as both elements show negative correlation (cf., [5,157,160,161]). Au-bearing arsenopyrite is commonly thinly zonal. Unstable conditions with short-period oscillations of local disequilibrium and some fluctuations in the fluid component fugacities ($f\ S_2$, $f\ Te_2$, $f\ O_2$, $f\ As_2$) contributed to the crystallisation of the mineral with a less perfect structure, which in turn favoured the entry of gold into the composition of arsenopyrite. Auriferous zones of arsenopyrite can contain nm-sized gold particles: TEM study in FIB foils [162] identified two types of nm-sized gold particles—elongated, rod-like (or disc-shaped?) Au grains about 35 nm in length and 5 nm in thickness, and roundish gold (or disc-shaped?) grains about 10 nm in diameter.

5.4. Crystal-Chemical Basics of Noble Metal Speciation in Sulphides

Several concepts are employed to describe crystal chemistry and to build structural classification schemes of the sulphides. Since the aim of this review is not a detailed analysis of the crystal structures of sulphides, we will only briefly describe the structures of the considered minerals with some preliminary analysis of the possibilities of isomorphic substitution of cations with noble metals (mainly Au, Ag, Pd and Pt). Table 29 lists the main crystallographic features of the studied minerals. With the exception of arsenopyrite FeAsS and chalcopyrite $CuFeS_2$, all the studied minerals are binary compounds. Pyrite and galena belong to the structure type of NaCl, marcasite and arsenopyrite to the structure type of TiO_2-rutile, sphalerite and chalcopyrite to the structure type of sphalerite, greenockite and würtzite to the structure type of ZnO and pyrrhotite to the structure type of NiAs.

Principle schemes of the crystal structures of the considered minerals are shown in Figure 43.

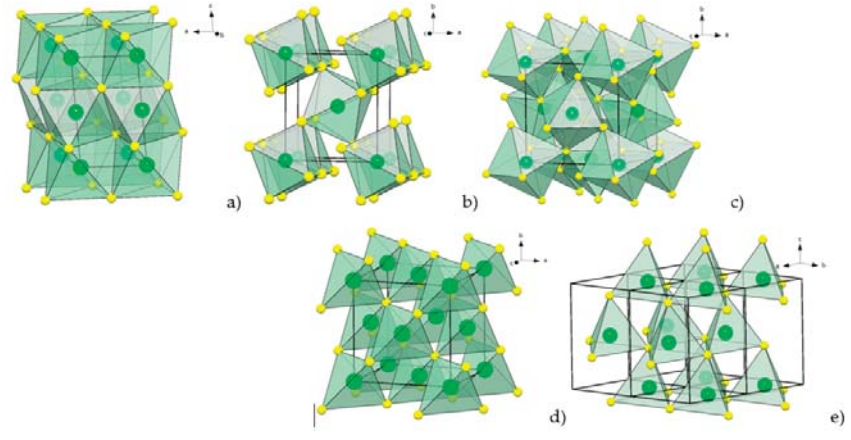

Figure 43. Crystal structures of sulphides: (**a**) pyrrhotite, (**b**) marcasite, löllengite, arsenopyrite, (**c**) pyrite, (**d**) sphalerite, chalcopyrite, (**e**) greenockite, würtzite. Green balls are cations, yellow balls are anions. In the structure of arsenopyrite, half of the anions are S ions, and half are As ions. In the structure of chalcopyrite, half of the cations are Cu ions and half are Fe ions.

The coordination of cations in the structures of sulphides depends on their size, charge and electron configuration [163,164]. Table 30 lists the hybridisation type and coordination numbers of the cations in the structures of sulphides. The coordination polyhedra of cations in the considered minerals are tetrahedra (sphalerite and ZnO structure types, CN = 4) and octahedra (rutile, NaCl and NiAs structure types, CN = 6).

Table 29. Crystal chemical parameters of the main sulphides.

Mineral	Formula	Space Group	Lattice Constants (Å)	Structure Type	Me-Me Distance	Me-S Distance	CN_{Me}	CP_{Me}	Ref
Pyrite	FeS_2	Pa-3	a = 5.416	NaCl	3.830	2.263	6	Octahedron	[165]
Marcasite	FeS_2	Pnnm	a = 4.445 b = 5.425 c = 3.386	Rutile	3.386	2 × 2.239 4 × 2.252	6	Octahedron	[165]
Arsenopyrite	FeAsS	$P2_1/c$	a = 5.761 b = 5.684 c = 5.767 β = 111.7210°	Rutile	2.734	S: 2.229, 2.230, 2.233 As: 2.370, 2.409, 2.412	6	Octahedron	[166]
Lollengite	$FeAs_2$	Pnnm	a = 5.300 b = 5.984 c = 2.882	Rutile	2.882	2 × 2.361 4 × 2.388	6	Octahedron	[167]
Galena	PbS	Fm-3m	a = 5.805	NaCl	4.105	2.903	6	Octahedron	[168]
Pyrrhotite	Fe_nS_{n+1}	$P6_3/mmc$	a = 3.446 c = 5.743	NiAs	2.871	2.453	6	Octahedron	[169]
Chalcopyrite	$CuFeS_2$	I-42d	a = 5.277 c = 10.441	ZnS	3.712	Cu: 2.295 Fe: 2.259	4	Tetrahedron	[170]
Greenockite	CdS	$P6_3mc$	a = b = 4.136 c = 6.716	ZnO	4.121	3 × 2.527 1 × 2.532	4	Tetrahedron	[171]
Sphalerite	ZnS	F-43m	a = b = c = 5.410	ZnS	3.826	2.343	4	Tetrahedron	[172]
Würtzite	ZnS	$P6_3mc$	a = b = 3.823 c = 6.261	ZnO	3.823	3 × 2.342 1 × 2.347	4	Tetrahedron	[173]

Table 30. Coordination number and type of hybridisation of some metals.

CN	Type of Hybridisation	Elements
2	$sp; p^2$	Cu^+, Cu^{2+}, $Ag^{+,}$ Au^+
4_{tetr}	sp^3	Cu^+, Ag^+, Au^+, Zn^{2+}, Fe^{2+}
4_{sq}	dsp^2	Pd^{2+}, Pt^{2+}, Cu^{2+}, Fe^{3+}
6	d^2sp^3	Pt^{4+}, Fe^{2+}

Table 31 lists the main structural characteristics of the sulphides of Au, Ag, Pd and Pt, and corresponding crystal structures are shown in Figure 44. Me-S chains are the main structural elements in the structures of Au_2S and Ag_2S. Me-S chains in the structure of Au_2S form a three-dimensional framework. The whole structure can be considered as an anti-cristobalite structure, i.e., a three-dimensional framework of anion-centered vertex-sharing SAu_4 tetrahedra. Ag in the structure of Ag_2S occupies two positions. AgI forms Ag-S chains along direction b of the unit cell. These chains are linked by AgII ions.

Table 31. Crystal chemical parameters of some noble metal sulphides.

Mineral	Formula	Space Group	Lattice Constants (Å)	Structure Type	Me-Me Distance	Me-S Distance	CN_{Me}	CP_{Me}	Ref
n/a	Au_2S	Pn-3m	5.0206	Cu_2O	3.550	2.174	2	Dumbbell	[174]
Acanthite	α-Ag_2S	$P12_1/c1$	a = 4.231 b = 6.930 c = 8.293 β = 110.71°	Ag_2S	3.084	AgI: 2.475, 2.511 AgII: 2.547, 2.563, 2.699	AgI: 2 AgII: 3	AgI: dumbbell AgII: coplanar triangle	[175]
Cooperite	PtS	$P4_2/mmc$	a = 3.4701 c = 6.1092	PtS	3.470	2.311	4	Square	[176]
n/a	PtS_2	P-3m1	a = 3.5432 c = 5.0388	CdI_2	3.543	2.421	6	Octahedron	[177]
n/a	PdS	$P4_2/m$	a = 6.429 c = 6.611	PdS	PdI-PdI: 3.305 PdII-PdIII: 3.389 PdIII-PdIII: 2.337	PdI: 2.341 PdII: 2.318 PdIII: 2 × 2.337, 2.346	4	Square	[178]
n/a	PdS_2	Pbca	a = 5.460 b = 5.541 c = 7.531	$PdSe_2$	3.889	PdI: 2 × 2.298, 2 × 2.304, 2 × 3.312	6	Octahedron	[179]

The coordination polyhedra of AgII is a coplanar triangle (Figure 44d). In terms of anion-centered polyhedra, the structure of α-Ag_2S is a set of layers composed of vertex-shared $SAgI_2AgII_3$ tetragonal pyramids. The layers are connected into a three-dimensional framework by AgI atoms. Two types of coordination polyhedra appear in the structures of Pt and Pd sulphides—a planar square in the PtS and PdS structures and an octahedron in the PtS_2 and PdS_2 structures (Figure 44e,g).

Speaking of isomorphic substitution, one must consider a difference in the sizes (ionic or atomic radii) and interatomic distances of host cations and their substitutes. The ionic radii of metals under question with coordination number 6 increases in the following order [180]: Pt < Pd < Ag <Au, which implies that Pt should be the most favourable and, probably, the most abundant admixture in the sulphides, while Au should be hypothetically the less probable isomorphic admixture. In addition, we have to compare Me-S and Me-Me (next nearest cation) distances in the structures of host sulphides and sulphides of the considered noble metals. Me-S distances in the sulphides listed in Table 29 vary between 2.231 Å (arsenopyrite) and 2.903 Å (galena), while Me-S distances in the sulphides of noble metals listed in Table 30 vary between 2.174 Å (Au_2S) and 2.699 Å (α-Ag_2S). It is worth noting that Me-Me distances are not correlated with the Me-S distance, i.e., Fe-S distance in pyrite equals ~2.26 Å, and the Fe-Fe distance equals ~3.83 Å, while Fe-S distance in arsenopyrite equals ~2.23 Å and Fe-Fe distance equals ~2.73 Å. However, in both base metal sulphides (except for galena) and noble metal sulphides (except for PdS_2), larger values of Me-Me distances correspond to smaller values of Me-S distances. The effect is not pronounced but can be detected.

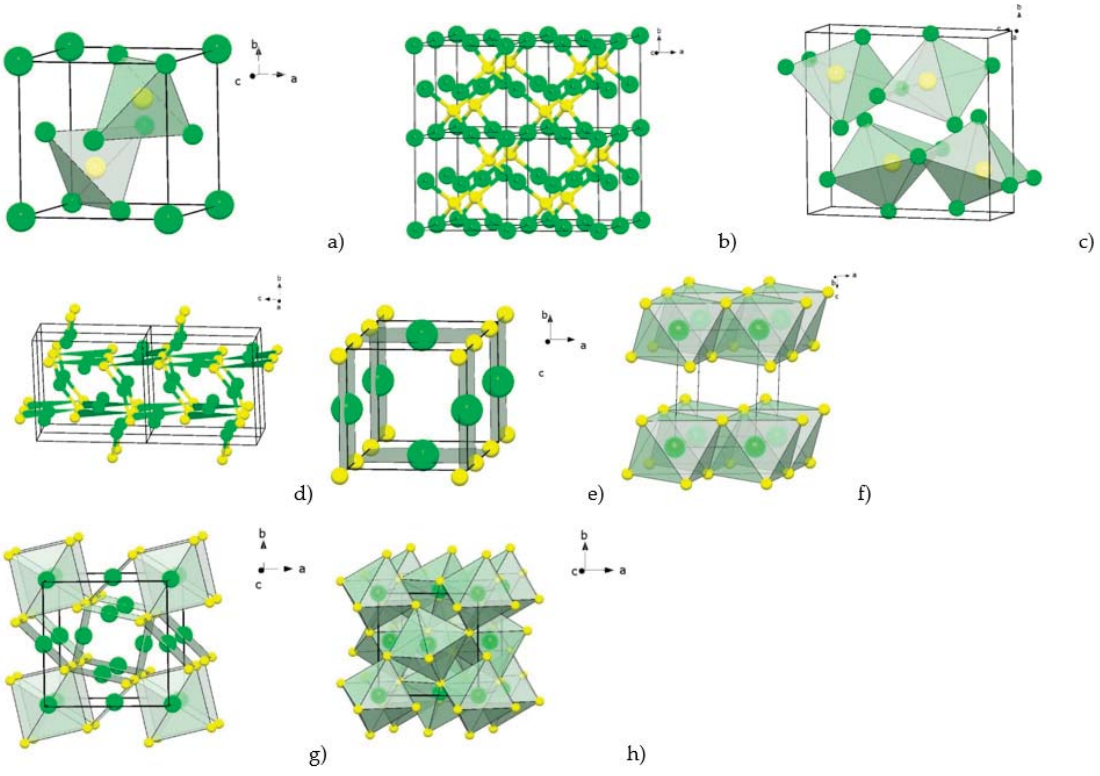

Figure 44. Crystal structures of NM-sulphides: (**a**) anion-centered polyhedra in the structure of Au_2S, (**b**) three-dimensional framework of Au-S bonds in the Au_2S, (**c**) anion-centered polyhedra in the structure of Ag_2S, (**d**) cation-centered polyhedra in the structure of Ag_2S, (**e**) crystal structure of PtS, (**f**) crystal structure of PtS_2, (**g**) crystal structure of PdS, (**h**) crystal structure of PdS_2.

X-ray absorption spectroscopy (XAS) investigations of minerals and their synthetic analogues showed that Au, Ag and Pt could form solid solutions with covellite [17], pyrite [19,22], arsenopyrite [18,19], pyrrhotite [23] and sphalerite [19,92]. However, the concentration of the admixtures is small. Thus, the measured maximum content of Au in natural and synthetic pyrite is ~300 and ~90 ppm accordingly. The concentration of Au in löllengite is about 800 ppm. The concentration of Ag in sphalerite is no more than 5 wt%. Synthetic pyrite hosts up to 7 wt% of Pt in the solid solution state. The measured concentrations of the considered admixtures in base metal sulphides correlate well with the ionic radii of the admixtures: the smaller the cation is, the higher its content in a host mineral. However, some experimental facts cannot be solely explained by the size factor. For example, the maximum content of Pt (the Pt^{2+}-S distance equals 2.31 Å, Table 30) in the solid solution state in pyrite is 7 wt% and is only 0.5 wt% in pyrrhotite [23], while the Fe-S distance is ~2.26 Å in pyrite and ~2.52 Å in pyrrhotite. Besides, the formation of the solid solution depends on the conditions of synthesis: Au forms a solid solution with pyrite in hydrothermal experiments only, and in the pyrites obtained using the salt flux technique, Au forms metal particles.

6. Conclusions

(1) For VMS and Carlin-style deposits as well as for gold-porphyry systems, avalanche deposition of sulphides on geochemical barriers in shallow-depth conditions from moderate- and high-concentrated solutions contributed to the rapid growth of imperfect and thin-zoned crystals, providing the entry of NM in sulphides in finely dispersed form (in the invisible state). Admixtures of metals and metalloids supplied both the increased defectiveness of crystal structure of the minerals (making them chemically more capacious in relation to NM), and the entry of NM impurities into sulphides by the mechanism of heterovalent isomorphism.

(2) For weakly metamorphosed VMS deposits, the following sequence of decrease in invisible gold concentration in sulphides was revealed: galena–chalcopyrite–pyrite–marcasite–sphalerite, in entire agreement with the hydrothermal experiments on the solubility of Au in sulphides (galena–bornite–chalcopyrite–pyrrhotite–pyrite–sphalerite). For highly metamorphosed VMS lodes, such sequence is pyrite–chalcopyrite–sphalerite/arsenopyrite–fahlore–bornite–pyrrhotite–galena, and, in general, the concentration of $C_{invis.\ gold}$ in sulphides is noticeably lower.

(3) In arsenopyrite crystals, the contents of invisible gold reach their maxima, and Fe is negatively correlated with Au. The ionic form of gold probably prevails in this mineral. Thin compositional zoning reflects short-period oscillations of local disequilibrium during crystal growth and some fluctuations in the fluid component fugacities ($f\ S_2$, $f\ Te_2$, $f\ Se_2$, $f\ O_2$, $f\ As_2$).

(4) Epigenetic hydrothermal and metamorphic processes, as well as the slower crystallisation of sulphides, favoured the nucleation of gold, coalescence of its clusters and enlargement of nano-sized NM isolations, and supported the formation of relatively large nuggets as a result of collective recrystallisation. Most Au deposits (except for Carlin-type and gold-porphyry deposits) originated at considerable depths, and the crystallisation of sulphides was in relatively stable conditions, providing the formation of more perfect sulphide crystals as well as co-crystallisation of proper NM minerals (except for the strongly scattered PGE), and a small fraction of NM remains in the sulphides in finely dispersed form (in the invisible state).

(5) Proper NM minerals are represented by groups of minerals that are similar, both for VMS and large gold deposits of the Urals: native gold (high-fineness gold and electrum), with sharply subordinated Ag-sulphosalts, Ag-, Au- and Au-Ag-tellurides, and to a lesser extent, native silver, Au-Ag-sulphides (petrovskaite, uytenbogaardtite, acanthite), Au-antimonide (aurostibite), Ag-sulphobismuthite (matildite) and Ag-selenotelluride (kurilite). In very sporadic cases, abundant NM-tellurides are comparable as host NM-minerals with native gold, in bulk ore composition (Svetlinsk deposit, etc.).

(6) Our experiments showed that admixture of In increases the solubility of Au in sphalerite up to 1 wt%. C_{Au} in sphalerite is higher (up to 1000 times) in samples synthesised at a higher (up to 10 bar) $f\ S_2$ in the system. Fe impurity also promotes the incorporation of Au in sphalerite (C_{Au} up to 0.01 wt%). In sphalerite synthesised under the same conditions without In, Fe, etc., C_{Au} does not exceed 0.001 wt% and does not depend on $f\ S_2$. EPMA and LA-ICP-MS analyses, revealing a homogeneous distribution of all studied elements, showed a clear positive correlation between the In, Fe and Au contents in sphalerite, as well as X-ray absorption spectroscopy confirmed the isomorphic entry of these elements according to the following scheme: $Au^+ + In^{3+}$ (Fe^{3+}) $\leftrightarrow 2\ Zn^{2+}$. A positive effect of $f\ S_2$ on the solubility of Au indicates the formation of vacancies in the cation sublattice, proving the existence of the second isomorphic scheme: $3Zn^{2+} \leftrightarrow 2In^{3+} + \square$. A part of Au doped in ZnS_{In} forms Au_2S clusters, according to the XAFS study. In general, the same pattern was noted for Ag in sphalerite, where Ag_2S and Ag^0 forms oCCur. Greenockite samples were used as model crystals for the würtzite type of structure, and the results confirm the same behaviour of Au in the presence of In and Fe as in sphalerite. In the samples consisting of both ZnS polytypes, C_{Au} does not exceed 50 g/t, and the distribution of doped elements is inhomogeneous.

Author Contributions: Conceptualisation, I.V.; Methodology, I.V., O.V. and E.T.; Field work and sampling, I.V., O.V., E.T., N.S., V.B. and A.S.; Synthesis experiments, D.T.; Laboratory investigations, I.V., O.V., E.T., J.I., D.T., D.B. and V.A.; Formal crystal chemical analysis, M.N.; Writing—original draft preparation, I.V., O.V., E.T., M.N., J.I., D.T. and N.S.; Reviewed and edited the draft, I.V., O.V., D.T. and G.P.; Discussion, I.V., O.V. and G.P.; Project leadership, I.V. All authors have read and agreed to the published version of the manuscript.

Funding: This study began with the support of the Russian Scientific Foundation grant No. 14–17-00693 (2014–2018—methodological approach, synthesis of Au/Ag-doped sulphides), and the Ministry of Science and Higher Education of the Russian Federation (field work, sampling, XRD and INAA study) and the Russian Foundation for Basic Research, projects No. 18–05-70041, 19-35-90115 (deposits of the Polar and North Urals; field work, sampling, SEM/EDS and LA-ICPMS study) and No. 20–05-00849 (ore deposits of the Middle and South Urals; field work, sampling, EPMA, SEM/EDS and LA-ICPMS study) funded this research. The present study contains parts of the PhD Theses of V.B., D.T., N.S., A.S. and D.B.

Data Availability Statement: Not applicable.

Acknowledgments: Experimental studies on the geochemistry of NM were carried out by the authors together with a group of our colleagues under the direction of B. Tagirov, the synthesis of chalgenides was performed according to the original method and under the supervision of D. Chareev with the participation of O. Filimonova. Some aspects of this work were fruitfully discussed with N. Bortnikov, V. Murzin, and B. Tagirov. We thank V. Sazonov, V. Murzin, V. Moloshag and A. Kisin, the managers and geological staff of the Uralian Mining and Metallurgical Company (Gai, Uchaly, Uzelga, Berezovsk Mines), JSC Uzhuralzoloto Group of Companies (UGC), CJSC Gold of Northern Urals (Polymetal), OJSC Yamalzoloto (YZC), for their assistance during fieldwork. Additionally, we thank S. Borisovsky, E. Kovalchuk, A. Tsepin, A. Kerzin, A. Mokhov, N. Trubkin, O. Doynikova, L. Magazina and N. Nekrasov for the analytical procedures, Timofey Pashko for preparing macrophotos, Anna Vikenteva for translation issues and Thomas Henderson for proofreading of the manuscript. EPMA, SEM/EDS and LA-ICPMS analyses were carried out at "IGEM-Analytics" Multi-User Centre and part of LA-ICPMS analyses in Université du Québec à Chicoutimi, Canada. The manuscript was improved through constructive and helpful reviews from the Academic Editor and anonymous reviewers.

Conflicts of Interest: The authors declare no conflict of interest.

Appendix A

Table A1. Standards used for routine mineral analysis by EPMA (I = 20 nA).

Element	X-ray	Crystal	Standard	Time		Detection Limit, 3 σ(wt%)
				Peak	Back	
			Py, Apy			
As	Lα	TAP	GaAs	30	15	0.05
Fe	Kα	LIF	Pyrite	10	5	0.06
S	Kα	PETH	Pyrite	10	5	0.02
Ni	Kα	LIF	NiSbS	10	5	0.04
Cu	Kα	LIF	$CuFeS_2$	10	5	0.07
Sb	Lα	PETH	NiSbS	10	5	0.05
Co	Kα	LIF	Co	30	15	0.06

Table A1. *Cont.*

Element	X-ray	Crystal	Standard	Time		Detection Limit, 3 σ(wt%)
				Peak	Back	
			CCp			
As	Lα	TAP	GaAs	30	15	0.05
Cu	Kα	LIF	$CuFeS_2$	10	5	0.06
S	Kα	PETH	$CuFeS_2$	10	5	0.02
Zn	Kα	LIF	ZnS	10	5	0.08
Fe	Kα	LIF	$CuFeS_2$	10	5	0.06
Cd	Lα	PETH	CdS	10	5	0.05
Ni	Kα	LIF	Ni	10	5	0.06
Mn	Kα	LIF	Mn	10	5	0.06
Co	Kα	LIF	Co	30	15	0.06
			Sp			
Cd	Lα	PETJ	CdS	30	15	0.11
Fe	Kα	LIF	Pyrite	20	10	0.05
S	Kα	PETH	ZnS	10	5	0.02
Zn	Kα	LIF	ZnS	10	5	0.1
In	Lα	PETJ	InSb	10	5	0.08
Mn	Kα	LIF	Mn	20	10	0.04
Ag	Lα	PETH	Ag	10	5	0.04
Cu	Kα	LIF	$CuFeS_2$	20	10	0.06
Hg	Mα	PETH	HgS	20	10	0.06
Sn	Lα	PETH	Sn	20	10	0.04
			Tnt			
Sb	Lα	PETJ	Sb_2S_3	10	5	0.10
As	Lα	TAP	GaAs	10	5	0.10
Zn	Kα	LIF	ZnS	10	5	0.09
S	Kα	PETH	$CuFeS_2$	10	5	0.02
Ag	Lα	PETJ	Ag	10	5	0.16
Se	Lα	TAP	CdSe	10	5	0.07
Cu	Kα	LIF	Cu	10	5	0.08
Hg	Mα	PETH	HgS	10	5	0.09
Te	Lα	PETJ	Te	10	5	0.11
Fe	Kα	LIF	$CuFeS_2$	10	5	0.06
Bi	Mα	PETH	Bi_2Te_3	10	5	0.09
Cd	Lβ	PETJ	CdSe	10	5	0.20
Pb	Mα	PETH	PbS	10	5	0.09
			Gn			
Pb	Mα	PETJ	PbS	20	10	0.22
Se	Lα	TAP	CdSe	10	5	0.09
Cu	Kα	LIF	$CuFeS_2$	20	10	0.09
S	Kα	PETH	PbS	10	5	0.02
Sb	Lα	PETJ	Sb_2S_3	20	10	0.09
As	Lα	TAP	GaAs	20	10	0.09
Fe	Kα	LIF	$CuFeS_2$	20	10	0.06
Ag	Lα	PETH	Ag	10	5	0.06
Bi	Mβ	PETH	Bi	30	15	0.10

References

1. Lincoln, F.C. Certain natural associations of gold. *Econ. Geol.* **1911**, *6*, 247–302. [CrossRef]
2. Schwartz, G.M. Host minerals of native gold. *Econ. Geol.* **1944**, *39*, 371–411. [CrossRef]
3. Burg, G.H. Sichtbarmachumg des Feinverteilten Goldes in Goldhoffigen Erzen und Ihre Wirtschaftliche Bedeutung. *Metall Erz.* **1930**, *27*, 333–338.
4. Bortnikov, N.S.; Genkin, A.D.; Chryssoulis, S. Deposition environment of gold–bearing arsenopyrite in mesothermal deposits. In *Current Research in Geology Applied to ore Deposits*; SGA: Granada, Spain, 1993; pp. 419–422.
5. McClenaghan, S.H.; Lentz, D.R.; Cabri, L.J. Abundance and speciation of gold in massive sulphides of the Bathurst Mining Camp, New Brunswick, Canada. *Can. Mineral.* **2004**, *42*, 851–871. [CrossRef]

6. Large, R.R.; Maslennikov, V.V.; Robert, F.; Danyushevsky, L.V.; Chang, Z. Multistage sedimentary and metamorphic origin of pyrite and gold in the giant Sukhoi Log deposit, Lena gold province, Russia. *Econ. Geol.* **2007**, *102*, 1233–1267. [CrossRef]
7. Large, R.R.; Danyushevsky, L.V.; Hollit, C.; Maslennikov, V.V.; Meffre, S.; E Gilbert, S.; Bull, S.W.; Scott, R.J.; Emsbo, P.; Thomas, H.; et al. Gold and trace element zonation in pyrite using a laser imaging technique: Implications for the timing of gold in orogenic and Carlin-style sediment-hosted deposits. *Econ. Geol.* **2009**, *104*, 635–668. [CrossRef]
8. Cook, N.J.; Ciobanu, C.L.; Mao, J. Textural control on gold distribution in As-free pyrite from the Dongping, Huangtuliang and Hougou gold deposits, North China Craton (Hebei Province, China). *Chem. Geol.* **2009**, *264*, 101–121. [CrossRef]
9. Vikent'ev, I.V.; Moloshag, V.P.; Yudovskaya, M.A. Speciation of noble metals and conditions of their concentration in massive sulphide ores of the Urals. *Geol. Ore Dep.* **2006**, *48*, 77–107. [CrossRef]
10. Kreiter, V.M. Gold particle sizes in sulphide deposits as a sign of postore metamorphosis. *Russ. Izv. Akad. Nauk SSSR Ser. Geol.* **1948**, *1*, 159–162.
11. Bürg, G.H. Natur des in den Pyriten nicht sichtbar enthaltenen Goldes. *Zeitschr. Prakt. Geol.* **1935**, *43*, 17–26.
12. Genkin, A.D.; Bortnikov, N.S.; Cabri, L.J.; Wagner, F.E.; Stanley, C.J.; Safonov, Y.G.; McMahon, G.; Friedl, J.; Kerzin, A.L.; Gamyanin, G.N. A multidisciplinary study of invisible gold in arsenopyrite from four mesothermal gold deposits in Siberia, Russian Federation. *Econ. Geol.* **1998**, *93*, 463–487. [CrossRef]
13. Tauson, V.L.; Pastushkova, T.M.; Bessarabova, O.I. On the limit and speciation of gold in hydrothermal pyrite. *Russ. Geol. Geophys.* **1998**, *39*, 924–933.
14. Tauson, V.L.; Kravtsova, R.G.; Smagunov, N.V. Structural and surface–bond gold in pyrite from deposits of various genetic types. *Russ. Geol. Geophys.* **2014**, *55*, 350–369. [CrossRef]
15. Vikentyev, I.V. Invisible and microscopic gold in pyrite: Methods and new data for massive sulfide ores of the Urals. *Geol. Ore Depos.* **2015**, *57*, 237–265. [CrossRef]
16. Tagirov, B.R.; Dikov, Y.P.; Buleev, M.I.; Koval'chuk, E.V.; Kokh, M.A.; Borisovskii, S.E.; Abramova, V.D.; Garas'ko, M.I.; Kovalenker, V.A.; Bortnikov, N.S.; et al. "Invisible" gold in covellite (CuS): Synthesis and studies by EPMA, LA–ICP–MS, and XPS techniques. *Dokl. Earth Sci.* **2014**, *459*, 1381–1386. [CrossRef]
17. Tagirov, B.R.; Trigub, A.L.; Kvashnina, K.O.; Shiryaev, A.A.; Chareev, D.A.; Nickolsky, M.S.; Abramova, V.D.; Kovalchuk, E.V. Covellite CuS as a matrix for "invisible" gold: X-ray spectroscopic study of the chemical state of Cu and Au in synthetic minerals. *Geochim. Cosmochim. Acta* **2016**, *191*, 58–69. [CrossRef]
18. Kovalchuk, E.V.; Tagirov, B.R.; Vikentyev, I.V.; Chareev, D.A.; Tyukova, E.E.; Nickolsky, M.S.; Borisovsky, S.E.; Bortnikov, N.S. «Invisible» gold in synthetic and natural crystals of arsenopyrite (Vorontsovka deposit, North Ural). *Geol. Ore Dep.* **2019**, *61*, 62–83. [CrossRef]
19. Trigub, A.L.; Tagirov, B.R.; Chareev, D.A.; Nickolsky, M.S.; Shiryaev, A.A.; Kovalchuk, E.V.; Mokhov, A.V.; Kvashnina, K.O.; Baranova, N.N. X–Ray spectroscopy study of the chemical state of "invisible" Au in synthetic minerals in the Fe–As–S system. *Am. Mineral.* **2017**, *102*, 1057–1065.
20. Kesler, S.E. Copper, molybdenum and gold abundances in porphyry copper deposits. *Econ. Geol.* **1973**, *68*, 106–112. [CrossRef]
21. Sillitoe, R.H. Gold–rich porphyry deposits: Descriptive and genetic models and their role in exploration and discovery. *Econ. Geol. Rev.* **2000**, *13*, 315–345.
22. Filimonova, O.N.; Nickolsky, M.S.; Trigub, A.L.; Chareev, D.A.; Kvashnina, K.O.; Kovalchuk, E.V.; Vikentyev, I.V.; Tagirov, B.R. The state of platinum in pyrite studied by X-ray absorption spectroscopy of synthetic crystals. *Econ. Geol.* **2019**, *114*, 1649–1663. [CrossRef]
23. Filimonova, O.N.; Trigub, A.L.; Nickolsky, M.S.; Chareev, D.A.; Kvashnina, K.O.; Kovalchuk, E.V.; Vikentyev, I.V.; Tagirov, B.R. The state of platinum in pyrrhotite: X-ray absorption spectroscopy study and implications for the role of Fe sulfides as plati-num carriers. *Ore Geol. Rev.* **2021**. in preparation.
24. Vikent'ev, I.V.; Moloshag, V.P.; Yudovskaya, M.A. Platinum group elements in ores of massive sulfide deposits of the Urals. *Dokl. Earth Sci.* **2002**, *385*, 488–492.
25. Vikentyev, I.V.; Yudovskaya, M.A.; Mokhov, A.V.; Kerzin, A.L.; Tsepin, A.I. Gold and PGE in sulphide massive sulphide ore of the Uzelginsk deposit, Southern Urals, Russia. *Can. Mineral.* **2004**, *42*, 651–665. [CrossRef]
26. Vikentyev, I.V.; Grabezhev, A.I.; Moloshag, V.P.; Novokreschenov, S.M.; Neustroeva, I.I. PGE in the ores of magnet-ite-copper-skarn deposits of the Urals. In *Yearbook-2004*; Zavaritsky Institute of Geology and Geochemistry, Uralian Branch, RAS: Yekaterinburg, Russia, 2005; pp. 328–331. (In Russian)
27. Murzin, V.V.; Varlamov, D.A.; Vikentyev, I.V. Copper-cobalt mineralization of the Pyshminsk-Klyuchevsk deposit in the Middle Urals: Mineral composition of ore and metasomatites, stages, P-T conditions of mineral formation. *Lithosphere* **2011**, *6*, 103–122.
28. Vikentyev, I.V.; Abramova, V.D.; Moloshag, V.P.; Shangguo, S. PGE in minerals of volcanogenic massive sulfide deposits of the Urals: Ore geochemistry and first LA-ICP-MS data. In *Abs.12th International Platinum Symposium*; Zavaritsky Institute of Geology and Geochemistry: Yekaterinburg, Russia, 2014; pp. 326–327.
29. Mansur, E.T.; Barnes, S.-J.; Duran, C.J. An overview of chalcophile element contents of pyrrhotite, pentlandite, chalcopyrite, and pyrite from magmatic Ni-Cu-PGE sulfide deposits. *Miner. Depos.* **2021**, *56*, 179–204. [CrossRef]
30. Reich, M.; Kesler, S.E.; Utsunomiya, S.; Palenik, C.S.; Chryssoulis, S.L.; Ewing, R.C. Solubility of gold in arsenian pyrite. *Geochim. Cosmochim. Acta* **2005**, *69*, 2781–2796. [CrossRef]

31. Franchini, M.; McFarlane, C.; Maydagán, L.; Reich, M.; Lentz, D.R.; Meinert, L.; Bouhier, V. Trace metals in pyrite and mar-casite from the Agua Rica porphyry–high sulphidation epithermal deposit, Catamarca, Argentina: Textural features and metal zoning at the porphyry to epithermal transition. *Ore Geol. Rev.* **2015**, *66*, 366–387. [CrossRef]
32. Fleet, M.E.; Chryssoulis, S.L.; MacLean, P.J.; Davidson, R.; Weisener, C.G. Arsenian pyrite from gold deposits; Au and As distribution investigated by SIMS and EMP, and color staining and surface oxidation by XPS and LIMS. *Can. Mineral.* **1993**, *31*, 1–17.
33. Leistel, J.M.; Marcoux, E.; Deschamps, Y.; Joubert, M. Antithetic behavior of gold in the volcanogenic massive sulphide de-posits of the Iberian Pyrite Belt. *Mineral. Dep.* **1997**, *33*, 82–97. [CrossRef]
34. Bi, S.-J.; Li, J.-W.; Zhou, M.-F.; Li, Z.-K. Gold distribution in As-deficient pyrite and telluride mineralogy of the Yangzhaiyu gold deposit, Xiaoqinling district, southern North China craton. *Miner. Depos.* **2011**, *46*, 925–941. [CrossRef]
35. Chen, L.; Li, X.; Li, J.; Hofstra, A.H.; Liu, Y.; Koenig, A.E. Extreme variation of sulphur isotopic compositions in pyrite from the Qiuling sediment–hosted gold deposit, West Qinling orogen, central China: An in situ SIMS study with implications for the source of sulphur. *Mineral. Dep.* **2015**, *50*, 643–656. [CrossRef]
36. Vikentyev, I.V. Invisible and microscopic gold in pyrite: New data for volcanogenic massive sulphide ores of the Urals. In *Mineral Resources in a Sustainable World*; Andre-Mayer, A.S., Ed.; SGA: Nancy, France, 2015; pp. 2113–2116.
37. Tseluyko, A.S.; Maslennikov, V.V.; Ayupova, N.R.; Maslennikova, S.P.; Danyushevsky, L.V. Tellurium–bearing minerals in clastic ores of Ybileynoe massive sulphide deposit (South Urals). *Geol. Ore Dep.* **2019**, *61*, 133–161. [CrossRef]
38. Ivanova, J.N.; Tykova, E.E.; Abramova, V.D.; Kovalchuk, E.V.; Vikentyev, I.V. Ores mineralogy and first data about "in-visible" form of Au in pyrite of the Novogodnee–Monto deposit (the Polar Urals, Russia). In *Mineral Resources in a Sustainable World*; Andre–Mayer, A.S., Ed.; SGA: Nancy, France, 2015; pp. 121–125.
39. Vikentiev, I.V.; Abramova, V.D.; Ivanova, Y.N.; Tyukova, E.E.; Kovalchuk, E.V.; Bortnikov, N.S. Trace elements in pyrite from the Petropavlovsk gold–porphyry deposit (Polar Urals): Results of LA-ICP-MS analysis. *Dokl. Earth Sci.* **2016**, *470*, 977–981. [CrossRef]
40. Vikentyev, I.V.; Mansurov, R.K.; Ivanova, Y.N.; Tyukova, E.E.; Sobolev, I.D.; Abramova, V.D.; Vykhristenko, R.I.; Trofimov, A.P.; Khubanov, V.B.; Groznova, E.O.; et al. Porphyry-style Petropavlovskoe gold deposit, the Polar Urals: Geological position, mineralogy, and formation conditions. *Geol. Ore Depos.* **2017**, *59*, 482–520. [CrossRef]
41. Vikent'eva, O.V.; Bortnikov, N.S. The large Svetlinsk Au-Te deposit, South Urals: Telluride mineralization for genetic recon-structions. In *Mineral Resources in a Sustainable World*; Andre-Mayer, A.S., Ed.; SGA: Nancy, France, 2015; pp. 851–854.
42. Vikent'eva, O.; Vikentev, I. Occurrence modes of As, Sb, Te, Bi, Ag in sulphide assemblages of gold deposits of the Urals. In *IOP Conference Series: Materials Science and Engineering*; IOP Publishing: Bristol, UK, 2016; Volume 123, pp. 1–4. [CrossRef]
43. Kampmann, T.C.; Jansson, N.F.; Stephens, M.B.; Olin, P.H.; Gilbert, S.; Wanhainen, C. Syn-tectonic sulphide remobilization and trace element redistribution at the Falun pyritic Zn-Pb-Cu-(Au-Ag) sulphide deposit, Bergslagen, Sweden. *Ore Geol. Rev.* **2018**, *96*, 48–71. [CrossRef]
44. Chareev, D.A. General principles of the synthesis of chalcogenides and pnictides in salt melts using a steady-state temperature gradient. *Crystallogr. Rep.* **2016**, *61*, 506–511. [CrossRef]
45. Chareev, D.A.; Volkova, O.S.; Geringer, N.V.; Koshelev, A.V.; Nekrasov, A.N.; Osadchii, V.O.; Osadchii, E.G.; Filimonova, O.N. Synthesis of chalcogenide and pnictide crystals in salt melts using a steady-state temperature gradient. *Crystallogr. Rep.* **2016**, *61*, 682–691. [CrossRef]
46. Widler, A.M.; Seward, T.M. The adsorption of gold(I) hydrosulphide complexes by iron sulphide surfaces. *Geochim. Cosmochim. Acta* **2002**, *66*, 383–402. [CrossRef]
47. Laptev, Y.V.; Rozov, K.B. Interaction of gold with sulphide surface as a factor of its concentration in hydrothermal ore formation. *Dokl. Earth Sci.* **2006**, *411*, 1229–1232. [CrossRef]
48. Cardile, C.M.; Cashion, J.D.; McGrath, A.C.; Renders, P.; Seward, T.M. ^{197}Au Mössbauer study of Au_2S and gold adsorbed onto As_2S_3 and Sb_2S_3 substrates. *Geochim. Cosmochim. Acta* **1993**, *57*, 2481–2486. [CrossRef]
49. Kozerenko, S.V.; Wagner, F.E.; Friedl, J.; Fadeev, V.V. Gold in pyrite formation processes: 3. Mössbauer study of synthetic gold–bearing iron sulphides. *Geochem. Intern.* **2001**, *39*, S167–S172.
50. Simon, G.; Huang, H.; Penner–Hahn, J.E.; Kesler, S.; Kao, L.S. Oxidation state of gold and arsenic in gold–bearing arsenian pyrite. *Am. Mineral.* **1999**, *84*, 1071–1079. [CrossRef]
51. Cabri, L.J.; Newville, M.; Gordon, R.A.; Crozier, E.D.; Sutton, S.R.; McMahon, G.; Jiang, D.-T. Chemical Speciation of Gold in Arsenopyrite. *Can. Miner.* **2000**, *38*, 1265–1281. [CrossRef]
52. Filimonova, O.N.; Tagirov, B.R.; Trigub, A.L.; Nickolsky, M.S.; Rovezzi, M.; Belogub, E.V.; Reukov, V.L.; Vikentyev, I.V. The state of Au and as in pyrite studied by X-ray absorption spectroscopy of natural minerals and synthetic phases. *Ore Geol. Rev.* **2020**, *121*, 103475. [CrossRef]
53. Taylor, S.R.; McLennan, S.M. *The Continental Crust: Its Composition and Evolution*; Blackwell Scientific: Oxford, UK, 1985; pp. 1–190.
54. Sillitoe, R.H. Gold deposit types: An overview. In *Geology of the World's Major Gold Deposits and Provinces*; Spec. Publ. No. 23; Society of Economic Geologists Inc.: Littleton, CO, USA, 2020; pp. 1–28.
55. Sazonov, V.N.; Van Herk, A.H.; de Boorder, H. Spatial and temporal distribution of gold deposits in the Urals. *Econ. Geol.* **2001**, *96*, 685–703. [CrossRef]
56. Prokin, V.A.; Buslaev, F.P. Massive copper–zinc sulphide deposits in the Urals. *Ore Geol. Rev.* **1998**, *14*, 1–69. [CrossRef]

57. Vikentyev, I.V.; Belogub, E.V.; Novoselov, K.A.; Moloshag, V.P. Metamorphism of volcanogenic massive sulphide deposits in the Urals. Ore geology. *Ore Geol. Rev.* **2017**, *85*, 30–63. [CrossRef]
58. Herrington, R.; Zaykov, V.V.; Maslennikov, V.V.; Brown, D.; Puchkov, V.N. Mineral deposits of the Urals and links to geo-dynamic evolution. *Econ. Geol.* **2005**, *100*, 1069–1095.
59. Bortnikov, N.S.; Vikentyev, I.V. Endogenous metallogeny of the Urals. In *Mineral Deposit Research for a High-Tech World Proceedings of the 12th Biennial SGA Meeting*; Jonsson, E., Ed.; SGA: Uppsala, Sweden, 2013; pp. 1508–1511.
60. Puchkov, V.N. General features relating to the occurrence of mineral deposits in the Urals: What, where, when and why. *Ore Geol. Rev.* **2017**, *85*, 4–29. [CrossRef]
61. Puchkov, V.N. *Geology of Urals and Cis–Urals (Actual Problems of Stratigraphy, Tectonics, Geodynamics and Metallogeny)*; Design Poligraph Service Publ.: Ufa, Russia, 2010. (In Russian)
62. Sazonov, V.N.; Murzin, V.V.; Grigor'ev, N.A. Vorontsovsk gold deposit: An example of Carlin–type mineralization in the Urals, Russia. *Geol. Ore Dep.* **1998**, *40*, 139–151.
63. Vikentyev, I.V.; Tyukova, E.E.; Vikent'eva, O.V.; Chugaev, A.V.; Dubinina, E.O.; Prokofiev, V.Y.; Murzin, V.V. Vorontsovka Carlin–style gold deposit in the north Urals: Mineralogy, fluid inclusion and isotope data for genetic model. *Chem. Geol.* **2019**, *508*, 144–166. [CrossRef]
64. Vikent'eva, O.V.; Bortnikov, N.S.; Vikentyev, I.V.; Groznova, E.O.; Lyubimtseva, N.G.; Murzin, V.V. The Berezovsk giant intrusion-related gold-quartz deposit, Urals, Russia: Evidence for multiple magmatic and metamorphic fluid reservoirs. *Ore Geol. Rev.* **2017**, *91*, 837–863. [CrossRef]
65. Sazonov, V.N.; Popov, V.A.; Grigoryev, N.A.; Murzin, V.V.; Metsner, E.I. *Crust–Mantle Mineralisation in the Salic Blocks of Eugeosyncline*; UrO USSR AN: Sverdlovsk, Russia, 1989. (In Russian)
66. Vikent'eva, O.; Prokofiev, V.; Borovikov, A.; Kryazhev, S.; Groznova, E.; Pritchin, M.; Vikentyev, I.; Bortnikov, N. Contrasting fluids in the Svetlinsk gold-telluride hydrothermal system, South Urals. *Minerals* **2020**, *10*, 37. [CrossRef]
67. Vikentyev, I.V. Precious metal and telluride mineralogy of large volcanic–hosted massive sulphide deposits in the Urals. *Mineral. Petrol.* **2006**, *87*, 305–326. [CrossRef]
68. Seravkin, I.B. Correlation of compositions of ore and host rocks in volcanogenic massive sulphide deposits (on the samples of South Urals). *Geol. Ore Dep.* **2013**, *55*, 68–83. [CrossRef]
69. Karpukhina, V.S.; Naumov, V.B.; Vikent'ev, I.V. Genesis of massive sulphide deposits in the Verkhneural'sk ore district, the South Urals, Russia: Evidence for magmatic contribution of metals and fluids. *Geol. Ore Dep.* **2013**, *55*, 125–143. [CrossRef]
70. Seravkin, I.B.; Kosarev, A.M.; Puchkov, V.N. Geodynamic conditions of formation of massive sulfide deposits in the Magnitogorsk Megazone, Southern Urals, and prospection criteria. *Geol. Ore Depos.* **2017**, *59*, 227–243. [CrossRef]
71. Vikentyev, I.V.; Simonov, V.A.; Borisova, A.Y.; Karpukhina, V.S.; Naumov, V.B. Volcanic–hosted massive sulphide deposits of the Urals, Russia: Evidence for a magmatic contribution of metals and fluid. In *Mineral Deposit Research for a High–Tech World*; Jonsson, E., Ed.; SGA: Uppsala, Sweden, 2013; pp. 1526–1529.
72. Vikentev, I. Selenium, tellurium and precious metal mineralogy in Uchalinsk copper-zinc-pyritic district, the Urals. In *IOP Conference Series: Materials Science and Engineering*; IOP Publishing: Bristol, UK, 2016; Volume 123, p. 012027.
73. Prokin, V.A.; Buslaev, F.P.; Vinogradov, A.M.; Moloshag, V.P.; Kuznetsov, S.I. *Gaisk Mining and Processing Company: Geology of Gaisk and Podolsk Copper-Zinc Pyritic Deposits on the Urals*; Nauka: Yekaterinburg, Russia, 2004; 148p. (In Russian)
74. Vikentyev, I.; Seravkin, I.; Moloshag, V.; Skuratov, V.; Yudovskaya, M.; Mokhov, A.; Kerzin, A.; Tsepin, A. Au and Ag in ores of the Gaisk giant VHMS deposit, South Urals. Extended Abs.12th IAGOD Symp. In *Understanding the Genesis of Ore Deposits to Meet the Demands of the 21st Century*; Elsevier: Amsterdam, The Netherlands, 2006; pp. 1305–1308.
75. Pshenichny, G.N. *Gai Copper–VMS Deposit of the South Urals*; Nauka: Moscow, Russia, 1975; 188p. (In Russian)
76. Vikentyev, I.V. *Formation Conditions and Metamorphism of Pyrite Ores*; Nauch: Moscow, Russia, 2004; 344p. (In Russian)
77. Yakubovich, O.V.; Podolskaya, M.M.; Vikentyev, I.V.; Fokina, E.L.; Kotov, A.B. U-Th-He geochronology of pyrite from the Uzelga VMS deposit (South Urals)—new perspectives for direct dating of the ore-forming processes. *Minerals* **2020**, *10*, 629. [CrossRef]
78. Vikentyev, I.; Chugaev, A.; Karpukhina, V.; Nosik, L.; Rimskaya–Korsakova, M. Origin of Uzelginsk Zn–Cu–Ag VHMS deposit, Southern Urals. Extended abs. In: 12th IAGOD Symp. In *Understanding the Genesis of ore Deposits to Meet the Demands of the 21st Century*; Elsevier: Amsterdam, The Netherlands, 2006; pp. 1233–1236.
79. Vikentyev, I.V.; Karpukhina, V.S. Uzelginsk Zn–Cu–Ag VMS deposit, South Urals: Genetic aspect. In *Applied Mineralogy*; Rammlmair, Ed.; Balkema: Rotterdam, The Netherlands, 2000; pp. 455–459.
80. Vikentyev, I.V.; Tyukova, E.E.; Murzin, V.V.; Vikent'eva, O.V.; Pavlov, L.G. *Vorontsovka Gold Deposit. Geology, Gold Modes, Genesis*; FortDialogIset Publ.: Ekaterinburg, Russia, 2016; 204p. (In Russian)
81. Akinfiev, N.N.; Vikentyev, I.V. Physicochemical modeling of ore formation at the gold and volcanogenic massive sulfide deposits of the Northern Urals. *Geochem. Int.* **2020**, *58*, 1437–1442. [CrossRef]
82. Zhukhlistov, A.P.; Vikent'ev, I.V.; Rusinova, O.V. Electron diffraction study of 1 M illites with interstratified trans- and cis-vacant 2:1 layers. *Crystallogr. Rep.* **2012**, *57*, 270–276. [CrossRef]
83. Udachin, V.; Williamson, B.J.; Purvis, O.W.; Spiro, B.; Dubbin, W.; Brooks, S.; Coste, B.; Herrington, R.; Mikhailova, I. As-sessment of environmental impacts of active smelter operations and abandoned mines in Karabash, Ural Mountains, Russia. *J. Sustain. Dev.* **2003**, *11*, 133–142. [CrossRef]

84. Mercier–Langevin, P.; Hannington, M.D.; Dubé, B.; Bécu, V. The gold content of volcanogenic massive sulphide deposits. *Mineral. Dep.* **2011**, *46*, 509–539. [CrossRef]
85. Wilson, S.A.; Ridley, I.; Koenig, A.E. Development of sulphide calibration standards for the laser ablation inductively–coupled plasma mass spectrometry technique. *J. Anal. At. Spec.* **2002**, *17*, 406–409. [CrossRef]
86. Wohlgemuth–Ueberwasser, C.C.; Ballhaus, C.; Berndt, J.; Stotter née Paliulionyte, V.; Meisel, T. Synthesis of PGE sulphide standards for laser ablation inductivelycoupled plasma mass spectrometry (LA-ICP-MS). *Contrib. Mineral. Petrol.* **2007**, *154*, 607–617. [CrossRef]
87. Vinokurov, S.F.; Vikentyev, I.V. Ionic mode of gold in sulphide ores. *Dokl. Earth Sci.* **2008**, *422*, 1062–1064. [CrossRef]
88. Vinokurov, S.F.; Vikent'ev, I.V. Quantifying the ionic form of gold in sulfide ores. *Her. Russ. Acad. Sci.* **2009**, *79*, 462–467. [CrossRef]
89. Vinokurov, S.F.; Vikent'ev, I.V.; Sychkova, V.A. Determining ionic gold species in massive sulphide ores. *Geochem. Intern.* **2010**, *48*, 510–516. [CrossRef]
90. Chareev, D.A.; Osadchii, V.O.; Shiryaev, A.A.; Nekrasov, A.N.; Koshelev, A.V.; Osadchii, E.G. Single-crystal Fe-bearing sphalerite: Synthesis, lattice parameter, thermal expansion coefficient and microhardness. *Phys. Chem. Miner.* **2017**, *44*, 287–296. [CrossRef]
91. Filimonova, O.N.; Minervina, E.A.; Kovalchuk, E.V.; Abramova, V.D.; Vikent'iev, I.; Tagirov, B.R.; Chareev, D.A.; Chvosti-cov, V.A. An experimental study of noble and base metals (Au, Ag, Pt, Pd, Zn) distribution in pyrite and pyrrhotite. In *Mineral Resources in a Sustainable World*; Andre–Mayer, A.S., Ed.; SGA: Nancy, France, 2015.
92. Filimonova, O.N.; Trigub, A.L.; Tonkacheev, D.E.; Nickolsky, M.S.; Kvashnina, K.O.; Chareev, D.A.; Chaplygin, I.V.; Kovalchuk, E.V.; Lafuerza, S.; Tagirov, B.R. Substitution mechanisms in In-, Au-, and Cu-bearing sphalerites studied by X-ray absorption spectroscopy of synthetic compounds and natural minerals. *Miner. Mag.* **2019**, *83*, 435–451. [CrossRef]
93. Vikentyev, I.V.; Vikentyeva, O.V. Precious metal minerals and «invisible» gold in sulfide ores of Urals. Mater. of XII Int. sci. conf. «Advanced technologies, equipment and analytical systems for materials and nano-materials». *Ust-Kamenogorsk East-Kazakhstan State Tech. Univ.* **2015**, *3*, 33–41.
94. Rogozhnikov, D.A.; Shoppert, A.A.; Dizer, O.A.; Karimov, K.A.; Rusalev, R.E. Leaching kinetics of sulfides from refractory gold concentrates by nitric acid. *Metals* **2019**, *9*, 465. [CrossRef]
95. Cabri, L.J.; Chryssoulis, S.L.; De Villiers, J.P.R.; Laflamme, J.H.G.; Buseck, P.R. The nature of "invisible" gold in arsenopyrite. *Can. Mineral.* **1989**, *27*, 353–362.
96. Fleet, M.E.; Mumin, A.H. Gold-bearing arsenian pyrite and marcasite and arsenopyrite from Carlin Trend gold deposits and laboratory synthesis. *Am. Miner.* **1997**, *82*, 182–193. [CrossRef]
97. Cepedal, A.; Fuertes–Fuente, M.; Martin-Izard, A.; González-Nistal, S.; Barrero, M. Gold–bearing As–rich pyrite and arsenopy-rite from the El Valle gold deposit, Asturias. Northwest Spain. *Can. Mineral.* **2008**, *46*, 233–247. [CrossRef]
98. Murzin, V.V.; Naumov, E.A.; Azovskova, O.B.; Varlamov, D.A.; Rovnushkin, M.Y.; Pirajno, F. The Vorontsovskoe Au-Hg-As ore deposit (Northern Urals, Russia): Geological setting, ore mineralogy, geochemistry, geochronology and genetic model. *Ore Geol. Rev.* **2017**, *85*, 271–298. [CrossRef]
99. Sidorova, N.V.; Vikent'ev, I.V.; Abramova, V.D.; Koval'chuk, E.V. Gold and other impurity elements in pyrite from the Berezovskoe deposit in the Middle Urals. *Lithosphere* **2019**, *2*, 327–336. [CrossRef]
100. Ciobanu, C.L.; Cook, N.J.; Pring, A.; Brugger, J.; Danyushevsky, L.V.; Shimizu, M. 'Invisible gold' in bismuth chalcogenides. *Geochim. Cosmochim. Acta* **2009**, *73*, 1970–1999. [CrossRef]
101. Steadman, J.A.; Large, R.R. Synsedimentary, diagenetic, and metamorphic pyrite, pyrrhotite, and marcasite at the Homestake BIF-Hosted gold deposit, South Dakota, USA: Insights on Au-As ore genesis from textural and LA-ICP-MS trace element studies. *Econ. Geol.* **2016**, *111*, 1731–1752. [CrossRef]
102. Tauson, V.L.; Babkin, D.N.; Pastushkova, T.M.; Krasnoshchekova, T.S.; Lustenberg, E.E.; Belozerova, O.Y. Dualistic distribution coefficients of elements in the system mineral-hydrothermal solution. I. Gold accumulation in pyrite. *Geochem. Int.* **2011**, *49*, 568–577. [CrossRef]
103. Vikent'ev, I.V. Composition of native gold in massive sulphide ores of the Urals. *Dokl. Earth Sci.* **2003**, *393*, 1284–1288.
104. Maslennikov, V.V.; Lein, A.Y.; Maslennikova, S.P.; Bogdanov, Y.A. Phanerozoic "black smokers" as indicator of host rocks composition. *Lithosphere* **2010**, *10*, 153–162.
105. Zaykov, V.V.; Melekestseva, I.Y. Gold and silver minerals in the ore facies from gold–polymetallic deposits of Baimak ore district, the South Urals. *Lithosphere* **2011**, *11*, 71–90.
106. Petrovskaya, N.V. *Native Gold*; Nauka Publ.: Moscow, Russia, 1973. (In Russian)
107. Boyle, R.W. The Geochemistry of Gold and Its Deposits. *Bull. Geol. Surv. Can.* **1979**, *280*, 584.
108. Trofimov, N.D.; Trigub, A.L.; Tagirov, B.R.; Filimonova, O.N.; Evstigneeva, P.V.; Chareev, D.A.; Kvashnina, K.O.; Nickolsky, M.S. The state of trace elements (In, Cu, Ag) in sphalerite studied by X-ray absorption spectroscopy of synthetic minerals. *Minerals* **2020**, *10*, 640. [CrossRef]
109. Pring, A.; Wade, B.; McFadden, A.; Lenehan, C.E.; Cook, N.J. Coupled substitutions of minor and trace elements in co-existing sphalerite and wurtzite. *Minerals* **2020**, *10*, 147. [CrossRef]
110. Tonkacheev, D.E.; Chareev, D.A.; Abramova, V.D.; Yudovskaya, M.A.; Minervina, E.A.; Tagirov, B.R. Sphalerite as a matrix for noble, non–ferrous metals and semimetals: A EPMA and LA–ICP–MS study of synthetic crystals. In *Mineral Resources in a Sustainable World*; Andre–Mayer, A.S., Ed.; SGA: Nancy, France, 2015; pp. 847–850.

111. Tonkacheev, D.E.; Chareev, D.A.; Abramova, V.D.; Trofimov, N.D.; Tagirov, B.R. "Invisible" gold and PGE elements in synthetic crystals of sphalerite, greenockite and covellite: A EPMA, LA–ICP–MS and XAFS study. In Proceedings of the Fifteenth International Symposium on Experimental Mineralogy, Petrology and Geochemistry (EMPG-XV), ETH Zurich, Switzerland, 5–8 June 2016.
112. Palyanova, G.A. Gold and silver minerals in sulfide ore. *Geol. Ore Deposits* **2020**, *62*, 383–406. [CrossRef]
113. Safonov, Y.G. Topical issues of the theory of gold deposit formation. *Geol. Ore Deposits* **2010**, *52*, 438–458. [CrossRef]
114. Simmons, S.F.; Tutolo, B.M.; Barker, S.L.L.; Goldfarb, R.J.; Robert, F. Hydrothermal gold deposition in epithermal, Carlin, and orogenic deposits. In *Geology of the World's Major Gold Deposits and Provinces*; Spec. Publ. No. 23; Society of Economic Geologists Inc.: Littleton, CO, USA, 2020; pp. 823–845.
115. Vikent'ev, I.V.; Belen'kaya, Y.A.; Ageev, B.I. The Aleksandrinsk polymetallic massive sulphide deposit (the Urals, Russia). *Geol. Ore Dep.* **2000**, *42*, 221–246.
116. Ganzhenko, G.D.; Yudovskaya, M.A.; Vikentyev, I.V. Gold–polymetallic mineralization of the Ridder–Sokolnoye deposit in the Rudny Altai (Eastern Kazakhstan). *Mineralogy* **2018**, *4*, 8–34.
117. Bortnikov, N.S.; Cabri, L.; Vikent'ev, I.V.; McMahon, G.; Bogdanov, Y.A. Invisible gold in sulphides from recent submarine hydrothermal mounds. *Dokl. Earth Sci.* **2000**, *373*, 863–866.
118. Bortnikov, N.S.; Cabri, L.J.; Vikentiev, I.V.; Tagirov, B.R.; Mc Mahon, G.; Bogdanov, Y.A.; Stavrova, O.O. Invisible gold in sulphides from seafloor massive sulphide edifices. *Geol. Ore Dep.* **2003**, *45*, 201–212.
119. Bortnikov, N.S.; Vikent'ev, I.V. Modern base metal sulphide mineral formation in the world ocean. *Geol. Ore Dep.* **2005**, *47*, 13–44.
120. Sayab, M.; Suuronen, J.-P.; Molnar, F.; Villanova, J.; Kallonen, A.; O'Brien, H.; Lahtinen, R.; Lehtonen, M. Three-dimensional textural and quantitative analyses of orogenic gold at the nanoscale. *Geology* **2016**, *44*, 739–742. [CrossRef]
121. Chryssoulis, S.L.; McMullen, J. Mineralogical investigation of gold ores. *Dev. Miner. Process.* **2005**, *15*, 21–71.
122. Tauson, V.L.; Lipko, S.V.; Smagunov, N.V.; Kravtsova, R.G. Trace element partitioning dualism under mineral–fluid interaction: Origin and geochemical significance. *Minerals* **2018**, *8*, 282. [CrossRef]
123. Novgorodova, M.I. *Native Metals in Hydrothermal Ores*; Nauka Publ.: Moscow, Russia, 1983. (In Russian)
124. Nekrasov, I.Y. *Geochemistry, Mineralogy, and Origin of Gold Ore Deposits*; Nauka Publ.: Moscow, Russia, 1991; 304p. (In Russian)
125. Pal'yanova, G.; Mikhlin, Y.; Kokh, K.; Karmanov, N.; Seryotkin, Y. Experimental constraints on gold and silver solubility in iron sulfides. *J. Alloys Compd.* **2015**, *649*, 67–75. [CrossRef]
126. Pal'yanova, G.A.; Mikhlin, Y.L.; Karmanov, N.S.; Kokh, K.A.; Seryotkin, Y.V. Visible and "invisible" forms of gold and silver in the products of melt crystallization in the Fe–S–Ag–Au system: Experimental data. *Dokl. Earth Sci.* **2017**, *474*, 636–640. [CrossRef]
127. Large, R.R.; Maslennikov, V.V. Invisible gold paragenesis and geochemistry in pyrite from orogenic and sediment-hosted gold deposits. *Minerals* **2020**, *10*, 339. [CrossRef]
128. Lipko, S.; Tauson, V.; Bychinskii, V. Gold partitioning in a model multiphase mineral-hydrothermal fluid system: Distribution coefficients, speciation and segregation. *Minerals* **2020**, *10*, 890. [CrossRef]
129. Johan, Z. Indium and germanium in the structure of sphalerite: An example of coupled substitution with Copper. *Miner. Pet.* **1988**, *39*, 211–229. [CrossRef]
130. Murakami, H.; Ishihara, S. Trace elements of Indium-bearing sphalerite from tin-polymetallic deposits in Bolivia, China and Japan: A femto-second LA-ICPMS study. *Ore Geol. Rev.* **2013**, *53*, 223–243. [CrossRef]
131. Zhang, Y.; Chu, F.; Li, Z.; Dong, Y.; Wang, H.; Li, X.; Long, J. Gold enrichment in hydrothermal sulfides from the Okinawa Trough: An in situ LA-ICP-MS study. *Ore Geol. Rev.* **2020**, *116*, 103255. [CrossRef]
132. Wohlgemuth-Ueberwasser, C.C.; Viljoen, F.; Petersen, S.; Vorster, C. Distribution and solubility limits of trace elements in hydrothermal black smoker sulfides: An in-situ LA-ICP-MS study. *Geochim. Cosmochim. Acta* **2015**, *159*, 16–41. [CrossRef]
133. Osadchii, V.O. Trivalent iron in the structure of sphalerite. In *Lomonosov Reading–2016*; Moscow State University: Moscow, Russia, 2016. Available online: https://istina.msu.ru/conferences/presentations/19830602/ (accessed on 26 April 2021). (In Russian)
134. Cook, N.J.; Ciobanu, C.L.; Brugger, J.; Etschmann, B.; Howard, D.L.; De Jonge, M.D.; Ryan, C.; Paterson, D. Determination of the oxidation state of Cu in substituted Cu-In-Fe-bearing sphalerite via XANES spectroscopy. *Am. Miner.* **2012**, *97*, 476–479. [CrossRef]
135. Belissont, R.; Muñoz, M.; Boiron, M.-C.; Luais, B.; Mathon, O. Distribution and oxidation state of Ge, Cu and Fe in sphalerite by μ-XRF and K-edge μ-XANES: Insights into Ge incorporation, partitioning and isotopic fractionation. *Geochim. Cosmochim. Acta* **2016**, *177*, 298–314. [CrossRef]
136. Tonkacheev, D.E.; Chareev, D.A.; Abramova, V.D.; Kovalchuk, E.V.; Vikentyev, I.V.; Tagirov, B.R. The substitution mechanism of Au in In–, Fe– and In–Fe–bearing synthetic crystals of sphalerite, based on the data from EPMA and LA–ICP–MS study. *Lithosphere* **2019**, *19*, 148–161. [CrossRef]
137. Koelmans, H. Association and dissociation of centres in luminescent ZnS-In. *J. Phys. Chem. Solids* **1960**, *17*, 69–79. [CrossRef]
138. Pattrick, R.A.D.; Mosselmans, J.F.W.; Charnock, J.M. An X-ray absorption study of doped sphalerites. *Eur. J. Miner.* **1998**, *10*, 239–250. [CrossRef]
139. Di Benedetto, F.; Bernardini, G.P.; Costagliola, P.; Plant, D.; Vaughan, D.J. Compositional zoning in sphalerite crystals. *Am. Miner.* **2005**, *90*, 1384–1392. [CrossRef]
140. Lin, Y.; Cook, N.J.; Ciobanu, C.L.; Liu, Y.P.; Zhang, Q.; Liu, T.G.; Gao, W.; Yang, Y.L.; Danyushevskiy, L. Trace and minor elements in sphalerite from base metal deposits in South China: A LA-ICPMS study. *Ore Geol. Rev.* **2011**, *39*, 188–217.

141. Pokrovski, G.S.; Akinfiev, N.N.; Borisova, A.Y.; Zotov, A.V.; Kouzmanov, K. Gold speciation and transport in geological fluids: Insights from experiments and physical-chemical modelling. *Geol. Soc. Lond. Spéc. Publ.* **2014**, *402*, 9–70. [CrossRef]
142. Tauson, V.L.; Mironov, A.G.; Smagunov, N.V.; Bugaeva, B.G.; Akimov, V.V. Gold in sulphides: State of the art of occurrence and horizons of experimental studies. *Rus. Geol. Geophys.* **1996**, *37*, 1–11.
143. Pals, D.W.; Spry, P.G.; Chryssoulis, S. Invisible gold and tellurium in arsenic-rich pyrite from the Emperor gold deposit, Fiji: Implications for gold distribution and deposition. *Econ. Geol.* **2003**, *98*, 479–493. [CrossRef]
144. McClenaghan, S.H.; Lentz, D.R.; Martin, J.; Diegor, J. Gold in the Brunswick No. 12 volcanogenic massive sulphide deposit, Bathurst Mining Camp, Canada: Evidence from bulk–ore analysis and laser–ablation ICP–MS–data on sulphide phases. *Mineral. Dep.* **2009**, *44*, 523–557. [CrossRef]
145. Tauson, V.L.; Lustenberg, E.K. Quantitative determination of modes of gold occurrence in minerals by the statistical analysis of analytical data samplings. *Geochem. Int.* **2008**, *46*, 423–428. [CrossRef]
146. Economou–Eliopoulos, M.; Eliopoulos, D.G.; Chryssoulis, S. A comparison of high–Au massive sulphide ores hosted in ophiolite complexes of the Balkan Peninsula with modern analogues: Genetic significance. *Ore Geol. Rev.* **2008**, *33*, 81–100. [CrossRef]
147. Clark, L.A. The Fe-As-S system; phase relations and applications. *Econ. Geol.* **1960**, *55*, 1631–1652. [CrossRef]
148. Arehart, G.B.; Chryssoulis, S.L.; Kesler, S.E. Gold and arsenic in iron sulfides from sediment-hosted disseminated gold deposits; implications for depositional processes. *Econ. Geol.* **1993**, *88*, 171–185. [CrossRef]
149. Palenik, C.S.; Utsunomiya, S.I.; Reich, M.; Kesler, S.E.; Wang, L.; Ewing, R.C. "Invisible" gold revealed: Direct imaging of gold nanoparticles in a Carlin-type deposit. *Am. Miner.* **2004**, *89*, 1359–1366. [CrossRef]
150. Griffin, W.L.; Ashley, P.M.; Ryan, C.G.; Sie, S.H.; Suter, G.F. Pyrite geochemistry in the North Arm Epitermal Ag–Au deposit, Queensland, Australia. A Proton microprobe study. *Can. Mineral.* **1991**, *29*, 185–198.
151. Aylmore, M.G. Distribution and Agglomeration of Gold in Arsenopyrite and Pyrite. Ph.D. Thesis, Curtin University of Technology, Perth, Australia, 1995; 209p.
152. Su, W.; Zhang, H.; Hu, R.; Ge, X.; Xia, B.; Chen, Y.; Zhu, C. Mineralogy and geochemistry of gold–bearing arsenian pyrite from the Shuiyindong Carlin–type gold deposit. Guizhou. China: Implications for gold depositional processes. *Mineral. Dep.* **2012**, *47*, 653–662. [CrossRef]
153. Sack, P.J.; Large, R.R.; Gregory, D.D. Geochemistry of shale and sedimentary pyrite as a proxy for gold fertility in the Selwyn basin area, Yukon. *Miner. Depos.* **2018**, *53*, 997–1018. [CrossRef]
154. Cathelineau, M.; Boiron, M.-C.; Holliger, P.; Marion, P.; Denis, M. Gold in arsenopyrites: Crystal chemistry, location and state, physical and chemical conditions of deposition. *Econ. Geol. Monogr.* **1989**, *6*, 328–341.
155. Cook, N.; Chryssoulis, S. Concentration of "invisible" gold in the common sulphides. *Can. Mineral.* **1990**, *28*, 1–16.
156. Vaughan, J.P.; Kyin, A. Refractory gold ores in Archaean greenstones, Western Australia: Mineralogy, gold paragenesis, metallurgical characterization and classification. *Miner. Mag.* **2004**, *68*, 255–277. [CrossRef]
157. Kovalev, K.R.; Kalinin, Y.A.; Naumov, E.A.; Kolesnikova, M.K.; Korolyuk, V.N. Gold–bearing arsenopyrite in eastern Kazakhstan gold–sulfide deposits. *Russ. Geol. Geophys.* **2011**, *52*, 178–192. [CrossRef]
158. Benzaazoua, M.; Marion, P.; Robaut, F.; Pinto, A. Gold–bearing arsenopyrite and pyrite in refractory ores: Analytical refinements and new understanding of gold mineralogy. *Mineral. Mag.* **2007**, *71*, 123–142. [CrossRef]
159. Mumin, A.H.; Fleet, M.E.; Chryssoulis, S.L. Gold mineralization in As-rich mesothermal gold ores of the Bogosu-Prestea mining district of the Ashanti gold belt, Ghana: Remobilization of 'invisible' gold. *Mineral. Dep.* **1994**, *29*, 445–460. [CrossRef]
160. Yang, S.; Blum, N.; Rahders, E.; Zhang, Z. The nature of invisible gold in sulfides from the Xiangxi Au-Sb-W ore deposit in North-western Hunan, People's republic of China. *Can. Mineral.* **1998**, *36*, 136l–1372.
161. Sung, Y.-H.; Brugger, J.; Ciobanu, C.L.; Pring, A.; Skinner, W.; Nugus, M. Invisible gold in arsenian pyrite and arsenopyrite from a multistage Archaean gold deposit: Sunrise Dam, Eastern Goldfields province, Western Australia. *Miner. Depos.* **2009**, *44*, 765–791. [CrossRef]
162. Goldmann, S.; Junge, M.; Wirth, R.; Schreiber, A. Distribution of trace elements in sphalerite and arsenopyrite on the nano-metre scale — Discrete phases versus solid solution. *Europ. J. Miner.* **2019**, *31*, 325–333. [CrossRef]
163. Belov, N.V.; Godovikov, A.A.; Bakakin, V.V. *Ocherki po Teoreticheskoy Mineralogii (Essays on Theoretical Mineralogy)*; Publ. House Nauka: Moscow, Russia, 1982. (In Russian)
164. Makovicky, E. Crystal structures of sulphides and other chalcogenides. *Rev. Mineral. Geochem.* **2006**, *61*, 7–125. [CrossRef]
165. Rieder, M.; Crelling, J.C.; Šustai, O.; Drábek, M.; Weiss, Z.; Klementová, M. Arsenic in iron disulphides in a brown coal from the North Bohemian Basin, Czech Republic. *Inter. J. Coal Geol.* **2007**, *71*, 115–121. [CrossRef]
166. Bindi, L.; Moelo, Y.; Léone, P.; Suchaud, M. Stoichiometric arsenopyrite, FeAsS, from La Roche–Balue Quarry, Loire–Atlantique, France: Crystal structure and Mössbauer study. *Can. Mineral.* **2012**, *50*, 471–479. [CrossRef]
167. Lutz, H.D.; Jung, M.; Wäschenbach, G. Kristallstrukturen des Löllingits $FeAs_2$ und des Pyrits $RuTe_2$. *Z. Anorg. Allg. Chem.* **1987**, *554*, 87–91. [CrossRef]
168. Slipukhina, I.V.; Bercha, D.M. Elementary energy bands in isovalent IV–VI orthorhombic and cubic crystals and their solid solutions. *Phys. Status Solidi* **2007**, *244*, 650–668. [CrossRef]
169. Sidhu, S.S.; Heaton, L.; Mueller, M.H. Neutron diffraction techniques and their applications to some problems in physics. *J. Appl. Phys.* **1959**, *30*, 1323. [CrossRef]
170. Kratz, T.; Fuess, H. Simultane Strukturbestimmung von Kupferkies und Bornit an einem Kristall. *Z. Krist.* **1989**, *186*, 167.

171. Sowa, H. On the mechanism of the pressure–induced würtzite–to NaCl–type phase transition in CdS: An X–ray diffraction study. *Solid State Sci.* **2005**, *7*, 73–78. [CrossRef]
172. Jamieson, J.C.; Demarest, H.H., Jr. A note on the compression of cubic ZnS. *J. Phys. Chem. Solids* **1980**, *41*, 963–964. [CrossRef]
173. Kisi, E.H.; Elcombe, M.M. U parameters for the wurtzite structure of ZnS and ZnO using powder neutron diffraction. *Acta Crystallogr. Sect. C Cryst. Struct. Commun.* **1989**, *45*, 1867–1870. [CrossRef]
174. Ishikawa, K.; Isonaga, T.; Wakita, S.; Suzuki, Y. Structure and electrical properties of Au_2S. *Solid State Ionics* **1995**, *79*, 60–66. [CrossRef]
175. Sadanaga, R.; Sueno, S. X–ray study on the α–β transition of Ag_2S. *Mineral. J.* **1967**, *5*, 124–143. [CrossRef]
176. Kjekshus, A.; Skansen, T.; Ehrenberg, L.; Brunvoll, J.; Bunnenberg, E.; Djerassi, C.; Records, R. On the homogeneity range of the PtS phase. *Acta Chem. Scand.* **1966**, *20*, 577–579. [CrossRef]
177. Furuseth, S.; Selte, K.; Kjekshus, A.; Gronowitz, S.; Hoffman, R.A.; Westerdahl, A. Redetermined crystal structures of $NiTe_2$, $PdTe_2$, PtS_2, $PtSe_2$, and $PtTe_2$. *Acta Chem. Scand.* **1965**, *19*, 257–258. [CrossRef]
178. Brese, N.E.; Squattrito, P.J.; Ibers, J.A. Reinvestigation of the structure of PdS. *Acta Crystallogr. Sect. C Cryst. Struct. Commun.* **1985**, *41*, 1829–1830. [CrossRef]
179. Grønvold, F.; Røst, E. The crystal structure of $PdSe_2$ and PdS_2. *Acta Crystallogr.* **1957**, *10*, 329–331. [CrossRef]
180. Shannon, R.D. Revised effective ionic radii and systematic studies of interatomic distances in halides and chalcogenides. *Acta Crystallogr. A* **1976**, *32*, 751–767. [CrossRef]

minerals

MDPI

Article

Geochemistry of Tourmaline from the Laodou Gold Deposit in the West Qinling Orogen, Central China: Implications for the Ore-Forming Process

Xiaoye Jin [1,2,3,*] and Jixiang Sui [4]

[1] School of Earth Resources, China University of Geosciences, Wuhan 430074, China
[2] State Key Laboratory of Geological Processes and Mineral Resources, China University of Geosciences, Wuhan 430074, China
[3] Engineering Technology Innovation Center of Mineral Resources Explorations in Bedrock Zones, Ministry of Natural Resources, Guiyang 550081, China
[4] Yifu Museum, China University of Geosciences, Wuhan 430074, China; suijx@cug.edu.cn
* Correspondence: xiaoye.jin@cug.edu.cn

Received: 26 June 2020; Accepted: 20 July 2020; Published: 22 July 2020

Abstract: The Laodou gold deposit, located in the West Qinling Orogen of central China, is a newly recognized intrusion-related gold deposit. It consists of auriferous quartz-sulfide-tourmaline and minor quartz-stibnite veins that are structurally controlled by fault zones transecting the host quartz diorite porphyry. Two types of tourmaline were identified in this study: Type 1 tourmaline occurs as quartz-tourmaline nodules within the quartz diorite porphyry, whereas type 2 tourmaline occurs as quartz-sulfide-tourmaline veins in auriferous lodes. Here, we present a major and trace element analysis by electron microprobe and laser ablation inductively coupled plasma mass spectrometry on these two types of tourmaline. Both tourmaline types fall into the alkali group, and are classified under the schorl-dravite solid solution series. The substitutions of $FeMg_{-1}$, $FeAl_{-1}$, $AlO((Fe, Mg)(OH))_{-1}$, and X-site $vacancyCa_{-1}$ are inferred by the variations of their major element compositions. Field and mineralogy observations suggest that type 1 tourmaline is a product of the late crystallization process of the quartz diorite porphyry, whereas type 2 tourmaline coexists with Au-bearing arsenopyrite and is crystallized from the ore-forming fluids. Their rare earth element compositions record the related magmatic hydrothermal evolution. The Co and Ni concentrations of the coexisting type 2 tourmaline and arsenopyrite define a regression line (correlation coefficient = 0.93) with an angular coefficient of 0.66, which represents the Co/Ni ratio of the tourmaline and arsenopyrite-precipitating fluids. This value is close to the Co/Ni ratios of the host quartz diorite porphyry, indicating a magma origin of the ore-forming fluids. The substitution of Al^{3+} by Fe^{3+} in both tourmaline types shows that type 1 tourmaline approaches the end member of povondraite whereas type 2 tourmaline occurs in opposite plots near the end member of Oxy-dravite, reflecting a more oxidizing environment for type 2 tourmaline formation. Moreover, the redox-sensitive V and Cr values of type 2 tourmaline are commonly 1–2 orders of magnitude higher than those of type 1 tourmaline, which also suggests that type 2 tourmaline forms from more oxidizing fluids. Combined with gold occurrence and fluid properties, we propose that the increasing of oxygen fugacity in the ore-forming fluids is a trigger of gold precipitation.

Keywords: tourmaline; geochemistry; ore-forming process; Laodou gold deposit; West Qinling Orogen

1. Introduction

Tourmaline is common in a variety of hydrothermal ore deposits such as granite related W–Sn polymetallic mineralization [1–3], porphyry Cu ± Mo [4,5], orogenic gold [6–8], volcanic-hosted

massive sulfide [9–11], and iron oxide–copper–gold deposits [12–14]. These diverse deposit types cover a broad spectrum of chemical environments and pressure-temperature conditions, suggesting a wide stability range for tourmaline [15]. This mineral phase is a borosilicate with large variations in chemical composition, containing most of the rock-forming elements and a certain number of volatile components (e.g., B, F, and OH) intrinsic to hydrothermal systems [16]. Chemical compositions and changes in tourmaline textures may provide evidence for changes in the process related to the crystallization history, and with proper decoding can elucidate the chemical evolution of the hydrothermal system [17,18].

Previous studies have shown that selected major and trace element compositions of tourmaline in hydrothermal deposits can be used as good indicators for the source and evolution of ore-forming fluids [19–21]. In this study, we present an in-situ dataset on major and trace element compositions of two types tourmaline from a newly recognized intrusion-related Laodou gold deposit in the West Qinling Orogen of central China. This gold deposit is characterized by an abundance of tourmaline occurring within the host quartz diorite porphyry and the hydrothermal auriferous lodes, in response to the parental magma evolution (late magmatic or early hydrothermal fluids) and subsequent ore-forming events, respectively. Characterization of chemical compositions of these two types of tourmaline growth during progressive exsolution of magma and subsequent hydrothermal crystallization has provided new insights into magmatic hydrothermal evolution, and the related ore-forming process.

2. Geological Setting

The West Qinling Orogen (WQO) is the western segment of the Qinling Orogen, which is bounded by the Linxia-Wushan-Tianshui Fault and Shangdan suture zone to the north and by the A'nimaque-Mianlue suture zone to the south (Figure 1a). The Shangdan suture zone witnesses the middle Paleozoic northward subduction of the Shangdan ocean (proto-Tethyan ocean) crust and subsequent collision between the North Qinling belt and Qinling terrane [22–24]. The A'nimaque-Mianlue Suture zone recorded the late Paleozoic to early Mesozoic subduction of the paleo-Tethyan oceanic crust and subsequent collision between the Yangtze Block, the Songpan-Ganzi terrane, and the Qinling terrane [25,26]. Lithologically, the WQO is dominated by a thick sequence of Paleozoic to early Mesozoic marine sedimentary rocks, with Archean to Proterozoic basement rocks exposed locally [23,24]. Brittle faults are well developed along several nearly E–W-trending fold and thrust belts in the WQO, and the thrust faults broadly coincide with the boundaries of major lithologic contacts [27]. Granitoid intrusions are widespread in the region. Available geochronological data indicate that most granitoid intrusions in the eastern part of the WQO were emplaced at 225–200 Ma [28,29], whereas the equivalents in the western part were mostly formed at 249–230 Ma [30,31], which has been interpreted to reflect a westward closure of the paleo-Tethyan ocean.

The Xiahe-Hezuo district is located in the western portion of the WQO (Figure 1a). It is dominated by weakly metamorphosed to unmetamorphosed Carboniferous to Middle Triassic marine sedimentary rocks [32], which were folded during the Triassic as outlined by the Xinpu-Lishishan anticline (Figure 1b). The district is divided into the western and eastern zones by the NW-striking Xiahe-Hezuo Fault. Secondary or higher order faults broadly parallel to the Xiahe-Hezuo Fault are well developed throughout the region (Figure 1b). Several Mesozoic granitoid plutons form a discontinuous NW-trending magmatic belt in the eastern zone, whereas numerous mafic to intermediate dikes are emplaced in the western zone. Some andesitic to dacitic volcanic rocks also outcrop sporadically (Figure 1b). Zircon U-Pb geochronology indicates that these igneous rocks emplaced and/or erupted between 252 and 233 Ma [30,31,33,34]. Combining the geology and geochemistry data, previous studies suggest these igneous rocks have formed along an active continental margin associated with the paleo-Tethyan subduction [31,35], or in a post-collision setting [30,36].

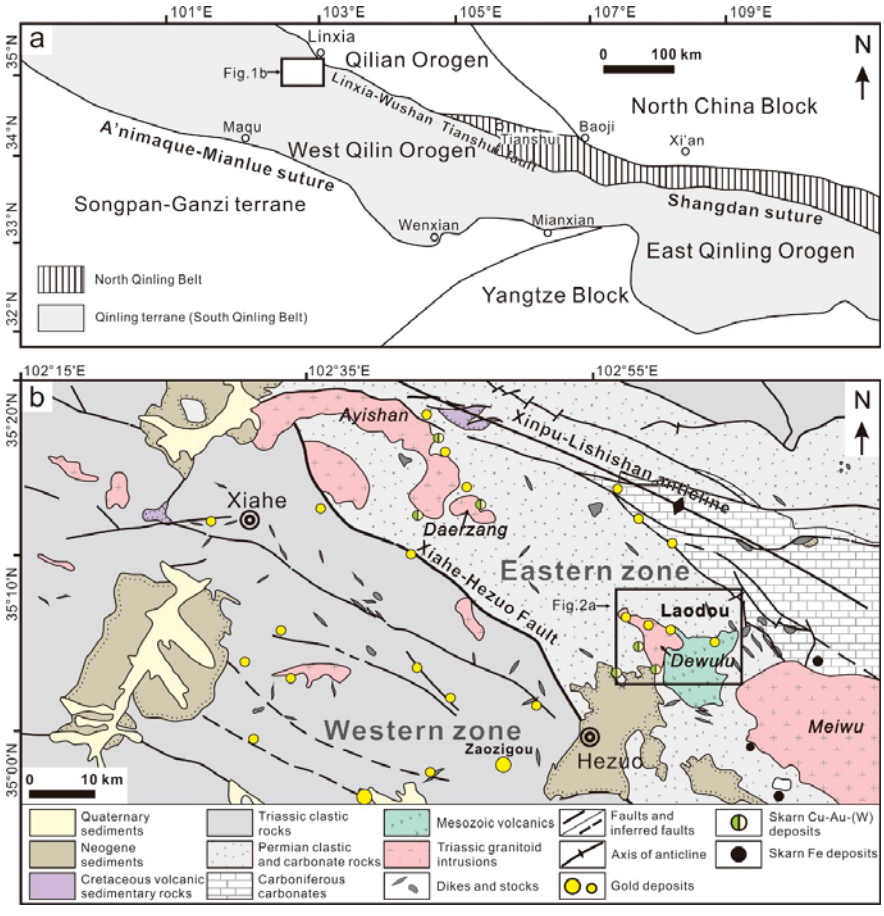

Figure 1. (**a**) Simplified map showing geotectonic terranes in the Qinling Orogen with the location of the study area [37,38]; (**b**) geologic map of the Xiahe-Hezuo district showing the distribution of major sedimentary facies, igneous rocks, and Au, Cu-Au-(W), and Fe deposits [39].

The Laodou gold deposit is a recently identified intrusion-related mineralization hosted in the quartz diorite porphyry of the Dewulu intrusive complex (Figure 2a). It has close spatial, temporal, and genetic relationships with igneous rocks, as well as the regional Cu-Au skarns and Au-Cu-As-W veins [33,37,39,40] (Figure 2a). The host quartz diorite porphyry consists of plagioclase, quartz, amphibole, and minor biotite. Zircon, apatite, and ilmenite are the main accessory minerals [31]. Tourmaline is locally abundant as disseminated crystals or tourmaline-quartz nodules. The magma origin has been interpreted as partial melting of K-rich meta-basaltic rocks in a thickened lower continental crust [31,41]. The deposit consists of five NNW- to N-striking auriferous lodes within the hydrothermally altered fault zones (F1–F5; Figure 2b). For example, the F1 altered fault zone contains five orebodies of Au2, Au2–1, Au8, Au8–1, and Au10, which strike at 286–354° and dip 27–38° to the east, and are 80–158 m long and 2.15–5.16 m thick, with a minimum vertical extent of 45–103 m (Figure 2c). The auriferous lode main includes quartz-sulfide-tourmaline and minor quartz-stibnite veins that are enveloped by potassic and phyllic alteration in the host quartz diorite porphyry (Figure 3). The mineral assemblages comprise mostly quartz, sericite, tourmaline, pyrite, arsenopyrite, and stibnite, with minor amounts of galena, sphalerite, chalcopyrite, tetrahedrite, and enargite. Gold occurs mainly

as "invisible gold" in pyrite (up to 66.65 ppm) and arsenopyrite (up to 4.32 ppm), and locally as submicrometer-sized particles of native gold [39,42]. The ore fluids are intermediate temperature (220–295 °C), low salinity (2–11 wt. % NaCl equiv), CO_2-rich, and moderately acidic to neutral aqueous fluids [42,43]. Stable isotopes of H-O-S-B-Pb supported a magmatic origin of the ore fluids, with minor external meteoric-derived groundwater also thought to be involved [39]. Two sericite samples—coeval with gold-bearing sulfides and native gold particles—yield indistinguishable plateau ages at 249 ± 1.5 Ma that, within analytical errors, agree with the zircon U-Pb age (247.6 ± 1.3 Ma) of the host quartz diorite porphyry [39].

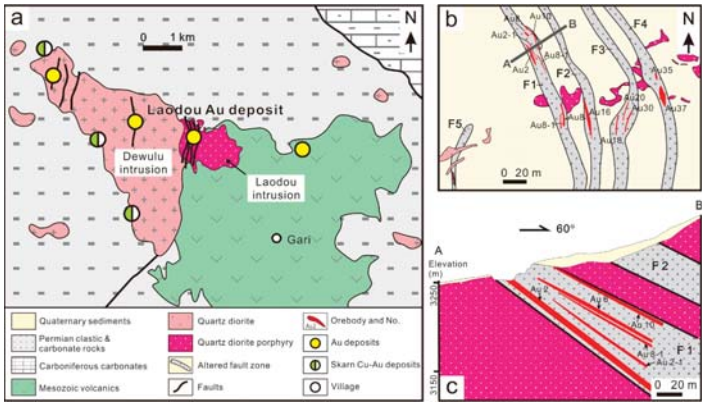

Figure 2. (**a**) Geologic map of the Dewulu intrusive complex with the location of the Laodou gold deposit. Other hydrothermal lode Au deposits and Cu-Au skarn deposits are also shown [44]; (**b**) simplified geologic map of the Laodou gold deposit; (**c**) representative cross section in (**b**) showing the geological relations between structures, alterations, and gold ores [39].

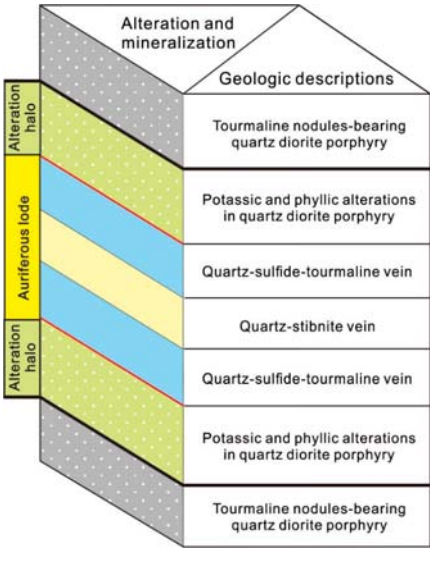

Figure 3. Idealized sketch of the auriferous lode that was enveloped by potassic and phyllic alteration in the host Laodou quartz diorite porphyry.

3. Tourmaline Occurrences

Tourmaline from the Laodou gold deposit is commonly black in field observations. According to the distinct occurrences and associated mineral assemblages, two types of tourmaline have been identified, including disseminated quartz-tourmaline nodules (type 1) in the host quartz diorite porphyry and quartz-sulfides-tourmaline veins (type 2) in the auriferous lodes.

3.1. Type 1 Tourmaline

Type 1 tourmaline is locally disseminated in the Laodou quartz diorite porphyry (Figure 4a) as quartz-tourmaline nodules that are usually several centimeters in diameter (Figure 4b). Some nodules display a leucocratic halo, which is mainly composed of fine-grained subhedral quartz and minor fine scaly sericite interstitial between quartz grains (Figure 4c). In most cases, quartz and tourmaline are intergrown and commonly characterized by a subhedral to anhedral granular texture, with straight or ragged boundaries (Figure 4d). In addition, some small tourmaline grains or fragments are wrapped by quartz that grew interstitially between the tourmaline grains (Figure 4d,e). The quartz-tourmaline nodules show a close spatial relationship with plagioclase, sericite, and muscovite (Figure 4e,f). Plagioclase is somewhat corroded, metasomatized, and then replaced by tourmaline (Figure 4e). Sericite and muscovite occur as fine scaly within the quartz-tourmaline nodules (Figure 4c), and remain the pseudomorph of plagioclase or biotite around the quartz-tourmaline nodules (Figure 4c,e,f).

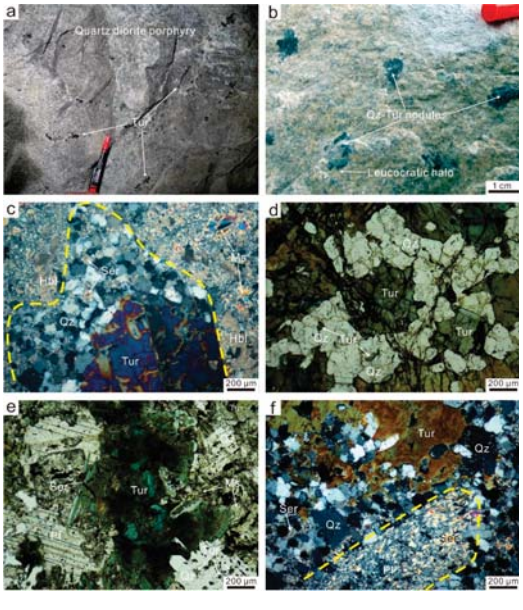

Figure 4. (**a**) Tourmaline occurs as disseminations in the quartz diorite porphyry; (**b**) quartz-tourmaline nodules in the quartz diorite porphyry display leucocratic haloes; (**c**) the leucocratic halo around a quartz-tourmaline nodule is mainly composed of fine-grained quartz and fine scaly sericite; (**d**) quartz and tourmaline in most nodules are intergrown and characterized by subhedral to anhedral granular textures with straight or ragged boundaries; (**e**) relationships between tourmaline, quartz, plagioclase, sericite, and muscovite; (**f**) sericite aggregates remain the pseudomorph of plagioclase or biotite around the quartz-tourmaline nodule. Tur—tourmaline; Qz—quartz; Hbl—hornblende; Ser—sericite; Pl—plagioclase; Ms—muscovite.

3.2. Type 2 Tourmaline

Type 2 tourmaline is represented by the open-space filling quartz-sulfide-tourmaline veins transecting the Laodou quartz diorite porphyry (Figure 5a), which are commonly several centimeters to half a meter wide with a variable length in auriferous lodes (Figure 2c). In this case, type 2 tourmaline is closely associated with arsenopyrite and commonly occurs either within the arsenopyrite vein (Figure 5a) or intergrown with the arsenopyrite disseminations (Figure 5b). Some fine-grained quartz-sulfide-tourmaline assemblages are present as the hydrothermal cement of breccias of altered quartz diorite porphyry (Figure 5c). Under microscope, type 2 tourmaline is characterized by an oscillatory-zoned texture of blue green to brown color, which has sharp, straight boundaries in contact with quartz and arsenopyrite (Figure 5d). In back scattered electron image, arsenopyrite exhibits either emulsion or hydrothermal filling textures in type 2 tourmaline (Figure 5e), implying they formed approximately at the same time. Other sulfides, including pyrite, tetrahedrite, and chalcopyrite, are generally interstitial between tourmaline grains (Figure 5f).

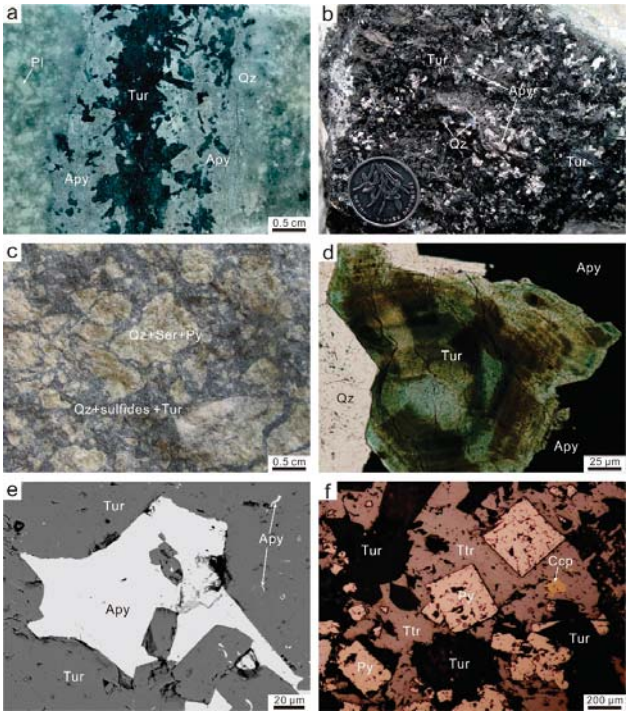

Figure 5. (**a**) Tourmaline occurs as quartz-sulfide-tourmaline veins transecting the quartz diorite porphyry; (**b**) tourmaline intergrown with arsenopyrite in a quartz-sulfide-tourmaline vein; (**c**) fine-grained quartz-sulfide-tourmaline cement the breccias of the altered quartz diorite porphyry; (**d**) tourmaline is characterized by an oscillatory-zoned texture of blue green to brown color, which has sharp, straight boundaries in contact with quartz and arsenopyrite; (**e**) arsenopyrite exhibits either emulsion or hydrothermal filling textures in type 2 tourmaline; (**f**) pyrite, tetrahedrite, and chalcopyrite are generally interstitial between tourmaline grains. Tur—tourmaline; Qz—quartz; Pl—plagioclase; Apy—arsenopyrite; Ser—sericite; Py—pyrite; Ttr—tetrahedrite; Ccp—chalcopyrite.

4. Sampling and Analytical Methods

Type 1 and type 2 tourmaline samples were collected from underground works and drill holes for this study. Double-polished thin sections of each type of tourmaline were examined under an optical microscope to reveal the paragenetic relationships and textural features.

4.1. Electron Microprobe Analysis

Back scattered electron (BSE) imaging and major element analysis using a JEOL JXA-8230 electron microprobe analyzer (EMPA) were completed at the Center for Global Tectonics, School of Earth Sciences, China University of Geosciences (Wuhan, China). The operating conditions were described in Wang et al. [45] and Ning et al. [46] in detail. We used the conditions of 15 kV accelerating voltage, 20 nA probe current, and a 1-micron beam diameter. The dwell times were 10 s on the element peaks and half that on the background locations adjacent to the peaks. Raw X-ray intensities were corrected using a ZAF (atomic number, absorption, fluorescence) correction procedure. A series of natural and synthetic SPI standards were utilized and changed based on the analyzing minerals. The following standards were used: andradite for Si and Ca, rutile for Ti, corundum for Al, hematite for Fe, rhodonite for Mn, pyrope garnet for Mg, albite for Na, sanidine for K, and apatite for P. We routinely analyzed two or three points from the core to rim of some large grains to check for chemical variations. The analyses were normalized to 15 cations (T + Z + Y) exclusive of Na, Ca, and K as suggested by Henry et al. [16]. All iron was assumed to be Fe^{2+}. The proportion of X site vacancies (□) was calculated as [1 − (Na + Ca + K)]. The B_2O_3 and H_2O contents were calculated from stoichiometric constraints assuming B = 3 atoms per formula unit (apfu) and OH^- = 3.5 apfu. Mineral formulae were calculated assuming 31 total anions (O^{2-} and OH^-).

4.2. Laser Ablation-ICPMS Analysis

Trace element analysis was conducted by LA-ICP-MS at the State Key Laboratory of Geological Processes and Mineral Resources (GPMR), China University of Geosciences (CUG), Wuhan, China. Detailed operating conditions for the laser ablation system and the ICP-MS instrument and data reduction have been previously described by Liu et al. [47]. Laser sampling was performed using a GeoLas 2005. An Agilent 7500a ICP-MS instrument was used to acquire ion-signal intensities, and the beam spot size was 44 μm. A "wire" signal smoothing device is included in this laser ablation system, by which smooth signals are produced even at very low laser repetition rates down to 1 Hz [48]. Helium was applied as a carrier gas. Argon was used as the make-up gas and mixed with the carrier gas via a T-connector before entering the ICP. Nitrogen was added into the central gas flow (Ar + He) of the Ar plasma to decrease the detection limit and improve precision [49]. Each analysis incorporated a background acquisition of approximately 20–30 s (gas blank) followed by 50 s of data acquisition from the sample. The Agilent Chemstation was utilized for the acquisition of each individual analysis. Element contents were calibrated against multiple-reference materials (BCR-2G, BIR-1G, BHVO-2G, and SRM610). Off-line selection and integration of background and analyte signals, and time-drift correction were performed by ICPMSDataCal [47], and quantitative calibration was undertaken using the method described by Chen et al. [50].

5. Results

5.1. Major Element Compositions

The major element compositions of type 1 and type 2 tourmaline samples from the Laodou gold deposit are listed in Table S1, and graphically shown in Figure 6. Type 1 tourmaline contains SiO_2 (33.6–35.1 wt.%), MgO (1.22–4.33 wt.%), Al_2O_3 (27.1–30.2 wt.%), FeO (14.6–19.8 wt.%), K_2O (0.034–0.056 wt.%), and MnO (0.16–0.31 wt.%). In contrast, type 2 tourmaline contains higher contents of SiO_2 (34.7–36.6 wt.%), MgO (5.69–9.72 wt.%), and Al_2O_3 (28.2–32.8 wt.%), and lower contents of FeO (5.79–13.5 wt.%), K_2O (0.015–0.032 wt.%), and MnO (0.013–0.028 wt.%) (Figure 6a–e).

Moreover, type 1 tourmaline shows narrow variations in CaO (0.97–1.66 wt.%), P_2O_5 (0.013–0.018 wt.%), and Na_2O (1.74–2.05 wt.%), while large variations in CaO (0.61–2.11 wt.%), P_2O_5 (0–0.023 wt.%), and Na_2O (1.49–2.23 wt.%) are observed in type 2 tourmaline (Figure 6f–h).

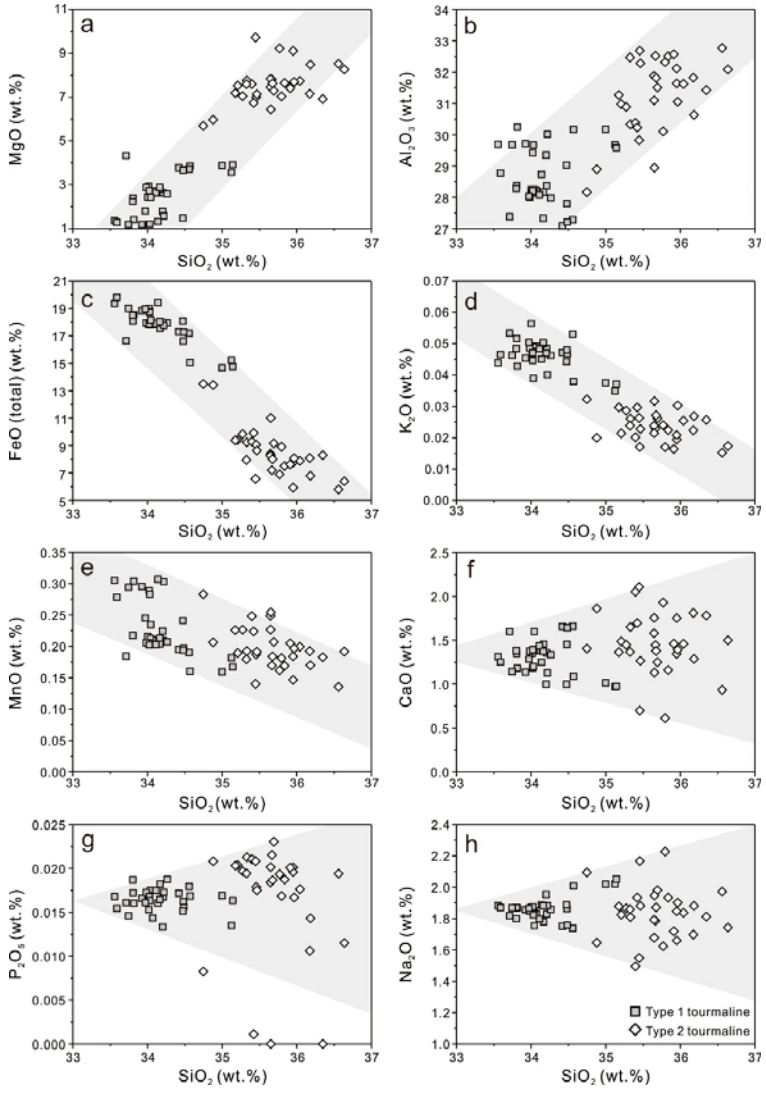

Figure 6. Major element variation diagrams for tourmaline from the Laodou gold deposit, showing the compositional differences between type 1 and type 2 tourmaline. (**a**) SiO_2 versus MgO; (**b**) SiO_2 versus Al_2O_3; (**c**) SiO_2 versus FeO (total); (**d**) SiO_2 versus K_2O; (**e**) SiO_2 versus MnO; (**f**) SiO_2 versus CaO; (**g**) SiO_2 versus P_2O_5; (**h**) SiO_2 versus Na_2O.

Both type 1 and type 2 tourmalines are classified in the alkali group based on the X-site occupancy [51] (Figure 7a). Type 1 tourmaline samples belong to schorl, with higher Fe/(Fe + Mg) ratios (0.68–0.90) and a narrow range of Na/(Na + Ca) ratios (0.65–0.79), whereas most type 2 tourmaline samples are dravite, with lower Fe/(Fe + Mg) ratios (0.27–0.57) and a larger range of Na/(Na + Ca) ratios

(0.57–0.87) [52] (Figure 7b). According to the ternary Al-Fe-Mg and Ca-Fe-Mg diagrams [53], both types of tourmaline are Al-rich and Ca-poor. Type 1 tourmaline has high Fe concentrations and plots in the fields of Li-poor granitoids and associated pegmatites and aplites, Fe^{3+}-rich quartz-tourmaline rocks (hydrothermally altered granites), and near Li-rich granitoids and associated pegmatites and aplites, whereas type 2 tourmaline contains high Mg and plots in the fields of metapelites and metapsammites not coexisting with an Al-saturating phase, Fe^{3+}-rich quartz-tourmaline rocks, calc silicate rocks, and metapelites, and Ca-poor metapelites, metapsammites, and quartz-tourmaline rocks (Figure 7c,d).

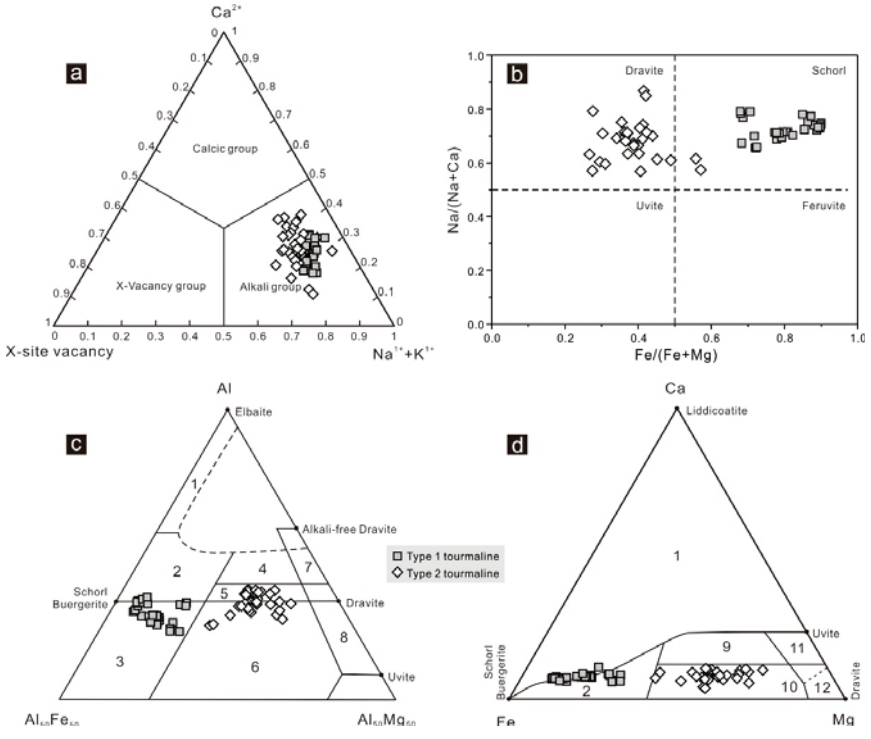

Figure 7. (**a**) Classification of the principal groups of tourmaline based on X-site occupancy [51]; (**b**) nomenclature of the tourmaline based on the classification diagram of Fe/(Fe + Mg) versus Na/(Na + Ca) [52]; (**c**,**d**) ternary Al-Fe-Mg and Ca-Fe-Mg diagrams showing compositions of tourmaline [53]. The regions define the compositions of tourmaline from different rock types. 1. Li-rich granitoids and associated pegmatites and aplites; 2. Li-poor granitoids and associated pegmatites and aplites; 3. Fe^{3+}-rich quartz-tourmaline rocks (hydrothermally altered granites); 4. Metapelites and metapsammites coexisting with an Al-saturating phase; 5. Metapelites and metapsammites not coexisting with an Al-saturating phase; 6. Fe^{3+}-rich quartz-tourmaline rocks, calc silicate rocks, and metapelites; 7. Low Ca metaultramafics and Cr, V-rich metasediments; 8. Metacarbonates and metapyroxenites; 9. Ca-rich metapelites, metapsammites, and calc-silicate rocks; 10. Ca-poor metapelites, metapsammites, and quartz-tourmaline rocks; 11. Metacarbonates; 12. Metaultramafics.

The binary diagrams show the compositional variation and substitution in type 1 and type 2 tourmaline samples. $FeMg_{-1}$ is suggested by the negative correlations between Fe and Mg in the two types of tourmaline samples (Figure 8a). However, the shift of the plots out of the northward arrow of $FeMg_{-1}$ suggest a substitution of Fe by Al (Figure 8b). This is proven by the strong negative correlation between Al and (Fe + Mg) (Figure 8c). The substitutions of $FeMg_{-1}$ and $FeAl_{-1}$ in type 1 and type 2 tourmaline are also supported by the projection of the data along the povondraite-"oxy-dravite" join,

because these plots fall roughly parallel to the $FeAl_{-1}$ and $AlO((Fe, Mg)(OH))_{-1}$ exchange vectors (Figure 8d). The positive correlation between X-site vacancy and Al suggests that the substitution of X-site vacancy Al_{-1} is also involved, alongside $FeMg_{-1}$, and $FeAl_{-1}$ in type 1 and type 2 tourmaline (Figure 8e). The Na content randomly distributes, along with the increase of X-site vacancy and Al, indicating that it is not the main influencing factor controlling the proportion of X-site vacancy and Al in tourmaline (Figure 8f,g). However, the negative correlation between X-site vacancy and Ca suggests that the X-site vacancy decrease in the tourmaline is caused by an increase of Ca content (Figure 8h), which suggests the substitution of X-site vacancy Ca_{-1} in type 1 and type 2 tourmaline.

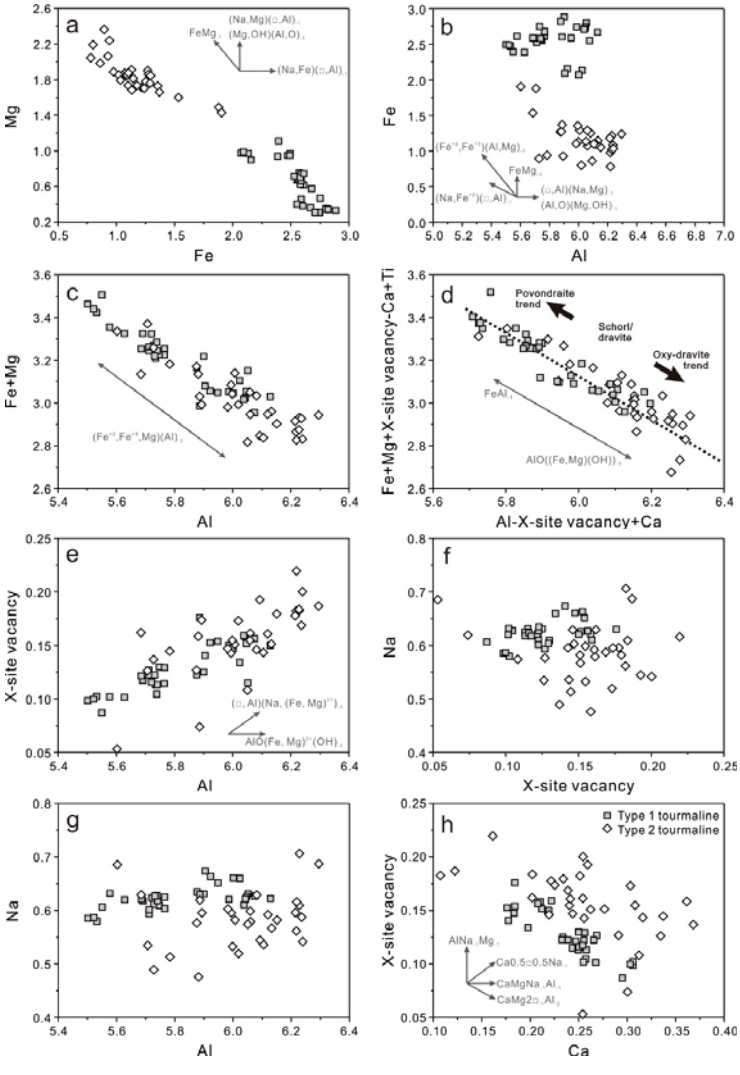

Figure 8. Binary composition diagrams of tourmaline expressed in terms atoms per formula unit (apfu). (**a**) Fe versus Mg; (**b**) Al versus Fe; (**c**) Al versus (Fe + Mg); (**d**) (Al-X-site vacancy + Ca) versus (Fe + Mg + X-site vacancy-Ca + Ti); (**e**) Al versus X-site vacancy; (**f**) X-site vacancy versus Na; (**g**) Ca versus X-site vacancy; (**h**) Al versus Na. Dominant substitution trends are indicated by arrows.

5.2. Trace and Rare Earth Element Compositions

The trace and rare earth element (REE) composition of type 1 and type 2 tourmaline samples from the Laodou gold deposit are summarized in Table S2 and plotted in Figures 9 and 10. Most trace element contents of type 1 and type 2 tourmaline vary between 0.1 and 10 ppm, except for some which are higher—up to hundreds of ppm in the cases of Sr, Sc, Sn, Cr, V, Mn, Zn, and Li, and some which are less than 0.1 ppm, such as Eu, Rb, Cs, Y, W, Bi, Th, and U (Table S2). Large ion lithophile elements (LILE) like Rb, Be, Ba, Cs, and K are relatively enriched in type 1 tourmaline compared to type 2 tourmaline, excluding Sr and Eu (Figure 9a). Most high field-strength elements (HFSEs), including Pb, Y, Sc, Nb, Ta, Ce, Hf, and REEs are also relatively enriched in type 1 tourmaline (Figure 9b). As for other elements, Sn, Cr, V, and Sb are enriched in type 2 tourmaline, whereas Mn, Zn, Li, Co, Cu, W, and Mo contents are higher in type 1 tourmaline (Figure 9c).

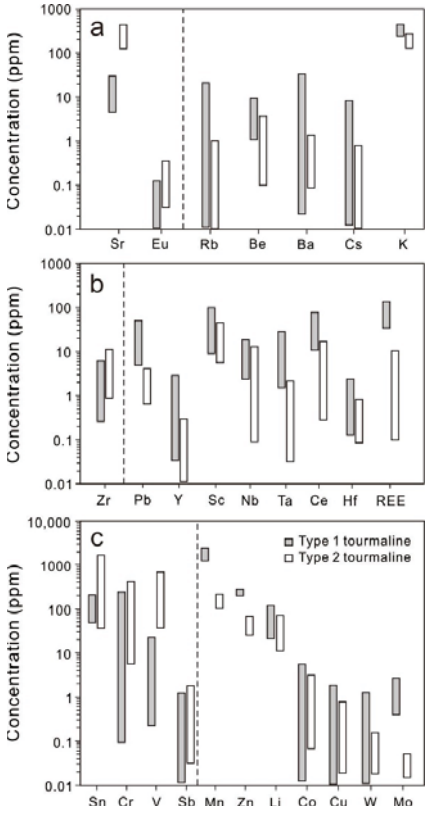

Figure 9. Concentration of (**a**) large ion lithophile elements (LILE); (**b**) high field-strength elements (HFSE); and (**c**) other trace elements in tourmaline from the Laodou gold deposit.

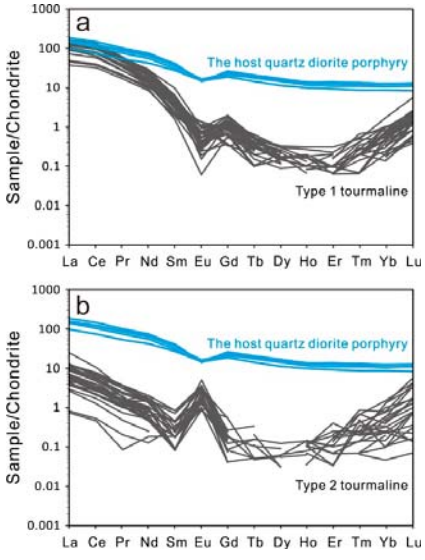

Figure 10. Chondrite-normalized [54] REE patterns of (**a**) type 1 tourmaline and (**b**) type 2 tourmaline from the Laodou gold deposit. Note that the chondrite-normalized REE patterns of the Laodou quartz diorite porphyry are also shown for comparison [31].

The REE concentrations and chondrite-normalized patterns of type 1 and type 2 tourmaline are different (Figure 10). As mentioned above, type 1 tourmaline contains higher REE concentrations than type 2 tourmaline (Figure 9b). Although both type 1 and type 2 tourmaline have similar asymmetric concave-upward shaped REE patterns with enrichment of LREE and HREE and depletion of MREE, type 1 tourmaline is characterized by a strong negative Eu anomaly (Eu* = 0–1.55; Figure 10a) whereas type 2 tourmaline has a strong positive Eu anomaly (Eu* = 2.33–40.15; Figure 10b). For comparison, the host quartz diorite porphyry has a similar asymmetric concave-upward shaped REE pattern, but typically has a higher REE concentration and relatively flat MREE and HREE patterns (Figure 10).

6. Discussion

6.1. Origin of Type 1 and Type 2 Tourmaline

Type 1 tourmaline occurs as disseminated quartz-tourmaline nodules in the Laodou quartz diorite porphyry. Quartz-tourmaline nodules in granite have been widely reported, and have been interpreted as (1) direct crystallization from a boron-rich granitic melt [55,56]; (2) magmatic-hydrothermal features related to the immiscible aqueous boron-rich fluids formed in the late stages of granite crystallization [20,57,58]; and (3) post-magmatic metasomatism by external boron-rich fluids through fractures [59]. Type 1 tourmaline occurs as inclusions in quartz, and grows interstitially between quartz grains (Figure 4d,e). This relationship suggests type 1 tourmaline and quartz formed at the same time. The presence of plagioclase replaced by tourmaline (Figure 4e) indicates that quartz-tourmaline nodules formed late in the crystallization sequence of the Laodou quartz diorite porphyry, rather than crystallizing directly from a boron-rich melt. The field observations showed that quartz-tourmaline nodules are texturally isolated aggregates dispersed in the quartz diorite porphyry without connections by any fractures (Figure 4b), indicating they are products of the crystallization of the quartz diorite porphyry and did not result from post-magmatic metasomatism by external boron-rich fluids infiltrating through fractures. Type 1 tourmaline samples are characterized by higher Fe and Al contents and lower Ca and Mg contents, and are mostly plotted in fields 2 and 3 of total Al-Fe-Mg and Ca-Fe-Mg

diagrams (Figure 7c,d), which is consistent with the fact that type 1 tourmaline is disseminated in the Laodou quartz diorite porphyry. Under the microscope, sericite and muscovite replacing plagioclase or biotite are distributed around the quartz-tourmaline nodules, reflecting the late internal infiltration of aqueous boron-rich fluids (Figure 4c,f). All these observations are consistent with the previous interpretation that quartz-tourmaline nodules formed from the magmatic hydrothermal fluids in the late crystallization sequence of the Laodou quartz diorite porphyry. This interpretation is also supported by the magmatic boron isotopic composition ($\delta^{11}B$ = –8.9–-5.5‰) of type 1 tourmaline [39].

Type 2 tourmaline occurs as radial crystal clusters in open-space filling quartz-sulfide-tourmaline veins (Figure 5a,b), indicating a hydrothermal origin. Type 2 tourmaline is commonly intergrown with arsenopyrite in the field, as shown by microscope observations (Figure 5). Mineral relations and textures, especially in the straight boundaries between arsenopyrite and tourmaline grains (Figure 5d) and the textures of arsenopyrite emulsion and/or infillings in tourmaline (Figure 5e), indicate the co-crystallization of type 2 tourmaline and arsenopyrite in the quartz-sulfide-tourmaline veins. Arsenopyrite is one of the gold-bearing sulfides in the Laodou deposit, containing detectable Au up to 4.32 ppm [42]. Thus, type 2 tourmaline, coexisting with Au-bearing arsenopyrite, can be interpreted as a hydrothermal product that crystallized from the ore-forming fluids of the Laodou gold deposit.

6.2. Records of Magmatic Hydrothermal Evolution

The composition of tourmaline is largely ruled by fluid/rock ratios and chemical equilibria with coexisting phases in the hydrothermal system [19]. In the Laodou deposit, type 1 tourmaline occurs as isolated quartz-tourmaline nodules in the quartz diorite porphyry, without connections by any fractures (Figure 4b), whereas type 2 tourmaline is represented as quartz-sulfide-tourmaline veins transecting the quartz diorite porphyry (Figures 2b and 5a). These field observations imply that type 1 tourmaline likely formed in a closed "rock-buffered" system with low fluid/rock ratios, whereas type 2 tourmaline crystallized in an open "fluid-buffered" system with high fluid/rock ratios. This interpretation is further supported by an oscillatory-zoned texture that is rare in type 1 tourmaline (Figure 4d) but is well-developed in type 2 tourmaline (Figure 5d), because the oscillatory zoning texture is commonly proposed as a record of high fluid/rock ratios in an open system [60]. Thus, type 1 tourmaline's chemistry is mainly controlled by the host quartz diorite porphyry, whereas type 2 tourmaline's chemistry retains some signatures of the ore-forming fluids. This is evidenced by the REE concentrations and REE patterns of type 1 and type 2 tourmaline, as discussed below.

Compared with the host quartz diorite porphyry, type 1 tourmaline has lower REE concentrations and a similar REE pattern, with a more negative Eu anomaly and higher contents of HREE. The lower REE concentrations in type 1 tourmaline are due to the co-crystallization of REE-rich apatite and zircon in the quartz diorite porphyry [20,31]. The similar REE patterns between type 1 tourmaline and the quartz diorite porphyry is the manifestation of the "source-inherited" characteristic. Tourmaline prefers Eu^{2+} over Eu^{3+}, but Eu^{3+} predominates in the magmatic melt [61]. This may explain type 1 tourmaline displaying a more negative Eu anomaly when crystallized from the low Eu^{2+} magmatic fluids generated by the exsolution of magmatic melt. The higher enrichment of HREE in type 1 tourmaline is mainly caused by the metasomatized and replaced plagioclase around the quartz-tourmaline nodules (Figure 4e,f), because HREE can be released from plagioclase more readily than Eu and LREE [62]. Likewise, this can also explain the enriched HREE in type 2 tourmaline, because quartz-sulfide-tourmaline veins are commonly enveloped by phyllic alteration (Figure 5a), reflecting the infiltration metasomatism represented by the formation of sericite as an alteration product of plagioclase [39]. Although type 2 tourmaline shows an asymmetric concave-upward REE pattern resembling type 1 tourmaline and the host quartz diorite porphyry, lower REE concentrations, and a strong positive Eu anomaly are exhibited (Figure 10b). Similar REE patterns are likely inherited from the magmatic fluids generated by the magma exsolution, which was evidenced by the below Co/Ni ratio constraints on the fluid provenance. The lower REE concentrations are likely caused by

the infiltration and dilution of the late inflow of meteoric fluids, characterized by low REE contents, which was supported by the reported H-O-B isotopic data of type 2 tourmaline [39]. The positive Eu anomaly of type 2 tourmaline does not reflect unusual redox conditions [7], except for the dominance of soluble Eu^{2+} over Eu^{3+} in fluids at temperature exceeding 200–250 °C [63]. This minimum temperature constraint is consistent with the microthermometry results of fluid inclusions (220–295 °C) in quartz from the quartz-sulfide-tourmaline veins [42,43].

6.3. Constraints on the Fluid Provenance

Previous studies have demonstrated that Co and Ni can partition strongly into tourmaline and arsenopyrite when they crystallize from ore-forming fluids [64,65]. In some cases, the Co/Ni ratio can be used as an index to place constraints on the source of ore-forming fluids [7,66]. In this study, type 2 tourmaline coexists with Au-bearing arsenopyrite in the auriferous lodes (Figure 5). It has been supposed that the Co/Ni ratios of coexisting arsenopyrite and tourmaline should represent the Co/Ni ratio of ore-forming fluids if they define a statistically significant linear trend [66]. The plotted Co and Ni contents of the coexisting type 2 tourmaline and arsenopyrite define a regression line with a squared correlation coefficient of 0.93 and an angular coefficient of 0.66 (Figure 11a). A correlation coefficient near 1 reflects the systematic tendency of Co and Ni to partition into tourmaline and arsenopyrite. The angular coefficient of 0.66 represents the Co/Ni ratio of the fluid from which the arsenopyrite and tourmaline precipitated. This value is close to the average Co/Ni ratio (0.43) of the Laodou quartz diorite porphyry [31]. We then plotted the Co and Ni contents of the Laodou quartz diorite porphyry for comparison. It is noted that these plots are comparable and restricted to the regression line that was defined by coexisting type 2 tourmaline and arsenopyrite (Figure 11a). The consistency of the projection data suggests that the related ore-forming fluids have a magmatic origin. This interpretation is further supported by the magmatic H-O-B isotopic signatures of type 2 tourmaline [39].

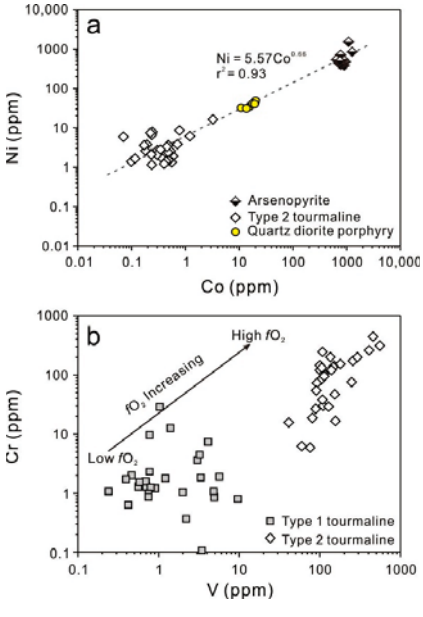

Figure 11. (**a**) Scatterplot of Co (ppm) versus Ni (ppm) in coexisting type 2 tourmaline and arsenopyrite [42] from the Laodou gold deposit. The Co and Ni contents of the host quartz diorite porphyry are shown for comparison [31]; (**b**) V (ppm) versus Cr (ppm) for type 1 and type 2 tourmaline samples from the Laodou gold deposit.

6.4. Redox State and Implications for Gold Precipitation

The ferric/ferrous ratios in tourmaline can be used as a monitor for changes in the redox state of hydrothermal fluids [19]. For example, it has been concluded that tourmaline in some porphyry Cu ± Mo deposits formed from oxidizing fluids based on their Al-poor composition and inverse Al-Fe correlations [67]. In this study, type 1 and type 2 tourmaline element plots showed a positive correlation between [Fe + Mg + X-site vacancy-Ca + Ti] and [Al-X-site + Ca], consistent with some involvement of the $FeAl_{-1}$ and/or $[AlO][(Fe, Mg)(OH)]_{-1}$ exchange vectors (Figure 8d). The compositions of tourmaline plots along the "oxy-dravite"–povondraite trend have been widely recognized in various hydrothermal systems [12,68]. This trend enables us to evaluate the significant proportion of the substitution of Al^{3+} by Fe^{3+}, and in turn implies changes of the redox state during tourmaline growth. Although there is some overlap of the type 1 and type 2 tourmaline points in the plot, type 1 tourmaline approaches the end member of povondraite, whereas type 2 tourmaline is plotted near the end member of oxy-dravite (Figure 8d). Accordingly, these plots show that more $[AlO][(Fe, Mg)(OH)]_{-1}$ is exchanged in type 2 tourmaline, and imply a more oxidizing environment for the formation of type 2 tourmaline.

The mobility of redox-sensitive trace elements is controlled by the changes of the redox state [69]. V and Cr are redox-sensitive elements and their concentrations in tourmaline are indicators of oxygen fugacity of the parental hydrothermal fluids [66]. This is because V is commonly transported in hydrothermal fluids as the soluble species V^{4+} and V^{5+}, rather than V^{3+} [70], whereas Cr is typically mobilized as Cr^{4+} under sufficiently oxidizing conditions [66]. Thus, the V and Cr concentrations in tourmaline have potential to act as an indicator of the redox state of hydrothermal fluids. In this study, type 2 tourmaline is characterized by remarkably higher V and Cr concentrations than type 1 tourmaline (Figure 11b), suggesting a higher oxygen fugacity of the parental fluids of type 1 tourmaline than type 2 tourmaline.

As mentioned above, type 2 tourmaline coexists with Au-bearing arsenopyrite in the auriferous lodes. Hence, the elevated concentrations of Fe^{3+}, V, and Cr in type 2 tourmaline fingerprint the increase of oxygen fugacity in the ore-forming fluids. This is consistent with the H-O-B isotopic data of type 2 tourmaline, which indicate the input of external meteoric-derived groundwater during precipitation of the quartz-sulfide-tourmaline veins [39]. The related fluid mixing would most likely lead to the increase of oxygen fugacity in the ore-forming fluids. In addition, gold as bisulfide ($Au(HS)_2^-$) complexes is widely acknowledged to account for gold transport in acidic reducing ore fluids in meso-epithermal ore-forming systems [71]. Increasing oxygen fugacity will destabilize $Au(HS)_2^-$ [72], facilitating the precipitation of gold in arsenopyrite and/or arsenian pyrite, and/or as native gold. Thus, we propose that the most important consequence of the increase of oxygen fugacity in the ore-forming fluids is acting as a trigger response for the precipitation of gold.

7. Conclusions

(1) Two types of tourmaline are recognized in the Laodou deposit. Type 1 tourmaline occurs as quartz-tourmaline nodules within the quartz diorite porphyry, whereas type 2 tourmaline occurs as quartz-sulfide-tourmaline veins in auriferous lodes.

(2) Both tourmaline types fall into the alkali group and are classified under the schorl-dravite solid solution series. The substitutions of $FeMg_{-1}$, $FeAl_{-1}$, $AlO((Fe, Mg)(OH))_{-1}$, and X-site vacancy Ca_{-1} are inferred by the variations of their major element compositions.

(3) Type 1 tourmaline samples are magmatic tourmaline, and were produced by the late crystallization process of the quartz diorite porphyry; type 2 tourmaline samples coexist with Au-bearing arsenopyrite and are crystallized from ore-forming fluids. Their REE compositions record the related magmatic-hydrothermal evolution.

(4) The Co/Ni ratios of the coexisting type 2 tourmaline and arsenopyrite are close to that of the host quartz diorite porphyry, indicating a magma origin of the ore-forming fluids.

(5) The elevated concentrations of Fe^{3+}, V, and Cr in type 2 tourmaline fingerprint the increase of the oxygen fugacity in the ore-forming fluids, which is a trigger of gold precipitation.

Supplementary Materials: The following are available online at http://www.mdpi.com/2075-163X/10/8/647/s1, Table S1: Major element compositions of type 1 and type 2 tourmaline samples from the Laodou gold deposit, Table S2: Trace element compositions of type 1 and type 2 tourmaline samples from the Laodou gold deposit.

Author Contributions: Conceptualization, X.J. and J.S.; investigation, X.J. and J.S.; data curation, X.J.; writing—original draft preparation, X.J.; writing—review and editing, X.J. and J.S. All authors have read and agreed to the published version of the manuscript.

Funding: This research was funded by the National Natural Science Foundation of China (Grant No. 41772081, 41072057).

Acknowledgments: We are grateful to Chenzhou Mining Limited for access to the mine and to Liangping Dong for geologic guidance. We also gratefully acknowledgment Zhaochu Hu, Jie Lin, and Chunfei Chen for their help with LA-ICPMS analysis.

Conflicts of Interest: The authors declare no conflict of interest.

References

1. Williamson, B.J.; Spratt, J.; Adams, J.T.; Tindle, A.G.; Stanley, C.J. Geochemical constraints from zoned hydrothermal tourmalines on fluid evolution and Sn mineralization: An example from fault breccias at Roche, SW England. *J. Petrol.* **2000**, *41*, 1439–1453. [CrossRef]
2. Sushchevskaya, T.; Ignatiev, A.; Velivetskaya, T. Magmatic Nature of Mineralizing Fluids in the Solnechnoye Sn Deposit (Russia) Deduced from Isotopic (H, O) Compositions of Tourmaline. *Resour. Geol.* **2011**, *61*, 407–413. [CrossRef]
3. Codeço, M.S.; Weis, P.; Trumbull, R.B.; Pinto, F.; Lecumberri-Sanchez, P.; Wilke, F.D.H. Chemical and boron isotopic composition of hydrothermal tourmaline from the Panasqueira W-Sn-Cu deposit, Portugal. *Chem. Geol.* **2017**, *468*, 1–16. [CrossRef]
4. Yavuz, F.; Iskenderoglu, A.; Jiang, S.Y. Tourmaline compositions from the Salikvan porphyry Cu-Mo deposit and vicinity, northeastern Turkey. *Can. Mineral.* **1999**, *37*, 1007–1023.
5. Dill, H.G.; Garrido, M.M.; Melcher, F.; Gomez, M.C.; Luna, L.I. Depth-related variation of tourmaline in the breccia pipe of the San Jorge porphyry copper deposit, Mendoza, Argentina. *Ore Geol. Rev.* **2012**, *48*, 271–277. [CrossRef]
6. Garda, G.M.; Trumbull, R.B.; Beljavskis, P.; Wiedenbeck, M. Boron isotope composition of tourmalinite and vein tourmalines associated with gold mineralization, Serra do Itaberaba Group, central Ribeira Belt, SE Brazil. *Chem. Geol.* **2009**, *264*, 207–220. [CrossRef]
7. Trumbull, R.B.; Garda, G.M.; Xavier, R.P.; Cavalcanti, J.A.D.; Codeço, M.S. Tourmaline in the Passagem de Mariana gold deposit (Brazil) revisited: Major-element, trace-element and B-isotope constraints on metallogenesis. *Miner. Depos.* **2019**, *54*, 395–414. [CrossRef]
8. Daver, L.; Jébrak, M.; Beaudoin, G.; Trumbull, R.B. Three-stage formation of greenstone-hosted orogenic gold deposits in the Val-d'Or mining district, Abitibi, Canada: Evidence from pyrite and tourmaline. *Ore Geol. Rev.* **2020**, *120*, 103449. [CrossRef]
9. Slack, J.F.; Palmer, M.R.; Stevens, B.P.J.; Barnes, R.G. Origin and significance of tourmaline-rich rocks in the Broken Hill district, Australia. *Econ. Geol.* **1993**, *88*, 505–541. [CrossRef]
10. Griffin, W.L.; Slack, J.F.; Ramsden, A.R.; Win, T.T.; Ryan, C.G. Trace elements in tourmalines from massive sulfides deposits and tourmalinites; geochemical controls and exploration applications. *Econ. Geol.* **1996**, *91*, 657–675. [CrossRef]
11. Jiang, S.Y.; Palmer, M.R.; Slack, J.F.; Shaw, D.R. Boron isotope systematics of tourmaline formation in the Sullivan Pb–Zn–Ag deposit, British Columbia, Canada. *Chem. Geol.* **1999**, *158*, 131–144. [CrossRef]
12. Tornos, F.; Wiedenbeck, M.; Velasco, F. The boron isotope geochemistry of tourmaline-rich alteration in the IOCG systems of northern Chile: Implications for a magmatic-hydrothermal origin. *Miner. Depos.* **2011**, *47*, 483–499. [CrossRef]

13. Xavier, R.P.; Wiedenbeck, M.; Trumbull, R.B.; Dreher, A.M.; Monteiro, L.V.S.; Rhede, D.; De Araujo, C.E.G.; Torresi, I. Tourmaline B-isotopes fingerprint marine evaporites as the source of high-salinity ore fluids in iron oxide copper-gold deposits, Carajás Mineral Province (Brazil). *Geology* **2008**, *36*, 743–746. [CrossRef]
14. Kelly, C.J.; Davis, W.J.; Potter, E.G.; Corriveau, L. Geochemistry of hydrothermal tourmaline from IOCG occurrences in the Great Bear magmatic zone: Implications for fluid source(s) and fluid composition evolution. *Ore Geol. Rev.* **2020**, *118*, 103329. [CrossRef]
15. Dutrow, B.L.; Henry, D.J. Tourmaline: A geologic DVD. *Elements* **2011**, *7*, 301–306. [CrossRef]
16. Henry, D.J.; Novák, M.; Hawthorne, F.C.; Ertl, A.; Dutrow, B.L.; Uher, P.; Pezzotta, F. Nomenclature of the tourmaline-supergroup minerals. *Am. Miner.* **2011**, *96*, 895–913. [CrossRef]
17. van Hinsberg, V.J.; Henry, D.J.; Dutrow, B.L. Tourmaline as a petrologic forensic mineral: A unique recorder of its geologic past. *Elements* **2011**, *7*, 327–332. [CrossRef]
18. Dutrow, B.L.; Henry, D.J. Tourmaline compositions and textures: Reflections of the fluid phase. *J. Geosci.* **2018**, *63*, 99–110. [CrossRef]
19. Slack, J.F.; Trumbull, R.B. Tourmaline as a recorder of ore-forming processes. *Elements* **2011**, *7*, 321–326. [CrossRef]
20. Yang, S.Y.; Jiang, S.Y.; Zhao, K.D.; Dai, B.Z.; Yang, T. Tourmaline as a recorder of magmatic–hydrothermal evolution: An in situ major and trace element analysis of tourmaline from the Qitianling batholith, South China. *Contrib. Mineral. Petrol.* **2015**, *170*, 1–21. [CrossRef]
21. Hu, D.L.; Jiang, S.Y. In-situ elemental and boron isotopic variations of tourmaline from the Maogongdong deposit in the Dahutang W-Cu ore field of northern Jiangxi Province, South China: Insights into magmatic-hydrothermal evolution. *Ore Geol. Rev.* **2020**, *122*, 103502. [CrossRef]
22. Kröner, A.; Zhang, G.W.; Sun, Y. Granulites in the Tongbai area, Qinling belt, China: Geochemistry, petrology, single zircon geochronology, and implications for the tectonic evolution of eastern Asia. *Tectonics* **1993**, *12*, 245–255. [CrossRef]
23. Zhang, G.W. *Qinling Orogenic Belt and Continental Dynamics*; Science Press: Beijing, China, 2001; 855p. (In Chinese)
24. Dong, Y.P.; Zhang, G.W.; Neubauer, F.; Liu, X.M.; Genser, J.; Hauzenberger, C. Tectonic evolution of the Qinling orogen, China: Review and synthesis. *J. Asian Earth Sci.* **2011**, *41*, 213–237. [CrossRef]
25. Meng, Q.R.; Zhang, G.W. Geologic framework and tectonic evolution of the Qinling orogen, central China. *Tectonophysics* **2000**, *323*, 183–196. [CrossRef]
26. Zhang, G.W.; Guo, A.L.; Yao, A.P. Western Qinling—Songpan continental tectonic node in China's continental tectonics. *Earth Sci. Front.* **2004**, *11*, 23–32, (In Chinese with English Abstract).
27. Zhu, L.M.; Zhang, G.W.; Yang, T.; Wang, F.; Gong, H.J. Geochronology, petrogenesis and tectonic implications of the Zhongchuan granitic pluton in the Western Qinling metallogenic belt, China. *Geol. J.* **2013**, *48*, 310–334. [CrossRef]
28. Sun, W.D.; Li, S.G.; Chen, Y.D.; Li, Y.J. Timing of synorogenic granitoids in the South Qinling, central China: Constraints on the evolution of the Qinling-Dabie Orogenic belt. *J. Geol.* **2002**, *110*, 457–468. [CrossRef]
29. Qin, J.F.; Lai, S.C.; Grapes, R.; Diwu, C.R.; Ju, Y.J.; Li, Y.F. Geochemical evidence for origin of magma mixing for the Triassic monzonitic granite and its enclaves at Mishuling in the Qinling orogen (central China). *Lithos* **2009**, *112*, 259–276. [CrossRef]
30. Luo, B.J.; Zhang, H.F.; Lü, X.B. U–Pb zircon dating, geochemical and Sr–Nd–Hf isotopic compositions of Early Indosinian intrusive rocks in West Qinling, central China: Petrogenesis and tectonic implications. *Contrib. Mineral. Petrol.* **2012**, *164*, 551–569. [CrossRef]
31. Jin, X.Y.; Li, J.W.; Sui, J.X.; Wen, G.; Zhang, J.Y. Geochronological and geochemical constraints on the genesis and tectonic setting of Dewulu intrusive complex in Xiahe-Hezuo district of Western Qinling Orogen. *J. Earth Sci. Environ.* **2013**, *35*, 20–38, (In Chinese with English Abstract).
32. Kou, X.H.; Zhang, K.X.; Lin, Q.X.; Zhu, Y.H.; Chen, F.N.; Luo, G.M.; Xu, Y.D. The distribution of Permian sedimentary sequences in the adjacent area of Qinling-Qilian-Kunlun, central China. *Earth Sci. J. China Univ. Geosci.* **2007**, *32*, 681–690, (In Chinese with English Abstract).
33. Sui, J.X.; Li, J.W.; Jin, X.Y.; Vasconcelos, P.; Zhu, R. $^{40}Ar/^{39}Ar$ and U-Pb constraints on the age of the Zaozigou gold deposit, Xiahe-Hezuo district, West Qinling orogen, China: Relation to early Triassic reduced intrusions emplaced during slab rollback. *Ore Geol. Rev.* **2018**, *101*, 885–899. [CrossRef]

34. Yu, H.C.; Qiu, K.F.; Nassif, M.T.; Geng, J.Z.; Sai, S.X.; Duo, D.W.; Huang, Y.Q.; Wang, J. Early orogenic gold mineralization event in the West Qinling related to closure of the Paleo-Tethys Ocean—Constraints from the Ludousou gold deposit, central China. *Ore Geol. Rev.* **2020**, *117*, 103217. [CrossRef]
35. Guo, X.Q.; Yan, Z.; Wang, Z.Q.; Wang, T.; Hou, K.J.; Fu, C.L.; Li, J.L. Middle Triassic arc magmatism along the northeastern margin of the Tibet: U-Pb and Lu-Hf zircon characterization of the Gangcha complex in the West Qinling terrane, central China. *J. Geol. Soc.* **2012**, *169*, 327–336. [CrossRef]
36. Zhang, C.L.; Wang, T.; Wang, X.X. Origin and tectonic setting of the early Mesozoic granitoids in Qinling orogenic belt, China. *Geol. J. China Univ.* **2008**, *14*, 304–316, (In Chinese with English Abstract).
37. Sui, J.X.; Li, J.W.; Hofstra, A.H.; Obrien, H.; Lahaye, Y.; Yan, D.R.; Li, Z.K.; Jin, X.Y. Genesis of the Zaozigou gold deposit, West Qinling orogen, China: Constraints from sulfide trace element and stable isotope geochemistry. *Ore Geol. Rev.* **2020**, *122*, 103477. [CrossRef]
38. Wang, J.P.; Liu, Z.J.; Liu, J.J.; Zeng, X.T.; Wang, K.X.; Liu, B.Z.; Wang, H.; Liu, C.H.; Zhang, F.F. Trace element compositions of pyrite from the Shuangwang gold breccias, Western Qinling Orogen, China: Implications for deep ore prediction. *J. Earth Sci.* **2018**, *29*, 564–572. [CrossRef]
39. Jin, X.Y.; Li, J.W.; Hofstra, A.H.; Sui, J.X. Magmatic-hydrothermal origin of the early Triassic Laodou lode gold deposit in the Xiahe-Hezuo district, West Qinling orogen, China: Implications for gold metallogeny. *Miner. Depos.* **2017**, *52*, 883–902. [CrossRef]
40. Sui, J.X.; Li, J.W.; Wen, G.; Jin, X.Y. The Dewulu Reduced Au-Cu skarn deposit in the Xiahe-Hezuo district, West Qinling orogen, China: Implications for an intrusion-related gold system. *Ore Geol. Rev.* **2016**, *80*, 1230–1244. [CrossRef]
41. Zhang, D.X.; Shu, Z.X.; Cao, H.; Lu, A.H. Indosinian magmatism and tectonic setting of Xiahe-Hezuo area, western Qinling Mountains—Implications from the Dewulu quartz diorite and Laodou quartz diorite porphyry. *Geol. China* **2015**, *42*, 1257–1273, (In Chinese with English Abstract).
42. Jin, X.Y. Genesis of the Laodou Gold Deposit, Xiahe-Hezuo Area, West Qinling Orogen: Constraints from the Geochemistry and Isotopic Geochronology. Master's Thesis, China University of Geosciences, Wuhan, China, 2013.
43. Wang, F. Discussion of the metallogenic geological conditions and ore genesis of the Laodou gold deposit in Gansu Province. *Gansu Metall.* **2004**, *26*, 16–18, (In Chinese with English Abstract).
44. Zhou, J.B. Study on geological characteristics and metallogenic mechanism of the Laodou gold deposit in Gansu province, China. *Gansu Metall.* **2011**, *33*, 56–60, (In Chinese with English Abstract).
45. Wang, J.P.; Li, X.W.; Ning, W.B.; Kusky, T.; Wang, L.; Polat, A.; Deng, H. Geology of a Neoarchean suture: Evidence from the Zunhua ophiolitic mélange of the Eastern Hebei Province, North China Craton. *GSA Bull.* **2019**, *131*, 1943–1964. [CrossRef]
46. Ning, W.B.; Wang, J.P.; Xiao, D.; Li, F.F.; Huang, B.; Fu, D. Electron probe microanalysis of monazite and its applications to U-Th-Pb dating of geological samples. *J. Earth Sci.* **2019**, *30*, 952–963. [CrossRef]
47. Liu, Y.S.; Hu, Z.C.; Gao, S.; Günther, D.; Xu, J.; Gao, C.G.; Chen, H.H. In situ analysis of major and trace elements of anhydrous minerals by LA-ICP-MS without applying an internal standard. *Chem. Geol.* **2008**, *257*, 34–43. [CrossRef]
48. Hu, Z.C.; Liu, Y.S.; Gao, S.; Xiao, S.Q.; Zhao, L.S.; Günther, D.; Li, M.; Zhang, W.; Zong, K.Q. A "wire" signal smoothing device for laser ablation inductively coupled plasma mass spectrometry analysis. *Spectrochim. Acta Part B At. Spectrosc.* **2012**, *78*, 50–57. [CrossRef]
49. Hu, Z.C.; Gao, S.; Liu, Y.S.; Hu, S.H.; Chen, H.H.; Yuan, H.L. Signal enhancement in laser ablation ICP-MS by addition of nitrogen in the central channel gas. *J. Anal. At. Spectrom.* **2008**, *23*, 1093–1101. [CrossRef]
50. Chen, C.F.; Liu, X.G.; Hu, Z.C.; Zong, K.Q.; Liu, Y.S. In situ analysis of the major and trace element compositions of hydrous silicate minerals by LA-ICP-MS. *Earth Sci. J. China Univ. Geosci.* **2014**, *39*, 525–536, (In Chinese with English Abstract).
51. Hawthorne, F.C.; Henry, D.J. Classification of the minerals of the tourmaline group. *Eur. J. Mineral.* **1999**, *11*, 201–216. [CrossRef]
52. Jiang, S.Y.; Palmer, M.R.; Yeats, C.J. Chemical and boron isotopic compositions of tourmaline from the Archean Big Bell and Mount Gibson gold deposits, Murchison Province, Yilgarn Craton, Western Australia. *Chem. Geol.* **2002**, *188*, 229–247. [CrossRef]
53. Henry, D.J.; Guidotti, C.V. Tourmaline as a petrogenetic indicator mineral- An example from the staurolite-grade metapelites of NW Maine. *Am. Mineral.* **1985**, *70*, 1–15.

54. Sun, S.S.; Mcdonough, W.F. Chemical and isotopic systematics of oceanic basalts: Implications for mantle composition and processes. *Geol. Soc. Lond. Spec. Publ.* **1989**, *42*, 313–345. [CrossRef]
55. Perugini, D.; Poli, G. Tourmaline nodules from Capo Bianco aplite (Elba Island, Italy): An example of diffusion limited aggregation growth in a magmatic system. *Contrib. Mineral. Petrol.* **2007**, *153*, 493–508. [CrossRef]
56. Longfellow, K.M.; Swanson, S.E. Skeletal tourmaline, undercooling, and crystallization history of the Stone Mountain granite, Georgia, USA. *Can. Mineral.* **2011**, *49*, 341–357. [CrossRef]
57. Samson, I.M.; Sinclair, W.D. Magmatic hydrothermal fluids and the origin of quartz-tourmaline orbicules in the Seagull Batholith, Yukon Territory. *Can. Mineral.* **1992**, *30*, 937–954.
58. Trumbull, R.B.; Krienitz, M.S.; Gottesmann, B.; Wiedenbeck, M. Chemical and boron-isotope variations in tourmalines from an S-type granite and its source rocks: The Erongo granite and tourmalinites in the Damara Belt, Namibia. *Contrib. Mineral. Petrol.* **2008**, *155*, 1–18. [CrossRef]
59. Rozendaal, A.; Bruwer, L. Tourmaline nodules: Indicators of hydrothermal alteration and Sn-Zn-(W) mineralization in the Cape Granite Suite, South Africa. *J. Afr. Earth Sci.* **1995**, *21*, 141–155. [CrossRef]
60. Taylor, B.E.; Slack, J.F. Tourmalines from Appalachian-Caledonian massive sulfide deposits; textural, chemical, and isotopic relationships. *Econ. Geol.* **1984**, *79*, 1703–1726. [CrossRef]
61. van Hinsberg, V.J. Preliminary experimental data on trace-element partitioning between tourmaline and silicate melt. *Can. Mineral.* **2011**, *49*, 153–163. [CrossRef]
62. Shibata, S.N.; Tanaka, T.; Yamamoto, K. Crystal structure control of the dissolution of rare earth elements in water-mineral interactions. *Geochem. J.* **2006**, *40*, 437–446. [CrossRef]
63. Bau, M.; Möller, P. Rare earth element fractionation in metamorphogenic hydrothermal calcite, magnesite and siderite. *Mineral. Petrol.* **1992**, *45*, 231–246. [CrossRef]
64. Klemme, S.; Marschall, H.R.; Jacob, D.E.; Prowatke, S.; Ludwig, T. Trace-element partitioning and boron isotope fractionation between white mica and tourmaline. *Can. Mineral.* **2011**, *49*, 165–176. [CrossRef]
65. Cook, N.J.; Ciobanu, C.L.; Meria, D.; Silcock, D.; Wade, B. Arsenopyrite-Pyrite Association in an Orogenic Gold Ore: Tracing Mineralization History from Textures and Trace Elements. *Econ. Geol.* **2013**, *108*, 1273–1283. [CrossRef]
66. Cabral, A.R.; Koglin, N. Hydrothermal fluid source constrained by Co/Ni ratios in coexisting arsenopyrite and tourmaline: The auriferous lode of Passagem, Quadrilátero Ferrífero of Minas Gerais, Brazil. *Mineral. Petrol.* **2012**, *104*, 137–145. [CrossRef]
67. Slack, J.F. Tourmaline associations with hydrothermal ore deposits. *Rev. Mineral.* **2002**, *33*, 559–644.
68. Henry, D.J.; Sun, H.T.; Slack, J.F.; Dutrow, B.L. Tourmaline in meta-evaporites and highly magnesian rocks: Perspectives from Namibian tourmalinites. *Eur. J. Mineral.* **2008**, *20*, 889–904. [CrossRef]
69. Lee, C.T.A.; Leeman, W.P.; Canil, D.; Li, Z.X. Similar V/Sc systematics in MORB and arc basalts: Implications for the oxygen fugacities of their mantle source regions. *J. Petrol.* **2005**, *46*, 2313–2336.
70. Wanty, R.B.; Goldhaber, M.B. Thermodynamics and kinetics of reactions involving vanadium in natural systems: Accumulation of vanadium in sedimentary rocks. *Geochim. Cosmochim. Acta* **1992**, *56*, 1471–1483. [CrossRef]
71. Liu, X.D.; Lu, X.C.; Wang, R.C.; Zhou, H.Q.; Xu, S.J. Speciation of gold in hydrosulphide-rich ore-forming fluids: Insights from first-principles molecular dynamics simulations. *Geochim. Cosmochim. Acta* **2011**, *75*, 185–194. [CrossRef]
72. Hofstra, A.H.; Cline, J.S. Characteristics and models for Carlin-type gold deposits. *Rev. Econ. Geol.* **2000**, *13*, 163–220.

minerals

MDPI

Article

Porphyry-Related Metamorphosed Au-Ag and Cu-Mo Deposits in the Precambrian of the Fennoscandian Shield

Arkadii A. Kalinin * and Nikolay M. Kudryashov

Geological Institute, Kola Science Center, Russian Academy of Science, Apatity 184200, Russia; nik@geoksc.apatity.ru

* Correspondence: kalinin@geoksc.apatity.ru; Tel.: +7-921-663-68-36

Abstract: The Pellapahk Cu-Mo and Oleninskoe Au-Ag deposits in the western segment of the Russian Arctic in the Kolmozero–Voronya greenstone belt are considered two parts of an Archean (2.83–2.82 Ga) porphyry-epithermal system, probably the oldest one defined in the Fennoscandian Shield. Formation of the Oleninskoe Au-Ag deposit at the epithermal stage of the system is indicated by the spatial and genetic relationships with the sills of granite porphyry, the geochemical association of ore elements (Au, Ag, Cu, Pb, Sb, As), an Au/Ag ratio of <0.2, and the multiplicity of silver mineralization with different Ag, Cu, Pb, Sb sulfosalts. The geological–structural characteristics of the Oleninskoe and the Pellapahk, i.e., their location in a shear zone, the morphology and size of ore bodies, the scale of the deposits, and the intensity and zoning of rock alteration, do not oppose this model. Mineralized rocks of the Pellapahk Cu-Mo and Oleninskoe Au-Ag deposits were amphibolite metamorphosed in the Neoarchean and again in the Paleoproterozoic. Structures of sulfide melt crystallization formed in the ores during metamorphism, those are fine intergrowths of galena, argentotetrahedrite, pyrargyrite, pyrrhotite, ullmannite, stutzite, and other mineral phases of low-melting-point metals such as Ag, Cu, Pb, Sb, As, Bi.

Keywords: Fennoscandian Shield; Kolmozero–Voronya belt; Oleninskoe Au-Ag deposit; Pellapahk porphyry deposit; alteration, gold; silver

Citation: Kalinin, A.A.; Kudryashov, N.M. Porphyry-Related Metamorphosed Au-Ag and Cu-Mo Deposits in the Precambrian of the Fennoscandian Shield. *Minerals* **2021**, *11*, 139. https://doi.org/10.3390/min11020139

Academic Editor: Galina Palyanova
Received: 18 January 2021
Accepted: 25 January 2021
Published: 29 January 2021

1. Introduction

Porphyry deposits are the major sources of Cu, Mo, and Re in the world [1]; they also provide significant amounts of Ag, Au, and some other metals. These deposits are the products of large hydrothermal systems that developed due to magmatic–hydrothermal phenomena in and around intermediate-to-felsic intrusions, emplaced at relatively high levels in the crust (1–6 km below the paleosurface) [1,2]. Metal-rich fluids exsolve from the shallow-crustal intrusive complexes and alter and mineralize the upper parts of the causative intrusions and the surrounding country rocks. These may be simple systems, consisting of a single intrusion with an associated alteration halo and a high-temperature ore, or more complicated systems of numerous intrusions with overlapping stages of alteration and ore deposition that formed over a wide range of temperatures [3].

Rock crystallization occurs due to pressure quenching, generating the diagnostic porphyritic texture of the mineralizing intrusions. Episodic brittle failure and fluid release from the crystallizing magmas produce a multistage vein stockwork that hosts the bulk of the ore [4]. Mineralization styles include stockwork veins, hydrothermal breccias, disseminations in the groundmass and, rarely, wall-rock replacements.

Epithermal fluids can potentially dissolve significant amounts of gold and silver from porphyry deposits, because the solubility of precious metals, such as aqueous bisulfide complexes, increases with decreasing temperatures when aqueous H_2S contents remain high [5]. Late-stage processes commence the final stage of porphyry ore formation and the formation of peripheral Ag-Au ore deposits.

Porphyry Cu-Au-Mo deposits mostly formed in the tectonic setting of continental and oceanic arcs, concentrated in the Pacific Rim. They also occur in the Tethyan arc from Europe to Asia, and others are scattered in volcanic arcs of all ages, with rare examples as old as the Archean [6–8]. The rarity of porphyry deposits in the Precambrian provokes a particular interest in their investigation.

The Archean Cu-Mo porphyry deposit of Pellapahk in the Kolmozero–Voronya greenstone belt (Kola Peninsula) is the only porphyry deposit in the northeastern part of the Fennoscandian Shield [9]. Cu-Mo mineralization was discovered in 1975 and studied in the 1970s and 1980s by the Central Kola Expedition (Monchegorsk, Russian Federation), and later in 2003–2010 by JSC Black Fox Resources (Ovoca Gold group) with diamond drilling (total 68 drillholes) and minor trenching. As a result of the investigations, a large stockwork of a complicated form with poor ores (200.5 million tons of ore with an average Mo content of 0.028%, Cu 0.154%, 2.0 g/t Ag, and 0.08g/t Au) [10,11] was contoured and traced down to a depth of 360 m. Cu-Mo mineralization was shown to be economically valuable in the case of an increase in the price of molybdenum [9].

The Oleninskoe gold–silver deposit and numerous gold occurrences are located in a neighborhood of the Pellapahk. Gold mineralization in the Oleninskoe deposit was discovered in 1969–1972 [12], and studied in the 1970s and 1980s by the Central Kola Expedition (Monchegorsk, Russian Federation), in 1997–1998 by Voronya Minerals JSC (Boliden AB group), and later in 2005–2008 by Black Fox Resources JSC (Ovoca Gold group) with intense trenching and drilling (total 61 drillholes). The Oleninskoe is a medium gold deposit, consisting of a number of mineralized lenses, with average gold content of 7.6 g/t. Resources of Au in the deposit are estimated at 10 t [13], while Ag resources have not been estimated. The Oleninskoe differs from all other gold deposits in the northeastern part of the Fennoscandian Shield in diverse mineralization of Pb, Ag, Sb, and Au. We consider the Oleninskoe deposit as a part of an Archean porphyry-epithermal system. This new genetic model of the mineral deposits in the Kolmozero–Voronya belt is discussed below.

2. Materials and Methods

Gold, silver, and Cu-Mo mineralization was studied in the specimens and samples (1.5–10 kg), collected by the authors in the outcrops and trenches in 1981–1983, then in 1997–1998, and again in 2017. Investigations of wall-rock alteration, metasomatic zoning, and determination of pre-ore, ore-related, and post-ore mineral assemblages in altered rocks were based on the study of rocks in the outcrops and in drillcores, the examination of mineral relations in thin and polished sections, as well as on the results of assays of primary and altered rocks. The samples were assayed for major (rock-forming) elements, Au and Ag, in the chemical laboratory of the Geological Institute, Kola Science Centre of Russian Academy of Sciences, Apatity, Russia with flame atomic absorption spectrometry (FAAS), and with pre-concentration of gold and silver with p-alkylaniline and oil sulfides. The data on trace elements, which determined the geochemical characteristics of the deposits, were obtained by ICP-MS in the Institute of Geology and Geochemistry of the Ural Branch of the Russian Academy of Science, Ekaterinburg, and in the Institute of Geology of Ore Deposits, Mineralogy, Geochemistry, and Petrography (IGEM), Russian Academy of Science, Moscow.

Mineral composition of the ores was studied in thin and polished sections with the reflected light microscope Axioplan 2 Imaging (Karl Zeiss, Jena, Germany), and with the electron microscope LEO-1450 (Karl Zeiss, Jena, Germany) in the Geological Institute of the Kola Science Center.

The preliminary estimation of the composition of mineral species was performed with the energy-dispersive system Bruker XFlash-5010. Microprobe analysis (MS-46, CAMECA, Gennevilliers Cedex, France, 22 kV; 30–40 nA, standards (analytical lines): $Fe_{10}S_{11}$ (FeKα, SKα), Bi_2Se_3 (BiMα, SeKα), LiNd $(MoO_4)_2$ (MoLα), Co (CoKα), Ni (NiKα), Pd (PdLα), Ag (AgLα), Te (TeLα), Au (AuLα) was performed for grains larger than 20 μm (analyst Ye. Savchenko). The identification of some rare mineral phases was verified with X-ray

analysis in the Geological Institute of the Kola Science Center (analyst E. Selivanova). Visually homogenous material of 50 × 10 µm or more in size was extracted from the polished sections and examined with the X-ray powder diffraction (Debye–Scherer) on URS-1 (Burevestnik, Irkutsk, Russia) operated at 40 kV and 16 mA with an RKU-114.7 mm camera and FeKα radiation.

The assaying of fluid inclusions was performed by Vsevolod Prokofiev (IGEM) in 0.5 g quartz samples, collected from −0.5 + 0.25 mm fraction with methods described in [14] (analyst Yu.Vasyuta, TsNIGRI, Moscow, Russia). The inclusions in quartz were thermally disclosed at 500 °C. The quantity of water for the calculation of element concentration in the solution, carbonic acid, methane, and other hydrocarbons was defined with the method of gas chromatography on a TsVET-100 chromatograph (Dzerzhinsk, Russia). Cl, SO_4, and F were assayed with ion chromatography on a TsVET-3006 (detection limit 0.01 mg/L), and K, Na, Ca, and Mg with ICP-MS in aqueous extracts.

Zircon U-Pb dating was undertaken at the Geological Institute of the Kola Science Center. Prior to analysis, zircons were extracted using standard magnetic and heavy liquid separation, with surface contamination removed using alcohol, acetone, and 1 M HNO_3.

The zircon dissolution and chemical recovery of Pb and U was performed using the technique described in [15], with U and Pb concentrations determined by isotope dilution employing a Finnigan MAT-262 (RPQ) (Finnigan MAT, San Jose, CA, USA) mass spectrometer and a mixed 208Pb + 235U tracer, with silica gel used as an ion emitter. Blank levels had maximum values of 100 ng Pb and 10–50 ng U, and all isotope ratios were corrected for mass fractionation by analysis of the SRM-981 and SRM-982 standards (0.12 ± 0.44%). The uncertainties of the resulting U-Pb ratios are 0.5%. The raw experimental data were processed using PbDAT (Version 1.21) and ISOPLOT (Version 2.06) [16,17], with age values calculated using conventional U decay constant values [18] and common Pb corrections following [19]. All uncertainties are reported at a 2σ confidence level.

3. Geological Setting of the Kolmozero–VoronyaBelt

The Kolmozero–Voronya greenstone belt separates the Murmansk block from the Kola Province of the Fennoscandian Shield (Figure 1A). The belt has an approximately 140 km strike length and a width of up to 10–12 km.

The history of the formation of the belt, as described in [20], includes the following events: formation of an island arc at 2.87–2.83 Ga; a break of 50 million years, and subsequent accretion of the island arc to the Murmansk continent; formation of an accretionary orogen (2.78–2.76 Ga); probable collapse of the orogen with formation of post-orogenic (or possibly anorogenic) granite intrusions in the central and southern parts of the belt (2.74–2.72 Ga). The total time of the belt development was about 150 Ma [20].

The structure of the belt is considered a monoclinal set of thrust sheets, with volcanics showing indications of oceanic and island arc magmatism [21,22]. The Archean supracrustal sequences of the belt comprise volcanics of tholeiite–komatiite and dacite–andesite–basalt series (the Kolmozero series), and subordinate sedimentary rocks: pelites and sandstones (at the basement of the Kolmozero series and the Porosozero series) (Figure 1B,C). The total thickness of the cross-section is 1800–2000 m.

Supracrustal sequences in the northwestern part of the Kolmozero–Voronya belt were intruded by:

- Gabbro, pyroxenite, and peridotite co-magmatic to the Kolmozero series volcanics;
- Quartz porphyry intrusions of the gabbrodiorite–diorite–granodiorite–granite series (the U-Pb age is 2.82–2.83 Ga, more details are given below);
- Plagiomicrocline and tourmaline granites (the U-Pb age of zircon from the tourmaline granite is 2451 ± 60 Ma [23]);
- Rare metal and tourmaline pegmatite veins (the U-Pb age of microlite from the Cs-Li pegmatite Vasin-Mylk deposit is 2454 ± 8 Ma [24]);
- More than one generation of dolerite and picrite porphyry dykes of Proterozoic and possibly Paleozoic age.

The rocks of the Kolmozero–Voronya belt were metamorphosed twice under conditions of the lower amphibolite facies: in the Neoarchean (2.7–2.8 Ga) and Paleoproterozoic (1.9–1.8 Ga) [25,26]. The PT-parameters of the early metamorphism were T~600 °C, P = 3–4 kbar. At the late stage of metamorphism, the temperature was a little lower (530 °C on the average), but pressure was higher (~5.5 kbar) [26]. In the northwestern part of the belt, the mineral associations of the late metamorphic stage only partly replaced the early stage associations (paramorphoses of kyanite after andalusite, decomposition of cordierite in the outer parts of the grains (Figure 2), re-crystallization of biotite and muscovite).

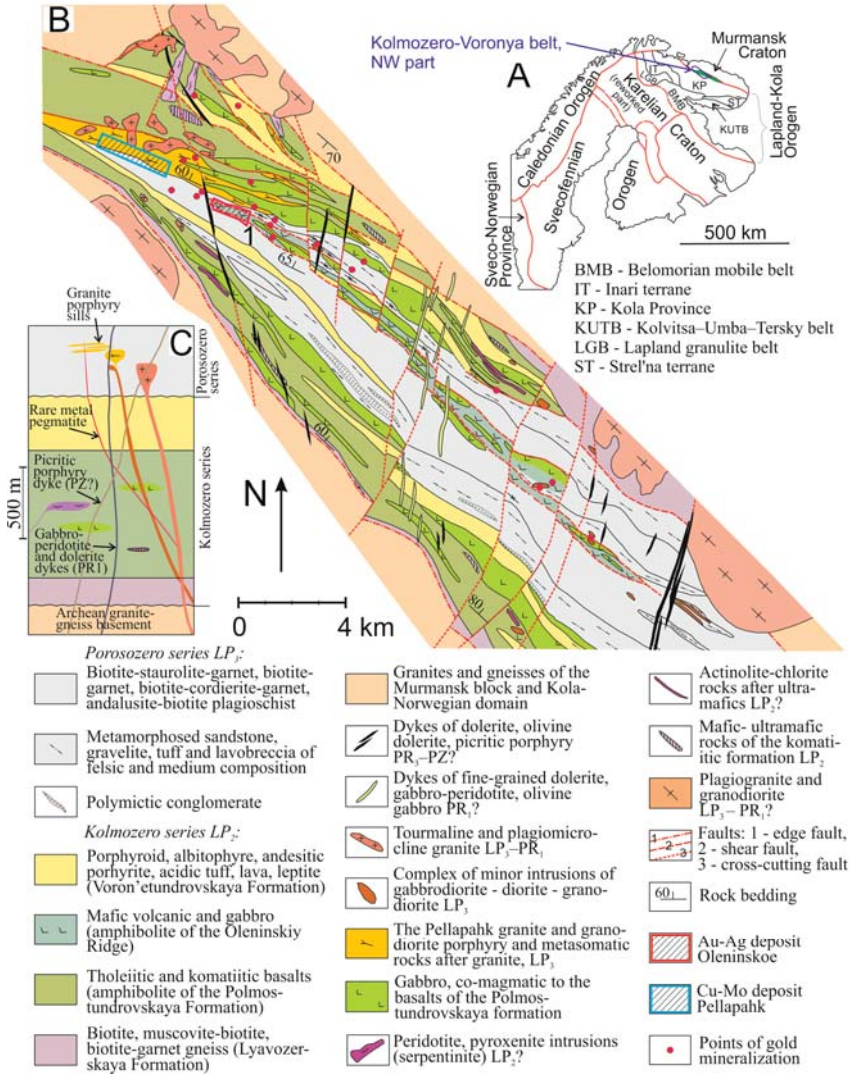

Figure 1. (**A**) Position of the Kolmozero–Voronya belt in the schematic tectonic map of the Fennoscandian Shield, modified from reference [27]. (**B**) Schematic geological map of the northwestern part of the Kolmozero–Voronya greenstone belt, modified from reference [28]. (**C**) Schematic stratigraphic column of the belt.

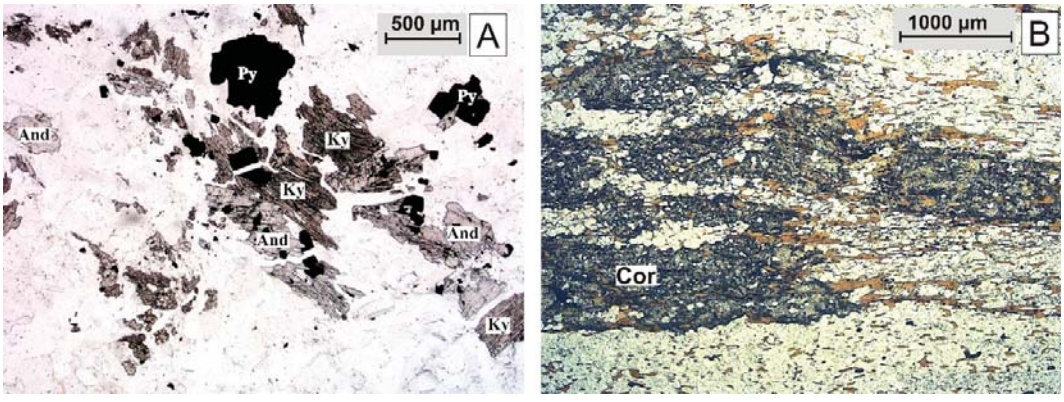

Figure 2. Paramorphoses of kyanite after andalusite in quartz–muscovite–kyanite schist (**A**) and decomposition of cordierite in biotite–cordierite plagioschist (**B**) as a result of the Early Proterozoic metamorphism. Thin section photo, plane polarized light. And—andalusite; Cor—cordierite; Ky—kyinite; Py—pyrite.

Three main fault systems are defined in the belt (Figure 1B) [29–31]. Deep faults of a NW direction along the boundaries of the belt comprise the first system. The second system unites strike–slip faults and shears of a NW up to latitudinal direction. These faults separate volcanic-sedimentary rock series or cut the stratigraphic boundaries at an acute angle of 5–15°. The faults of the second system can be traced for a few kilometers; the shears control zones of rock alteration [32]. The third fault system includes faults of a NE up to sub-meridional direction, which divide the belt into a number of blocks displaced for hundreds of meters. The faults of the third system are often marked by dolerite and picrite porphyry dykes (Figure 1).

4. Results

4.1. Mineral Deposits Associated with the Granite Porphyry Intrusions

More than 20 intrusions of the gabbrodiorite–diorite–granodiorite–granite porphyry series are located in the NW part of the belt. The rocks of mafic and intermediate composition form mainly small differentiated intrusions with the long axis less than 1000 m. More acidic rocks (granodiorite and granite porphyry) can form bigger intrusions up to 8 km long and 1.5 km wide (Figure 1). The biggest intrusion at Pellapahk hosts a Cu-Mo deposit. Granite porphyry also forms sills in metavolcanics and metasediments in the central part and northern flank of the belt (Figure 1). The Oleninskoe gold-silver deposit is associated with granite porphyry sills in the Oleny Ridge amphibolite.

4.1.1. The Pellapahk Cu-Mo Porphyry Deposit

The Pellapahk granite porphyry intrusion is of elongated form, orientated according to the general strike of the belt: in the southeast, it splits into a number of thin granite porphyry sills (Figure 1B). The granite porphyry intrudes mafic and intermediate volcanics of the Kolmozero series and high-alumina primary sedimentary rocks of the Porosozero series. Xenoliths of the high-alumina gneiss were noted in the southern part of the intrusion. In the north, the granite porphyry intrusion is cut by younger intrusions of tourmaline plagiomicrocline granite. The intrusions and the surrounding country metavolcanic-sedimentary rocks are crossed by numerous dykes of pyroxenite, dolerite, picrite porphyry, and by pegmatite veins (Figures 3 and 4).

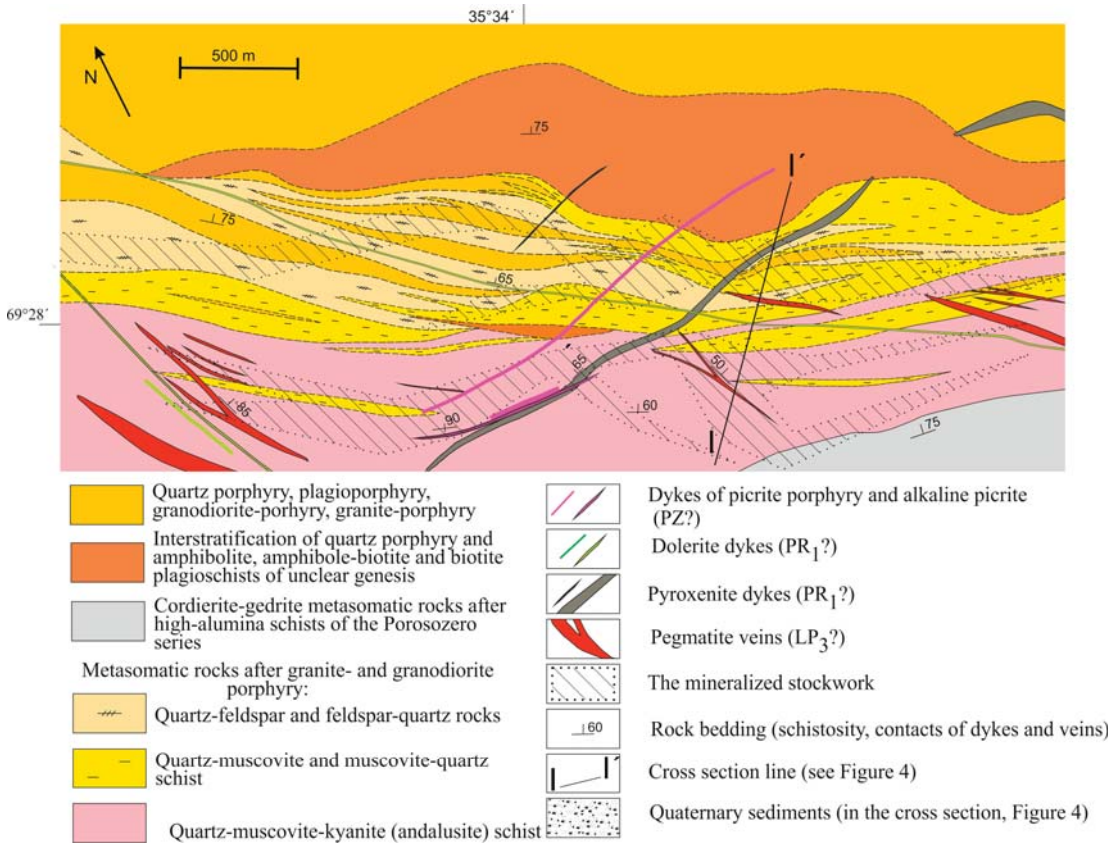

Figure 3. Schematic geological map of the Pellapahk Cu-Mo deposit, modified from Reference [9].

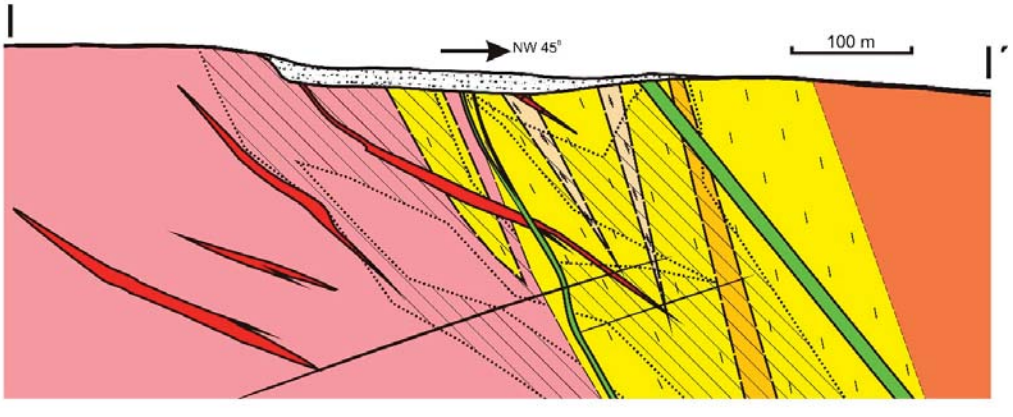

Figure 4. Cross-section of the mineralized stockwork of the Pellapahk Cu-Mo deposit along I–I′ line, modified from Reference [9]. See Figure 2 for Legend.

The age of zircon from the Pellapahk granite porphyry, defined by the U-Pb method, is 2828 ± 8 Ma [10]; i.e., the granite porphyry crystallized at the late stage of formation of the volcanic-sedimentary sequence, before the main metamorphic event (2770 ± 40 Ma) [25].

The rock-forming minerals in granite porphyry are quartz, 40–45 vol.%; oligoclase, 25–35%; muscovite, 10–15%; biotite, 5–10%; and microcline up to 5%. It is a fine-grained rock, with quartz and oligoclase phenocrysts up to 2 mm in size. The accessory minerals are titanite, ilmenite, rutile, tourmaline, apatite, and scheelite. The sulfides are pyrite, pyrrhotite, chalcopyrite, rare sphalerite and pentlandite.

Granite porphyry of the Pellapahk intrusion belongs to the calc-alkaline series (Table 1, Figure 5). Chemical composition of the rock corresponds to metaluminous I-type granite [33,34].

Table 1. Chemical composition (wt%) of granite porphyry and altered rocks of the Pellapahk intrusion.

Sample #	AK-107	AK-121	AK-289	AK-292	AK-293	AK-721	C-904	AK-120	AK-130	C-902
SiO_2	71.62	68.57	72.48	72.65	72.67	73.23	71.68	79.30	79.87	75.50
TiO_2	0.23	0.36	0.18	0.24	0.26	0.29	0.16	0.12	0.23	0.21
Al_2O_3	14.56	15.16	14.26	14.46	14.45	12.20	13.19	12.77	12.85	12.85
Fe_2O_3	0.37	2.12	0.78	0.55	1.04	n.a.	0.84	0.34	0.27	2.22
FeO	1.52	1.08	1.57	1.98	0.86	n.a.	1.61	0.27	0.37	1.65
FeO*	1.85	2.99	2.27	2.48	1.80	3.44	2.37	0.58	0.61	3.65
MnO	0.05	0.02	0.06	0.04	0.02	0.22	0.04	0.01	0.01	0.02
MgO	0.84	1.16	1.64	0.86	0.58	1.49	0.96	0.44	0.39	0.86
CaO	2.46	1.70	3.88	3.18	2.04	2.55	3.09	0.26	0.02	0.35
Na_2O	4.02	5.11	2.14	3.11	4.78	2.19	3.60	0.52	0.25	0.57
K_2O	2.50	1.91	1.38	1.70	1.86	0.68	2.62	3.64	3.45	2.62
P_2O_5	0.10	0.04	0.07	0.08	0.05	0.12	0.08	0.03	0.07	0.09
S	0.44	1.70	0.22	0.00	0.33	1.20	0.57	0.07	0.05	1.66
LOI	0.84	1.32	1.90	1.25	1.48	2.12	0.89	2.38	2.25	1.74
CO_2	0.01	0.00	0.05	0.05	0.06	<0.10	0.74	0.00	0.04	0.00
Total	99.56	100.25	100.61	100.15	100.48	99.73	100.07	100.15	100.12	100.34

Notes: AK-107, AK-121, AK-289, AK-292, AK-293, AK-721—granite porphyry; C-904—granite porphyry with quartz-epidote-carbonate veinlets; AK-120, AK-130, C-902—quartz-muscovite-kyanite schist. n.a. = not assayed. FeO* = FeO + 0.9*Fe_2O_3.

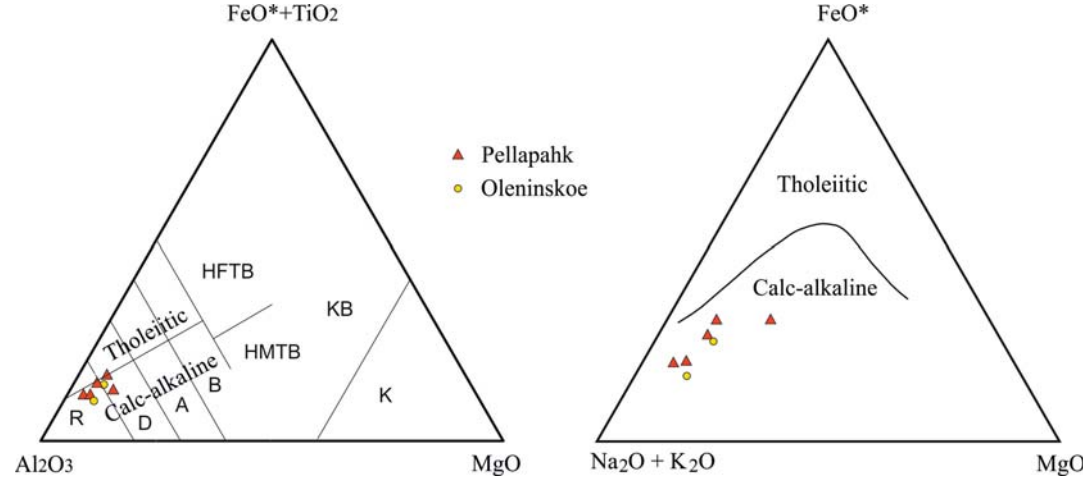

Figure 5. Composition of the Pellapahk and Oleninskoe granite-porphyry in the petrochemical diagrams (FeO* = FeO + 0.9*Fe_2O_3).

REE spectra (Figure 6), drawn with data from Table 2 and Table 5, are similar to the REE spectrum of I-type granite, formed under conditions of subduction and island arc [34].

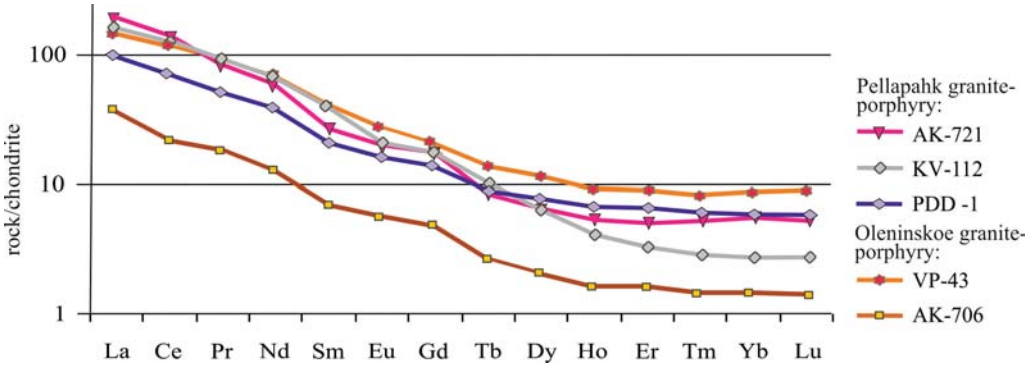

Figure 6. REE spectra for granite porphyry of the Pellapahk Cu-Mo and the Oleninskoe Au-Ag deposits, normalized by chondrite [35].

Table 2. ICP-MS data for granite porphyry (AK-721), and mineralized (KV-112, PDD-1) metasomatic rocks of the Pellapahk deposit, g/t.

Element	AK-721	KV-112	PDD-1	Element	AK-721	KV-112	PDD-1
Li	184	57	17	Ba	227	507	664
Be	0.86	1.53	0.52	La	46	41	25
Sc	1.70	4.38	2.67	Ce	93	82	45
V	39	32	25	Pr	7.96	9.03	5.05
Cr	826	164	164	Nd	28	34	18.4
Co	6.31	13.5	7.17	Sm	4.25	6.07	3.17
Ni	47	16.7	13.2	Eu	1.12	1.22	0.90
Cu	26	1150	1516	Gd	3.65	3.88	2.71
Zn	51	45	21	Tb	0.33	0.40	0.31
Ga	27	20	14.2	Dy	1.79	1.62	1.87
As	10.0	0.97	6.63	Ho	0.31	0.24	0.36
Se	0.33	3.51	1.26	Er	0.90	0.55	1.03
Rb	59	166	168	Tm	0.14	0.07	0.15
Sr	393	139	537	Yb	1.02	0.47	0.95
Y	12.9	6.05	10.5	Lu	0.14	0.07	0.14
Zr	171	145	137	Hf	3.27	4.36	3.02
Nb	4.30	4.40	6.75	Ta	0.31	0.30	0.37
Mo	3.52	167	173	W	1.61	31.02	12.96
Ag	1.30	2.30	3.16	Tl	0.85	2.46	0.55
Cd	0.22	0.40	n.a.	Pb	153	115	15
Sn	0.98	5.32	1.57	Bi	0.32	11.3	2.65
Sb	0.44	1.91	2.98	Th	8.38	7.66	6.67
Te	0.17	0.61	0.18	U	2.15	3.19	1.91
Cs	14.7	6.25	2.87	-	-	-	-

n.a. = not assayed.

The zone of intense rock alteration has a total thickness of more than 700 m and follows the contact of the granite porphyry with high-alumina gneiss (Figure 3). The general zoning of the alteration is the following (from north to south): (0) slightly altered granite porphyry; (1) quartz-microcline rock; (2) muscovite schist; (3) muscovite–kyanite (or/and andalusite) schist; (4) altered (gedrite, cordierite) high-alumina schist, and (5) non-altered biotite-andalusite schist (Figure 3). Rocks in zones (1)–(3) formed after granite porphyry, and in (4), after the high-alumina schist (5) of the Porosozero series.

Muscovite and muscovite–kyanite schists contain phenocrysts of quartz preserved from the primary porphyry (3–4 vol.%), newly formed porphyroblasts of andalusite and/or kyanite (up to 6–8 vol.%), and pyrite metacrystals up to 3 mm in size (1–3 vol.%).

Alteration processes caused the decomposition of plagioclase and microcline, the formation of high-alumina minerals andalusite and kyanite (Figure 2A), and the replacement of biotite by muscovite in the granite porphyry. The muscovite and muscovite–kyanite schists have high SiO_2 and K_2O content, compared to the composition of the primary rock, but are poorer in MgO, CaO, and Na_2O (Table 1).

All altered rocks contain sulfide mineralization. Cordierite–gedrite rock after high-alumina schists contains disseminated pyrrhotite in intergrowths with chalcopyrite, pyrite, rarely sphalerite, arsenopyrite, cobaltite–gersdorfite, and pentlandite; the main oxide minerals are ilmenite and magnetite. Muscovite, muscovite–kyanite schists and quartz–microcline rocks after granite porphyry contain pyrite mineralization up to 3 vol.% with minor chalcopyrite, pyrrhotite, and sphalerite. Rutile is the main oxide mineral in these rocks and replaces ilmenite.

The Cu-Mo mineralization comprises a stockwork of quartz and quartz–calcite–epidote veinlets in the zone of alteration of granite porphyry. The stockwork was traced for 1500–1600 m along the strike; its width varies from 350 to 600 m (Figures 3 and 4). The mineralization was drilled down to a depth of 360 m in the NW part of the stockwork, and probably goes deeper [9].

Geochemical association of the metals in the mineralized altered rocks in the stockwork includes Mo, Cu, Ag, Bi, W, Se, and Sb (Figure 7, Table 2).The content of Cu, Mo, Bi, and W in the altered rocks is 10 or more times higher than in the primary granite porphyry.

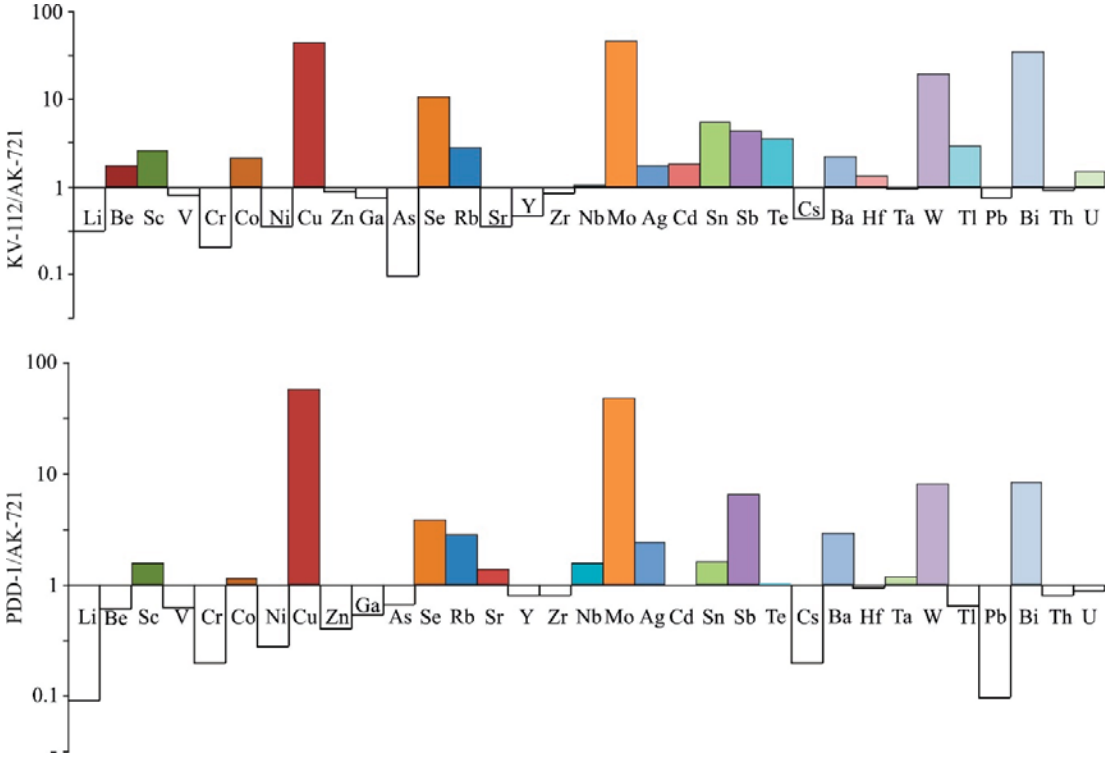

Figure 7. Trace elements spectra in the muscovite–kyanite schist (KV-112 and PDD-1) in the mineralized stockwork compared to the slightly altered granite porphyry (AK-721).

In the stockwork, the main ore minerals are pyrite, chalcopyrite, and rutile. Sporadic ore minerals are molybdenite, sphalerite, galena, tetrahedrite, pyrrhotite, cubanite, ilmenite,

scheelite. The rare minerals are native bismuth, gudmundite, tennantite, löllingite, lillianite, and pentlandite [9,36]. The oxidation zone is not well developed in the deposit, but bornite and covellite were rarely noted to replace chalcopyrite in the outer parts of the grains.

Pyrite is the most abundant sulfide mineral both within the mineralized Cu-Mo stockwork, and outside of it. Idiomorphic grains of pyrite are regularly disseminated in the rock groundmass, but the content of pyrite and the size of its grains (cubic crystals may reach 3 mm) increase in the quartz–carbonate–epidote veinlets.

The main productive minerals are chalcopyrite and molybdenite. Chalcopyrite forms irregular grains up to 0.5 mm in the rock mass; it develops in fractures in pyrite grains and along cleavage in kyanite, but much more rarely in andalusite (Figure 8B).

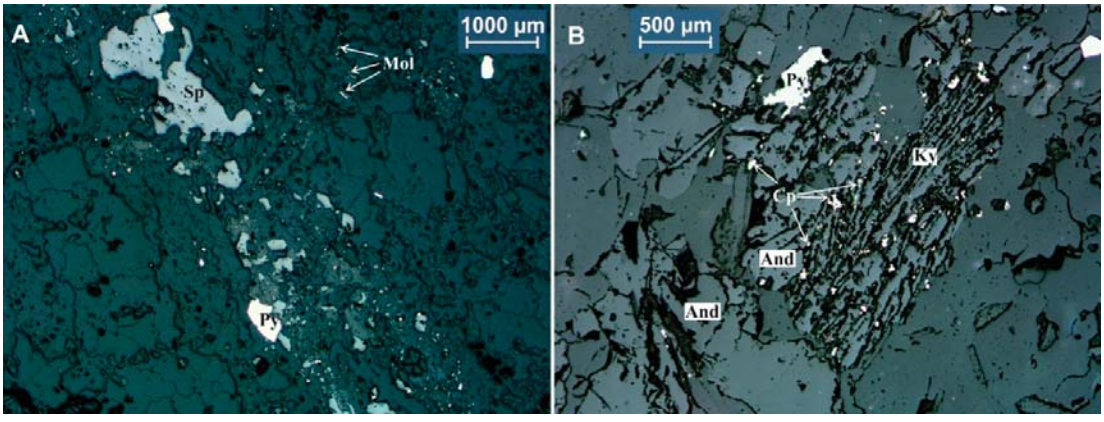

Figure 8. Quartz–calcite–epidote veinlet with sphalerite–pyrite mineralization (**A**) and kyanite with disseminated chalcopyrite along the cleavage, Pellapahk Cu-Mo deposit (**B**). Polished section photo, plane polarized light. Cp—chalcopyrite; Mol—molybdenite; Py—pyrite; Sp—sphalerite.

Molybdenite forms fine flakes (mainly 0.05–0.1 mm, rarely up to 0.5 mm) along cleavage in muscovite or along quartz grain boundaries. Chains of molybdenite flakes cross pyrite crystals, chalcopyrite, and sphalerite grains [36].

Galena and sphalerite are rare in the rock groundmass, but their content significantly increases in the quartz–epidote–calcite veinlets. The rare minerals of As, Sb, and Bi (fahlore, gudmundite, lillianite) are associated mainly with galena.

4.1.2. The Oleninskoe Au-Ag Deposit

The Oleninskoe Au-Ag deposit is located at the northwestern thinning of the Oleny Ridge amphibolite strata (Figure 1) in a shear zone of northwest strike [37–39]. The amphibolite and high-alumina metasedimentary schist host numerous granite porphyry sills with a thickness of 0.1–6.0 m (Figures 9 and 10).

The Oleny Ridge amphibolite borders biotite–andalusite gneiss of the Porosozero series in the south, and a stratum of alternation of amphibolite, biotite–cordierite, and biotite–andalusite gneisses in the north. Both southern and northern contacts are tectonic.

The latest rocks in the deposit are granite–pegmatite veins, which cut all rocks, including those that are mineralized. The thickest veins can be traced in a NW direction for hundreds of meters (Figure 9).

The rock in the sills is very fine-grained; the size of plagioclase, quartz grains, and biotite and muscovite flakes in the groundmass is less than 0.05 mm; quartz phenocrysts are <0.5 mm. Phenocrysts of plagioclase were not found.

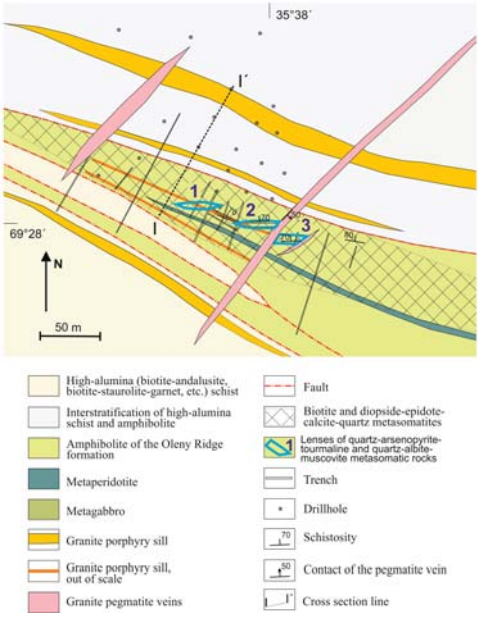

Figure 9. Schematic geological map of the Oleninskoe deposit, modified from References [28,37].

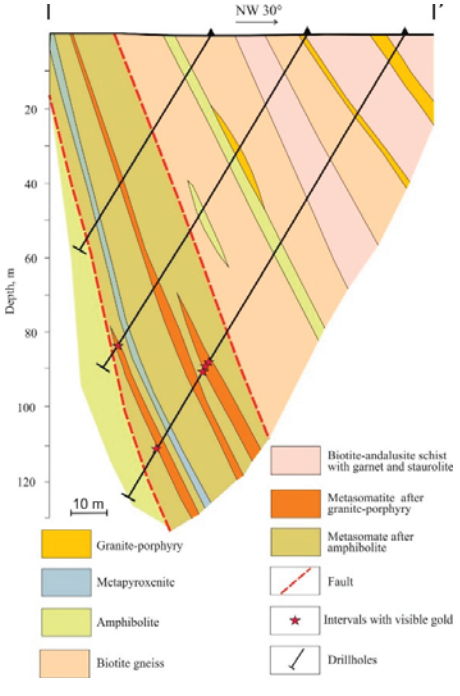

Figure 10. Schematic cross-section of the main mineralized zone of the Oleninskoe deposit along I–I′ line (Figure 9).

The age of the granite porphyry sill in the Oleninskoe deposit was defined by a U-Pb geochronological study of zircons. Zircons (sample AK-706) are long-prismatic, idiomorphic and sub-idiomorphic, from 50 to 100 μm in size, of brownish color, and with fine growth zoning suggesting a magmatic origin. The zircon fractions yield a discordia with an upper intercept at 2817 ± 9 Ma (MSWD = 0.54, Table 3, Figure 11) that represents the crystallization age of the granite porphyry sill.

Table 3. Results of U–Pb geochronological studies of zircons from the Oleninskoe deposit.

Sample #	Weight, mg	Pb (ppm)	U (ppm)	Isotope Ratios		
Fraction #				$^{206}Pb/^{204}Pb$ *	$^{207}Pb/^{206}Pb$ *	$^{208}Pb/^{206}Pb$ *
AK-706/1	0.3	250	483	1250	0.2040 ± 0.0002	0.1034 ± 0.0002
AK-706/2	0.3	65	130	796	0.2090 ± 0.0004	0.1309 ± 0.0003
AK-706/3	0.2	109	192	1552	0.2061 ± 0.0002	0.1109 ± 0.0002
AK-706/4	0.2	178	355	1271	0.2033 ± 0.0003	0.1099 ± 0.0003

Sample #	Isotope Ratios		Rho	Age, Ma		
Fraction #	$^{206}Pb/^{238}U$	$^{207}Pb/^{235}U$		$^{206}Pb/^{238}U$	$^{207}Pb/^{235}U$	$^{207}Pb/^{206}Pb$
AK-706/1	0.4559 ± 0.0022	12.234 ± 0.061	0.93	2422 ± 12	2623 ± 13	2782 ± 3
AK-706/2	0.4293 ± 0.0030	11.497 ± 0.072	0.91	2303 ± 16	2564 ± 20	2778 ± 6
AK-706/3	0.5080 ± 0.0025	13.820 ± 0.069	0.93	2648 ± 13	2742 ± 14	2812 ± 5
AK-706/4	0.4410 ± 0.0023	11.802 ± 0.064	0.91	2355 ± 14	2589 ± 16	2777 ± 5

* Isotope ratios are corrected for the blank and common lead. Rho—the correlation coefficient of the 207Pb/235U-206Pb/238U ratios.

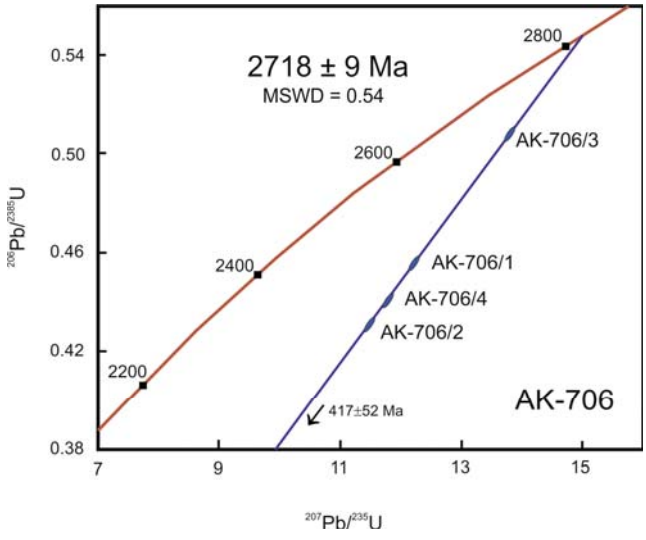

Figure 11. Diagram with concordia for granite porphyry from the Oleninskoe deposit.

The chemical composition of the non-altered granite porphyry sills is generally similar to the granite porphyry of the Pellapahk intrusion (Table 4, Figure 5), and the granite porphyry from the Oleninskoe deposit belongs to the series of calc-alkaline I-type granites.

The spectrum of REE in sample AK-706 (Oleninskoe) differs in the lower content of REE (Figure 6), but the form of the curve is very similar to the one in the REE spectra of the Pellapahk granite-porphyry.

The mineralized zone consists of a number of ore lenses within an area of 900 × 50 m (Figure 9). The zone is orientated according to the general strike of the rocks. The ore lenses are up to 3.5 m thick (1.5 m on average) with the length up to 50 m; they form an

echelon-like series of lenticular bodies, cutting general schistosity in the host rocks at an acute angle of 10–15° (Figure 9). Three lenses are outcropped on the surface, but drilling shows their number is more than three. The mineralization is traced by drilling down to a depth of 200 m, and goes deeper. The thickness of the ore intervals and Au grades increase with the depth [31]. The weighted average gold content is 7.6 g/t; inferred resources are estimated at 10 t Au down to a depth of 100 m [13].

The amphibolite is intensely altered. Diopsidization (diopside-zoisite, diopside-epidote, diopside-epidote-carbonate, diopside-epidote-garnet associations) and biotitization cover the whole mineralized zone, and quartz-arsenopyrite-tourmaline metasomatic rocks are spatially confined to the ore lenses. Granite porphyry is turned to quartz-albite-muscovite, quartz-arsenopyrite-tourmaline, and quartz metasomatic rocks: the latter formed the most recently and very locally (ellipsoidal bodies, ~30 × 10 cm) (Figure 12). All kinds of metasomatic rocks and the zoning of alteration can be seen in lens 2, outcropped with a trench along the strike (Figure 12).

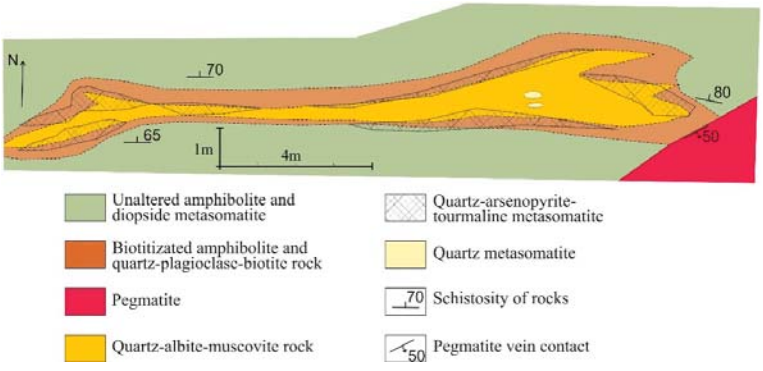

Figure 12. Scheme of zoning of metasomatic rocks in lens 2 (see Figure 9), logging of the trench.

Table 4. Chemical composition (wt%) of granite porphyry and altered rocks of the Oleninskoe deposit.

Sample #	VP-10	AK-706	AK-710	AK-712	AK-900K	AK-900C	AK-900T	AK-707	AK-711
SiO_2	69.53	71.56	64.22	59.53	61.07	65.58	55.93	62.38	92.55
TiO_2	0.23	0.34	0.97	1.22	0.98	0.89	1.22	0.28	0.10
Al_2O_3	16.20	14.69	11.91	14.06	10.75	13.22	13.38	2.71	1.30
Fe_2O_3	0.48	0.00	1.62	3.48	4.25	2.32	5.44	7.99	0.00
FeO	1.36	2.38	5.18	4.53	4.28	2.20	4.05	6.39	3.38
FeO*	1.79	2.38	6.64	7.66	8.11	4.29	8.95	13.58	3.38
MnO	0.03	0.03	0.02	0.02	0.02	0.01	0.02	0.02	0.02
MgO	1.18	1.18	0.19	0.33	0.24	0.24	0.22	0.43	0.18
CaO	1.74	2.50	0.39	0.51	0.52	0.30	0.23	0.65	0.06
Na_2O	6.28	4.89	2.28	3.97	3.33	3.33	2.67	0.49	0.22
K_2O	1.56	1.01	1.94	1.68	1.06	1.82	2.30	0.26	0.07
P_2O_5	0.06	0.07	0.42	0.37	0.19	0.49	0.28	0.46	0.05
S	0.01	0.07	1.15	2.93	3.47	0.54	4.27	3.57	0.27
LOI	0.84	0.84	3.04 *	1.53	1.57	7.75 *	3.46 *	4.53 *	1.13
CO_2	<0.10	<0.10	<0.10	<0.10	<0.10	<0.10	<0.10	<0.10	<0.10
Total	99.50	99.56	99.85	94.16 **	91.73 **	98.69	93.47 **	90.16 **	99.33
Ag (ppm)	n.a.	0.80	20.72	17.49	110.38	9.96	11.17	96.50	114.14
Au (ppm)	n.a.	<0.004	3.29	0.15	2.36	1.62	0.24	3.16	90.93

* High loss on ignition is connected with carbonaceous matter in the rocks. ** The deficit appears due to high content of arsenopyrite mineralization, the samples were assayed for As with ICP-MS, see Table 5. VP-10, AK-706—granite porphyry; AK-710, AK-712, AK-900K, AK-900C, AK-900T—quartz-albite-muscovite metasomatite; AK-707—quartz-arsenopyrite-tourmaline metasomatite; AK-711—quartz metasomatite. n.a. = not assayed.

Table 5. ICP-MS data for granite porphyry and altered rocks of the Oleninskoe deposit, g/t.

Sample #	AK-706	ВП-43	AK-707	AK-710	AK-712	AK-711
Li	174	16	18	107	103	19
Be	0.89	0.67	0.13	0.44	0.64	0.09
Sc	1.88	2.42	7.76	34	29	3.99
V	25	22	59	247	296	11
Cr	281	400	34	219	166	917
Co	5.16	4.50	29	9.78	31	5.76
Ni	29	18	69	12	29	67
Cu	12	19	270	207	400	78
Zn	20	110	91	47	63	204
Ga	24	19	3.49	15	15	1.47
As	29	n.a.	67792	41304	18825	1385
Se	n.a.	n.a.	2.30	<1.00	n.a.	n.a.
Rb	48	56	18	95	35	3.46
Sr	151	117	25	57	67	6.74
Y	3.22	14	1.40	1.20	0.82	0.48
Zr	101	127	6.79	12	15	2.25
Nb	1.46	6.64	0.33	0.73	0.85	0.13
Mo	1.29	2.30	0.52	0.44	0.47	4.84
Ag	1.05	0.49	228	15	149	145
Cd	0.11	n.a.	1.03	0.16	0.49	1.76
Sn	0.57	1.08	0.55	1.07	1.02	0.90
Sb	2.11	0.30	717	60	48	5.28
Te	n.a.	n.a.	1.04	1.48	0.19	2.67
Cs	9.73	13	5.76	8.85	5.16	1.34
Ba	187	395	42	154	79	5.80
La	9.00	36	1.01	1.34	0.69	0.34
Ce	14	75	2.01	3.41	1.89	0.76
Pr	1.81	8.93	0.26	0.55	0.39	0.09
Nd	6.24	33	1.18	2.73	2.06	0.43
Sm	1.12	6.47	0.28	0.67	0.63	0.10
Eu	0.35	1.65	0.09	0.17	0.18	0.03
Gd	1.05	4.47	0.23	0.48	0.45	0.07
Tb	0.10	0.53	0.04	0.05	0.05	0.01
Dy	0.54	3.07	0.25	0.24	0.25	0.07
Ho	0.10	0.56	0.05	0.05	0.05	0.02
Er	0.29	1.55	0.16	0.14	0.15	0.06
Tm	0.04	0.22	0.02	0.02	0.02	0.01
Yb	0.26	1.55	0.19	0.15	0.15	0.05
Lu	0.04	0.24	0.02	0.03	0.02	0.01
Hf	1.96	3.90	0.18	0.41	0.48	0.07
Ta	0.16	0.54	0.02	0.07	0.06	n.a.
W	3.34	n.a.	3.75	15.64	20.51	4.06
Tl	0.24	0.80	4.77	0.47	0.38	0.03
Pb	9.66	88	2238	133	137	20
Bi	n.a.	n.a.	1.91	0.12	0.16	0.05
Th	3.42	9.44	0.08	0.17	0.16	0.06
U	0.89	2.95	0.07	0.07	0.10	0.08

n.a. = not assayed.

The geochemical association of the metals in the mineralized altered rocks includes Au–As–Ag–Sb–Cu–Pb–W (Table 5). The concentration coefficient of As, Ag, and Sb in the mineralized rocks is more than 100 if compared to the unaltered granite porphyry (Figure 13). The highest content of As, Ag, Pb, and Sb was found in quartz-arsenopyrite-tourmaline rock (Figure 13, Table 5). Quartz metasomatic rock is not as rich in Pb, Ag, and Sb as quartz-albite-muscovite and quartz-arsenopyrite-tourmaline metasomatites (Table 5), but it is rich in Au (Table 4). The Au/Ag ratio in the mineralized rocks is <0.2 [29], except the quartz metasomatite.

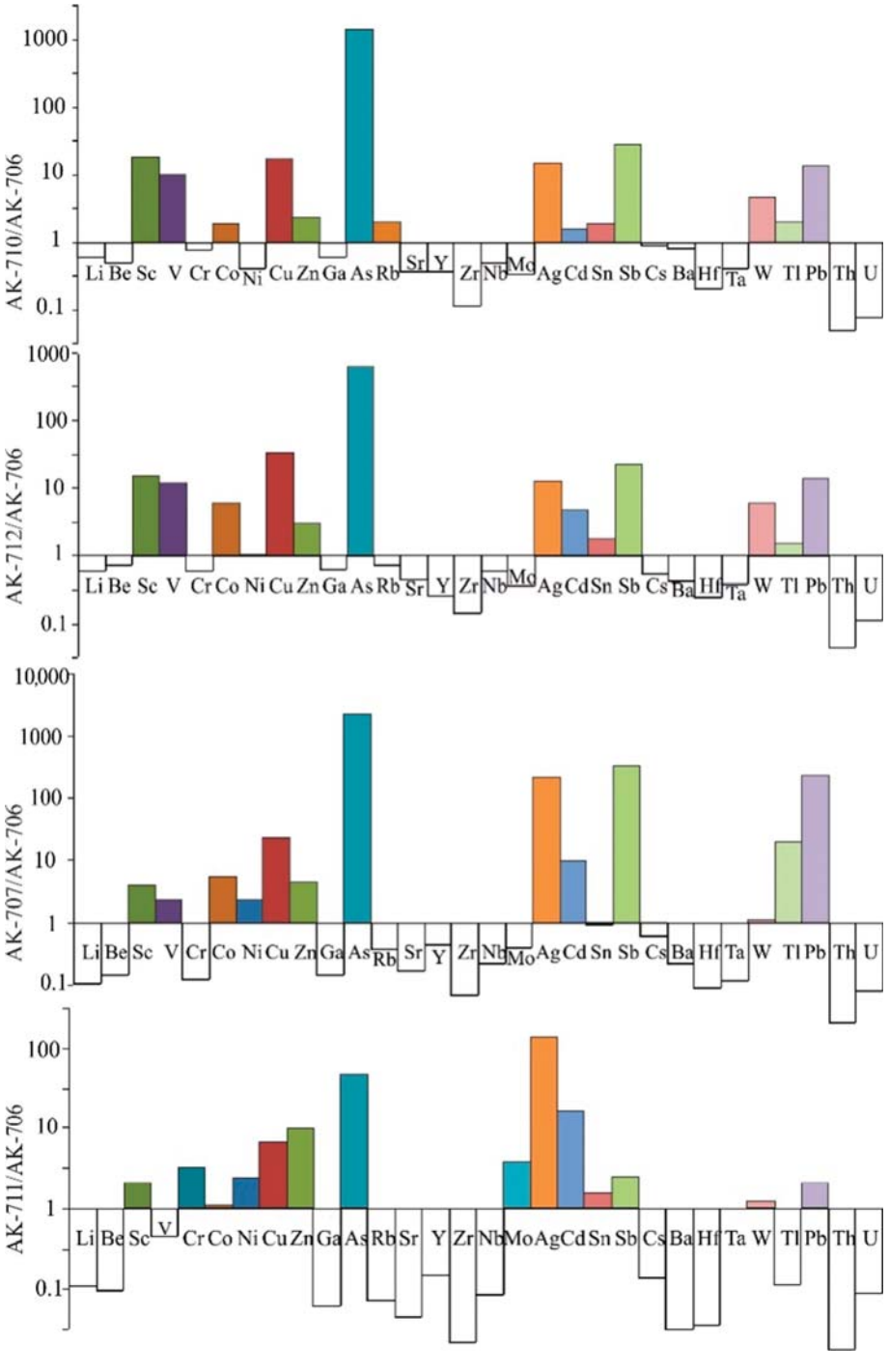

Figure 13. Trace elements spectra of quartz-albite-muscovite (AK-710 and AK-712), quartz-arsenopyrite-tourmaline (AK-707), and quartz (AK-711) metasomatic rocks from lens 2, compared to granite porphyry (AK-706).

The geochemical characteristics of the rocks correspond well to the composition of mineralization (Table 6). Arsenopyrite, pyrrhotite, and ilmenite are the most abundant ore minerals, which are present in all altered rocks [37,38]. Sporadic ore minerals in biotitizated and diopsidizated amphibolite are chalcopyrite and sphalerite; pentlandite and electrum are rare. Quartz–arsenopyrite–tourmaline and quartz metasomatic rocks in the exocontact zones of granite porphyry contain rich Pb–Ag–Sb–Au mineralization totaling more than 50 mineral phases: 20 of them are the minerals of the precious metals Ag and Au (Tables 6 and 7). Ilmenite in quartz–arsenopyrite–tourmaline and quartz metasomatic rocks is partly (in the outer parts of the grains) or fully replaced by rutile [37,38].

Four types of minerals of the Au-Ag series were recognized in the deposit: 1—electrum 25–32 mas.% Au in association with arsenopyrite, löllingite, and pyrrhotite; 2—electrum 33–47 mas.% Au in intergrowths with galena, dyscrasite, and sulfosalts; 3—gold (78–95 mas.% Au) in quartz; 4—native silver (<7 mas.% Au) in the crust of weathering of the ore [37]. Types 1 and 3 are widespread in the deposit, and 2 and 4 relate only to the quartz–arsenopyrite–tourmaline rocks rich in Pb-Ag-Sb. Mustard gold was found in the oxidized ore with high Ag–Sb electrum. These mineral aggregates consist of electrum, Fe and Sb oxides, Ag chlorides, and bromides [38].

In the Oleninskoe ores we see fine intergrowths of Ag, Cd, Pb, As, Sb and Te minerals. These multiphase aggregates are up to 0.2 mm in size, and the size of individual micrograins in the intergrowths is <5 μm. The polymineral intergrowths adjoin bigger grains of argentotetrahedrite, pyrrhotite, and galena host sulfides (Figures 14 and 15).

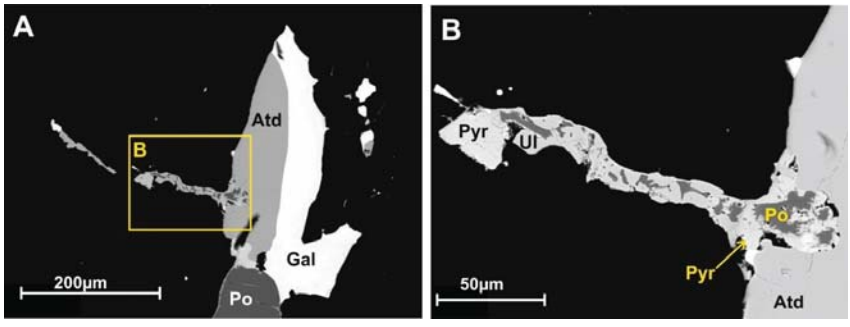

Figure 14. Aggregate of ulmannite (Ul), pyrrhotite (Po), and pyrargyrite (Pyr) at the boundary of argentotetrahedrite (Atd) grain: (**A**) general view, (**B**) detailed area. Back scattered electron images (BEI).

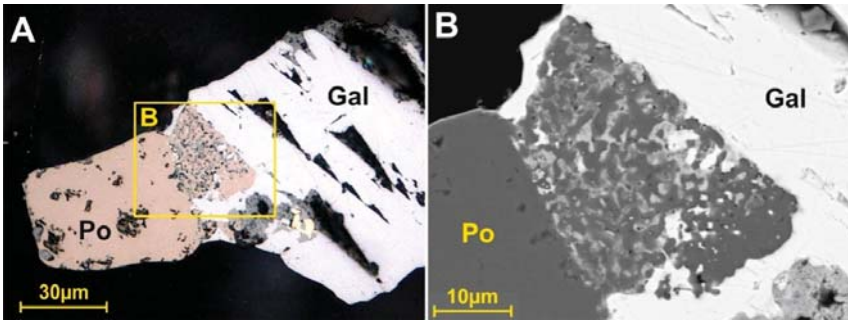

Figure 15. (**A**) aggregate of pyrrhotite (Po), galena (Gal), argentotetrahedrite (gray), and chalcopyrite (yellow) in galena, polished section photo under plane polarized light; (**B**) BEI of the aggregate.

Table 6. Ore minerals (native metals, sulfides, and their analogues) in the rocks of the Oleninskoe deposit.

Mineral Phases	Unaltered Amphibolite	Mineralized Rocks, Not Connected with Quartz Porphyry		Metasomatic Rocks After Granite Porphyry and in ExocontactZones		
		Biotitizated and DiopsidizatedAmphibolite	Quartz-Arsenopyrite-Tourmaline Rock	Quartz-Albite-Muscovite	Quartz-Arsenopyrite-Tourmaline Rock	Quartz
1	2	3	4	5	6	7
Pyrrhotite	+++	++++	++++	++++	+++	+++
Chalcopyrite	++	+++	+++	+++	++	+
Pentlandite	+	+	-	-	-	-
Pyrite	-	-	-	-	++	++
Marcasite (primary)	-	-	-	-	++	-
Sphalerite	+	++	+++	+++	++++	++
Galena	-	++	++	++	++++	++
Molybdenite	-	-	-	-	-	++
Bornite	-	-	-	-	+	-
Covellite	-	-	-	-	+	-
Greenockite	-	-	-	-	++	-
Acanthite	-	-	-	-	+++	++
Uytenbogaardtite	-	-	-	-	+++	+++
Mckinstryite	-	-	-	-	+	-
Arsenopyrite	-	++++	++++	++++	++++	++++
Lollingite	-	+++	+++	-	-	+
Gersdorfite	-	+	-	-	+	-
Safflorite	-	+	-	-	-	-
Nickeline	-	+	-	-	-	-
Gudmundite	-	-	-	-	+++	-
Ullmannite	-	-	-	-	++	-
Nisbite	-	-	-	-	+	-
Breithauptite	-	-	-	-	+	-
Dyscrasite	-	-	-	-	+++	-
Aurostibite	-	-	-	-	+	-
Argentotetrahedrite *	-	-	-	-	++++	++
Polybasite	-	-	-	-	+	+
Boulangerite	-	-	-	-	+++	-
Falkmanite	-	-	-	-	+++	-
Semseyite	-	-	-	-	+++	-
Meneginite	-	-	-	-	++	-
Bournonite	-	-	-	-	++	-
Owyheeite	-	-	-	-	++	-

Table 6. *Cont.*

Mineral Phases	Unaltered Amphibolite	Mineralized Rocks, Not Connected with Quartz Porphyry		Metasomatic Rocks After Granite Porphyry and in ExocontactZones		
		Biotitizated and DiopsidizatedAmphibolite	Quartz-Arsenopyrite-Tourmaline Rock	Quartz-Albite-Muscovite	Quartz-Arsenopyrite-Tourmaline Rock	Quartz
1	2	3	4	5	6	7
Diaphorite	-	-	-	-	+++	-
Ramdohrite	-	-	-	-	++	-
Uchucchacuaite	-	-	-	-	++	-
Fizelyite	-	-	-	-	++	-
Pyrargyrite	-	-	-	-	+++	-
Stephanite	-	-	-	-	++	-
Miargyrite	-	-	-	-	+	-
Billingsleyite	-	-	-	-	+	-
Dervillite	-	-	-	-	+	-
Proustite	-	-	-	-	+	-
Hessite	-	-	-	-	++	++
Stutzite	-	-	-	-	+	-
Cervelleite	-	-	-	-	+	-
Calaverite	-	-	-	-	+	-
Petzite	-	-	-	-	+	-
Canfieldite-Te	-	-	-	-	+	-
Native Bismuth	-	-	-	-	+	-
Native Gold	-	++	++	++	+++	+++
Native Arsenic	-	-	-	-	+	-

Notes: ++++—abundant ore minerals; +++—frequent; ++—scanty; +—very rare (1–3 grains). * Earlier this mineral phase was called freibergite, but in the IMA-lists 2019 and 2020 "freibergite" was changed to "argentotetrahedrite".

Table 7. Electron microprobe data in wt.% for selected Ag, Pb, and Sb mineral phases from the Oleninskoe deposit.

Mineral	Dyscrasite	Dyscrasite	Argentotetrahedrite	Argentotetrahedrite	Argentotetrahedrite	Bournonite	Meneghinite	Owyheeite	Diaphorite	Uchucchacuaite	Fyzeliite	Pyrargyrite	Uytenbogaardtite	Hessite
S	0.03	bdl	21.92	20.19	20.37	19.02	16.50	18.52	19.23	20.32	21.39	17.84	11.15	0.04
Mn	n.a.	n.a.	n.a.	bdl	n.a.	0.03	bdl	bdl	n.a.	2.70	0.58	n.a.	n.a.	n.a.
Fe	bdl	0.01	5.34	5.14	5.18	0.06	0.07	0.04	n.a.	0.46	0.83	bdl	0.15	bdl
Co	n.a.	n.a.	0.01	bdl	bdl	n.a.	n.a.	n.a.	n.a.	bdl	n.a.	n.a.	bdl	n.a.
Ni	n.a.	bdl	bdl	bdl	0.01	bdl	bdl	bdl	n.a.	bdl	n.a.	n.a.	bdl	bdl
Cu	0.01	0.02	22.01	16.02	15.00	12.49	1.46	bdl	n.a.	0.07	n.a.	bdl	n.a.	bdl
Zn	n.a.	0.01	0.78	0.69	0.61	n.a.	n.a.	bdl	n.a.	bdl	n.a.	n.a.	n.a.	n.a.
As	bdl	bdl	bdl	0.28	0.22	bdl	bdl	bdl	n.a.	bdl	n.a.	bdl	bdl	0.15
Se	n.a.	n.a.	bdl	bdl	bdl	n.a.	n.a.	bdl	n.a.	n.a.	n.a.	0.02	n.a.	n.a.
Ag	72.61	69.84	22.47	30.38	31.92	n.a.	0.18	4.74	24.01	6.16	9.05	58.68	59.86	62.00
Cd	n.a.	n.a.	n.a.	0.27	n.a.	bdl	bdl	n.a.	n.a.	bdl	1.50	bdl	n.a.	n.a.
Sb	24.03	19.00	26.72	26.66	26.06	24.41	17.78	26.20	25.73	34.21	33.96	22.28	n.a.	0.24
Te	n.a.	n.a.	bdl	n.a.	bdl	n.a.	n.a.	bdl	n.a.	n.a.	n.a.	n.a.	n.a.	37.52
Au	2.29	10.46	bdl	n.a.	bdl	n.a.	n.a.	n.a.	n.a.	n.a.	n.a.	bdl	26.88	0.35
Pb	bdl	0.07	0.33	bdl	0.73	42.73	64.27	bdl	n.a.	n.a.	n.a.	n.a.	n.a.	n.a.
Bi	n.a.	n.a.	0.03	n.a.	0.11	n.a.	n.a.	50.18	31.22	34.52	32.71	0.18	n.a.	n.a.
Total	98.96	99.41	99.60	99.63	100.20	98.74	100.26	99.68	100.19	98.44	100.03	99.00	98.04	100.28
Formulae coefficients in Ag, Pb, and Sb mineral phases.														
S	0.005	0.001	13.000	13.000	13.000	3.000	24.000	28.000	8.000	12.000	24.000	2.998	2.000	0.004
Mn	-	-	-	0.000	-	0.002	0.000	0.000	-	0.931	0.378	-	-	-
Fe	0.000	0.001	1.819	1.901	1.897	0.005	0.056	0.035	-	0.156	0.536	0.000	0.016	0.000
Co	-	-	0.004	0.000	0.000	-	-	-	-	0.000	-	-	0.000	-
Ni	-	0.000	0.000	0.000	0.002	0.000	0.000	0.000	-	0.000	-	-	0.000	0.000
Cu	0.001	0.002	6.588	5.207	4.833	0.994	1.074	0.000	-	0.020	-	0.000	-	0.000
Zn	-	0.001	0.226	0.219	0.191	-	-	0.000	-	0.000	-	-	-	-
As	0.000	0.000	0.000	0.077	0.060	0.000	0.000	0.000	-	0.000	-	0.000	0.000	0.007
Se	-	-	0.000	-	-	-	-	0.000	-	-	-	0.002	-	-
Ag	3.394	4.144	3.961	5.817	6.057	-	0.078	2.130	2.970	1.080	3.020	2.932	3.191	1.923
Cd	-	-	-	0.049	-	0.000	0.000	-	-	0.000	0.826	0.000	-	-
Sb	0.995	0.999	4.174	4.521	4.381	1.014	6.809	10.430	2.819	5.319	10.034	0.986	-	0.006
Te	-	-	0.000	-	-	-	-	0.000	-	-	-	-	-	0.984
Au	0.059	0.340	0.000	-	0.000	-	-	-	-	-	-	0.000	0.785	0.006
Pb	0.000	0.000	0.030	0.000	0.072	1.043	14.464	0.000	-	-	-	-	-	-
Bi	-	-	0.003	-	0.010	-	-	11.741	2.010	3.154	5.678	0.005	-	-

Bdl = below the detection limit. Formulae coefficients are calculated for Sb + As + S = 1 for dyscrasite; S = 13 (argentotetrahedrite); S = 3 (bournonite); S = 24 (meneghinite); S = 28 (owyheeite); S = 8 (diaphorite); S = 12 (uchucchacuaite); S = 24 (fyzeliite); S + Se = 3 (pyrargyrite); S = 2 (uytenbogaardtite); Te + S + As + Sb = 2 (hessite). n.a. = not assayed.

We interpret the origin of these multiphase grains as a product of sulfide melt crystallization [40]. It is known that in the case of temperature increases, partial melting of sulfides begins when the whole rock is solid, before the melting of silicate phases ("sulfide anatexis"). A low melting temperature is characteristic of Zn, Ga, Ag, Cd, In, Hg, Tl, Pb, As, Sb, Bi, Se, and Te sulfides, and the first melt appears in the systems Ag–Pb–S, Pb-Sb-S, Ag–Sb–S, PbS-CuS-Sb_2S_3 and other triple and pseudotriple systems in the temperature interval 300–500 °C [39]. In the case of metamorphism under conditions of amphibolite–granulite facies (T = 500–800°C), partial melting of low-melting-point sulfides begins in the rocks, and later, when the temperature decreases, the sulfide melt crystallizes and forms multiphase intergrowths of sulfides, sulfosalts, tellurides, and selenides. These structures of sulfide melt crystallization were described in the ores of many polymetal and gold deposits in metamorphic complexes, for example, Broken Hill (Australia) [39], Montauban [41] and Hemlo (Canada) [42,43], and Bleikvassli (Norway) [44].

The following mineral associations were found in the multiphase intergrowths in the Oleninskoe deposit [45]: galena + argentotetrahedrite ± pyrrhotite (PbS-CuS-Ag_2S-FeS-Sb_2S_3 system); pyrrhotite + pyrargyrite (FeS-Ag_2S-Sb_2S_3); galena + ullmannite + argentotetrahedrite (PbS-NiS-CuS-Sb_2S_3); diaphorite + pyrargyrite + galena (PbS-Ag_2S-Sb_2S_3); galena + fyzeliite (or uchucchacuaite) (PbS-Ag_2S-Sb_2S_3); intergrowths of argentotetrahedrites with different Ag and Cu content (CuS-Ag_2S-Sb_2S_3).

The rocks of the Oleninskoe Au-Ag deposit were metamorphosed under conditions of lower amphibolite facies at 500–600 °C [26]. This temperature was high enough to start melting Pb, Ag, Cu, and Sb sulfides. The signs indicating the origin of the multiphase aggregates as a product of crystallization of sulfide melt are the following: multiphase composition of the grains, where minerals of the low-melting-point metals Pb, Ag, Sb, and Te are necessarily present; absence of signs of replacement of the earlier formed minerals by the later ones; drop-like or roundish irregular forms of the aggregates, which adjoin a larger grain of host sulfide; multiphase sulfide filling of fractures in quartz rock mass. These points fully correspond to the signs of sulfide melt crystallization in sulfide ores as they are given in [39].

4.2. Fluid Composition

Total salinity of fluid in the inclusions in quartz from the studied deposits varies from medium to high (Table 8) [46]. Quartz from the Pellapahk mineralized rocks shows high salinity of fluid inclusions of 341 g/kg H_2O (Table 8). In the Oleninskoe deposit, total salinity varies, depending on the metasomatic rocks: in quartz–albite–muscovite and quartz metasomatites it is moderate at ~130 g/kg H_2O, and in quartz–arsenopyrite–tourmaline rock it is even more than 400 g/kg H_2O. The latter corresponds well to the data obtained earlier for the same rocks [47].

Table 8. Concentration of the main components in fluids from the Oleninskoe and Pellapahk deposits, g/kg H_2O [46].

Deposit	**Oleninskoe**			**Pellapahk**
Sample #	**AK-707**	**AK-710A**	**AK-711**	**AK-721**
Cl^-	131.8	64.5	47.7	52.6
SO_4^{2-}	134.2	9.85	40.1	137.8
HCO_3-	0.55	2.42	1.10	32.84
F^-	0.00	0.00	0.00	0.00
Na^+	47.0	15.9	10.1	62.1
K^+	31.5	6.96	0.49	36.3
Ca^{2+}	61.8	21.1	34.8	10.6
Mg^{2+}	7.60	1.99	0.30	9.00
Total salinity	414.4	122.7	134.6	341.2
CO_2	416.7	625.0	282.6	206.6
CH_4	2.84	0.61	0.76	1.74

Ca and Na (Ca > Na) are the two main cations in the fluids in quartz from the Olenickoe gold–silver deposit; potassium and magnesium content is much lower, especially in quartz metasomatic rock. In the Pellapahk Cu-Mo deposit (Table 8), alkaline metals (sodium and potassium) are predominant: together they make up 85% of mole shares of cations in the inclusions in quartz.

The anion composition of the fluids is also different. In the Oleninskoe deposit, it is characterized by a prevalence of Cl^- over SO_4^{2-} (in mole shares). The mole share of Cl reaches 95% in quartz–albite–muscovite rock. HCO_3^- content is low. In the Pellapahk deposit, the mole share of Cl^- is relatively low: 43% of the anions, close to the one of SO_4^{2-} (41%); HCO_3^- accounts for 15%.

The Na/Cl ratio in the inclusions varies from 0.33 to 0.55 in quartz from the Oleninskoe deposit. This indicates a significant role of Ca and Mg chlorides in the fluids. The (Na + K)/Cl ratio in quartz from the Pellapahk deposit is 1.97. This means that sodium and potassium sulfates and carbonates are present in the fluid inclusions.

5. Discussion

The fact that the intrusions, which host the Pellapahk and the Oleninskoe deposits, refer to one and the same intrusive complex, can be proved by the age of the rocks and by their geochemical characteristics.

The age of the Pellapahk intrusion is 2828 ± 8 Ma, and the age of the Oleninskoe granite porphyry sills is 2817 ± 9 Ma; the values match within the error limits. The difference between the older and the younger ages does not exceed the typical duration of porphyry systems development (10–20 Ma) defined in the Phanerozoic belts [2].

Chemical composition of the unaltered rocks from the deposits does not differ significantly: all of them belong to the calc-alkaline series of metaluminous granites with moderate alkalinity, and the fields of rock composition overlap in the classification diagrams (Figure 5).

The REE spectra of granite porphyry from the studied deposits are of the same form, characterized by enrichment in light REE and the absence of the Eu anomaly (Figure 6). This form of spectrum is typical for I-granites formed in zones of subduction and island arcs [34], and differs significantly from the REE spectra of tourmaline plagiomicrocline anorogenic granites from the intrusions located north of the Pellapahk (Figure 1) [48].

In the Phanerozoic belts, the porphyry intrusions form at a depth of 1–6 km and produce magmatic porphyry-epithermal ore systems, which occur in near-surface conditions. These systems show a specific vertical and lateral zoning in rock alteration and in the distribution of the mineralization, from deep to shallow horizons (and from the center to the edge) (Mo, Cu)–(Cu)–(Pb, Zn)–(Au, Ag, As, Sb); the zoning can be full or fragmentary [2,40,49,50]. Similar systems formed in the Precambrian, or even in the Archean, but the probability they were preserved and have not been eroded since that time is low.

If we consider the Pellapahk and the Oleninskoe deposits as parts of an Archean porphyry-epithermal system, then the Pellapahk Cu-Mo deposit is located at its centre, and the Oleninskoe (Au, Ag, As, Sb) is a distal epithermal deposit in relation to the Pellapahk deposit.

Porphyry Cu deposits in the Phanerozoic are known to display a consistent, broad-scale alteration zoning that comprises, centrally from the bottom upward, zones of sodic-calcic, potassic, chlorite-sericite, sericitic, and advanced argillic (quartz–pyrophyllite, quartz-alunite, quartz-kaolinite) alteration [2,4]. In the Pellapahk deposit, we see zones of quartz-microcline (potassic alteration), quartz-muscovite (sericitic zone), and quartz-andalusite-muscovite (advanced argillic zone) metasomatic rocks (Figures 2 and 3). This zoning generally corresponds that described for the Phanerozoic deposits, but the altered rocks of the Pellapahk deposit were later metamorphosed: sericite was replaced by muscovite, and alumina silicates of the argillic zone (pyrophyllite, alunite, kaolinite) by andalusite during the Neoarchean metamorphism of lower amphibolite facies. Subsequently, during the Paleoproterozoic metamorphism, kyanite formed paramorphoses after

andalusite. The origin of the quartz-muscovite-andalusite schists of the Pellapahk deposit as altered and later metamorphosed volcanic rocks was first published by Glagolev [51], who studied petrography of the Kolmozero–Voronya belt in early 1970s when the Cu-Mo mineralization was unknown.

Generally, the Pellapahk granite porphyry was Si-K altered, and Na, Mg, Ca, and Fe were partly removed from the rock (Table 1). Sodium was taken away from the porphyry system, but Mg, Ca, and Fe were re-deposited in the zone of alteration of high-alumina gneiss in the mineral forms of gedrite and cordierite [36].The zone of gedrite–cordierite alteration is 100–150 m thick and follows the contact with the altered granite porphyry (part of it is shown in Figure 3).

The metamorphism of the mineralized rocks in the Pellapahk deposit can be confirmed by findings of multiphase grains with structures of sulfide melt crystallization, which in the Pellapahk deposit are not as frequent as in the Oleninskoe. Multiphase fine aggregates from the Pellapahk deposit consist of minerals of Pb, Ag, Bi, and Zn galena, argentotetrahedrite, lillianite [45], or minerals of Cu, Sb, and As tetrahedrite and tennantite, löllingite, and chalcopyrite (Figure 16). It is interesting to note formation of löllingite and the absence of arsenopyrite in the rocks with intense pyrite dissemination.

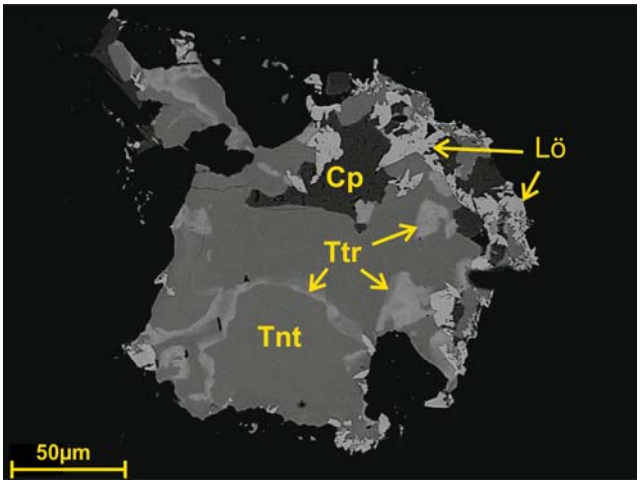

Figure 16. Aggregate of tennantite (Tnt), tetrahedrite (Ttd), chalcopyrite (Cp), and löllingite (Lö) from the Pellapahk deposit. BEI.

Other signs of metamorphism of the ore in the Pellapahk deposit are recrystallization of chalcopyrite with deposition along cleavage in kyanite, which replaces andalusite (Figures 2 and 8), and recrystallization of molybdenite along cleavage in muscovite.

The fact that large amounts of pyrite are preserved within the Pellapahk deposit indicates that high $f(S_2)$ conditions must have prevailed during metamorphism.

Alteration processes in the Oleninskoe deposit differ from those in Pellapahk: we see here calcium alteration (diopsidization), potassic alteration (biotitization), and Si $\pm$ K, Na alteration (quartz-albite-muscovite, quartz-arsenopyrite-tourmaline, quartz metasomatites).

The following distinctive features show metamorphism of the mineralized rocks in the Oleninskoe deposit. First, there are numerous findings of multiphase sulfide grains with structures of sulfide melt crystallization [45], described in Section 4.1.2. Then, late metamorphism is indicated by the mineral composition of the altered rocks, where chlorite is absent, calcite is very rare, and actinolite-hornblende and diopside are abundant. Chlorite and carbonates are typical minerals (together with quartz) in altered amphibolite, but

during amphibolite metamorphism, when H_2O and CO_2 are removed from the rocks, chlorite is replaced by amphiboles [52,53], and the content of carbonates reduces.

Then, pyrite in the Oleninskoe deposit is sporadic, and pyrrhotite is the most abundant sulfide mineral. This can be a result of metamorphism: pyrrhotite replaces pyrite under the conditions of amphibolite metamorphism [53,54].

The composition of the fluid inclusions in quartz varies depending on the character of rock alteration: in the Pellapahk deposit, the fluids are alkaline (Na, K) and SO_4^{2-} rich, and in the Oleninskoe deposit, they are Ca-Mg-Cl dominant.

Mineralogical and geochemical features of the Oleninskoe deposit indicate its genesis with high oxidizing fluids, which could be generated by a magmatic source [55]. The spatial and genetic relationship of mineralization with the sills of granite porphyry, the geochemical association of metals, an Au/Ag ratio of <0.2, and the multiplicity of silver mineralization with different Ag, Cu and Pb sulfosalts are all characteristics that enable the classification of the Oleninskoe deposit as a sub-epithermal deposit located in the vicinity of a big granite porphyry intrusion; the Pellapahk intrusion being the most probable. The geological–structural characteristics of the Oleninskoe deposit—its position in a shear zone, the morphology and size of ore bodies, the scale of the deposit, the intensity and zoning of host rocks alteration—do not oppose this model.

If the Oleninskoe and Pellapahk deposits are the parts of the Pellapahk–Oleninskoe porphyry-epithermal system, then the age of primary mineralization is close to the time of the formation of granite porphyry at 2.83–2.81 Ga. The deposits were later lower amphibolite metamorphosed together with the hosting volcanic-sedimentary rocks in the Neoarchean (T = 550–600 °C, P = 3–4 kBar) and in the Paleoproterozoic (T ~ 530 °C, P ~ 5.5 kBar) [26], and the mineralized rocks demonstrate signs of metamorphism of the ore.

Mineral deposits, associated with granite porphyry intrusions and dykes, are well known in the Fennoscandian and other Precambrian shields around the world. In the Fennoscandian Shield, we can mention the Cu porphyry (with gold) deposit of Aitik in Norbotten, Sweden [56], the molybdenum porphyry deposit ofLobash and neighboring gold deposit Lobash-1 in the Central Karelia [57,58], the minor gold deposits of Taloveis and Falaley in the Kostamuksha greenstone belt, Western Karelia [59], Mo-W with gold occurrences of Yalonvaara and Hatunoya in Southern Karelia [60], etc. The deposits and occurrences in Karelia formed not at the time of crystallization of the porphyry intrusions, but at the stage of the Paleoproterozoic (or rarer, Neoarchean) regional metamorphism [61]. The geological setting, morphology and size of the ore bodies, geochemical characteristics, and mineralogy show these deposits belonging to the orogenic genetic class [62]. In the Kolmozero–Voronya belt, the Nyalm-1 deposit is considered an orogenic gold deposit, associated with a granodiorite porphyry intrusion [63,64].

Some deposits in the Fennoscandian Shield are classified as metamorphosed epithermal: those are the gold deposit of Kutemajarvi in the Tampere belt in South Finland, and the silver (with base metals) deposit of Taivaljarvi in the Tipasjarvi belt in Central Finland.

The Kutemajarvi gold deposit comprises eight tube-like ore bodies, located 500 m south from the Pukala monzogranite–porhyry tonalite intrusion in the intermediate metavolcanics. The intrusion and the deposit are of the Paleoproterozoic age of 1.90–1.88 Ga [65].

The Taivaljarvi is an Archean stratiform Ag-Zn-Pb deposit, consisting of four mineralized horizons formed by fluids of magmatic origin, which migrated along shear zones in felsic pyroclastic rocks (rhyolite tuffs) [66]. The average gold content in the deposit is 0.29 g/t. The age of the rocks hosting the mineralization is 2.83–2.75 Ga [66].

Thus, the Pellapahk–Oleninskoe porphyry-epithermal system is the oldest system with complex Cu-Mo and Au-Ag mineralization in the Fennoscandian Shield. Distinctive geochemical and mineralogical features distinguish the Oleninskoe deposit from all other gold deposits in Fennoscandia.

6. Conclusions

Gabbro-diorite-granodiorite-granite porphyry intrusions formed at the late stages of the formation of the volcanic-sedimentary sequences of the Kolmozero–Voronya greenstone belt. The age of the intrusions is 2.83–2.82 Ga. Cu-Mo, Au-Ag, and Au deposits are associated with the quartz porphyry series.

The Pellapahk Cu-Mo and the Oleninskoe Au-Ag deposits are considered two parts of the Pellapahk–Oleninskoe porphyry-epithermal system: the Cu-Mo deposit in a big granite porphyry intrusion makes its central part, and the gold-silver deposit is located in the flank where it is associated with granite porphyry sills.

The following distinctive features indicate the sub-epithermal origin of the Au-Ag mineralization in the Oleninskoe deposit: the spatial and genetic relationships with the sills of granite porphyry, the geochemical association of ore elements, an Au/Ag ratio of <0.2, and the multiplicity of silver mineralization with different Ag, Cu, Pb, and Sb sulfosalts. The geological–structural characteristics of the Oleninskoe deposit (i.e., its location in a shear zone, the morphology and size of ore bodies, the scale of the deposit, the intensity and zoning of host rocks alteration) do not oppose this model.

The Pellapahk–Oleninskoe porphyry-epithermal ore system is probably the oldest one in the Fennoscandian Shield. Mineralized rocks of the Pellapahk and Oleninskoe deposits were later lower amphibolite metamorphosed. An important sign of ore metamorphism is the formation of structures of crystallization of sulfide melt of the low-melting-point metals. In the Oleninskoe ores we see fine intergrowths of Ag, Cd, Pb, As, Sb, Te minerals galena, argentotetrahedrite, pyrargyrite, pyrrhotite, ullmannite, stutzite, etc. In the Pellapahk Cu-Mo deposit, multiphase fine aggregates consist of Bi, Pb, Sb, and As minerals. Other signs of metamorphism of the ore in the Pellapahk deposit are recrystallization of chalcopyrite with re-deposition along cleavage in kyanite, and recrystallization of molybdenite along cleavage in muscovite. Late metamorphism of the ore in the Oleninskoe deposit is indicated by the absence of chlorite and the scarcity of carbonate in altered amphibolite.

Author Contributions: Methodology: A.A.K.; Conceptualization: A.A.K., N.M.K.; Geochronological Study: N.M.K.; Mineralogical Investigations: A.A.K.; Original Draft Writing: A.A.K., N.M.K.; Editing and Review: A.A.K. All authors have read and agreed to the published version of the manuscript.

Funding: The work was carried out under Project 0226-2019-0053 of the Russian Academy of Science.

Institutional Review Board Statement: Not applicable.

Informed Consent Statement: Not applicable.

Data Availability Statement: The data presented in this study are available on request from the corresponding author.

Acknowledgments: The authors thank Vsevolod Prokofiev (IGEM RAS) for study of fluid inclusions composition, Yevgeny Savchenko and Yekaterina Selivanova (GI KSC RAS) for microprobe and X-ray study of minerals, and Alexandr Volkov (IGEM RAS) for helpful discussion of the results. The authors are grateful to the reviewers for their comments, which helped to improve the manuscript.

Conflicts of Interest: The authors declare no conflict of interest.

References

1. Seedorff, E.; Dilles, J.H.; Proffett, J.M.; Einaudi, M.T.; Zurcher, L.; Stavast, W.J.A.; Johnson, D.A.; Barton, M. Porphyry deposits—Characteristics and origin of hypogene features. *Econ. Geol.* **2005**, *100*, 251–298.
2. Sillitoe, R.H. Porphyry-copper systems. *Econ. Geol.* **2010**, *105*, 3–41. [CrossRef]
3. Cooke, D.R.; Hollings, P.; Wilkinson, J.J.; Tosdal, R.M. Geochemistry of Porphyry Deposits. In *Treatise on Geochemistry*, 2nd ed.; Holland, H.D., Turekian, K.K., Eds.; Elsevier: Oxford, UK, 2014; pp. 357–381.
4. Kesler, S.E.; Chryssoulis, S.L.; Simon, G. Gold in porphyry copper deposits: Its distribution and fate. *Ore Geol. Rev.* **2002**, *21*, 103–124. [CrossRef]
5. Cooke, D.R.; Simmons, S.F. Characteristics and genesis of epithermal gold deposits. *Rev. Econ. Geol.* **2000**, *13*, 221–244.
6. Cooke, D.R.; Hollings, P.; Walshe, J. Giant porphyry deposits—Characteristics, distribution and tectonic controls. *Econ. Geol.* **2005**, *100*, 801–818. [CrossRef]

7. Richards, J.P. Postsubduction porphyry Cu-Au and epithermal Au deposits: Products of remelting of subduction-modified lithosphere. *Geology* **2009**, *37*, 247–250. [CrossRef]
8. Sillitoe, R.H. Some metallogenic features of gold and copper deposits related to alkaline rocks and consequences for exploration. *Miner. Depos.* **2002**, *37*, 4–13. [CrossRef]
9. Kalinin, A.A.; Galkin, N.N. The Precambrian Copper-Molybdenum porphyry deposit Pellapahk (Kolmozero-Voron'ya greenstone belt). *Vestnik KNTs RAN* **2012**, *44*, 80–92. (In Russian)
10. Kalinin, A.A.; Kudryashov, N.M.; Galkin, N.N. Occurrences of gold, copper, and molybdenum mineralization in the Kolmozero-Voron'ya greenstone belt (Kola Peninsula): Geological characteristics and age. In *Gold in the Kola Peninsula and Adjacent Territories*; K&M: Apatity, Russia, 2010; pp. 51–59. (In Russian)
11. Ovoca Gold plc Operational Update 13/09/2007. Available online: http://www.ovocagold.com/upload/20070913_ayax__kola_&_goltsovoye_update.pdf (accessed on 2 April 2017).
12. Rozhkov, I.S.; Zhadnova, T.P. On the problem of gold mineralization in the Russian Platform. *Doklady AN SSSR* **1972**, *203*, 434–437. (In Russian)
13. Korovkin, V.A.; Turyleva, L.V.; Rudenko, D.G.; Zhuravlev, V.A.; Klyuchnikova, G.N. *Underground of the North-West of Russian Federation*; VSEGEI: Sankt-Peterburg, Russia, 2003; 754p. (In Russian)
14. Kryazhev, S.G.; Prokofiev, V.Y.; Vasyuta, Y.V. Use of ICP-MS method for assaying of ore-forming fluids. *Vestn. Mosc. State Univ. Ser. 4 Geol.* **2006**, *4*, 30–36. (In Russian)
15. Krogh, T.E. A low-contamination method for hydrothermal decomposition of zircon and extraction of U and Pb for isotopic age determination. *Geochim. Cosmochim. Acta* **1973**, *37*, 485–494. [CrossRef]
16. Ludwig, K.R. *PbDat for MS-DOS, Version 1.21*; U.S. Geological Survey Open-File Report; U.S. Geological Survey: Reston, VA, USA, 1991; pp. 88–542.
17. Ludwig, K.R. *ISOPLOT/Ex. Version 2.06. A Geochronological Toolkit for Microsoft Excel*; Berkley Geochronology Center Special Publication: Berkeley, CA, USA, 1999; 49p.
18. Steiger, R.H.; Jager, E. Subcomission of geochronology: Convention of the use of decay constants in geo- and cosmochronology. *Earth Planet. Sci. Lett.* **1976**, *36*, 359–362. [CrossRef]
19. Stacey, J.S.; Kramers, I.D. Approximation of terrestrial lead isotope evolution by a two-stage model. *Earth Planet. Sci. Lett.* **1975**, *26*, 207–221. [CrossRef]
20. Mints, M.V.; Suleimanov, A.K.; Babayants, P.S. *Deep Structure, Evolution, and Minerals in the Early Precabrian Basement of the East European Platform: Interpretation of Materials on Referent Profile 1-EV, Profiles 4V and TATSEIS*; Geokart Geos: Moscow, Russia, 2010; ISBN 978-5-89118-531-9. (In Russian)
21. Nikitin, I.V. Tectonics of the Kolmozero-Voron'ya belt in the light of the conception of horizontal moving. In *Regional Tectonics of the Early Precambrian of the USSR*; Nauka: Leningrad, Russia, 1980; pp. 104–111. (In Russian)
22. Mints, M.V.; Glaznev, V.N.; Konilov, A.N.; Nikitichev, A.P.; Raevskiy, A.B.; Sedykh, Y.N.; Stupak, V.M.; Fonaryov, V.I. *The Early Precambrian of the North-Eastern Part of the Baltic Shield: Paleogeodynamics, Structure and Evolution of the Continental Crust*; Nauchny Mir: Moscow, Russia, 1996; 287p. (In Russian)
23. Kudryashov, N.M.; Udoratina, O.V.; Coble, M.A.; Steshenko, E.N.; Gabov, D.A. Age and sources of matter for rare metal pegmatite in the Archean Kolmozero-Voronya greenstone belt: Isotope geochronological study of zircons from muscovite-tourmaline granites. *Proc. Fersman Sci. Sess. GIKSC RAS* **2018**, *15*, 222–225. (In Russian) [CrossRef]
24. Kudryashov, N.M.; Lyalina, L.M.; Apanasevich, E.A. Age of rare metal pegmatites from the VasinMyl'k deposit (Kola region): Evidence from of U-Pb geochronology of microlite. *Dokl. AN* **2015**, *461*, 321–325. [CrossRef]
25. Astafiev, B.Y.; Viskunova, K.G.; Voinova, O.A.; Glaznev, V.N. *State GeologicalMap of Russian Federation. Scale 1:1000000 (the Third Generation). Series Severo-Karsko-Barentsevomorskaya. Sheet R—37, 38—Cape Svyatoy Nos, Cape Kanin Nos. Explanatory Note*; Cartographic Factory of VSEGEI: Sankt-Peterburg, Russia, 2008; 251p. (In Russian)
26. Drugova, G.M.; Glebovitskiy, V.A.; Duk, V.L.; Kitsul, V.I.; Savel'eva, T.L.; Sedova, I.S.; Semyonov, A.S. *High Gradient Regimes of Metamorphism in Development of the Earth crust*; Nauka: Leningrad, Russia, 1982; 229p. (In Russian)
27. Daly, J.S.; Balagansky, V.V.; Timmerman, M.J.; Whitehouse, M.J. The Lapland-Kola orogen: Palaeoproterozoic collision and accretion of the northern Fennoscandian lithosphere. *Geol. Soc. Lond. Mem.* **2006**, *32*, 579–598. [CrossRef]
28. Kalinin, A.A. *Gold in Metamorphic Complexes of the North-Eastern Part of the Fennoscandian Shield*; Federal Research Centre 'Kola Science Centre': Apatity, Russia, 2018; 250p. (In Russian)
29. Nikitin, I.V.; Gavrilenko, B.V. Structural and geodynamical diversity of exhumated 'roots' of the Archean interplate suture (Kola Peninsula). In *Postcollisional Evolution of Mobile Belts*; Institute of Geology and Geochemistry, the Ural Branch of the RAS: Ekaterinburg, Russia, 2001; pp. 126–129. (In Russian)
30. Gavrilenko, B.V.; Nikitin, I.V.; Zozulya, D.R.; Kudryashov, N.M.; Petrovskiy, M.N.; Korsakova, O.P.; Galkin, N.N. Geology, tectonics, age, and metallogeny of the Archean suture zone Kolmozero-Voron'ya. *Vestn. Murm. State Tech. Univ.* **2002**, *5*, 43–60. (In Russian)
31. Galkin, N.N. Geology and Mineralogy of Gold Occurrences in the Pellaphk–Oleninsky Ore Unit. Ph.D. Thesis, Kola Science Centre, Apatity, Russia, 2006; 22p. (In Russian).
32. Roizenman, F.M.; Ezhov, S.V.; Ronenson, B.M. Ore-formong metasomatic processes in metamorphic complexes. In *Metamorphic Ore Genesis*; Kola Science Center: Apatity, Russia, 1980; pp. 77–83. (In Russian)

33. Frost, B.R.; Barnes, C.G.; Collins, W.J.; Arculus, R.J.; Ellis, D.J.; Frost, C.D. A geochemical classification for granitic rocks. *J. Petrol.* **2001**, *42*, 2033–2048. [CrossRef]
34. Turkina, O.M. *Lections on Geochemistry of Magmatic and Metamorphic Processes*; Novosibirsk State University: Novosibirsk, Russia, 2014; 118p.
35. Sun, S.-S.; McDonough, W.F. Chemical and isotopic systematics of oceanic basalts: Implications for mantle composition and processes. *Geol. Soc. Lond. Spec. Publ.* **1989**, *42*, 313–345. [CrossRef]
36. Belolipetskiy, A.P.; Kalinin, A.A.; Petrov, S.I. *Mineralogy and Geochemistry of Metasomatites in Deep Fault Zones*; Kola Filial of Academy of Science of the USSR: Apatity, Russia, 1987; 115p. (In Russian)
37. Kalinin, A.A.; Kazanov, O.V.; Bezrukov, V.I.; Prokofiev, V.Y. Gold Prospects in the Western Segment of the Russian Arctic: Regional Metallogeny and Distribution of Mineralization. *Minerals* **2019**, *9*, 137. [CrossRef]
38. Kalinin, A.A.; Savchenko, Y.E.; Selivanova, E.A. Mustard Gold in the Oleninskoe Gold Deposit, Kolmozero–Voronya Greenstone Belt, Kola Peninsula, Russia. *Minerals* **2019**, *9*, 786. [CrossRef]
39. Frost, B.R.; Mavrogenes, J.A.; Tomkins, A.G. Partial melting of sulfide ore deposits during medium- and high-grade metamorphism. *Can. Miner.* **2002**, *40*, 1–18. [CrossRef]
40. Lang, J.R.; Eastoe, C.J. Relationships between a porphyry Cu-Mo deposit, base and precious metal veins, and Laramide intrusions, Mineral Park, Arizona. *Econ. Geol.* **1988**, *83*, 551–567. [CrossRef]
41. Tomkins, A.G. Three mechanisms of ore re-mobilisation during amphibolite facies metamorphism at the Montauban Zn—Pb—Au—Ag deposit. *Miner. Depos.* **2007**, *42*, 627–637. [CrossRef]
42. Tomkins, A.G.; Frost, B.R.; Pattison, D.R.M. Arsenopyrite melting during metamorphism of sulfide ore deposits. *Can. Miner.* **2006**, *44*, 1025–1042. [CrossRef]
43. Tomkins, A.G.; Pattison, D.R.M.; Zaleski, E. The Hemlo gold deposit, Ontario: An example of melting and mobilization of a precious metal–sulfosalt assemblage during amphibolite facies metamorphism and deformation. *Econ. Geol.* **2004**, *99*, 1063–1084. [CrossRef]
44. Vokes, F.M. Some aspects of the regional metamorphic mobilization of preexisting sulphide deposits. *Miner. Depos.* **1971**, *6*, 122–129. [CrossRef]
45. Kalinin, A.A.; Savchenko, Y.E. Structures of sulfide melt crystallization as an indication of metamorphism of the ores in the Oleninskoe gold deposit. *Vestn. MSTU* **2020**, *23*, 29–37. (In Russian) [CrossRef]
46. Kalinin, A.A.; Prokofiev, V.Y. Specific features of genesis of precious and base metals deposits in the Voron'yetundrovsky ore area (Kolmozero-Voronya belt). In *Rock and Ore Formation: Achievements and Prospects of Investigations. Proceeding of the 90-th Anniversary of IGEM RAS, Moscow, Russia, 5–9 April 2021*; Bortnikov, N.S., Petrov, V.A., Eds.; IGEM RAS: Moscow, Russia, 2020; pp. 128–131. ISBN 978-5-88918-060-9. Available online: http://www.igem.ru/igem_90/ (accessed on 15 January 2021). (In Russian)
47. Volkov, A.V.; Novikov, I.A. The Oleninskoe gold sulfide deposit (Kola peninsula, Russia). *Geol. Ore Depos.* **2002**, *44*, 361–372.
48. Kudryashov, N.M.; Udoratina, O.V.; Coble, M.A.; Steshenko, E.N. Geochronological and Geochemical Study of Zircon from Tourmaline-Muscovite Granites of the Archaean Kolmozero–Voronya Greenstone Belt: Insights into Sources of the Rare-Metal Pegmatites. *Minerals* **2020**, *10*, 760. [CrossRef]
49. Korobeinikov, A.F.; Anan'ev, Y.S.; Gusev, A.I.; Voroshilov, V.G. *Ore-Metasomatic and Geochemical Zonation of Gold Fields and Deposits in Folded Belts of Siberia*; Tomsk Polytechnical University: Tomsk, Russia, 2013; 458p. (In Russian)
50. Cox, D.P.; Singer, D.A. *Mineral Deposit Models. U.S. Geological Survey Bulletin 1693*; U.S. Geological Survey: Washington, DC, USA, 1992; 379p.
51. Glagolev, A.A. Influence of the early post-volcanic processes on composition of the metamorphic rocks of the Voron'y Tundry. In *Geochemistry, Mineralogy, and Petrology*; Book 5; Bolgarian Academy of Sceince: Sofia, Bulgaria, 1976; pp. 108–116. (In Russian)
52. Phillips, G.N.; Powell, R. Formation of gold deposits: A metamorphic devolatilization model. *J. Metamorph. Geol.* **2010**, *28*, 689–718. [CrossRef]
53. Gaboury, D. Parameters for the formation of orogenic gold deposits. *Appl. Earth Sci.* **2019**, *128*, 124–133. [CrossRef]
54. Phillips, G.N. Metamorphic fluids and gold. *Mineral. Mag.* **1993**, *57*, 365–374. [CrossRef]
55. Saunders, J.A.; Hofstra, A.H.; Goldfarb, R.J.; Reed, M.H. Geochemistry of hydrothermal gold deposits. In *Treatise on Geochemistry*, 2nd ed.; Elsevier: Amsterdam, The Netherlands, 2014; pp. 383–424. [CrossRef]
56. Juhani, O.V.; Iljina, M. (Eds.) *Metallogeny and Tectonic Evolution of the Northern Fennoscandian Shield*; Guidebook 33 IGC excursion No. 15, 15–21 August 2008; 33 IGC: Oslo, Norway, 2008; 113p.
57. Pokalov, V.T.; Semenova, N.V. The first big molybdenum deposit of the Precambrian age. *Geol. Ore Dep.* **1993**, *35*, 262–270.
58. Kuleshevich, L.V.; Tytyk, V.M.; Korotaeva, N.N. Mineralogy of ore and near-ore altered rocks in the gold-polymetsl deposit Lobash-1. *Zapiski RMO* **2004**, *4*, 39–51.
59. Kuleshevich, L.V.; Dmitrieva, A.V. Geochemical characteristics and gold mineralization of the Late Archean Taloveis diorite granite porphyry complex, Kostomuksha structure, Karelia. *Proc. Karelian Sci. Cent. RAS* **2014**, *1*, 63–75. (In Russian)
60. Ivashchenko, V.I.; Lavrov, O.B. Complex porphyry deposit Jalonvaara in the Archean of Karelia (Russia). *Geol. Ore Dep.* **1996**, *5*, 412–423.
61. Samsonov, A.V.; Larionova, Y.O.; Nosova, A.A.; Ruch'ev, A.M. The Problem of Age Position and Genesis of Gold Mineralization in the Archean Greenstone Belts of the Karelian Block: An Experience of Complex Reconstructions. (In Russian). Available online: http://www.minsoc.ru/viewreports.php?cid=338&rid=1395 (accessed on 25 November 2020).

62. Ivashchenko, V.I.; Golubev, A.I. *Gold and Platinum in Karelia: Formational-Genetic Types of Mineralization and Prospects*; Karelian Science Center: Petrozavodsk, Russia, 2011; 369p. (In Russian)
63. Kudryashov, N.M.; Kalinin, A.A.; Lyalina, L.M.; Serov, P.A.; Elizarov, D.V. Geochronological and isotope geochemical characteristics of rocks, hosting gold occurrences in the Archean greenstone belt Kolmozero-Voron'ya (Kola region). *Lithosphere* **2015**, *6*, 83–100. (In Russian)
64. Kalinin, A.A.; Bakaev, G.F. Gold occurrence Nyal'm-1 in the Kolmozero-Voron'ya belt: Geological and mineralogical-geochemical characteristics. In *Science and Education in the Arctic Region, Proceedings of the International Scientific-Practical Conference, Murmansk, Russia, 3–7 April 2017*; MSTU: Murmansk, Russia, 2017; pp. 70–76. (In Russian)
65. Eilu, P.; Pankka, H. *Fingold—A Public Database on Gold Deposits in Finland*; Geological Survey of Finland: Espoo, Finland, 2013. Available online: http://en.gtk.fi/informationservices/palvelukuvaukset/fingold.html (accessed on 21 March 2016).
66. Maier, W.D.; Lahtinen, R.; O'Brien, H. (Eds.) *Mineral Deposits of Finland*; Elsevier: Amsterdam, The Netherlands, 2015; 792p, ISBN 978-0-12-410438-9.

minerals

MDPI

Article

Disseminated Gold–Sulfide Mineralization in Metasomatites of the Khangalas Deposit, Yana–Kolyma Metallogenic Belt (Northeast Russia): Analysis of the Texture, Geochemistry, and S Isotopic Composition of Pyrite and Arsenopyrite

Maxim V. Kudrin [1,*], Valery Yu. Fridovsky [1], Lena I. Polufuntikova [1,2] and Lyudmila Yu. Kryuchkova [3]

[1] Diamond and Precious Metal Geology Institute, SB RAS, 677000 Yakutsk, Russia; 710933@list.ru (V.Y.F.); pli07@list.ru (L.I.P.)
[2] M.K. Ammosov North-Eastern Federal University, 677000 Yakutsk, Russia
[3] Centre for X-ray Diffraction Studies of the Research Park, Saint Petersburg State University, 199034 St Petersburg, Russia; kryuchkova.2106@gmail.com
* Correspondence: kudrinmv@mail.ru; Tel.: +7-4112-33-58-72

Abstract: At the orogenic gold deposits of the Yana–Kolyma metallogenic belt (northeast Russia) both Au–quartz-sulfide mineralization with native gold and disseminated sulfide mineralization with invisible Au developed. The textural and mineralogical-geochemical features, isotope-geochemical characteristics of gold-bearing sulfides from proximal metasomatites, and possible forms of Au occurrence in pyrite and arsenopyrite have been studied using electron microprobe, atomic absorption, LA-ICP-MS trace element, isotope analysis, and computed microtomography. Four generations of pyrite (Py1, diagenetic; Py2, metamorphic; Py3, metasomatic; Py4, veined) and two generations of arsenopyrite (Apy1, metasomatic; Apy2, veined) have been identified at the Khangalas deposit. In the proximal metasomatites, the most common are Py3 and Apy1. Studying their chemical composition makes it possible to identify the features of the distribution patterns of typochemical trace elements in pyrite and arsenopyrite, and to establish the nature of the relationship between Au and these elements. In Py3 and Apy1, structurally bound (solid solution) Au^{+} prevails, isomorphically entering the crystal lattice or its defects. Isotope characteristics of hydrothermal sulfides ($\delta^{34}S = -2.0$ to -0.6‰) indicate that mantle/magmatic sulfur was involved in the formation of the deposit, though the participation of sulfur from the host rocks of the Verkhoyansk clastic complex cannot be ruled out. The Khangalas deposit has much in common with other gold deposits of the Yana–Kolyma metallogenic belt, and from this point of view, the results obtained will help to better reveal their gold potential and understand their origin.

Keywords: LA-ICP-MS; invisible gold; trace elements; pyrite; arsenopyrite; metasomatite; orogenic gold deposit; Khangalas; northeast Russia

Citation: Kudrin, M.V.; Fridovsky, V.Y.; Polufuntikova, L.I.; Kryuchkova, L.Y. Disseminated Gold–Sulfide Mineralization in Metasomatites of the Khangalas Deposit, Yana–Kolyma Metallogenic Belt (Northeast Russia): Analysis of the Texture, Geochemistry, and S Isotopic Composition of Pyrite and Arsenopyrite. *Minerals* **2021**, *11*, 403. https://doi.org/10.3390/min11040403

Academic Editor: Galina Palyanova

Received: 28 February 2021
Accepted: 7 April 2021
Published: 12 April 2021

1. Introduction

The Late Jurassic–early Early Cretaceous Yana–Kolyma metallogenic belt (YKMB) is located in the central part of the Verkhoyansk–Kolyma folded region, in the boundary zone between the northeastern margin of the Siberian craton and the Kolyma–Omolon superterrane. Within the belt, gold deposits are concentrated in three sectors: Upper Kolyma, Upper Indigirka, and Adycha. The length of the belt is approximately 1000 km and the width is approximately 200 km. This is the richest gold province in northeast Russia, including the large Natalka (1500 t Au) and Degdekan (400 t Au) deposits. It is of global economic importance. Production of gold from the Yana–Kolyma belt since the 1930s was ~3200 t, with current estimated resources of about 5000 t Au [1,2]. This is comparable with the output of major Paleozoic–Mesozoic gold provinces of the world (Jiaodong, China; Juneau gold belt, AK, USA; Lachlan fold belt, Australia; Baikal fold

belt, Russia; and Southern Tien Shan, Uzbekistan) [3]. To date, the areas with the most economic value within the YKMB are orogenic gold deposits with Au-quartz vein and/or Au-sulfide-quartz veinlet-disseminated types of mineralization. The origin and conditions of the localization of the first mineralization type have been much studied (e.g., [4–9] and many others). Recent research has shown great economic value of the insufficiently studied disseminated gold-bearing pyrite and arsenopyrite mineralization in the YKMB (see [10–15] and references therein). Disseminated sulfide mineralization is known both within the gold deposits [10,11,15–19] and in regional sulfidation zones [17,20–22] localized in transcrustal faults [12,23].

This work presents the mineralogy, geochemistry, isotopic composition, and gold content of disseminated mineralization in clastic rocks of the Khangalas orogenic gold deposit located in the Upper Indigirka sector of the YKMB [24,25]. In early research of the geology and ore content of the deposit, attention was focused on Au–quartz mineralization [26–28], its supergene alteration [28–30], and placer-to-primary source relationships [31]. In recent years, extensive prospecting work has been carried out within the Khangalas ore cluster. A large number of surface and underground mined workings have been completed. This made it possible to obtain new data on the mineralogy and geochemistry of the Khangalas deposit. Despite the fact that the current estimated reserves and resources of gold at the deposit are small (11 tonnes of Au, with a high average grade of 11.2 g/t Au [32]), the presence of gold-bearing pyrite and arsenopyrite in the wall–rock metasomatites is evidence that the total contained tonnage may be much higher. The Khangalas deposit has much in common with other gold deposits of the YKMB. From this standpoint, the findings presented here will help geologists and prospectors evaluate the overall potential gold resources of the region.

2. Regional Geology and Mineralization

2.1. Regional Tectonic Framework

The Khangalas deposit is located in the central part of the Yana–Kolyma metallogenic belt, which includes the Kular–Nera and the more easterly Polousny–Debin terranes, as well as the eastern part of the Verkhoyansk fold-and-thrust belt (Figure 1). The Kular–Nera terrane consists of Upper Permian, Triassic, and Lower Jurassic clastic sedimentary rock sequences, metamorphosed to initial stages of greenschist facies, and the Polousny–Debin terrane is composed mainly of Upper Triassic–Upper Jurassic turbidites. The terranes are separated by the Charky–Indigirka and Chai–Yureya faults. To the southwest, the regional-scale Adycha–Taryn fault separates the Kular–Nera terrane from the Verkhoyansk fold-and-thrust belt made of Mesoproterozoic–Lower Carboniferous carbonate–clastic and carbonate rocks and Upper Paleozoic–Mesozoic clastic rocks of the passive continental margin of the Siberian craton. The structural pattern of the Yana–Kolyma metallogenic belt is defined by linear folds and faults of NW strike, manifesting several deformation stages [9,33].

Magmatism in the Upper Indigirka sector is manifested by granitoids of intermediate to felsic intrusions and volcanics of the Tas–Kystabyt magmatic belt (J_3–K_1). Also present are mafic (162 ± 4 Ma, whole rock, Rb–Sr [34]), intermediate, and felsic dikes of the Nera–Bohapcha complex (151–145 Ma, U–Pb SHRIMP-II, zircons [23]). According to Parfenov et al. [35] and Parfenov and Kuzmin [33], the emplacement of the Late Jurassic granitoids was related to collision events. More recent data indicate that subduction processes were involved in their formation [36,37]. Tectonic structures, magmatism, and ore deposits of the YKMB were closely related to the Late Jurassic to earliest Early Cretaceous subduction, accretionary events at the eastern active continental margin of the Siberian craton [33]. The Upper Indigirka sector of the YKMB includes, from northeast to southwest, the Inyali–Debin, Olchan–Nera, Adycha–Taryn, and Adycha metallogenic zones. The Olchan–Nera zone hosts the Khangalas orogenic gold deposit.

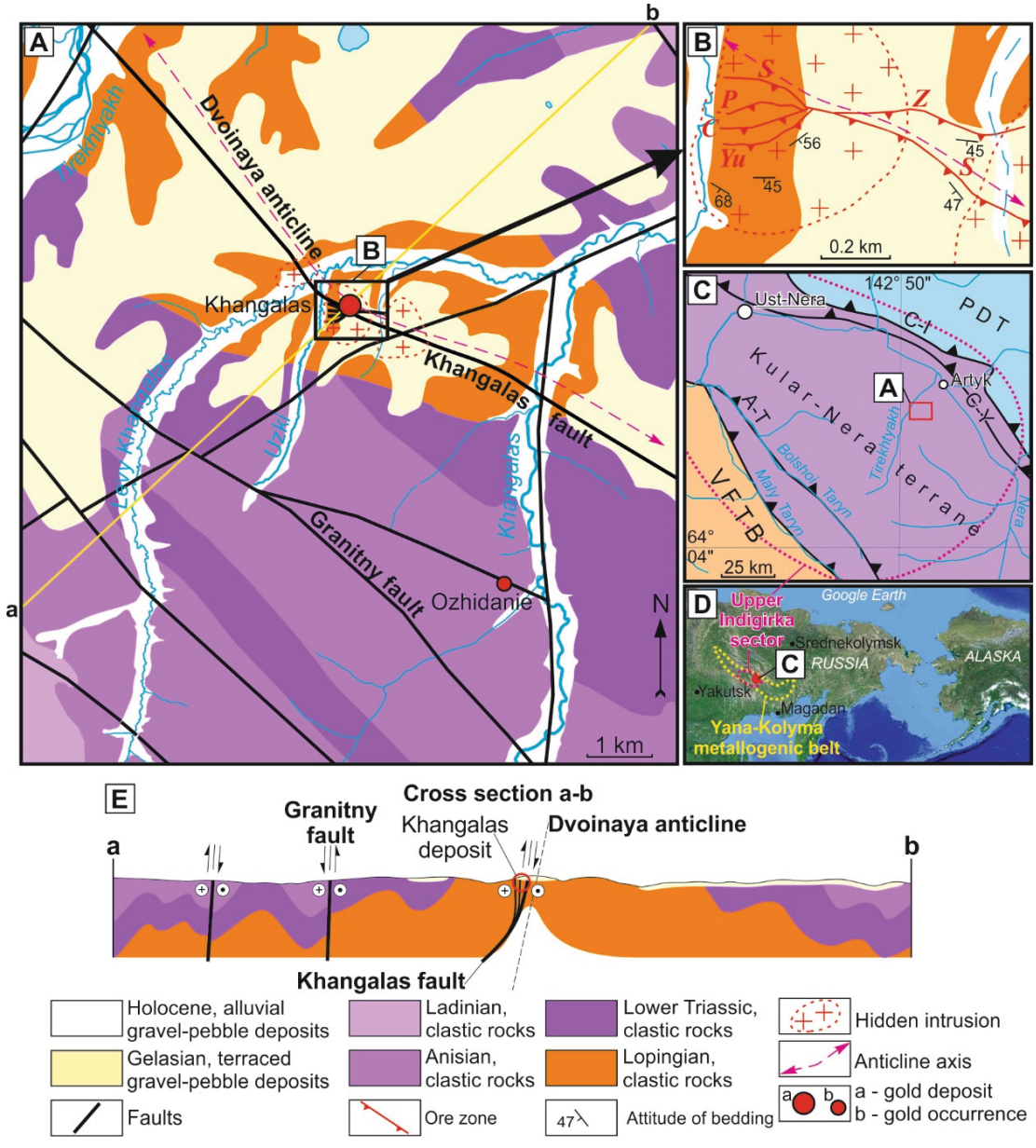

Figure 1. (**A**,**C**,**D**) Regional location, (**B**) geological structure, and (**E**) cross-section of Khangalas deposit. Inset map: VFTB, Verkhoyansk fold-and-thrust belt; PDT, Polousny–Debin terrane; C-I, Charky–Indigirka fault; C-Y, Chai–Yureya failt; A-T, Adycha–Taryn fault. Mineralized crushed zones: S, Severnaya; P, Promezhutochnaya; C, Centralnaya; Yu, Yuzhnaya; Z, Zimnyaya.

2.2. Geology of the Khangalas Deposit

2.2.1. Structures and Host Rocks

The geology and structural-tectonic conditions of the formation and localization of the Khangalas deposit are described in detail in [25]. Here we give only a brief summary of the necessary information. Extraction of alluvial gold started in 1933, when the Khangalas Creek placers were first discovered. Later on, in 1947, the Khangalas lode gold deposit was discovered, and production of gold from quartz veins with pyrite, arsenopyrite, galena, sphalerite, and chalcopyrite began. The veins occur mostly at the border between sandy and shaly intervals, due to competency contrast. The deposit is localized in the crest of the Dvoinaya anticline of the Nera (Nera–Omchug) anticlinorium (Figure 1). The core of the anticline is composed of Upper Permian (Lopingian, P_3) deposits. In the lower part of the section, with a thickness of more than 350 m, these are mainly massive brownish-gray and gray sandstones with thin siltstone interbeds. The upper part is dominated by a more than 450 m thick sequence of dark gray to black siltstones with included pebbles of sedimentary, igneous, and metamorphic rocks. The limbs of the anticline are made of Lower Triassic (T_1) deposits (mainly dark gray shales, mudstones, and siltstones with rare interlayers of light gray sandstones with a thickness of 680–750 m) and Middle Triassic (T_2a) sediments of the Anisian stage (alternating sandstones and siltstones with a thickness of 700–800 m). The Ladinian strata (T_2l) consist of interbedded siltstones and sandstones with a total thickness of 850–950 m. The main ore-controlling tectonic structure is the Khangalas fault with a NW strike. This is represented at the Khangalas deposit by five extensive (up to 1400 m) mineralized ore zones (Severnaya, Promezhutochnaya, Centralnaya, Yuzhnaya, Zimnyaya) with low-sulfidation Au-type mineralization localized in the Dvoinaya anticline crest (Figures 1 and 2A). The ore zones are up to 32 m thick and dip to the SW, S, and SE at 30°–50° to 70°–80° [25]. No evidence of magmatic activity is observed within the Khangalas deposit. Geophysical data suggest the presence of a granitoid pluton at depth [38]. The mineralization formed as a result of progressive fold-and-thrust deformations in the Verkhoyansk–Kolyma fold belt. These were initiated by orogenic processes in late Late Jurassic–early Early Cretaceous [25].

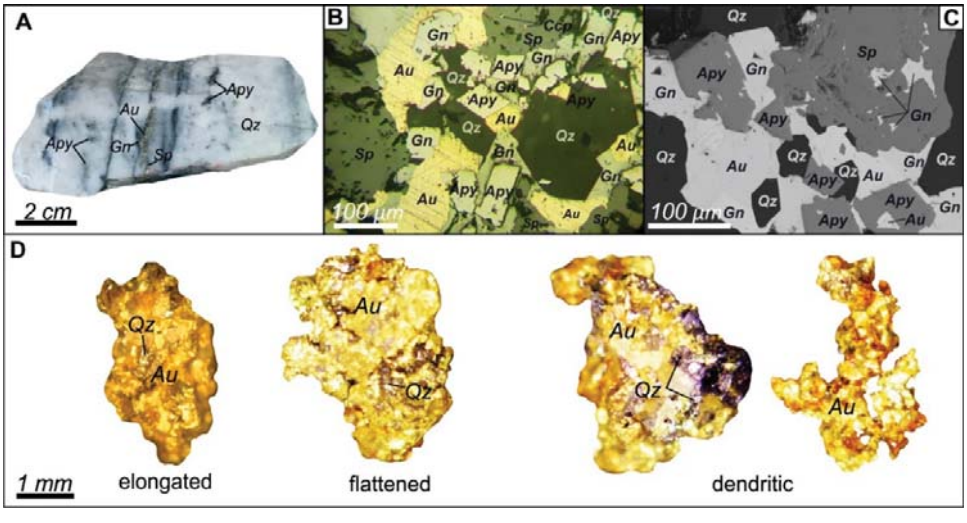

Figure 2. (**A**–**C**) Mineral composition of vein-type ores, and (**D**) morphology of native gold of Khangalas deposit. (**A**) Banded quartz with inclusions of native gold (Au), galena (Gn), sphalerite (Sp), and arsenopyrite (Apy); (**B**,**C**) intergrowths of native gold (Au), galena (Gn), sphalerite (Sp), and chalcopyrite (Ccp) of the Au–polysulfide vein association and anhedral arsenopyrite (Apy) of quartz–pyrite–arsenopyrite vein association: (**B**) in reflected light, (**C**) in backscattered electrons. Hereafter, abbreviations for minerals are from [39].

2.2.2. Mineralization

Gold mineralization in the Khangalas deposit is present as two types: Au–quartz-sulfide veins with native gold and sulfide–quartz disseminations with invisible gold hosted in quartz–sericite–carbonate metasomatites (Figure 3). The Au–quartz-sulfide mineralization is characterized as concordant and discordant quartz veins 0.1–1 m thick in swells up to 5 m (Figures 2 and 3B,C). The content of sulfides reaches 1–3 vol.%. The main ore minerals are pyrite and arsenopyrite, with less common galena, sphalerite, and chalcopyrite. Accessory minerals include freibergite, boulangerite, tetrahedrite, Fe-gersdorffite, acanthite, and native gold. The veinlet-disseminated sulfide–quartz mineralization with invisible gold is localized both in the ore zones and in their walls (Figure 3D,E). The sulfide content reaches 3–3.5 vol.%, and pyrite and arsenopyrite predominate. Galena, sphalerite, chalcopyrite, native gold, and freibergite are rare. Gold content in the metasomatites varies from <1 ppm up to 5.29 ppm Au, with an average of 0.73 ppm.

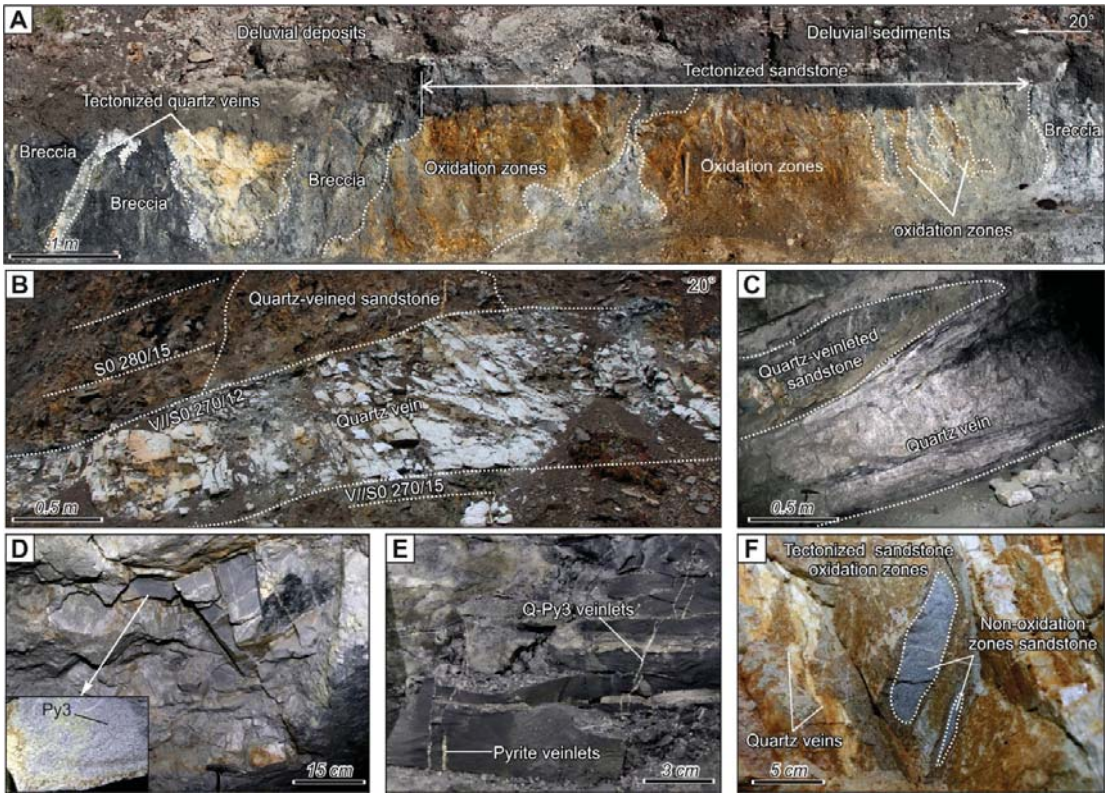

Figure 3. Ore bodies of the Khangalas deposit: (**A**) Yuzhnaya oxidized mineralized fault zone; (**B**) quartz–carbonate vein. Photographs taken in underground mine workings: (**C**) vein-type Au–quartz mineralization with native gold, Centralnaya zone, alt. 920 m a.s.l.; (**D**) disseminated type of mineralization with invisible gold in quartz–sericite–carbonate metasomatites, Centralnaya zone, alt. 920 m a.s.l.; (**E**) pyrite and quartz veinlets in sandstones, Centralnaya zone, alt. 920 m a.s.l.; (**F**) oxidized pyrite in sandstones, alt. 945 m a.s.l.

At the Khangalas deposit, four stages of mineral formation are distinguished: two pre-ore preparatory (sedimentary and metamorphic), ore (hydrothermal), and post-ore (supergene) (Figure 4). During the sedimentary stage, accumulation of clastic material, a change in redox potential, mobilization of ore matter, and formation of diagenetic sulfide mineralization (Py1) took place. The metamorphic stage was marked by alteration of clastic

rocks as a result of regional metamorphism and deformation processes, disseminated sulfide mineralization (Py2), and sericitization and chloritization of clastic rocks. The hydrothermal stage is characterized by four successive paragenetic associations:

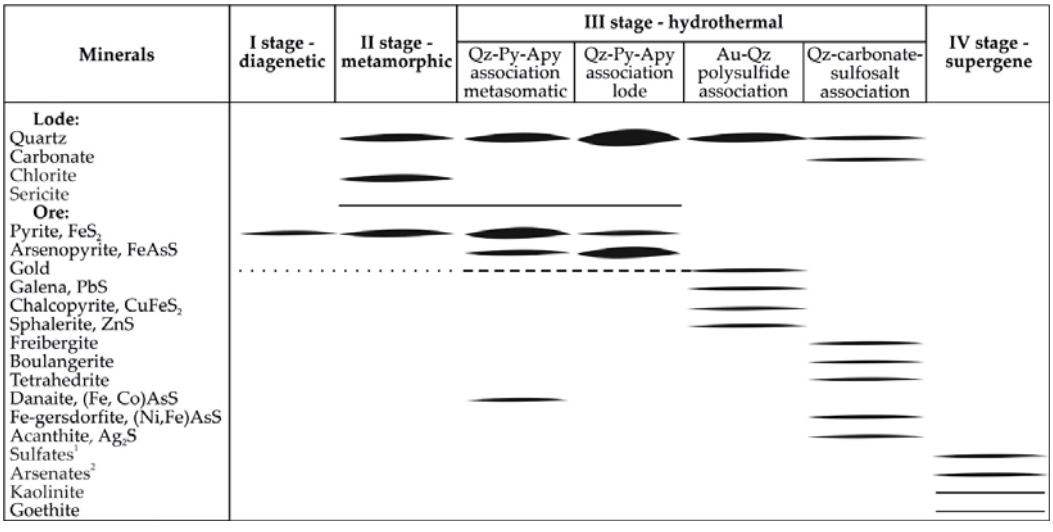

Figure 4. Mineral paragenesis for Khangalas deposit. [1] Sulfates: gypsum, jarosite, mangazeite, amarantite, meta-aluminite, meta-alunogen, tamarugite, pickeringite, unknown hydrous iron sulfate [40]. [2] Arsenates: scorodite, kankite, bukovskiite, unknown Fe-Al arsenate-phosphate-sulfate [41].

1. The metasomatic quartz–pyrite–arsenopyrite association is localized in quartz veinlets within the wall rock with a quartz–carbonate–sericite matrix. The main ore minerals are auriferous pyrite (Py3) and arsenopyrite (Apy1), which occur as individual crystals, intergrowths, small aggregates ranging in size from fractions of a millimeter to 2–3 mm, and veins up to a few mm thick. Also observed are microcrystals and microaggregates of high-Co arsenopyrite (danaite), ranging in size from tens to 100–200 microns. Native gold is present here in an invisible, finely dispersed form. It forms very thin films and nanoinclusions in pyrite and arsenopyrite, and also occurs as an isomorphic impurity.

2. The vein quartz–pyrite–arsenopyrite association is present mainly in the ore bodies, composed of coarse and medium crystalline anhedral quartz. Pyrite (Py4) and arsenopyrite (Apy2) occur as aggregates up to 3–4 cm in size, veinlets up to 1 mm thick, and individual crystals up to 1–2 mm long (Figure 3A).

3. Au–Qz–polysulfide association is represented by small aggregates and microveinlets of sphalerite, chalcopyrite, and galena, and by native gold segregations (Figure 3B,C). They fill voids in quartz and cracks in pyrite and arsenopyrite of early associations. Native gold is elongated, flattened, and dendritic in form (Figure 3D). The size ranges from small to large (most common fractions are 0.5–0.8 mm) and the distribution is extremely uneven. The fineness of native gold averages 820‰–830‰ (min 780‰–max 850‰).

4. The quartz–carbonate–sulfosalt association is localized in cracks and voids of the early ore and vein minerals in the form of aggregates and individual grains. The principal mineral type is carbonate, represented by ankerite and ankerite–dolomite. Sulfosalts are sporadic and mainly include freibergite, tetrahedrite, and boulangerite.

The post-ore stage is characterized by supergene minerals. This is one of the characteristic features of the Khangalas deposit [29,40,42]. They are expressed as an oxidation zone with the formation of sulfates, arsenates, iron oxides, clay, and other minerals, extending to a depth of 50–100 m (Figure 2F). The authors have previously identified two

unknown minerals from the oxidation zone: hydrous iron sulfate [40] and Fe–Al arsenate–phosphate–sulfate [41].

3. Materials and Methods

Samples for mineralogical-geochemical and isotope-geochemical studies were collected from natural outcrops and the walls and dumps of surface and underground mined workings. For mineralogical and geochemical studies of disseminated sulfide mineralization, thick polished sections (40 in total) and epoxy-mounted grains (90 sulfide grains in 8 mounts) were prepared. The textural and structural features of the ores were studied using a Karl Zeiss Axio M1 optical microscope. The qualitative chemical and mineral compositions of the samples were studied with the use of a JEOL JSM-6480LV scanning electron microscope equipped with an Energy 350 Oxford energy dispersive spectrometer (20 kV, 1 nA, beam diameter 1 μm) (analysts S.K. Popova and N.I. Khristoforova, Diamond and Precious Metal Geology Institute, Siberian Branch, Russian Academy of Sciences, Yakutsk).

The major element compositions of pyrite and arsenopyrite were determined by standard X-ray spectral analysis on a Camebax-Micro microanalyzer (analyst N.V. Khristoforova, Diamond and Precious Metal Geology Institute, Siberian Branch, Russian Academy of Sciences, Yakutsk). The analytical conditions were as follows: accelerating voltage of 20 kV; beam current of 25 nA; measurement time of 10 s; K series for Fe, Co, Ni, Cu and S; M series for Au and Pb; L series for As and Sb.; and wavelength-dispersive spectrometer (WDS) with LiF, PET, and TAP crystals. The standards used were: FeS_2 for Fe and S, FeAsS for As, Fe-Ni-Co alloy for Co, Ni, Au-Ag alloy of fineness for Au and Ag, $CuSbS_2$ for Sb, and PbS for Pb. The detection limits 0.01%. Trace elements in pyrite were studied on 9 grains of pyrite-3 and arsenopyrite-1 using a New Wave Research UP-213 laser ablation system (USA) coupled with an Agilent 7700x quadrupole mass spectrometer (Agilent Technologies, Santa Clara, CA, USA) (analyst D.A. Artemiev, Institute of Mineralogy, Ural Branch of the Russian Academy of Sciences, Miass). The measurements were carried out using a 213 nm Nd:YAG UV laser with fluence set at 1.8–5.5 J/cm^2 (1.8–3.0 J/cm^2 for pyrite, 3.0–4.5 J/cm^2 arsenopyrite) and a rate of flow of He carrier gas at 0.5–0.65 L/min. Mass spectrometer settings were: RF power 1550 W, carrier gas Ar, flow rate 0.85–0.95 L/min, plasma-forming gas (Ar) flow rate 15 L/min, and auxiliary gas (Ar) flow rate 0.9 L/min. Data were acquired by singe spot and line analyses using a laser spot diameter of 25 to 80 μm and a frequency of 5–10 Hz. The analysis time for each sample was 90 s, comprising a 30 s measurement of background (laser off) and a 60 s analysis with laser on. Pre-ablation was performed for 3–4 s before each analysis. Between the analyses, and between analysis and pre-ablation, blowing with gas was done for 60–90 s.

The mass spectrometer was calibrated using calibration multi-element solutions and the NIST SRM-612 reference material. The amount of molecular oxides ($^{232}Th^{16}O/^{232}Th$) was kept below 0.2%. The $^{238}U/^{232}Th$ ratio, when adjusted according to NIST SRM-612, was 1:1. External calibration standards USGS MASS-1 [43] and UQAC FeS-1 were used to analyze every 7–13 spots to account for drifting of the laser and mass spectrometer. Mass contents of elements for NIST SRM-612 and USGS MASS-1 were taken from the GeoReM database. Data processing and calculation were carried out using the Iolite software package [44]. As internal standard (IS) for pyrite, we used ^{57}Fe measured by SEM-EMF. In some cases, normalization to 100% of the total components was performed according to standard techniques [45].

The Au and Ag contents were determined on powdery monomineral samples by atomic absorption spectrometry with electrothermal atomization on a Thermo Scientific iCE 3500 spectrometer (analysts A.E. Sannikova, E.L. Naryshkina, and E.I. Mikhailov, Diamond and Precious Metal Geology Institute, Siberian Branch, Russian Academy of Sciences, Yakutsk). Au and Ag content of more than 2 ppm was determined on an Agilent 4200 MP-AES atomic emission spectrometer with microwave-saturated plasma. X-ray computed microtomography was used to study the internal structure of minerals and identify

high-density phases in sulfide grains; this non-destructive method makes it possible to visualize in 3D the distribution of phases with different density in the sample [46–53], etc. Microtomographic studies were carried out at the Centre for X-ray Diffraction Studies of the Research Park of St. Petersburg State University (analyst L.Yu. Kryuchkova). Samples of pyrite and arsenopyrite (31 in total) were studied by x-ray computed microtomography. Monomineral fractions 0.25–1.0 mm in size were hand-picked under a binocular microscope. The studies were carried out on a SkyScan-1172 microtomography scanner (Bruker microCT, Belgium). To reconstruct the array of shadow images, NRecon software (Bruker microCT) was used, which allows leveling instrument artifacts and setting the range of gray gradations corresponding to the value of x-ray absorption and, accordingly, x-ray density. To analyze the obtained microtomographic data, DataViewer and CTVox software (Bruker microCT) were used. For sulfur isotope analysis we used monosulfide fractions (5 samples) selected by hand and ground into powder. The analysis was performed in the Laboratory of Stable Isotopes of the Far Eastern Geological Institute, Far Eastern Branch of the Russian Academy of Sciences (Vladivostok; analyst T.A. Velivetskaya) using a Flash EA-1112 elemental analyzer (Thermo Scientific, Germany) in the S configuration according to the standard protocol for converting sulfur from sulfide to SO_2. The $^{34}S/^{32}S$ isotope ratios were measured on a MAT-253 mass spectrometer (Thermo Scientific, Waltham, MA, USA) in continuous He flux mode. The measurements were performed against a standard laboratory gas SO_2 calibrated according to international standards IAEA-S-1, IAEA-S-2, IAEA-S-3, and NBS-127. The results of $\delta^{34}S$ measurements are given in reference to the international VCDT standard.

4. Results

4.1. Pyrite and Arsenopyrite Types and Textures

At the Khangalas deposit, four generations of pyrite and two generations of arsenopyrite are established.

4.1.1. Diagenetic Pyrite (Py1)

Pyrite (Py1) was formed during sedimentation and diagenesis due to bacterially mediated sulfate reduction (Figure 5A,B). Framboids are represented by spherical aggregates ranging in size from 10 to 100 μm (Figure 5A,B). They are composed of pyrite microcrystals, sometimes have a zonal structure with a carbonaceous-silicic matrix, and form diffused or bedding-plane dissemination in sedimentary rocks (Figure 6C).

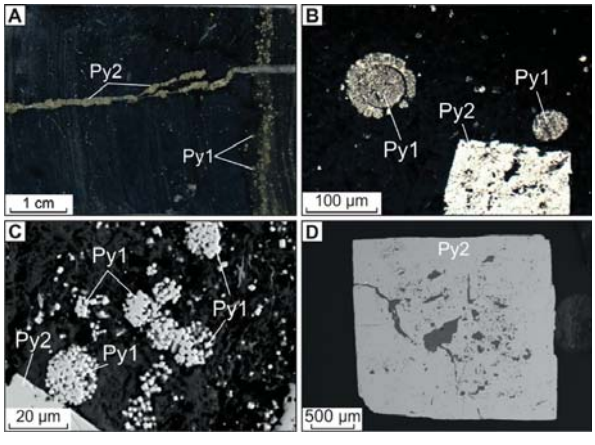

Figure 5. (**A**) Photo and (**B**) photomicrographs of Py1 and Py2 of Khangalas deposit in reflected light, and (**C**,**D**) backscattered electrons: (**A**) Py2 veinlets and Py1 bedding-plane dissemination in siltstone; (**B**,**C**) diagenetic Py1 and metamorphic Py2; (**D**) metamorphic Py2.

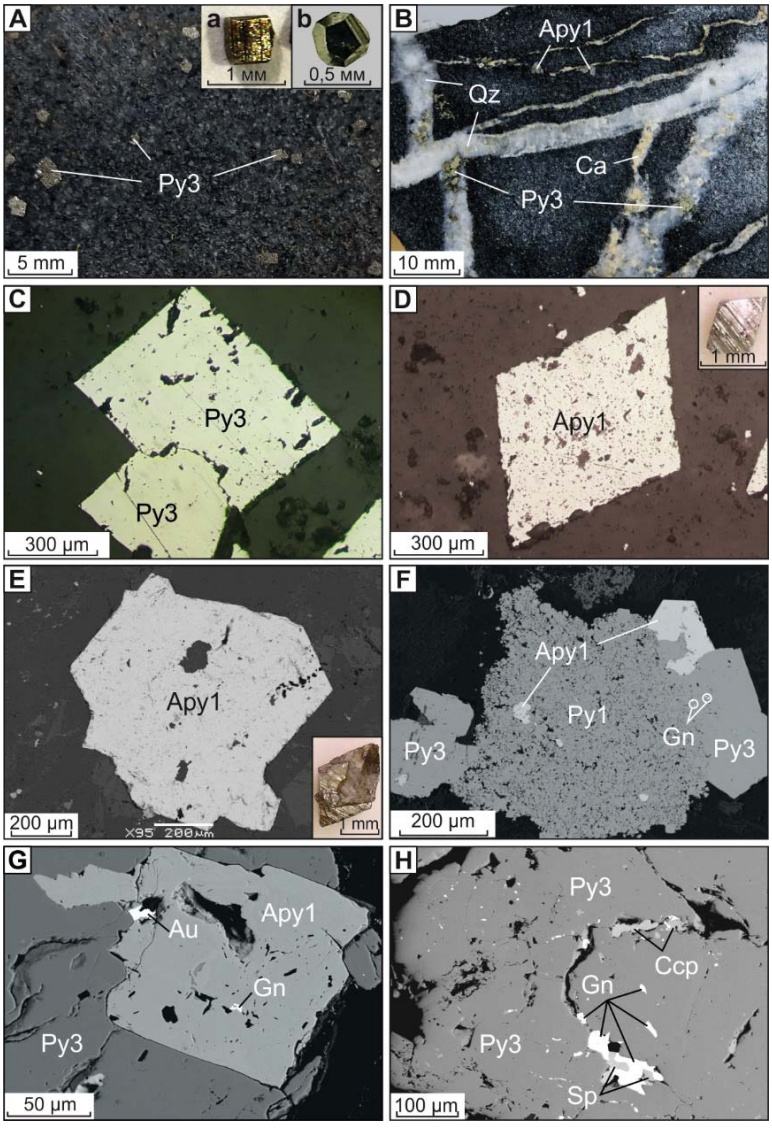

Figure 6. (**A**,**B**) Photos and (**C**,**D**) photomicrographs of Py3 and Apy1 of Khangalas deposit in reflected light and (**E**–**H**) backscattered electrons: (**A**) disseminations of metasomatic Py3 in sandstone; (**B**) vein-disseminated quartz-Py3-Apy1 mineralization; (**C**) Py3 veinlets and bedded-plane Py1 dissemination in siltstone; (**D**) euhedral Apy1; (**E**) Apy1 aggregate; (**F**) intergrowths of Py1, Py3, and Apy1 with galena inclusions (Gn); (**G**) inclusions of native gold (Au) and galena (Gn) in Py3 and Apy1. (**H**) inclusions of sulfides of gold–polysulfide association (Gn, galena; Ccp, chalcopyrite; Sp, sphalerite) in Py3. Insets: (**A**, inset a) cubic Py3; (**A**, inset b) pyritohedra Py3; (**D**, inset) short prismatic Apy1; (**E**, inset) pseudo-pyramidal Apy1.

4.1.2. Metamorphic Pyrite (Py2)

Metamorphic inequigranular cubic pyrite (Py2) forms disseminated mineralization and fills in microcracks in sedimentary rocks (Figure 5B,D). Crystal size ranges from

5–150 microns to 1–3 mm. Large crystals have microtextures characteristic of cataclasis and corrosion (Figure 5D).

4.1.3. Metasomatic Pyrite (Py3) and Arsenopyrite (Apy1)

The metasomatic quartz–pyrite–arsenopyrite association forms the basis of the vein-disseminated mineralization type with invisible gold in the wall rock metasomatites. Metasomatic Py3 and Apy1 occur as individual crystals, intergrowths, small aggregates, and veinlets up to a few mm thick in thin quartz veins (Figure 6). Apy1 is characterized by short prismatic to pseudo-pyramidal crystal shapes (Figure 6D,E, insets), while Py3 features complicated cubic shapes up to pyritohedra (Figure 6A, inset). The crystals size to 1–1.5 mm, less often to 2–3 mm. Py3 and Apy1 contain superimposed microinclusions of minerals of polysulfide and sulfosalt–carbonate associations (Figure 6F–H). In ~20% of Py3 and ~12% of Apy1 grains, inclusions of galena and rare inclusions of sphalerite and chalcopyrite (Figure 6F–I) were found. Microinclusions of tetrahedrite and freibergite were recorded in single samples. In only one sample, K-4-17, in interstices between crystals of arsenopyrite Apy1 and pyrite Py3, we found native gold about 15 μm in size with a fineness of 827‰ (Figure 6G).

X-ray computed microtomography (3D) of arsenopyrite (Apy1) and pyrite (Py3) grains from two samples collected from the Khangalas deposit showed that they consist of x-ray contrasting phases (Figure 7). Dense minerals are light to white in color, have isometric, subisometric, and flattened shapes, and are up to 10–15 μm in size in Apy1 (Figure 7A) and from a few to 30–40 μm in Py3 (Figure 7C,D). They form an impregnated texture. One can observe a linear-planar distribution of dense phases (or aggregates), probably confined to the defect and crystal growth zones. Uniform arsenopyrite grains are noted (Figure 7B). Native gold and galena are denser than pyrite and arsenopyrite.

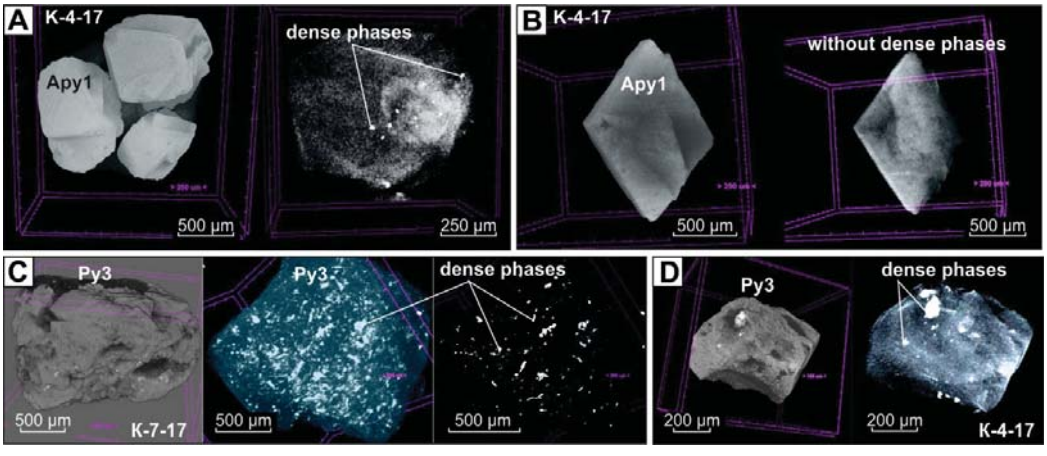

Figure 7. Three-dimensional visualization of Py3 and Apy1 of Khangalas deposit. (**A**) Apy1 grains with inclusions of dense minerals (galena, gold); (**B**) Apy1 without inclusions of x-ray contrasting phases; (**C**,**D**) Py3 aggregate with included dense minerals (galena, gold).

4.1.4. Vein Pyrite (Py4) and Arsenopyrite (Apy2)

The veined quartz–pyrite–arsenopyrite association forms the basis of the vein ore bodies of the deposit (Figure 8). Arsenopyrite Apy2 and pyrite Py4 crystallized simultaneously with quartz, and they occur as scattered small euhedral and anhedral grains and nests up to 1–2 cm in size, less often up to 3–5 cm, as well as veinlets oriented along carbonaceous bands in quartz (Figure 8A,B). Galena, chalcopyrite, sphalerite, and native

gold form microinclusions in Apy2, Py4, and quartz crystals, and are confined to their fractures and growth zones (Figure 8C,D).

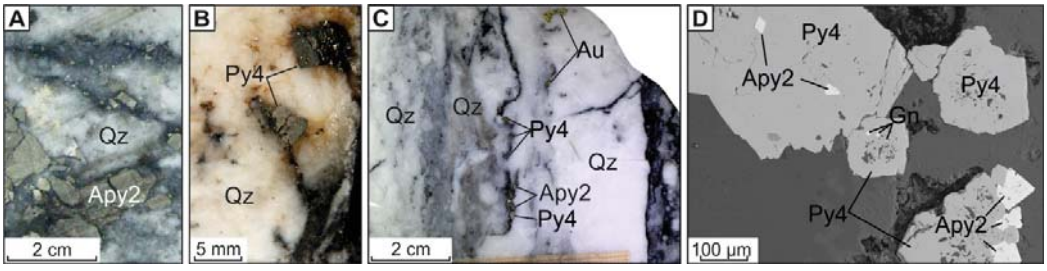

Figure 8. (**A**–**C**) Photographs and (**D**) photomicrograph of Py4 and Apy2 of Khangalas deposit (in backscattered electrons): (**A**) nest-like clusters and individual idiomorphic Apy2 crystals in quartz; (**B**) idiomorphic Py4 grains in quartz; (**C**) gold–polysulfide association with Py4, Apy2 in banded quartz; (**D**) Py4-Apy2 intergrowths with scattered galena (Gn) in quartz.

4.2. Composition of Pyrite and Arsenopyrite

4.2.1. EPMA Results: Major and Minor Elements CAPS

The results of electron probe micro-analyzer (EPMA) spot analysis of the different varieties of pyrite are given in Table 1. All types of pyrite contain As, Co, Ni, Cu, and Sb impurities, the most abundant of which is As.

Table 1. Chemical composition of pyrites and arsenopyrites determined by EPMA (all values in wt.%.; nd, not detected).

No	Sample	Fe	S	As	Co	Ni	Cu	Sb	Pb
				Diagenetic Py1					
1	K-40-14; n = 11	47.48−45.99 * / 46.79	55.82−51.78 / 54.37	0.31−0.03 / 0.15	0.13−0.05 / 0.09	0.17−0.02 / 0.06	0.06−0.01 / 0.03	0.05−0.01 / 0.03	nd
2	K-55-14; n = 10	46.63−46.93 / 46.45	53.89−52.77 / 53.27	0.31−0.06 / 0.22	0.18−0.06 / 0.08	0.19−0.01 / 0.07	0.06−0.01 / 0.03	0.05−0.07 / 0.03	nd
3	K-61-14; n = 5	46.99−45.78 / 46.66	54.44−52.93 / 53.84	0.30−0.08 / 0.18	0.11−0.05 / 0.07	0.05−0.01 / 0.02	0.02−0.01 / 0.02	0.06−0.03 / 0.04	nd
4	K-23-14; n = 5	45.69−44.54 / 45.04	52.41−51.17 / 52.00	0.23−0.01 / 0.07	0.07−0.05 / 0.06	0.33−0.13 / 0.03	0.03−0.01 / 0.02	0.06−0.03 / 0.05	0.10−0.05 / 0.08
5	Kpr2-4-14; n = 4	46.61−46.30 / 46.44	51.76−50.96 / 51.45	0.12−0.01 / 0.06	0.05−0.03 / 0.04	0.01	nd	0.04−0.02 / 0.03	0.05−0.02 / 0.04
6	K-4-14; n = 6	46.51−45.73 / 46.17	54.62−52.13 / 53.18	0.23−0.09 / 0.16	0.19−0.07 / 0.10	0.03−0.01 / 0.02	0.03	0.07−0.01 / 0.03	nd
7	K-7-17; n = 19	47.40−45.06 / 46.04	53.89−51.41 / 52.74	0.28−0.02 / 0.17	0.20−0.02 / 0.11	0.14−0.01 / 0.07	0.04−0.01 / 0.01	0.11−0.01 / 0.05	nd
8	KG-32-19, n = 1	46.80	53.66	0.18	nd	0.02	nd	0.06	nd
9	KG-7-19, n = 1	46.50	52.31	0.01	nd	0.01	nd	0.05	nd
				Metamorphic Py2					
10	K-40-14; n = 4	46.97−45.91 / 46.65	54.89−50.60 / 53.73	0.15−0.09 / 0.13	0.15−0.08 / 0.10	0.06−0.03 / 0.05	0.04−0.02 / 0.03	0.03−0.01 / 0.02	nd
11	K-55-14; n = 3	46.74−45.53 / 46.60	52.97−52.67 / 52.67	0.27−0.20 / 0.24	0.09−0.07 / 0.09	0.32−0.01 / 0.13	0.03−0.01 / 0.02	0.05−0.03 / 0.04	nd
12	K-4-14; n = 4	46.70−46.13 / 46.50	52.88−51.71 / 52.14	0.25−0.03 / 0.16	0.07−0.05 / 0.06	0.02−0.01 / 0.01	0.03−0.01 / 0.02	0.03−0.02 / 0.03	nd
13	K-23-14; n = 7	45.93−45.31 / 45.67	53.14−51.35 / 51.88	0.23−0.02 / 0.08	0.10−0.06 / 0.08	0.23−0.04 / 0.15	0.12−0.01 / 0.04	0.06−0.01 / 0.03	0.13−0.03 / 0.08
14	KG-29-19; n = 4	46.98−46.48 / 46.74	53.95−52.66 / 53.32	0.14−0.01 / 0.06	0.05−0.03 / 0.04	0.01	0.06−0.01 / 0.03	0.03−0.01 / 0.02	0.11−0.02 / 0.07
				Hydrothermal-metasomatic Py3					
15	K-32-14; n = 16	46.17−45.14 / 45.50	51.95−50.37 / 50.94	2.14−1.01 / 1.57	0.08−0.04 / 0.05	0.07−0.01 / 0.02	0.02−0.01 / 0.01	0.05−0.01 / 0.02	nd
16	K-51-14; n = 27	46.91−44.91 / 46.00	53.59−50.25 / 51.84	2.22−0.56 / 1.31	0.17−0.05 / 0.09	0.25−0.01 / 0.04	0.05−0.01 / 0.03	0.04−0.01 / 0.02	nd
17	K-52-14; n = 24	47.01−45.98 / 46.59	55.10−50.93 / 53.71	2.49−0.97 / 1.58	0.11−0.03 / 0.05	0.14−0.01 / 0.03	0.03−0.01 / 0.01	0.04−0.01 / 0.02	nd
18	K-55-14; n = 6	46.59−46.02 / 46.36	53.32−51.30 / 52.24	1.03−0.31 / 0.67	0.21−0.07 / 0.12	0.10−0.01 / 0.06	0.04−0.01 / 0.03	0.06−0.02 / 0.04	nd
19	K-61-14; n = 17	47.15−45.24 / 46.45	55.48−50.89 / 52.63	1.86−0.34 / 0.98	0.08−0.05 / 0.06	0.07−0.01 / 0.02	0.12−0.01 / 0.03	0.12−0.02 / 0.05	nd
20	K-9-17/1; n = 18	46.63−44.87 / 45.98	54.16−51.04 / 52.81	1.71−0.31 / 0.95	0.12−0.06 / 0.08	0.11−0.01 / 0.03	0.06−0.01 / 0.03	0.10−0.01 / 0.03	nd
21	K-4-17; n = 13	46.53−45.58 / 46.15	52.60−50.76 / 51.98	1.28−0.40 / 0.77	0.13−0.04 / 0.06	0.38−0.01 / 0.16	0.03−0.01 / 0.02	0.08−0.01 / 0.02	nd
22	K-14-17; n = 19	46.85−45.36 / 46.22	54.28−52.82 / 53.63	1.59−0.38 / 0.81	0.50−0.05 / 0.11	0.48−0.01 / 0.16	0.03−0.01 / 0.01	0.04−0.01 / 0.02	0.01
23	K-35-17; n = 24	46.98−45.59 / 46.43	53.39−50.31 / 51.56	1.81−0.45 / 1.03	0.13−0.04 / 0.06	0.24−0.01 / 0.06	0.06−0.01 / 0.02	0.06−0.01 / 0.03	0.13−0.01 / 0.07

Table 1. *Cont.*

No	Sample	Fe	S	As	Co	Ni	Cu	Sb	Pb
24	KG-12-19; n = 25	47.39−45.33 / 46.60	55.27−52.25 / 53.93	1.45−0.32 / 0.82	0.10−0.03 / 0.05	0.09−0.01 / 0.02	0.02−0.01 / 0.01	0.08−0.01 / 0.04	0.12−0.01 / 0.06
25	KG-13-19; n = 39	46.95−45.50 / 46.35	54.02−51.59 / 53.04	2.23−0.33 / 0.93	0.54−0.04 / 0.08	0.15−0.01 / 0.03	0.05−0.01 / 0.02	0.05−0.01 / 0.02	0.06−0.01 / 0.02
26	KG-9-19; n = 5	46.95−45.97 / 46.43	54.02−52.58 / 53.47	1.27−0.42 / 0.78	0.10−0.04 / 0.06	0.15−0.01 / 0.05	0.05−0.01 / 0.02	0.06−0.01 / 0.03	0.03−0.01 / 0.01
27	KG-18-19; n = 26	46.86−45.82 / 46.48	53.61−50.76 / 52.89	2.29−0.56 / 1.27	0.13−0.04 / 0.07	0.27−0.01 / 0.04	0.04−0.01 / 0.01	0.08−0.01 / 0.02	0.05−0.01 / 0.02
28	KG-24-19; n = 21	46.32−46.76 / 45.99	54.78−52.66 / 53.97	2.40−0.36 / 1.28	0.08−0.04 / 0.06	0.04−0.01 / 0.02	0.03−0.01 / 0.01	0.04−0.01 / 0.02	0.07−0.01 / 0.03
29	KG-29-19; n = 20	47.17−45.78 / 46.51	53.62−58.88 / 52.51	1.88−0.42 / 1.08	0.62−0.03 / 0.08	0.23−0.01 / 0.04	0.06−0.01 / 0.02	0.05−0.01 / 0.02	0.13−0.01 / 0.05
30	KG-30-19/1; n = 21	47.18−45.86 / 45.81	53.93−51.92 / 53.00	1.05−0.32 / 0.58	0.08−0.02 / 0.05	0.33−0.01 / 0.10	0.04−0.01 / 0.02	0.04−0.01 / 0.02	0.14−0.01 / 0.05
31	Kpr-4-14; n = 9	46.84−44.87 / 46.52	51.87−48.88 / 51.38	0.97−0.31 / 0.75	0.08−0.02 / 0.05	0.04−0.01 / 0.02	0.02−0.01 / 0.01	0.07−0.01 / 0.03	0.03
32	KG-30-19/2; n = 9	46.29−45.86 / 45.86	53.64−52.10 / 53.06	0.81−0.32 / 0.53	0.08−0.03 / 0.05	0.33−0.01 / 0.12	0.04−0.01 / 0.01	0.04−0.01 / 0.02	nd
33	K-7-17; n = 10	46.99−45.44 / 46.08	53.88−49.99 / 52.44	1.96−0.98 / 1.37	0.02	0.04−0.01 / 0.01	0.02−0.01 / 0.01	0.01	nd
34	K-5-14/1; n = 27	50.61−44.99 / 45.89	55.31−52.48 / 52.48	1.52−0.45 / 1.09	0.17−0.04 / 0.09	0.15−0.01 / 0.08	0.02−0.01 / 0.01	0.03	nd
	Hydrothermal vein Py4								
35	KG-1-19; n = 14	47.56−46.30 / 46.88	54.41−52.86 / 53.65	1.14−0.35 / 0.85	0.08−0.05 / 0.06	0.04−0.01 / 0.02	0.05−0.01 / 0.02	0.05−0.01 / 0.03	nd
36	K-45-14; n = 9	46.71−41.62 / 45.42	52.63−43.86 / 49.70	2.50−0.45 / 1.21	0.06−0.03 / 0.04	0.05−0.01 / 0.02	0.02−0.01 / 0.01	0.07−0.01 / 0.03	nd
	Hydrothermal-metasomatic Apy1								
37	K-32-14; n = 10	33.60−32.12 / 33.00	20.78−18.88 / 19.98	44.83−40.40 / 42.36	0.05−0.03 / 0.04	0.10−0.01 / 0.03	0.03−0.01 / 0.01	0.10−0.02 / 0.05	nd
38	K-51-14; n = 4	33.85−33.16 / 33.60	21.46−20.34 / 20.72	48.45−46.61 / 47.57	0.11−0.07 / 0.09	0.05−0.01 / 0.03	0.02−0.01 / 0.01	0.03−0.01 / 0.01	nd
39	K-52-14; n = 5	35.24−34.36 / 34.69	23.70−21.77 / 22.37	44.21−41.93 / 43.52	0.04−0.02 / 0.03	0.05−0.01 / 0.03	0.02−0.01 / 0.01	0.13−0.05 / 0.09	nd
40	K-4-17; n = 5	33.96−33.16 / 33.56	20.83−19.93 / 21.30	44.51−43.22 / 43.80	0.15−0.03 / 0.08	0.69−0.04 / 0.27	0.06−0.01 / 0.03	0.09−0.03 / 0.07	nd
41	KG-9-19; n = 5	34.29−33.53 / 34.02	21.90−20.64 / 21.30	45.06−43.05 / 43.81	0.07−0.04 / 0.06	0.02−0.01 / 0.02	0.01	0.05−0.03 / 0.04	nd
42	KG-30-19/1; n = 5	34.51−33.96 / 34.10	22.25−20.55 / 21.33	44.16−42.02 / 43.21	0.08−0.04 / 0.05	0.12−0.05 / 0.08	nd	0.15−0.02 / 0.08	nd
43	K-7-17; n = 15	36.96−33.77 / 34.58	35.80−20.96 / 23.12	43.92−4.99 / 42.23	0.10−0.03 / 0.06	0.22−0.01 / 0.03	nd	0.16−0.01 / 0.06	nd
	Hydrothermal vein Apy2								
44	KG-11-19; n = 43	35.66−31.59 / 33.02	22.62−19.03 / 20.50	49.97−41.76 / 47.52	0.07−0.02 / 0.03	0.16−0.01 / 0.04	0.002	0.22−0.01 / 0.06	nd
45	K-21-14; n = 24	35.57−33.24 / 34.58	23.09−19.18 / 21.70	47.53−41.11 / 43.46	0.07−0.03 / 0.05	0.04−0.01 / 0.01	0.02−0.01 / 0.01	0.16−0.03 / 0.08	nd

* $\frac{\text{Maximum}-\text{Minimum}}{\text{Mean}}$.

In Py1 and Py2, the total content of minor elements varies from 0.04 to 0.8 wt.%. The As concentrations are within 0.01–0.31 wt.%, making up 30–70% of the total. About 10% of the analyzed pyrite grains refer to the arsenic-free variety because their As values are below the detection limit of the probe. Py1 and Py2 have permanent minor elements of Co (coefficient of variation (CV) = 48%) and Ni (CV = 104%). Their contents range as follows: 0.02–0.2 wt.% Co and 0.02–0.33 wt.% Ni (Figure 9A,B). The Co/Ni ratio varies from 0.2 to 18.5; 70% of the analyzed grains have $C_{Co} > C_{Ni}$, which are characterized by a strong correlation (r = 0.74). Copper constitutes 5–6% of the total amount of trace elements in Py1 and Py2 (0.02–0.11 wt.% Cu), and its content is variable, even within the same crystal. Another constant but quantitatively insignificant minor element in Py1 and Py2 is Sb (0.03–0.1 wt.% Sb). Correlation analysis revealed a Co–Ni–Pb geochemical association in Py1. The empirical formula of sedimentary and metamorphic pyrite is $Fe_{0.96–1.04}Ni_{0.0–0.01}S_{2.00}$ (Ni is present in 18% of the analyzed grains).

In Py3, the total amount of minor elements varies from 0.38 to 3.27%, with the As proportion higher than 75%. The As content in 47% of the analyzed grains is 1–3 wt.%. The amounts Co, Ni, Cu, and Sb in Py3 are most subject to variation, but are generally comparable with those in Py1 and Py2 (Figure 9C). Cu is present in all analyzed grains, and its content varies from 0.02 to 0.2 wt.%, in rare cases ranging as high as 0.6 wt.%. Nickel is present in significant amounts in 60% of the analyzed grains (0.02–0.48 wt.% Ni). The Co/Ni ratio is from 0.2 to 32.5. In Py3, Co prevails over Ni, and their correlation coefficient is moderate (r = 0.6). The Cu content does not exceed 0.12 wt.%, and in 48% of the analyzed grains its concentration is below the detection limit. There is a moderate correlation between Cu and Au (r = 0.48). About 30% of the analyzed

grains have Pb with an average content of 0.04 wt.%. The metasomatic Py3 formula is $Fe_{0.98–1.08}Ni_{0.0–0.01}Co_{0.0–0.01}S_{1.95–2.00}As_{0.01–0.05}$.

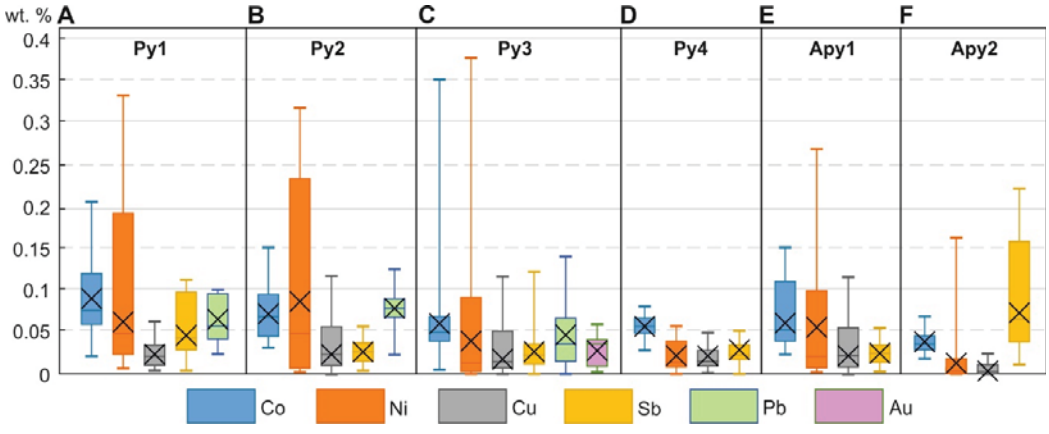

Figure 9. Trace element contents by EPMA: (**A**) Py1; (**B**) Py2; (**C**) Py3; (**D**) Py4; (**E**) Apy1; (**F**) Apy2. Box boundaries are first and third quartiles, and line in middle of box is median. Lower border of line shows minimum value, upper shows maximum value, cross shows average value.

In veined Py4, the total content of minor elements varies from 0.49 to 2.62 wt.%, of which 80–90% is As. Py4 is characterized by the permanent presence of Co, Ni, Cu, and Sb, but their total content is low (0.04–0.18 wt.%) (Figure 9D). Co is the most stable element (CV = 26%) with a content of 0.025–0.077 wt.%. The Ni in Py4 is the lowest of all pyrite generations (0.002–0.054 wt.%). The Co/Ni ratio is >1.0, so there is no correlation between these elements. The contents of Cu and Sb in Py4 remain unchanged, averaging 0.02–0.03 wt.%. A positive Sb–As correlation is observed (r = 0.6). A negative correlation between As and S (r = –0.42; Figure 10B) indicates isomorphic As → S substitution in the pyrite structure. The vein Py4 formula is $Fe_{0.98–1.07}S_{1.96–1.99}As_{0.01–0.04}$.

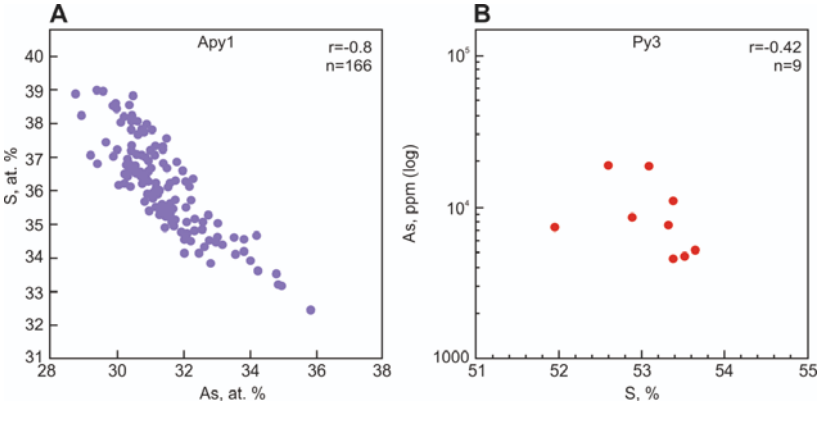

Figure 10. Ratio of As and S in (**A**) Apy1 and (**B**) Py3.

In Apy1 and Apy2, Co, Ni, Cu, and Sb are typochemical minor elements. In 70% of analyzed Apy1 grains, the total content of trace elements does not exceed 0.2 wt.%. Ni shows uneven distribution in Apy1 (CV = 179%) and is the most abundant trace element (0.003–0.687 wt. % Ni) (Figure 9E). In 50% of analyzed Apy1 grains, the Cu concentration is below the detection limit of the probe, and it seldom exceeds 0.01 wt.%. The content of Co and Sb amounts to 0.06 wt.% on average. The formula of metasomatic Apy1 is $Fe_{0.93–1.04}As_{0.86–1.01}S_{0.99–1.14}$.

In veined Apy2, the contents of Co, Ni, Cu, and Sb are lower than in Apy1 and do not exceed 0.24 wt.% in total (Figure 9F). Cobalt is a constant minor element; its content is two times lower than in Apy1 (0.015–0.067 wt.% Co), but always exceeds the nickel amount (Co/Ni = 1.1–22.5). Sb is steady and the most quantitatively significant minor element in Apy1, accounting for about 60% of the total volume (0.01–0.22 wt.% Sb). Cu concentration above the detection limit was recorded in only 20% of the analyzed grains and did not exceed 0.02 wt.%.

4.2.2. Gold and Trace Element Concentrations in Py3 and Apy1 According to LA-ICP-MS Data

The chemical composition of Py3 and Apy1 was studied in more detail, because these generations are the most widespread and have an elevated content of invisible gold (Table 2). According to the LA-ICP-MS data, Py3 contains, apart from typochemical elements (As, Co, Ni, Cu, and Sb), a number of trace elements, such as Zn (3.5–6.4 ppm, avg. 4.5 ppm), Ag (0.008–1.01 ppm, avg. 0.448 ppm), Cd (0.024–0.065 ppm, avg. 0.038 ppm), Te (0.06–0.31 ppm, avg. 0.15 ppm), Pb (0.5–860 ppm, avg. 110.0 ppm), Bi (0.02–0.93 ppm, avg. 0.26 ppm), Hg (0.01–0.36 ppm, avg. 0.21 ppm), and Au (0.1–15.9 ppm, avg. 3.4 ppm) (Table 2). Correlation analysis revealed several geochemical associations. Au has a high correlation with As (r = 0.9), Cu (r = 0.92), and Cd (r = 0.97).

According to LA-ICP-MS data, Apy1 grains contain, along with typochemical Co, Ni, Cu, and Sb elements, a number of trace elements including Zn (0.7–15.0 ppm, avg. 3.9 ppm), Ag (0.2–1.5 ppm, avg. 0.6 ppm), Te (0.01–8.00 ppm, avg. 1.87 ppm), Pb (2.0–76.0 ppm (avg. 18.7 ppm), Bi (0.1–1.4 ppm, avg. 0.6 ppm), Hg (0.25–1.95 ppm, avg. 0.72 ppm), and Au (0.3–6.1 ppm, avg. 1.5 ppm) (Table 2). Correlation analysis revealed several geochemical associations. Au has a moderate correlation with Cu (r = 0.59) and Zn (r = 0.63).

4.3. Gold Content of Sulfides from Proximal Metasomatites and in Veins

Table 3 shows the results of atomic absorption analysis of proximal metasomatites, their sulfides, and sulfides in veins. The average Au content in Py3 is 12.51 ppm and in Ag is 5.89 ppm. In Apy1, Au varies from 12.3 to 23.8 ppm (17.51 ppm on average), and Ag from 0.43 to 11.83 ppm (6.48 ppm on average). Proximal metasomatites contain Au from 0.001 to 5.29 ppm (0.81 ppm on average), and Ag from 0.007 to 0.14 ppm (0.06 ppm on average). The Au grade in Py4 averages 29.30 ppm and in Ag 6.35 ppm; in Apy2 the Au value amounts to 20.49 ppm, and in Ag 2.06 ppm.

Table 2. Data of LA-ICP-MS trace element analysis of Py3 and Apy1 of Khangalas gold deposit (all values in ppm; bdl, below detection limit; nd, not detected).

Sample	Spot Position	As	Ti	V	Cr	Mn	Co	Ni	Cu	Zn	Ga	Ge	Se	Mo	Ag	Cd	In	Sn	Sb	Te	W	Tl	Pb	Bi	Au	Pd	Ba	Pt	Hg	Au/Ag
K-4-17	Asp10-6	-	218	1.23	6.3	1.04	521	565	15.9	15	0.036	1.99	323	1.53	0.9	nd	0.048	0.09	890	5.9	2.44	0.045	9.7	0.71	3.31	0.025	2.25	0.051	1.26	3.68
K-4-17	Asp11-11	-	2060	5.07	3.4	1.45	57.5	93	7	4.2	0.035	2.36	104	0.56	0.55	0.57	0.122	0.68	385	0.5	0.83	0.01	7.41	0.417	2	0.012	2.49	0.033	0.41	3.64
K-4-17	Asp12-14	-	37.5	0.204	2.6	1.16	524	534	14	3.7	0.055	1.8	268	21.6	0.6	0.16	0.119	0.18	721	1.97	0.129	0.11	13.5	0.99	0.574	0.003	0.29	0.006	0.3	0.96
K-4-17	Asp13-15	-	0.8	0.077	3.3	1.09	3.24	6.3	4.6	5.7	0.019	1.86	156	7.16	0.186	0.07	0.076	0.22	416	0.35	0.016	0.026	1.95	0.466	0.255	bdl	0.28	bdl	0.42	1.37
K-4-17	Asp14-15	-	8	0.132	2.3	0.3	7.2	50	7.9	3.3	0.085	1.95	66.9	7.72	0.47	nd	0.119	bdl	883	6.2	0.22	0.03	38.9	0.402	0.352	0.002	0.33	0.028	0.82	0.75
K-4-17	Asp15-25	-	0.97	0.194	2.9	1.71	4.22	13.6	19	10	0.013	2.01	187	1.38	0.41	0.043	0.133	0.13	778	bdl	bdl	0.012	5.49	0.89	6.13	0.001	0.08	0.057	0.98	14.95
K-4-17	Asp16-26	-	1.06	0.069	0.59	1.35	1070	1680	7.8	3.6	0.021	2.17	329	9.9	0.55	0.036	0.114	0.07	1414	8	0.19	0.043	7.83	1.42	0.7	0.017	0.34	0.01	1.95	1.27
K-4-17	Asp17-33	-	21.7	0.29	2.7	1.29	35.7	76	9.8	2.55	0.059	2.01	107	20	0.5	nd	0.097	bdl	926	0.01	0.082	0.019	7.12	0.77	0.88	bdl	0.11	0.018	0.63	1.76
K-4-17	LineA1-1	-	295	0.62	1.15	nd	65	122.1	8	2	0.014	3.82	126.2	9.22	0.57	nd	0.062	0.126	550	0.74	1.68	0.0239	9.18	0.641	0.488	bdl	3.1	bdl	0.51	0.86
K-4-17	LineA1-2	-	242	0.42	0.71	nd	3.7	8.9	3.44	0.69	bdl	4.19	98	3.05	0.35	0.1	0.06	0.3	378	bdl	1.17	0.0038	5.43	0.56	0.44	bdl	2.2	bdl	1.03	1.26
K-4-17	LineA1-3	-	32	0.111	0.27	nd	728	1182	4.57	1.63	0.0079	3.88	145.7	6.03	0.388	nd	0.059	0.1	429	0.7	0.27	0.0049	5.79	0.636	0.715	bdl	0.29	0.004	0.64	1.84
K-4-17	LineA2	-	3.1	0.089	89	nd	56.5	184	6.5	4.3	0.058	4.06	48.9	0.156	0.341	nd	0.035	0.12	193.8	2.34	0.035	0.044	36.3	0.113	2.7	bdl	4.2	0.012	0.43	7.92
K-4-17	LineA2	-	2.93	0.025	5.6	nd	10.32	26.1	2.46	2.47	0.0086	3.8	93.1	2.34	0.698	nd	0.062	0.091	208.8	0.24	0.026	0.0176	76	0.226	3.16	bdl	2.61	0.02	0.95	4.53
K-4-17	LineA2	-	399	0.945	1.89	nd	401	874	2.27	2.3	0.051	3.89	118.5	1.5	0.54	nd	0.0534	0.262	328.3	0.28	0.93	0.0297	11.4	0.454	0.715	bdl	2.82	0.033	0.72	1.32
K-4-17	LineA2	-	72	0.201	2.2	nd	109.7	250.8	2.05	1.69	0.022	4.09	71.2	8.68	0.448	nd	0.052	0.184	495	bdl	0.13	0.0178	6.16	0.712	0.833	0.016	0.54	0.008	0.46	1.86
K-4-17	LineA2	-	99	0.334	1.98	nd	140	276	2.07	2.28	0.0314	3.76	118.5	11.85	0.376	0.0031	0.0544	0.182	512.6	0.255	0.451	0.0087	7.46	0.659	0.319	bdl	1.08	0.011	0.57	0.85
K-4-17	LineA2	-	278	0.61	3.1	nd	14.84	37.5	6.3	2.29	0.0114	3.67	130.3	11.07	0.732	nd	0.051	0.218	550.6	0.35	0.76	0.0067	60.2	0.759	0.562	0.024	1.16	0.010	0.61	0.77
K-4-17	LineA2	-	7790	15	14.8	nd	32.6	50	7.91	2.08	0.16	3.92	112.9	11.18	1.49	nd	0.037	0.8	534.3	0.21	22.6	0.0071	27.4	0.693	2.43	0.011	30.5	0.017	0.25	1.63
	Minimum		0.8	0.0	0.3	0.3	3.2	6.3	2.1	0.7	0.0079	1.8	48.9	0.2	0.2	0.0	0.04	0.07	193.8	0.01	0.02	0.004	2.0	0.1	0.3	0.001	0.08	0.004	0.25	0.75
	Maximum		7790.0	15.0	89.0	1.7	1070.0	1680.0	19.0	15.0	0.16	4.2	329.0	21.6	1.5	0.6	0.13	0.80	1414.0	8.00	22.60	0.110	76.0	1.4	6.1	0.025	30.5	0.057	1.95	14.95
	Average		642.3	1.4	8.0	1.2	210.3	335.0	7.3	3.9	0.040	3.1	144.7	7.5	0.6	0.1	0.08	0.23	588.5	1.87	1.88	0.026	18.7	0.6	1.5	0.012	3.04	0.021	0.72	2.84
	Std dev		1846.3	3.6	20.5	0.4	309.8	471.4	4.8	3.5	0.038	1.0	82.0	6.3	0.3	0.2	0.0	0.2	302.5	2.5	5.2	0.025	21.0	0.3	1.6	0.009	6.97	0.017	0.41	3.52
	CV		287%	252%	254%	35%	147%	141%	66%	89%	94%	32%	57%	84%	51%	140%	43%	89%	51%	133%	279%	98%	112%	46%	105%	74%	229%	79%	57%	
K-4-17	Py1-1	4890	2470	7.16	10.3	0.85	1.13	14.4	3.96	3.51	0.197	2.49	4.4	0.079	0.92	nd	0.005	0.23	10.19	0.056	9.71	0.0076	66	0.243	0.955	0.008	3.88	0.062	bdl	1.04
K-4-17	Py2-3	7110	0.7	0.028	0.38	0.57	0.233	8.2	0.54	3.62	0.055	2.67	6.2	0.21	0.0076	nd	0.0021	0.11	0.25	0.21	0.067	0.018	0.479	0.048	0.502	bdl	0.008	0.0073	0.02	66.05
K-4-17	Py3-4	4390	8.6	0.116	0.39	0.82	17.5	13.4	1.58	3.8	0.056	2.59	2.6	0.64	0.196	nd	0.021	0.059	2	0.13	0.055	0.0074	3.71	0.084	0.236	0.01	0.16	0.034	0.01	1.20
K-9-17	Py4-7	4220	0.78	0.058	0.52	0.41	1.15	74.9	3	4.2	0.018	2.46	7.2	0.059	0.85	0.024	0.0033	0.033	407	0.083	0.019	0.065	860	0.93	0.507	0.0036	0.008	0.029	0.2	0.60
K-9-17	Py5-8	17480	36.1	0.35	0.98	0.4	7.05	39	19	4.7	0.19	2.71	3.5	0.047	0.055	0.036	0.017	0.07	6.19	bdl	0.08	0.047	3.35	0.09	8.83	0.01	1.83	0.037	0.33	160.55
K-9-17	Py6-10	17260	2390	8.42	7.9	1.53	21.3	56.9	18	5.3	0.191	2.66	4.5	0.71	0.8	0.065	0.0105	0.31	40.1	0.06	8.66	0.089	26.7	0.446	15.85	0.013	4.68	0.064	0.36	19.81
K-14-17	Py7-11	10280	77	0.235	0.58	7.55	505	690	7.3	6.4	0.009	2.69	52.1	1.04	1.01	0.027	0.0012	0.07	8.42	0.31	0.112	0.03	23.3	0.457	2.5	0.0027	0.151	0.044	0.33	2.48
K-14-17	Py8-13	6820	79	0.105	1.09	0.74	41.6	1298	1.4	4.65	0.036	2.7	40.3	0.29	0.062	nd	bdl	0.1	1.05	0.21	0.096	0.0028	2.75	0.043	0.143	0.0028	0.05	0.013	bdl	2.31
K-42-17	Py9-18	8030	208	0.274	0.77	0.73	43.5	64.9	1.29	4.22	0.018	2.63	73.6	bdl	0.128	nd	0.0031	0.03	1	bdl	0.56	bdl	3.34	0.024	1.028	0.007	0.008	0.01	bdl	304.69
	Minimum	4220.0	0.7	0.028	0.38	0.40	0.23	8.2	0.5	3.5	0.0	2.5	2.6	0.05	0.01	0.024	0.001	0.03	0.3	0.1	0.0	0.003	0.5	0.02	0.1	0.003	0.01	0.01	0.01	0.6
	Maximum	17480.0	2470.0	8.42	10.30	7.55	505.0	1298.0	19.0	6.4	0.2	2.7	73.6	1.04	1.01	0.065	0.021	0.31	407.0	0.3	9.7	0.089	860.0	0.93	39.0	0.013	4.68	0.06	0.36	304.7
	Average	8942.2	585.6	1.86	2.55	1.51	70.9	251.1	6.2	4.5	0.1	2.6	21.6	0.38	0.45	0.038	0.008	0.11	52.9	0.2	2.2	0.033	110.0	0.26	7.6	0.007	1.20	0.03	0.21	62.1
	Std dev	5147.9	1047.8	3.38	3.77	2.29	163.6	448.4	7.2	0.9	0.1	0.1	26.7	0.37	0.43	0.023	0.007	0.10	133.4	0.1	4.0	0.031	282.1	0.30	12.9	0.004	1.85	0.02	0.16	105.3
	CV	58%	179%	182%	148%	151%	231%	179%	116%	20%	96%	3%	124%	96%	96%	61%	95%	85%	252%	70%	186%	94%	257%	115%	170%	60%	155%	63%	79%	

Table 3. Results of atomic absorption analysis of proximal metasomatites, their sulfides, and sulfides in quartz veins.

Sample	Mineral/Rock	Content		Au/Ag
		Au, ppm	Ag, ppm	
K-4-17	Py3	7.39	8.73	0.8
K-9-17	Py3	21.4	5.64	3.8
K-9-17	Py3	22.37	7.8	2.9
K-14-17	Py3	3.54	1.31	2.7
K-14-17	Py3	0.76	1.15	0.7
KG-9-19	Py3	4.89	2.74	1.8
KG-32-19	Py3	10.06	5.44	1.8
KG-20-19	Py3	11.87	6.54	1.8
K-13-18	Py3	3.67	6.95	0.5
KG-8-19	Py3	39.32	17.38	2.3
KG-30-19	Py3	12.36	1.13	10.9
	Average	12.51	5.89	
	Std dev	11.32	4.71	
	CV	91%	80%	
K-4-17	Apy1	12.3	0.43	28.6
KG-26-19	Apy1	16.44	11.83	1.4
KG-29-19	Apy1	23.8	7.2	3.3
	Average	17.51	6.49	
	Std dev	5.82	5.73	
	CV	33%	88%	
KG-23-19	Py4	27.07	4.46	6.1
K-5-17	Py4	9.42	3.47	2.7
KG-34-19	Py4	51.42	11.13	4.6
	Average	29.30	6.35	
	Std dev	21.09	4.17	
	CV	72%	66%	
KG-35-19	Apy2	20.49	2.06	9.9
K-4-17	Sandstone with sulfides and quartz veinlets	0.084	0.088	1.0
K-9-17	Sandstone with sulfides and quartz veinlets	0.740	0.084	8.8
K-14-17	Sandstone with sulfides	0.001	0.032	0.0
K-25-17	Sandstone with sulfides	0.240	0.042	5.7
K-27-17	Sandstone with sulfides	0.059	0.007	8.4
K-28-17	Sandstone with sulfides	0.064	0.097	0.7
K-40-17	Sandstone with sulfides	5.29	0.142	37.3
K-41-17	Siltstone with pyrite	0.006	0.041	0.1
	Average	0.81	0.07	
	Std dev	1.83	0.04	
	CV	225%	66%	

4.4. Sulfur Isotopic Composition of Sulfides

The sulfur isotopic composition of sulfides at the Khangalas deposit has a narrow range of negative $\delta^{34}S$ values close to 0 (−2.0 to 0.6‰) (Table 4), for gold-bearing Py3 it is $\delta^{34}S = -0.6$‰ (21.4 ppm Au, K-9-17), for Apy1 it is $\delta^{34}S = -1.2$‰ (12.3 ppm Au, K-4-17), and for Apy2 it is $\delta^{34}S = -2.0$ ‰ (KG-35-19).

Table 4. Sulfur isotopic composition of sulfides from metasomatites of Khangalas deposit.

№	Sample	Generation	$\delta^{34}S_{VCDT}$ (‰)
1	K-4-17	Apy1	−1.2
2	KG-9-19	Apy1	−1.4
3	K-9-17	Py3	−0.6
4	KG-32-19	Py3	−1.3
5	KG-35-19	Apy2	−2.0

5. Discussion

5.1. Pyrite and Arsenopyrite Types and Textures

The formation of pyrites took place for a long time, under changing physicochemical conditions, which is reflected in the morphology of crystals and the place of their formation. The morphology becomes more complex: from framboid and cubic forms to pentagonal dodecahedra. Rounded (framboid) microaggregates of Py1 were formed during the sedimentary–diagenetic stage of the clastic strata deposition subsequent to a change in the redox potential of the sedimentation environment. Py1 accumulations are often arranged parallel to the rock bedding. Some framboids have a zonal structure with fragments of rocks and minerals present in the central part. In part, early pyrites served as a substrate/nucleus for metamorphic Py2 formed during recrystallization. Accumulations of finely crystalline Py2 are confined to microfractures and foliation planes formed in the process of dislocation-metamorphic transformation of rocks. Py2 underwent cataclasis under the effect of late deformation processes. Py3 was developed in the wall rock zones; it has cubic and pentagonal-dodecahedral forms. The complication of crystal forms is accompanied by a change in the type of conductivity and the appearance of defects in the crystal lattice, which is a positive factor for isomorphic Au substitution into pyrite. Py3 is also characterized by a zonal or block structure, which provides the possibility for gold adsorbtion at interphase boundaries and crystal growth planes [54]. In quartz veins, Py4 occurs as intergrowths and aggregates, less often as individual grains altered in the course of cataclasis and corrosion processes. They contain numerous inclusions of late sulfides and native gold.

In the zone of wall rock metasomatism, along with Py3, euhedral short prismatic Apy1 is developed. It forms disseminated grains and intergrowths, as well as aggregates and microveinlets. Macroinclusions are most often represented by silicate minerals entrapped during the crystal growth. Late sulfides, sulfosalts, and native gold are recorded as microinclusions, which are confined to the crystal growth zones. From the results of AFM analysis, Vorobiev and Kozyrev [54] came to the conclusion that Au (III) is sorbed to a greater extent on the FeAsS surface, being reduced to Au (0). Thus, it can be assumed that the gold content of metamorphic arsenopyrite is partially related to the adsorption of gold nanoparticles on the crystal growth surfaces. Vein Apy2 forms nests and clusters, often in association with Py4. In some Apy2 grains, zoning is observed, which is expressed by microtextures of replacement of the central part of the crystals by late sulfides and native gold.

5.2. Composition of Pyrite and Arsenopyrite

All generations of pyrite and arsenopyrite from the Khangalas deposit have a non-stoichiometric composition. Elevated and reduced Fe/(S + As) values are observed (Py1: 0.48–0.52; Py2: 0.48–0.53; Py3: 0.47–0.54; Py4: 0.49–0.53; Apy1: 0.42–0.52; Apy2: 0.45–0.51).

The As/S atomic ratio is an indicator of the temperature in the sulfur-buffer group, i.e., it increases with increasing temperature (see [55–57], etc.). Apy1 from the Khangalas deposit has As/S < 1 (0.81 to 0.93). For Apy2, this ratio is higher: 30% of the analyzed grains have As/S > 1 (1.01 to 1.08). Kovalchuk et al. [55] studied the composition of arsenopyrite at the Vorontsovskoye deposit (Northern Urals, Russia) and showed that in arsenopyrite enriched in sulfur and depleted in gold, the ratio is As/S < 1, and in arsenopyrite depleted in sulfur and enriched in gold it is As/S > 1. The crystallization temperature and fugacity of sulfur in Apy1 are higher than in Apy2. These data suggest that the Apy2 vein of the Khangalas deposit crystallized at a higher temperature and S fugacity than Apy1. Arsenopyrite from the Khangalas deposit is characterized by negative correlation coefficients between As and S (r = –0.65 for Apy1 (Figure 10A) and r = –0.85 for Apy2), which reflects their pairwise replacement during crystallization [56,58–61].

Microprobe analysis of the chemical composition of pyrite and arsenopyrite revealed a range of stable minor and trace elements in them. The main indicator element in pyrite is As. Pre-ore pyrite has As $\leq$ 0.3 wt.%, while syn-ore pyrite exhibits As $\geq$ 0.3 wt.%. In

diagenetic and metamorphic pyrites, As makes up 30–35% of the total volume of trace elements; in the ore-stage metasomatic and vein pyrite, the proportion of As reaches 85–91% (max 3.19 wt.% As). The distribution of As in pyrite is uneven even within one grain. For Py1 and Py2, increased As content in the center of grains is often observed; for Py3 and Py4, blocks of maximum As content are characteristic.

Other typochemical minor elements (Co, Ni, Sb, Cu, Pb) are present in all generations of pyrite and arsenopyrite, and their proportion decreases from the pre-ore to the hydrothermal stage (Figure 11).

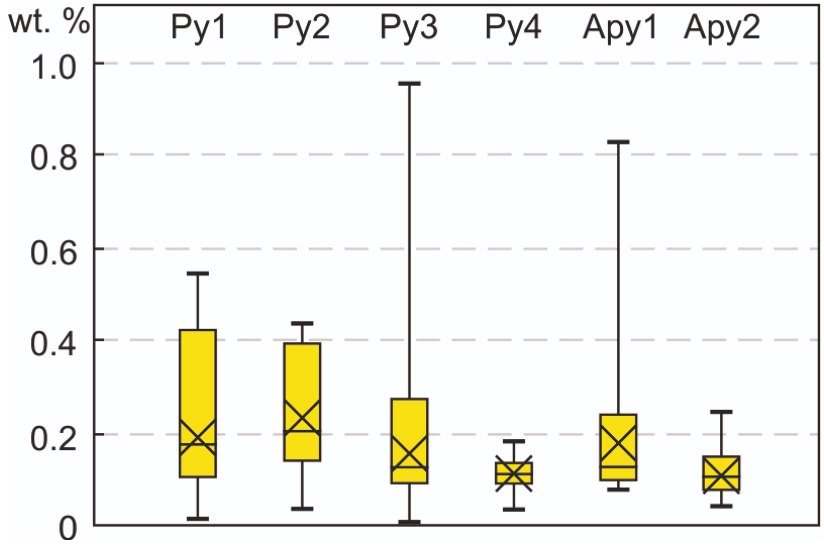

Figure 11. Variations in total content of Co, Ni, Sb, Cu, and Pb (wt.%) in sulfides of different generations, Khangalas deposit. Box boundaries are first and third quartiles, and line in middle of box is median. Lower border of line shows minimum value, upper shows maximum value, cross shows average value.

Pyrite of early generations (Py1, Py2) is persistent in Cu content. In hydrothermal-metasomatic Py3 and Py4, the Cu content is reduced, and in Apy1 and Apy2, Cu concentration above the detection limit is found in only few grains. Most likely, this is due to the isomorphic Cu → Au substitution in sulfides.

Sb is a permanent trace element in pyrites and arsenopyrites. It can enter the pyrite structure isomorphically by replacing S to form $[S–Sb]^{3-}$ or $[Sb–Sb]^{4-}$ dumbbells [62]. The negative correlation (r = 0.3–0.6) between antimony and iron indicates the possibility of isomorphic Fe → Sb substitution.

The presence of As, Co, Ni, Sb, Cu, and Au in Py1 is related to muds enriched in organic matter laid down by the water of marginal oceanic basins or inland seas [63,64]. They were isomorphically incorporated into Py1. During regional dislocation-metamorphic events, the processes of recrystallization of Py1 and redistribution of trace elements in it took place. For example, in Py2, a drop in Co and Sb content and a slight increase in Ni value are observed. Under the influence of hydrothermal-metamorphic solutions, pyrite gets freed of early trace elements and becomes enriched in As, Sb, and Au. Thus, according to the results of microprobe analysis, we observe regular changes in the range and content of trace elements in pyrite and arsenopyrite during their formation and transformation. This is evidenced by the concentration of elements and the degree of supersaturation of the solution during crystallization and recrystallization of sulfides [65].

5.3. Invisible Gold and Its Relationship with Other Elements in Py3 and Apy1 According to LA-ICP-MS Data

Trace elements revealed by the LA-ICP-MS method in Py3 and Apy1 can be divided into several independent groups according to the degree of their connection. A stable paragenetic association with strong correlations (r = 0.8–0.9) in both pyrite and arsenopyrite is formed by the trace elements of the first group: Ti, V, W, Sn, Ga, Ba, Ag, Pt, and Pd. Py3 also includes Cr and Au, with a moderate degree of correlation (r = 0.5–0.6). They do not form isomorphic substitutions in pyrite and arsenopyrite; they are present as nanoinclusions. The enrichment of sulfides with trace elements of the first group could partly be due to the entrapment of microinclusions of early minerals during crystal growth. The second stable geochemical association, Cu–Zn–Au, is connected with a polysulfide vein association of the hydrothermal stage of mineral formation. The minerals of these elements (chalcopyrite, sphalerite, and native gold) are present in Py3 and Apy1 in the form of nano- and microinclusions. Both pyrite and arsenopyrite are characterized by strong Sb–Bi and Se–Te correlations. In Apy1, these elements can be combined into one geochemical association, which also includes Co and Ni. For Py3, the Sb–Bi pair is supplemented by Pb, and one more stable Co–Mn–Mo–Se–Te geochemical association is observed. It is possible that the enrichment with these elements occurred at later stages of mineral formation, due to a deeper source. In general, these data confirm the conclusions of many researchers regarding different depth sources for fluids at the gold ore objects of the YKMP [66,67].

LA-ICP-MS trace element analysis of metasomatic Py3 and Apy1 made it possible not only to determine a range of trace elements, but also to analyze the relationship between Au and various components of the system. Trace elements, including Au, can be found in pyrite in various forms: solid solution, nanoparticles, and microinclusions [15,17,61,68,69].

Using a scanning electron microscope, microinclusions of native gold about 15 μm in size were detected in only one sample out of about 200 examined Py3 and Apy1 grains (Figure 6G). All other inclusions are galena, sphalerite, and chalcopyrite, and less often tetrahedrite and freibergite. This allows us to conclude that the elevated Au content in Py3 and Apy1 may be due to the presence of micro- and nanoinclusions of native gold. Low content is typical for gold incorporated in the crystal lattice of pyrite or its defects [17,60,68,70–72].

5.3.1. Invisible Gold in Py3

For Py3, a negative correlation is observed between Fe and Au (r = −0.6) (Figure 12A), which indicates an isomorphic Au ↔ Fe substitution [61]. A comparison of the physical characteristics of iron (atomic mass 55.85; Fe^{2+} ionic radius r = 0.80 Å) and gold (atomic mass 196.96; Au^{3+} ionic radius r = 0.85 Å; Au^{+} r = 1.37 Å) also confirms the possibility of isomorphic incorporation of Au into pyrite [73,74]. Chouinard et al. [75] proposed a conjugate substitution mechanism of $Au^{3+} + Cu^{+} \leftrightarrow 2Fe^{2+}$ or $Au^{+} + Cu^{+} + Co^{2+} + Ni^{2+} \leftrightarrow 3Fe^{2+}$ types (Figure 13B,C). According to Wang et al. [61], the marked negative relationship between (Au + As) and Fe in Py3 (Figure 12D) suggests that Au and As entered the lattice through isomorphic substitution for Fe under conditions of high oxygen fugacity (fO_2).

There is a very close correlation between Au and As in Py3 from the Khangalas deposit (r = 0.9) (Figure 12E). Such a close relationship between Au and As (r > 0.5) in pyrite and arsenian pyrite from various types of gold deposits has been noted by many authors [17,60,68,71,76], etc. Elevated As content is characteristic of pyrite with excess iron (S/Fe = 1.9–1.98). In the pyrite structure, As isomorphically replaces S ($Fe_{1.00}(S_{1.98}As_{0.02})_{2.00}$) to form, in some cases, arsenian pyrite (As > 1.7 %), which is typical for reducing conditions (see [60,77], etc.). Reich et al. [60] noted for epithermal and Carlin-type deposits increased Au solubility in the pyrite structure with increasing As content: $C_{Au} = 0.02 \cdot C_{As} + 4 \times 10^{-5}$.

Based on EPMA, LA-ICP-MS, SIMS, and l-PIXE analyses, Deditius and co-authors [71] studied the mechanism of Au and As incorporation and the solubility of gold in pyrite from various types of deposits. In addition to the Carlin and epithermal types, pyrites from porphyry Cu, Cu–Au, orogenic (OGD), volcanic-massive sulfide (VMS), iron-oxide

copper-gold (IOCG), Witwatersrand Au, and coal deposits were studied. Deditius et al. [71] found that on the Au–As diagram, the analysis of pyrite from gold deposits showed that they form a wedge-shaped zone and most of the data points fall below the Au saturation line of the solution determined by Reich et al. [60] (Figure 12E). They show that Au^+ is the dominant form of gold in the arsenian pyrite of the studied deposits. Analytical data [60] indicate that the Au solubility limit in arsenian pyrite of epithermal deposits is defined by an Au/As ratio of ~0.02. The solubility limit of Au in pyrite of orogenic deposits is lower (~0.004) [71].

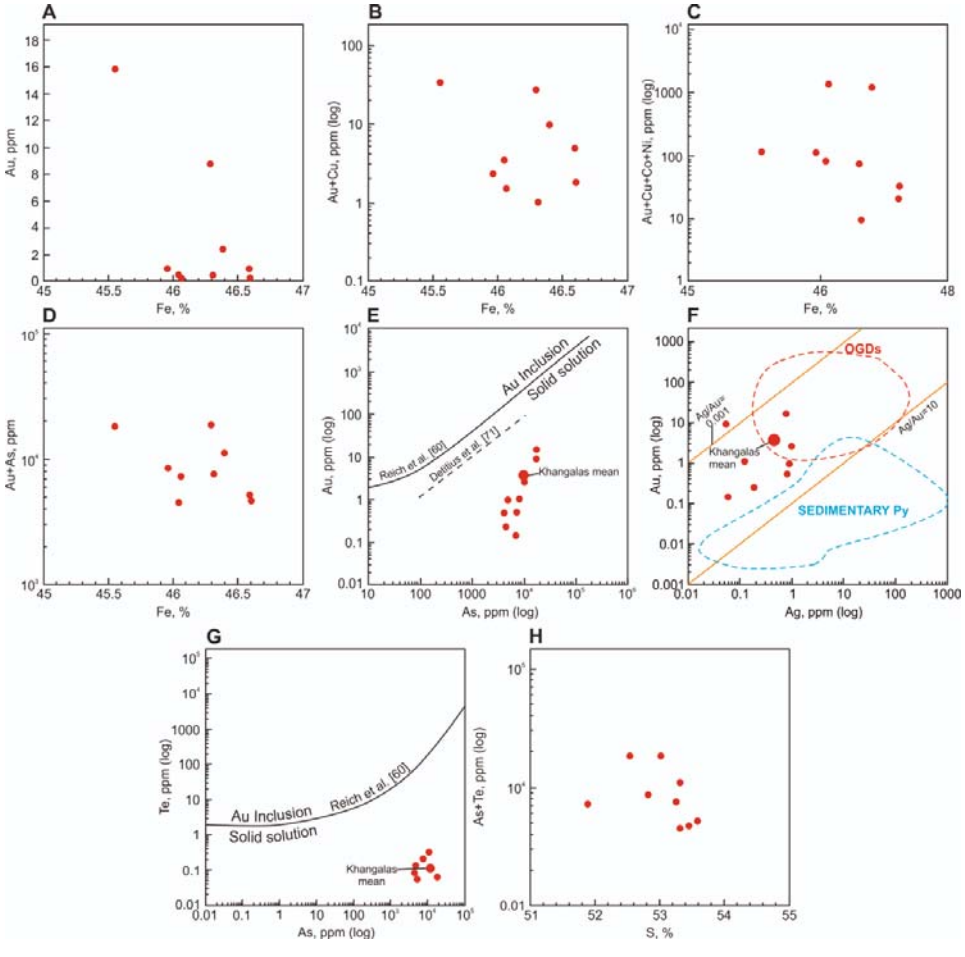

Figure 12. Binary correlation diagrams for Py3: (**A**) Fe vs. Au; (**B**) Fe vs. Au + Cu; (**C**) Fe vs. Au + Cu + Co + Ni; (**D**) Fe vs. Au + As; (**E**) As vs. Au; (**F**) Ag vs. Au, field of orogenic gold deposits (OGDs) and sedimentary Py after Large and Maslennikov [68]; (**G**) As vs. Te; (**H**) S vs. Te + As.

Our LA-ICP-MS results for Py3 are in good agreement with those of Reich et al. [60] and Deditius et al. [71]. Figure 13F shows that, in the Au–As (ppm, log) coordinates, all samples of the studied Py3 from the Khangalas deposit fall into the field of structurally bound gold (Au^+). These results are confirmed by the rather low Au content in the analyzed Py3: in most samples, Au does not exceed 2.5 ppm (Table 2). Earlier, Tauson et al. [76] showed that the content of the Au^+ structural form in the studied pyrite samples from deposits

of different genetic types in Russia (large Natalka and Degdekan orogenic gold-quartz deposits, Dukat volcanogenic-plutonogenic Au–Ag deposit, Dalnee and Oroch volcanic Au–Ag deposits, Sukhoi Log giant deposit with a debated genesis, Pokrovskoye epithermal Au–Ag deposit, Amur Dikes deposit with an unconventional type of mineralization, and Zun–Kholbinskoye deposit with a controversial genesis) and Uzbekistan (Kochbulak and Kyzylalmasay epithermal Au–Ag deposits) does not exceed ~5 ppm. Similar results were obtained by Deditius et al. [71] for pyrite from orogenic gold deposits, which, according to their data, contains less than 100 ppm Au. The higher Au content is mainly due to the presence of nano- and microparticles of native gold [78]. The occurrence of native superficially bound Au^0 in sulfides of metasomatites is reported from deposits of various genetic types [60,68,76,79].

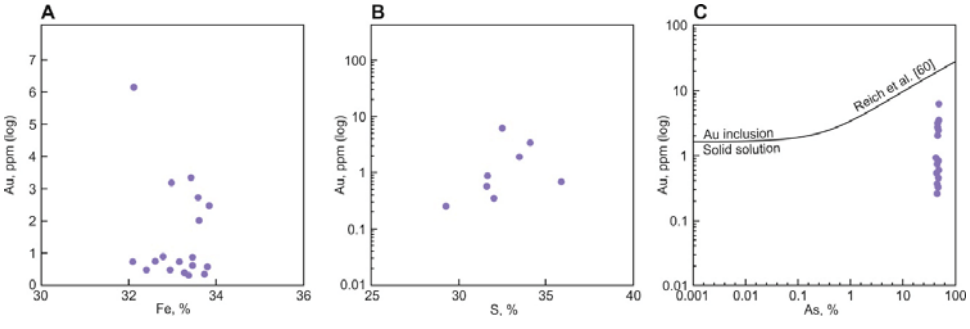

Figure 13. Binary correlation diagrams for Apy1: (**A**) Fe vs. Au; (**B**) Au vs. S; (**C**) As vs. Au.

Keith et al. [70] applied the Au solubility line [60] to the Te–As system, which made it possible to distinguish between Te in a solid solution and Au-tellurides in inclusions in pyrite. As shown in Figure 12G, the Te–As values are below the Au solubility line, which indicates that Te is incorporated in the Py3 lattice. This is confirmed by the fact that no Au-telluride microinclusions were found in Py3 grains under a scanning electron microscope. There is a weak positive correlation between As and Te (r = 0.24), while the relationship between As + Te and S in Py3 is negative (Figure 12H); nevertheless, it is known that As significantly affects the appearance of Te nano- and microinclusions in pyrite due to structural distortions [70].

One of the criteria for discriminating between sedimentary and hydrothermal-metasomatic disseminated orogenic pyrite in sedimentary rocks is the Ag/Au ratio. According to Large and Maslennikov [68] and Gregory et al. [80], disseminated arsenian pyrite from deposits with Au–As associations (Mt. Olympus, Macraes) has small Ag/Au values (up to 1), while sedimentary pyrite features a higher Ag/Au ratio (up to 1000). The Ag/Au ratio in Py3 from the Khangalas deposit ranges from 0.01 to 1.7 (0.5 on average). Figure 12F shows the average Ag/Au ratio for Py3 of the Khangalas deposit, which falls within the field of orogenic deposits and is consistent with the results of [68].

5.3.2. Invisible Gold in Apy1

The relationship between Au and Fe indicates the form of gold occurrence in arsenopyrite (see [55,58], etc.). Figure 13A shows an inverse correlation between Au and Fe in Apy1 of the Khangalas deposit, which is strong (r = −0.9) at Au > 2 ppm, and weak at Au < 2 ppm (r = −0.18). The strong inverse correlation between Au and Fe is due to isomorphic Au → Fe substitution in the arsenopyrite structure at Au > 2 ppm [55].

No direct Au vs. S or Au vs. As correlations are identified (Figure 13B,C), which is probably due to the heterogeneous composition of Apy1. As shown in Figure 13C, the Au/As values fall into the zone below the Au saturation line [60], which indicates the predominance of the Au^+ structurally bound form in Apy1. This is confirmed by

the low Au content (<6.1 ppm) in Apy1. At the same time, the results of atomic absorption analysis revealed high Au content in the bulk samples of Apy1 (Table 2), which indicates the presence of nano- and microparticles of native gold.

Correlation plots for Au concentrations with Ag, Pb, Cu, Ni, Co, Bi, Sb, and Te in Apy1 are shown in Figure 14A–H. Gold and silver do not show a significant correlation (Figure 14A), but gold has a noticeable positive correlation with Cu and Zn. A close positive correlation between Cu, Zn, and Pb elements and Au is recorded for arsenopyrite from layered quartz veins of the Samgwang deposit (Korea) [58]. In the Au vs. Pb correlation diagram (Figure 14B), a weak negative relationship (r = −0.39) is observed for Apy1 from the Khangalas deposit.

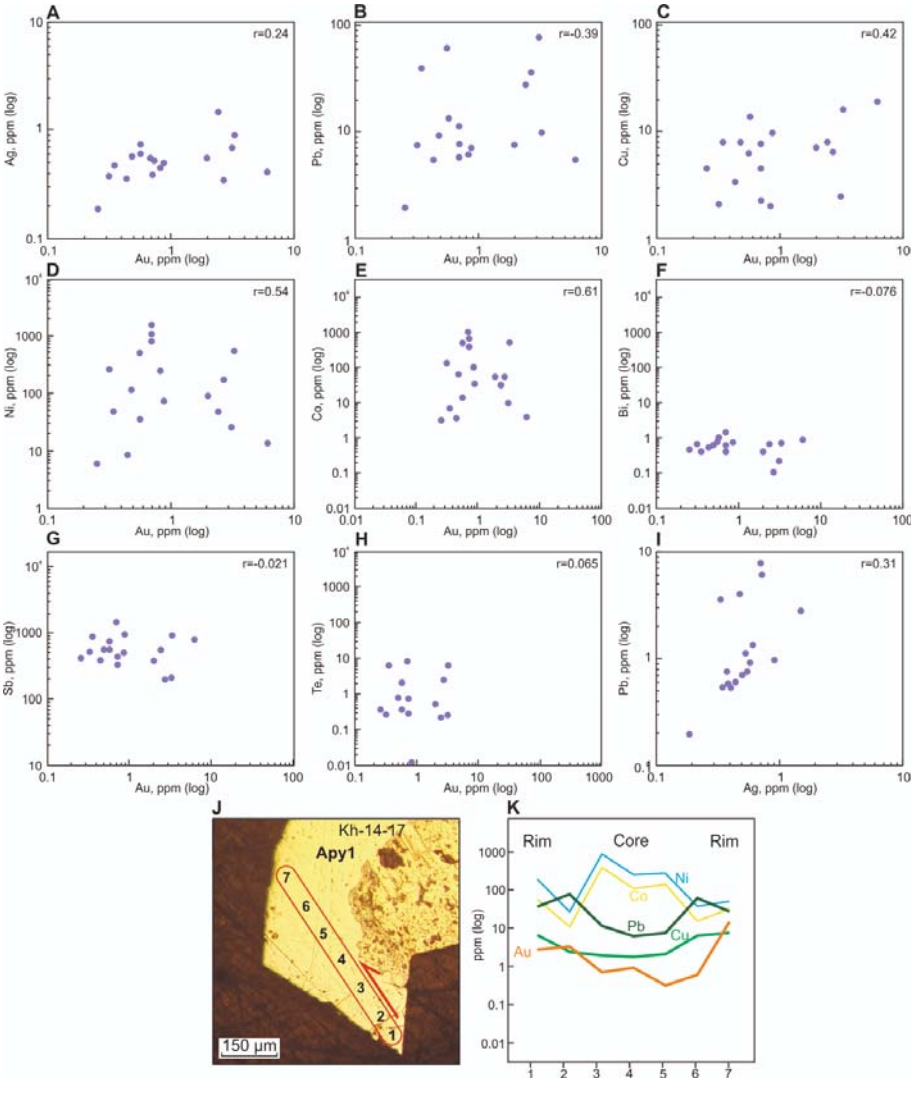

Figure 14. Correlation diagrams for Apy1: (**A**) Au vs. Ag; (**B**) Au vs. Pb; (**C**) Au vs. Cu; (**D**) Au vs. Ni; (**E**) Au vs. Co; (**F**) Au vs. Bi; (**G**) Au vs. Sb; (**H**) Au vs. Te; (**I**) Ag vs. Pb. Distribution of some elements (**K**) inside Apy1 grain (sample K-14-17) (**J**).

At the same time, Figure 14K shows that Au–Pb–Cu have a highly positive relationship in the Apy1 crystal. Qualitative line scanning with the use of LA-ICP-MS analysis has proved to be effective in recognizing variations in trace element concentrations in zoned or altered sulfide grains (Py, Apy) [58,81–83]. Using this method, we found that concentrations of invisible Au, Pb, and Cu tend to decrease from the rim to the core of the grains, while the contents of Co and Ni are noticeably higher in the central zones of the crystals (Figure 14K). A similar variation in the amount of trace elements within arsenopyrite of the Samgwang orogenic deposit (Korea) was shown by Lee et al. [58], who attributed this fact to later hydrothermal alteration. For the Khangalas deposit, the increased Au, Pb, and Cu in the rim of the Apy1 grain is associated with the input of a portion of fluids enriched in Au-polysulfide association. The rest of the trace elements do not show any clear regularity in their distribution within the Apy1 grain.

Apy1 from the Khangalas deposit shows a noticeable positive correlation of Au with Ni and Co (Figure 14D,E). This may indicate [58] the involvement of basic and ultrabasic sources in ore formation at the Khangalas deposit. The lack of correlation between Au and Bi, Sb, and Ag in Apy1 (Figure 14A,F,G) and the marked positive correlation between Ag and Pb (Figure 14I) indicate the contribution of Ag-, Bi-, and Sb-containing fluids to the formation of deposits, which is typical for the metallogenic specialization of the region [8,84,85].

Thus, LA-ICP-MS trace element analysis data show that Au in Apy1 and Py3 of the Khangalas deposit is present in the form of both invisible gold (solid solution in the crystal lattice/nanoparticles with a size of <100 nm) and native gold. The predominant form is the solid solution Au^+ in the Py3 and Apy1 crystal lattices.

5.4. Gold Content of Proximal Metasomatites and Their Sulfides

The results of atomic absorption analysis of the proximal metasomatites and their sulfides at the Khangalas deposit showed that average Au content in Py3 (12.51 ppm) and Apy1 (17.51 ppm) is lower than in veined Py4 (29.30 ppm) and Apy2 (20.49 ppm, one measurement). For the proximal metasomatites, average Au content with a highly uneven distribution (CV = 225%) was 0.81 ppm. Taking the average Au content at 0.5 ppm, the length of the ore body at 1400 m, and the thickness of the proximal metasomatites at 50 m, the gold resources of Khangalas deposit to a depth of 100 m would amount to 9.1 t Au. A significant contribution of disseminated mineralization to gold reserves is also reported for other orogenic deposits of the Yana–Kolyma metallogenic belt (Natalka [10,11], Degdekan [11], Drazhnoe [86], etc.). For example, for the Drazhnoe deposit (Upper Indigirka sector of the YKMB), with reserves of 49.8 tonnes of gold with an average grade of 2.86 ppm, the contribution of disseminated sulfide ores with invisible gold is estimated at 75% [86,87].

5.5. Sources of Metals

5.5.1. Pyrite Genesis as Evidenced by Co/Ni Ratio

The Co/Ni ratio reflects the genesis of pyrite [61,88–90]. In the studied samples, Co/Ni varied over a wide range (0.2–46.0), but in most analyses $C_{Co} > C_{Ni}$ (Co/Ni > 1.0). Increased Ni content (Co/Ni = 0.2–0.8) is characteristic of Py1 and Py2, and is recorded in the central part of zoned Py3 crystals. Variable correlations are observed between Co and Ni: a strong positive correlation (r = 0.64–0.73) in Py1 and Py2, a negative correlation (r = −0.6) in grains with elevated Ni content, and no correlation between Co and Ni in vein Py4 and Apy2. High concentrations of Ni in sulfides suggest, according to Lee et al. [58], that mafic and ultramafic components introduced into hydrothermal fluids were involved in the precipitation of sulfides (maximum 2230 ppm for Apy1, 1620 ppm for Apy2, 4830 ppm for Py3). Negative correlations between Co and Fe (r = −0.6) (Figure 15B) and Ni and Fe (r = −0.1, Figure 15C) in Py3 indicate the presence of Ni and Co in the crystal lattice through isomorphic substitution for Fe [61].

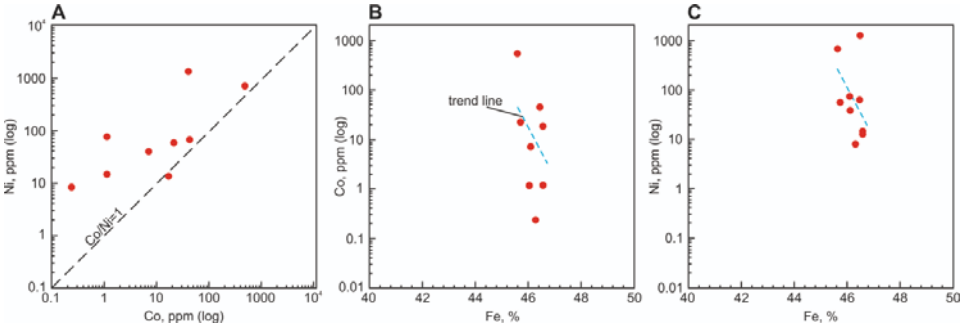

Figure 15. Ratio diagrams of (**A**) Co/Ni, (**B**) Fe/Co, and (**C**) Fe/Ni for Py3.

5.5.2. Origin of Hydrothermal Sulfides According to Stable Sulfur Isotopes

Examining stable isotopes in geological objects (rocks, mineralizing fluids, vein minerals, and ore deposits) has proven to be a powerful method that allows one to study their genesis in detail [91]. The genesis and sources of ore matter in orogenic Au deposits are controversial; first of all, the issue concerns the identification and assessment of the role of host rocks and deep-seated (magmatogenic and/or metamorphic) ore-bearing fluids in the process of ore formation (see [92–94] and references therein). The reported $\delta^{34}S$ values for sulfide minerals from orogenic gold deposits range from −20‰ to + 25‰ [92]. As sulfur is an important complexing agent for gold, understanding the S source may be critical in identifying the source areas of gold. A number of researchers came to the conclusion that the $\delta^{34}S$ composition in Phanerozoic deposits changes depending on the age of the host rock [92,95,96]. The sulfur isotopic composition of sulfides from the Khangalas deposit is in good agreement with these results (Figure 15B).

Based on the example of deposits in the Juneau gold belt [97] and on a comprehensive analysis of Jiaodong Province, China [92], it was shown that sulfur entered the composition of ore-forming fluids during the metamorphic conversion of pyrite into pyrrhotite. The sulfur source must have been a disseminated syngenetic/diagenetic pyrite in terranes being devolatilized at depth [95,96].

For gold deposits of the Yilgarn craton, at $\delta^{34}S \sim 0$, it was determined that the ore-forming fluid had a felsic magmatic or mantle-level source of sulfur [98]. The sulfur isotopic composition ($\delta^{34}S$ = 0.0 to −3.3‰) in a number of gold–sulfide deposits in Kazakhstan indicates that the ore matter had a mantle-level source of sulfur with some contribution from the crust [99,100].

The sulfur isotopic composition in clastic strata of the Upper Kolyma region varies widely from −23.1 to +5.6‰ (Figure 16A) [19]. Tyukova and Voroshin [19] compared the $\delta^{34}S$ of accessory sulfides of host rocks with the $\delta^{34}S$ of sulfides of gold deposits in the Upper Kolyma gold-bearing region, and suggested the involvement of sulfur mobilized from clastic strata in the hydrothermal process. It is believed that the most probable source of sulfur in sulfides ($\delta^{34}S$ −6.3 to + 2.6) from the Natalka orogenic deposit, the largest in the region, is the host rocks of the Verkhoyansk clastic complex [101,102]. Sulfur and arsenic were mobilized as a result of phase transformations of iron sulfides from clastic strata during the transformation of pyrite to pyrrhotite in the course of metamorphism.

For the orogenic gold deposits of the Adycha–Taryn metallogenic zone of the YKMB, a narrower interval of $\delta^{34}S$ values is established: from −2.1‰ to +2.4‰ (Apy), from −6.6 to +5.4‰ (Py), and from −6.1‰ to +4.2‰ (antimonite) (Figure 16) [8]. For example, the $\delta^{34}S$ values in sulfides are close to zero: −0.2‰ to +2.4‰ for Malo-Tarynskoe, −2.9‰ to −1.5‰ for Avgustovskoe, −3.6‰ to 1.3‰ for Kinyas, −1.7‰ to −1.2‰ for Pil, and −4.4‰ to −0.7‰ for Elginskoe and other gold deposits. These data are interpreted by

the authors as indicating a magmatic source of sulfur with some contribution from the host rocks of the Verkhoyansk clastic complex.

We studied the S isotopic composition of Py3, Apy1, and Apy2 in five samples from the Khangalas deposit, and obtained a narrow range of negative $\delta^{34}S$ values from −2.0‰ to −0.6‰ (Figure 16, Table 4). Similar sulfur isotopic compositions of arsenopyrite and pyrite of ore veins and disseminated mineralization of ore-hosting strata indicate their formation during a single hydrothermal event. The $\delta^{34}S$ values of sulfides from the Khangalas deposit are close to those of the well-studied orogenic gold-sulfide deposits: Natalka (Upper Kolyma region) [103]; Suzdalskoe, Zhaima, Bolshevik, and Zherek (Kazakhstan) [99,100]; and deposits of the Adycha-Taryn metallogenic zone [8] (Figure 16A). For the large Nezhdaninskoe orogenic gold deposit in the Allakh–Yun metallogenic zone, deep magma chambers (−5‰ to +1‰ for vein ores) and sulfides of host rocks (Figure 16A) are considered as sulfur sources [104]. At the same time, the conclusions about the genesis of the fluid components here are ambiguous, as in the case of the Muruntau deposit [105]. Thus, mantle/magmatic sulfur was involved in the formation of the Khangalas deposit, but the participation of sulfur from the host rocks of the Verkhoyansk clastic complex cannot be ruled out. The small volume of the conducted isotope studies does not make it possible to represent the entire range of $\delta^{34}S$ values for the Khangalas deposit. To obtain more information about the sources of ore matter, a comprehensive analysis of all generations of pyrite and arsenopyrite as well as thermobarometric and microelemental analysis of fluid inclusions are required.

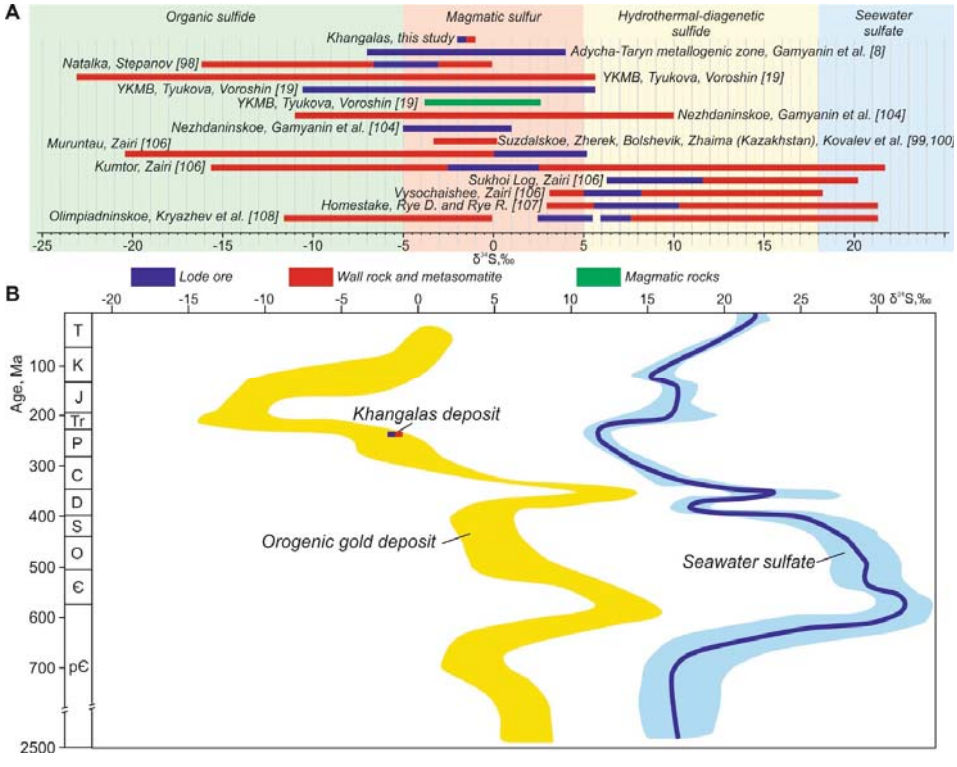

Figure 16. (**A**) S isotope composition of sulfides of Khangalas deposit [106–108]. Range of values of sulfur sources after Ohmoto [109] and Kryazhev [94]. (**B**) Variation in $\delta^{34}S$ values of sulfides in global sediment-hosted orogenic gold deposits after Goldfarb et al. [96]. Heavy line and blue error envelope indicate seawater sulfate evolution curve from Claypool et al. [110].

6. Conclusions

Four generations of pyrite (Py1, diagenetic; Py2, metamorphic; Py3, metasomatic; and Py4, veined) and two generations of arsenopyrite (Apy1, metasomatic, and Apy2, veined) have been identified at the Khangalas deposit. All sulfide generations are characterized by nonstoichiometric compositions: Fe/(S + As) (Py1: 0.48–0.52; Py2: 0.48–0.53; Py3: 0.47–0.54; Py4: 0.49–0.53; Apy1: 0.42–0.52; Apy2: 0.45–0.51) and contain As, Co, Ni, Cu, and Sb. The main trace element is As, making up a major portion of the total amount.

For diagenetic Py1 and metamorphic Py2, the total content of trace elements varies from 0.04 to 0.8 wt.%, and the share of As is from 30% to 70%. The most widespread and commercially significant pyrite with a high content of invisible gold is Py3, which formed in the wall rock metasomatites and occupies up to 3% to 3.5% of their volume. The total content of trace elements in Py3 varies from 0.38% to 3.27%, and the proportion of As is more than 75%.

The results of LA-ICP-MS trace element analysis provide information on the form of occurrence of invisible gold in Py3 and Apy1. Some aspects of Au behavior in sulfides indicate the predominance of structurally bound Au^{+}. A low Au content in sulfides (Py3, avg. 1.5 ppm; Apy2, avg. 7.6 ppm) is interpreted by some researchers [76] as an indicator of the structurally bound form of Au. In addition, the negative correlation between Au and Fe established for Py3 and Apy1 indicates isomorphic Au ↔ Fe substitution [52,55,58]. The close correlation between Au and As indicates that they have a common genesis. Their distribution patterns relative to the line limiting the transition of the solid solution Au^{+} to Au^{0} [57,71] also indicate the development of Au^{+} in Apy1 and Py3 from proximal metasomatites (Figure 13F,H). At the same time, a higher Au content was found in sulfides and proximal metasomatites (Py3: 39.32 ppm Au by atomic absorption; Apy1: 39.0 ppm by LA-ICP-MS). This may indicate the presence of micro- and nanoinclusions of native gold in sulfides, which is confirmed by the detection, with the use of a scanning electron microscope, of an Au^{0} microinclusion in the Py3 and Apy1 intergrowth in 1 out of about 200 grains studied. Indirect evidence of the presence of native gold inclusions in sulfides may be the large number of dense phases detected by computed microtomography. Isotope characteristics of hydrothermal sulfides ($\delta^{34}S = -2.0‰$ to $-0.6‰$) indicate that mantle/magmatic sulfur was involved in the formation of the deposit, but the participation of sulfur from the host rocks of the Verkhoyansk clastic complex cannot be ruled out.

The gold content of sulfides and proximal metasomatites determined during this study indicate that the Khangalas deposit has higher commercial potential than was thought before. It has much in common with other deposits of the Yana-Kolyma metallogenic belt. The results of this work make it possible to re-evaluate the reserves of orogenic gold deposits based on the study of disseminated sulfide mineralization with invisible gold. In these respects, Khangalas provides an exploration model useful in targeting similar gold deposits from the local to the regional scale.

Author Contributions: Conceptualization: V.Y.F. and M.V.K.; methodology, L.I.P., L.Y.K., V.Y.F. and M.V.K.; validation, V.Y.F., L.I.P. and M.V.K.; writing—original draft preparation, M.V.K., V.Y.F. and L.I.P.; writing—review and editing, V.Y.F., M.V.K. and L.I.P.; visualization, M.V.K.; supervision, V.Y.F.; project administration, V.Y.F.; funding acquisition, V.Y.F. and M.V.K. All authors have read and agreed to the published version of the manuscript.

Funding: This work was supported by the Diamond and Precious Metals Geology Institute, Siberian Branch of the Russian Academy of Sciences (DPMGI SB RAS), was partially funded by Russian Foundation for Basic Research (RFBR) (grant number 18-45-140040 r a), and by State scholarship of the Republic of Sakha (Yakutia) young researchers and graduate students.

Data Availability Statement: Not applicable.

Acknowledgments: The authors are grateful to all engineers for their accurate, timely and prompt analytical work. The authors are grateful to the engineer of DPMGI SB RAS Tarasov Ya.A. for his help in the preparation and selection of samples. The authors appreciate the staff of DPMGI SB RAS

Zayakina N.V. and Vasileva T.I. for their interest and advice that helped improve the article. We are sincerely grateful to Alekseenko E.V. for translating the text.

Conflicts of Interest: The authors declare no conflict of interest.

References

1. Goryachev, N.A.; Pirajno, F. Gold deposit and gold metallogeny of Far East Russia. *Ore Geol. Rev.* **2014**, *59*, 123–151. [CrossRef]
2. Mikhailov, B.K.; Struzhkov, S.F.; Aristov, V.V.; Natalenko, M.V.; Tsymbalyuk, N.V.; Tyamisov, N.E.; Uzyunkoyan, A.A. Gold potensial of the Yana–Kolyma province. *Ore Met.* **2007**, *5*, 4–17. (In Russian)
3. Kerrich, R.; Goldfarb, R.; Groves, D.; Garwin, S.; Jia, Y. The characteristics, origins, and geodynamic settings of supergiant gold metallogenic provinces. *Sci. China Ser. D Earth Sci.* **2000**, *43*, 68. [CrossRef]
4. Goryachev, N.A. *Geology of Mesozoic Gold–Quartz Vein Belts of Northeast Asia*; NEISRI FEB RAS: Magadan, Russia, 1998. (In Russian)
5. Gamyanin, G.N. *Mineralogical and Genetic Aspects of Gold Mineralization of the Verkhoyansk–Kolyma Mesozoids*; GEOS: Moscow, Russia, 2001. (In Russian)
6. Fridovsky, V.Y. Structures of gold ore fields and deposits of Yana–Kolyma ore belt. In *Metallogeny of Collisional Geodynamic Settings*; Mezhelovsky, N.V., Gusev, G.S., Eds.; GEOS: Moscow, Russia, 2002; Volume 1, pp. 6–241. (In Russian)
7. Amuzinsky, V.A. *Metallogenic Epochs and Content of Ore Complexes of the Verkhoyansk Folded System*; YSU Publishing House: Yakutsk, Russia, 2005. (In Russian)
8. Gamyanin, G.N.; Fridovsky, V.Y.; Vikent'eva, O.V. Noble-metal mineralization of the Adycha–Taryn metallogenic zone: Geochemistry of stable isotopes, fluid regime, and ore formation conditions. *Russ. Geol. Geophys.* **2018**, *59*, 1271–1287. [CrossRef]
9. Fridovsky, V.Y. Structural control of orogenic gold deposits of the Verkhoyansk–Kolyma folded region, northeast Russia. *Ore Geol. Rev.* **2018**, *103*, 38–55. [CrossRef]
10. Goryachev, N.A.; Vikentyeva, O.V.; Bortnikov, N.S.; Prokofiev, V.Y.; Alpatov, V.A.; Golub, V.V. World-class Natalka gold deposit: REE distribution, fluid inclusions, stable oxygen isotopes and ore formation conditions (North-East of Russia). *Geol. Rudn. Mest.* **2008**, *50*, 414–444. (In Russian)
11. Goryachev, N.A.; Sotskaya, O.T.; Mikhalitsyna, T.I.; Goryacheva, E.M.; Manshin, A.P. Estimation of Au-Pt-Pd-Ni in ores of typical deposits (Natalka, Degdekan) in the black shale strata of the Yana-Kolyma gold belt. *Vestnik ONZ RAS* **2012**, 325–336. (In Russian)
12. Goryachev, N.A.; Sotskaya, O.T.; Ignatiev, A.V.; Velivetskaya, T.I.; Goryacheva, E.M.; Semyshev, F.I.; Berdnikov, N.V.; Malinovsky, M.A.; Alshevsky, A.V. About sulfide mineralization of the zones of large faults of the Yana-Kolyma orogenic belt. *Bull. Northeast Sci. Center FEB RAS* **2020**, *1*, 11–29. (In Russian) [CrossRef]
13. Sotskaya, O.T.; Goryachev, N.A. Micromineral forms of gold and silver in disseminated sulfide "black shale" ores (North-East of Russia). Geology and mineral resources of the North-East of Russia. In Proceedings of the All-Russian Conference, Yakutsk, Russia, 29–30 March 2012. (In Russian)
14. Voroshin, S.V.; Tyukova, E.E.; Newberry, R.J.; Layer, P.W. Orogenic gold and rare metal deposits of the Upper Kolyma District, Northeastern Russia: Relation to igneous rocks, timing, and metal assemblages. *Ore Geol. Rev.* **2014**, *62*, 1–24. [CrossRef]
15. Sidorova, N.V.; Aristov, V.V.; Grigorieva, A.V.; Sidorov, A.A. "Invisible" gold in pyrite and arsenopyrite from the Pavlik deposit (North-East of Russia). *Dokl. Earth Sci.* **2020**, *495*, 821–826. [CrossRef]
16. Palyanova, G.A. Minerals of gold and silver in sulfide ores. *Geol. Ore Depos.* **2020**, *62*, 426–449. [CrossRef]
17. Volkov, A.V.; Sidorov, A.A. Invisible gold. *Bull. RAS* **2017**, *87*, 40–49. (In Russian) [CrossRef]
18. Tyukova, E.E.; Voroshin, S.V. *Composition and Paragenesis of Arsenopyrite in Deposits and Host Rocks of the Upper Kolyma Region (to the Interpretation of the Genesis of Sulfide Associations)*; NEISRI FEB RAS: Magadan, Russia, 2007. (In Russian)
19. Tyukova, E.E.; Voroshin, S.V. Isotopic composition of sulfur in sulfides from ores and host rocks of the Upper Kolyma region (Magadan region). *Russ. J. Pac. Geol.* **2008**, *27*, 29–43. (In Russian)
20. Babkin, P.V.; Gelman, M.L.; Veldyaksov, F.F.; Pavlyuchenko, L.A. Prospects for identifying gold mineralization in sulfidization zones in the black shale strata of the North-East USSR. *Kolyma* **2001**, *2*, 14–22. (In Russian)
21. Izmailov, L.I. *Pyrrhotite Mineralization of Metal-Bearing Zones of the Kolyma River Basin*; Science: Novosibirsk, Russia, 1976. (In Russian)
22. Volkov, A.V.; Sidorov, A.A.; Goncharov, V.I.; Sidorov, V.A. Disseminated gold-sulfide deposits in the Russian Northeast. *Geol. Ore Dep.* **2002**, *44*, 159–174.
23. Fridovsky, V.Y.; Yakovleva, K.Y.; Vernikovskaya, A.E.; Vernikovsky, V.A.; Matushkin, N.Y.; Kadilnikov, P.I.; Rodionov, N.V. Geodynamic Emplacement Setting of Late Jurassic Dikes of the Yana–Kolyma Gold Belt, NE Folded Framing of the Siberian Craton: Geochemical, Petrologic, and U–Pb Zircon Data. *Minerals* **2020**, *10*, 1000. [CrossRef]
24. Fridovsky, V.Y.; Kudrin, M.V. Deformation structures of the Khangalassky ore cluster. Geology and mineral resources of the North-East of Russia. In Proceedings of the All-Russian scientific-practical Conference, Yakutsk, Russia, 31 March–2 April 2015; pp. 537–540. (In Russian)
25. Fridovsky, V.Y.; Kudrin, M.V.; Polufuntikova, L.I. Multi-stage deformation of the Khangalas ore cluster (Verkhoyansk–Kolyma folded region, northeast Russia): Ore-controlling reverse thrust faults and post-mineral strike-slip faults. *Minerals* **2018**, *8*, 270. [CrossRef]

26. Rozhkov, I.S.; Grinberg, G.A.; Gamyanin, G.A.; Kukhtinskiy, Y.G.; Solovyev, V.I. *Late Mesozoic Magmatism and Gold Mineralization of the Upper Indigirsky Region*; Science: Moscow, Russia, 1971. (In Russian)
27. Amuzinsky, V.A.; Anisimova, G.S.; Zhdanov, Y.Y. *Native Gold of Yakutia, Upper Indigirsky District*; VO Nauka: Novosibirsk, Russia, 1992. (In Russian)
28. Nesterov, N.V. *Supergene Enrichment of Gold Deposits in Northeast Asia*; Nauka: Novosibirsk, Russia, 1985. (In Russian)
29. Kudrin, M.V.; Zayakina, N.V.; Vasilieva, T.I. Minerals of the oxidation zone of the Khangalas gold deposit (Eastern Yakutia). Geology and mineral resources of the North-East of Russia. In Proceedings of the VIII All-Russian Scientific-Practical Conference, Yakutsk, Russia, 18–20 April 2018; pp. 77–80. (In Russian)
30. Kudrin, M.V.; Vasilieva, T.I.; Fridovsky, V.Y.; Zayakina, N.V.; Polufuntikova, L.I. Minerals of the weathering crust of the Khangalassky ore cluster (North-East of Russia). Geology and mineral resources of the North-East of Russia. In Proceedings of the IX All-Russian Scientific and Practical Conference, Yakutsk, Russia, 10–12 April 2019; pp. 53–56. (In Russian)
31. Skryabin, A.I. *Reconstruction of the Lateral Zoning of Gold Mineralization (Yano-Kolyma Belt)*; YSC SB RAS: Yakutsk, Russia, 2010. (In Russian)
32. GeoInfoComLLC. Available online: http://mestor.geoinfocom.ru/publ/1-1-0-55 (accessed on 15 January 2021).
33. Parfenov, L.M.; Kuzmin, M.I. *Tectonics, Geodynamics and Metallogeny of the Territory of the Republic of Sakha (Yakutia)*; Parfenov, L.M., Kuzmin, M.I., Eds.; MAIK Nauka/Interperiodika: Moscow, Russia, 2001. (In Russian)
34. Zaitsev, A.I.; Fridovsky, V.Y.; Vernikovskaya, A.E.; Kudrin, M.V.; Yakovleva, K.Y.; Kadilnikov, P.I. Rb–Sr isotopic study of basites of the dyke complex of the Taryn ore-magmatic system (Northeast Russia). *Russ. J. Domes. Geol.* **2018**, *5*, 50–61. (In Russian)
35. Parfenov, L.M.; Berzin, N.A.; Khanchuk, A.I.; Badarch, G.; Belochenko, V.G.; Bulgatov, A.I.; Dril, C.I.; Kirillova, G.L.; Kuzmin, M.I.; Nokleberg, W.J.; et al. Model of orogenic belt formation in Central and Northeast Asia. *Russ. J. Pac. Geol.* **2003**, *22*, 7–41. (In Russian)
36. Akinin, V.V.; Prokopiev, A.V.; Toro, J.; Miller, E.L.; Wooden, J.; Goryachev, N.A.; Alshevsky, A.V.; Bakharev, A.G.; Trunilina, V.A. U–PB SHRIMP ages of granitoids from the Main batholith belt (North East Asia). *Dokl. Acad. Sci.* **2009**, *426*, 216–221.
37. Akinin, V.V.; Miller, E.L.; Toro, J.; Prokopiev, A.V.; Gottlieb, E.S.; Pearcey, S.; Trunilina, V.A. Episodicity and the dance of late mesozoic magmatism and deformation along the northern circum-pacific margin: NE Russia to the Cordillera. *Earth-Sci. Rev.* **2020**, *208*, 103272. [CrossRef]
38. Akimov, G.Y. New age data on gold–quartz mineralization in the Verkhnyaya Indigirka area, Yakutia. *Dokl. Acad. Sci.* **2004**, *398*, 80–83. (In Russian)
39. Whitney, D.L.; Ewans, B.W. Abbreviations of names of rock forming minerals. *Am. Miner.* **2010**, *95*, 185–187. [CrossRef]
40. Kudrin, M.V.; Zayakina, N.V.; Fridovsky, V.Y.; Galenchikova, L.T. Hydrous ferric sulfate–$Fe(SO_4)(OH)\cdot 2H_2O$ from the supergene zone of the Khangalas gold deposit, Eastern Yakutia, Russia. *Notes Rus. Min. Soc.* **2020**, *149*, 126–141.
41. Zayakina, N.V.; Kudrin, M.V.; Fridovsky, V.Y. Unknown sulfate-arsenate-phosphate Al and Fe from the Khangalas deposit (Eastern Yakutia). Geology and Mineral Resources of the North-East of Russia. In Proceedings of the X All-Russian Scientific-Practical Conference with International Participation, Yakutsk, Russia, 8–10 April 2020; pp. 210–214. (In Russian)
42. Nesterov, N.V. Secondary zoning of gold ore deposits in Yakutia. In *Bulletin of the Tomsk Polytechnic University*; TPU: Tomsk, Russia, 1970; pp. 242–247. (In Russian)
43. Wilson, S.A.; Ridley, W.I.; Koenig, A.E. Development of sulphide calibration standards for the laser ablation inductively-coupled plasma mass spectrometry technique. *J. Anal. At. Spectrom.* **2002**, *17*, 406–409. [CrossRef]
44. Paton, C.; Hellstrom, J.; Paul, B.; Woodhead, J.; Hergt, J. Iolite: Freeware for the visualisation and processing of mass spectrometric data. *J. Anal. Atomic Spectrom.* **2011**, *26*, 2508–2518. [CrossRef]
45. Longerich, H.P.; Jackson, S.E.; Günther, D. Inter-laboratory note. Laser ablation inductively coupled plasma mass spectrometric transient signal data acquisition and analyte concentration calculation. *J. Anal. Atomic Spectrom.* **1996**, *11*, 899–904. [CrossRef]
46. Nadeev, A.; Mikhailov, D.; Chuvilin, E.; Koroteev, D.; Shako, V. Visualization of clay and frozen substances inside porous rocks using X-ray micro-computed tomography. *J. Microsc. Anal.–Tomogr. Suppl.* **2013**, *27*, 8–11.
47. Mayorova, T.P.; Statsenko, E.O.; Trifonov, A.A.; Nesterenko, G.V. X-ray microtomography and field emission electron microscopy – new possibilities for studying highly dispersed gold ores. *Bull. Inst. Geol. KSC UB RAS.* **2013**, *11*, 34–38. (In Russian)
48. Krupskaya, V.V.; Zakusin, S.V.; Zhukhlistov, A.P.; Dorzhieva, O.V.; Sudin, V.V.; Kryuchkova, L.Y.; Zubkov, A.A. Newly formed smectite as an indicator of transformations of the geological environment under the influence of highly reactive solutions accompanying liquid radioactive waste. *J. Geoecol. Engin. Geol. Hydrogeol. Geocr.* **2016**, *5*, 412–421.
49. Jarzyna, J.A.; Krakowska, P.I.; Puskarczyk, E.; Wawrzyniak-Guz, K.; Bielecki, J.; Tkocz, K.; Tarasiuk, J.; Wro'nski, S.; Dohnalik, M. X-ray computed microtomography—A useful tool for petrophysical properties determination. *Comput. Geosc.* **2016**, *20*, 1155–1167. [CrossRef]
50. Voitenko, V.N. Form of crystallization of native gold in arsenopyrite ores of the Bazovskoye deposit (according to X-ray microtomography data). In *Practical Microtomography, Proceedings of the III All-Russian Scientific Conference*; SPBGU: St. Petersburg, Russia, 2014; pp. 26–28. (In Russian)
51. Naumov, E.A.; Kovalev, K.R.; Kalinin, Y.A.; Palyanova, G.A.; Voitenko, V.N. The use of high-resolution X-ray tomography methods in mineralogical research. In *Scientific and Methodological Foundations of Forecasting, Prospecting, Evaluation of Diamond, Precious and Non-Ferrous Metal Deposits*; TSINIGRI: Moscow, Russia, 2019; pp. 126–127. (In Russian)

52. Korost, D.V.; Kalmykov, G.A.; Yapaskurt, V.O.; Ivanov, M.K. Application of computer microtomography to study the structure of terrigenous reservoirs. *Geol. Oil Gas.* **2010**, *2*, 36–42. (In Russian)
53. Korost, D.V.; Ariskin, A.A.; Pshenitsyn, I.V.; Khomyak, A.N. X-ray computed tomography as a method for reconstructing the 3d characteristics of dispersed sulfides and spinel in plagiodunites of the Yoko-Dovyren intrusion. *Petrol* **2019**, *27*, 401–419. (In Russian) [CrossRef]
54. Vorobiev, A.E.; Kozyrev, E.N.; Honore, C. Communication nanorelief Pyrite and Arsenopyrite with the values of adsorption of gold. In *Science, Education, Culture and Information and Educational Activities-the Basis of Sustainable Development of Mountain Territories, Proceedings of the VIII International Scientific-Practical Conference*; SKGMI: Vladikavkaz, Russia, 2015; pp. 264–272. (In Russian)
55. Kovalchuk, E.V.; Tagirov, B.R.; Vikentyev, I.V.; Chareev, D.A.; Tyukova, E.E.; Nikolsky, M.S.; Bortnikov, N.S. "Invisible" Gold in Synthetic and Natural Arsenopyrite Crystals, Vorontsovka Deposit, Northern Urals. *Geol. Ore Dep.* **2019**, *61*, 447–468. [CrossRef]
56. Sharp, Z.D.; Essene, E.J.; Kelly, W.C. A re-examination of the arsenopyrite geothermometer; pressure considerations and applications to natural assemblages. *Can. Mineral.* **1985**, *23*, 517–534.
57. Lentz, D.R. Sphalerite and arsenopyrite at the Brunswick No. 12 massive sulfide deposit, Bathurst camp, New Brunswick: Constraints on P-T evolution. *Can. Mineral.* **2002**, *40*, 19–31. [CrossRef]
58. Lee, M.; Shin, D.; Yoo, B.; Im, H.; Pak, S.; Choi, S. LA-ICP-MS trace element analysis of arsenopyrite from the Samgwang gold deposit, South Korea, and its genetic implications. *Ore Geol. Rev.* **2019**, *114*, 103147. [CrossRef]
59. Fleet, M.E.; Mumin, A.H. Gold-bearing arsenian pyrite and marcasite and arsenopyrite from Carlin Trend gold deposits and laboratory synthesis. *Am. Mineral.* **1997**, *82*, 182–193. [CrossRef]
60. Reich, M.; Kesler, S.E.; Utsunomiya, S.; Palenik, C.S.; Chryssoulis, S.L.; Ewing, R.C. Solubility of gold in arsenian pyrite. *Geochim. Cosmochim. Acta.* **2005**, *69*, 2781–2796. [CrossRef]
61. Wang, C.; Shao, Y.; Huang, K.; Zhou, H.; Zhang, J.; Liu, Z.; Liu, Q. Ore-Forming Processes at the Xiajinbao Gold Deposit in Eastern Hebei Province: Constraints from EPMA and LA-ICPMS Analysis. *Minerals* **2018**, *8*, 388.
62. Pshenichkin, A.Y. On the form of finding trace elements in pyrite. *Expl. Prot. Min. Resour.* **2010**, *11*, 46–49. (In Russian)
63. Large, R.R.; Bull, S.W.; Maslennikov, V.V. A carbonaceous sedimentary source rock model for Carlin-type and orogenic gold deposits. *Econ. Geol.* **2011**, *106*, 331–358. [CrossRef]
64. Maslennikov, V.V.; Large, R.R.; Maslennikova, S.P.; Arkhireeva, N.S. Typochemism of pyrite and pyrrhotite as a reflection of the evolution of gold-bearing carbonaceous deposits in marginal oceanic structures. *Metall. Anc. Mod. Oceans* **2013**, *19*, 32–35.
65. Samusikov, V.P. Regularities of the concentration of isomorphic-impurity elements in minerals during hydrothermal ore formation. *Russ. Geol. Geoph.* **2010**, *51*, 338–352.
66. Bortnikov, N.S.; Gamyanin, G.N.; Vikentieva, O.V.; Prokofiev, V.Y.; Alpatov, V.A.; Bakharev, A.G. Composition and origin of fluids in the hydrothermal system of the Nezhdaninsky gold ore deposit (Sakha-Yakutia, Russia). *Geol. Ore Depos.* **2007**, *49*, 99–145. [CrossRef]
67. Aristov, V.V.; Kryazhev, S.G.; Ryzhov, O.B.; Volfson, A.A.; Prokofiev, V.Y.; Sidorova, N.V.; Sidorov, A.A. Sources of fluids and ore matter of gold and antimony mineralization of the Adychansk ore region (Eastern Yakutia). *Pap. Acad. Sci.* **2017**, *476*, 174–180.
68. Large, R.R.; Maslennikov, V.V. Invisible Gold Paragenesis and Geochemistry in Pyrite from Orogenic and Sediment-Hosted Gold Deposits. *Minerals* **2020**, *10*, 339. [CrossRef]
69. Maslennikov, V.V.; Maslennikova, S.P.; Large, R.R.; Danyushevsky, L.V. Study of trace element zonation in vent chimneys from the Silurian Yaman-Kasay volcanic-hosted massive sulfide deposit (southern Urals, Russia) using laser ablation–inductively coupled plasma mass spectrometry (LA-ICPMS). *Econ. Geol.* **2009**, *104*, 1111–1141. [CrossRef]
70. Keith, M.; Smith, D.J.; Jenkin, G.R.; Holwell, D.A.; Dye, M.D. A review of Te and Se systematics in hydrothermal pyrite from precious metal deposits: Insights into ore-forming processes. *Ore Geol. Rev.* **2018**, *96*, 269–282. [CrossRef]
71. Deditius, A.P.; Reich, M.; Kesler, S.E.; Utsunomiya, S.; Chryssoulis, S.L.; Walshe, J.; Ewing, R.C. The coupled geochemistry of Au and As in pyrite from hydrothermal ore deposits. *Geochim. Cosmochim. Acta* **2014**, *140*, 644–670. [CrossRef]
72. Vikentiev, I.V. Invisible and microscopic gold in pyrite: Research methods and new data for pyrite ores of the Urals. *Geol. Ore Depos.* **2015**, *57*, 267–298.
73. Voitkevich, G.V.; Miroshnikov, A.E.; Povarenykh, A.S.; Prokhorov, V.G. *A Short Guide to Geochem.*, 2nd ed.; Nedra: Moscow, Russia, 1977. (In Russian)
74. Belikova, G.I.; Salikhov, D.N.; Berdnikov, P.G. On the question of gold isomorphism in pyrite. *Geol. Collect. GI USC RAS* **2002**, *3*, 190–193. (In Russian)
75. Chouinard, A.; Paquette, J.; Williams-Jones, A.E. Crystallographic controls on trace-element incorporation in auriferous pyrite from the Pascua epithermal high-sulfidation deposit, Chile-Argentina. *Can. Miner.* **2005**, *43*, 951–963. [CrossRef]
76. Tauson, V.L.; Kravtsova, R.G.; Smagunov, N.V.; Spiridonov, A.M.; Grebenshchikova, V.I.; Budyak, A.E. Structurally and superficially bound gold in pyrite from deposits of different genetic types. *Russ. Geol. Geophys.* **2014**, *55*, 273–289. [CrossRef]
77. Gao, F.; Du, Y.; Pang, Z.; Du, Y.; Xin, F.; Xie, J. LA-ICP-MS Trace-Element Analysis of Pyrite from the Huanxiangwa Gold Deposit, Xiong'ershan District, China: Implications for Ore Genesis. *Minerals* **2019**, *9*, 157. [CrossRef]
78. Vaughan, J.P.; Kyin, A. Refractory gold ores in Archaean greenstones, Western Australia: Mineralogy, gold paragenesis, metallurgical characterization and classification. *Miner. Magaz.* **2004**, *68*, 255–277. [CrossRef]

79. Moskvitina, L.V.; Moskvitin, S.G.; Anisimova, G.S. Research of Nanoscale Gold by Methods of Tunneling and Atomic-Powered Microscopy with Chemical and Ion-Plasma Etching in the Kuchus Deposit (Republic Sakha (Yakutia). In *International Science and Technology Conference "Earth Science"-Section One, Proceedings of the Iop Conference Series: Earth and Environmental Science, Russky Island, Russia, 4–6 March 2019*; IOP Publishing Ltd.: Bristol, UK, 2019; Volume 272, pp. 1–7.
80. Gregory, D.D.; Large, R.R.; Halpin, J.A.; Baturina, E.L.; Lyons, T.W.; Wu, S.; Danyushevsky, L.; Sack, P.J.; Chappaz, A.; Maslennikov, V.V.; et al. Trace element content of sedimentary pyrite in black shales. *Econ. Geol.* **2015**, *110*, 1389–1410. [CrossRef]
81. Tomkins, A.G.; Mavrogenes, J.A. Redistribution of gold within arsenopyrite and lollingite during pro-and retrograde metamorphism: Application to timing of mineralization. *Econ. Geol.* **2001**, *96*, 525–534. [CrossRef]
82. Morey, A.A.; Tomkins, A.G.; Bierlein, F.P.; Weinberg, R.F.; Davidson, G.J. Bimodal distribution of gold in pyrite and arsenopyrite: Examples from the Archean Boorara and Bardoc shear systems, Yilgarn craton, Western Australia. *Econ. Geol.* **2008**, *103*, 599–614. [CrossRef]
83. Sung, Y.H.; Brugger, J.; Ciobanu, C.L.; Pring, A.; Skinner, W.; Nugus, M. Invisible gold in arsenian pyrite and arsenopyrite from a multistage Archaean gold deposit: Sunrise Dam, Eastern Goldfields Province, Western Australia. *Miner. Dep.* **2009**, *44*, 765. [CrossRef]
84. Zaitsev, A.I.; Fridovsky, V.Y.; Yakovleva, K.Y.; Kudrin, M.V.; Vernikovskaya, A.E. Composition and age of the basitic dikes of the Nastenka site of the Malo–Tarynskoe orogenic gold deposit (Verkhoyansk–Kolyma folded region, Northeast Russia). In Proceedings of the 19th International Multidisciplinary Scientific GeoConference-SGEM, Albena, Bulgaria, 30 June–6 July 2019; pp. 99–108.
85. Bortnikov, N.S.; Gamyanin, G.N.; Vikent'eva, O.V.; Prokof'ev, V.Y.; Prokop'ev, A.V. The Sarylakh and Sentachan gold–antimony deposits, Sakha-Yakutia: A case of combined mesothermal gold–quartz and epithermal stibnite ores. *Geol. Ore Dep.* **2010**, *52*, 339–372. (In Russian) [CrossRef]
86. Aristov, V.V.; Prokofiev, V.Y.; Imamendinov, B.N.; Kryazhev, S.G.; Alekseev, V.Y.; Sidorov, A.A. Features of ore formation at the Drazhnoe gold-quartz deposit (Eastern Yakutia, Russia). *Dokl. Earth Sci.* **2015**, *464*, 879–884. [CrossRef]
87. GV GOLD. Available online: https://www.gvgold.ru/ru/our-assets/taryn-business-unit/ (accessed on 25 January 2021).
88. Bralia, A.; Sabatini, G.; Troja, F. A revaluation of the Co/Ni ratio in pyrite as geochemical tool in ore genesis problems. *Miner. Depos.* **1979**, *14*, 353–374. [CrossRef]
89. Cook, N.J.; Ciobanu, C.L.; Mao, J.W. Textural control on gold distribution in As-free pyrite from the Dongping, Huangtuliang and Hougou gold deposits, North China craton (Hebei Province, China). *Chem. Geol.* **2009**, *264*, 101–121. [CrossRef]
90. Azovskova, O.B.; Utochkina, N.V.; Zubova, T.P. Geochemical features of pyrite and marcasite from weathering crusts and "ancient" loose deposits of the Aktai area (Northern Urals). In *EZHEGODNIK-2013, Tr. IGG UrO RAN*; URO RAN: Ufa, Russia, 2014; Volume 161, pp. 238–245. (In Russian)
91. Shanks, W. *Stable Isotope Geochemistry of Mineral Deposits*; Elsevier Ltd.: Amsterdam, The Nederland, 2014.
92. Goldfarb, R.J.; Groves, D.I. Orogenic gold: Common or evolving fluid and metal sources through time. *Lithos* **2015**, *233*, 2–26. [CrossRef]
93. LaFlamme, C.; Sugiono, D.; Thébaud, N.; Caruso, S.; Fiorentini, M.L.; Selvaraja, V.; Jeon, H.; Voute, F.; Martin, L. Multiple sulfur isotopes monitor fluid evolution of an orogenic gold deposit. *Geoch. Cosmoch. Acta* **2018**, *222*, 436–446. [CrossRef]
94. Kryazhev, S.G. Isotope-geochemical and genetic models of gold deposits in carbonaceous-terrigenous strata. *Domest. Geol.* **2017**, *1*, 28–38. (In Russian)
95. Chang, Z.; Large, R.; Maslennikov, V. Sulfur isotopes in sediment-hosted orogenic gold deposits: Evidence for an early timing and a seawater sulfur source. *Geology* **2008**, *36*, 971–974. [CrossRef]
96. Goldfarb, R.J.; Miller, L.D.; Leach, D.L.; Snee, L.W. Gold deposits in metamorphic rocks of Alaska. *Econ. Geol.* **1997**, *9*, 151–190.
97. Goldfarb, R.J.; Leach, D.L.; Rose, S.C.; Landis, G.P. Fluid inclusion geochemistry of gold-bearing quartz veins of the Juneau Gold Belt, southeastern Alaska-implications for ore genesis. *Econ. Geol.* **1989**, *6*, 363–375.
98. Xue, Y.; Campbell, I.H.; Ireland, T.R.; Holden, P.; Armstrong, R. No mass-independent sulfur isotope fractionation in auriferous fluids supports a magmatic origin for Archean gold deposits. *Geology* **2013**, *41*, 791–794. [CrossRef]
99. Kovalev, K.R.; Kalinin, Y.A.; Naumov, E.A.; Kolesnikova, M.K.; Korolyuk, V.N. Gold content of arsenopyrite of gold-sulfide deposits of East Kazakhstan. *Geol. Geoph.* **2011**, *52*, 225–242.
100. Kovalev, K.R.; Kuzmina, O.N.; Dyachkov, B.A.; Vladimirov, A.G.; Kalinin, Y.A.; Naumov, E.A.; Kirillov, M.V.; Annikova, I.Y. Gold-sulfide disseminated mineralization of the Zhaima deposit (East Kazakhstan). *Geol. Ore Dep.* **2016**, *58*, 116–133. [CrossRef]
101. Mikhalitsyna, T.I.; Sotskaya, O.T. The role of black-shales in the formation of gold-ore deposits Natalka and Pavlik (Yano-Kolymsky orogene belt). *Russ. Geol. Geoph.* **2020**, *61*, 1648–1671.
102. Eremin, R.A.; Voroshin, S.V.; Sidorov, V.A.; Shakhtyrov, V.G.; Pristavko, V.A.; Gashtold, V.V. Geology and genesis of the Natalka gold deposit, Northeast Russia. *Inter. Geol. Rev.* **1994**, *36*, 1113–1138. [CrossRef]
103. Stepanov, V.A. *Zoning of Gold-Quartz Mineralization in Central Kolyma (Magadan Region, Russia)*; Dalnauka: Vladivostok, Russia, 2001. (In Russian)
104. Gamyanin, G.N.; Bortnikov, N.C.; Alpatov, V.V. *The Nezhdaninskoe Gold Ore Deposit is A Unique Deposit in the North-East of Russia*; GEOS: Moscow, Russia, 2000. (In Russian)
105. Seltmann, R.; Goldfarb, R.; Zu, B.; Creaser, R.; Dolgopolova, A.; Shatov, V. Muruntau, Uzbekistan: The World's Largest Epigenetic Gold Deposit. *Soc. Econ. Geol.* **2020**, *23*, 497–521.

106. Zairi, N.M. Isotope-Geochemical Models of the Formation of Deposits of Gold-Carbon Formation. Ph.D. Thesis, TSINIGRI, Moscow, Russia, 1992. (In Russian)
107. Rye, D.M.; Rye, R.O. Homestake Gold Mine, South Dakota: I. Stable Isotope Studies. *Econ. Geol.* **1974**, *69*, 293–317. [CrossRef]
108. Kryazhev, S.G.; Glukhov, A.P.; Rusinova, O.V.; Kuznetsova, S.V. Isotope-geochemical regime of the formation of the gold-quartz deposit Sovetskoe. In *Applied Geochemistry (Analytical Research)*, 4th ed.; IMGRE: Moscow, Russia, 2003; pp. 154–164. (In Russian)
109. Ohmoto, H. Stable isotope geochemistry of ore deposits. In *High Temperature Geological Processes (Review in Mineralogy)*; Mineralogical Society of America: Washington, DC, USA, 1986; pp. 491–559.
110. Claypool, G.E.; Holser, W.T.; Kaplan, I.R.; Sakai, H.; Zak, I. The age curves of sulfur and oxygen isotopes in marine sulfate and their mutual interpretation. *Chem. Geol.* **1980**, *28*, 199–260. [CrossRef]

minerals

MDPI

Article

Types of Tellurium Mineralization of Gold Deposits of the Aldan Shield (Southern Yakutia, Russia)

Larisa A. Kondratieva *, Galina S. Anisimova and Veronika N. Kardashevskaia

Diamond and Precious Metal Geology Institute, SB RAS, 677000 Yakutsk, Russia; gsanisimova1952@mail.ru (G.S.A.); kardashevskaya92@mail.ru (V.N.K.)
* Correspondence: lkon12@yandex.ru; Tel.: +7-4112-33-58-72

Abstract: The published and original data on the tellurium mineralization of gold ore deposits of the Aldan Shield are systematized and generalized. The gold content is related to hydrothermal-metasomatic processes caused by Mesozoic igneous activity of the region. The formation of tellurides occurred at the very late stages of the generation of gold mineralization of all existing types of metasomatic formations. 29 tellurium minerals, including 16 tellurides, 5 sulfotellurides and 8 tellurates have been identified. Tellurium minerals of two systems predominate: Au-Bi-Te and Au-Ag-Te. Gold is not only in an invisible state in sulfides and in the form of native gold of different fineness, but also is part of a variety of compounds: montbrayite, calaverite, sylvanite, krennerite and petzite. In the gold deposits of the Aldan Shield, three mineral types are distinguished: Au-Ag-Te, Au-Bi-Te, and also a mixed one, which combines the mineralization of both systems. The decrease in the fineness of native gold is consistent with the sequence and temperatures of the formation of Te minerals and associated mineral paragenesis from the epithermal–mesothermal Au-Bi-Te to epithermal Au-Ag-Te. The conducted studies allowed us to determine a wide variety of mineral species and significantly expand the area of distribution of Au-Te mineralization that indicates its large-scale regional occurrence in the Aldan Shield.

Keywords: tellurides; gold; Au-Bi-Te; Au-Ag-Te and mixed Au-Ag-Bi-Te mineral types; igneous activity; alkaline magmatism; metasomatites; Aldan Shield

Citation: Kondratieva, L.A.; Anisimova, G.S.; Kardashevskaia, V.N. Types of Tellurium Mineralization of Gold Deposits of the Aldan Shield (Southern Yakutia, Russia). *Minerals* **2021**, *11*, 698. https://doi.org/10.3390/min11070698

Academic Editors: Galina Palyanova and Liqiang Yang

Received: 30 April 2021
Accepted: 25 June 2021
Published: 29 June 2021

1. Introduction

One of the main sources of gold in Russia for many decades has been gold mineralization of the Aldan-Stanovoy Shield—the largest outcrop of the Early Precambrian basement of the Siberian platform. The geological structure of the area includes two structural stages: the lower, crystalline basement, composed of metamorphosed Early Archean gneisses, schists, and granites, and the upper, platform cover formed by the Vendian-Lower Cambrian carbonate and Jurassic terrigenous rocks. Two large gold-bearing provinces, Aldan and Stanovaya, are identified on the territory of the Aldan-Stanovoy Shield, located respectively in the geoblocks (shields) of the same name.

The main gold reserves of the Aldan Shield (AS) are concentrated on the territory of the Central Aldan ore District (CAD). The gold content is associated with hydrothermal-metasomatic processes caused by large-scale Mesozoic igneous activity of the region, involving the intrusion of massifs of subalkaline and alkaline high-potassium igneous rocks of the Jurassic-Cretaceous age [1–12]. Ore-bearing hydrothermal-metasomatic formations are represented by sericite-microcline metasomatites, beresites, gumbaites, jasperoids, and argillizites.

Tellurium mineralization in the area of the Aldan Shield was first recorded in the 1970s to 1980s. Epithermal gold-telluride mineralization was described by S. V. Yablokova (1975) and A. A. Kim (1982, 1988, 1990, 2000) in the Kuranakhsky ore cluster of the CAD (Bokovoye and Delbe deposits). In addition to the well-known tellurium and selenium minerals, new mineral types of tellurates have been established: kuranakhite [13], yafsoanite, kuksite,

cheremnykhite and V, Si-dugganite [14–17]. Recently, new information has appeared on tellurium mineralization in the deposits and ore occurrences of the CAD in the ores of Lebedinsky [18,19], Elkonsky [20–22], Dzhekondinsky [23,24], Yukhtinsky [25,26], and the Nimgerkansky [27] ore fields, as well as a number of other gold ore objects outside the CAD-Verkhne-Tokkinsky [28,29], Verkhneamginsky [30–34], Tyrkandinsky, Guvilgrinsky, Altan-Chaidakhsky, and Verkhnealgominsky [35–38] (Figure 1).

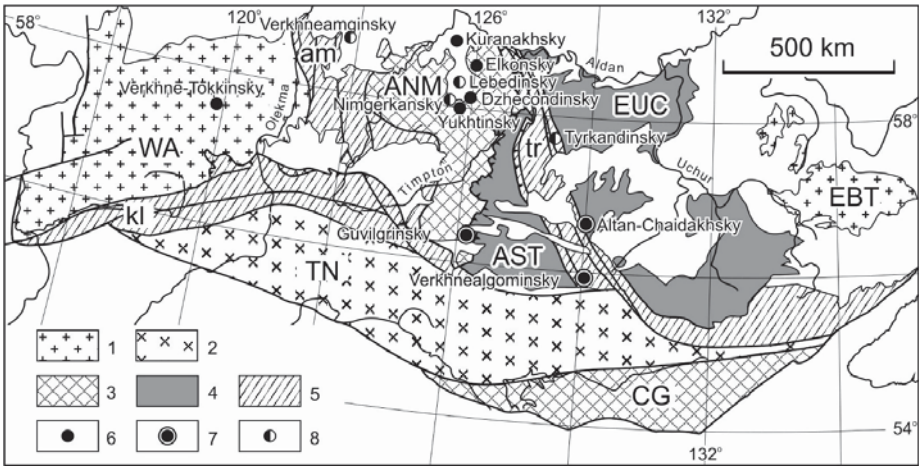

Figure 1. The position of deposits and ore occurrences with telluride mineralization in the structures of the Aldan geoblock of the Aldan-Stanovoy shield. Based on [39]: 1–4—terrains: granite-greenstone (WA—West-Aldan, EBT—Batomgsky, 2—tonalite-trondhjemite gneissic (TN—Tyndinsky), 3—granulite-gneissic (ANM—Nimnyrsky, CG—Chogarsky), 4—granulite-paragneissic (AST—Sutamsky, EUC—Uchursky); 5—zones of tectonic melange (am—Amginskaya, kl—Kalarskaya, tr—Tyrkandinskaya); 6–8—ore districts with Te mineralization: 6—Au-Ag-Te, 7—Au-Bi-Te, 8—mixed.

The significance of the research of tellurides is proved by their important role as indicator minerals of the physical and chemical conditions of the formation of gold mineralization, as well as accessory minerals, containing a significant proportion of the gold reserves.

The purpose of the research: to systematize and summarize the scattered information on Te mineralization of the region, to clarify their typomorphic properties and conditions of ore formation, to typify and determine the patterns of their spatial position in the structures of the Aldan Shield.

2. Materials and Methods

Typification of tellurium mineralization of gold deposits of the Aldan shield is carried out on the basis of systematization and generalization of scattered known and original data. About three hundred and fifty samples were collected from mine working of the Verkhneamginsky, Nimgerkansky, Tyrkandinsky, Guvilgrinsky, Altan-Chaidakhsky, and Verkhnealgominsky ore fields. The polished sections made from the samples were optically examined using a Jenavert ore microscope in reflected light, with special attention being directed toward identifying sulfides, sulfosalts, tellurides and native elements. These minerals were analyzed on a Camebax-micro X-ray spectral microanalyzer and a JEOL JSM-6480LV scanning electron microscope with an OXFORD energy spectrometer, where the Back Scattered Electron images were taken at the Diamond and Precious Metal Geology Institute, Siberian Branch, Russian Academy of Sciences (Yakutsk, Russia) (analysts N.V. Khristoforova, S. K. Popova, S. A. Karpova). The quantitative analysis was carried out using Software INCA Energy (Version 4.17, Oxford Instruments, Abingdon, Oxfordshire, UK) with XPP matrix correction scheme developed by Pouchou and Pichoir. Operating conditions included 20 kV voltage, a beam current of 1.08 nA and a beam diameter of 1 μm,

measurement time 10 s. Analitical lines: Bi–Mα; Te, Pb, Ag, Sb, S–Lα; Cu, Fe, Zn, S–Kα. Standards: gold 750%–Au, Ag, Bi_2S_3–Bi (bismuthinite), HgTe (coloradoite)–Hg, Te, $CuSbS_2$ (chalcostibite)–Cu, Sb, S, Tl (Br,I)—Tl, ZnS (sphalerite)–Zn, $CuFeS_2$ (chalcopyrite)–Fe, PbS (galena)–Pb, FeAsS (arsenopyrite)–As. Element detection limits (wt%) X-ray spectral microprobe analysis: Au 0.117, Ag 0.061, Hg 0.083, Cu 0.031, Fe 0.019, Pb 0.066, Bi 0.095. Limits of element detection (wt%) scanning electron microscope equipped with energy spectrometer: Au 1.84, Ag 0.96, Hg 1.6, Cu 1.22, Fe 1.04, Pb 1.78, Bi 2.7.

Microthermometric studies of fluid inclusions were carried out at the Department of Mineralogy of St. Petersburg State University in a thermal chamber mounted on a POLAM P-211 microscope, and also at the "Geomodel" Resource Center Saint Petersburg State University on Olympus BX53F optical microscope complete with microthermometric system THMSG-600-ec with LNP95 liquid nitrogen sample cooling system at temperature range from −196 to +600 °C. The accuracy of temperature measurements is ±0.1 °C in the temperature range from −20 to +20 °C. The composition of the liquid and vapour phases of fluid inclusions in quartz was analyzed there on the Horiba LabRam HR800 Raman spectrometer at the «Geomodel» Resource Center SPSU (analyst V.N. Bocharov), an Ar laser with a wavelength of 514.5 nm and 488 nm, an exposure time of 3 s, the number of repetitions—5, the laser power-50 MW, and the magnification of the microscope-50×.

3. Results

3.1. Tellurium Minerals

The tellurium mineralization of AS is characterized by a wide diversity of mineral species. Currently, 29 tellurium minerals are found in the ores: 16 tellurides, 5 sulfotellurides, and 8 tellurates, of which 2 are unidentified (Table 1). They usually form micro-and nano-inclusions with a size of 1–20 μm, with the exception of the ores of the Bodorono and Khatyrkhay deposits, where the sizes of tellurobismuthite and/or tetradymite reach 3 mm. The shape of the grains is round-oval, elongated, needle-like, or irregular angular. Tellurium minerals occur both as monoinclusions and in ensembles of two or three tellurides.

Table 1. Tellurium minerals of the Aldan Shield.

Tellurides	Sulfotellurides	Tellurates
calaverite ($AuTe_2$)	Te-canfieldite ($Ag_8Sn(S,Te)_6$)	smirnite (Bi_2TeO_5)
montbrayite Au_2Te_3	cervelleite (Ag_4TeS)	kuranakhite ($PbMnTeO_6$)
krennerite ($AuAgTe$)	tetradymite Bi_2Te_2S	yafsoanite ($(Zn,Ca,Pb)_3TeO_6$)
sylvanite $(AuAg)_2Te_4$	sulphotsumoite (Bi_3Te_2S)	kuksite $(Pb_3Zn_3TeO_6(PO_4)_2)$
petzite (Ag_3AuTe_2)	goldfieldite	cheremnykhite
stutzite ($Ag_{4.7}Te$)	($Cu_{12}(Te,Sb,As)_4S_{13}$)	$(Pb_3Zn_3TeO_6(VO_4)_2)$
hessite (Ag_2Te)		V,Si-dugganite
volynskite ($AgBiTe_2$)		$(Pb_3Zn_3Te(As,V,Si)_2O_4(OH))$
tellurobismuthite (Bi_2Te_3)		Unidentified Tl tellurates
hedleyite (Bi_7Te_3)		Unidentified Tl
tsumoite ($BiTe$)		telluroantimonates
rucklidgeite ($PbBi_2Te_4$)		
merenskyite ($(Pd,Pt)(Bi,Te)_2$)		
melonite ($NiTe_2$)		
altaite ($PbTe$)		
coloradoite ($HgTe$)		

Tellurium minerals of two systems predominate: Au-Bi-Te and Au-Ag-Te. The tellurides of the Au-Ag-Te system are characterized by the greatest diversity. Seven minerals have been identified. These minerals often form inclusions in pyrite, and are also found in calcite, quartz, bornite, and tennantite (Figure 2). Among the minerals of the Au-Bi-Te system, the most common are the tellurides of the tetradymite group (tellurobismuthite, tetradymite, tsumoite, sulfotsumoite, and hedleyite). Tellurides are commonly found in pyrite, galena, galenobismutite, chalcopyrite, pyrrhotite, and quartz (Figure 3).

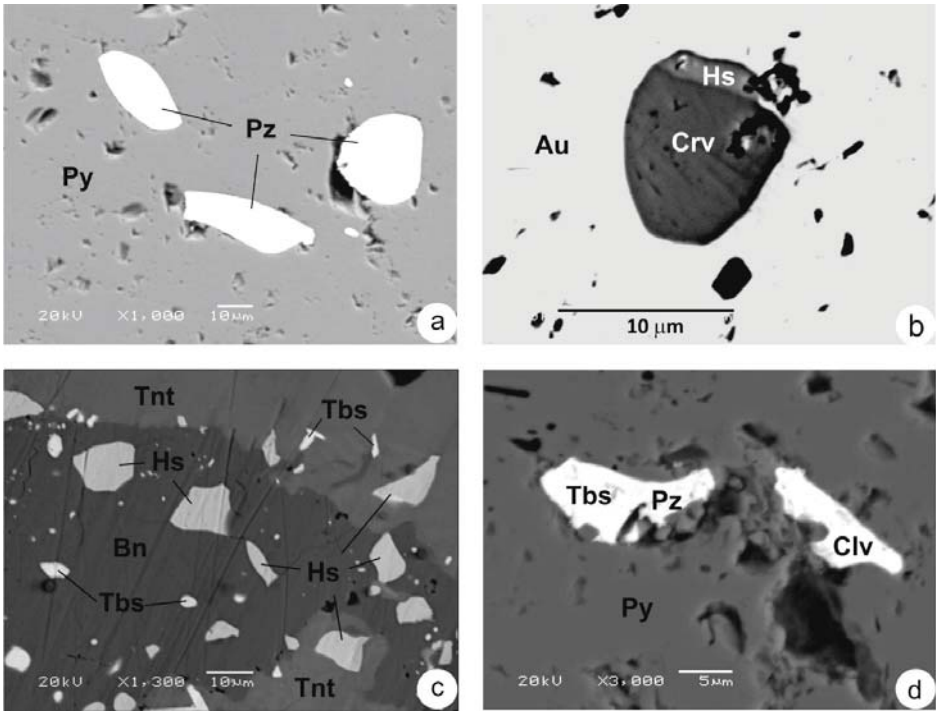

Figure 2. Au-Ag-Te mineralization: (**a**)—round-oval petzite (Pz) grains in pyrite (Py). Maiskoye ore field of the Tyrkandinsky cluster, (**b**)—grain of cervelleite (Crv) with hessite (Hs) rim in native gold (Au), Spokoinoye ore field of the Tyrkandinsky cluster, (**c**)—angular grains of hessite (Hs) and tellurobismuthite (Tbs) in the bornite (Bn)-tennantite (Tnt) matrix, Obman ore occurrence of the Nimgerkansky cluster, (**d**)—intergrowth of tellurobismuthite (Tbs) with petzite (Pz) and calaverite (Clv) grain in pyrite (Py), Granitnoye ore occurrence of the Nimgerkansky cluster.

3.2. Typification of Telluride Mineralization

The analysis of the species composition of Te minerals in the AS gold deposits allowed us to identify three mineral types: Au-Ag-Te, Au-Bi-Te, as well as the type, where the mineralization of both systems is combined and identified as a mixed one (Table 2).

3.2.1. Au-Ag-Te Mineral Type

The first type includes the deposits of the CAD–Kuranakhsky, Elkonsky, Yukhtinsky, and Dzhekondinsky fields, as well as the mineralization of the Upper-Tokkinsky cluster and the Khokhoy deposit of the Verkhneamginsky cluster. The Au-Ag-Te type is represented more often by petzite, hessite, and supergene Te minerals, and less often by coloradoite, altaite, and calaverite (Figure 2, Tables 3, 5 and 6). Bi tellurides are absent, the exception is tellurobismuthite of the Podgolechnoye deposit, where it plays a subordinate role. The extensive and diverse list of associated minerals includes selenides (clausthalite (PbSe), naumannite (Ag_2Se), tiemannite (HgSe)); sulfides (cinnabar (HgS), stibnite (Sb_2S_3), orpiment (As_2S_3), acanthite (Ag_2S), uytenbogaardtite (Ag_3AuS_2)); Ag chlorides and bromides (chlorargyrite (AgCl), bromargyrite (AgBr)); emphasizes the epithermal of Au-Ag-Te type ores. This mineral type also includes the low-temperature thallium mineralization of the Khokhoy deposit of the Verkhneamginsky cluster, represented by thallium tellurates and telluroantimonates with weissbergite ($TlSbS_2$), avicennite (Tl_2O_3) and thallium antimonates (Table 7) [33,40]. A characteristic feature of ores bearing Au-Ag-Te mineralization is the susceptibility to supergene changes. In the ores of the Kuranakh deposit, the largest in AS,

tellurides are represented exclusively by Au and Au-Ag species (sylvanite predominates), Ag tellurides have not been identified. The minerals are characterized by a noticeable concentration of Hg and Se, as well as a certain excess of Te in the composition (Table 3). The sulfides associated with them are characterized by an impurity of Te and a deficiency of S [14].

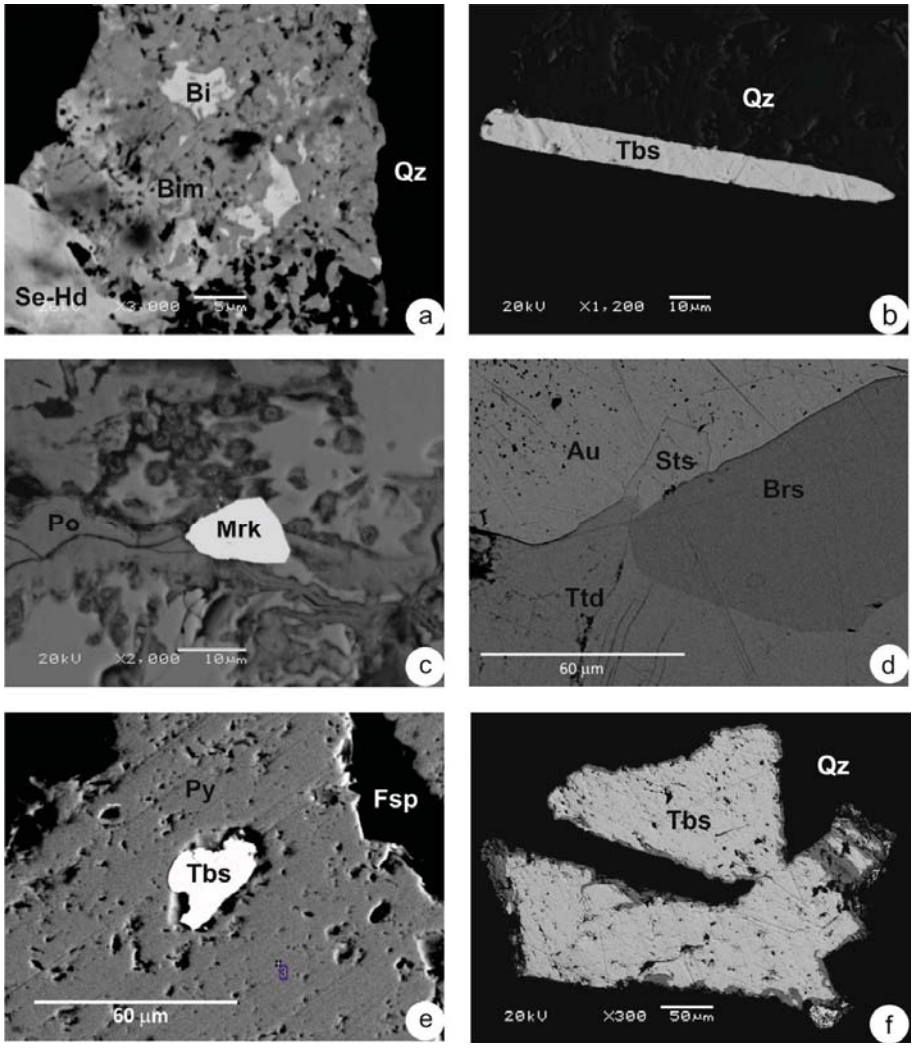

Figure 3. Au-Bi-Te mineralization: (**a**)—particles of native bismuth in bismuthinite (Bim) and Se-hedleyite (Se-Hd) grain in quartz (Qz), the Bodorono deposit of the Verkhnealgominsky cluster, (**b**)—needle-shaped grain of tellurobismuthite (Tbs) in quartz (Qz), the Bodorono deposit of the Verkhnealgominsky cluster, (**c**)—merenskyite (Mrk) in pyrrhotite (Po), the Dyvok ore occurrence of the Verkhnealgominsky cluster, (**d**)—the relationship of tetradymite (Ttd), bursaite (Brs), sulphotsumoite (Sts) and native gold (Au), the Lagernoye ore occurrence of the Altan-Chaidakhsky ore cluster, (**e**)—grain of tellurobismuthite (Tbs) in pyrite (Py) among feldspar (Fsp), the Malenkoye ore occurrence of the Guvilgrinsky ore cluster, (**f**)—tabular grains of tellurobismuthite (Tbs) in quartz (Qz), the Khatyrkhay ore occurrence of the Verkhneamginsky ore cluster.

Table 2. Types of telluride mineralization of the Aldan shield.

Ore Node	Deposit, Ore Occurrence	Metasomatites	Geochemical Association	Te Minerals	Associated Minerals	Fineness of Native Gold	Formation Temperature	References
Au-Ag-Te Mineral Type								
Kuranakhsky	Bokovoye and Delbe	Jasperoids	Au-Te in pyrite-quartz metasomatites	Altaite, coloradoite, petzite, krennerite, calaverite, sylvanite	Cinnabar, arsenopyrite, stibnite	700–900%	200–150	[14]
			Au-Te-Se and Au-tellurates in calcite veins	Altaite, coloradoite, petzite, kuranakhite, yafsoanite, kuksite, cheremnykhite, V,Si-dugganite	Clausthalite, naumannite, tiemannite, cinnabar, orpiment, descloizite	720–920%	120–70	[13–17]
Yukhtinsky	Samolazovskoye	Jasperoids	Au-Ag-Te	Hessite, coloradoite, calaverite	Cinnabar, tiemannite, acanthite, native Ag, sulvanite, roscoelite			[18,21,25,26]
Elkonsky	Fedorovskoye (Lunnoye)	Gumbeites	Au-Ag-Te	Te-canfieldite, hessite, Ag sulphotelluride	Native Ag, acanthite, chlorargyrite, bromargyrite, Ag-Tl sulphosalts			[20–22]
	Ryabinovoye (Muscovitoviy and Noviy)	Sericite-microcline	Au-Ag-Te	Hessite, petzite, Pt-Pd tellurides	Uytenbogaardtite			[21]
Dzhekon-dinsky	Podgolechnoye	Sericite-microcline	Au-Ag-Te	Hessite, petzite, montbrayite, stutzite, tellurobismuthite	Roscoelite			[24]
Verkhne-Tokkinsky	Gross	Gumbeites	Au-Ag-Te	Hessite, petzite, Te-canfieldite	Acanthite			[29]
	Tabornoye	Gumbaites	Au-Ag-Te	Au and Ag tellurides				[28,29]
Verkhneam-ginsky	Khokhoy	Jasperoids	Au-Te-Sb-Tl	Tl tellurates and telluroantimonates	Weissbergite, avicennite, acanthite, chlorargyrite, Tl antimonates	834–992%		[32,33,40]
Complex Au-Ag-Te-Bi Mineral Type								
Lebedinsky	Lebedinoye, Radostnoye	Jasperoids	Au-Ag-Bi-Te	Hessite, calaverite, altaite, tetradymite	Native Ag, Bi, cinnabar, aikinite, lillianite, bursaite, Bi tennantite-annivite, tennantite, arsenosulvanite			[19,41]

Table 2. *Cont.*

Ore Node	Deposit, Ore Occurrence	Metasomatites	Geochemical Association	Te Minerals	Associated Minerals	Fineness of Native Gold	Formation Temperature	References
Nimger-kansky	Obman, Granitnoye	Argillizites	Au-Ag-Bi-Te	Hessite, petzite, calaverite, tellurobismuthite, volynskite, goldfieldite	Tennantite, jalpaite	776–809%		[27]
Verkhne-amginsky	Khatyrkhay	Gumbeites, beresites	Au-Ag-Bi-Te	Tellurobismuthite, hessite, petzite, altaite, calaverite, tsumoite	Tennantite	858–878%	230–210	[30–32,34]
Verkhealgominsky	Dyvok	Argillizites, beresites	Au-Ag-Bi-Te	Hessite, altaite, volynskite, merenskyite, melonite, rucklidgeite		650–830%	230–200	[38] and unpublished authors' data
Tyrkandinsky	Spokoinoye, Maiskoye	Argillizites, beresites, sericite-microcline	Au-Ag-Bi-Te	Petzite, hessite, cervelleite, tellurobismuthite	Acanthite, galena, matildite, native Bi and Sn, scheelite	761–783%		unpublished authors' data
Au-Bi-Te Mineral Type								
Verkhe-algominsky	Bodorono	Beresites, argillizites	Au-Bi-Te	Tellurobismuthite, tetradymite, hedleyite, Se hedleyite, smirnite	Native Bi, bismuthinite, lillianite, Se galena, laitakarite	830–940%	200–150	[35,37]
Altan-Chai-dakhsky	Lagernoye	Beresites, argillizites	Au-Bi-Te	Tetradymite, tellurobismuthite, sulphotsumoite	Bursaite, lillianite, cosalite, galenobismutite	862–893%	365–276	[36]
Guvilgrin-sky	Malenkoye	Argillizites	Au-Bi-Te	Tellurobismuthite, petzite	Galena, scheelite	898–999%		unpublished authors' data

Table 3. Chemical composition of tellurides and sulfotellurides of Au, Ag by EMP analysis.

Mineral	Te	Au	Ag	Bi	Hg	Cu	Fe	Ni	Sn	Se	S	References
Kuranakh. Pyrite-Quartz Metasomatites												
Petzite (7)	36.60	20.94	40.51		1.33							[14]
Krennerite (7)	59.01	33.12	7.27									
Calaverite (9)	57.91	41.52	0.33									
Sylvanite (5)	63.33	25.62	10.21		0.30							
Kuranakh. Calcite Veins												
Petzite (5)	33.90	20.05	41.10		2.00					1.11	0.09	[14]
Maiskoye												
Hessite (5)	37.60–38.59 38.40		61.61–62.74 62.34									unpublished authors' data
Cu cervelleite	23.12–23.46 23.29		65.32–65.77 65.55			2.64–3.47 3.06					4.63–4.83 4.73	
Petzite (13)	34.38–37.32 35.60	17.63–24.08 21.71	41.78–45.89 43.17									
Spokoinoye												
Hessite (4)	38.46–40.29 39.33		60.14–61.32 60.59									unpublished authors' data
Cervelleite (2)	25.12–27.37 26.25		65.19-68.23 66.71								4.59–5.07 4.83	
Cu cervelleite (3)	24.14–24.41 24.31		66.00-66.83 66.32			5.15–5.92 5.53					4.93–5.38 5.22	
Dyvok												
Hessite (2)	37.2–40 38.60		55.88–58.92 57.40	0–0.69 0.35			1.81–2.96 2.39	0–0.99 0.50				unpublished authors' data
Nimgerkan												
Hessite (14)	33.99–38.99 36.32		59.27–63.44 61.32			0–2.92 1.77						[27]
Petzite (3)	31.73–32.95 32.20	23.68–24.79 24.40	40.96–41.53 41.24			0–3.85 2.46	0–2.41 0.80					
Calaverite (2)	47.98–48.73 48.35	46.85–46.96 46.9					1.79–2.36 2.07					
Podgolechnoye												
Montbrayite	46.60	53.40										[24]
Petzite (8)	30.78–34.92 33.54	21.98–27.21 25.29	38.81–42.00 41.25									
Stutzite (2)	43.21–45.03 44.12		54.97–56.79 55.88									
Hessite (13)	35.61–40.22 38.06	0-4.4 0.34	58.31–64.39 61.66									

Table 3. *Cont.*

Mineral	Te	Au	Ag	Bi	Hg	Cu	Fe	Ni	Sn	Se	S	References
Lunnoye												
Te-canfieldite (7)	18.63–19.17 18.96		62.98–63.65 63.40						7.81–8.20 8.01		9.22–9.56 9.42	[22]
Khatyrkhay												
Petzite	32.67	25.31	41.86									[34]
Hessite	34.62	4.91	60.71				0.48					

Note. The Tables 3–5 and 7 above the line show the minimum and maximum values, below the line–the average value, in parentheses–the number of analyses.

Table 4. Chemical composition of tellurides and sulfotellurides Bi.

Mineral	Te	Ag	Bi	Pb	Cu	Fe	Sb	Se	S	References
Altan-Chaidakhsky										
Tellurobismuthite (3)	45.25–46.3 45.72		51.46–52.47 51.98							
Tetradymite (19)	31.63–35.14 34.36	0–0.5 0.03	56.09–59.55 57.63	0–4.48 1.05				0–0.2 0.07	4.67–5.34 4.95	[36]
Pb-tetradymite (7)	30.6–31.12 30.90	0	53.46–55.01 54.53	6.00–7.97 7.06				0.02–0.15 0.09	5.64–5.84 5.72	
Sulphotsumoite (2)	21.57–22.64 22.11	0–0.02 0.01	71.01–71.86 71.44	0.38–1.45 0.92				0.07–0.08 0.08	2.98–3.19 3.09	
Khatyrkhay										
Tellurobismuthite (18)	47.36–49.67 48.54	0–0.30 0.05	49.27–52.17 50.31	0–0.08 0.01	0–0.11 0.03	0–0.09 0.04			0–0.03 0.00	[32]
Tetradymite (3)	36.53–37.50 37.12	0.00	56.67–58.02 57.19	0–0.07 0.02	0–0.08 0.03	0.02–0.04 0.03			4.19–4.33 4.27	
Tsumoite (3)	34.59–38.00 35.75		62.00–65.41 64.25							[30]
Bodorono										
Hedleyite	19.71		80.14							
Se hedleyite (2)	13.77–16.59 15.18		80.06–80.89 8.47					3.72–5.17 4.44		[37]
Sulphotsumoite	22.49		64.86	4.4					5.59	
Tetradymite	35.84		59.32						4.84	
Guvilgra										
Tellurobismuthite	48.4		53.41							unpublished authors' data

Table 4. *Cont.*

Mineral	Te	Ag	Bi	Pb	Cu	Fe	Sb	Se	S	References
Nimgerkan										
Tellurobismuthite (10)	42.93–46.38 44.91		49.42–55.68 52.57		0–5.81 1.47	0–2.65 0.88				[27]
Volynskite (4)	40.01–42.35 40.79	18.02–20.58 19.77	32.11–36.30 34.03		4.00–4.94 4.44	0–1.48 0.37				
Dyvok										
Volynskite	41.48	18.53	34.48	1.6		2.69			0.69	unpublished authors' data
Rucklidgeite	47.35		36.78	12.62		4.49			0.59	
Maiskoye										
Tellurobismuthite (6)	47.69–49.16 48.21		51.17–52.60 51.95							unpublished authors' data
Podgolechnoye										
Tellurobismuthite (2)	47.32–48.91 48.00		51.09–52.24 52.00							[24]
Lebedinoye										
Tetradymite (2)	34.66–35.44 35.05	0.03	58.13–58.85 58.49	0–0.61 0.3	0.08–0.18 0.13	0–0.03 0.01	0.25–0.33 0.29		4.55–4.59 4.57	[19]

Table 5. Chemical composition of Pb, Hg, Pd and Cu tellurides and sulfotellurides.

Mineral	Te	Ag	Bi	Pb	Hg	Cu	Fe	As	Ni	Pd	Se	S	References
Kuranakh. Pyrite-Quartz Metasomatites													
Altaite	39.64	0.52		59.36									[14]
Coloradoite	39.90			0.82	58.05								
Kuranakh. Calcite Veins													
Altaite	31.83			63.54							1.35	2.97	[14]
Coloradoite	38.58				0.80						1.00	0.11	
Dyvok													
Merenskyite	66.9		5.44				1.05		4.01	24.55			unpublished authors' data
Altaite	37.2			60.25			2.92						
Melonite	74.34						4.22		20.15			2.58	
Nimgerkan													
Goldfieldite (2)	14.43–15.07 14.75					49.66–50.70 50.18	0–1.08 0.54	8.92–9.53 9.23				26.14–26.58 26.36	[27]

Table 6. Chemical composition of supergene Te minerals of the Kuranakh deposit.

Mineral	TeO_3	ZnO	CaO	PbO	As_2O_3	P_2O_5	V_2O_5	Sb_2O_5	SiO_2	MnO	H_2O	References
Yafsoanite (crystals) (11)	42.11	24.65	16.79	12.82					0.21		2.02	[14]
Yafsoanite (Concentric-zonal) (15)	39.91	27.38	18.47	8.86					1.56		2.77	
Zn-yafsoanite (5)	38.33	50.23	0.60	9.19					2.13		1.16	
Kuksite (9)	14.30	20.76	1.45	50.59		10.38	1.81		0.40			[16]
Cheremnykhite (10)	13.76	18.89		53.04	2.02		9.25		2.16			
V,Si-dugganite (8)	14.15	18.33		51.94	7.10		4.30	0.25	2.37		0.25	[15]
Kuranakhite	38.20			45.40						15.40		[13]

Table 7. Chemical composition of supergene Te minerals of the Khokhoy deposit.

Mineral	Te	Sb	Tl	O	References
Tl tellurates (3)	20.22–21.89 21.00		60.85–61.77 61.29	17.24–17.45 17.37	unpublished authors' data
Tl telluroantimonates (4)	6.00–6.91 6.45	9.37–11.20 10.30	65.25–67.50 66.25	17.17–18.34 17.73	

3.2.2. Au-Bi-Te Mineral Type

The deposits of the Guvilgrinsky and Altan-Chaidakhsky clusters, as well as the Bodorono deposit of the Verkhnealgominsky cluster, are classified as the Au-Bi-Te type. Bi tellurides are developed here, mainly tellurobismuthite, less often hedleyite, and Bi sulfotellurides–tetradymite and sulphotsumoite (Figure 3, Table 2). The associated minerals are native Bi, bismuthinite, Pb sulphobismuthites–lillianite ($Pb_3Bi_2S_6$), bursaite ($Pb_5Bi_4S_{11}$) and cosalite ($Pb_5Bi_2S_5$). Fe, Cu, and Pb impurities in Te minerals are often related to the capture of the elements from matrix minerals–pyrite, pyrrhotite, galena, and chalcopyrite (Table 4). Note the presence of Se-containing hedleyite and associated laitakarite and Se-containing galena in the ores of the Bodorono deposit, as well as Pb-containing tetradymite in the Altan-Chaidakh deposit. A large role of lead is generally characteristic of the Au-Bi-Te type ores, as evidenced by the composition of the associated minerals.

3.2.3. Mixed Au-Ag-Bi-Te Mineral Type

The mixed-type deposits of the Lebedinsky, Nimgerkansky, Tyrkandinsky, and the Khatyrkhay ore occurrences of the Verkhneamginsky and Dyvok of the Verkhnealgominsky clusters contain minerals of both systems, and there are also single grains of such rare minerals as merenskyite, rucklidgite, and melonite in the ores of the Dyvok occurrence (Table 2) [38]. The associated minerals are diverse: native bismuth, galena, acanthite, scheelite, tin, and Pb sulfobismuthides–lillianite ($Pb_3Bi_2S_6$), bursaite ($Pb_5Bi_4S_{11}$) and aikinite ($PbCuBiS_3$), Ag sulfobismuthide–matildite ($AgBiS_2$), as well as Bi-containing tennantite-annivite and tennantite. In the Te minerals of the Nimgerkan ore occurrence, Cu and Fe impurities are recorded, captured from the surrounding minerals–pyrite, tennantite, and bornite. A typical feature of the rare sulfotelluride Ag, cervelleite, is an impurity of Cu up to 6wt%. The relationships of tellurides of both systems in the ores of the Nimgercansky cluster demonstrate their syngenenticity, expressed in the spatial combination of angular grains of tellurobismuthite and hessite without signs of substitution or intersection, as well as the facts of intergrowth of tellurobismuthite and petzite (Figure 2c,d).

3.3. Gold Speciations

Gold in the ores of the AS deposits is present in three varieties: invisible gold in pyrite, native gold, and gold in the composition of tellurides.

Studies of invisible gold by inductively coupled plasma mass spectrometry (LA-ICP-MS) were carried out in pyrite from the Lunnoye, Samolazovskoye and Ryabinovoye deposits (the Muscovitoviy and Noviy sites) [21]. It is noted that the primary ores of the Lunnoye and Samolazovskoye deposits belong to refractory ores due to the significant amount of gold associated with sulfides. It is identified that pyrite from fine-grained aggregates is enriched with gold, as well as with As, Sb, Hg, and Tl correlating with it, where its content at the Samolazovskoye field reaches 600 g/t, at the Lunnoye–300 g/t, which exceeds the Au content in the coarser grained idiomorphic pyrite by two orders or higher. The dynamics of ablation shows a relatively uniform distribution of impurities in pyrite.

The average Au content in the pyrite of the Muscovitoviy ore occurrence of the Ryabinovoye deposit is only 0.14 g/t, the Noviy ore occurrence in the porous pyrite is

about 0.96 g/t, and in the massive one, 0.06 g/t. Cu, Pb, and Te are characterized by top-cut grades associated with inclusions of minerals that concentrated of the corresponding metals. The graph of changes in the contents of Au, Ag, and Te during ablation indicates that the noble metals are present as inclusions of native gold with an Ag impurity and Au and Ag tellurides. Gold in the porous pyrite of the Noviy site positively correlates with Ag and Te; no significant correlations were found for the pyrite of the Muscovitoviy site [21].

Native gold, which is associated with tellurides, is of a usually porous structure. Spongy and mustard gold is often found in Au-Ag-Te deposits (Figure 4) [14,33,41,42]. The grain size varies, and relatively large gold is typical for the Au-Bi-Te type. Native gold associated with Au-Ag-Te type minerals usually has a dimension from the dust to the fine class, while in the sypergene zone there is a noticeable increase in size of the gold. There are few data on the fineness of native gold, which is directly associated with Te mineralization (Table 2). The fineness of native gold ranges from 650 to 999%. The comparison of the fineness of different types of telluride mineralization is complicated by the fact that post-ore supergene processes are widely developed in Au-Ag-Te ores, where Au refinement occurs. Nevertheless, the lower limits of the fineness of native gold of mineralization of the Au-Ag-Te type begin with 700% [14], in the mixed type–range from 650 to 878% (excluding the ores of the Lebedinsky deposit, also subjected to the processes of supergene) and finally, in the Au-Bi-Te type, the fineness is 830–999%. Thus, we can state a decrease in the fineness of native gold from the Au-Bi-Te type to the Au-Ag-Te. The decrease in the fineness of native gold is consistent with the sequence and temperatures of formation of Te minerals and associated mineral paragenesis from epithermal–mesothermal Au-Bi-Te (830–999%) to the epithermal Au-Ag-Te (>700%).

3.4. Fluid Inclusions

There is not much information on fluid inclusions (FI) in gold-telluride ores of AS. We studied the FI in the Au-Bi-Te the mineral type ores of the Bodorono (Verkhnealgominsky cluster) and Lagernoye (Altan-Chaidakhsky cluster) deposits, as well as the mixed Au-Ag-Bi-Te type of the Dyvok ore occurrence (Verkhnealgominsky cluster).

Three types of inclusions were found in quartz from the gold-tellurium-bismuth-quartz association of the Bodorono deposit: Type I—monophase aqueous inclusions; type II—two-phase gas-liquid inclusions, according to Raman spectroscopy data they contain H_2O liquid and CO_2 vapour. The homogenisation temperature is ranging from 145 to 200 °C; type III—three-phase carbon dioxide-water inclusions (H_2Oliq+CO_2liq+CO_2vap) sometimes with impurities of CH_4 and N_2 vapour. The temperature of homogenisation of liquid CO_2 into gas was 28–29 °C. The density of liquid CO_2 is 0.63–0.65 g/cm^3. The pressure is estimated at 0.4–0.6 kbar. Composition of the vapour phase (mol.%): CO_2 95.2, N_2 2.9, CH_4 1.9. The formation temperature of the earlier gold-polymetallic assemblage is estimated at 270–300 °C [37].

FI data on the Dyvok ore occurrence suggest the formation of the early auriferous mineral assemblage (arsenopyrite-pyrite-quartz) at temperatures of 300–335 °C and a pressure of 0.7 kbar. Studies of quartz from the middle gold-chalcopyrite-sphalerite assemblage showed homogenisation temperatures of 250–280 °C. The latest quartz-telluride association is characterised by an average homogenisation temperature of 210–230 °C.

Microthermometric studies of the FI of the Altan-Chaidakh ore cluster have determined that the formation of the gold-polymetallic assemblage occurred at temperatures of 300–331 °C from Mg,Cl-solutions, with CO_2 and impurities of CH_4 in the vapour phase. The gold-tellurium-bismuth assemblage was formed at close temperature values (276–365 °C) from Mg-Na-KCl- solutions with a predominant CO_2 content in the vapour phase.

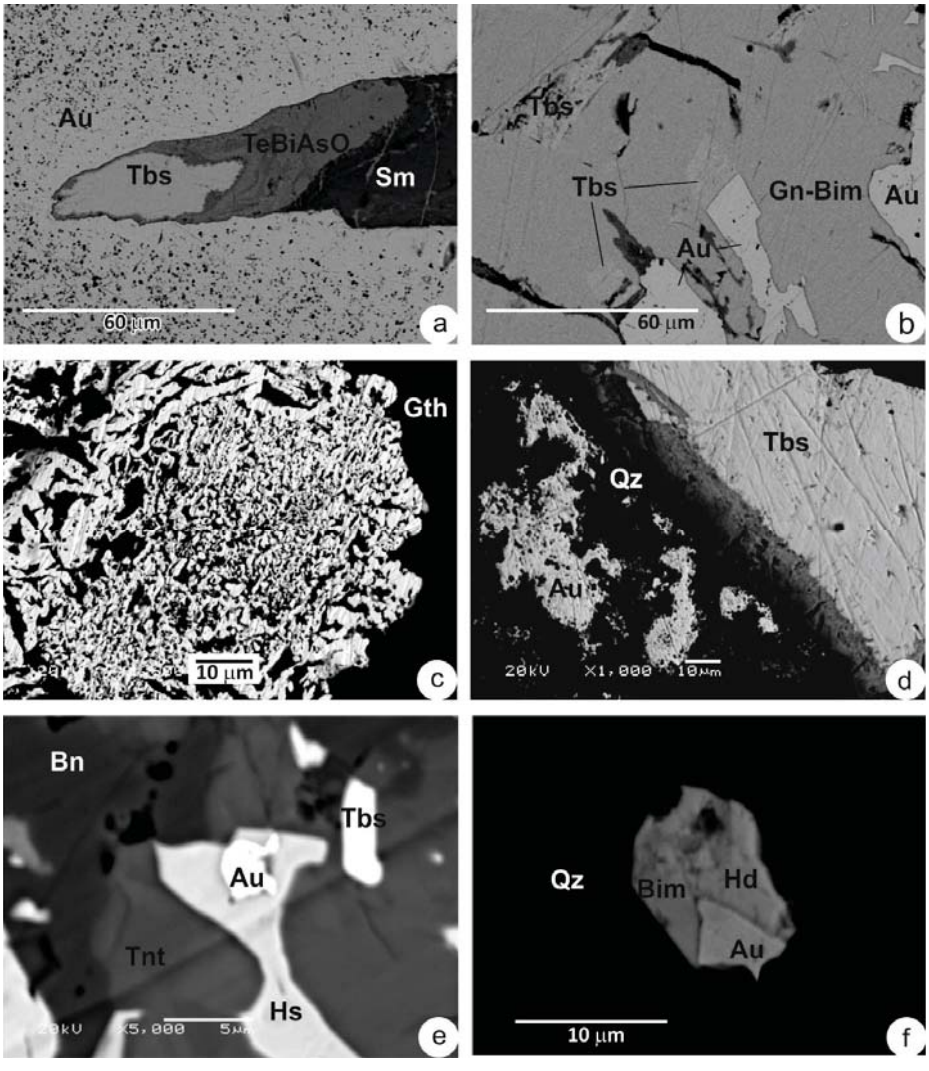

Figure 4. Native gold: (**a**)—substitution of tellurobismuthite (Tbs) for smirnite (Sm) and tellurates (TeBiAsO) in porous gold (Au), the Lagernoye ore occurrence of the Altan-Chaidakhsky ore cluster, (**b**)—replacement of platy grains of tellurobismuthite (Tbs) for native gold (Au) in galenobismutite (Gn-Bim), the Lagernoe ore occurrence of the Altan-Chaidakhsky ore cluster, (**c**)—spongy gold in goethite (Gth), the Khokhoy ore occurrence of the Verkhneamginsky ore cluster, (**d**)—porous gold (Au) and tabular grain of tellurobismuthite (Tbs) in quartz (Qz), the Khatyrkhay ore occurrence of the Verkhneamginsky ore cluster; (**e**)—native gold (Au) in hessite (Hs) and tellurobismuthite (Tbs) grain in bornite (Bn)-tennantite (Tnt) matrix, the Obman ore occurrence of the Nimgercansky ore cluster, (**f**)—the relationship of native gold (Au), bismuthinite (Bim) and hedleyite (Hd) in quartz (Qz), the Bodorono deposit of the Verkhnealgominsky cluster.

The ore mineralization of quartz-chlorite-feldspar metasomatites of the Khatyrkhay ore occurrence in the Verkhneamginsky region, represented by two assemblages, was studied by I.Prokopyev (2019). The first association represented by sulfide minerals: pyrite, chalcopyrite, galena, sphalerite, molybdenite, boulangerite, etc. is formed from highly concentrated (44–22 wt.% NaCl-eq.) of fluid $CO_2 \pm N_2$ solutions at temperatures

of 330–400 °C and at a pressure of 1150 bar. The late gold-telluride ore mineralization was formed from low-concentrated (3.3–9.2 wt.% NaCl-eq.) of fluid CO_2 solutions at temperatures of 210–230 °C [34].

Pressure-Temperature (P-T) parameters of the formation of the Lebedinoye deposit were studied in quartz of different paragenesis of the first (tremolite-quartz-magnetite-sulfide) and second (quartz-carbonate-gold-bismuth-sulfide) stages (Orekhovaya and Vodonosnaya deposits) [19]. The results of studies of ore mineralization of the Orekhovaya deposit showed that the temperatures of fluid homogenisation in tremolite are 342–316 °C, quartz, which is in the same paragenesis with tremolite, 321 °C. T_{hom} of inclusions in later quartz generations decreases: 284–223 °C and 195–157 °C. Pressure—570–440 bar. The study of fluid inclusions in quartz of ore samples of the Vodonosnaya deposit shows T_{hom} of fluid inclusions of 500–484 °C, pressure—2040–1260 bar. T_{hom} values of inclusions of later quartz generations are close to the quartz temperatures in ore samples of the Orekhovaya ore deposit, but the pressure values vary significantly from 450 to 3180 bar.

High salt concentrations (46.9–51.5 wt.% NaCl-eq.) obtained at T_{hom} 186–162 °C and a pressure of 2250–2130 bar. In other samples, at T_{hom} 339–310 °C, 231 °C, 177–136 °C and a pressure drop (1530–640 bar), the salt concentration decreases and is 10.9–6.2, 9.2 and 1.2–0.5 wt.% NaCl-eq. [19].

According to the results of the study of FI at the Kuranakh deposit, the temperature of formation of the early quartz-pyrite assemblage with fine-grained quartz 1 and finely-dispersed gold in pyrite is 350–200 °C, quartz-polysulfide assemblage with pyrite and riziform quartz 2 and visible gold-250–200 °C. The formation of Au-Ag-Te mineralization in quartz veins occurs at temperatures of 220–150 °C, and the Au-Te-Se and Au-tellurate mineralization in calcite veins decreases to 120–70 °C. Thus, there is a regressive regime of the ore formation process with temperature inversions in the range of 50–100 °C, as well as a change in mineral assemblages [14].

4. Discussion

The Aldan alkaline volcanogenic-intrusive complex was formed in several stages [5]. In the first stage (Late Triassic–Early Jurassic), sills of quartz porphyry, orthophyre, and nordmarkite were intruded into the platform cover, accompanied on the surface by domes and trachyte covers. In the second stage (Middle–Late Jurassic), concentric-zonal plutons of platinum-bearing dunites, wehrlites, and gabbroids were formed, followed by alkaline volcanic plutons, stocks, dikes of alkaline gabbroids and syenites, and their effusive analogues (alkaline trachytes, pseudoleucitic phonolites). In the third stage (Late Jurassic–Early Cretaceous), laccoliths, stocks, dikes of monzonites, subalkaline syenites, and granosyenites were intruded. In the fourth stage (Late Cretaceous), the stocks of aegirine granites and regional dike belts of syenite-porphyry, orthophyre, minette, bostonite, and picrite were formed.

The formation of the Aldan alkaline volcanogenic-intrusive complex involved metasomatic changes in rocks. In the Central Aldan region, four metasomatic formations are gold-producing: gumbaite, sericite-microcline metasomatites, jasperoid and argillizited [5,11].

The gold mineralization of AS is diverse. The metasomatites of the gumbaite formation are represented by pyrite-carbonate-K-feldspar metasomatites, which are related to the main gold-uranium deposits of the Elkonsky ore cluster. Gold-copper-porphyry (Ryabinovsky) type of mineralization, including veined-disseminated sulfide mineralization in alkaline volcanic plutons (Ryabinovoye and Noviy deposits) is associated with the formation of sericite-microcline metasomatites. The jasperoid type of mineralization is represented by deposits formed in three geostructural settings: in the contact zones of the Mesozoic alkaline and subalkaline intrusions with carbonate rocks of the Vendian among hydrothermally altered dolomite marbles, magnesian skarns and syenites (Samolazovsky subtype); in zones of layered and transverse fracturing in the Vendian-Lower Cambrian carbonate rocks (Lebedinsky subtype) and at the contact of Lower Cambrian limestones with Jurassic sandstones (Kuranakhsky subtype). Gold-argillizited mineralization of the

Nimgerkansky type is spatially confined to the intrusions of syenite-porphyry of Cretaceous age and is associated with crystal-bearing and amethyst-bearing mineralization [11].

The systematization of Te mineralization demonstrates its presence in all available types of ore-bearing metasomatites, that indicates a regional large-scale manifestation in the area of AS. The process of ore formation is long, multi-stage, but in general, three producing stages are distinguished in most deposits—the early pyrite-quartz assemblage with finely-dispersed gold is replaced by (gold)-polysulfide-quartz and ends with gold-telluride.

The typification of gold mineralization on Te minerals and mineral assemblages revealed a certain zoning in the location of gold deposits on the area of AS. In general, the Aldan-Stanovoy Shield is characterized by zoning in the distribution of the Mesozoic magmatism derivatives. The Stanovoy geoblock is characterized by granitoid intrusions, while the Aldan geoblock mainly by subalkaline and alkaline ones. When considering the position of objects with Au-Ag-Te and Au-Bi-Te mineralization, zoning is traced, which is consistent with the distribution of derivatives of the Mesozoic magmatism. Au-Bi-Te mineralization is typical for deposits that are close to the Stanovoy plutonogenic region in the areas of dikes and small intrusions of acid composition in the Guvilgrinsky (granodiorites), Verkhnealgominsky (diorite porphyrites), and Altan-Chaidakhsky (granodiorites, diorite porphyrites, dacites) clusters. Au-Ag-Te mineralization is developed in the northern and central parts of the Aldan geoblock, where massifs of rocks of mainly subalkaline and alkaline composition were formed.

Lateral zoning is also observed in the distribution of mineralization types in the CAD area: mixed Au-Ag-Bi-Te mineralization with predominance of Bi is developed in ores of the Lebedinsky cluster, located in the center of the magmatogenic structure, where the most intense magmatism in the CAD occurs, covering all 4 stages of igneous activity, and mixed and the Au-Ag-Te ores in the Kuranakh and Yukhtin jasperoids, the Elkon and Jekondin gumbeites are developed on the periphery at a distance of 10–30 km.

Available data on the temperatures of formation of Au-Te mineralization (Table 2), as a rule, show their epithermal. Thus, the formation of the Au-Te mineralization of the Kuranakhsky cluster in quartz veins occurs at temperatures of 220–150 °C, and in calcite veins it decreases to 120–70 °C [14]. Au-Bi-Te mineralization can classed as the epithermal-mesothermal, the highest temperature of ore formation is shown by the mineralization of the Altan-Chaidakhsky cluster—365–276 °C. The Bodorono deposit, judging by the presence of Se-containing hedleyite and galena, as well as laitakarite and the formation temperature of 200–150 °C, has features of epithermal mineralization.

High-temperature inclusions of the Lebedinoye deposit with mixed Au-Ag-Bi-Te mineral type probably belong to the period of scarification, which strengthens the argument in favor of the connection of the hydrothermal process with magmatism. At the same time, the high pressure of ore-forming fluids may indicate a significant depth of the source. The large range of variations in salt concentrations may be due to the presence of two sources of ore-forming fluids: one is associated with dilute solutions, and the other with brines, the concentration of salts in which decreases with a drop in pressure. The data obtained indicate the heterogeneity of ore-bearing solutions, their connection with magmatism, the depth of formation of hearths in each specific deposit, and different sources of ore-forming hydrothermal solutions [19].

Te ores of the AS are characterized by a number of properties typical for the epithermal alkaline gold-telluride type (A-type). This was previously shown by Leontiev for the Samolazovskoye and Podgolechnoye deposits [24,26]. The characteristic features of A-type deposits are a close spatial relationship with alkaline magmatism, and a typical "mantle" association of elements (Te, V, and F), an important role in the minerals of Au and Ag tellurides, fluorite and vanadium-containing minerals (roscoelite, descloizite, sulvanite, arsenosulvanite, cheremnykhite and dugganite) [43,44]. Examples of A-type deposits are world-class facilities such as Cripple Creek (Colorado, USA, 673 t Au), Acupan (Philippines, 500 t Au, ~500 t Ag), Emperor (Fiji, >120 t Au), Ladolam (Papua New Guinea, 680 t Au), Kochbulak (Uzbekistan), etc.

The Kuranakh and Khokhoy deposits have features of Carlin-type mineralization: they are located in the area of tectonic-magmatic activation, are conjugated with intrusions of monzonite-granodiorite series, and are of normal and high alkalinity, strata of carbonate rocks, stratoidal disseminated deposits, presence of jasperoids, low content of sulfides, finely-dispersed gold in pyrite, typomorphic elements—Au-Tl-As-Hg-Sb-Te-Ba-F [4,33,40].

Numerous studies show the presence of gold of three varieties: invisible in pyrite or arsenopyrite, native gold and gold tellurides. With the advent in recent decades of the highly sensitive inductively coupled plasma mass spectrometry (LA-ICP-MS) method and, especially, the local version of this method with laser ablation of the substance directly from the sample, it became possible to determine gold and other trace elements in pyrite [45–49].

The gold and tellurium studies of the Emperor deposit [45] showed that gold is found in three different forms: as "invisible" or submicrometer-size inclusions of gold and tellurium in arsenian pyrite, as visible native gold and tellurium, and as tellurides. The pyrite from Emperor is among the most Au-(up to 11,057 ppm Au), Te-(up to 5796 ppm Te), and As-rich (up to 16.60 wt.% As) yet reported from any mineral deposit type.

In addition, Large, and Maslennikov (2020) [47] report a distinct chemical association of invisible gold in pyrite in the deposits studied. For example, in the Gold Quarry (Carlin type), Mt Olympus, Macraes and Konkera, the invisible gold is principally related to the arsenic content of pyrite. In contrast, in Kumtor and Geita Hill, the invisible gold is principally related to the tellurium content of pyrite. Other deposits (Golden Mile, Bendigo, Spanish Mountain, Witwatersrand Carbon Leader Reef (CLR)) exhibit both the Au-As and Au-Te association in pyrite. Some deposits of the Au-As association have late orogenic Au-As-rich rims on pyrite, which substantially increase the value of the ore. In contrast, deposits of the Au-Te association are not known to have Au-rich rims on pyrite but contain nano- to micro-inclusions of Au-Ag-(Pb-Bi) tellurides.

As a result of the studies conducted by Belogub [21] at the deposits of the Aldan Shield, it was found that fine-grained aggregates of iron disulfides are significantly enriched with impurities compared to idiomorphic pyrite. This may be due to both the higher growth rate of fine-grained aggregates and their more significant specific surface area, which contributes to the capture of impurities, and the defectiveness of the disulfides themselves, which contain submicron or nano-inclusions of minerals that concentrate of impurities, since the association of impurities observed for fine-grained aggregates of iron disulfides, in general, corresponds to the set of rare mineral species found in ores. In larger idiomorphic crystals, the impurity content is significantly lower, that is related to a lower growth rate, which does not contribute to the capture of incoherent (non-structural) impurities.

Au-Ag tellurides are important accessory minerals, carrying a significant proportion of the gold endowment in some low to medium temperature hydrothermal vein deposits [50]. At the Kochbulak and Kairagach deposits (Uzbekistan) [51–55], Golden Mile in Kalgoorlie, Western Australia [56] about 20% of Au is in telluride form, Cripple Creek, [57]; Emperor, Fiji—10–50% in the form of tellurides [58]; and Săcărîmb, Romania [59], at the Bereznyakovskoye deposit (S.Ural) about 80% of gold [60], Sandaowanzi [61] more than 95% of the extracted gold occurs in the form of tellurides. We assume that the tellurides of the gold deposits of the Aldan Shield are also an additional source of at least 20% of the total gold reserve.

The mechanism of formation of native gold from gold and silver tellurides was experimentally shown in the works [62–65]. The formation of spongy gold as a result of the decomposition of maldonite under supergene conditions was considered in studies [66,67] and hypogenic [68–73]. The porous gold in the studied ores is also the result of the decomposition of tellurides, as we have shown by the example of native gold from the Khokhoy deposit of the Verkhneamnginsky node [33]. Thus, the Au-Ag-Bi-Te minerals are one of the most important sources of gold in the world.

5. Conclusions

Systematization and generalization of published and original data on Te mineralization enables us to demonstrated a wide variety of mineral species and significantly expand the territory of distribution of Au-Te mineralization, which indicates its large-scale regional occurrence in the Aldan Shield. At the same time, tellurium minerals are developed in all known types of metasomatic formations. Gold is not only in an invisible state in sulfides and in the form of native particles of different fineness, but is also part of a variety of compounds: montbrayite (Au_2Te_3), calaverite ($AuTe_2$), sylvanite $(AuAg)_2Te_4$, krennerite (AuAgTe) and petzite (Ag_3AuTe_2). Au-Ag-Bi tellurides are important accessory minerals containing a significant proportion of the gold reserve.

Author Contributions: L.A.K. and G.S.A. conceived and designed the study, the paper, provided field work on gold deposits, provided valuable insights, interpreted the results, and wrote the paper. V.N.K. provided field work on gold-ore objects, performed mineralogical description and photographing of polished sections, conducted microthermometric studies. All authors have read and agreed to the published version of the manuscript.

Funding: The research was carried out within the framework of the state task of the Diamond and Precious Metals Geology Institute of the Siberian Branch of the Russian Academy of Sciences, funded by the Ministry of Science and Higher Education of the Russian Federation, project No 0381-2019-0004 and supported by grants of the Russian Foundation for basic Research No 18-45-140045 and No 19-35-90051.

Institutional Review Board Statement: Not applicable.

Informed Consent Statement: Not applicable.

Data Availability Statement: Not applicable.

Acknowledgments: The authors thank N. Khristoforova, S. Popova, and S. Karpova for their help in carrying out a large amount of work on the scanning electron microscope and X-ray spectral microanalyzer (Diamond and Precious Metals Geology Institute of the Siberian Branch of the Russian Academy of Sciences), V. Bocharov for his help using the Raman Spectroscopy (Saint Petersburg State University) and E. Sokolov for the organization of field work at gold mining facilities (JSC "Yakutskgeologiya") and for discussing the results of the research. The authors are grateful to anonymous reviewers for their comments and constructive suggestions.

Conflicts of Interest: The authors declare no conflict of interest.

References

1. Bilibin, Y. *Fundamentals of Placer Geology*; State United Scientific and Technical Publishing House: Moscow, Russia, 1938; 504p. (In Russian)
2. Petrovskaya, N.V.; Fastolovich, A.I. Nature of mineralization in Lebedinoe gold deposit (Aldan). *Sov. Geol.* **1940**, *2–3*, 54–65. (In Russian)
3. Petrovskaya, N.V.; Kazarinov, A.I. Gold deposits of the Central Aldan. In *Geology of the Main Gold Deposits of the USSR*; TsNIGRI: Moscow, Russia, 1951; Volume 2, 154p.
4. Vetluzhskikh, V.G.; Kim, A.A. Geological and commercial types of gold deposits in Southern Yakutia. *Otechestvennaya Geol.* **1997**, *1*, 16–24. (In Russian)
5. Ugriumov, A.N.; Dvornik, G.P. Altered formations and gold mineralization in the ore region of the Mesozoic tectonic-magmatic activation (Aldan Shield). *Proc. Ser. Geol. Geophys.* **2000**, *10*, 119–128. (In Russian)
6. Vetluzhskikh, V.G.; Kazansky, V.I.; Kochetkov, A.Y.; Yanovskiy, V.M. Central Aldan gold deposits. *Geol. Ore Depos.* **2002**, *44*, 405–434.
7. Kazansky, V.I. The unique Central Aldan gold-uranium ore district (Russia). *Geol. Ore Depos.* **2004**, *46*, 167–181.
8. Kochetkov, A.Y. Mesozoic gold-bearing ore-magmatic systems of the Central Aldan. *Geol. Geophys.* **2006**, *47*, 850–864. (In Russian)
9. Boitsov, V.E.; Pilipenko, G.N.; Dorozhkina, L.A. Gold and gold-uranium deposits of Central Aldan. In *Proceedings of the Large and Superlarge Deposits of Ore Minerals*; Strategic Types of Ore Raw Materials; IGEM RAS: Moscow, Russia, 2006; Volume 2, pp. 215–240. (In Russian)
10. Maksimov, E.P.; Uyutov, V.I.; Nikitin, V.M. The Central Aldan gold-uranium ore magmatogenic system, Aldan-Stanovoy shield, Russia. *Russ. J. Pac. Geol.* **2010**, *4*, 95–115.
11. Dvornik, G.P. Gold-ore metasomatic formations of the Central Aldan region. *Lithosphere* **2012**, *2*, 90–105. (In Russian)

12. Molchanov, A.V.; Terekhov, V.V.; Shatov, V.V.; Petrov, O.V.; Kukushkin, K.A.; Kozlov, D.S.; Shatova, N.V. Gold ore districts and ore clusters of the Aldanian metallogenic province. *Reg. Geol. Metallog.* **2017**, *71*, 93–111. (In Russian)
13. Yablokova, S.V.; Dubakina, L.S.; Dmitrak, A.L.; Sokolova, T.V. Kuranakhite—New hypergenic mineral of tellurium. *Zap. Vsesoyuznogo Mineral. Obs.* **1975**, *3*, 310–313. (In Russian)
14. Kim, A.A. Gold-telluride-selenide mineralization in the Kuranakh deposit (Central Aldan). *Zap. Vserossiyskogo Mineral. Obs.* **2000**, *5*, 51–57. (In Russian)
15. Kim, A.A.; Zayakina, N.V.; Lavrent'yev, Y.G. Yafsoanite, $(Zn_{1.38}Ca_{1.36}Pb_{0.26})_3TeO_6$, a new tellurium mineral. *Zapiski Vsesoyuznogo Mineral. Obshchestva* **1982**, *111*, 118–121. (In Russian)
16. Kim, A.A.; Zayakina, N.V.; Lavrentiev, Y.G.; Makhotko, V.F. Si-variety of dugganite—The first find in the USSR. *Mineral. J.* **1988**, *10*, 85–89. (In Russian)
17. Kim, A.A.; Zayakina, N.V.; Makhotko, V.F. Kuksite $Pb_3Zn_3TeO_6(PO_4)_2$ and cheremnukhite $Pb_3Zn_3TeO_6(VO_4)_2$–New tellurates from the Kuranakh gold deposit (Central Aldan, Southern Yakutia). *Zap. Vsesoyuznogo Mineral. Obs.* **1990**, *5*, 50–57. (In Russian)
18. Eluev, V.K.; Kiskin, V.A.; Kislyi, A.V. *Report on the Results of the Detailed Exploration of the Samolazovskoe Gold Deposit Conducted in 1999–2000*; Book I. The Text of the Report; Aldan, Russia, 2000, Unpublished work.
19. Dobrovolskaya, M.G.; Razin, M.V.; Prokofiev, V.Y. The Lebedinoe gold deposit (Central Aldan): Mineral paragenesis, stages and conditions of formation. *Geol. Ore Depos.* **2016**, *58*, 308–326. [CrossRef]
20. Grechishnikov, D.N.; Krajyshkin, S.A.; Bugrova, N.S. Russia, 2013 Report on the Completed Exploration Work at the Lunnoe Field for 2008–2013 with the Estimation of Reserves as of 01.01.2013. Unpublished work.
21. Belogub, E.V.; Novoselov, K.A.; Artemyev, D.A.; Palenova, E.E. Trace contaminations of pyrite from the Elkonsky and Ryabinovsky types of gold deposits in the Central Aldan ore region (Sakha-Yakutia). *Metallog. Anc. Mod. Oceans* **2018**, *1*, 146–150. (In Russian)
22. Novoselov, K.A.; Belogub, E.V.; Blinov, I.A. Te-canfieldite from ores of the Lunnoe Au-U deposit (Aldan region, Republic Sakha of Yakutia). *Mineralogy* **2019**, *5*, 49–56. (In Russian)
23. Leont'ev, V.I.; Platonova, N.V. Features of the occurrence of gold mineralization of the Lebedinsky type in the Dzhekondinsky ore cluster (Central Aldan ore region). *Reg. Geol. Metallog.* **2016**, *65*, 84–92. (In Russian)
24. Leont'ev, V.I.; Bushuev, Y.Y. Ore mineralization in adular-fluorite metasomatites: Evidence of the Podgolechnoe alkalic-type epithermal gold deposit (Central Aldan Ore District, Russia). *Key Eng. Mater.* **2017**, *743*, 417–421. [CrossRef]
25. Krasnov, A.N.; Dorozhkina, L.A.; Trubkin, N.V.; Groznova, E.O.; Myznikov, I.K. Vanadium mineralization of Samolazovsky gold deposit, Central Aldan District. *Izv. Vuzov. Geol. I Razved.* **2004**, *5*, 70–72. (In Russian)
26. Leontiev, V.I.; Bushuev, Y.Y.; Chernigovtsev, K.A. Samolazovskoe gold deposit (Central Aldan ore region): Geological structure and features of deep horizons mineralization. *Reg. Geol. Metallog.* **2018**, *75*, 90–103. (In Russian)
27. Kondratieva, L.A.; Minakov, A.V.; Kravchenko, A.A. Gold-telluride mineralization of the Nimgerkan ore cluster (Aldan shield). In *Proceedings of the VNPK*; Publishing House of the NEFU: Yakutsk, Russia, 2020; pp. 224–229. (In Russian)
28. Glushkova, E.G.; Nikiforova, Z.S. Comparative analysis of the proximal wash off placer gold and gold from metasomatites of Tabornoe ore field (West part of Aldan shield). *Proc. Russ. Mineral. Soc.* **2014**, *CXLIII*, 66–73. (In Russian)
29. Zubkov, Y.A.; Sagir, A.V.; Chvarova, N.V. "Uguysky" type of large-volume gold deposits formed in the linear weathering crust (South-Western Yakutia). *Otechestvennaya Geol.* **2020**, *2*, 32–45. (In Russian)
30. Terekhov, A.V.; Molchanov, A.V.; Shatov, V.V.; Khorokhorina, E.I.; Soloviev, O.L. Typomorphism of native gold from the Cenozoic deposits of the Gorely creek and its connection with primary sources within the Verkhneamginskiy ore-alluvial cluster (Southern Yakutia). *Reg. Geol. Metallog.* **2016**, *65*, 93–103. (In Russian)
31. Kazhenkina, A.G. Micromineral inclusions in native gold of the Tayakhtakh creek (Khatyrkhaysky ore-alluvial cluster). In Proceedings of the Congress of the Russian Mineralogical Society "200 years of RMO", Saint-Petersburg, Russia, 9–12 October 2017; Volume 1, pp. 229–231. (In Russian).
32. Anisimova, G.S.; Kondratieva, L.A.; Sokolov, E.P.; Kardashevskaya, V.N. Gold mineralization of the Lebedinsky and Kuranakh types in the Verkhneamginsky district (South Yakutia). *Otechestvennaya Geol.* **2018**, *5*, 3–13. (In Russian)
33. Anisimova, G.S.; Kondratieva, L.A.; Kardashevskaia, V.N. Characteristics of Supergene Gold of Karst Cavities of the Khokhoy Gold Ore Field (Aldan Shield, East Russia). *Minerals* **2020**, *10*, 139. [CrossRef]
34. Prokopyev, I.R.; Doroshkevich, A.G.; Ponomarchuk, A.V.; Redina, A.A.; Yegitova, I.V.; Ponomarev, J.D.; Sergeev, S.A.; Kravchenko, A.A.; Ivanov, A.I.; Sokolov, E.P.; et al. U-Pb SIMS and Ar-Ar geochronology, petrography, mineralogy and gold mineralization of the late Mesozoic Amga alkaline rocks (Aldan shield, Russia). *Ore Geol. Rev.* **2019**, *109*, 520–534. [CrossRef]
35. Anisimova, G.S.; Sokolov, E.P. The Bodorono deposit—New gold ore object of the Southern Yakutia. *Ores Met.* **2014**, *5*, 49–57. (In Russian)
36. Anisimova, G.S.; Sokolov, E.P. Altan-Chaidakh—Promising object of the Southern Yakutia. *Otechestvennaya Geol.* **2015**, *5*, 3–10. (In Russian)
37. Anisimova, G.S.; Sokolov, E.P.; Kardashevskaya, V.N. Gold-rare-metal (Au-Mo-Te-Bi) mineralization of the Upper-Algominsky gold-bearing region (Southern Yakutia). *Otechestvennaya Geol.* **2017**, *5*, 12–22. (In Russian)
38. Kardashevskaia, V.N.; Anisimova, G.S. Tellurides Pd, Ni, Bi, Pb and Ag from quartz veins of Dyvok ore occurrence (South Yakutia). In *Proceedings of the VNPK*; Publishing House of the NEFU: Yakutsk, Russia, 2019; pp. 32–35. (In Russian)
39. MAIK. *Tectonics, Geodynamics and Metallogeny of the Territory of the Republic of Sakha (Yakutia)*; MAIK(International Academic Publishing Company) "Nauka/Interperiodics": Moscow, Russia, 2001; 571p. (In Russian)

40. Anisimova, G.S.; Kondratieva, L.A.; Kardashevskaya, V.N. Weissbergite (TlSbS2) and avicennite (Tl2O3)—Rare thallium minerals. The first finds in Yakutia. *Proc. Russ. Mineral. Soc.* **2021**, *2*, 18–27. (In Russian)
41. Petrovskaya, N.V.; Fastalovich, A.I.; Ivanov, A.A. *Materials on Gold Mineralogy*; General Directorate for the Production of Special Non-Ferrous Metals: Moscow, Russia, 1952; 347p. (In Russian)
42. Nikolaeva, L.A.; Gavrilov, A.M.; Nekrasova, A.N.; Yablokova, S.V.; Shatilova, L.V. *Native Gold of Ore and Placer Deposits of Russia*; TSNIGRI: Moscow, Russia, 2015; 200p. (In Russian)
43. Groves, D.I.; Goldfarb, R.J.; Gebre-Mariam, M.; Hagemann, S.G.; Robert, F. Orogenic gold deposits: A proposed classification in the context of their crustal distribution and relationship to other gold deposit types. *Ore Geol. Rev.* **1998**, *13*, 7–27. [CrossRef]
44. Kovalenker, V.A. Ore-forming systems of epithermal gold and silver deposits: Concepts, reality, models. *Probl. Ore Geol. Petrol. Mineral. Geochem.* **2004**, *39*, 160–184. (In Russian)
45. Pals, D.W.; Spry, P.G.; Chryssoulis, S. Invisible gold and tellurium in arsenic rich pyrite from the Emperor gold deposit, Fiji: Implications for gold distribution and deposition. *Econ. Geol.* **2003**, *98*, 479–493. [CrossRef]
46. Large, R.R.; Maslennikov, V.; Robert, F.; Danyushevsky, L.V.; Chang, Z. Multistage sedimentary and metamorphic origin of pyrite and gold in the giant Sukhoi Log deposit, Lena gold province, Russia. *Econ. Geol.* **2007**, *102*, 1233–1267. [CrossRef]
47. Large, R.R.; Maslennikov, V. Invisible Gold Paragenesis and Geochemistry in Pyrite from Orogenic and Sediment-Hosted Gold Deposits. *Minerals* **2020**, *10*, 339. [CrossRef]
48. Vikentyev, I.V. Invisible and microscopic gold in pyrite: Methods and new data for massive sulfide ores of the Urals. *Geol. Ore Depos.* **2015**, *57*, 237–265. [CrossRef]
49. Gao, F.; Du, Y.; Pang, Z.; Du, Y.; Xin, F.; Xie, J. LA-ICP-MS Trace-Element Analysis of Pyrite from the Huanxiangwa Gold Deposit, Xiong'ershan District, China: Implications for ore genesis. *Minerals* **2019**, *9*, 157. [CrossRef]
50. Zhao, J.; Pring, A. Mineral Transformations in Gold–(Silver) Tellurides in the Presence of Fluids: Nature and Experiment. *Minerals* **2019**, *9*, 167. [CrossRef]
51. Kovalenker, V.A.; Safonov, Y.G.; Naumov, V.B.; Rusinov, V.L. The Epithermal Gold-Telluride Kochbulak Deposit. *Geol. Ore Depos.* **1997**, *39*, 107–128.
52. Kovalenker, V.A.; Plotinskaya, O.Y.; Koneev, R.I. Mineralogy of epithermal gold-sulfide-telluride ores of the Kairagach deposit (Uzbekistan). *New Data Miner.* **2003**, *38*, 45–56. (In Russian)
53. Islamov, F.; Kremenetsky, A.; Minzer, E.; Koneev, R. The Kochbulak-Kairagach ore field. In *Au, Ag, and Cu Deposits of Uzbekistan. Excursion Guidebook*; GFZ: Potsdam, Germany, 1999; pp. 91–106.
54. Koneev, R.I. *Nanomineralogy of Gold in Epithermal Ore Deposits of the Chatkalo-Kuramin Region*; Delta: Saint Petersburg, Russia, 2006; 218p. (In Russian)
55. Koneev, R.I.; Khalmatov, R.A.; Mun, Y.S. Nanomineralogy and nanochemistry of ores from gold deposits of Uzbekistan. *Geol. Ore Depos.* **2010**, *52*, 755–766. [CrossRef]
56. Shackleton, J.M.; Spry, P.G.; Bateman, R. Telluride mineralogy of the Golden Mile deposit, Kalgoorlie, Western Australia. *Can. Miner.* **2003**, *41*, 1503–1524. [CrossRef]
57. Kelley, K.D.; Romberger, S.B.; Beaty, D.W.; Pontius, J.A.; Snee, L.W.; Stein, H.J.; Thompson, T.B. Geochemical and geochronological constraints on the genesis of Au-Te deposits at Cripple Creek, Colorado. *Econ. Geol.* **1998**, *93*, 981–1012. [CrossRef]
58. Ahmad, M.; Solomon, M.; Walshe, J.L. Mineralogical and geochemical studies of the Emperor gold telluride deposit, Fiji. *Econ. Geol.* **1987**, *82*, 234–270. [CrossRef]
59. Cook, N.J.; Ciobanu, C.L.; Capraru, N.; Damian, G.; Cristea, P. Mineral assemblages from the vein salband at Sacarimb, Golden Quadrilateral, Romania: II. Tellurides. Geochem. *Miner. Petrol.* **2005**, *43*, 56–63.
60. Plotinskaya, O.Y.; Novoselov, K.A.; Kovalenker, V.A.; Zeltmann, R. Variations of the Forms of Finding Commercial Components at the Bereznyakovskoye Field (Southern Urals). Materials of the Annual Meeting of the RMO. 2006. Available online: http://www.minsoc.ru/2006-2-51-0 (accessed on 17 October 2006). (In Russian)
61. Zhai, D.; Liu, J. Gold-telluride-sulfide association in the Sandaowanzi epithermal Au-Ag-Te deposit, NE China: Implications for phase equilibrium and physicochemical conditions. *Miner. Petrol.* **2014**, *108*, 853–871. [CrossRef]
62. Zhao, J.; Brugger, J.; Xia, F.; Ngothai, Y.; Chen, G.; Pring, A. Dissolution-reprecipitation vs. solid-state diffusion: Mechanism of mineral transformations in sylvanite, $(AuAg)_2Te_4$, under hydrothermal conditions. *Am. Miner.* **2013**, *98*, 19–32. [CrossRef]
63. Zhao, J.; Brugger, J.; Grundler, P.V.; Xia, F.; Chen, G.; Pring, A. Mechanism and kinetics of a mineral transformation under hydrothermal conditions: Calaverite to metallic gold. *Am. Miner.* **2009**, *94*, 1541–1555. [CrossRef]
64. Xu, W.; Zhao, J.; Brugger, J.; Chen, G.; Pring, A. Mechanism of mineral transformations in krennerite, Au_3AgTe_8, under hydrothermal conditions. *Am. Miner.* **2013**, *98*, 2086–2095. [CrossRef]
65. Palyanova, G.A. Gold and Silver Minerals in Sulfide Ore. *Geol. Ore Deposits* **2020**, *62*, 383–406. [CrossRef]
66. Nesterenko, G.V. *Forecast of Gold Mineralization by Placers (on the Example of the Regions of Southern Siberia)*; Nauka: Novosibirsk, Russia, 1991; p. 191. (In Russian)
67. Murzin, V.V.; Malyugin, A.A. *Gold Typomorphism of the Supergene Zone (on the Example of the Urals)*; Ural Scientific Center AS: Sverdlovsk, Russia, 1987; p. 96. (In Russian)
68. Gamyanin, G.N.; Nekrasov, I.Y.; Samusikov, V.P. Maldonite from the gold ore occurrences of the Eastern Yakutia. *Mineral. J.* **1986**, *8*, 65–71. (In Russian)
69. Nekrasov, I.Y. *Geochemistry, Geology and Genesis of Gold Deposits*; Nauka: Moscow, Russia, 1991; p. 302. (In Russian)

70. Ciobanu, C.L.; Cook, N.J.; Pring, A. Bismuth tellurides as gold scavengers. In *Mineral Deposit Research: Meeting the Global Challenge*; Mao, J.W., Bierlein, F.P., Eds.; Springer: Berlin, Germany, 2005; pp. 1383–1386.
71. Tooth, B.; Brugger, J.; Ciobanu, C.L.; Liu, W. Modelling of gold-scavenging by bismuth melts coexisting with hydrothermal fluids. *Geology* **2008**, *36*, 815–818. [CrossRef]
72. Okrugin, V.M.; Andreeva, E.; Etschmann, B.; Pring, A.; Li, K.; Zhao, J.; Griffiths, G.; Lumpkin, G.R.; Triani, G.; Brugger, J. Microporous gold: Comparison of textures from Nature and experiments. *Am. Miner.* **2014**, *99*, 1171–1174. [CrossRef]
73. Tolstykh, N.D.; Palyanova, G.A.; Bobrova, O.V.; Sidorov, E.G. Mustard Gold of the Gaching Ore Deposit (Maletoyvayam Ore Field, Kamchatka, Russia). *Minerals* **2019**, *9*, 489. [CrossRef]

minerals

MDPI

Article

Gold Mineralization at the Maletoyvayam Deposit (Koryak Highland, Russia) and Physicochemical Conditions of Its Formation

Evgeny G. Sidorov [1], Andrey A. Borovikov [2], Nadezhda D. Tolstykh [2,3,*], Daria S. Bukhanova [1], Galina A. Palyanova [2,3] and Valery M. Chubarov [1]

[1] Institute of Volcanology and Seismology, Far East Branch of Russian Academy of Sciences, Piipa Blvd., 9, Petropavlovsk-Kamchatsky 683006, Russia; eg_sidorov@mail.ru (E.G.S.); dasha-snejinka@yandex.ru (D.S.B.); camebax@gmail.com (V.M.C.)

[2] Sobolev Institute of Geology and Mineralogy, Siberian Branch of Russian Academy of Sciences, Koptyuga Ave., 3, Novosibirsk 630090, Russia; borovikov.57@mail.ru (A.A.B.); palyan@igm.nsc.ru (G.A.P.)

[3] Department of Geology and Geophysics, Novosibirsk State University, Pirogova Ave., 2, Novosibirsk 630090, Russia

* Correspondence: tolst@igm.nsc.ru

Received: 25 October 2020; Accepted: 3 December 2020; Published: 5 December 2020

Abstract: Microthermometry study of fluid inclusions in quartz veins of the Maletoyvayam deposit (Koryak Highland, Russia) was carried out. This epithermal gold deposit contains unique Au compounds including maletoyvayamite, which has not been reported anywhere else. Two paragenetic mineral associations (pyrite-quartz and maletoyvayamite-quartz) with quartz of different generations corresponding to different pulses were also described. Only early generations of quartz (Q^1) include ore minerals: pyrite for the first mineral assemblage, and in Au-bearing minerals, sulfosalts, bismuthinite, and others—for the second assemblage. A study on fluid inclusions in quartz showed a salinity (mainly NaCl + KCl) range from 0.2 to 4.3 wt.% NaCl eq., increasing from the first mineral association to the second due to boiling fluids. The obtained temperature variations for quartz crystallization were 295–135 °C, the fluid pressure ranged from 79 to 4 bar. On the other hand, the range of conditions obtained for the gold productive ore association is more narrow: salinity of the fluid inclusions is 4.3 wt.% NaCl eq., the temperatures vary from 255 °C to 245 °C, and the pressure from 39 to 32 bar. These physicochemical characteristics of the Maletoyvayam ore deposit greatly coincide with other HS-type epithermal deposits; however, within the Central Kamchatka Volcanic Belt it is so far the only deposit of this type reported.

Keywords: Central Kamchatka Volcanic Belt; HS epithermal deposit; maletoyvayamite-quartz association; fluid inclusions; gold

1. Introduction

The term "epithermal" was defined by W. Lindgren [1] to include a broad range of tellurides, antimonides or selenides of Au, Ag and base metals deposits which he estimated to be formed from aqueous fluids at low temperatures (less than 200 °C) and moderate pressures. It is, however, now generally accepted that mainly magmatic fluids at slightly higher temperatures (200–300 °C) and pressures of less than a few hundred bars participate in the formation of these type of deposits. Nevertheless, the term "epithermal" is still widespread [2].

Taylor, Hedenquist and coauthors [3,4] consider that an epithermal Au deposit consists of three subtypes: high sulfidation (HS), intermediate sulfidation (IS), and low sulfidation (LS), each represented by characteristic alteration mineral assemblages, occurrences, textures, and characteristic suites of

associated geochemical elements. The term HS (high sulfidation) is now widely used [5], and combines many other previously described types: enargite–gold [6], Goldfield-type [7,8], high-sulfur [9,10], quartz-alunite [11] and alunite–kaolinite [12] which were assigned to a group of epithermal deposits based on their mineralogical and geochemical features. HS type deposits are characterized by the presence of diagnostic minerals of high sulfidation conditions (e.g., enargite), acidic hydrothermal conditions (e.g., alunite, kaolinite) and relatively oxidized conditions of sulfur (SO_2-rich) in the hydrothermal system. HS deposits are associated with some types of hydrothermal systems due to influence of a deep magma chamber [13] and also with andesitic volcanoes in which surface manifestations include high-temperature fumaroles and acid sulfate-chloride hot springs. In contrast, LS deposits of reduced (H_2S-rich) hydrothermal fluids with neutral pH are similar to those found in geothermal systems [13], that exhibit in the surface: sinter-terraces of silica, hot springs and steam-heated acid-sulfate alterations [14].

Within the Kamchatka Peninsula, Au-Ag epithermal deposits are localized in volcanic belts of different ages (Eocene-Oligocene Koryak-West Kamchatka, Oligocene-Quaternary Central Kamchatka, and Pliocene-Quaternary East Kamchatka), extending along the modern subduction trend [15–19]. All of the Au-Ag mines located there (Aginskoe, Asacha, Ametistovoe, Zolotoe, Baran'evskoe, Kungurtsevskoe, Oganchinskoe, Ozernovskoe), as well as most of the known Au-Ag deposits and prospects, fit into the LS epithermal type [19–23]. These deposits are characterized by the presence of quartz, adularia, illite and calcite in Au-Ag-bearing veins.

The Maletoyvayam deposit located in the Central Kamchatka Volcanic Belt (CKVB) is restricted to volcano–tectonic structures within the Vetrovayam volcanic zone situated in the northeastern part of the CKVB (southwestern part of the Koryak Highland) [24,25]. On the contrary to the above mentioned deposits, Maletoyvayam deposit belongs to the HS type category of epithermal deposits [26], which are also known in the Eastern part of Russia (Belaya Gora and Svetloye) [27]. The predominance of andesite and basaltic andesite rocks in the CKVB is a reflection of the mafic composition of its basement. This factor determines the particularity of the metallogeny on this zone, characterized by a wide development of near-surface mineralization of tellurides as subtypes of the main gold-silver deposits [28]. The veins of massive quartz are included in the vuggy silica, and both are Au(Ag)-bearing. The central vuggy silica zones are rimmed along the periphery of the ore field by quartz-alunite-kaolinite association. The Maletoyvayam HS type deposit differs from others known on the Kamchatka Peninsula, which are of the LS type, by a great variety of mineral phases: native gold, chalcogenides of Au and Ag, Cu-sulfosalts with Sb and As, as well as complexes including Au-bearing oxides among which some are considered rare or unique. Contrary to the other deposits of the CKVB, native gold in these ores is not dominant. The study of other styles of gold occurrences in sulfide-telluride-selenide ores and the physicochemical conditions of their formation are of great interest from a mineralogical, genetic and technological point of view [29]. The first results on the mineral composition of Maletoyvayam deposit were obtained recently [26,30–35]. Typical and uncommon minerals of epithermal systems were reported in this deposit: senarmontite (Sb_2O_3), tripuhyite ($FeSbO_4$), bismite (Bi_2O_3), rooseveltite ($Bi(AsO_4)$), tiemannite (HgSe), antimonselite (Sb_2Se_3), Te-,Sb-bearing guanajuatite: ($Bi_2(Se,Te)_3$ and $(Bi,Sb)_2Se_3$), bismuthinite ((Bi_2S_3) and $(Bi,Sb)_2(S,Se)_3$), unnamed phase ($(Sb,Bi,Te,As,Fe)_2O_5$), tellurium (Te,Se). In addition, unique compounds, that had not been previously found in nature, were reported: maletoyvayamite and its S-rich analogue ($Au_3Se_4Te_6$ and $Au_3S_4Te_6$), AuSe and Au(Te,Se); their occurrence is due most likely to specific properties of the hydrothermal solutions. Microthermometric study of these ores had not previously been carried out. Thus, the purpose of this study is to present mineralogical and microthermometric measurement data of this particular type of ore and to show the physicochemical conditions that played an important role in the ore accumulation.

2. Regional Geology and Mineralization

The Central Kamchatka Volcanic Belt (Russia) is about 1800 km long, controlled by the Main Kamchatka deep fault, displaying a significant number of gold-silver epithermal deposits [22,28]. The Maletoyvayam deposit is particularly confined to a volcano-tectonic structure (up to 30 km) within the Vetrovayam volcanic zone located in the northeastern region of the Central Kamchatka Volcanic Belt and delimited by the Koryak Highland in the southwestern part [24,25]. This whole structure is controlled by the Vyvensky northeast-striking deep fault and the northwest-striking faults zone [36,37]. Stratified subvolcanic and intrusive formations, as well as Quaternary sediments, are the constituent elements of the ore field (Figure 1).

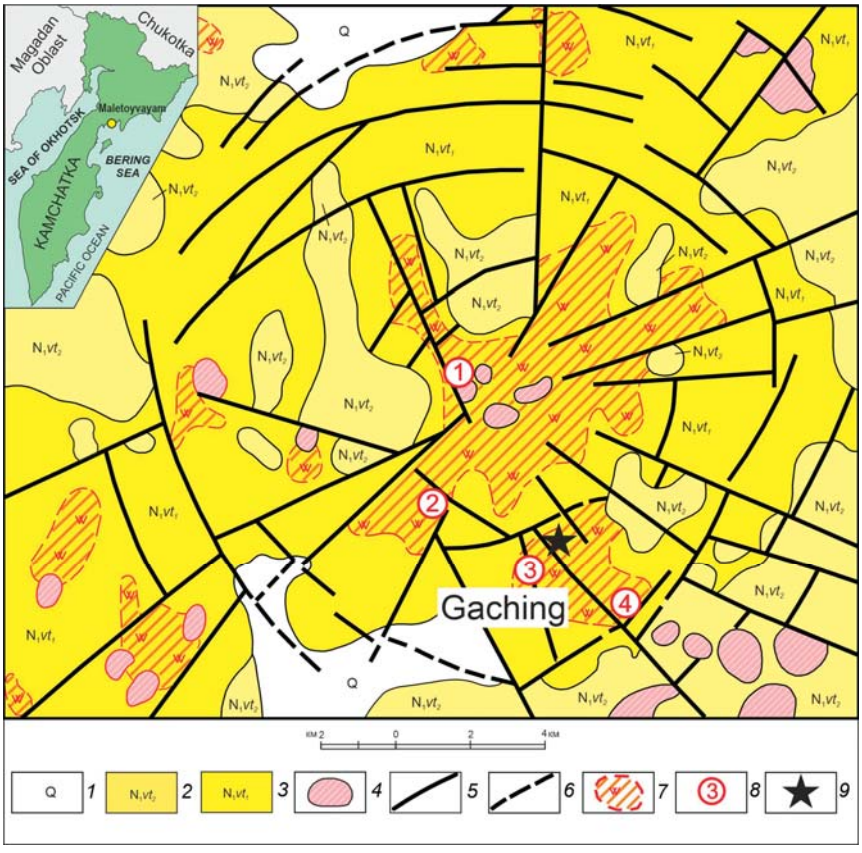

Figure 1. Schematic geological map (volcano-tectonic structure) of the Maletoyvayam gold deposit, modified after Stefanov and Schiroky [37]. 1—Quaternary deposits; 2,3—rocks of the upper member (2) and the lower member (3) of the Vetrovayam Formation (Middle-Late Miocene); 4—Vetrovayam volcanic complex (Late Miocene); 5—main faults; 6—faults covered by Quaternary deposits; 7—hydrothermally altered rocks; 8—ore occurrences (numbers in circles): 1—Yubileyny, 2—Yugo-Zapadny, 3—Gaching, 4—Tyulul; 9—Sampling location.

Stratified deposits are represented by effusive, pyroclastic, and tuffaceous-sedimentary rocks of the Vetrovayam Formation (Figure 1), which are divided into two lithostratigraphic members. The lower member (N_1vt_1) is composed of tuff and tuff breccia of intermediate to basic composition, andesite, basaltic andesite, and, less often, dacite and felsic tuff. At the base of this member, there are lenses

and interlayers of tuffaceous sandstone, tuff conglomerate, tuff siltstone, and brown coal. The upper member (N_1vt_2) of the Vevetrovayam Formation is 10–30 m thick and composed mainly by effusive rocks: andesite and basaltic andesite. Interlayers of basalt, tuff, tuff breccia, and tuff conglomerates of intermediate and mafic composition are less common. The radiometric age for effusive rocks (K/Ar method) is 7–18 Ma [38]. Intrusive subvolcanic bodies and dikes form a single volcanic complex (Vetrovayam), which is represented by diorite, quartz diorite and granodiorite. The age of this complex was determined as Middle-Late Miocene [38]. Volcanic rocks in the area exhibit different degrees of hydrothermal alteration, which are associated with areas of gold mineralization and sulfur deposits explored in 1971 [25,36,38]. The Maletoyvayam deposit includes four areas (ore occurrences) where gold ore reserves have been identified and estimated: Yubileyny, Yugo-Zapadny, Gaching and Tyulul.

Based on the types of mineral assemblages [26], these ore occurrences are associated to a HS epithermal type [4,39,40]. However, they differ among themselves in the degree of oxidation of the primary mineralization. For instance, at the Gaching occurrence, the ores are less oxidized (about 10% sulfate iron and 90% sulfide iron), compared to the Yugo-Zapadny occurrence, where sulfide iron is only 8%. Hence, the primary mineralization at the Gaching ore occurrence is considered to be more preserved and for that reason it was selected and analyzed in the present study.

Maletoyvayam deposit is composed of rocks of the lower member of the Vetrovaym Formation. Vuggy silica was identified in the central part of the ore field, transitioning outwards into quartrz-alunite, quartz-kaolinite, quartz-sericite-kaolinite and then to argillic- and propylitic-altered rocks. Gold was found both in vuggy silica remnants located on the watershed in the Gachingalhovayam river valley (Figure 2a), and in quartz veins. The color in rock samples showing vuggy and massive silica texture is light gray to gray (Figure 2b). In the samples with texture the main mineral phase is quartz—85–90 vol.%; kaolinite—5 vol.%, and alunite—4–5 vol.%; the rest of the minerals correspond to potassium feldspar, barite, anglesite, muscovite, etc.

Figure 2. (**a**) Vuggy silica in the Gachingalhovayam river valley, (**b**) Vuggy silica sample with quartz veins, (**c**) fragment of quartz vein containing the maletoyvayamite-quartz association, Gaching ore occurrence.

The dark zones in samples exhibiting vuggy silica texture are due to the presence of an intense dissemination of mainly pyrite, or sulfosalts along with gold mineralization. Au content in samples with vuggy silica texture reaches 8.8 ppm, whereas Ag—47.2 ppm. The white quartz veins also contain a fine-grained dissemination of ore minerals, which is irregularly distributed (Figure 2c). The concentration of Au in quartz veins vary within the range 1.40–144 ppm, and for Ag—147–724 ppm. Other ore elements show concentrations of: Cu—1.38–3.18; As—up to 2; S—up to 2.26; Sb, Se, Te—more than 0.2 (wt.%) [25].

3. Samples and Analytical Methods

Quartz veins samples selected for this study are shown in (Table 1). In the first stage, thin polished sections were made from these samples. To determine the phases' transition temperatures in quartz fluid inclusions, cryo- and thermometry methods were used (Linkam THMSG-600 heating-freezing chamber

(Linkam Scientific Instruments, Tadworth Surrey, United Kingdom, https://www.linkam.co.uk/) with a measurement range of −196/+600 °C). The composition of the gas phase and corresponding identification of solid phases in the inclusions were carried out by Raman spectroscopy (JobinYvon "Ramanor U-1000" spectrometer, MillenniaProS2 laser (532 nm), HORIBA JOBIN YVON detector, Novosibirsk, Russia).

Table 1. List of samples with their main characteristics

Sample	Texture	Morphology	Minerals Included in Quartz or Filling Cracks and Cavities
3053_a	Filling of cavities	Segregation	Fe-hydroxide, Fe-antimonite/tellurite, sulfosalts, Au-Fe(Sb,As,Te) oxide
3053_b	Filling of cavities	Segregation	Sulfosalts, maletoyvayamite, tellurium
3058_a	Interspersed	Inclusions	Pyrite
3058_b	Interspersed	Inclusions	Pyrite
3058_c	Interspersed	Inclusions	Bismuthinite, maletoyvayamite, Sb(Bi,Te,As,Se) oxide, sulfosalts

Note. All samples are a vein of white quartz.

The total salt concentrations in fluid inclusions and their corresponding water–salt system were determined using the cryometry method [41,42]. The assessment of the pressure of mineral formation environment was carried out using the published pressure-temperature-composition data for NaCl-H_2O systems. The AqSo_NaCl [43], ISOHOR [44] and FLINCOR [45] software packages were also used to estimate the pressure of mineral formation from microthermometric data obtain in the study of fluid inclusions.

The chemical compositions of the minerals (samples 3053-8_a,d,c) and texture of mineral aggregates were studied at the Analytical Center for multi-elemental and isotope research of the Sobolev Institute of Geology and mineralogy Russian Academy of Sciences (SB RAS) in Novosibirsk, using a LEO-413VP scanning electron microscope (SEM) with the INCA Energy 350 microanalysis system (Oxford Instruments Ltd.) equipped with an energy dispersive spectrometer (EDS) (analysts: Dr. N. Karmanov, M. Khlestov), operated at an accelerating voltage of 20 kV, current intensity 0.4 nA, 50 sec. measuring time, and beam diameter ~1 μm. The following standards were used: pure metals (Ag, Au, Bi, Se, Sb, Fe, Cu), pyrite (S), synthetic HgTe (Te), sperrylite (As). The detection limit was 0.02%. The following X-ray lines were selected: Lα for Ag, Te, As, Sb and Se; Kα for S, Fe, Cu and O; and Mα for Au and Bi. Analytical data for the samples 3053-3 a,b was obtained at the Institute of Volcanology and Seismology of Far Eastern Branch of RAS, using a TescanVega-3 scanning electron microscope equipped with an energy dispersive spectrometer, EMF X-MAX (analyst: V.M. Chubarov), operated at an accelerating voltage of 20 kV, current intensity 3–0.7 nA, 50 sec. measuring time, and beam diameter ~1 μm. The following standards were used: pure metals (Au, Ag, Se, Sb), synthetic FeS_2 (Fe), InAs (As), CdTe (Te), $CuSbS_2$ (Sb), Bi_2S_3 (Bi), $CuFeS_2$ (S, Cu). The detection limit was 0.1 wt.%. The following X-ray lines were selected: Lα for Ag, Te, As, Sb and Se; Kα for S, Fe, Cu and O; and Mα for Au and Bi.

4. Results

4.1. Mineralogy of Studied Maletoyvayam Deposit Ores

The studied samples are represented by quartz veins with abundant spotty dissemination of fine grain ore minerals. In some of the ore samples only pyrite is present, whereas Au minerals are completely absent. These samples are considered to be related to early pyrite-quartz assemblage (Figure 3a,b). Other samples contain fine dissemination of Au compounds along with other ore minerals; however, pyrite is absent or only represented as subordinate inclusions within other minerals. These samples are genetically associated to the later gold-bearing assemblage [26], which in the context of our study was named as: the maletoyvayamite-quartz association.

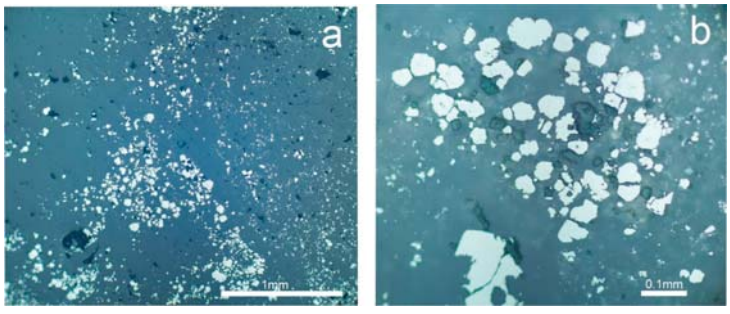

Figure 3. Impregnation of pyrite in quartz: irregular (sample 3058-8_a) (**a**) and spotted (**b**) from the pyrite-quartz association (sample 3058-8_b).

The studied ore-bearing samples correspond to quartz veins. The concentrations of noble metals vary depending on the dissemination density within the ore samples: Au from 0.8 to 147 ppm and Ag from 0.5 to 200 ppm. In Au-Ag enriched samples (3053-3), quartz contains very small quartz druses; these cavities are partially or completely filled with a finely dispersed reddish-gray mass, represented by a mixture of iron hydroxides, tellurites and iron antimonates, sulfosalts (Figure 4a), native and secondary (mustard) gold and other rare minerals including unique compounds of Au-sulfoselenotellurides and complex Au-bearing oxides (Figure 4b).

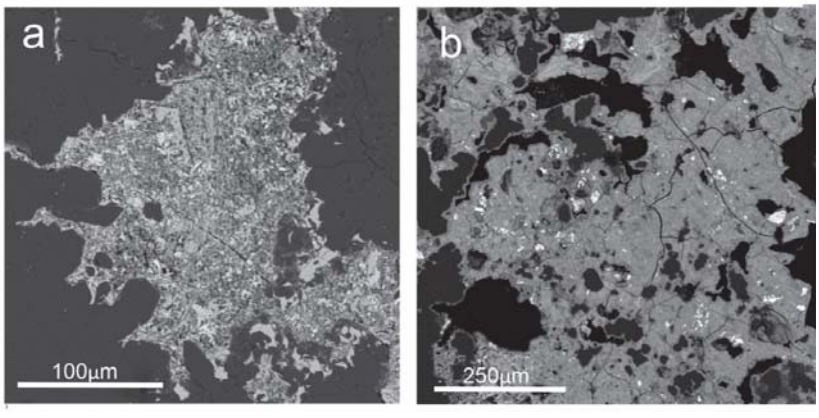

Figure 4. SEM image of sample 3053-3_a. The cavities in quartz filled with a finely dispersed mass represented by a mixture of iron hydroxides, tellurites, iron antimonates, and sulfosalts (**a**); and the same masses, but impregnated with complex oxides of Au (Au-Fe-Sb-Te-O compounds) (**b**).

Sulfosalts are widespread in the ore associations of the Maletoyvayam deposit. Two main groups of sulfosalts were identified in the Gaching area: the tetrahedrite-group $Cu_{12}(As,Sb,Te)_4S_{13}$ and enargite-group $Cu_3(As,Sb)S_4$ [33]. In the samples with highest noble metals enrichment, maletoyvayamite occurs as independent grains intergrown with tellurium and sulfosalts. It is often found along cracks or in the intergranular space of quartz (Figure 5a), or confined to the margins of large grains of sulfosalts (Figure 5b).

Au-bearing minerals range in size from a few μm to 80 μm, while sulfosalt grains reach up to 2.5 mm. The sulfosalts are enriched in Se within a range of 5.84–10.42 wt.%. The substitution of Se for S is ubiquitous (Table 2). The presence of selenium in sulfosalts indicates specific conditions for their formation.

Table 2. Compositions of ore minerals shown in Figure 5 from the maletoyvayamite-quartz. association (sample 3053-3), wt.%.

No	S	Cu	As	Se	Sb	Te	Au	Total	Formula
1	21.49	42.37		5.84	8.46	20.75		99.28	$Cu_{11.82}(Te_{2.86}\ Sb_{1.22})_{4.08}(S_{11.80}Se_{1.30})_{13.10}$
2	21.43	40.28	2.30	8.76	6.40	21.38		100.56	$Cu_{11.05}(Te_{2.92}Sb_{0.92}\ As_{0.54})_{4.38}(S_{11.65}\ Se_{1.93})_{13.58}$
3	6.34			6.24		50.5	37.80	100.88	$Au_{2.89}Te_{5.95}(S_{2.97}Se_{1.19})_{4.16}$
4	6.35			5.60		50.47	37.76	100.19	$Au_{2.91}Te_{6.00}(S_{3.01}Se_{1.08})_{4.09}$
5	3.38			11.03		49.89	36.16	100.46	$Au_{2.91}Te_{6.20}(Se_{2.22}S_{1.67})_{3.89}$
6				6.97		92.99		99.95	$Te_{0.89}Se_{0.11}$
7	25.81	42.65	6.15	7.50	17.88	0.73		100.72	$Cu_{4.09}(Sb_{0.89}As_{0.50}\ Se_{0.48}Te_{0.04})_{1.91}(S_{4.90}Se_{0.10})_{5.00}$
8	20.59	42.59	1.02	7.74	12.34	15.75		100.03	$Cu_{11.79}(Te_{2.17}\ Sb_{1.78}As_{0.24})_{4.19}(S_{11.30}Se_{1.73})_{13.02}$
9				32.8		66.68		99.49	$Te_{0.56}Se_{0.44}$
10	2.95			12.15		48.75	36.40	100.26	$Au_{2.96}Te_{6.11}(Se_{2.46}S_{1.47})_{3.93}$
11	19.71	40.94		9.99	8.85	20.00		99.49	$Cu_{11.57}(Te_{2.82}Sb_{1.31})_{4.13}(S_{11.04}Se_{2.27})_{13.31}$
12	26.94	45.54	16.52	10.42	2.34			101.76	$Cu_{2.97}(As_{0.91}Sb_{0.08})_{0.99}(S_{3.49}Se_{0.55})_{4.04}$

Note. 1,2,8,11—goldfieldite $Cu_{12}(Te,Sb)_4(S,Se)_{13}$; 3,4—S-rich analogue of maletoyvayamite $Au_3Te_6(S,Se)_4$; 5,10—maletoyvayamite $Au_3Te_6(Se,S)_4$; 6,9—tellurium; 7—watanabeite $Cu_4(Sb,As)_2(S,Se)_5$; 12—enargite $Cu_3(As,Sb)(S,Se)_4$.

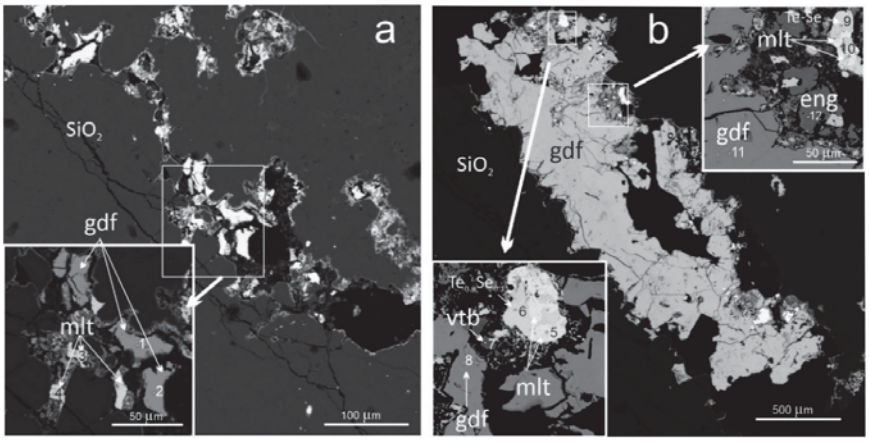

Figure 5. SEM image. The maletoyvayamite-quartz association in the sample 3053-3_b, highest enrichment in noble metals (Au is 144 ppm, Ag is 200 ppm); (**a**) ore minerals localized along cracks in the intergranular space of quartz; (**b**) maletoyvayamite confined to the margins of sulfosalts grains; mlt—maletoyvayamite, gdf—goldfieldite, wtb—watanabeite, $Te_{0.9}Se_{0.1}$—Te-Se solid solution. Points with numbers correspond to the analysis numbers in Table 2.

Another sample (3053-8_a,d,c) containing the maletoyvayamite-quartz ore association with concentrations of Au and Ag 1.4 and 12.3 ppm, respectively, contains large bismuthinite inclusions. In addition, sulfosalts of various compositions (tetrahedrite, goldfieldite, enargite, etc.), which are described in [33], are also found in association with bismuthinite (Figure 6a,c,d). Bismuthinite has an unusual composition, since Sb and Te in its structure are substituted for Bi, whereas Se and Te for S (Figure 6a,b; Table 3). Furthermore, it was found that bismuthinite has an S/Se = 2 ratio. Moreover, we suggest the possibility of this mineral phase corresponding to a potentially new mineral Bi_2S_2Se. This phase has also been reported from the HS-IS epithermal Perama Hill deposits, in Greece [46]. It is intergrown with the Se-bearing tellurium (Figure 6c). Complex oxides of various oxidation states in primary minerals, including maletoyvayamite, are common in the Maletoyvayam deposit [26,31]. In the analyzed sample, bismuthinite and similar phases are replaced by oxides of Sb, Bi, As, Te and Se in variable proportions; Fe, Cu and occasionally Ag are minor elements. The oxidation state also varies in these compounds from $(Sb,Bi,Te,As,Se)_{0.31}O_{0.69}$ to $(Sb,Bi,Te,As,Se)_{0.24}O_{0.76}$ (Figure 7) depending mainly on the oxygen fugacity: $\log fO_2$ ranging from −29.8 to −27.3; values previously calculated for the ore-bearing mineral association [26].

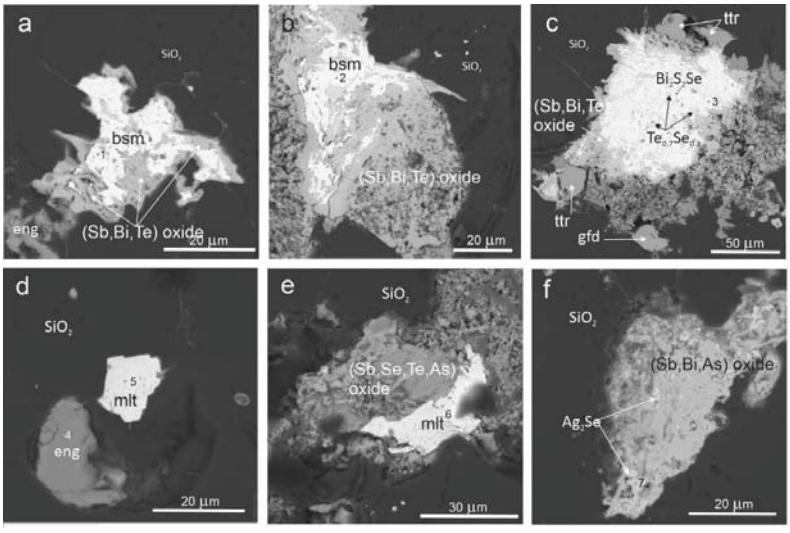

Figure 6. SEM image. The maletoyvayamite-quartz association in the sample 3053-8-c (Au is 1.37 ppm and Ag is 12.3 ppm): (**a**) Sb,Te,Se-bearing bismuthinite (bsm) replaced by (Sb,Bi,Te)-oxide in intergrowths with enargite (eng) hosted in quartz; (**b**) bismuthinite replaced by (Sb,Bi,Te)-oxide; (**c**) unnamed phase Bi_2S_2Se with inclusions of Se-rich tellurium ($Te_{0.7}Se_{0.3}$) replaced by (Sb,Bi,Te)-oxide, in intergrowth with tetrahedrite (ttr) and goldfieldite (gfd); (**d**) inclusions of maletoyvayamite (mlt) and enargite in quartz; (**e**) maletoyvayamite in intergrowths with (Sb,Se,Te,As)-oxide; (**f**) grain of (Sb,Bi,As)-oxide containing the naumannite (Ag_2Se) inclusions in quartz. Points with numbers correspond to the analysis numbers in Table 3.

Table 3. Compositions of ore minerals shown in Figure 6 from the maletoyvayamite-quartz. association (sample 3053-8_c), wt.%.

No.	Au	Cu	Ag	Bi	Sb	Te	As	Se	S	Total	Formula
1				62.41	8.46	2.89		10.89	14.16	98.81	$(Bi_{1.54}Sb_{0.36}Te_{0.12})_{2.01}(S_{2.28}Se_{0.71})_{2.99}$
2				65.07	5.19	3.20		11.36	13.45	98.27	$(Bi_{1.65}Sb_{0.23}Te_{0.13})_{2.01}(S_{2.23}Se_{0.76})_{2.99}$
3				72.54				14.13	11.34	98.01	$Bi_{1.97}S_{2.01}Se_{1.02}$
4		47.11			2.86		15.93	1.07	31.32	98.29	$Cu_{3.01}(As_{0.86}Sb_{0.10})_{0.96}(S_{3.97}Se_{0.06})_{4.03}$
5	35.10					47.38		14.80	2.03	99.31	$Au_{2.89}Te_{6.03}(Se_{3.04}S_{1.03})_{4.07}$
6	55.87					47.07		14.67	2.14	99.75	$Au_{2.95}Te_{5.97}(Se_{3.01}S_{1.08})_{4.09}$
7			71.84					26.49		98.33	$Ag_{2.00}Se_{1.00}$

Note. 1,2—Sb,Te,Se-bearing bismuthinite $(Bi,Sb,Te)_2(S,Se)_3$, 3—unnamed phase, 4 enargite, 5,6—maletoyvayamite, 7—naumannite.

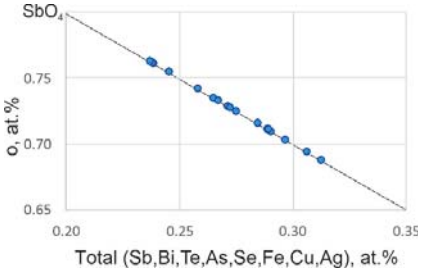

Figure 7. Oxygen versus the sum of the rest atoms in complex oxides (iron tellurites and iron antimonates) showing the variations in their composition due to the degree of oxidation of the primary phases.

4.2. Quartz Generations and Corresponding Types of Fluid Inclusions

The ore-bearing samples selected to study of fluid inclusions are represented by two main associations: pyrite-quartz and maletoyvayamite-quartz.

4.2.1. Pyrite-Quartz Association

In the studied samples showing this mineral association, there are at least three successively crystallized generations of quartz (Figure 8a). The earliest generation is represented by a grayish to dark gray fine-grained quartz aggregate with abundant dissemination of fine pyrite grains. Subsequent generations of quartz are represented by veins that cut the early pyrite-bearing quartz. In late veinlets, crustified, microdruse, cockade and, less often, collomorphic textures can be observed (Figure 8a). These textures are also representative of mineral associations in other gold-bearing low sulfidation epithermal deposits in the Kamchatka Peninsula [19]. Late quartz veins also contain sporadic pyrite, but very rarely. Separate large grains of quartz in late veinlets are characterized by a zonal structure. The central parts of quartz grains contain single two-phase inclusions with isometric shape (Figure 9b). Growth zones on the periphery of quartz crystals are traced by abundant fluid inclusions with oval vacuoles, elongated perpendicular to the faces of quartz crystals (Figure 9c).

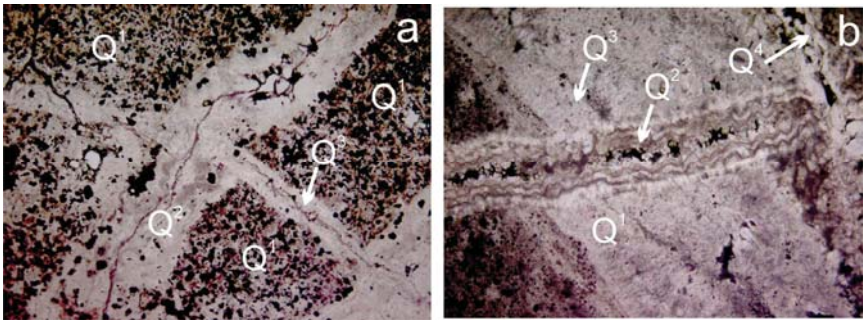

Figure 8. Quartz generations. (**a**) pyrite-quartz mineral association: Early quartz (Q^1) is presented in association with abundant pyrite grains (black spots) and intersected by veins of quartz (Q^{2-4}), containing rare pyrite inclusions; (**b**) maletoyvayamite-quartz mineral association: In this sample, early quartz (Q^1) contains inclusions of bismuthinite and maletoyvayamite. This quartz generation is intersected by late quartz veins (Q^{2-4}).

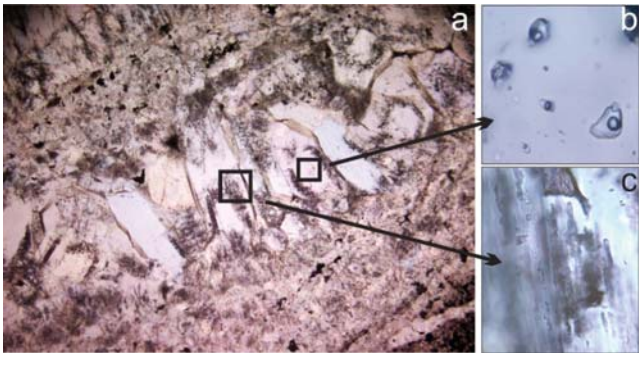

Figure 9. (**a**) quartz exhibiting zoning pattern with crustified texture from a pyrite-quartz association; (**b**) a group of isolated two-phase inclusions in the center part of the quartz crystal, (**c**) two-phase inclusions with elongated shape trace the growth zone at the periphery of the quartz crystal.

Crystallization of some quartz generations with different textures occurred close in time or almost simultaneously, since smooth transitions are often observed among them. It is likely that several hydrothermal pulses at very short time intervals were consistently segregated during the formation of ores. Thus, different quartz generations represent the observed textural varieties as a result of these rhythmic pulses. On this subject, when presenting the results on fluid inclusions, showed by textural features, we will divide the quartz in the pyrite-quartz association into only two generations—the early fine-grained generation with abundant dissemination of pyrite and the late one, represented by veinlets cutting the first one.

4.2.2. Maletoyvayamite–Quartz Association

Quartz associated with this mineral assemblage is similar to those of the pyrite-quartz association in respect to the textural and structural features, as well as in the distribution of fluid inclusions. Quartz displaying crustified texture also contain inclusions of ore minerals. Pyrite in the studied sample is represented by single small crystals whereas Au minerals (maletoyvayamite) are the most abundant (Figure 6 d,e); among Ag minerals, naumannite Ag_2Se and hessite Ag_2Te occur in association (Figure 6f). The quartz of the maletoyvayamite-quartz association, as in the pyrite-quartz association, also contains two types of fluid inclusions (Figure 10a,b) with the characteristic that they belong to the primary phase, and less often to the pseudo-secondary phase according to [47,48]. The first type is represented by two-phase inclusions close to isometric, containing a gas bubble and liquid in vol. ratios 1/10–1/12, which does not exceed 10 μm in size (Figure 10c). The second type is represented by two-phases, which are close to the faces of the quartz crystal and delimitate its growth zones. They have an elongated or tubular shape of up to 30 μm in length and 5–10 μm in cross-section (Figure 10d), and as a rule, they are associated with single-phase vapor inclusions, also elongated with channel-shaped, of up to 50 μm in length.

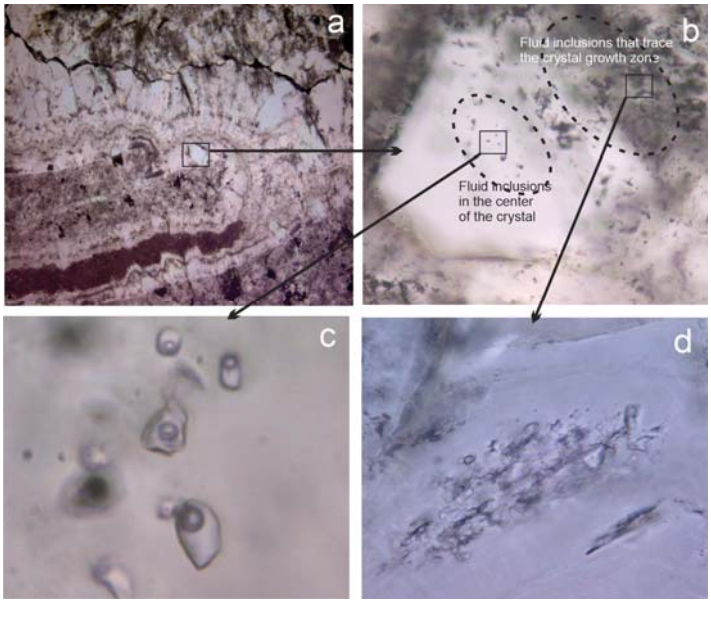

Figure 10. (**a**) quartz exhibiting zonation texture from a maletoyvayamite-quartz association; (**b**) group of isolated fluid inclusions in the central part of the quartz crystal and elongated shape of inclusions at the periphery of the crystal; close-up showing the representative shape and details of the inclusions in the center of quartz crystals (**c**) and in the growth zones (**d**).

The origin of elongated fluid inclusions is related with the repulsion of mineral particles by the growing face of the crystal, or with the processes of dissolution of quartz and subsequent healing of the formed tunnel-like hollows [47]. The presence of single-phase vapor inclusions seems to be due to boiling processes of the mineral-forming fluid. Judging by the significant elongation of the vacuoles of fluid inclusions located perpendicular to the faces of the quartz crystal, the boiling process is suggested to be quite long [47].

4.3. Results of the Fluid Inclusions Microthermometry

The results of fluid inclusions study from different types of quartz veins associations make it possible to characterize the main physicochemical parameters related to their formation. Table 4 summarizes these main parameters for two types of quartz from the different associations discussed before.

Table 4. Results of fluid inclusions microthermometry in quartz from early and late generations.

Quartz Generation	T °C Homogenization, (n *)	T °C Eutectic	T °C Ice Melting	NaCl, wt.%	KCl, wt.%	Total Salinity, wt.%	Pressure **, Bar
Pyrite-Quartz Association							
Early (Q^1)	290–288 (5)	−25 (−38–−35)	−0.5–−0.4	0.6	0.3	0.9	70–68
	270–260 (6)	−24–−23	−0.6–−0.4	0.6	0.3	0.9	50–43
	295 (2)	25 (−38–−35)	−0.5–−0.4	0.6	0.3	0.9	76
	245 (4)	−24.5	−0.5	0.6	0.3	0.9	32
	264–268 (3)	−26–−25	−2	2.5	0.8	3.3	49
Late ($Q^{2–4}$)	260–240 (4)	−38	−0.1	0.1	0.1	0.2	43
	200 (2)	−38–−35	−0.1	0.1	0.1	0.2	13
Maletoyvayamite-Quartz Association							
Early (Q^1)	255–245 (4)	−38–−35	−2.5–−2	3.3	1.0	4.3	39–32
	250–245 (2)	−38–−35	−2.4–−2.2	3.3	1.0	4.3	36–32
Late ($Q^{2–4}$)	228–210 (6)	−38	−0.7–−0.5	1.0	0.5	1.5	23–16
	220–135 (3)	−38	−0.6–−0.3	0.9	0.3	1.2	20–4

Note. * Number of inclusions; ** pressure value calculated for the concentration of solutions (wt.%) to NaCl eq.

4.3.1. Pyrite-Quartz Association

Two-phase water–salt inclusions from early quartz are homogenized at temperatures ranging from 290 to 260 °C. Ice is formed in these inclusion solutions when they are cooled, and melts again when heated at a temperature range from −2 to −0.4 °C. The first melting of ice is observed in a temperature range from −38 to −35 °C, although intense, ice melting and the appearance of liquid in is recorded in the range from −26 to −23 °C. In small inclusions, the first melting is distinguished in the same temperature interval (from −26 to −23 °C), which is close to the melting temperature of the eutectic NaCl + KCl + H_2O water–salt system (−23.5 °C). This may indicate that the main salt components in the inclusions are probably NaCl and KCl with a diminutive admixture of other soluble salts, which somewhat lower the eutectic of the solutions. One of such impurities may correspond to K_2CO_3, since the melting temperatures of eutectics in the water–salt systems Na_2CO_3 + K_2CO_3 + H_2O and K_2CO_3 + H_2O correspond to −37 and −36.4 °C [48], that also coincides with a temperature interval of the ice first melting in large inclusions −38–35 °C.

According to the method used by Borisenko [41] it was revealed that the concentrations of Na and K chlorides prevailing in the composition of solutions in the inclusions are estimated as 2.5–0.1 wt.% NaCl and 0.8–0.1 wt.% KCl, however, the presence of Fe and Mg chlorides in the composition of the inclusions is unlikely. Mg compounds are not typical for the studied mineral associations. $FeCl_2$ and $FeCl_3$ in water–salt systems would cause a metastable state, which also would involve incomplete crystallization of the cooled solution and, as a consequence, a decrease in the melting point of the eutectic [49,50], which was not observed in our studies.

Cryometric study of individual vapor inclusions and the gas component of water–salt inclusions did not reveal the presence of a dense gas phase. The cooling down to −190 °C did not result in any gases' liquefaction or crystallization. The absence of a dense gas phase is also confirmed by the study of fluid inclusions with Raman spectroscopy. Raman spectra of the gas phase of inclusions do not contain bands characteristic of CO_2, N_2, and CH_4 [51].

The pressure values were calculated for the concentration of solutions (wt.%) equivalent to NaCl. These values decrease from early generations of quartz to later ones and are in the range of 70–13 bar for the pyrite-quartz association.

4.3.2. Maletoyvayamite-Quartz Association

Two-phase inclusions in the early quartz of the maletoyvayamite-quartz association were homogenized in a temperature range from 255 to 245 °C. Ice is formed in cooled solutions of two-phase inclusions, which then is melted at temperatures ranging from −2.5 to −2 °C. The beginning of ice melting in cooled solutions occur in the range from −38 to −35 °C. Fluid inclusions in late quartz from veinlets were homogenized in a temperature range from 225 to 135 °C (Table 4).

The rate of ice melting in cooled inclusions increases sharply at temperatures above −23 °C, and lastly ice melts in a temperature range from −0.7 to −0.3 °C. The temperature ranges for the initial melting point of cooled solutions in the inclusions are close to the melting temperature of the eutectic of the water–salt systems $Na_2CO_3 + K_2CO_3 + H_2O$ and $K_2CO_3 + H_2O$: −37 °C and −36.4 °C, respectively. A quick acceleration of ice melting in cooled solutions at a temperature of −23 °C suggests the presence of NaCl and KCl solutions along with Na_2CO_3 and K_2CO_3 as part of the composition.

The water–salt inclusions of the ore-bearing minerals from the maletoyvayamite-quartz association are more saturated in salts in comparison with the inclusions from the pyrite-quartz association (Table 4). Salt concentrations were calculated by the method of Borisenko [41], reaching NaCl = 3.3 and 1.0, and KCl = 1.0 and 0.5 (wt.%) in early quartz and late quartz, respectively. These values decrease from early generations of quartz to later ones and are in the range of 39–4 bar for the maletoyvayamite-quartz association (Table 4, Figure 10).

5. Discussion

The results obtained from fluid inclusions microthermometry in vein quartz of the Maletoyvayam deposit (Gaching area) indicate that the quartz was formed in a wide range of temperatures from nearly 300 to 180 °C and even below. In the same way, the pressure also varies from 80 to 10 bar (average). At high temperatures (295–255 °C) and pressures (50–75 bar), pyrite is the main ore mineral (pyrite-quartz association) (Figure 11a), while maletoyvayamite, bismuthinite, Cu-sulfosalts, etc. occurred in a rather narrow range of temperatures and pressures (245–255 °C and 32–39 bar) (Figure 12).

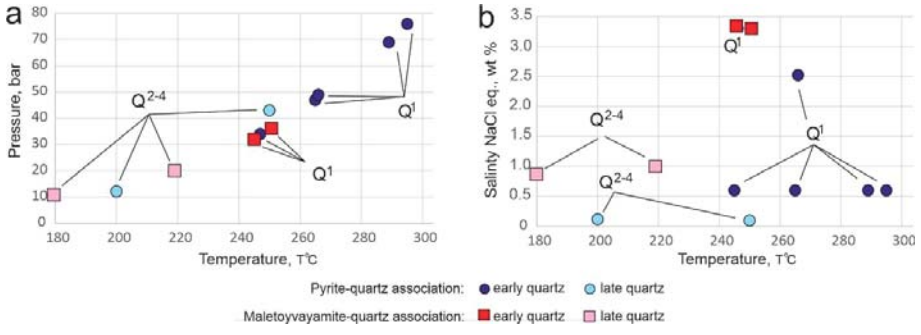

Figure 11. (**a**) Diagrams of pressure versus temperature and (**b**) salinity of NaCl eq. versus temperature on the basis of the microthermometry study of the different quartz generations.

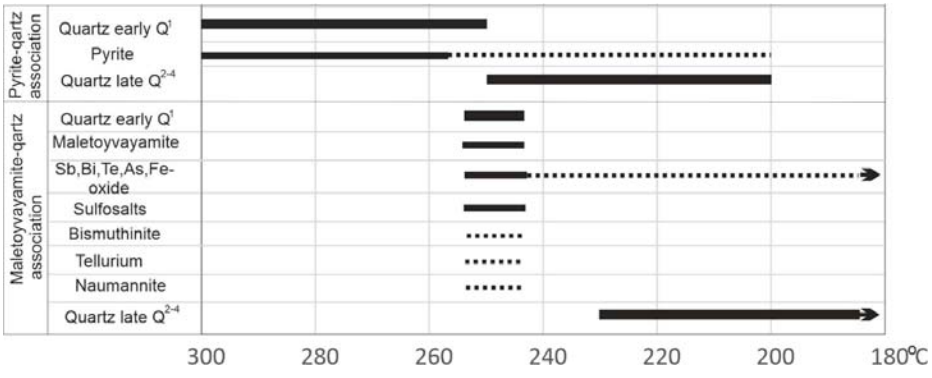

Figure 12. Paragenetic diagram showing the stages of mineral formation. The thick line – main mineral, line - less common mineral, dotted line – rare mineral.

Both of the diagrams in (Figure 11) display a gradual change between the mineral associations, moving from pyrite-quartz to maletoyvayamite-quartz; the late quartz generation of the first association coincides with the early quartz generation of the second association in P-T parameters (Figure 11a); however, they do differ in salt content (Figure 11b). For instance, the salinity percentage in fluid inclusions of the productive gold-bearing association (maletoyvayamite-quartz) is considerably bigger (3.3 versus 0.6).

Sulfosalts are an important indicator of mineral formation conditions in hydrothermal deposits of various types [52–54]. Enargite in particular is a formation conditions indicator of HS type epithermal deposits [2]. This mineral has been found in ores of well-known HS epithermal deposits: Goldfield (Nevada, USA), Red Mountain, Lake City II and Summitville (Colorado, USA), Julcani (Peru) [2,55,56] and others. It is also common among the sulfosalts described at Maletoyvayam [33], and, in particular, in the studied samples (Figure 5). Enargite-bearing epithermal deposits develop when fluid rapidly rises to higher levels of the earth's crust without interacting with groundwater. Then, its gradual cooling and partial neutralization due to its reaction with the host rocks leads to the formation of a pyrite–enargite association, including alunite and barite [57].

Earlier, we made the assumption that pyrite formation and maletoyvayamite are divergent in time based on the fact that they have never been encountered in equilibrium intergrowths [26]. Indeed, the microthermometry study on fluid inclusions in quartz confirmed this hypothesis: the most abundant dissemination of pyrite grains occur in the earliest generations of the fine-grained quartz aggregate (Figure 8a), with temperatures that correspond to a range of 295–245 °C, whereas the Au minerals, sulfosalts and other associated minerals of the main ore stage crystallized at 255–245 °C (Table 3, Figures 10 and 12). Moreover, pyrite crystallization precedes enargite in many HS-type epithermal deposits [58].

The fluid inclusions data for HS epithermal deposits (Table 5) indicate that ore deposition occurred mainly at temperatures similar to the LS and IS types. For example, the homogenization temperatures of primary inclusions in quartz from the Aginskoye deposit (LS type) were 230–280 °C, with the ore phase being in the range of 250–260 °C [59]. Similar temperature ranges have been established both for the LS type deposits (Rodnikovoye and Asachinskoye in South Kamchatka, Russia) [19,21,60] and in regard to the IS type deposit (Cheshmeh Hafez, Iran) [61], the homogenization temperatures of the primary inclusions are in the range of 140–280 °C with peaks at around 180–250 °C. This is also compatible with all HS type deposits, and with the obtained formation parameters of the Maletoyvayam deposit (Table 5).

The salinity of ore-forming solutions differs both between the deposit types (LS and HS) and even within the same type (Table 5). The salinity range can be strongly influenced on one hand by the

mixing with meteoric water (dilution), or, on the other hand, by boil-off (concentrating) [57,62]. Fluid inclusions with high salinity reflect the fluid history after crystallization of underlying magmas [63,64]. The strongly acidic hot fluids interaction with host rocks typically dissolve the surrounding rock, leaving only silica. Then, brines containing gold ascend from the magma and precipitate metals in the vuggy quartz forming the HS deposits. In general, the salinity of HS type deposits show a wide range of values. For example, the highest salinity values of HS type ore deposits range from 5 to 24 wt.% NaCl eq. for Julcani, Summitville and Goldfield [65,66] (Table 5). The ranges of 3–12 wt.% NaCl eq. are typical of the Kairagach and Shelekhovskoe [67,68]. However, data from fluid inclusions in quartz associated with the main gold stage from Red Mountain, Mt Carlton, Lepanto, Agan, Danchenkovskoe and Belaya Gora [27,69–72], including Maletoyvayam, indicate salinities of up to 4.5 wt.% NaCl eq. (Table 5).

Table 5. Crystallization conditions parameters for HS type epithermal deposits.

District	Measured		Selected Ore Representative		References
	T °C	Salinity	T °C	Salinity	
Red Mountain, BC, Canada	215–265 (?)	1.6	240	1.6	[69]
Summitville, CO	231–276 (?)	7–21			[65]
Goldfield, NV	150–325 (?)	5–18			[65,66]
Julcani, Peru	161–275 (?)	5–24			[65]
Mt Carlton, NE Australia	163–264 (57)	0–1.6	222		[70]
Lepanto, Philippines	166–285	0.2–4.5			[71]
Kairagach, Uzbekistan	120–300	<12			[67]
Agan, Russia	88–184 (6)	0.2–2.6	136		[27]
Danchenkovskoe, Russia	297–336	1–4			[72]
Belaya Gora, Russia	≈100	<1			[68]
Shelekhovskoe, Russia	180–250	3–8			
Maletoyvayam * Russia	295–245 (23)	0.9–3.3	270	2	This study
Maletoyvayam **	255–245(6)	4.3	250	4.3	This study
Maletoyvayam ***	228–135(9)	1.3	180	1.3	This study

Note. *—pyrite-quartz association (early Q^1); **—maletoyvayamite-quartz association (early Q^1); ***—maletoyvayamite-quartz association (later Q^{2-4}). Salinity in wt. % NaCl eq. Selected Temperature and Salinity related to the productive stage.

The HS mineralization associated with the dilute to moderately saline solutions (<5 to ~10 wt.% NaCl eq.) occur at temperatures between 180 and 320 °C [71]. The hotter and more saline fluid inclusions occur in rocks of deep horizons closer to the magma fluid source [14,73]. The reduction in the sulfidation state of fluids due to interaction with wallrocks can change HS fluids to IS ones, as confirmed by paragenetic transitions from HS to IS mineralization [74]. In the IS-type epithermal deposits, salinity ranges vary widely and reaches high values, for example, 4.7–18 wt.% NaCl eq. at the Cheshmeh Hafez field [61]. While the salinity in inclusions from LS-type deposits of the Aginskoye deposit of the Central Kamchatka volcanic belt is no more than 2 wt.% NaCl equiv. [59], as in the Juliet field (LS-type), at the Okhotsk-Chukotka volcanic belt, the salinity of the inclusions is about 1.2–5.6 wt.% NaCl eq. [75]. In this respect, it is clear that the salinity of fluid inclusions is not intimately related to the type of deposit, but more dependent on the conditions of ore deposition.

Based on the formation model for HS epithermal deposits [4,39,64,76,77], it can be assumed that gold–copper–porphyry mineralization may be found at deeper horizons in the Maletoyvayam area since the models for epithermal deposits form in a relatively near-surface magmatic-hydrothermal environment associated with volcanic rocks that overlie cogenetic intrusive rocks.

6. Conclusions

Two mineral associations were indentified during the study of quartz mineralization at the Maletoyvayam Au-deposit: the earlier pyrite-quartz and the Au-bearing maletoyvayamite-quartz associations. Each of them contains different generations of quartz, but only the early quartz generations

in each of the mentioned associations include either pyrite (pyrite-quartz association) or sulfosalts with gold compounds and other rare associating minerals (maletoyvayamite-quartz association). Maletoyvayamite is the main Au mineral of the maletoyvayamite-quartz association, which has never been reported in any other epithermal gold deposit in the world. It was particularly identified in samples having high Au concentrations, and occurs in the marginal parts of sulfosalts, intergrown with complex oxides of chalcogenides and native tellurium, and also as individual inclusions in quartz.

The following features and physicochemical conditions on the formation of a productive ore association were identified based on the fluid inclusions study (Figures 11 and 12):

The composition of primary fluid inclusions in the quartz is represented by the dominant NaCl and KCl, as well as Na_2CO_3 and K_2CO_3. The total percentage of salinity varies from 4.3 wt.%. in the early quartz from the maletoyvayamite-quartz association to 0.2 in late quartz from the pyrite-quartz association. The temperature of fluids varied from 290 to 135 °C, decreasing during the crystallization of the later generations of quartz (Figure 11). The calculated pressure of the fluid varies from 79 to 4 bar, and most likely corresponds to hydrostatic fluid. The fluids that formed the maletoyvayamite-quartz association differ from those forming the pyrite-quartz association with lower temperatures (255–135 °C), and increased salt concentration (4.3 wt.%). The increase in the total concentration of salts in the hydrothermal solutions that formed the maletoyvayamite-quartz association is due to the boiling of fluids. All parameters before presented and discussed agree in all respects with other HS-type epithermal deposits around the world; however, they do not provide further evidence of the particularities in ore mineral composition of the Maletoyvayam deposit, which is as yet the only known occurrence of the HS type on the Central Kamchatka Volcanic Belt.

Author Contributions: E.G.S. and V.M.C. provided the samples from the Maletoyvayam deposit. Conceptualization and methodology: E.G.S., N.D.T., G.A.P. and D.S.B. Investigation: A.A.B., N.D.T. and V.M.C. Writing—original draft preparation, N.D.T. and D.S.B. Editing, E.G.S. and G.A.P. Visualization, N.D.T. Supervision, E.G.S. and N.D.T. All authors have read and agreed to the published version of the manuscript.

Funding: The studies were carried out within the framework of the state assignment of the Sobolev Institute of Geology and Mineralogy of the Siberian Branch of the Russian Academy of Sciences, and the Institute of Volcanology and Seismology of the Far East Branch of the Russian Academy of Sciences. Financial support was provided by the Russian Foundation of Basic Research, project No. 19-05-00316 and the grant No. 13.1902.21.0018 "Fundamental Problems of the Development of the Mineral Resource Base of the High-Tech Industry and Energy in Russia" from Ministry of Science and Higher Education of the Russian Federation.

Acknowledgments: The authors thank N. Karmanov and M. Khlestov for helping with the utilization of the scanning electron microscope and an X-ray spectral microanalyzer (Analytical Center for multi-elemental and isotope research in Sobolev Institute of Geology and Mineralogy, SBRAS). We are grateful to editors and reviewers for their constructive and helpful comments, which significantly improved the manuscript.

Conflicts of Interest: The authors declare no conflict of interest.

References

1. Lindgren, W. *Mineral. Deposits*; McGraw-Hill Book Company, Inc.: New York, NY, USA; London, UK, 1933; p. 930.
2. Heald, P.; Hayba, D.O.; Foley, N.K. Comparative anatomy of volcanic-hosted epithermal deposits: Acid-sulfate and adularia-sericite types. *Econ. Geol.* **1987**, *82*, 1–26. [CrossRef]
3. Taylor, B.E. Epithermal gold deposits. In *Mineral. Deposits of Canada: A Synthesis of Major Deposit-Types, District Metallogeny, the Evolution of Geological Provinces, and Exploration Methods*; Goodfellow, W.D., Ed.; Mineral Deposits Division, Special Publication; Geological Association of Canada: Saint John, NL, Canada, 2007; Volume 5, pp. 113–139.
4. Hedenquist, J.W.; Arribas, A.; Gonzalez-Urien, E. Exploration for epithermal gold deposits. *Rev. Econ. Geol.* **2000**, *13*, 245–277.
5. Hedenquist, J.W. Mineralization associated with volcanic-related hydrothermal systems in the Circum-Pacific basin. In *Transactions of the Fourth Circum Pacific Conference on Energy and Mineral Resources Conference, Singapore*; American Association of Petroleum Geologists: Tulsa, OK, USA, 1987; pp. 513–524.

6. Ashley, R.P. Occurrence model for enargite-gold deposits. In *U.S. Geological Survey Open-File Report 82-795*; U.S. Department of the Interior, Geological Survey USA: Reston, VA, USA, 1982; pp. 144–147.
7. Bethke, P.M. Controls on base- and precious-metal mineralization in deeper epithermal environments. In *US Geological Survey Open-File Report 84–890*; U.S. Dept. of the Interior, Geological Survey USA: Reston, VA, USA, 1984; 39 p.
8. Ransome, F.L. The association of alunite with gold in the Goldfield district, Nevada. *Econ. Geol.* **1907**, *2*, 801–803. [CrossRef]
9. Bonham, H.F. Three major types of epithermal precious metal deposits. *Geol. Soc. Am. Abstr. Programs* **1984**, *16*, 449.
10. Bonham, H.F., Jr. Models for volcanic-hosted epithermal precious metal deposits: A review. In *Proceedings Symposium 5th, Volcanism, Hydrothermal Systems and Related Mineralisation*; International Volcanological Congress: Auckland, New Zealand, 1986; pp. 13–17.
11. Berger, B.R. Descriptive model of low-sulfide Au-quartz veins. In *Mineral deposit models, US Geological Survey Bulletin*; United States Government Printing Office: Washington, DC, USA, 1992; p. 239.
12. Berger, B.R.; Henley, R.W. Advances in the understanding of epithermal gold-silver deposits, with special reference to the western United States. *Econ. Geol. Monogr.* **1989**, *6*, 405–423.
13. Henley, R.W.; Ellis, A.J. Geothermal systems ancient and modern: A geochemical review. *Earth Sci. Rev.* **1983**, *19*, 1–50. [CrossRef]
14. Arribas, A., Jr. Characteristics of high-sulfidation epithermal deposits, and their relation to magmatic fluid. *Mineral. Assoc. Can. Short Course* **1995**, *23*, 419–454.
15. Kubota, Y. Temporal and spatial relationship and significance of island arc junctions on Late Cenozoic gold deposits in the Japanese Islands. *Res. Geol.* **1994**, *44*, 17–24.
16. Okrugin, V.; Kokarev, S.; Okrugina, A.; Chubarov, V.; Shuvalov, R. An unusual example of the interaction of modern hydrothermal system with Au-Ag veins (Southern Kamchatka). *Miner. Mag.* **1994**, *58A*, 669–670. [CrossRef]
17. Khanchuk, A.I.; Ivanov, V.V. Meso-Cenozoic geodynamic settings and gold mineralization of the Russian Far East. *Russ. Geol. Geophys.* **1999**, *40*, 1607–1617.
18. Konstantinov, M.M.; Vargunina, N.P.; Kosovets, T.N.; Struzhkov, S.F.; Syngaevskii, E.D.; Shishakova, L.N. *Gold-Silver Deposits. Series: Models of Noble-and Nonferrous-Metal Deposits*; TsNIGRI: Moscow, Russia, 2000; 239p. (In Russian)
19. Borovikov, A.A.; Lapukhov, A.S.; Borisenko, A.S.; Seryotkin, Y.V. The Asachinskoe epithermal Au-Ag deposit in southern Kamchatka: Physicochemical conditions of formation. *Russ. Geol. Geophys.* **2009**, *50*, 693–702. [CrossRef]
20. Takahashi, R.; Matsueda, H.; Okrugin, V.M. Hydrothermal gold mineralization at the Rodnikovoe deposit in South Kamchatka, Russia. *Res. Geol.* **2002**, *52*, 359–369. [CrossRef]
21. Takahashi, R.; Matsueda, H.; Okrugin, V.M.; Ono, S. Epithermal gold-silver mineralization of the Asachinskoe deposit in South Kamchatka, Russia. *Resour. Geol.* **2007**, *57*, 354–373. [CrossRef]
22. Okrugin, V.M.; Shishkanova, K.O.; Yablokova, D.A. About ores of Amethystovoe deposits (Kamchatka). *Mt. Bull. Kamchatka* **2015**, *3-4*, 33–34. (In Russian)
23. Andreeva, E.D.; Matsueda, H.; Okrugin, V.M.; Takahashi, R.; Ono, S. Au–Ag–Te mineralization of the low-sulfidation epithermal Aginskoe deposit, Central Kamchatka, Russia. *Res. Geol.* **2013**, *63*, 337–349. [CrossRef]
24. Golyakov, V.I. *Geological Map of the USSR Scale 1: 200 000*; Pogozhev, A.G., Ed.; Series Koryak; Sheets P-5 8-XXXIII, O-58-III.; VSEGEI Cartographic Factory: St. Peterburg, Russia, 1980. (In Russian)
25. Melkomukov, B.H.; Razumny, A.V.; Litvinov, A.P.; Lopatin, W.B. New highly promising gold objects of Koryakiya. *Min. Bull. Kamchatka* **2010**, *14*, 70–74. (In Russian)
26. Tolstykh, N.; Vymazalova, A.; Tuhy, M.; Shapovalova, M. Conditions of formation of Au-Se-Te mineralization in the Gaching ore occurrence (Maletoivayam ore field), Kamchatka, Russia. *Min. Mag.* **2018**, *82*, 649–674. [CrossRef]
27. Volkov, A.V.; Sidorov, A.A.; Chizhova, I.A.; Alekseev, V.Y.; Savva, N.E.; Kolova, E.E. The Agan epithermal gold-silver deposit and prospects for the discovery of high-sulfidation mineralization in Northeast Russia. *Geol. Ore Depos.* **2015**, *57*, 21–41. [CrossRef]

28. Goryachev, N.A.; Volkov, A.V.; Sidorov, A.A.; Gamyanin, G.N.; Savva, N.Y.; Okrugin, V.M. Au-Ag-mineralization of volcanogenic belts of the northeast. Asia. *Lithosphere* **2010**, *3*, 36–50. (In Russian)
29. Palyanova, G.A. Gold and Silver Minerals in Sulfide Ore. *Geol. Ore Depos.* **2020**, *62*, 383–406. [CrossRef]
30. Tolstykh, N.D. Gold ore mineralization of the Maletoyvayam ore occurrence. In *Materials of the Anniversary Congress of the Russian Mineralogical Society "200 Years of RMO"*; LLC Publishing House LEMA: St. Peterburg, Russia, 2017; Volume 2, pp. 339–341.
31. Tolstykh, N.; Palyanova, G.; Bobrova, O.; Sidorov, E. Mustard gold of the Gaching ore occurrence (Maletoyvayam deposit, Kamchatka, Russia). *Minerals* **2019**, *9*, 489. [CrossRef]
32. Tolstykh, N.D.; Tuhý, M.; Vymazalová, A.; Plášil, J.; Laufek, F.; Kasatkin, A.V.; Nestola, F.; Bobrova, O.V. Maletoyvayamite, $Au_3Se_4Te_6$, a new mineral from Maletoyvayam deposit, Kamchatka peninsula, Russia. *Min. Mag.* **2020**, *84*, 117–123. [CrossRef]
33. Shapovalova, M.; Tolstykh, N.; Bobrova, O. Chemical composition and varieties of sulfosalts from gold mineralization in the Gaching ore occurrence (Maletoyvayam ore field). *IOP Conf. Ser. Earth Environ. Sci.* **2019**, *319*, 012019. [CrossRef]
34. Palyanova, G.A.; Tolstykh, N.D.; Zinina, V.Y.; Koh, K.A.; Seretkin, Y.V.; Bortnikov, N.S. Synthetic gold chalcogenides in the Au-Te-Se-S system and their natural analogs. *Dokl. Earth Sci.* **2019**, *487*, 929–934. [CrossRef]
35. Palyanova, G.; Mikhlin, Y.; Zinina, V.; Kokh, K.; Seryotkin, Y.; Zhuravkova, T. New gold chalcogenides in the Au-Te-Se-S system. *J. Phys. Chem. Solids.* **2020**, *138*, 109276. [CrossRef]
36. Vlasov, G.M. *Volcanic Sulfur Deposits and Some Problems of Hydrothermal ore Formation*; Nauka: Moscow, Russia, 1971. (In Russian)
37. Stefanov, Y.M.; Schiroky, B.I. *Metallogeny of the Upper Structural Floor of Kamchatka*; Science: Moscow, Russia, 1980. (In Russian)
38. Melkomukov, V.N.; Amelin, S.A.; Razumny, A.V.; Kudrin, A.S. *State Geological Map of the Russian Federation on a Scale of 1: 200 00*; Lopatin, V.B., Ed.; Series Olyutorsky; Sheet P-58-XXXIII, O-58-III.; VSEGEI Cartographic Factory: St. Petersburg, Russia, 2010. (In Russian)
39. White, N.C.; Hedenquist, J.W. Epithermal gold deposits: Styles, characteristics and exploration. *Publ. SEG Newsl.* **1995**, *23*, 9–13.
40. Hedenquist, J.W.; Arribas, R.A. Epithermal ore deposits: First-order features relevant to exploration and assessment. In Proceedings of the 14th SGA Biennial Meeting, Québec City, QC, Canada, 20–23 August 2017; Volume 1, pp. 47–50.
41. Borisenko, A.S. Analysis of the salt composition of solutions of gas-liquid inclusions in minerals by cryometry. In *The Use of Methods of Thermobarogeochemistry in the Search and Study of Ore Deposits*; Nedra: Moscow, Russia, 1982; pp. 37–47. (In Russian)
42. Bodnar, R.J.; Vityk, M.O. Interpretation of microthermometric data for NaCl-H_2O fluid inclusions. In *Fluid Inclusions in Minerals: Methods and Applications*; Virginia Polytechnic Institute State University: Blacksburg, VA, USA, 1994; pp. 117–131.
43. Bakker, R.J. AqSo_NaCl: Computer program to calculate p-T-V-x properties in the H2O-NaCl fluid system applied to fluid inclusion research and pore fluid calculation. *Comput. Geosci.* **2018**, *115*, 122–133. [CrossRef]
44. Bakker, R.J. Fluids: New software package to handle microthermometric data and to calculate isochors. *Mem. Geol. Soc.* **2001**, 23–25.
45. Brown, P.E. FLICOR: A microcomputer program for the reduction and investigation of fluid-inclusion data. *Am. Min.* **1989**, *74*, 1390–1393.
46. Voudouris, P.; Melfos, V.; Spry, P.G.; Moritz, R.; Papavassiliou, K.; Falalakis, G. Mineralogy and geochemical environment of formation of the Perama Hill high-sulfidation epithermal Au-Ag-Te-Se deposit, Petrota Graben, NE Greece. *Min. Petrol.* **2011**, *103*, 79–100. [CrossRef]
47. Roedder, E. Fluid inclusions. In *Reviews in Mineralogy*; Mineralogical Society of America: Washington, DC, USA, 1984; Volume 12, pp. 79–108.
48. Ermakov, N.P. *Geochemical Systems of Inclusions in Minerals*; Nedra: Moscow, Russia, 1972. (In Russian)
49. Lecumberri-Sanchez, P.; Steele-MacInnis, M.; Bodnar, R.J. Synthetic fluid inclusions XIX. Experimental determination of the vapor-saturated liquidus of the system H_2O–NaCl–$FeCl_2$. *Geochim. Cosmochim. Acta* **2015**, *148*, 34–49. [CrossRef]

50. Borovikov, A.A.; Gushchina, L.V.; Borisenko, A.S. Determination of iron (II, III) and zinc chlorides in solutions of fluid inclusions during cryometric studies. *Geochemistry* **2002**, *1*, 70–79. (In Russian)
51. Frezzotti, M.L.; Tecce, F.; Casagli, A. Raman spectroscopy for fluid inclusion analysis. *J. Geochem Explor.* **2012**, *112*, 1–20. [CrossRef]
52. Spiridonov, E.M. Typomorphic specific features of Fahlore from some plutonogenic, volcanogenic, and telethermal gold deposits. *Geol. Rudn. Mestorozhd.* **1987**, *29*, 83–92. (In Russian)
53. Repstock, A.; Voudouris, P.; Kolitsch, U. New occurrences of watanabeite, colusite, "arsenosulvanite" and Cu-excess tetrahedrite-tennantite at the Pefka high-sulfidation epithermal deposit, northeastern Greece. *Neues Jahrb. Fur Mineral. Abh. J. Mineral. Geochem.* **2015**, *192*, 135–149. [CrossRef]
54. Kovalenker, V.A.; Bortnikov, N.S. Chemical composition and mineral associations of sulphosalts in the precious metal deposits from different geological environment. *Geol. Carpathica* **1985**, *36*, 283–291.
55. Buchanan, L.J. Precious metal deposits associated with volcanic environments in the southwest. *Ariz. Geol. Soc. Dig.* **1981**, *14*, 237–262.
56. Hayba, D.O.; Bethke, P.M.; Heald, P.; Foley, N.K. Geologic, mineralogic and geochemical characteristics of volcanic-hosted epithermal precious metal deposits. *Rev. Econ. Geol.* **1985**, *2*, 129–167.
57. Corbett, G. Epithermal Au-Ag Deposit Types—Implications for Exploration. 2005. Available online: https://www.researchgate.net/publication/237489786 (accessed on 30 August 2014).
58. Jannas, R.; Bowers, T.S.; Petersen, U.; Beane, E. High-Sulfidation Deposit Types in the El Indio District, Chile. In *Geology and Ore Deposits of the Central Andes*; Skinner, B.J., Ed.; Society Economic Geologists Special Publication: Littleton, CO, USA, 1999; Volume 7, pp. 27–59.
59. Okrugin, V.M.; Andreeva, E.D.; Yablokova, D.A.; Okrugina, A.M.; Chubarov, V.M.; Ananiev, V.V. The new data on the ores of the Aginskoye gold-telluride deposit (Central Kamchatka). In *"Volcanism and Its Associated Processes" Conference*; Petropavlovsk-Kamchatsky: Kamchatka Krai, Russia, 2014; pp. 335–341. (In Russian)
60. Takahashi, R.; Matsueda, H.; Okrugin, V. Epithermal gold and silver mineralization at the Rodnikovoe deposit related to the hydrothermal activity in the Mutnovsko-Asachinskaya geothermal area, Southern Kamchatka, Russia. In Proceedings of the International Symposium on Gold and Hydrothermal Systems, Fukuoka, Japan, 4 November 2001; pp. 51–57.
61. Mehrabi, B.; Siani, M.G. Intermediate sulfidation epithermal Pb-Zn-Cu (±Ag-Au) mineralization at Cheshmeh Hafez deposit, Semnan Province. *J. Geol. Soc. India* **2012**, *80*, 563–578. [CrossRef]
62. Hedenquist, J.W.; Henley, R.W. Hydrothermal eruptions in the Waiotapu geothermal system, New Zealand: Their origin, associated breccias, and relation to precious metal mineralization. *Econ. Geol.* **1985**, *80*, 1640–1668. [CrossRef]
63. Hedenquist, J.W.; Arribas, A.; Reynolds, T.J. Evolution of an intrusion-centered hydrothermal system: Far Southeast-Lepanto porphyry andepithermal Cu-Au deposits, Philippines. *Econ. Geol.* **1998**, *93*, 373–404. [CrossRef]
64. Heinrich, C.A.; Dreisner, T.; Steffánson, A.; Seward, T.M. Magmatic vapor contraction and the transport of gold from the porphyry environment to epithermal ore deposits. *Geology* **2004**, *32*, 761–764. [CrossRef]
65. Bruha, D.I.; Noble, D.C. Hypogenequartz-alunite±pyrite alteration formed by moderately saline, ascendant hydrothermal solutions. *Geol. Soc. Am. Abstr. Programs* **1983**, *15*, 325.
66. Jensen, M.L.; Ashley, R.P.; Albers, J.P. Primary and secondary sulfates at Goldfield, Nevada. *Econ. Geol.* **1971**, *66*, 618–626. [CrossRef]
67. Kovalenker, V.A.; Plotinskaya, O.Y.; Prokofev, V.Y.; Gertman, Y.L.; Koneev, R.I.; Pomortsev, V.V. Mineralogy, geochemistry, and genesis of gold-sulfide-selenide-telluride ores from the Kairagach deposit (Uzbekistan). *Geol. Ore Depos.* **2003**, *45*, 171–200.
68. Mishin, L.F.; Berdnikov, N.V. Nature of high-alumina secondary quartzite by data of thermobarogeochemistry and isotopic analysis of oxygen and hydrogen. *Russ. J. Pac. Geol.* **2001**, *20*, 123–139. (In Russian)
69. Nash, J.T. Fluid inclusion studies of vein, pipe, and replacement deposits, northwestern San Juan Mountains, Colorado. *Econ. Geol.* **1975**, *70*, 1448–1462. [CrossRef]
70. Sahlstrom, F. The Mt Carlton High-Sulfidation Epithermal Deposit, NE Australia: Geologic Character, Genesis and Implications for Exploration. PhD. Thesis, James Cook University, Singapore, 2018.
71. Mancano, D.P.; Campbell, A.R. Microthermometry of enargite-hosted fluid inclusions from the Lepanto, Philippines, high-sulfidation Cu-Au deposit. *Geochim. Cosmochim. Acta* **1995**, *59*, 3909–3916. [CrossRef]

72. Lapukhov, A.S.; Borovikov, A.A.; Guzman, B.V.; Miroshnichenko, L.V.; Rasvorotneva, L.I. Hieratite in hydrothermally altered volcanic rocks of Danchenkovskoye deposit (the Urup Island). *Zap. RMO* **2012**, *141*, 52–59. (In Russian)
73. Arribas, A., Jr.; Cunningham, C.G.; Rytuba, J.J.; Rye, R.O.; Kelly, W.C.; Podwysocki, M.H.; McKee, E.H.; Tosdal, R.M. Geology, geochronology, fluid inclusions, and isotope geochemistry of the Rodalquilar gold-alunite deposit, Spain. *Econ. Geol.* **1995**, *90*, 795–822. [CrossRef]
74. Sillitoe, R.H.; Hedenquist, J.W. Linkages between volcanotectonic settings, ore-fluid compositions, and epithermal precious metal deposits. In *Volcanic, Geothermal, and Ore-Forming Fluids: Rulers and Witnesses of Processes within the Earth*; Simmons, S.F., Graham, I.J., Eds.; Society Economic Geologists Special Publication: Johnson Printing, Littleton, CO, USA, 2003; Volume 10, pp. 315–343.
75. Prokof'ev, V.Y.; Ali, A.A.; Volkov, A.V.; Savva, N.E.; Kolova, E.E.; Sidorov, A.A. geochemical peculiarities of ore forming fluidof the juliette Au–Ag epithermal deposit (Northeastern Russia). *Dokl. Earth Sci.* **2015**, *460*, 87–91. [CrossRef]
76. Cooke, D.R.; Simmons, S.F. Characteristics and genesis of epithermal gold deposits. *Rev. Econ. Geol.* **2000**, *13*, 221–244.
77. Sillitoe, R.H. Porphyry copper systems. *Econ. Geol.* **2010**, *105*, 3–41. [CrossRef]

minerals

MDPI

Article

Au-Ag-S-Se-Cl-Br Mineralization at the Corrida Deposit (Russia) and Physicochemical Conditions of Ore Formation

Elena E. Kolova [1], Nataly E. Savva [1], Tatiana V. Zhuravkova [2,3], Anton N. Glukhov [1] and Galina A. Palyanova [2,3,*]

[1] Shilo North-East Interdisciplinary Scientific Research Institute, Far Eastern Branch of the Russian Academy of Sciences, 16 Portovaya St., 685000 Magadan, Russia; kolova@neisri.ru (E.E.K.); savva@neisri.ru (N.E.S.); gluhov76@list.ru (A.N.G.)
[2] Sobolev Institute of Geology and Mineralogy, Siberian Branch of Russian Academy of Sciences, 3 Koptyuga Ave., 630090 Novosibirsk, Russia; zhur0502@rambler.ru
[3] Department of Geology and Geophysics, Novosibirsk State University, 1 Pirogova St., 630090 Novosibirsk, Russia
* Correspondence: palyan@igm.nsc.ru

Abstract: The mineral and chemical compositions of ores from the Corrida epithermal Au-Ag deposit (Chukchi Peninsula, Russia) were studied using the optical and scanning electron microscopy with X-ray energy-dispersion microanalysis. The deposit was formed at the time close to the period when the basic volume of acid magmas had been emplaced within the Okhotsk–Chukotka belt (84 to 80 Ma). The Au–Ag mineralization is distinguished with Au-Ag sulphides and selenides (uytenbogaardtite-fischesserite solid solution, Se-acanthite, S-naumannite) and Ag halides of the chlorargyrite-embolite-bromargyrite series. The ores were formed in two stages. Using microthermometric methods, it has been established that the ore-bearing quartz was formed in the medium-temperature environment (340–160 °C) with the participation of low-salt (3.55 to 0.18 wt.% NaCl eq.) hydrotherms, mostly of the NaCl composition with magnesium, iron and low-density CO_2. According to our results of thermodynamic modeling at temperatures from 300 to 25 °C and data on mineral metasomatic alterations of the host rocks, the Au-Ag-S-Se-Cl-Br mineralization was formed at decreasing temperature and fugacity of sulphur ($\log fS_2$ from −6 to −27), selenium ($\log fSe_2$ from −14 to −35), and oxygen ($\log fO_2$ from −36 to −62), with near-neutral solutions replaced by acid solutions. Analysis of the obtained data shows that the Corrida refers to the group of the LS-type epithermal deposits. This deposit is a new example of epithermal deposits with significant quantities of Au–Ag chalcogenides (acanthite, uytenbogaardtite, fischesserite, naumannite and others).

Keywords: Arctic; epithermal mineralization; Corrida deposit (Chukchi Peninsula, Russia); LS-type of deposits; Au-Ag-S-Se-Cl-Br mineralization; physicochemical parameters of ore formation (T, P, fO_2, fS_2, fSe_2, pH)

Citation: Kolova, E.E.; Savva, N.E.; Zhuravkova, T.V.; Glukhov, A.N.; Palyanova, G.A. Au-Ag-S-Se-Cl-Br Mineralization at the Corrida Deposit (Russia) and Physicochemical Conditions of Ore Formation. *Minerals* **2021**, *11*, 144. https://doi.org/10.3390/min11020144

Academic Editor: Stefano Salvi
Received: 29 November 2020
Accepted: 26 January 2021
Published: 30 January 2021

1. Introduction

The exploitation of the Northern Sea Route and technological solutions of arranging production in the severe climatic conditions make the Arctic part of Eurasia increasingly interesting for investors [1]. Over the last 20 years, in Central and West Chukotka, more than 10 epithermal gold deposits have been explored and involved in mining production, though in the second half of the 20th century they were considered unfeasible. The resource base re-evaluation, which led to the successful exploration of mining objects, was based on their comprehensive study [2–7] and on the accumulated world insight into epithermal mineralization [8–13]. The Chukchi Peninsula is located to the east of the 180° meridian (Figure 1). For some primarily infrastructure reasons, manifestations of different ore types, including epithermal Au-Ag ones, known ever since the 1970s, have so far been insufficiently studied. Some practical and research works generally characterize only their geological structure and the morphology of ore bodies exposed on the surface [14,15].

The accumulated data on the epithermal Au-Ag deposits illustrate that they are formed in the areas of calc-alcaline volcanism associated with convergent tectonic regimes, at the depth of no more than 2 km from the surface and temperatures from 300 to 100 °C, from low-salt hydrothermal fluids [11,12,16]. Depending on the chemical compositions and acidity of ore-forming solutions, and the degree of their interaction with host rocks, the fugacities of sulphur and oxygen [10,17–19], T, and P-parameters of the ore-formation process, three contrasting types of Au-Ag mineralization are formed at different levels of the ore system. High-sulphidation (HS), intermediate-sulphidation (IS), and low-sulphidation (LS) types differ in mineral compositions, ore textures, geochemistry, hydrothermal-metasomatic alterations, and ore potentials for depth [9–13,16]. Examples of HS deposits include Lepanto (Philippines), Summitville (CO, USA) [13,20]; IS deposits—Silbak-Premier (British Columbia) [13]; LS deposits—Creede (CO, USA), Hishikari (Japan), and Apacheta (Peru) [13,21,22].

In 2013, E.E. Kolova participated in prospecting works arranged by a private geological company in East Chukotka. The greatest attention was drawn to the Corrida deposit (145 km to the east of the settlement of Egvekinot, in the Erguveyem River basin), discovered by geologists V.I. Plyasunov and G.A. Tynankergav in 1975.

The aim of this study is to investigate the features of Au-Ag-S-Se-Cl-Br mineralization at the epithermal Au-Ag Corrida deposit (Chukchi Peninsula, Russia) and to estimate the physicochemical conditions of its formation based on the fluid inclusions study and thermodynamic modeling.

2. Geological Situation

The Corrida deposit is located in the central part of the East-Chukotka flank zone of the Okhotsk–Chukotka volcanic belt (OCVB). It is the largest province of the Cretaceous calc-alkaline magmatism, localized at the joint of the North-Asian continent and the North Pacific, where it forms a marginal continental Andean-type belt [23]. The deposit was discovered by 1:50,000-scale geologic mapping in the Soviet-period [24].

The Corrida deposit belongs to the Erguveyem ore district [15], confined to the similarly named volcanic–tectonic structure of circular type, which is 90 km in diameter. It is built from periclinally deposited Late Cretaceous volcanites of the calc-alkaline series (Na_2O/K_2O ratio ranges between 1.5 and 5.6) [24]; among these, the Nyrvakinot Formation, composed of andesites (U-Pb zircon age ca. 88.1 Ma) and felsic volcanites of the Amgen' Formations (U-Pb zircon age ca. 84–80 Ma) prevail [23,25]. The stock (Figure 1) exposed in the central part of the volcanic structure is about 15 km in diameter, built from quartz syenites and monzonites of the Late Cretaceous Ekityn complex of the estimated age U-Pb 84 ± 1.2 Ma (Na_2O/K_2O ratio ranges between 0.5 and 3.0) [24]. Small intrusions and dykes of granites, granodiorites, monzonites, syenites, subvolcanic bodies of fluidal and spherolite rhyolites and andesites of the Early and Late Cretaceous age are widely spread [24]. The structure basement is composed of Late Triassic to Early Cretaceous volcanic-terrigenous-siliceous masses and associated gabbroids and ophiolites of the Velmay island-arc terrane [26]; their debris is observed in coarsely fragmented tuffs in the basement of the Amgen' rocks [27]. All known occurrences in the Erguveyem ore district are located at the joints of circular fractures bounding the volcanic–tectonic structure with regional faults of the north-north-eastern strike.

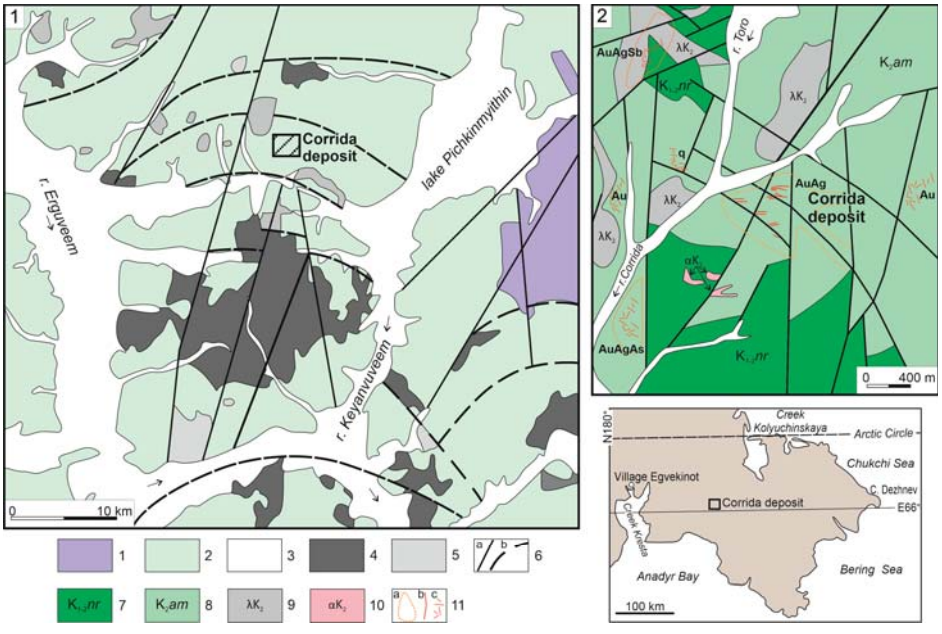

Figure 1. Geological map of the Erguveyem ore district (1) and the Corrida ore field (2) [24,26]. 1–6—illustration (1): 1—Late Triassic–Early Cretaceous volcanogenic-terrigenous-siliceous formation; 2—Cretaceous volcanic rocks; 3—Quaternary aqueoglacial and alluvial formations, with the main water flow directions; 4—Late Cretaceous granitoids; 5—Late Cretaceous subvolcanic rhyolite and andesite bodies; 6—tectonic dislocations: a—faults; b—dislocations of volcanic–tectonic structures; 7–11—illustration (2): 7—volcanic rocks of the Nyrvakinot Formation; 8—volcanic rocks of the Amgen' Formation; 9, 10—Late Cretaceous subvolcanic bodies: 9—rhyolite; 10—andesite; 11—ore features: a—hydrothermal-metasomatic alteration zones; b—lodes; c—stockwork veinlet zones.

In the ore field of the Corrida deposit, the Nyrvakinot Formation is overlapped by acid effusives of the Amgen' Formation (Figure 1). The latter contains three benches. The first includes multicolored lapilli, and, more seldom, agglomerate tuffs of rhyolites and rhyodacites with lenses of tuff conglomerates with a lot of coarsely fragmented pyroclastic material and basement rock fragments. The second is composed of vitric tuffs of rhyolites and rhyodacites, with fragments of feldspar, quartz, and glass crystals prevailing in their composition. The third consists of rhyolite ignimbrites with rare interbeds of vitric tuffs and dacites [28]. On watershed tops, rare isolated stacks built from cenotypal andesibasalts of the Nulingran Formation are found. Volcanites are broken by extrusions, subvolcanic bodies and dykes of andesites, basalts, massive and fluidal rhyolites.

The most intense alterations with clear vertical zoning are observed in the felsic tuffs of the Amgen' Formation. Coarse-grained tuffs with sericite and sericite-quartz alterations, with adularia-quartz veining including Au-Ag mineralization, occur within the elevation interval of 200–350 m. At 350–400 m, we observe intense argillic alteration and hematitization. Within 400–450 m, there are kaolinite-alunite-quartz advanced argillic alterations ("secondary quartzites" by Russian therminology) that host rare quartz veinlets with poor sulphide mineralization. Within the interval of 450–500 m, welded ash tuffs are weakly altered. The unaltered ignimbrites occur above 500 m.

The ore bodies present the adularia-quartz veining zones with rare thin (0.1–0.5 m) veins. The bodies have mostly northwestern and northeastern strike, north and north-east dip (50–60°) and extremely uneven thickness, from 5 to 15 m, with swells of up to 35 m. Along the strike, they are traced from the surface for 1.3 km. From data [24], it can be seen that gold grade in ores varies from 1 to 33 ppm, and silver grade from 116 to 622 ppm.

Veins and veinlets are built mostly from medium-, fine-grained, cryptocrystalline chalcedonic quartz, seldom associated with adularia. They often have colloform-banded, framboidal-platy, massive, porous, brecciform, and breccia structures, and seldom have drusy structures (Figure 2). In breccia aggregates, numerous rubbles are presented by host rocks (Figure 2) cemented by cryptocrystalline quartz. The ore mineralization is disseminated unevenly from fine and uniform to sporadic and nested.

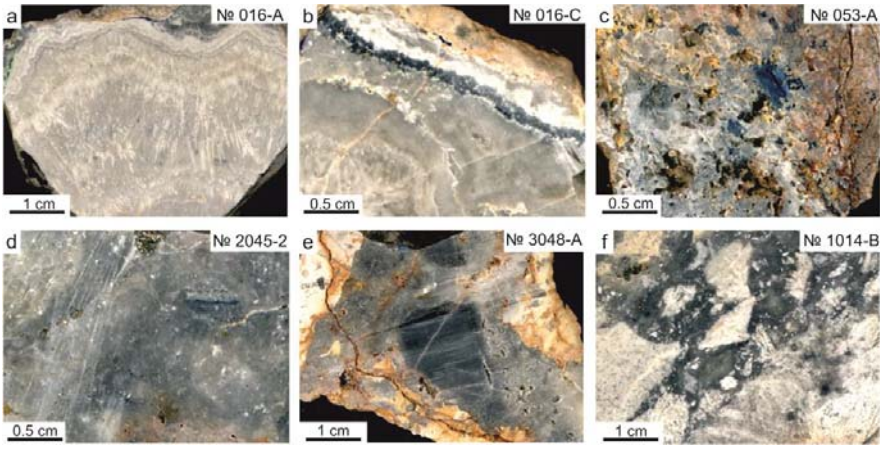

Figure 2. Typical textures of Corrida ores: (**a**)—combination of crustify-platy and colloform-banded; (**b**)—banded; (**c**)—massive; (**d**)—fragmentally brecciform; (**e**)—porous; (**f**)—breccia (fragments of monoquartzites in cryptocrystalline quartz).

3. Materials and Methods

The ore has been studied in polished sections under the AXIOPLAN Imagin microscope.(NEISRI FEB RAS, Magadan, Russia) The chemical compositions of the minerals were determined with the Camebax X-ray electron-probe microanalyzer (FEB RAS, Magadan, Russia) (analyst E.M. Goryacheva) (EDS) and QEMSCAN attached to the EVO50 scanning electron microscope (FEB RAS, Magadan, Russia) (SEM) with the Quantax Esprit system of X-ray energy-dispersion microanalysis system using the standard P/B-ZAF method (analyst T.V. Subbotnikova). The content range was 0.0n–100% with an error for the main components not exceeding 1 wt.%. Statistic calculations of native gold grades were made with the GOLD software (IVerison) developed by S.V. Preis.

Additional analyses of composition of sphalerite and associated minerals were carried out using a MIRA 3 LMU (Tescan Orsay Holding, Novosibirsk, Russia) with EDS INCA Energy 450+ (Analytical Center for Multi-elemental and Isotope Research, Siberian Branch, Russian Academy of Sciences, Novosibirsk, Russia, analyst N.S. Karmanov). The operation conditions were: an accelerating voltage of 20 kV, a probe current of 1 nA and a spectrum recording time of 20 s. The detection limits of elements were <0.1%. The uncertainty was $\leq$1% for major components (>10–15 wt.%) and <2% for minor ones (1–10 wt.%). These dates were used for thermodynamic modeling.

Microthermometry of fluid inclusions was conducted in NEISRI FEB RAS with the measuring set based on the THMSG-600 stage (made by Linkam, London, UK), Motic microscope, Moticam camcorder, Olympus x50 long-focus lens, and the control computer. Individual fluid inclusions (FI) were studied following the methodologies from [29,30]. The fill factor (FF) was calculated considering FI, flattened in shape, by the formula: FF = Sf $\div$ Sv $\times$ 100, where Sf stands for the area of the fluid phase, and Sv, for that of the vacuole. The salt composition of solutions was determined by eutectic temperatures [31]; salt concentration, by the ice melting temperature ($T_{ice.\ mel.}$), according to [32]. Salt concen-

trations as well as water vapor density and pressures were calculated using the FLINCOR software [33] according to the system outlined in [34]. Compositions of gas mixtures (CO_2, N_2, CH_4) in fluid inclusions were determined by Raman analyses on the Lab Ram HR 800 Raman dispersion spectrometer in the wide spectrum range of 150–3800 cm^{-1}, with the exciting line 532 nm of the He-Ne laser and the spectral slit 1.8 cm^{-1}. Complex contours were disintegrated with the Origin 7.5 software. Raman-spectroscopy was carried out at the Analytical Center for Multielemental and Isotope Research, Siberian Branch, Russian Academy of Sciences, Novosibirsk, Russia.

LogfS_2–(logfSe_2, logfO_2) and logfO_2–pH diagrams at 25–300 °C were calculated by the method suggested by Garrels and Christ [35]. Gibbs free energies (G_T) used in calculating chemical equations, involving Fe, Cu, Zn, and Pb minerals, were taken from the databases of the Selector software package for Windows [36]: for sulphides and oxides—s_sprons07.DB [37]; for selenides and sulphates—s_Yokokawa.DB [38]. Thermodynamic constants for iron sulphides were taken from the Thermodem database [39]; for arsenopyrite and loellingite, from [40]; for arsenic, from [41]. Calculations G_T for Au-Ag minerals involve the thermodynamic data from [42–44]. Thermodynamic properties for Ag chlorides and bromides were taken from [45,46]. Sulphur fugacity (fS_2) and temperatures of mineral formation were estimated using the electrum-sphalerite geothermometer based on the data on Fe-content of sphalerite (x_{FeS}) and the amount of Ag (x_{Ag}) in the coexisting native gold ($Au_{1-x}Ag_x$). Calculations were performed using the related equations from [17,47].

4. Results

4.1. Mineral Composition of Ores

The present research has established over 20 ore and 11 vein minerals at the Corrida deposit (Table 1).

Table 1. Mineral composition of Corrida ores.

Groups	Basic	Secondary	Rare
Vein	Quartz	Adularia Albite Hydromica Kaolinite Jarosite	Carbonate Zeolite Epidote Actinolite
Ore	Pyrite Galena Acanthite * Naumannite *	Sphalerite Arsenopyrite Native gold * Chalcopyrite Fahlores Bromargyrite * Au-chlorargyrite *	Argyrodite * Polybasite * Pyrargyrite * Miargyrite * Clausthalite * Andorite Lenaite * Sternbergite * Argentopyrite * Uytenbogaardtite * Fischesserite * Native silver
Hypergene	Limonite Chalcocite	Anglesite	Chlorargyrite * Acanthite

* Chemical compositions of minerals are presented in Tables 2 and 3.

Table 2. Compositions of sulphides (below, and in Tables 3–5, the analyses are not 100% standardized).

Mineral	Element Concentrations, wt.%					Sum
	Ag	Zn	As	Fe	S	
Pyrite				45.55	54.45	100.00
				46.45	53.55	100.00
				47.84	52.16	100.00
				48.37	51.63	100.00
Arsenopyrite			43.75	37.44	18.80	100.00
Sphalerite	4.66	55.66		5.96	33.72	100.00
	2.45	61.97		4.45	31.02	100.00
	3.50	62.07		1.53	32.89	100.00
		62.95		1.98	35.07	100.00
	1.68	63.30	1.03		33.60	99.95
		65.09	2.25		32.67	100.00

Table 3. Compositions of clausthalite and minerals of Au and Ag.

Mineral	Element Concentrations, wt.%										Sum
	Fe	Pb	Zn	Ge	Cu	Au	Ag	Sb	Se	S	
Clausthalite		72.02							27.90		99.92
		72.54							26.99		99.53
Naumannite							72.76		27.24		100.00
							73.36		25.60	1.04	100.00
							74.51		24.50	0.98	100.00
							76.29		21.49	2.22	100.00
							77.75		19.26	2.98	100.00
Uytenbogaardtite-fischesserite						3.00	76.34		18.36	2.30	100.00
						13.78	77.73			7.15	100.00
Argyrodite				4.97			72.69		13.25	9.09	100.00
				5.53			72.57		10.74	11.17	100.00
				5.94			69.90		10.60	10.43	98.87
Andorite		13.22					22.72	18.31	3.70	11.40	99.61
		18.52					17.22	22.17	1.81	22.62	98.40
Pyrargyrite							59.70	20.58	3.43	14.33	98.04
Miargyrite							45.99	41.19	4.55	8.28	100.00
							35.02	40.35	1.80	22.00	100.97
							36.15	41.00	1.16	20.46	98.77
Acanthite							78.06		15.73	6.21	100.00
							78.88		12.71	8.41	100.00
	2.99						84.41		4.14	11.45	100.00
			1.67				79.14		3.54	11.30	100.00
	0.94						82.59		3.27	13.21	100.00
							87.41		1.27	11.32	100.00
			5.97				65.70			7.15	100.00
							77.16			14.63	97.76
Polybasite	4.57				10.35		43.04	23.02		19.02	100.00
							65.77	21.70		12.53	100.00
Argentopyrite-lenaite-sternbergite	15.12						61.76			23.12	100.00
	9.06						72.59			18.15	100.00
	8.20						72.82			16.98	100.00
	8.24						80.63			11.13	100.00

Table 4. Compositions of native gold in the Corrida ores.

Mineral	Element Concentrations. wt.%		Sum
	Ag	Au	
Native gold (electrum)	28.45	71.55	100.00
	29.50	70.50	100.00
	34.04	65.96	100.00
	38.95	61.05	100.00
	41.46	58.20	100.00
	44.60	55.40	100.00
	48.50	51.50	100.00
	57.51	42.49	100.00
	60.64	39.36	100.00
	65.67	34.33	100.00
	67.11	32.89	100.00

Table 5. Compositions of silver halides in the Corrida ores.

Mineral	Element Concentrations, wt.%						Sum
	S	Cl	Br	Fe	Au	Ag	
Bromargyrite		18.32	6.01			75.68	100.00
		18.18	4.19			77.63	100.00
Chlorargyrite		22.76				77.25	100.01
	1.22	22.57				76.21	100.00
	0.57	21.00				78.43	100.00
		18.61				81.39	100.00
Au-chlorargyrite (or phase mixture)	5.85	9.63			20.95	63.57	100.00
		4.51			40.63	54.87	100.00

Quartz is the most widely spread mineral in lode-veinlet zones. Most narrow veins and veinlets, as well as lode central parts, are usually filled with medium- to finely-grained, sometimes platy, light quartz, often associated with adularia (Quartz Type 1) (Figure 2a,b); finely-grained light-shade quartz with massive and porous structures with impregnated Pb, Zn and Ag sulphides (Quartz Type 2) (Figure 2c,d). The cementing mass in the aggregates has a brecciated structure; fine "enriched" rhythms of colloform-striped formations, narrow veins and veinlets of massive structure are built from dark, finely-grained, cryptocrystalline, to chalcedonic quartz (Quartz Type 3) (Figure 2e,f), saturated with abundant and even submicroscopic impregnation of ore minerals (Au-Ag sulphoselenides, halides, selenides, and sulphides of silver) (Figures 2 and 3; Tables 2 and 3).

Adularia does not exceed 15% of lode fill; besides, it is observed in combination with sericite and kaolinite in near-lode metasomatic formations. It is light-crème in colour and is presented by hypidiomorphic aggregates, its position in rhythmically striped aggregates is clearly seen in the structure pattern (Figure 2).

Pyrite and arsenopyrite fill fine impregnations (1–2 μm to 0.2 mm, seldom to 3–5 mm) both in lode bodies and in wallrock zones of metasomatic alterations. Joint locations of pyrite and arsenopyrite are observed extremely rarely: they are predominantly located separately. Pyrite is abundant and found in association with all established sulphides (Figures 3 and 4). The signs of pyrite cataclasis and recrystallization are widepsread. Arsenopyrite forms practically no mineral associations and often occurs as disseminated inclusions in fine-grained quartz. The pyrite composition is stoichiometric; in the arsenopyrite composition, Fe grades exceed stoichiometric while As and S ones are lower: $Fe_{1.10}As_{0.95}S_{0.95}$ (Table 2).

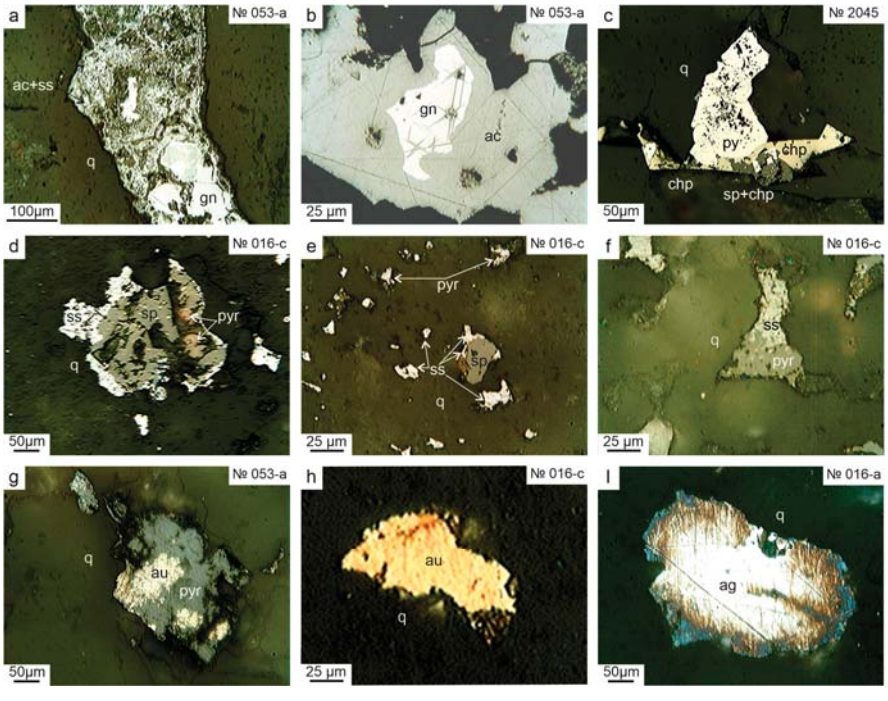

Figure 3. Mineral interrelations at the Corrida deposit: (**a**)—acanthite grown on galena; (**b**)—acanthite around galena and acanthite tabular isolations in galena; (c)—assemblage of pyrite, chalcopyrite, and sphalerite impregnated with chalcopyrite emulsion; (**d**,**e**)—sphalerite and pyrargyrite with the rim of the mineral mixture of Au-Ag sulphides; (**f**)—pyrargyrite with the mineral mixture of Au-Ag sulphides; (**g**)—native gold intergroup with pyrargyrite; (**h**)—interstitial grain of native gold; (**i**)—interstitial grain of native silver. ***Mineral abbreviation in*** **Figures 3 and 4*:*** au—native gold, ag—native silver, fis—fischesseritie, uyt—uytenbogaardtite, ac—acanthite, nmt—naumannite, se-argd—Se-bearing argyrodite, pyr—pyrargyrite, an—andorite, chl—chlorargyrite, br—bromargyrite, py—pyrite, apy—arsenopyrite, sp—sphalerite, chp—chalcopyrite, gn—galena, claus—clausthalite, q—quartz, ss—fischesseritie-uytenbogaardtite solid solution.

Sphalerite and chalcopyrite are observed in medium-grained quartz, more seldom in chalcedonic, in the form of uneven impregnation and pockets of up to 1 mm in size (Figure 3c–e). Sphalerite with fine impregnation of chalcopyrite is episodic (Figure 3c). Sphalerite is often observed with acanthite and naumannite (Figure 4e,f), which grow around and penetrate into it through fractures. Sphalerite $(Zn,Fe)_{0.99}S_{1.01}$ contains up to 6 wt.% Fe and up to 4.6 wt.% Ag (in half of the grains studied) (Table 2). We suggest that Ag admixture is related to microscopic or submicroscopic inclusions of discrete Ag-minerals [48].

Galena is marked in medium-fine-grained light quartz both as fine impregnations and pockets of up to 4–5 mm in size (Figure 3a,b). In the dark chalcedonic quartz, it is seldom observed in the shape of unevenly distributed submicroscopic grains. Acanthite is often developed on the edges of galena aggregates as well as on their joints. The Se-analog of galena, clausthalite, is found in the paragenesis with naumannite. They occur as submicroscopic impregnations in grey quartz (Figure 4, Table 3,) and in direct proximity to acanthite, pyrite, and sphalerite (Figure 4).

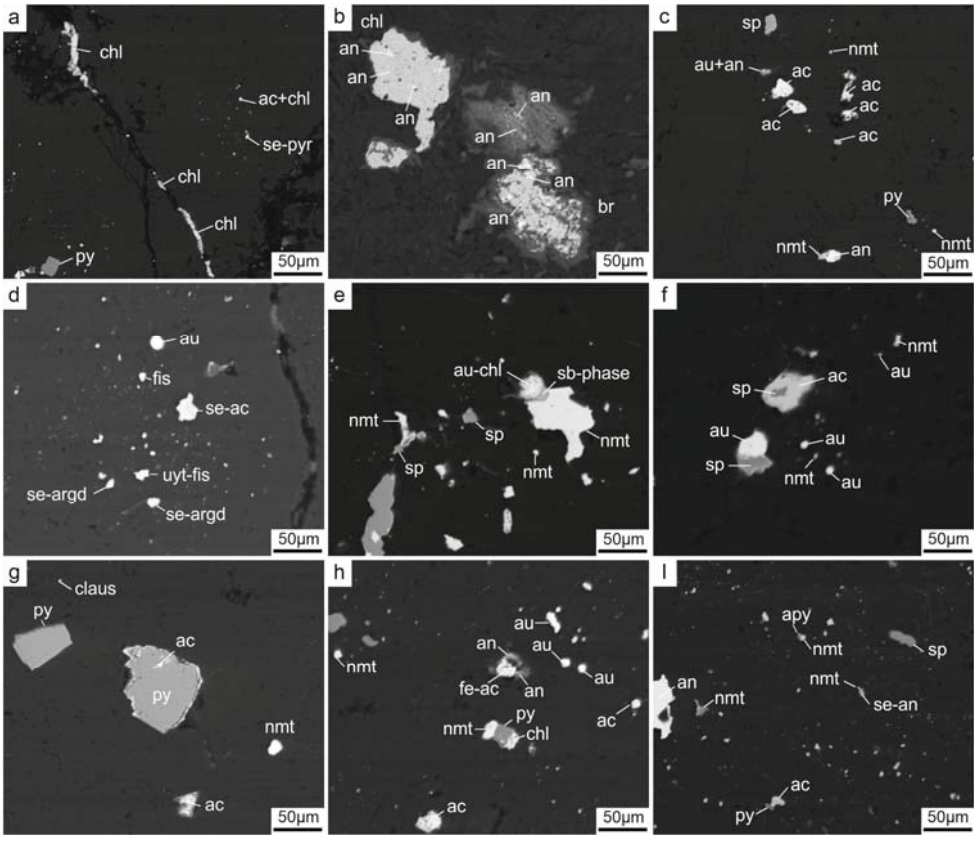

Figure 4. BSE (Backscattered electron) image of microscopic and submicroscopic particles of ore minerals in chalcedonic quartz: (**a**)—chlorargyrite (chl), acanthite (ac), pyrargyrite (pyr) in fissures; (**b**)—andorite (an), chlorargyrite (chl) and bromargyrite (br) in relatively large pores filled with anglesite and clay material; (c)—native gold (au), acanthite (ac), naumannite (nmt), sphalerite (sp), pyrite (py) in smaller pores; (**d**)—acanthite (ac), argyrodite (argd), uytenbogaardtite (uyt) and fischesserite (fis) impregnation; (**e**,**f**)—naumannite (nmt), chlorargyrite (chl), sphalerite (sp) and native gold (au) impregnation; (**g**)—pyrite (py) and acanthite (ac) impregnation; (**h**)—native gold (au), naumannite (nmt), acanthite (ac) and pyrite (py) in smaller pores; (**I**)—naumannite (nmt), acanthite (ac) and arsenopyrite (apy) in smaller pores.

In chalcedonic quartz, submicroscopic impregnations (Figure 4, Table 3) consist of clausthalite, naumannite, uytenbogaardtite-fischesserite series, argyrodite, andorite, pyrargyrite, lenaite, and acanthite. There is also polybasite, which is characterized by a lower content of Ag, higher Cu and Fe contents, and absence of As. Rarely observed mineral mixtures of the argentopyrite-lenaite-sternbergite series are characterized by lower Fe and higher Ag contents (Table 3).

The most common Ag-bearing mineral in ores is acanthite, which occurs in associations with galena (Figure 3b), naumannite, argyrodite, clausthalite, and jarosite. It has the non-stoichiometric composition, and often contains Se (1.3 to 15.7 wt.%) and Fe (up to 3 wt.%) (Table 3). Naumannite shows up to 3 wt.% S.

Native gold commonly occurs as submicroscopic particles in chalcedonic quartz associated with acanthite (Figure 3) and galena; less often it forms larger (up to 0.5 mm), xenomorphic insets in medium- and fine-grained quartz (Figure 3h) in association with

pyrite and sphalerite. The fineness of native gold varies from 330 to 720‰ (Table 4), and averages 458‰; values are distributed bimodally, with peaks at 300–400‰ and 550–600‰.

Native silver is rare in association with acanthite and galena. Silver grains in quartz do not exceed 0.7 mm in size (Figure 3i).

Among ore mineralization, various chlorides and bromides of Ag are present as finely dispersed dissemination in chalcedony (Figure 3, Table 5). They are frequently localized in fissures and interstitions, and associated with anglesite (Figure 4a,b,h) and jarosite.

Mineralogical analysis showed three productive mineral associations in Corrida ores: pyrite-arsenopyrite-sphalerite-chalcopyrite with native gold and acanthite; galena with native gold and Au-Ag sulphides and selenides; limonite-anglesite with acanthite, silver chlorides and bromides. Basic Au- and Ag-bearing minerals are native gold (electrum) and, to a lesser extent, minerals of the uytenbogaardtite-fischesserite series, acanthite, and naumannite.

4.2. Fluid Inclusions

In quartz samples from ore bodies of the Corrida deposit, 55 individual primary and primary-secondary FI were studied (Table 6). Under the ambient temperature, all FI are two-phase, gas-liquid in their phase composition (Figure 5). They vary in size from 5 to 20 μm, of which 28% smaller than 10 μm. FI are unevenly distributed, both in groups and individually, in the central zones of quartz crystals (Figure 5), are elongated, and, more rarely, round in shape. About 23% can be referred to FI with a prevailing gas phase (FF lower than 67) (Table 6, Figure 5b). FI with different FF are typically localized in growth zones and can be considered syngenetic (Figure 5c).

Table 6. Results of microthermometry studies of individual fluid inclusions in the Corrida productive quartz.

Sample	n	Experimental Data				Calculation Data		
		$T_{hom.}$, °C	$T_{eut.}$, °C	$T_{ice.mel.}$, °C	FF, %	C, wt.% NaCl eq.	d, g/cm^3	P, bar
016c Quartz Type 1	3	340–320	−20	−1.4	75	2.41	0.63	140–108
	6	314–280	−25	−2–−1.8	50–67	3.39–3.06	0.7	82–60
	7	314–292	−26–−20	−2.1–−1.5	75–83	3.55–2.57	0.75	100–72
	2	290–288		−0.1	75	0.18	0.7	70–68
	5	286–280	−29–−23	−2–−1.8	80	3.39–3.06	0.7	66–60
	4	279–240	−29–−25.6	−2–−0.1	75–86	3.39–0.18	0.8–0.7	59–27
	3	240–237	-	−0.1	50–67	0.18	0.8	29
	3	235–192	−25	−0.1	75–80	0.18	0.8	27–11
053 Quartz Type 2	3	307	−28	−0.1	66	0.18	0.67	90
	3	279	−25	−0.1	75	0.18	0.73	59
	5	233–223	−28	−0.3–−0.1	83–75	0.53–0.18	0.83–0.8	26–21
	5	182–172	−32–−25	−0.3–−0.1	85–83	0.53–0.18	0.9	8–7
1014B Quartz Type 3	3	205	−23.8	−0.1	91	0.18	0.8	14
	5	183–158	−27.5–−23	−0.1	88–80	0.18	0.9–0.8	9–6
	1	163	−22	−0.1	67	0.18	0.9	6

n—number of measurements with similar values, united in one group; FF—fluid inclusion fill factor: ratio of voluminous parts of the liquid phase to the gas one.

In 4 out of 8 compositions of FI "gas" phases, Raman-spectroscopy established CO_2 with density from 0.05 to 0.19 g/cm^3 (calculated according to [49]), with minor contents of N_2 and CH_4 (Figure 6) and $CO_2/N_2/CH_4$ ratios from 0.97/0/0.03 to 0.92/0.07/0.01.

Most FI are homogenized within the temperature range of 163 °C to 340 °C (Table 6). FI with predominant gas phase (FF = 50) are homogenized at 237–300 °C (Table 6), and those with the liquid phase (FF = 89–92), at 158–205 °C. Homogenization temperatures are distributed bimodally, with peaks at 275–300 °C and 150–175 °C.

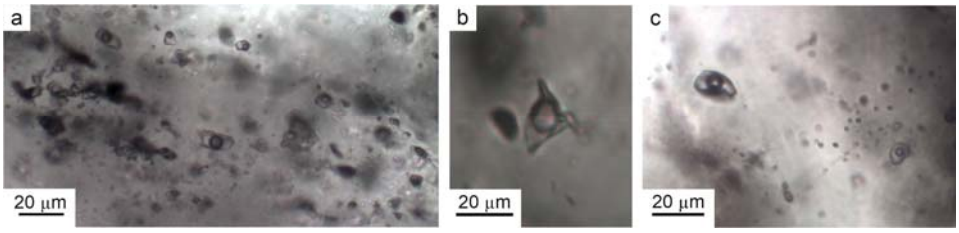

Figure 5. Photomicrographs showing different types of fluid inclusions in the ore-bearing quartz: (**a**)—fluid inclusions in quartz (sample 053); (**b**)—fluid inclusion (16C_2fi, see Figure 6), with the gas phase represented by the CO_2 mixture not exceeding 0.05 g/cm^3 in density, N_2, and CH_4 in ratio 0.92/0.07/0.01; (**c**)—coexistence of two-phase fluid inclusions with different fill factors (sample 016 C).

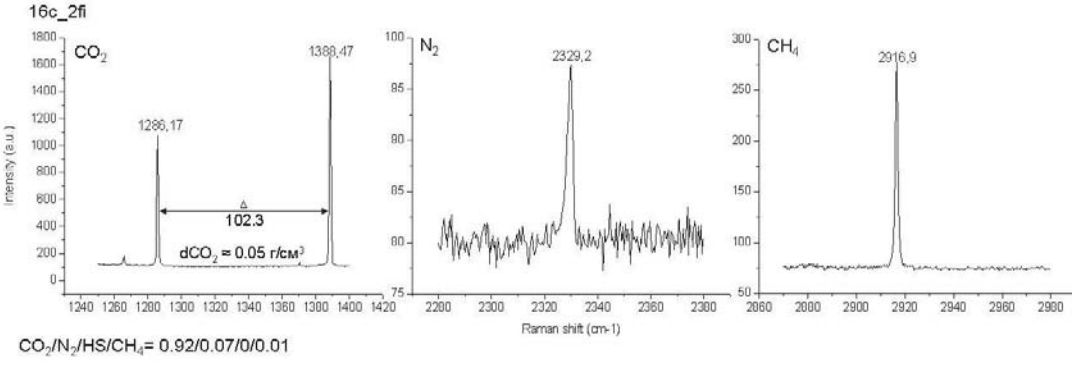

Figure 6. Raman-spectra, showing the gas composition (CO_2, N_2, CH_4) of the fluid inclusion (16c_2fi) in the Corrida ore-bearing quartz.

Cryometric research shows that the last ice crystal in FI melts at temperatures between −2.1 and −0.1 °C (Table 6, Figure 7), which corresponds to salt concentration in solutions from 3.55 to 0.18 wt.% NaCl eq. FI containing solutions with salt concentration from 3.5 to 2.4 wt.% NaCl eq. are homogenized at temperatures from 240 to 340 °C, and form a group on the diagram (Figure 7). FI have the eutectic temperature range of −32 °C to −20 °C, which suggests the presence of NaCl with $MgCl_2$ and $FeCl_2$ in the solution (Table 6, Figure 7). Salt composition of the solutions from FI remains stable throughout the ore process (Figure 7).

4.3. Physicochemical Parameters (fO_2, fS_2, fSe_2, pH) of Ore Formation

Based on the data of mineral compositions of ores and hydrothermal alterations as well as on the results of fluid inclusions study, some physicochemical parameters of mineralization (fS_2, fSe_2, fO_2, and pH) have been evaluated.

The presence of pyrite, arsenopyrite, Fe-bearing sphalerite, and native gold in Corrida ores permits one to estimate the range of sulphur and oxygen fugacities. At 300 °C, the pyrite + arsenopyrite + $Ag_{0.75}Au_{0.25}$ + acanthite are stable at logfS_2 = −11–−6 and log fO_2 < −26 (Figure 8a,b, field 1). Absence of the Se-bearing mineralization suggests low values of fSe_2 (logfSe_2 < −13) during ore formation. According to Figure 8a,b at 300 °C, the fields of pyrite and native silver do not intersect, which implies lower temperatures of their formation. This association is stable at 200 °C and logfS_2 = −16.5–−10.5, log fSe_2 < −18, and logfO_2 < −36 (Figure 8c,d, field 2).

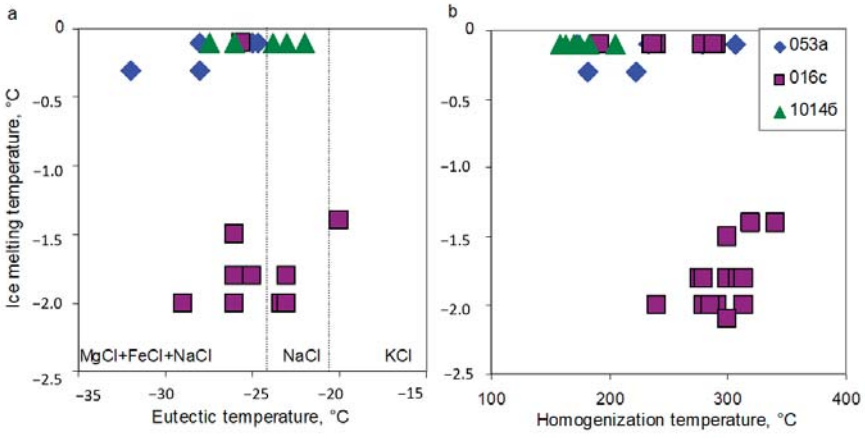

Figure 7. Plots of the last ice crystal melting temperature vs. eutectic temperature (**a**) and last ice crystal melting temperature vs. homogenization temperature (**b**), illustrating the distribution patterns of the data points for different types of quartz.

The emergence of Se-containing minerals (Ag sulphoselenides–Se-acanthite, S-naumannite; fischesserite, clausthalite) in the ores testifies to the increasing role of selenium in the mineral formation process. According to the genetic model, at this stage hydrothermal solutions may have boiled. As a result of boiling, porous chalcedony is formed and micromineral phases are deposited in pores with S and Se subliming by the scheme: Se-acanthite − S-naumannite + clausthalite + native gold − native silver + chlorargyrite + bromargyrite − uytenbogaardtite + fischesserite. At 100 °C, Se-acanthite with the composition Ag_2S – $Ag_{1.94}S_{0.52}$ $Se_{0.54}$ is formed at logfS_2 = −21−−16, log fSe_2 = −28−−22 and logfO_2 < −48 (Figure 9a,b, field 3); the upper stability limit of fS_2 corresponds to the line of uytenbogaardtite occurrence. The stability field of naumannite ($Ag_{1.94}S_{0.33}Se_{0.73}$–$Ag_2Se$) combined with clausthalite at 100 °C is limited within the intervals of logfS_2 from −25 to −16, logfSe_2 from −26.5 to −21 and logfO_2 < −48 (Figure 9a,b, field 4).

The stability field of native silver (Figure 9a,b, field 5) corresponds to the lower values of logfS_2 < −21 and logfSe_2 < −27. The minimum value of logfS_2 = −24.6 was evaluated by the pyrite-pyrrhotite (FeS_2/Fe_7S_8) stability line, and the maximum limit for logfO_2 = −54, by the line of oxides (hematite, cuprite) and sulphates (anglesite, Ag_2SO_4) appearance. The association of $Au_{0.5}Ag_{0.5}$ with petrovskaite or $Ag_{0.75}Au_{0.25}$ with uytenbogaardtite at this temperature is formed at the values of logfS_2 = −13.9 and −16.3. The association of $Ag_{0.75}Au_{0.25}$ with fischesserite or $Au_{0.5}Ag_{0.5}$ with fischesserite or naumannite ($Ag_{0.5}Au_{0.5}$ + Ag_2Se/Ag_3AuSe $_2$+ Au) is formed at logfSe_2 = −21.1 and −18.4. AuSe is formed at log fSe_2 < −14. Minerals of the uytenbogaardtite-fischesserite series below 100 °C are stable at logfS_2 from −25 to −14, logfSe_2 < −14, and logfO_2 < −48 (Figure 9a,b, field 6).

The Corrida ores' mineral composition is peculiar for the presence of Ag chlorides and bromides in the hypergene association with acanthite, jarosite, anglesite, limonite, and chalcocite, which permits evaluation of their stability fields. Below 100 °C, chlorargyrite and bromargyrite are formed at logfO_2 > −46 and pH< 6; under 25 °C, at logfO_2 > −60 and pH < 9 (Figure 9c,d); consequently, Ag halides are more stable under lower temperatures. For the hypergene association, critical values of sulphur and selenium fugacity correspond to the stability lines of copper sulphide (Cu_2S, chalcocite) and selenide Cu_2Se (logfS_2 from −44 to −20.6, logfSe_2 < −18) (Figure 9a), while oxygen fugacities are limited by the anglesite stability lines (logfO_2 from −62 to −50).

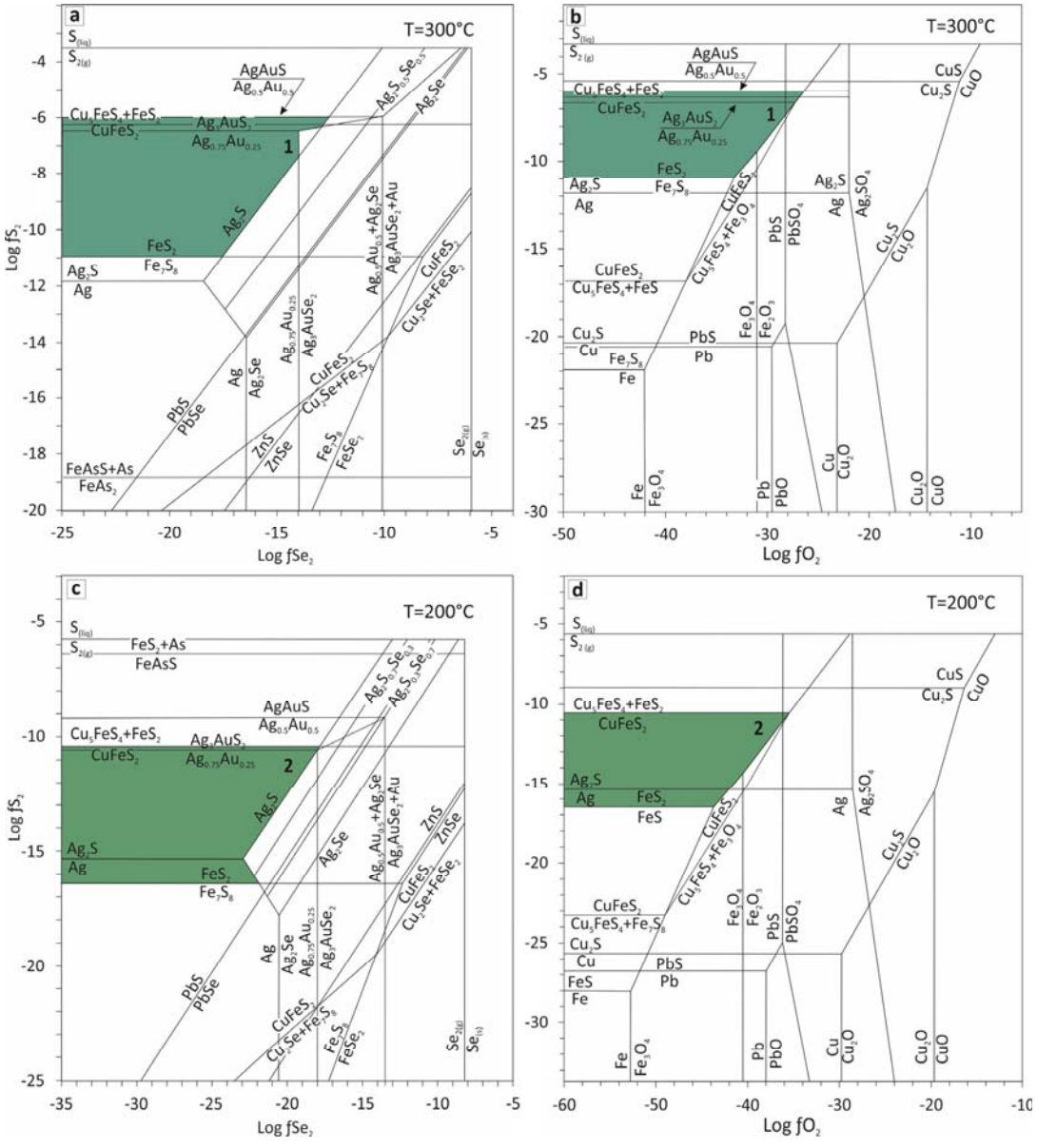

Figure 8. LogfS_2—logfSe_2 and logfS_2—logfO_2 diagrams at 300°C (**a**,**b**) and 200 °C (**c**,**d**) and stability fields of the Corrida mineral associations: field 1—pyrite + arsenopyrite + native gold + acanthite-1; field 2—pyrite + chalcopyrite + acanthite-2 + native silver.

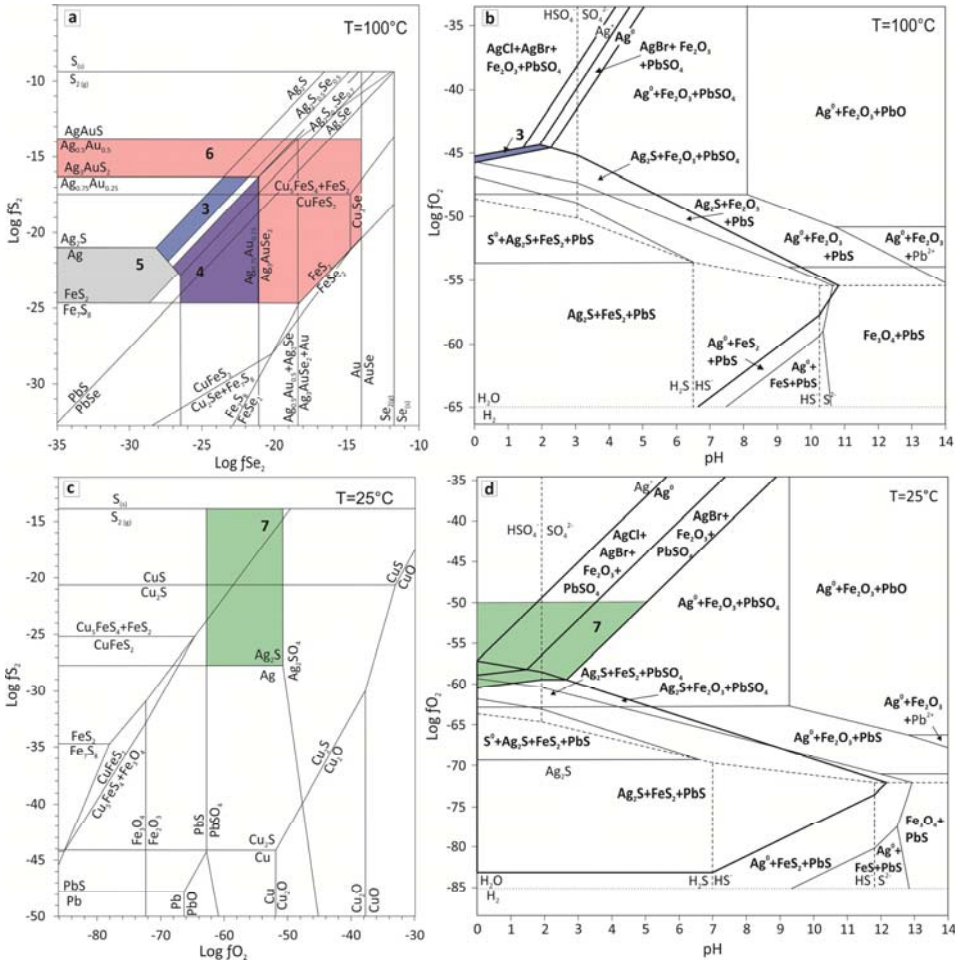

Figure 9. Diagrams of logfS_2–logfSe_2 (**a**) and logfO_2–pH (**b**) at 100 °C, logfS_2–logfO_2 (**c**) and logfO_2–pH (**d**) at 25 °C, and stability fields of the Corrida mineral associations: field 3—Se-acanthite ($Ag_2S - Ag_{1.94}S_{0.52}Se_{0.54}$) + Ag halides; field 4—S-naumannite ($Ag_{1.94}S_{0.33}Se_{0.73} - Ag_2Se$) + clausthalite (PbSe); field 5—Au-Ag solid solutions; field 6—uytenbogaardtite-fischesserite; field 7—acanthite + chlorargyrite + bromargyrite + anglesite ($PbSO_4$). Element concentrations used in calculation: [S] = 10^{-2} M, [Cl] = 10^{-1} M, [Br] = 10^{-2} M, [Ag] = 10^{-7} M.

The electrum-sphalerite geothermometer is used for calculating the temperature and S fugacity values. In the present research, we studied the homogeneous grains of native gold in paragenesis with sphalerite. The composition of native gold from this paragenesis varies within the range x_{Ag} = 0.630–0.731; mole fraction of FeS in sphalerite (x_{FeS}) is between 0.019 and 0.055. The calculations show that the formation of this mineral assemblage, with the above-mentioned compositions of native gold and sphalerite, requires temperatures from 192 to 274 °C and logfS_2 from −15.6 to −11.4. Calculated by different equations [17,47], these characteristics are close in value (Table 7) and do not exceed the above-estimated boundary values of fS_2.

Table 7. Estimated values of the mineral formation temperature and sulphur fugacities.

№	x_{FeS}	x_{Ag}	T°, C [17]/[47]	$\log fS_2$ [17]/[47]	№	x_{FeS}	$\log fS_2$ [17]/[47]	
							175 °C	150 °C
	Sphalerite with native gold					Sphalerite with Ag-minerals		
1	0.022	0.731	214.9/192.0	−14.06/−15.62	6	0.120	−18.35/−17.63	−20.39/−19.57
2	0.027	0.719	223.5/201.1	−13.67/−15.14	7	0.094	−18.13/−17.41	−20.17/−19.35
3	0.049	0.631	270.4/250.6	−11.53/−12.60	8	0.020	−16.79/−16.07	−18.83/−18.00
4	0.055	0.630	274.2/254.6	−11.42/−12.46	9	0.096	−18.16/−17.44	−20.19/−19.37
5	0.019	0.631	237.3/216.1	−12.55/−13.86	10	0.089	−18.08/−17.36	−20.12/−19.30

In evaluating sulphur fugacity, based on the composition of sphalerite associated with Ag- sulphoselenides and sulphosalts, we used mineral formation temperatures according to the data from the FI research (150–175 °C) that supposedly corresponds to the formation of later Ag-containing minerals. The presence of argentopyrite in the association indicates temperatures below 150 °C [50]. The mole fraction of FeS in sphalerite (x_{FeS}) in this association varies between 0.020 and 0.120. Calculations using equations from [17,47] show that sphalerite forms within the range of temperatures from 150 to 175 °C and sulfur fugacity $\log fS_2 = -20.4 - -16.0$, which remains within the fS_2 boundary values estimated above.

Hydrothermal-metasomatic alterations of Corrida host rocks are represented by hydromica-quartz metasomatites, argillisites, and secondary quartzites replacing them on higher horizons. According to the research on metasomatic rocks [51], weakly acid to near-neutral solutions are typical of argillization, and ultra-acid solutions are typical for secondary quartzites. Moreover, the presence of jarosite in ores at the final stages of Corrida mineralization also suggests participation of acid hydrothermal solutions [52]. At the original stages, mineral-forming solutions might have had weakly acid to near-neutral pH and were later replaced with acid and ultra-acid solutions.

5. Discussion

The research showed three productive mineral associations in the ores of the Corrida deposit: (1) pyrite-arsenopyrite-sphalerite-chalcopyrite with native gold and acanthite; (2) galena with native gold and silver and Au-Ag sulphides and selenides; (3) limonite-anglesite with acanthite and silver chlorides and bromides. A specific feature of the ores is a broad range of Au-Ag-S-Se-Cl-Br minerals. The observed mineral interrelations and bimodal distribution of native gold fineness values imply a two-stage model formation of Au-Ag ores at the Corrida deposit: plutogenic-volcanogenic and hypergenic; the first stage can be divided into two substages.

The FI study revealed that the lode body quartz was formed from low-salt (3.55 wt.% to 0.18 wt.% NaCl eq.) hydrotherms, saturated with ions of chlorine, sodium, magnesium, and iron at temperatures from 340 to 158 °C. A low level of salt concentration in hydrothermal solutions is characteristic of epithermal systems. This may be a consequence of the condensation of magmatic vapor [53–55], and the boiling process [56,57]. Most FI were trapped in two temperature intervals, which show that the first ore-forming stage contained two substages: 300–275 °C and 175–150 °C. It was found that three kinds of quartz filling ore formations were formed successively on cooling of the system: (1) light, medium- to fine-grained quartz (Type 1), building quartz-adularia lode-veinlet aggregates of the colloform-banded and crustified-platy structures (Sample 016c) (Figure 2a,b; Table 5), was formed at 340 to 192 °C; (2) fine-grained quartz (Type 2), forming aggregates of massive, brecciform, and porous structures, with mostly galena mineralization (Sample 053) (Figure 2c,d; Table 5), at 307 to 172 °C; (3) grey, cryptocrystalline (Type 3), which builds dark rhythms of colloform-banded and banded aggregates, serves as the cementing material for breccia formation, and contains submicroscopic impregnations of gold and silver minerals (Sample 1014B) (Figure 2e,f; Table 5), at 205 to 158 °C. In ore-forming

solutions, trapped by the light quartz FI (Type 1), salt concentration is seven times as large (Table 5; Figure 7) as that in the grey quartz FI (Type 3). Simultaneously, low-density CO_2 with minor N_2 and CH_4 (Figure 6) was found only in the light quartz FI, which means that in the initial period, up to approximately 300 °C, the ore-forming fluid contained low-density gases. Vapor phases, according to [57,58], are capable of transporting gold in the form of colloid particles of heterogeneous trapping. Prokofiev et al. [59] determined the presence of gold as nanoparticles in fluid inclusions by optical and spectroscopic methods. The FI in quartz from the Corrida deposit are very small. We observed no gold as nanoparticles in them. Possible species of gold transport in the ore-forming epithermal system are chloride and hydrosulfide complexes [43,60,61]. Breccia ore formations, cemented by the low-temperature variety of quartz, indicate that the hypogene stage is complicated by tectonic, probably seismic, fluctuations.

Thermodynamic modeling showed that the pyrite-arsenopyrite-argentite (acanthite) assemblage can be formed at 300 °C with $\log fS_2$ from −11 to −6, $\log fSe_2$ from −25 to −13, $\log fO_2$ from −50 to −26; pyrite-chalcopyrite-argentite(acanthite) assemblage, at 200 °C with $\log fS_2$ from −16.5 to −10.5, $\log fSe_2$ from −25 to −15, $\log fO_2$ from −50 to −36; Se-bearing mineralization, at 100°C with $\log fS_2$ from −16 to −24.6, $\log fSe_2 > -28$ and $\log fO_2 > -54$. At the same time, chlorargyrite and bromargyrite can be formed at the pH < 6 at 100 °C and pH < 3 at 25 °C.

According to experimental research and thermodynamic modeling results [51,52], in the core sample of hydrothermal-metasomatic alterations of host rocks, at the 400–500 m horizon, hydromica-quartz metasomatites and argillisites are replaced by kaolinite-alunite-quartz secondary quartzites and monoquartzites, which indicates the change of pH in the solutions from weakly acid–near-neutral to acid during mineral formation. The horizon, in which kaolinite-alunite-quartz metasomatism is manifested, presumably corresponds to the level of the Corrida ore system paleo surface, where geothermal processes were accompanied by boiling, solution oxidation, and formation of quartz platy aggregate [62]; these might have even had zero connection with the ore formation process ("overprinting ore") [9].

Thus, it was established that in the Corrida ore system, on the background of lowering temperature, boiling, decreasing fluid salt concentration, and pH changing from near-neutral to acid, the oxidation potential was increasing, sulphur activity was lowering, but selenium activity was growing. These factors resulted in the significant variation of sulphoselenides and selenides of Ag in ores. According to the results of thermodynamic modeling and experiments [63,64], at such physicochemical conditions, the role of selenium as an ideal precipitator of Ag is multiplied. Here, the buried waters of an oxygen-free marine paleobasin saturated with an organic matter could be the source of selenium [65]; the waters warmed to over 250 °C, and the biologically bound selenium could mobilize into a hydrothermal fluid [66]. Their deposition in the discussed area was favorably promoted by shallow deposition of the OCVB built by the flinty masses of the Velmay island-arc terrane, less permeable than the OCVB volcanites and, therefore, capable of confining water.

Comparatively high, for epithermal ores, initial temperature of ore-forming fluid, presence of low-density gases and broadly spread acanthite in ores suggest that an intrusion chamber could be the source of the ore-forming fluid [10]. Probably such chamber for the Corrida ore system was a stock built by syenites and monzonites of the Ekityn complex, of the estimated age 84 ± 1.2 Ma [24], which was formed during the evolution of the central part of the Erguveyem volcano-tectonic structure. The ore process occurred close to this time, which is indicated by hydrothermal-metasomatic alterations in the rocks of the Leurvaam and the Amgen' Formation (84–80 Ma) and complete absence of such alterations in the rocks of the Nunlingran Formation of the Campanian age [22,25]. These data allow one to estimate a possible period of the Corrida formation as 84 to 80 Ma [67], i.e., the time when the basic volume of OCVB acid magmas was formed [23,68].

The data obtained in the present study (adularia availability, colloform ore structures, development of arsenopyrite and sphalerite, wide range of Au-Ag minerals, absence of enargite, tennantite, tetrahedrite, and other sulfosalts characteristic for HS systems [17]) show near-neutral pH of ore-forming solutions in the basic part of the system. The presence of CO_2 in the ore-forming fluid at the initial stage, as an indicator of redox reactions under interaction of fluid with rocks [18], allows us to classify the Corrida deposit as an LS-type deposit. It was determined, for this group of objects, that the most favorable temperature conditions for the formation of rich ores are 180–280 °C [9]; temperatures above 280 °C (in this case, maximum ore formation temperature 340 °C) imply a high ore potential of the system.

The Corrida deposit is a new example of epithermal deposits in which Au–Ag chalcogenides (acanthite, uytenbogaardtite, fischesserite, naumannite and others) are found in significant quantities [3,7,69–71]. Au–Ag chalcogenides and other gold and silver minerals found in sulfide ores (argyrodite, andorite, pyrargyrite, lenaite, chlorargyrite, bromargyrite) can be of economic importance in the future [72].

6. Conclusions

The studied Corrida Au-Ag deposit, located at the periphery of the Erguveyem volcanic–tectonic depression, belongs to the group of epithermal LS-type deposits. The mineral composition of ore bodies here is characterized by a broad range of Au-Ag-S ± Se-Cl-Br minerals. Basic Au- and Ag-bearing minerals are native gold and, to a lesser extent, minerals of the uytenbogaardite-fishesserite series, acanthite and naumannite. The ores were formed in two stages. The first hypogenic stage was from 84 to 80 Ma. Basic ore mineralization was formed in the medium- to low-temperature environment (340–150 °C) from low-salt (3.55 to 0.18 wt.%wt.% NaCl eq.) chloride hydrotherms, in the context of fluid boiling, pH change from near-neutral to acid, decreasing sulfur, and increasing selenium contents. The buried waters of the oxygen-free marine paleobasin saturated with the organic matter could be the source of Se, Cl and Br.

Author Contributions: Conceptualization, E.E.K., G.A.P.; methodology, E.E.K., N.E.S., T.V.Z.; validation E.E.K., A.N.G.; formal analysis, E.E.K., N.E.S., T.V.Z.; investigation, E.E.K., N.E.S., T.V.Z., A.N.G.; resources, A.N.G.; writing—original draft preparation, E.E.K., N.E.S., T.V.Z., A.N.G., G.A.P.; writing—review and editing, E.E.K., G.A.P.; project administration, G.A.P. All authors have read and agreed to the published version of the manuscript.

Funding: The studies were carried out by the grant № 13.1902.21.0018 "Fundamental Problems of the Development of the Mineral Resource Base of the High-Tech Industry and Energy in Russia" from the Ministry of Science and Higher Education of the Russian Federation.

Institutional Review Board Statement: The study was conducted according to the guidelines of the Declaration of Helsinki, and approved by the Institutional Review Board (or Ethics Committee) of NEISRI FEB RAS (protocol 1.12.2020).

Informed Consent Statement: Informed consent was obtained from all subjects involved in the study.

Data Availability Statement: Not applicable.

Acknowledgments: The authors thank N. Karmanov (Sobolev Institute of Geology and Mineralogy, Siberian Branch, Russian Academy of Sciences) for help in carrying out work on a scanning electron microscope and an X-ray spectral microanalyzer. We would like to thank the academician N.S. Bortnikov for useful comments in the preparation of this article. We are very grateful to the anonymous reviewers for their comments, which helped to improve the quality of the paper. Appreciation is given to the Academic Editor for careful reading of the manuscript and comments.

Conflicts of Interest: The authors declare no conflict of interest.

References

1. Bortnikov, N.S.; Lobanov, K.V.; Volkov, A.V.; Galyamov, A.L.; Vikentev, I.V.; Tarasov, N.N.; Distler, V.V.; Lalomov, A.V.; Aristov, V.V.; Murashov, K.Y.; et al. Strategy metal deposits in the Arctic zone. *Geol. Ore Depos.* **2015**, *57*, 479–500. [CrossRef]
2. Volkov, A.V.; Prokofyev, V.Y.; Savva, N.Y.; Sidorov, A.A.; Byankin, M.A.; Uyutnov, K.V.; Kolova, E.E. Ore formation at the Kupol epithermal Au-Ag deposit (Russia's North-East) according to the data from fluid inclusions studies. *Geol. Ore Depos.* **2012**, *54*, 295–303. [CrossRef]
3. Savva, N.E.; Pal'yanova, G.A.; Byankin, M.A. The problem of genesis of gold and silver sulfides and selenides in the Kupol deposit (Chukci Peninsula, Russia). *Rus. Geol. Geophys.* **2012**, *53*, 457–466. [CrossRef]
4. Savva, N.E.; Kolova, E.E.; Fomina, M.I.; Kurashko, V.V. Gold mineralization in explosive breccia bodies: Mineralogical characterization and genetic aspects (Sentyabrsky NE Deposit, Chukotka Region, Arctic Russia). *Arktos* **2017**, *3*, 6. [CrossRef]
5. Kolova, E.E.; Volkov, A.V.; Savva, N.Y.; Prokofyev, V.Y.; Sidorov, A.A. Features of ore formation at the Dvoynoye epithermal Au-Ag deposit (West Chukotka). *Dokl. Earth Sci.* **2018**, *478*, 561–565. [CrossRef]
6. Volkov, A.V.; Prokofyev, V.Y.; Sidorov, A.A.; Vinokurov, S.F.; Yelmanov, A.A.; Murashov, K.Y.; Sidorova, N.V. Conditions of the Au-Ag epithermal mineralization formation in the Amguema-Kanchalan volcanic field (East Chukotka). *Voclanol. Seismol.* **2019**, *13*, 335–347. [CrossRef]
7. Zhuravkova, T.V.; Palyanova, G.A.; Kalinin, Y.A.; Goryachev, N.A.; Zinina, V.Y.; Zhutova, L.M. Physicochemical conditions of formation of gold and silver paragenesis at the Valunistoe deposit (Chukchi Peninsula). *Rus. Geol. Geophys.* **2019**, *60*, 1247–1256.
8. Heald, P.; Hayba, D.O.; Foley, N.K. Comparative anatomy of volcanic-hosted epithermal deposits: Acid sulfate and adularia-sericite types. *Econ. Geol.* **1987**, *82*, 1–26. [CrossRef]
9. White, N.C.; Hedenquist, J.W. Epithermal environments and styles of mineralization: Variations and their causes, and guidelines for exploration. *J. Geochem. Explor.* **1990**, *36*, 445–474. [CrossRef]
10. Hedenquist, J.W.; Lowenstern, J.B. The role of magmas in the formation of hydrothermal ore deposits. *Nature* **1994**, *370*, 519–527. [CrossRef]
11. Hedenquist, J.W.; Arribas, A.; Gonzalez-Urien, E. Exploration for epithermal gold deposits. *Rev. Econ. Geol.* **2000**, *13*, 245–277.
12. Sillitoe, R.H.; Hedenquist, J.W. Linkages between volcanotectonic settings, ore-fluid compositions, and epithermal precious metal deposits. *Spec. Publ. Soc. Econ. Geol.* **2003**, *10*, 315–343.
13. Taylor, B.E. Epithermal Gold Deposits. In *Mineral Deposits of Canada: A Synthesis of Major Deposit Types, District Metallogeny, the Evolution of Geological Provinces and Exploration Methods*; Goodfellow, W.D., Ed.; Mineral Deposits Division Special Publication; Geological Association of Canada: St. John's, NL, Canada, 2007; Volume 5, pp. 113–139.
14. Volkov, A.V.; Goncharov, V.I.; Sidorov, A.A. *Gold and Silver Deposits in Chukotka*; Neisri Feb Ras: Magadan, Russia, 2006. (In Russian)
15. Struzhkov, S.F.; Konstantinov, M.M. *Gold and Silver Metallogeny in the Okhotsk-Chukotka Volcanogenic Belt*; Science World: Moscow, Russia, 2005. (In Russian)
16. White, N.C.; Hedenquist, J.W. Epithermal gold deposits: Styles, characteristics and exploration. *SEG Newsl.* **1995**, *23*, 9–13.
17. Barton, P.B., Jr.; Skinner, B.J. Sulfide Mineral Stabilities. In *Geochemistry of Hydrothermal Ore Deposits*, 2nd ed.; Barnes, H.L., Ed.; Wiley Interscience: New York, NY, USA, 1979; pp. 278–403.
18. Giggenbach, W.F. Isotopic shifts in waters from geothermal and volcanic systems along convergent plate boundaries and their origin. *Earth Planet. Sci. Lett.* **1992**, *113*, 495–510. [CrossRef]
19. Rye, R.O. The evolution of magmatic fluids in the epithermal environment; the stable isotope perspective. *Econ. Geol.* **1993**, *88*, 733–752. [CrossRef]
20. Mancano, D.P.; Campbell, A.R. Microthermometry of enargite-hosted fluid inclusions from the Lepanto, Philippines, high-sulfidation CuAu deposit. *Geochim. Cosmochim. Acta* **1995**, *9*, 3909–3916. [CrossRef]
21. Izawa, E.; Urashima, Y.; Ibaraki, K.; Suzuki, R.; Yokoyama, T.; Kawasaki, K.; Taguchi, S. The Hishikari gold deposit: High-grade epithermal veins in Quaternary volcanics of southern Kyushu, Japan. *J. Geochem. Explor.* **1990**, *36*, 1–56. [CrossRef]
22. André-Mayer, A.S.; Leroy, A.S.; Bailly, J.L.; Chauvet, A.; Marcoux, E.; Grancea, L.; Rosas, J. Boiling and vertical mineralization zoning: A case study from the Apacheta low-sulfidation epithermal gold-silver deposit, southern Peru. *Miner. Depos.* **2002**, *37*, 452–464. [CrossRef]
23. Akinin, V.V.; Miller, E.L. Evolution of lime-alkaline magmas in the Okhotsk-Chukotka volcanic belt. *Petrol* **2011**, *19*, 237–277. [CrossRef]
24. Isayeva, Y.P.; Zvizda, T.V.; Ushakova, D.D. *State Geological Map of the Russian Federation, Scale 1:1 000 000 (3rd Generation), Ser. Chukotka, Sheet Q-60—Anadyr, Explanatory Note*; Vsegei Map Factory: St. Petersburg, Russia, 2016; Available online: ftp://ftp.vsegei.ru/Q-60/Q-60_ObZap.pdf (accessed on 28 October 2020).
25. Sakhno, V.G.; Polin, V.F.; Akinin, V.V.; Sergeev, S.A.; Alenicheva, A.A.; Tikhomirov, P.L.; Moll-Stalcup, E.J. The diachronous formation of the Enmyvaam and Amguema-Kanchalan volcanic fields in the Okhotsk-Chukotka volcanic belt (NE Russia): Evidence from isotopic data. *Dokl. Earth Sci.* **2010**, *434*, 365–371. [CrossRef]
26. Ledneva, G.V.; Piis, V.L.; Bazylev, B.A. Upper Triassic siliceous-volcanogenic-terrigenous deposits of the Chukchi Peninsula. *Rus. Geol. Geophys.* **2016**, *57*, 1423–1442. [CrossRef]

27. Akinin, V.V.; Gelman, M.L.; Sedov, B.M.; Amato, J.M.; Miller, E.L.; Toro, J.; Calvert, A.T.; Fantini, R.M.; Wright, J.E.; Natal'in, B.A. Koolen metamorphic complex, NE Russia: Implications for the tectonic evolution of the Bering Strait region. *Tectonics* **1997**, *16*, 713–729.
28. Glukhov, A.N.; Kolova, E.E.; Savva, N.Y. Gold-silver mineralization of East Chukotka. In *Geology & Mineral Resources of Russia's North-East; Proceedings of the 10th All-Russia Conference with International Participation, Yakutsk, Russia, 8–20 April 2020*; Neefu Publishers: Yakutsk, Russia, 2020; pp. 192–195.
29. Redder, E. *Fluid Inclusions in Minerals*; Nauka: Moscow, Russia, 1987.
30. Van den Kerkhof, A.M.; Hein, U.F. Fluid inclusion petrography. *Lithosphere* **2001**, *55*, 27–47. [CrossRef]
31. Borisenko, A.S. Studies of the salt composition of gaseous-fluid inclusions in minerals by cryometry. *Rus. Geol. Geophys.* **1977**, *8*, 16–27.
32. Bodnar, R.J.; Vityk, M.O. Interpretation of microterhrmometric data for H_2O–NaCl fluid inclusions. In *Fluid Inclusions in Minerals: Methods and Applications*; Pontignano: Siena, Italy, 1994; pp. 117–130.
33. Brown, P. FLINCOR: A computer program for the reduction and investigation of fluid inclusion data. *Am. Mineral.* **1989**, *74*, 1390–1393.
34. Zhang, Y.G.; Frantz, J.D. Determination of the homogenization temperatures and densities of supercritical fluids in the system NaCl-KCl-$CaCl_2$-H_2O using synthetic fluid inclusions. *Chem. Geol.* **1987**, *64*, 335–350. [CrossRef]
35. Garrels, R.M.; Christ, C.L. *Solutions, Minerals, and Equilibria*; Mir: Moscow, Russia, 1968. (In Russian)
36. Chudnenko, K.V. *Thermodynamic Modelling in Geochemistry: Theory, Algorythms, Software, Applications*; GEO: Novosibirsk, Russia, 2010. (In Russian)
37. Helgeson, H.C.; Delany, J.M.; Nesbitt, H.W.; Bird, D.K. Summary and critique of the thermodynamic properties of rock-forming minerals. *Am. J. Sci.* **1978**, *278*, 1–229.
38. Yokokawa, H. Tables of thermodynamic properties of inorganic compounds. *J. Natl. Chem. Lab. Ind.* **1988**, *305*, 27–118.
39. Thermodderm Thermochemical and Mineralogical Tables for Geochemical Modeling. Available online: https://thermoddem.brgm.fr (accessed on 1 July 2020).
40. Perfetti, E.; Pokrovski, G.S.; Ballerat-Busserolles, K.; Majer, V.; Gibert, F. Densities and heat capacities of aqueous arsenious and arsenic acid solutions to 350 °C and 300 bar, and revised thermodynamic properties of $As(OH)_3^\circ$(aq), $AsO(OH)_3^\circ$(aq) and iron sulfarsenide minerals. *Geochim. Cosmochim. Acta* **2008**, *72*, 713–731. [CrossRef]
41. Pokrovski, G.; Gout, R.; Schott, J.; Zotov, A.; Harrichoury, J.C. Thermodynamic properties and stoichiometry of As(III) hydroxide complexes at hydrothermal conditions. *Geochim. Cosmochim. Acta* **1996**, *60*, 737–749. [CrossRef]
42. Tagirov, B.R.; Baranova, N.N.; Zotov, A.V.; Schott, J.; Bannykh, L.N. Experimental determination of the stabilities of Au_2S(cr) at 25 °C and $Au(HS)_2^-$ at 25–250 °C. *Geochim. Cosmochim. Acta* **2006**, *70*, 3689–3701. [CrossRef]
43. Pal'yanova, G.A. Physicochemical modeling of the coupled behavior of gold and silver in hydrothermal processes: Gold fineness, Au/Ag ratios and their possible implications. *Chem. Geol.* **2008**, *255*, 399–413. [CrossRef]
44. Pal'yanova, G.A.; Chudnenko, K.V.; Zhuravkova, T.V. Thermodynamic properties of solid solutions in the Ag_2S–Ag_2Se system. *Thermochim. Acta* **2014**, *575*, 90–96. [CrossRef]
45. Pankratz, L.B. *Thermodynamic Data for Silver Chloride and Silver Bromide*; US Bur Mines, Rep. Inv. 7430; US Department of Interior, Bureau of Mines: Washington, DC, USA, 1970.
46. Rycerz, L.; Szymanska-Kolodziej, M.; Kolodziej, P.; Gaune-Escard, M. Thermodynamic properties of AgCl and AgBr. *J. Chem. Eng.* **2008**, *53*, 1116–1119. [CrossRef]
47. Scott, S.D.; Barnes, H.L. Sphalerite geothermometry and geobarometry. *Econ. Geol.* **1971**, *66*, 653–669. [CrossRef]
48. Cook, N.J.; Ciobanu, C.L.; Pring, A.; Skinner, W.; Shimizu, M.; Danyushevsky, L.; Melcher, F. Trace and minor elements in sphalerite: A LA-ICPMS study. *Geochim. Cosmochim. Acta* **2009**, *73*, 4761–4791. [CrossRef]
49. Kawakami, Y.; Yamamoto, J.; Kagi, H. Micro-Raman densimeter for CO_2 inclusions in mantle-derived minerals. *Appl. Spectrosc.* **2003**, *57*, 1333–1339. [CrossRef]
50. Czamanske, G.K. The stability of argentopyrite and sternbergite. *Econ. Geol.* **1969**, *64*, 459–461. [CrossRef]
51. Zharikov, V.A.; Rusinov, V.L. *Metasomatism and Metasomatic Rocks*; Nauchny Mir: Moscow, Russia, 1998; p. 492. (In Russian)
52. Naboko, S.I. Jarosite deposition from acid sulfate water of the Lower Mendeleyev Spring (Kunashir Isle). *Proc. Mineral. Mus.* **1959**, *10*, 164–170. (In Russian)
53. Heinrich, C.A. The physical and chemical evolution of low-salinity magmatic fluids at the porphyry to epithermal transition: A thermodynamic study. *Miner. Depos.* **2005**, *39*, 864–889. [CrossRef]
54. Berger, B.R.; Henley, R.W. Magmatic-vapor expansion and the formation of high-sulfidation gold deposits: Structural controls on hydrothermal alteration and ore mineralization. *Ore Geol. Rev.* **2011**, *39*, 75–90. [CrossRef]
55. Rottier, B.; Kouzmanov, K.; Casanova, V.; Wälle, M.; Fontboté, L. Cyclic dilution of magmatic metal-rich hypersaline fluids by magmatic low-salinity fluid: A major process generating the giant epithermal polymetallic deposit of Cerro de Pasco, Peru. *Econ. Geol.* **2018**, *113*, 825–856. [CrossRef]
56. Wilkinson, J.J. Fluid inclusions in hydrothermal ore deposits. *Lithos* **2001**, *55*, 229–272. [CrossRef]
57. Banks, D.A.; Bozkaya, G.; Bozkaya, O. Direct observation and measurement of Au and Ag in epithermal mineralizing fluids. *Ore Geol. Rev.* **2019**, *111*, 102955. [CrossRef]

58. Gartman, A.; Hannington, M.; Jamieson, J.W.; Peterkin, B.; Garbe-Schönberg, D.; Findlay, A.J.; Kwasnitschka, T. Boiling-induced formation of colloidal gold in black smoker hydrothermal fluids. *Geology* **2018**, *46*, 39–42. [CrossRef]
59. Prokofiev, V.Y.; Banks, D.A.; Lobanov, K.V.; Selektor, S.L.; Milichko, V.A.; Akinfiev, N.N.; Borovikov, A.A.; Lüders, V.; Chicherov, M.V. Exceptional Concentrations of Gold Nanoparticles in 1,7 Ga Fluid Inclusions From the Kola Superdeep Borehole, Northwest Russia. *Sci. Rep.* **2020**, *10*, 1108. [CrossRef]
60. Pokrovski, G.S.; Akinfiev, N.N.; Borisova, A.Y.; Zotov, A.V.; Kouzmanov, K. Gold speciation and transport in geological fluids: Insights from experiments and physical-chemical modelling. *Geol. Soc. Lond. Spec. Publ.* **2014**, *402*, 9–70. [CrossRef]
61. Williams-Jones, A.E.; Bowell, R.J.; Migdisov, A.A. Gold in solution. *Elements* **2009**, *5*, 281–287. [CrossRef]
62. Simmons, S.F.; Christenson, B.W. Origins of calcite in a boiling geothermal system. *Am. J. Sci.* **1994**, *294*, 361–400. [CrossRef]
63. Akinfiev, N.N.; Tagirov, B.R. Selenium impact on silver transportation and sedimentation by hydrothermal solutions: Thermodynamic description of the Ag-Se-S-Cl-OH system. *Geol. Ore Depos.* **2006**, *48*, 460–472. [CrossRef]
64. Tagirov, B.R.; Baranova, N.N. On the role of selenium in the silver hydrothermal transportation (by experimental data). *Geochem. Int.* **2009**, *6*, 666–672.
65. Stotler, R.L.; Frape, S.K.; Shouakar-Stash, O. An isotopic survey of δ^{81}Br and δ^{37}Cl of dissolved halides in the Canadian and Fennoscandian shields. *Chem. Geol.* **2010**, *274*, 38–55. [CrossRef]
66. Layton-Matthews, D.; Leybourne, M.I.; Peter, J.M.; Scott, S.D.; Cousens, B.; Eglington, B.M. Multiple sources of selenium in ancient seafloor hydrothermal systems: Compositional and Se, S, and Pb isotopic evidence from volcanic-hosted and volcanic-sediment-hosted massive sulfide deposits of the Finlayson Lake district, Yukon, Canada. *Geochim. Cosmochim. Acta* **2013**, *117*, 313–331. [CrossRef]
67. Tikhomirov, P.L.; Glukhov, A.N. On the issue of the age of volcanites within the East Chukotka segment of the OCVB and the associated mineralization. In *Cretaceous Systems in Russia and Adjacent Countries: Problems of Stratigraphy and Paleogeography; Proceedings of the 10th All-Russia Meeting, Magadan, Russia, 20–25 September 2020*; MAOBTI: Magadan, Russia, 2020; pp. 250–252. (In Russian)
68. Tikhomirov, P.L.; Kalinina, E.A.; Moriguti, T.; Makishima, A.; Kobayashi, K.; Cherepanova, I.Y.; Nakamura, E. The Cretaceous Okhotsk-Chukotka volcanic belt (NE Russia): Geology, geochronology, magma output rates, and implications on the genesis of silicic LIPs. *J. Volcanol. Geotherm. Res.* **2012**, *221*, 14–32. [CrossRef]
69. Seryotkin, Y.V.; Pal'yanova, G.A.; Savva, N.E. Sulfur–selenium isomorphous substitution and morphotropic transition in the $Ag_3Au(Se,S)_2$ series. *Rus. Geol. Geophys.* **2013**, *54*, 646–651. [CrossRef]
70. Palyanova, G.A.; Savva, N.E.; Zhuravkova, T.V.; Kolova, E.E. Gold and silver minerals in low-sulfide ores of the Julietta deposit (northeastern Russia). *Russ. Geol. Geophys.* **2016**, *57*, 1171–1190. [CrossRef]
71. Sidorov, E.G.; Borovikov, A.A.; Tolstykh, N.D.; Bukhanova, D.S.; Palyanova, G.A.; Chubarov, V.M. Gold Mineralization at the Maletoyvayam Deposit (Koryak Highland, Russia) and Physicochemical Conditions of Its Formation. *Minerals* **2020**, *10*, 1093. [CrossRef]
72. Palyanova, G.A. Gold and Silver Minerals in Sulfide Ore. *Geol. Ore Depos.* **2020**, *62*, 383–406. [CrossRef]

minerals

MDPI

Article

Native Gold in the Chudnoe Au-Pd-REE Deposit (Subpolar Urals, Russia): Composition, Minerals in Intergrowth and Genesis

Galina Palyanova [1,2,*], Valery Murzin [3], Andrey Borovikov [1], Nikolay Karmanov [1] and Sergei Kuznetsov [4]

[1] Sobolev Institute of Geology and Mineralogy, Siberian Branch of Russian Academy of Sciences, Akademika Koptyuga Pr., 3, 630090 Novosibirsk, Russia; borovikov.57@mail.ru (A.B.); krm@igm.nsc.ru (N.K.)
[2] Department of Geology and Geophysics, Novosibirsk State University, Pirogova Str., 2, 630090 Novosibirsk, Russia
[3] Zavaritsky Institute of Geology and Geochemistry, Ural Branch of Russian Academy of Sciences, Akademika Vonsovskogo Str., 15, 620016 Ekaterinburg, Russia; murzin@igg.uran.ru
[4] Komi Science Center, Institute of Geology, Ural Branch, Russian Academy of Sciences, Pervomaiskaya Str., 54, 167982 Syktyvkar, Russia; kuznetsov@geo.komisc.ru
* Correspondence: palyan@igm.nsc.ru

Abstract: Composition of native gold and minerals in intergrowth of the Chudnoe Au-Pd-REE deposit (Subpolar Urals, Russia) was studied using optical microscopy, scanning electron microscopy, and electron microprobe analysis. Five varieties of native gold have been identified, based on the set of impurity elements and their quantities, and on intergrown minerals. Native gold in rhyolites from the Ludnaya ore zone is homogeneous and contains only Ag (fineness 720‰, type I). It is in intergrowth with fuchsite or allanite and mertieite-II. In rhyolites from the Slavnaya ore zone, native gold is heterogeneous, has a higher fineness, different sets and contents of elements: Ag, Cu, 840–860‰ (type II); Ag, Cu, Pd, 830–890‰ (III); Ag, Pd, Cu, Hg, 840–870‰ (IV). It occurs in intergrowth with fuchsite, albite, and mertieite-II (type II), or albite, quartz, and atheneite (III), or quartz, albite, K-feldspar, and mertieite-II (IV). High-fineness gold (930–1000‰, type V) with low contents of Ag, Cu, and Pd or their absence occurs in the form as microveins, fringes and microinclusions in native gold II–IV. Tetra-auricupride (AuCu) is presented as isometric inclusions in native gold II and platelets in the decay structures in native gold III and IV. The preliminary data of a fluid inclusions study showed that gold mineralization at the Chudnoe deposit could have been formed by chloride fluids of low and medium salinity at temperatures from 105 to 230 °C and pressures from 5 to 115 MPa. The formation of native gold I is probably related to fuchsitization and allanitization of rhyolites. The formation of native gold II-V is also associated with the same processes, but it is more complicated and occurred later with a significant role of Na-, Si-, and K-metasomatism. The presence of Pd and Cu in the ores and Cr in fuchsite indicates the important role of mafic-ultramafic magmatism.

Keywords: Chudnoe deposit (Russia); Au-Pd-REE mineralization; chemistry of native gold; Au-Cu intermetallides; P,T,X parameters of ore-forming fluids

Citation: Palyanova, G.; Murzin, V.; Borovikov, A.; Karmanov, N.; Kuznetsov, S. Native Gold in the Chudnoe Au-Pd-REE Deposit (Subpolar Urals, Russia): Composition, Minerals in Intergrowth and Genesis . *Minerals* **2021**, *11*, 451. https://doi.org/10.3390/min11050451

Academic Editor: Theodore J. Bornhorst

Received: 20 February 2021
Accepted: 22 April 2021
Published: 25 April 2021

1. Introduction

The Chudnoe deposit (Subpolar Urals, Russia) [1–3] and some other Ural deposits—Baronskoe [4], Volkovskoe, Nesterovskoe [1,3,5–7], and Ozernoe [8,9] are unique in the set of impurity elements in native gold (Ag, Cu, Pd, Hg), variability of their concentrations, and minerals in intergrowth with it. The Chudnoe deposit is a special type of Au-Pd-REE mineralization [1,3], which differs from the known hydrothermal or metamorphic gold deposits. Native gold at this deposit is associated with chromium muscovite (fuchsite), REE minerals, palladium arsenoantimonides in the absence of iron sulfides and carbonates. It was discovered by Ozerov in 1994 [10] on the eastern slope of the Maldynyrd ridge during prospecting works on primary deposits, which are probable sources of earlier discovered

placers with gold and palladium minerals in the Kozhim district. Since that time, numerous papers have been published on the mineralogy of the Chudnoe deposit in the form of a number of publications in the proceedings of Russian conferences, one monograph [3], three Ph.D. theses [5,11,12], and about ten articles [1–3,7,13–16].

In the earlier works on the mineralogy of gold from the Chudnoe deposit the authors distinguish from one to three varieties of native gold [1–3,16]. Native gold contains major (>10 wt.%), minor (1–10 wt.%), and trace (<1 wt.%) elements. The first data on the composition of native gold were reported by Tarbaev and coauthors [1], revealing that gold particles are concentrated near fuchsite veinlets. The first variety is the products of decomposition of Ag-Cu-Hg-Pd solid solution. The matrix is depleted in Pd (0.3–0.8 wt.%) relative to the Au-Cu phase of the platelets (0.7–1.1 wt.% Pd) and has a fineness of 840–870‰ (N_{Au} = Au × 1000/(Au + Ag + Cu + Hg + Pd)). The composition of platelets (1–2 μm thick and to 10 μm long) was determined approximately: maximum content of Cu is 10.5 wt.%, the amount of Hg is close to that in the matrix 0.1–1 wt.%, and Ag ranges from 2.5 to 11.6 wt.%. The second variety of native gold is represented by a higher fineness (to 1.9 wt.% Pd) porous gold in the form of isometric 3–15 μm inclusions in native gold of the first type or thin rims around it.

Galankina et al. [2] found one variety of native gold with high concentrations of Ag (to 20–25, occasionally to 50.5 wt.%) and low concentrations of Cu and Pd (no more than 0.2 wt.%) (fineness 510–800‰) in the absence of Hg. Gold particles to 3 mm in size were concentrated in fuchsite-quartz-allanite veinlets and often in intergrowth with mertieite or contained its inclusions. Shumilov and Ostashchenko [3] revealed three varieties of that native gold from the Chudnoe deposit, which are associated with either fuchsite or allanite localized in the axial part of mica veinlets. Native gold with a wide range of impurities, to 2.3 wt.% Pd, to 3.6 wt.% Cu, and to 1.4 wt.% Hg (840–870‰), was attributed to the first type. It has an intricate inner structure: some of gold particles (840–870‰) are rimmed with high-fineness gold (920–990‰) only with an impurity of Cu, whereas other gold particles contained the decomposition products of solid solutions. The platelets are from 0.1 to 1–3 μm thick, the amount of Cu in the platelets is higher (increase to 12.5 instead of 3–4 wt.%), and that of Ag is lower than in the matrix (decreases from 11–12 to 3–4 wt.%). Native gold of the second type is characterized by a low fineness (720–790‰, as low as 530‰) and absence of Cu, Hg, and Pd. This type of native gold occurs in the Ludnaya zone. To the third type, these authors [3] attribute porous and microcrystalline native gold that overgrows on larger gold particles of the first and second types. It is characterized by high fineness (to 990‰) and, respectively, lower contents of Ag and Cu at relatively high concentrations of Pd and absence of Hg.

Borisov [5] found that native gold from the Chudnoe deposit contained inclusions of the Au-Cu phases: Au_3Cu, Au_3Cu_2, and Au_2Cu with minor Pd. Kuznetsov et al. [8] also reported that native gold of heterogeneous composition (8.2–11.6 wt.% Ag, 1.3–3.0 wt.% Cu, about 1.3 wt.% Hg and to 1.7 wt.% Pd, fineness 850–906‰) contains inclusions of Au-Cu phases—tetra-auricupride AuCu and auricupride $AuCu_3$ and Pd minerals—mertieite Pd_5Sb_2, isomertieite Pd_5AsSb, atheneite $(Pd,Hg)_3As$, stillwaterite Pd_8As_3, and stibiopalladinite Pd_5Sb_3. It is worth noting that the stoichiometric formulas of some minerals reported by these authors differ from those of minerals with similar names from the IMA database [17]: mertieite-I $Pd_{5+x}(Sb,As)_{2-x}$ (x = 0.1−0.2), mertieite-II $Pd_8Sb_{2.5}As_{0.5}$, omertieite $Pd_{11}Sb_2As_2$, stibiopalladinite Pd_5Sb_2, atheneite $Pd_2(As_{0.75}Hg_{0.25})$. Onishchenko et al. [16] determined two varieties of native gold in the Slavnaya ore zone at the Chudnoe deposit. The authors show a predominance of native gold containing 84–88 wt.% Au, 7–12 wt.% Ag, 1.3–5.5 wt.% Cu, 1–2 wt.% Pd and about 1 wt.% Hg. This native gold was found to be intergrown with small inclusions of high-fineness gold: 94–98 wt.% Au, 1.5–2 wt.% Pd, to 0.9 wt.% Cu and to 0.7 wt.% Ag.

Despite the numerous results, the reasons of compositional changes in native gold and the presence of a wide set of impurity elements are not clear yet. Although native gold is known to be concentrated in the fuchsite veinlets in rhyolites, there is little information on matrix minerals in close growth with it and physicochemical conditions of the formation of Au-Pd-REE mineralization. The aim of our study is to reveal the specific features of the chemical composition of native gold and to determine the minerals in the intergrowth with it in the Slavnaya and Ludnaya ore zones of the Chudnoe deposit. The first results of the fluid inclusions study at the Chudnoe deposit were obtained by Surenkov [12]. This study provides limited new microthermometric analyses of fluid inclusions which are used to estimate the compositional features and PTX parameters for two ore zones. These data will help us to determine the possible sources of trace elements in native gold and to receive new information on the genesis of unique Chudnoe Au-Pd-REE deposit.

2. Geological Settings and Localizations

The Chudnoe deposit occurs on the western slope of the Subpolar Urals (Russia) in the interformational contact zone of uralids (terrigeneous and sedimentary rocks O_{1-2}) and preuralids (volcanogenic rocks of effusive and subvolcanic facies of acidic and basic composition R_3-V) in the axial part of the Maldinskaya anticline. In the contact zone of the Precambrian and Ordovician rocks there are lenses of chloritoid-pyrophylite slates which are considered to be the relicts of metamorphosed weathering crusts of the Precambrian age [10].

Numerous dislocations with a break in continuity of mainly NE strike are developed in the area of the deposit. The largest of them is the Maldinskiy fault, a zone in which the Chudnoe deposit is localized [1,7]. Metasomatites and associated zones of pyritization, hydrothermal quartz veins, many of which are crystal-bearing, are widespread in the area. Occurrences of rare-earth, polymetallic, molybdenum, silver, and uranium-copper mineralization are present as well. Lying 1.5–2 km to the southeast of the Chudnoe deposit is the Nesterovskoe occurrence localized in the terrigenous formations of uralids (aleuroschists, sandstones and gritstone O_1) with gold-platinoid-fuchsite mineralization. Gold-palladium mineralization formed much later than the host rocks and it is of Paleozoic age (250–260 Ma), according to the ^{39}Ar-^{40}Ar datings on fuchsite [13].

The northwestern part of the Chudnoe deposit is composed of rocks of basic composition rich in Na (Figure 1). These rocks consist of metabasalts transformed into dark-gray schists and, to a lesser degree, of metadolerites and gabbrodolerites of more massive appearance [7]. Alterations of rocks develop as chloritization, albitization, and epidotization. The accessory minerals of metabasic rocks are magnetite, ilmenite, titanite, and sulfides (pyrite, chalcopyrite). The content of gold in basaltoids is insignificant.

The southeastern part of the deposit area is made up of mainly dark porphyric rhyolites with flow bandings. Along the dislocations with a break in continuity, rhyolites are often lightened. In addition, dark rhyolites contain lightened zones extending to 1 m, oriented according to fluidality. The dark color of rhyolites is due to the scattered fine (to 0.01 mm) impregnations of hematite, which is absent in light rocks [14]. The groundmass of rhyolites is composed of varying amounts of quartz, albite, K-feldspar, and sericite. The accessory minerals of rhyolites are ilmenite, titanite, allanite, apatite, zircon, monazite, and xenotime. As for dark rhyolites, lightened zones contain similar quantities of major components and low concentrations of Fe_2O_3 (Table 1).

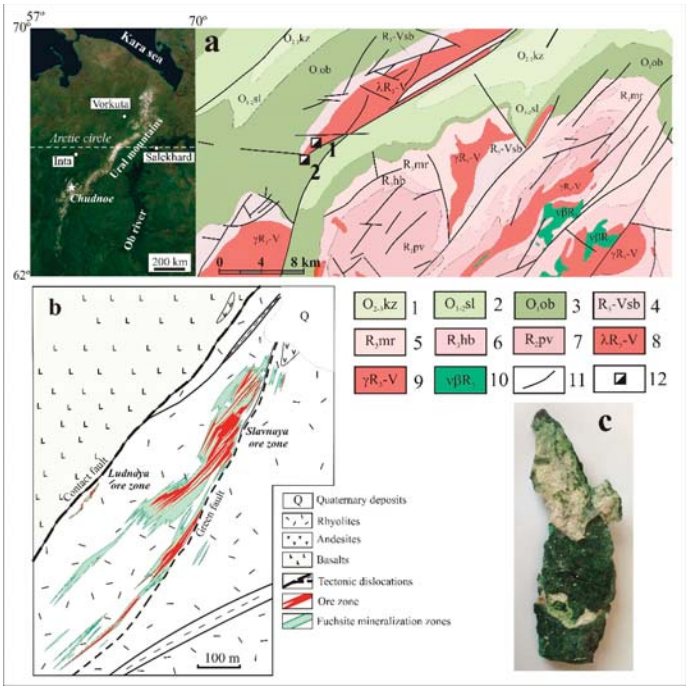

Figure 1. 200-km (inset), 8-km (**a**), and 100-m (**b**) scale maps of the Chudnoe deposit according to [7] and photograph of ore sample (size 5 cm × 13 cm) from this deposit (**c**). 1—Kozhim Formation: limestones, calcareous shales and sandstones; 2—Saled Formation: chlorite-sericite-quartz shale, sandstone; 3—Obizskaya suite: quartzite sandstones, conglomerates, gravelstones; 4—Sablegorskaya suite: felsic and basic effusive rocks, tuffs, phyllitic schists; 5—Moroinskaya Formation (R_3mr): phyllitic schists, marbles, quartzites; 6—Khobein suite: quartzites, conglomerates, chlorite-sericite-quartz schists; 7—Puivinskaya suite: mica-quartz schists, calcareous schists, interlayers of quartzites, marbles; 8—subvolcanic rhyolites; 9—granites; 10—gabbro, gabbro-dolerites; 11—tectonic faults; 12—Chudnoe (1) and Nesterovskoe (2) deposits.

Table 1. Chemical composition of light (L) and dark (D) rhyolites from the Chudnoe deposit [14].

No.	SiO_2	TiO_2	Al_2O_3	Fe_2O_3	FeO	MnO	MgO	CaO	Na_2O	K_2O	P_2O_5	LOI	Σ
41 L	77.32	0.17	11.63	0.62	0.50	0.02	0.06	0.19	1.99	6.40	0.02	0.21	99.13
42 D	75.08	0.17	11.75	2.40	0.72	0.02	0.09	0.18	1.72	6.60	0.02	0.41	99.16
43 L	76.42	0.17	12.14	1.00	0.65	0.02	0.10	0.16	1.85	6.60	0.02	0.27	99.40
44 D	73.56	0.19	12.64	2.55	0.65	0.04	0.16	0.37	1.45	6.60	0.05	0.74	99.00
62 L	75.44	0.19	13.66	0.50	1.01	0.02	0.04	0.21	4.90	3.60	0.03	0.14	99.74
63 D	73.06	0.19	14.29	1.49	0.79	0.02	0.06	0.23	4.80	3.80	0.04	0.38	99.15
64 L	74.94	0.19	13.91	0.30	0.58	0.02	0.01	0.22	5.70	3.10	0.02	0.05	99.04
65 D	75.34	0.19	13.15	1.86	0.65	0.02	0.05	0.23	5.00	3.20	0.02	0.21	99.92
21 L	77.76	0.17	12.17	0.13	0.60	0.01	0.04	0.15	2.78	5.70	0.02	0.18	99.71
22 D	75.36	0.18	12.68	1.78	0.43	0.01	0.06	0.14	2.90	5.30	0.02	0.27	99.13
71 L	73.42	0.19	14.20	0.21	0.86	0.01	0.06	0.17	4.50	5.70	0.03	0.15	99.53
72 D	72.00	0.19	14.54	2.41	0.29	0.02	0.05	0.16	5.60	4.70	0.02	0.17	100.15
4–2 L	78.92	0.10	10.80	0.37	1.22	0.01	0.10	0.18	3.67	3.40	0.02	0.6	99.39
4–1 D	75.67	0.12	12.11	1.59	1.08	0.01	0.12	0.20	4.41	3.65	0.02	0.4	99.38

Notes: The CO_2 content in the samples does not exceed 0.22 wt.%, the F content < 0.02 wt.%. LOI—loss on ignition.

Onishchenko and Kuznetsov [7] report that in gold-bearing rhyolites, the content of Cr reaches 0.03–0.05 wt.%, and the concentrations of Au, Ag and As are no more than few tens of ppm: 25 Au, 3.4 Ag (which corresponds to Au/Ag ≈ 7), and 6–21 As. The contents of some elements amount to hundreds of ppm: 480–970 Ba, 80–100 La, 160–230 Ce, 60–110 Y, 30–40 Nb, 180–260 Zr. The total contents of REE in rhyolites with fuchsite from the Chudnoe deposit average 544 ppm [5]. The concentrations of Hg to 18 ppm are typical of fuchsite ores, barren rhyolites contain up to 18 ppb Hg [18]. In gold-bearing rhyolites the content of S is no more than 0.01 wt.%. Higher sulfur contents (to 0.5 wt.%) were found in some poorly productive zones among andesites [7].

Au-Pd-REE mineralization occurs in several schist and brecciate zones 100 to 460 m in length and up to 60 m in thickness in rhyolites (Figure 1). The ore zones have a steep (50–70°) northwestern dip and northeastern strike. Au-Pd-REE mineralization in the schist and brecciated zones occurs among fuchsite, quartz, and quartz-albite veinlets ranging in thickness from few mm to 1–1.5 cm. The Chudnoe deposit includes the Slavnaya and Lyudnaya ore zones (Figure 1). The main zone is the Slavnaya located in the central part of the deposit. This zone contains the richest ores with highest Au concentrations ~22 ppm [7]. A rather small Ludnaya ore zone is localized in schistose rhyolites at the contact with mafic rocks (andesites and basalts). It occurs to the southwest of the Slavnaya ore zone at a distance of 200–250 m and rises for 50 m above the relief [3]. The Ludnaya ore zone has a lentiform-discontinuous structure and contains rich ores with visible native gold. The content of noble metals is nonuniform—from few to hundreds ppm.

3. Materials and Methods

Samples of Au-bearing rhyolites collected from exploration trenches were used. Numerous polished and thin sections were made of them. For our study we selected typical samples of rhyolite from the ore zones Ludnaya (No.1a—1154-6; No.1b—1154-6b) (Figure 2a) and Slavnaya (No.2—1122-5, No.3—1122-12, No.4a—1122-1, No.4b—1122-1b; No.5—1122-13) (Figures 6a–8a), in which native gold was found visually or under a microscope.

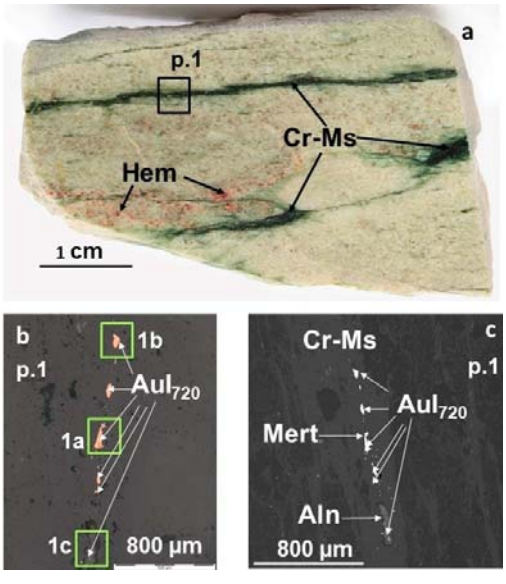

Figure 2. Macrophotograph of a polished section of rhyolite from the Ludnaya zone (**a**) and reflected light microscopy image (**b**) and BSE (**c**) micrograph of its fragment (p.1) with a fuchsite (Cr-Ms) veinlet containing native gold of type I (AuI), allanite (Aln), and mertieite (Mert).

A macro- and microscopic study of the ore samples was conducted. Mineralogical research was carried out using an optical microscope Olympus BX51 (in the Sobolev Institute of Geology and Mineralogy of the Siberian Branch of the Russian Academy of Sciences (IGM SB RAS) (Novosibirsk, Russia). Chemical analyses of minerals were conducted at the Analytical Center for Multi-elemental and Isotope Research in the IGM SB RAS (Novosibirsk, Russia) by electron probe microanalysis (EPMA) using a MIRA 3 LMU scanning electron microscope (Tescan Orsay Holding, Brno, Czech Republic) equipped with an X-ray energy dispersive spectrometer (EDS) AZtec Energy XMax-50 (Oxford Instruments Nanoanalysis, Oxford, UK) (analysts Dr. N. Karmanov, M. Khlestov).

The composition of native gold and accessory minerals was studied at the following parameters: accelerating voltage was 20 kV, live spectrum acquisition time was 60 sec (total area of spectra ~10^6 counts). The following X-rays were selected: *K* series for Fe, Cu, As and *L* series for Pd, Ag, Sb, Au, Hg. We used pure metals (Fe, Cu, Pd, Ag, Au) and InAs for As and HgTe for Hg as the standards. The detection limits (in wt.%) were: 0.1 Fe, 0.15 Cu, 0.25 Pd, Ag, Sb, 0.3 As, 0.6 Au, and 0.8 Hg. Error in determining the main components with the contents higher than 10 wt.% did not exceed 1 relative (rel.) %, and when the content of components ranged 2–10 wt.%, the error was no higher than 6–8 rel. %. Close to the limit of detection, the error was 15–20 rel. %. In some cases the spectrum acquisition time increased to 120 s, the lower limits of determined contents and the random error of the analysis decreased about 1.4 times. To reduce the effect of microrelief of samples on the quality of analysis, data on the primary homogeneous gold were obtained in the scanning mode of individual sections from 10 × 10 to 50 × 50 μm^2 in size. In the same mode, we obtained the average composition of native gold in the presence of decay structures. The compositions of small gold particles (<10 μm) and platelets of decay structure were determined with a 10 nm point probe, but the size of the generation region of X-ray emission in gold with the electron beam energy 20 kV was 1 μm. Therefore, the data of analysis cannot be considered quantitative if the minimum size of the studied object is less than 2 μm.

It is worth noting that in the obtained back scattered-electron (BSE) micrographs, albite and quartz as well as K-feldspar and muscovite (fuchsite) are hardly distinguishable when they are intergrown with each other. For better visualization of the matrix minerals, we used multi-layered colorful EDS maps.

Fluid inclusion microthermometry was used to analyze the composition of fluids and to estimate the pressure-temperature conditions during ore forming processes (fluid inclusion study was carried out in the Laboratory of Prediction-Metallogenic studies, IGM SB RAS, Novosibirsk, Russia). Phase transition temperatures in fluid inclusions (samples No.1b—1154-6b; No.4b—1122-1b) were determined using cryo- and thermometry procedures (Linkam THMSG-600 heating-freezing chamber with the measurement range of –196 to +600 °C). According to the data of cryometry, the fluids are attributed to the water-salt system [19,20]. To estimate the pressure and other parameters of mineral formation from the microthermometric data of fluid inclusion study, we used the AqSo_NaCl software [21].

4. Results

Detailed mineralogical studies reveal the varieties of native gold and the minerals in the intergrowths with it from the Ludnaya and Slavnaya ore zones of the Chudnoe Au-Pd-REE deposit. Native gold is intergrown with one up to five minerals. The intergrowths of native gold with minerals are common. In the subsections below, we describe the features of the revealed varieties of native gold and minerals in the intergrowths with it from two ore zones.

4.1. Native Gold in Rhyolites from the Ludnaya Ore Zone

Figure 2 shows the macrophotograph of a polished section of typical rhyolite from the Ludnaya zone (a) and micrographs (b,c) of its fragment (p.1) with a fuchsite veinlet containing native gold. The sizes of gold particles vary from barely discernible 0.1 to 70–100 μm. Small gold particles are virtually of isometric shape, occasionally with elements

of faceting, whereas larger individuals are of elongated interstitial shape. Figures 3–5 show the reflected light microscopy image (Figures 3a and 4a), BSE micrographs (Figure 5a,b), multi-layered colorful EDS maps (Figures 3b and 4b), and maps of areal distribution of elements in characteristic rays (Figures 3c–i and 4c–g) of fragments (p.1a, p.1b) with gold particles of various morphologies and sizes (Figure 2b). The gold particles have a homogeneous texture, which is clearly seen from these figures.

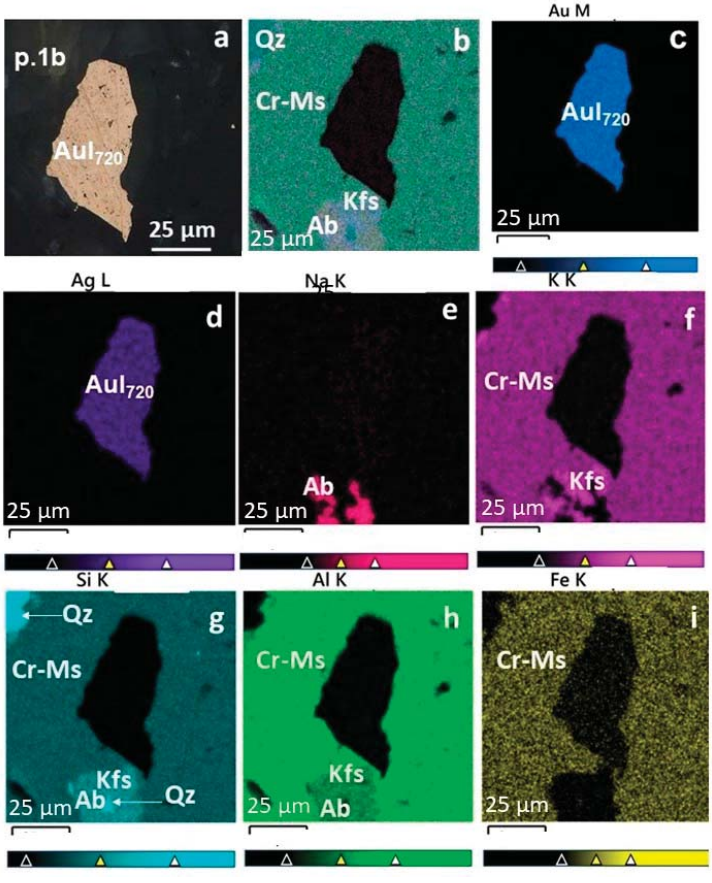

Figure 3. Native gold (type I) (AuI) (fineness 720‰, Ag impurity) in intergrowth with fuchsite (Cr-Ms) in rhyolite from the Ludnaya zone (Figure 2b—p.1b). (**a**)—reflected light microscopy image, (**b**)—multi-layered colorful EDS map, (**c**–**i**)—maps of areal distribution of elements in characteristic rays. Abbreviations of minerals: quartz (Qz), albite (Ab), K-feldspar (Kfs).

It is well seen on the multi-layered colorful EDS maps (Figures 3b and 4b) and maps of areal distribution of elements (Au, Ag, Pd, Na, K, Si, Al, Fe, Sb, As) in characteristic rays (Figures 3c–i and 4c–g) that native gold in the analyzed fragments—points p.1a and p.1b—is localized in the interstices of fuchsite and has no common borders with quartz, albite, and K-feldspar. Figure 4 demonstrates that native gold (p.1a) is intergrown with fuchsite and mertieite. Mertieite also occurs as separate particles in fuchsite (Figure 4a).

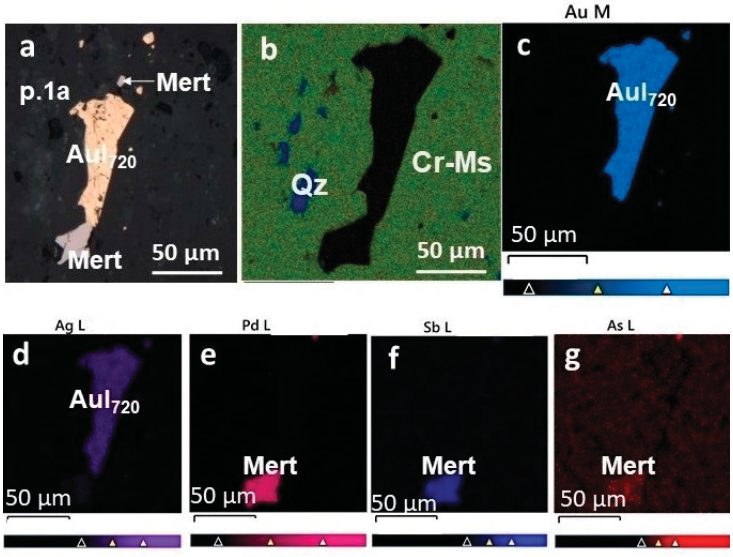

Figure 4. Native gold (type I) (AuI) (fineness 720‰, Ag impurity) in intergrowth with fuchsite (Cr-Ms) and mertieite (Mert) (**b**–**d**) in rhyolite from the Ludnaya zone (Figure 2b—p.1a). (**a**)—reflected light microscopy image, (**b**)—multi-layered colorful EDS map, (**c**–**g**)—maps of areal distribution of elements in characteristic rays.

Figure 5a,b shows relatively small particles of native gold (type I) (Figure 2b—p.1c), surrounded by fuchsite or allanite. Allanite is localized in the axial part of the fuchsite veinlet (Figures 2c and 5a). It is seen from Figure 5b that one of the gold particles is intergrown with mertieite and allanite, and between allanite and fuchsite there are aggregates of quartz and K-feldspar, which also proves the absence of joint boundaries of native gold (type 1) with these minerals in rhyolite.

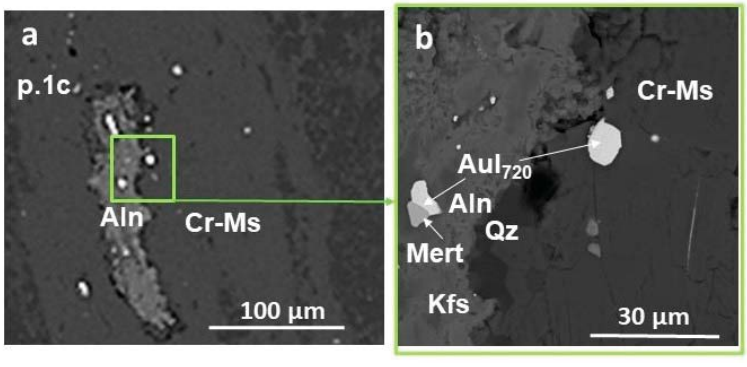

Figure 5. BSE micrographs of a fuchsite (Cr-Ms) vein with allanite (Aln), native gold (type I) (AuI) (Figure 2b—p.1c) and other minerals in rhyolite from the Ludnaya zone (**a**) and its enlarged fragment (**b**): on the right are gold microparticles in intergrowth with fuchsite, on the left, in intergrowth with allanite (Aln) and mertieite (Mert). Abbreviations of minerals: quartz (Qz), K-feldspar (Kfs).

Native gold (type I) in intergrowth with fuchsite, allanite, and mertieite in green veinlets of rhyolite sample No.1 from the Ludnaya ore zone (Figure 2a) has a constant composition and major Ag impurity (fineness 716–724‰, N_{Au} = Au * 1000/(Au + Ag))

(Table 2). It is worth noting that Pd, Cu, Hg, and other elements were not detected even when the acquisition time of the spectra was increased to 120 s.

Table 2. Representative analyses of native gold (type I) and minerals in intergrowth with it in rhyolite No.1 (Figures 2–5) from the Ludnaya ore zone (EPMA data in wt.% and formula).

N	Au	Ag	∑ wt.%	N_{Au}	Formula	Minerals in Intergrowth
p.1a	69.54	27.6	97.14	716	$Au_{0.58}Ag_{0.42}$	Cr-Ms; U-Mert
	70.52	27.22	97.74	722	$Au_{0.59}Ag_{0.41}$	- " -
p.1b	71.44	27.29	98.72	717	$Au_{0.58}Ag_{0.42}$	Cr-Ms
	70.52	27.22	97.74	724	$Au_{0.59}Ag_{0.41}$	- " -
p.1c	69.91	27.12	97.03	720	$Au_{0.59}Ag_{0.41}$	Cr-Ms
	69.95	27.46	97.41	722	$Au_{0.59}Ag_{0.41}$	Aln; Cu-Mert

Abbreviations of minerals: fuchsite (Cr-Ms), allanite (Aln) and U or Cu-mertieite (U- or Cu-Mert).

Fuchsite from the Ludnaya ore zone, in addition to 0.4–1.1 Cr, also contains 6.4–6.5 Fe, 0.3–0.6 Mg, and 0.2–0.3 Ti (in wt.%). Its stoichiometric formula corresponds to $K_{0.98}Fe_{0.52}Ti_{0.02}Cr_{0.01}Mg_{0.09}Al_{2.24}Si_{3.24}O_{11}H_{4.5}$. Allanite has a varying composition with impurities of (in wt.%): 0.1–0.3 Ce and Nd, up to 0.5 Pr, up to 0.1 La, Sm, Cr, and Mn ($Ca_{3.2–3.8}Fe_{2–2.1}La_{0–0.1}Ce_{0–0.3}Nd_{0–0.3}Pr_{0–0.1}Mn_{0.1}Cr_{0–0.1}Al_{3.9–4.1}Si_{6.2}O_{25}H_{1.9}$). In some allanite crystals, we observed REE together with about 1 wt.% Sr, which corresponds to ($Ca_4Fe_{2.1}Sr_{0.1}La_{0.1}Ce_{0.3}Nd_{0.3}Pr_{0.1}Sm_{0.1}Al_{4.1}Si_{6.2}O_{25}H_{1.9}$). The stoichiometric formula of palladium arsenoantimonide, according to IMA data, is similar to mertieite-II ($Pd_8Sb_{2.5}As_{0.5}$). The difference between mertieite-I and mertieite-II is chemical: mertieite-I $Pd_{5+x}(Sb,As)_{2-x}$ (x = 0.1 − 0.2), mertieite-II $Pd_8Sb_{2.5}As_{0.5}$. The stoichiometric formula of this phase in the fuchsite matrix is $Pd_{7.7}Sb_{2.6}As_{0.6}U_{0.1}$ (content of U impurity is about 2 wt.%), and in the intergrowth with allanite it revealed higher contents of As, presence of Cu, and absence of U: $Pd_{7.5}Cu_{0.5}Sb_{1.6}As_{1.4}$.

Fuchsite veinlets also contain titanite $CaTiSiO_6$ and Y mineral, which is similar in composition to keiviite ($Y_2Si_2O_7$). Rhyolite, in addition to quartz, albite, and K-feldspar, contains hematite (Figure 2a), less frequently, zircon and apatite. In zircon, hafnium (1–1.4 wt.%) was present. Titanite was found to contain (in wt.%): 1–1.2 Nb, 0.3 Cr, and 0.9 Fe.

Results of studies showed that native gold of type I occurs in the form of individual particles or in intergrowth with mertieite-II in the allanite-fuchsite matrix in rhyolite from the Ludnaya ore zone and has direct contacts with these minerals, which suggests simultaneous formation of Au-Pd-REE mineralization and fuchsite veinlets and, probably, similar physicochemical conditions of deposition.

4.2. Native Gold in Rhyolites from the Slavnaya Ore Zone

Native gold in rhyolites from the Slavnaya ore zone, in contrast to the Ludnaya ore zone, along with silver contains copper, palladium, and mercury in various combinations and concentrations. The fineness of native gold ($N_{Au,}$ ‰) was calculated using the equation: Au (in wt.%) * 1000/(Au + Ag + Cu + Pd + Hg) (in wt.%). Depending on the set and contents of impurity elements in native gold, its reference symbols were adopted-$Au(N_{Au})_{AgCuPdHg}$ (elements are given in order of decreasing concentrations). Several varieties of native gold were established (Tables 3–6): (1) Native gold with major content of Ag and minor Cu (fineness 860‰) (type II) ($AuII_{860AgCu}$); (2) native gold with major Ag and insignificant amounts of Cu and Pd (fineness 830–890‰) (type III) ($AuIII_{830–890AgCuPd}$); (3) native gold with major Ag and insignificant amounts of Cu, Pd, and Hg (fineness 830–860‰) (type IV) ($AuIV_{830–860AgCuPdHg}$); (4) high-fineness gold (930–1000‰) with insignificant amounts of Ag, Cu, and (or) Pd (type V) ($AuV_{930AgCuPd}$-AuV), the total content of which does not exceed 7 wt.%, or pure gold (AuV). We found Au-Cu intermetallides in association with native gold of types II–IV.

Results of study of the composition and amount of impurity elements in native gold and minerals in intergrowth with it in rhyolites from the Slavnaya ore zone are reported in the subsections below in the order of revealed varieties.

4.2.1. Native Gold with Ag and Cu Impurities

Native gold containing major Ag and minor Cu (type II) was identified in two rhyolite samples from the Slavnaya ore zone No.2 (p.1a, 2, 6, 7) (Figure 6) and No.3 (p.1b, 1c, 3b, 3c, 4a) (Figure 7). Table 3 shows typical compositions of this type of native gold and provides a list of intergrown minerals.

In sample No.2 this native gold is localized in albite veins accompanying fuchsite veins (Figure 6a–c). It is intergrown with both minerals albite and fuchsite (Figure 6c,e,g,h) as well as with mertieite (Figure 6d–g) and allanite (Figure 6g,h). As an example, Figure 6b–j shows optical and BSE micrographs of xenomorphic particles of native gold (type II) (20–40 μm in size) in intergrowth with albite, fuchsite, and mertieite (sample No.2, p.1a,6,7). The particles contain 11.4–12.7 wt.% Ag and 1.5–1.8 wt.% Cu, which corresponds to the fineness 860–865‰ (Table 3).

Table 3. Representative analyses of native gold (type II) and minerals in intergrowth with it in rhyolites from the Slavnaya ore zone (Nos. 2, 3, Figures 6 and 7) (EPMA data in wt.% and formula).

N	Au	Ag	Cu	∑wt.%	N_{Au}	Formula	Minerals in Intergrowth
				No.2			
p.1a	85.03	11.58	1.72	98.34	865	$Au_{0.76}Ag_{0.19}Cu_{0.05}$	Cr-Ms; Ab; Cu,Ag-Mert
p.1a	84.64	12.41	1.65	98.7	858	$Au_{0.76}Ag_{0.19}Cu_{0.05}$	- " -
p.2	84.55	11.51	4.12	100.19	844	$Au_{0.71}Ag_{0.18}Cu_{0.11}$	Cr-Ms; Ab; Kfs; AuCu; $AuIII_{840–890}$
p.2	84.76	12.72	1.55	99.03	856	$Au_{0.75}Ag_{0.21}Cu_{0.04}$	- " -
p.6	83.68	12.24	1.61	97.53	858	$Au_{0.75}Ag_{0.20}Cu_{0.04}$	Cr-Ms; Ab; Aln; $AuV_{930–990}$
p.6	83.78	12.19	1.77	97.73	857	$Au_{0.75}Ag_{0.20}Cu_{0.05}$	- " -
p.7	85.38	11.44	1.48	98.3	869	$Au_{0.77}Ag_{0.19}Cu_{0.04}$	Cr-Ms; Ab; Cu,Ag,Au-Mert; AuV_{990}
p.7	85.73	11.87	1.62	99.23	864	$Au_{0.77}Ag_{0.19}Cu_{0.04}$	Cr-Ms; Ab; AuV_{990}
p.7	85.67	12.28	1.54	99.48	861	$Au_{0.76}Ag_{0.20}Cu_{0.04}$	- " -
p.7	84.41	12.38	1.4	98.19	860	$Au_{0.76}Ag_{0.20}Cu_{0.04}$	Ms; Ab; Aln; AuV_{990}
				No.3			
p.1b	85.22	11.86	1.88	98.96	861	$Au_{0.76}Ag_{0.19}Cu_{0.05}$	Ab; Ms; Kfs; Qz; $AuV_{1000–970}$; AuCu; X1
p.1b	84.93	11.95	2.04	98.92	859	$Au_{0.75}Ag_{0.19}Cu_{0.06}$	- " -
p.1b	84.21	12.57	1.51	98.29	857	$Au_{0.75}Ag_{0.21}Cu_{0.04}$	- " -
p.1e	83.62	11.75	4.64	100.01	836	$Au_{0.70}Ag_{0.18}Cu_{0.12}$	Ab; Kfs; Qz; $AuIII_{840–890}$
p.2	86.84	12.83	2.24	101.9	852	$Au_{0.74}Ag_{0.20}Cu_{0.06}$	Ab; Ms; Qz
p.2	84.57	12.9	2.11	99.58	849	$Au_{0.74}Ag_{0.21}Cu_{0.05}$	- " -
p.2	86.36	12.27	1.71	100.35	861	$Au_{0.76}Ag_{0.20}Cu_{0.05}$	- " -
p.2	85.39	12.98	2.02	100.39	851	$Au_{0.75}Ag_{0.21}Cu_{0.06}$	- " -
p.2	83.16	14.85	1.35	99.36	837	$Au_{0.73}Ag_{0.23}Cu_{0.04}$	- " -
p.2	84.86	12.29	2.42	99.57	852	$Au_{0.73}Ag_{0.20}Cu_{0.07}$	- " -
p.3b	84.13	12.21	1.67	98.01	858	$Au_{0.75}Ag_{0.2}Cu_{0.05}$	Ab; Ms
p.3c	84.82	12.19	1.76	98.77	859	$Au_{0.75}Ag_{0.2}Cu_{0.05}$	Ab
p.4a	84.54	12.33	1.93	98.81	856	$Au_{0.75}Ag_{0.2}Cu_{0.05}$	Ab; Kfs; Cu-Mert; X1
p.4a	84.07	12.34	2.07	98.48	854	$Au_{0.74}Ag_{0.2}Cu_{0.06}$	- " -

Abbreviations of minerals: native gold of type II, III and V (AuII, AuIII and AuV), fuchsite (Cr-Ms), muscovite (Ms), allanite (Aln), quartz (Qz), albite (Ab), K-feldspar (Kfs) Cu, Ag, U-mertieite (Cu, Ag, U-Mert), tetra-auricupride (AuCu) and amoeba phase (X1).

Figure 6g shows native gold of type II in the intergrowth with allanite, albite, fuchsite, and mertieite in the same sample No.2 (p.7). The contact between native gold and allanite is not resorbed, which suggests that they formed simultaneously. In some albite-fuchsite veinlets of sample No.2 (p.6) (Figure 6h–j) gold particles in the marginal parts are replaced by higher-fineness gold (fineness 930–965‰) (type V): the content of Ag decreases to 2.2 wt.%, and that of Cu increases to 2.3 wt.% and Pd appears (0.9–1.9 wt.%) (Table 6). The texture of such native gold becomes porous (Figure 6j). The albite-fuchsite-allanite veinlet contains apatite inclusions ($Ca_{4.9}P_{2.82}O_{12}F_1$) (Figure 6h).

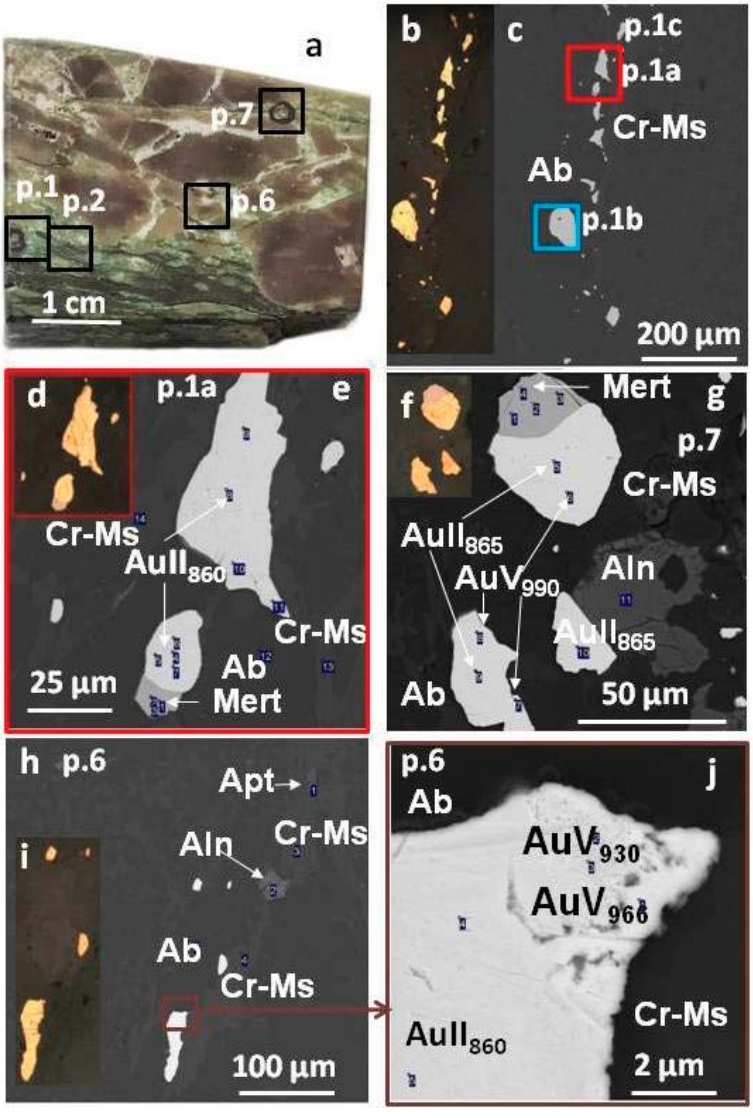

Figure 6. Macrophotograph of a polished section of rhyolite No.2 from the Slavnaya ore zone (**a**) with albite-fuchsite veins and its fragments with native gold (types II, V) (p.1,2,6,7) (**b**–**j**). (**b**,**d**,**f**,**i**) Reflected light microscopy image; (**c**,**e**,**g**,**h**,**j**) BSE micrographs. (**j**) Enlarged fragment on h. Abbreviations of minerals: native gold (type II, V) (AuII, AuV), fuchsite (Cr-Ms), allanite (Aln), albite (Ab), apatite (Apt), mertieite (Mert).

In sample No.3 (Figure 7a), native gold of type II is concentrated in albite veinlets with rare fragments of fuchsite and it is intergrown with albite (p.3c) or albite and fuchsite (p.3b) (Figure 7b) or albite, fuchsite, and mertieite (p.4a) (Figure 7c) or albite, fuchsite, quartz, and K-feldspar (p.1b,1c) (Figure 7d,f). It is localized in the monomineral albite matrix (sample No.3, p.3c) or bimineral albite-fuchsite matrix (sample No.3, p.3b) (Figure 7b), it is homogeneous and contains 11.5–12.8 wt.% Ag and 1.5–2.4 wt.% Cu, its fineness is 860‰ (Table 3).

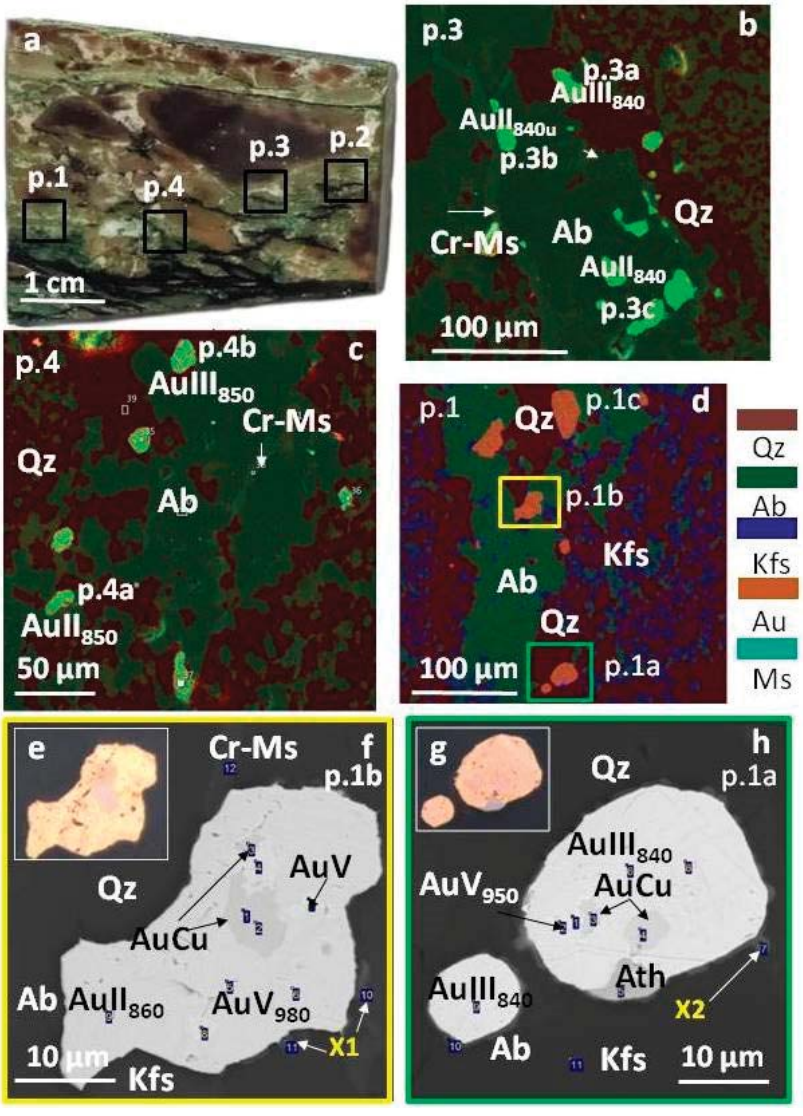

Figure 7. Macrophotograph of a polished section of rhyolite No.3 from the Slavnaya ore zone (**a**), multi-layered colorful EDS maps of its fragments (p.3,4,1) (**b**–**d**), reflected light microscopy image (**e**,**g**) and BSE micrographs (**f**,**h**) of native gold (types II, III, V, AuCu) in intergrowth with quartz (Qz), albite (Ab), fuchsite (Cr-Ms), K-feldspar (Kfs), amoeba phase (X1) (**f**) (p.1b) or with quartz, albite, atheneite (Atn) and amoeba phase (X2) (**h**) (p.1a). Abbreviations of minerals: native gold (type II, III, V) (AuII, AuIII, AuV), tetra-auricupride (AuCu).

Native gold of type II in the polymineral matrix p.1b (sample No.3) (Figure 7d), consisting of albite, fuchsite, quartz, and K-feldspar, has a heterogenous texture (Figure 7f). It contains isometric inclusions (to 10 × 12 µm^2 in size) of tetra-aucupride with trace concentrations of Pd (0.9 wt.%) ($Au_{1.07}Cu_{0.91}Pd_{0.02}$) (III type) (Table 7), and microinclusions of higher-fineness (fineness 980‰, with trace contents of Cu, Ag, no Pd) or pure gold

(fineness 1000‰, without impurities) (type V) (Table 6). In most gold particles the content of Cu is 1.9–2.0 wt.% and that of Ag is 11.9–12.6 wt.%, which corresponds to fineness 860‰. In the marginal parts of these gold particles one can observe amoeboid-like rims. The chemical composition of these rims is similar to the mixture of albite with the X1 phase, containing, along with main elements Na, Al, Si, and O, impurities of Y (2.1), Zr (2.8), Ce (0.6), U (1.3), Fe (0.2), and As (0.9) (in wt.%) (Figure 7f, p.1b).

The stoichiometric formula of palladium arsenoantimonide, according to IMA data, is similar to mertieite-II, but contains 5.5 wt.% Cu (No.3, p.4a) or 5.1–5.4 wt.% Cu and 0.7–0.9 wt.% Ag (No.2, p.1a), and occasionally Au too (No.2, p.7): 2.6–2.9 Cu; 0–0.8 Ag, 1.3–2.7 Au (in wt.%). This phase has elements of faceting. The boundaries between the particles of mertieite-II and native gold of type II are straight. Fuchsite contains the following impurities (in wt.%): 1.1–1.7 Cr, 4.6–5.7 Fe, 0.2 Ti, 0.5–0.8 Mg, 0.8 Mn, and 0.3 Ba.

4.2.2. Native Gold with Ag, Cu, and Pd Impurities

Native gold containing major Ag, minor Cu, and trace Pd impurities (type III) (Table 4) was found in rhyolite samples Nos. 3 (Figure 7a, p.1, 3, 4) and 4 (Figure 8a, p.2).

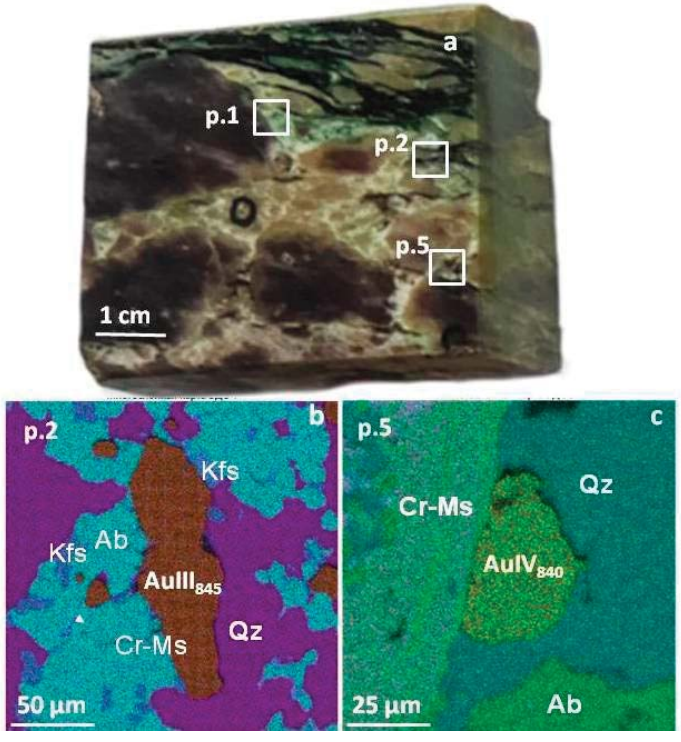

Figure 8. Macrophotograph of a polished section of rhyolite No.4 from the Slavnaya ore zone (**a**) and multi-layered colorful EDS maps of its fragments (p.2 and p.5) (**b**,**c**) with native gold (types III—**b**, IV—**c**) in poly—(**b**) and bimineral (**c**) matrices: (**b**) Quartz, albite, K- feldspar, fuchsite; (**c**) Quartz, fuchsite. Abbreviations of minerals: native gold (type III, IV) (AuIII, AuIV), fuchsite (Cr-Ms), quartz (Qz), albite (Ab), K-feldspar (Kfs).

In sample No.3 (Figure 7a), the minerals intergrown with gold particles are quartz, albite, and K-feldspar (p.3a, 4b—Figure 7b,c), (p.1c—Figure 7d–f), (p.1a—Figure 7g,h). Native gold of type III (grains of 50–70 µm in size), surrounded mainly by quartz, occasionally occurs in contact with albite and K-feldspar (sample No.3, p.1a) (Figure 7d,h), contains (in

wt.%): 12.8–13.1 Ag, 1.8–2.2 Cu, 0.7–1.0 Pd, and its fineness varies in a narrow range of 840–860‰ (Table 4).

Table 4. Representative analyses of native gold (type III) and minerals in intergrowth with it in rhyolites from Slavnaya ore zone (Nos. 3, 4—Figures 7a and 8a) (EPMA data in wt.% and formula).

N	Au	Ag	Cu	Pd	∑wt.%	N_{Au}	Formula	Minerals in Intergrowth
No.3								
p.1a	83.35	12.76	1.92	0.96	98.98	842	$Au_{0.73}Ag_{0.20}Cu_{0.06}Pd_{0.01}$	Qz; Ab; Kfs; Ath; AuCu; AuV_{950}; X2
p.1a	83.46	13.05	2.21	0.67	99.39	840	$Au_{0.72}Ag_{0.21}Cu_{0.06}Pd_{0.01}$	- " -
p.1c	82.71	7.77	6.46	1.01	97.96	844	$Au_{0.70}Ag_{0.12}Cu_{0.16}Pd_{0.02}$	Qz; Ab; Kfs; X2
p.1c	84.79	12.9	1.92	0.47	100.08	847	$Au_{0.74}Ag_{0.20}Cu_{0.05}Pd_{0.01}$	- " -
p.1c	84.63	12.56	2.05	1.03	100.28	844	$Au_{0.73}Ag_{0.20}Cu_{0.05}Pd_{0.02}$	- " -
p.1c	89.11	9.17	1.15	1.14	100.56	886	$Au_{0.80}Ag_{0.15}Cu_{0.03}Pd_{0.02}$	- " -
p.1c	84.5	12.37	2.46	0.88	100.21	843	$Au_{0.73}Ag_{0.19}Cu_{0.07}Pd_{0.01}$	- " -
p.3a	83.87	12.46	1.76	0.62	98.71	850	$Au_{0.74}Ag_{0.2}Cu_{0.05}Pd_{0.02}$	Qz; Ab; Cr-Ms; Ath; AuV_{930}
p.3a	83.93	12.73	1.61	0.57	98.84	849	$Au_{0.73}Ag_{0.21}Cu_{0.05}Pd_{0.02}$	- " -
p.3a	82.19	8.88	7.64	0.41	99.12	829	$Au_{0.67}Ag_{0.13}Cu_{0.19}Pd_{0.01}$	- " -
p.4b	82.42	8.43	7.24	1.2	99.3	830	$Au_{0.67}Ag_{0.13}Cu_{0.18}Pd_{0.02}$	Qz; Ab; Kfs
p.4b	82.6	12.81	1.9	0.98	98.29	840	$Au_{0.73}Ag_{0.21}Cu_{0.05}Pd_{0.02}$	- " -
p.4b	82.03	13.41	1.54	1.11	98.09	836	$Au_{0.73}Ag_{0.21}Cu_{0.05}Pd_{0.02}$	- " -
No.4								
p.2	83.64	12.3	2.16	1.14	99.24	843	$Au_{0.74}Ag_{0.2}Cu_{0.06}Pd_{0.02}$	Qz; Ab; Kfs; Cr-Ms
p.2	83.64	11.97	1.41	0.75	97.78	855	$Au_{0.75}Ag_{0.2}Cu_{0.04}Pd_{0.01}$	- " -
p.2	82.57	11.21	3.05	1.2	98.03	842	$Au_{0.73}Ag_{0.19}Cu_{0.06}Pd_{0.02}$	- " -
p.2	84.02	11.18	2.69	1.07	98.96	849	$Au_{0.73}Ag_{0.18}Cu_{0.07}Pd_{0.02}$	- " -

Abbreviations of minerals: native gold (type II, V) (AuII, AuV), fuchsite (Cr-Ms), quartz (Qz), albite (Ab), K-feldspar (Kfs), atheneite (Atn), tetra-aucupride (AuCu) and amoeba phase (X2).

Native gold III is heterogeneous in texture (Figure 7h) and contains microveinlets and microinclusions of higher fineness gold (950‰) (Table 6) and idiomorphic inclusions of tetra-auricupride (to 10–20 μm in size) of composition $Au_{1.06}Cu_{0.92}Pd_{0.03}$ (0.7–1.1 wt.% Pd) (Table 7). In high-fineness gold, the amount of impurities of Cu increases to 2.3–2.8 wt.% and that of Pd, to 2.2–2.4 wt.%, whereas the content of Ag decreases up to complete disappearance (<0.4 wt.%). The marginal parts of the intergrowth with native gold of type III contain atheneite (Figure 7h, p.1a). The atheneite composition $Pd_{2.62}As_{0.93}Hg_{0.29}$ differs from the ideal stoichiometric formula $Pd_2(As_{0.75}Hg_{0.25})$ in the higher contents of Pd and As. Native gold of type III is frequently surrounded by thin amoeba-shaped rims (Figure 7h, p.1a). The composition of rim substance (phase X2) was not identified. Most likely, this is a mixture of phases (quartz + X2) because, in addition to major elements Si and O, it also contains such elements as Y (3.2), Zr (2.4), Th (1.3), Ce (0.9) (in wt.%) etc.

Native gold of type III in association with quartz, albite, and K-feldspar (p.1c) (Figure 7d), (p.3a) (Figure 7b) and (p.4b) (Figure 7c) of sample No.3 is characterized by a wider range of the contents of elements (in wt.%): from 7.8 to 12.9 Ag and 1.1 to 7.6 Cu, with the same amount of Pd (0.4–1.2), which corresponds to the fineness of 830–890‰ (Table 4). The elevated concentrations of Cu (to 6.5* wt.%, Table 4) are, most likely, due to the presence of the AuCu phase. In native gold of type III we found microinclusions of higher-fineness gold (930–960‰): the content of Ag decreases down to complete disappearance, Cu is 1.2 wt.%, and Pd increases to 2.8 wt.% (Table 6).

In sample No.4 (p.2) (Figure 8a) naive gold of type III is mainly surrounded by quartz and albite and occasionally has the contact with K-feldspar and fuchsite (Figure 8b). Its fineness is 840–850‰, the contents of elements vary (in wt.%): 11.2–12.3 Ag, 1.4–3.1 Cu and 0.8–1.2 Pd (Table 4).

In native gold of type III, the amount of elements is not higher than 13.4 wt.% for Ag, 9.6 wt.% Cu and 1.2 wt.% Pd (Table 4). The elevated contents of Cu in native gold of type III can be related to the presence of Au-Cu intermetallide in the point probe.

4.2.3. Native Gold with Ag, Cu, Pd, and Hg Impurities

Native gold of type IV with four elements Ag, Cu, Pd, and Hg was found in rhyolite sample No.4 (p.1, 5) (Figure 8a,c and Figure 9a). Gold particles are in intergrowth with quartz, albite, and K-feldspar (Figure 9b, p.1) or quartz and fuchsite (Figure 8c). Figure 9a,f show discernible lattice decay structures with tetra-auricupride. The contents of the following elements in this native gold are (in wt.%): 11.9–12.5 Ag, 1.7–2.5 Cu, 0.6–0.8 Pd, and 0.7–1 Hg (Table 5). Its fineness varies in the range of 840–870‰. Variations in copper concentrations are likely due to the presence of platelets of AuCu phase. In native gold of type IV there are inclusions of U-mertieite-II (Figure 9e) and microinclusions of high-fineness gold (type V) (Figure 9a).

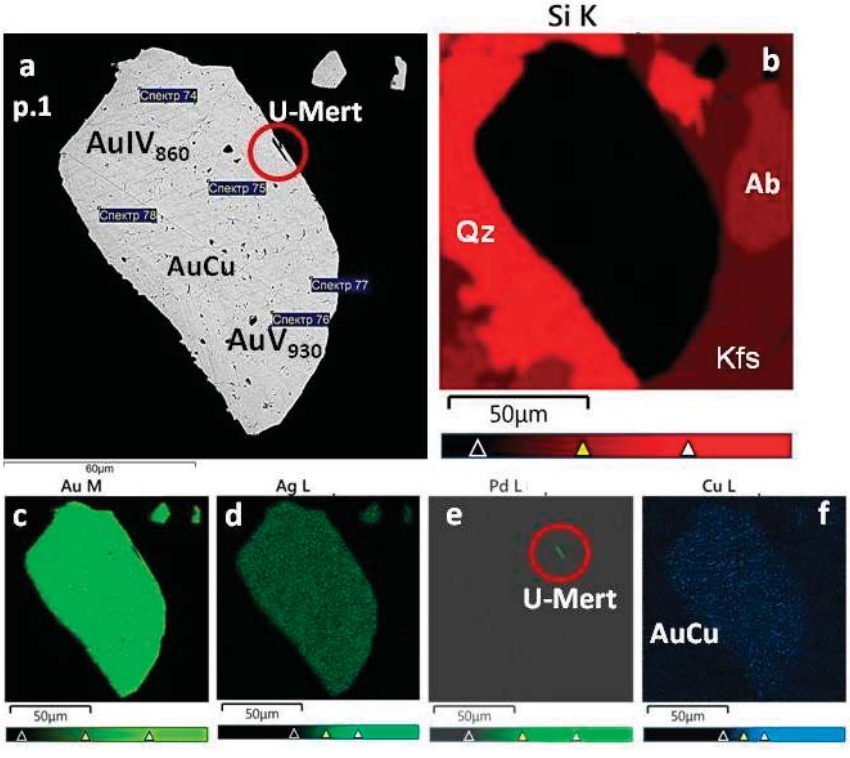

Figure 9. Native gold of type IV with decay structures (matrix—fineness 860‰, AuCu platelets) and inclusions of higher-fineness gold (type V) and mertieite (with U impurity) in the quartz-albite-K-feldspar vein of rhyolite (No.4, p. 1) (Figure 8a): (**a**) BSE micrograph; (**b**–**f**) maps of areal distribution elements (Si, Au, Ag, Pd, Cu) in characteristic rays. Abbreviations of minerals: native gold of type IV and V (AuIV, AuV), quartz (Qz), albite (Ab), K-feldspar (Kfs), U-mertieite (U-Mert), tetra-auricupride (AuCu).

Table 5. Representative analyses of native gold (type IV) and minerals in intergrowth with it in rhyolite from the Slavnaya ore zone (No.4; Figure 8a) (EPMA data in wt.% and formula).

N	Au	Ag	Cu	Pd	Hg	∑wt.%	N_{Au}	Formula	Minerals in Intergrowth
p.1	81.41	11.92	2.32	0.70	0.79	97.43	866	$Au_{0.72}Ag_{0.19}Cu_{0.07}Pd_{0.01}Hg_{0.01}$	Qz; Ab; Kfs; AuCu; AuV_{930}; U-Mert
p.1	82.42	12.02	2.46	0.82	0.96	98.9	865	$Au_{0.72}Ag_{0.19}Cu_{0.07}Pd_{0.01}Hg_{0.01}$	- " -
p.5	81.77	12.2	1.69	0.55	0.76	96.97	843	$Au_{0.74}Ag_{0.2}Cu_{0.04}Pd_{0.01}Hg_{0.01}$	Qz; Cr-Ms; AuCu
p.5	82.23	12.41	1.8	0.52	0.65	97.61	842	$Au_{0.73}Ag_{0.2}Cu_{0.05}Pd_{0.01}Hg_{0.01}$	- " -
p.5	83.03	12.5	1.89	0.72	0.86	99.00	839	$Au_{0.73}Ag_{0.2}Cu_{0.05}Pd_{0.01}Hg_{0.01}$	- " -

Abbreviations of minerals: fuchsite (Cr-Ms), quartz (Qz), albite (Ab), K-feldspar (Kfs), tetra-auricupride (AuCu), U-mertieite (U-Mert).

4.2.4. Native Gold of Fineness 930–1000‰

High-fineness gold (930–1000‰) (type V) is present in all studied rhyolite samples in the form of microveinlets and microinclusions in native gold of types II–IV (see Section 4.2.1, Section 4.2.2 and Section 4.2.3) (Tables 2–4). It contains 5.6 wt.% Ag and 2.8 wt.% Cu and Pd (Table 6). High-fineness gold with one or two of these impurity elements or pure gold without any impurity also occur (Figure 6g,j, Figure 7f,h and Figure 9a). It is worth noting that Hg is absent in native gold of type V.

Table 6. Representative analyses of high-fineness gold 930–1000‰ (type V) and minerals in intergrowth with it in rhyolites from the Slavnaya ore zone (Nos. 2–4, Figures 6a, 7a and 9a) (EPMA data in wt.% and formula).

N	Au	Ag	Cu	Pd	∑wt.%	N_{Au}	Formula	Minerals in Intergrowth
					No.2			
p.6	93.41	1.23	0.93	1.12	96.7	966	$Au_{0.93}Ag_{0.02}Cu_{0.03}Pd_{0.02}$	$AuII_{860}$
p.6	89.02	2.14	1.76	1.28	94.2	945	$Au_{0.88}Ag_{0.04}Cu_{0.05}Pd_{0.02}$	- " -
p.6	87.08	2.18	2.27	1.95	93.49	932	$Au_{0.86}Ag_{0.04}Cu_{0.07}Pd_{0}$	- " -
p.7	99.15	0.46	0	0.94	100.55	986	$Au_{0.97}Ag_{0.01}Pd_{0.02}$	- " -
					No.3			
p.1a	94	0.43	2.34	2.42	99.19	948	$Au_{0.88}Ag_{0.01}Cu_{0.07}Pd_{0.04}$	$AuIII_{840}$
p.1a	95.85	0	2.78	2.24	100.87	950	$Au_{0.88}Cu_{0.08}Pd_{0.04}$	- " -
p.1b	97.03	0	1.85	1.08	99.97	971	$Au_{0.93}Cu_{0.05}Pd_{0.02}$	$AuII_{860}$
p.1b	97.88	0	0	0	97.88	1000	$Au_{1.0}$	- " -
p.1b	99.04	1.65	0.23	0	100.91	981	$Au_{0.96}Ag_{0.03}Cu_{0.01}$	- " -
p.3a	93.49	5.64	0.55	1.04	100.72	928	$Au_{0.86}Ag_{0.1}Cu_{0.02}Pd_{0.02}$	$AuIII_{860}$
p.4b	97.02	0	1.16	2.78	100.96	961	$Au_{0.92}Cu_{0.05}Pd_{0.03}$	AuII840
					No.4			
p.1	97.68	0	1.66	1.33	100.17	930	$Au_{0.95}Cu_{0.03}Pd_{0.02}$	AuIV860

Abbreviations of minerals: native gold (type II, III, IV) (AuII, AuIII, AuIV).

The specific features of high-fineness gold are its high porosity, which resulted in the reduced total contents of components during the analysis (Table 6), and recrystallization. These features were observed in sample No.2 (p.6) (Figure 6j), in which we detected porous gold of type V with the highest content of Pd (2.8 wt.%) and lower concentrations of Ag and Cu than in the matrix of native gold of types II–IV, which suggests the removal of Ag and Cu and supply of Pd (Table 6). High-fineness gold (930–1000‰) (type V) in the marginal parts of Ag,Cu-bearing gold (type II) (Figure 6j) comes into contact with albite and fuchsite.

4.2.5. Au-Cu Intermetallides

Au-Cu phases were detected in the form of individual microinclusions of idiomorphic shape and thin platelets in lattice decay structures of solid solutions in some large particles of native gold (types II–IV) in rhyolite samples No.2–4. The compositions of Au-Cu intermetallides and matrix for two samples Nos.2, 3 are given in Table 7. These data show that Au-Cu intermetallides are similar to AuCu phase with minor amounts of Pd or Ag.

The AuCu phase intergrown with native gold of type II and an exsolution texture is absent (Figure 7e–h) in sample No.3 (Section 4.2.2). The size of inclusions is no more than 12 μm. The content of Pd is 0.6–1.1 wt.%, which corresponds to the formula $Au_{1.06–1.1}Cu_{0.92–0.88}Pd_{0.02}$.

The AuCu phase in the form of thin platelets (1–2 × 10–20 μm) in lattice decay structures is typical of native gold III in sample No.2 (Figure 6a, p.2) (Section 4.2.3) and native gold IV in sample No.4a (Figure 9a,f). The content of Pd in the thin platelets in sample No.2 (p.2) does not exceed 0.36 wt.% (Table 3), that of Ag varies in a narrow range of 0.3–0.8 wt.%, and the amount of Au is higher than the ideal composition of AuCu ($Au_{1.04–1.06}Cu_{0.92–0.94}Pd_{0.02–0.01}Ag_{0–0.01}$).

Table 7. Representative analyses of AuCu phases and mineral matrix (EPMA data in wt.% and formula).

N	Au	Ag	Cu	Pd	∑wt.%	N_{Au}	Formula	Minerals in Intergrowth
				No.3				
p.1a	76.58	0	21.26	0.75	98.59	777	$Au_{1.06}Cu_{0.92}Pd_{0.02}$	$AuIII_{840}$
p.1a	76.35	0	21.4	1.1	98.85	772	$Au_{1.06}Cu_{0.92}Pd_{0.02}$	- " -
p.1b	76.96	0	21.28	0.63	98.87	778	$Au_{1.07}Cu_{0.91}Pd_{0.02}$	$AuIII_{860}$
p.1b	77.04	0	21.29	0.73	99.06	778	$Au_{1.07}Cu_{0.91}Pd_{0.02}$	- " -
p.1b	77.01	0	19.80	0.62	97.43	790	$Au_{1.1}Cu_{0.88}Pd_{0.02}$	-" -
				No.2				
p.2	77.20	0.29	22.37	0.36	100.23	770	$Au_{1.04}Cu_{0.94}Pd_{0.01}Ag_{0.01}$	$AuII_{830–860}$
p.2	77.12	0.84	21.52	0	99.48	775	$Au_{1.06}Cu_{0.92}Ag_{0.02}$	- " -

Abbreviations: native gold of types II and III (AuII, AuIII).

We failed to determine the composition of the Au-Cu phases in native gold of type IV in sample No.4a (Figure 9a,f) owing to poor visualization on the optical and scanning microscopes and small thickness of the plates (<1 μm).

4.3. Reconnaissance of Fluid Inclusions

A limited number of fluid inclusions were studied in albite and quartz in rhyolites from the Slavnaya and Ludnaya ore zones (Figure 10). While the data are too few data to draw firm conclusions, they are sufficient to allow us to hypothesize about the nature of the hydrothermal system. In rhyolite samples from the Slavnaya zone, albite and quartz are associated with native gold of types II–IV, which suggests their synchronous crystallization (Figures 6c,e and 7a–e). In rhyolite samples from the Ludnaya zone, albite and quartz do not contain gold particles, but are intergrown with fuchsite in which native gold of type I is localized (Figures 3 and 4).

Fluid inclusions are classified as primary inclusions when they occur along growth zones (Figure 10a,b) or are isolated (Figure 10c,d). Secondary inclusions in quartz form trails in cracks. The size of fluid inclusions is no more than 10–15 μm.

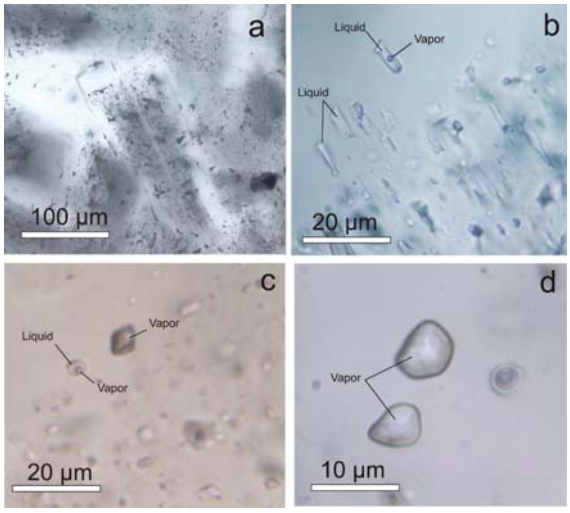

Figure 10. Albite crystals saturated with primary fluid inclusions (**a**); primary vapor-liquid two-phase and liquid single-phase fluid inclusions tracing the growth zone in albite (**b**) (**a**,**b**)—Slavnaya ore zone); primary two-phase and vapor inclusions in quartz (**c**); primary vapor inclusions in quartz (**d**) (**c**,**d**)—Ludnaya ore zone).

4.3.1. The Ludnaya Ore Zone

Only 9 primary fluid inclusions were analyzed from the Ludnaya ore zone. In albite and quartz, two-phase inclusions are homogenized in the temperature range of 186 to 139 °C (Table 8). Melting of eutectic takes place at −39 °C. The temperature is close to the eutectic temperature of the $MgCl_2$-KCl-H_2O system (−37.8 °C). Complete melting of ice in frozen inclusions in albite takes place at −0.3 to 0.1 °C. The salinity of solutions varies from 2.1 to 0.2 wt.% NaCl eq.

Table 8. Results of primary two-phase fluid inclusion study by cryo- and thermometry.

Sample	Mineral	Th °C	Teu °C	Tice °C	Salinity (wt.% NaCl eq.)
Rhyolite from Ludnaya ore zone					
3p-1154–2 (4)	albite	155–139	−39	−0.3 to −0.1	0.5–0.2
3p-1154–2 (5)	quartz	186–178	−39	−1.2 to −0.7	2.1–1.2
Rhyolite from Slavnaya ore zone					
3p-1122-1 (10) *	albite	130–113	−39 to −38	−15 to −7.5	18.6–11
3p-1122-1 (5)	quartz	165–105	−55	−10 to −7.5	13.9–11
3p-1122-13 (4)	albite	133–125	−49	−17 to −13	20.2–16.9

Note: * —number of fluid inclusions; Th—homogenization temperature, Teu—melting of eutectic and Tice—melting of ice.

4.3.2. The Slavnaya Ore Zone

Only 19 primary fluid inclusions were analyzed from the Slavnaya ore zone. In quartz and albite, two-phase fluid inclusions are homogenized in the temperature range from 165 to 105 °C. In these inclusions, melting of eutectic is observed at −49 °C, which is similar to the melting temperatures of eutectic of the $CaCl_2$-KCl-H_2O (−50.5 °C) and $CaCl_2$-H_2O (−49.8 °C) systems. Ice melts at temperatures from −15 to −7.5 °C. The salinity of solutions of fluid inclusions varies from 20.2 to 11 wt.% NaCl eq. (Table 8).

5. Discussion

The mechanism of formation of native gold of varying chemical composition is very complicated and depends on many factors [22–28]. The content of elements in native gold is determined by their concentrations in hydrothermal solutions, which are governed by temperature, redox conditions, pH, presence of ligand elements Cl, S, and elements such as Se, Te, As, Sb. A wide spectrum of impurity elements in native gold is related to different geochemical conditions in which mobilization, transportation, and deposition of gold-ore mineralization took place. Nowadays, several hypotheses on the role and ratios of magmatic, metamorphic, and hydrothermal processes during the formation of Au-Pd mineralization are discussed. Fluids are considered to play an important role in the genesis of mafic-ultramafic complexes with mineralization of noble metals [29–36]. The efficiency of mobilization, transportation, and deposition of noble metals with participation of fluids at the magmatic and post-magmatic stages of evolution of the ore-forming process is shown in the experiments [37]. The precipitation of these metals from hydrothermal solutions is the main process of concentrating of metals and they can form their own mineral phases or occur as an isomorphic impurity in other minerals. The fineness and set of impurity elements in native gold, and associated minerals are the indicators of different genetic origin [28,38–43].

Pd-bearing native gold occurs both in magmatic sulfide ores and in low-sulfide post-magmatic metasomatites [44,45]. Large occurrences of low-sulfide, essentially Au-Pd mineralization in different types of mafic-ultramafic complexes are known in the Norilsk district (Talnakhskoye, Norilsk-1 and 2, Chernogorskoe, Vologochanskoe), in the Skaergaard formation, in John Melville reef of the Stillwater complex and some others [46]. The elevated Cu content in native gold indicates the probable genetic relation of gold mineralization with mafic-ultramafic complexes or with the deposits of copper type (copper-skarn, copper-pyrite and porphyry copper) [47–50].

5.1. Compositions of Native Gold and Minerals in Intergrowth

The study reveals differences in the set and quantity of impurity elements in the composition of native gold, intergrown minerals, and PTX parameters of the deposition of Au-Pd mineralization in two ore zones of the Chudnoe deposit. The obtained results (Figure 11a) together with the earlier published data (Figure 11b) allowed us to distinguish five types of native gold. Both the data from previous works [2,3,5] and our results (Table 2) show that native gold (type I) from the Ludnaya ore zone contains only Ag. The fineness of native gold varies within the range of 510 to 790‰. Native gold in this ore zone occurs in the form of impregnated particles commonly intergrown with arsenoantimonide in a fuchsite or allanite matrix (Figures 2–5). Palladium arsenoantimonide intergrown with native gold (type I) is represented by U- or Cu-mertieite-II. In this type of native gold, we did not detect Pd, Cu, and Hg impurities even under long-term accumulation of spectra (see Section 3).

In rhyolites of the Slavnaya ore zone, native gold is heterogeneous, has a higher fineness, different sets and amounts of impurities: II type—Au-Ag-Cu solid solution (840–860‰); III—Au-Ag-Cu-Pd (830–890‰), IV—Au-Ag-Pd-Cu-Hg (840–870‰), as well as a specific mineral composition of the surrounding matrix-fuchsite or allanite, albite, and mertieite-II (II); albite, quartz, and atheneite (III); quartz, albite, K-feldspar, and mertieite-II (IV) (Tables 3–5, Figures 3–9). It is worth noting that native gold of II and IV types shows some similarity with native gold of type I, as it occurs in paragenesis with fuchsite or allanite (II type) and mertieite-II (types II and IV).

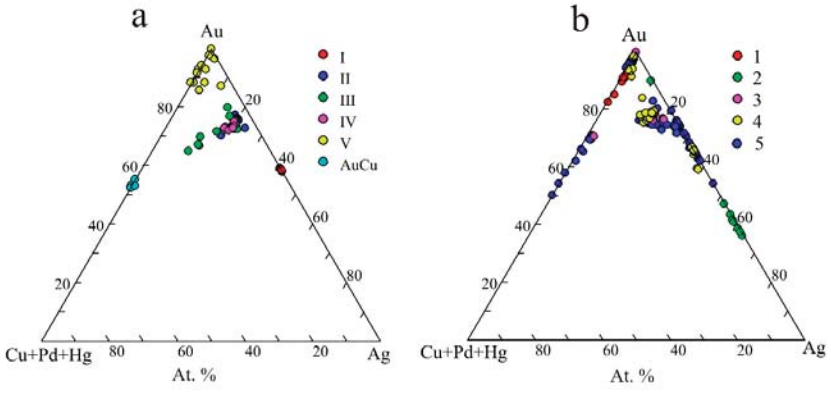

Figure 11. Chemical composition of various types of native gold from the Chudnoe deposit on the ternary diagram Au-Ag-Cu(+ Pd + Hg) from the results of present study (**a**) and data of other authors (**b**): 1—[1]; 2—[2]; 3—[5]; 4—[3]; 5 [7,14–16].

In this study we revealed lattice decay structures with tetra-auricupride AuCu for native gold of types III (Ag,Cu,Pd) and IV (Ag,Cu,Pd,Hg). AuCu intermetallide is present in native gold of type II but in the form of isometric microinclusions. Intermetallides of AuCu, Au_3Cu, Au_3Cu_2, Au_2Cu, $AuCu_3$ composition were reported by other authors [5,8,16,50,51].

The phase diagram Au-Cu [52] shows that the presence of lattice decay structures with thin platelets of tetra-aucupride AuCu in native gold indicates temperatures 410 °C. Au-Cu intermetallides of composition Au_3Cu and $AuCu_3$ are formed at temperatures below 390 and 240 °C. The formation of decay structures in the initially homogeneous solid solution results from the decrease in the miscibility of components and their redistribution with decreasing in temperature. Such structures were also found at other objects: Zolotaya Gora, Melent'evskoe deposits (Southern Urals, Russia) [53,54], Agardag ultramafic massif (S. Tuva, Russia) [44], the 15 Mile deposit (the Dease Lake district, British Columbia) [55], Au-Pd ores of the Skaergaard massif (Greenland) [45].

5.2. Inferences on the PTX Parameters of Au-Pd-REE Mineralization

Data on the PTX parameters of formation of Au-Pd-REE mineralization at the Chudnoe deposit were for the first time obtained by Surenkov et al. [12,56]. They used thermocryometry to analyze 110 vapor-liquid inclusions of which the vapor-liquid inclusions in albite and pre-ore quartz were attributed to primary inclusions. In early veined quartz, homogenization temperature ranged from 230 to 400 °C, and salt concentrations, from 2.1 to 17 wt.% NaCl eq. For late generations of quartz, albite and calcite, which reflect the conditions for the formation of Au-Pd mineralization, temperature ranged from 100 to 180 °C and the concentrations of salts, from 2.5 to 23 wt.% NaCl eq. Surenkov [12] suggests that at the early stage, the Chudnoe deposit was formed with participation of metamorphic fluids and the formation of Au-Pd mineralization took place at lower temperatures with participation of meteoric, marine, or buried waters.

Our limited study of fluid inclusions are generally consistent with the data of Surenkov et al. [12,56]. Ore-forming fluids of Ludnaya and Slavnaya ore zones range salinity from 2.1 to 0.2 and from 20.2 to 11 wt.% NaCl eq., respectively. It is known, however, that mineral parageneses with quartz, albite and sericite (fuchsite) in gold deposits are formed at the temperatures higher than 200–230 °C [57]. At lower temperatures, argillisites form, in which sericite is commonly replaced by mixed-layer minerals of clay series. These data allow us to estimate the possible pressure of ore formation by comparing the formation temperature of the quartz-albite-sericite (fuchsite) mineral association in gold deposits with isochores of fluid inclusions solutions.

Gold mineralization at the Ludnaya ore zone was formed synchronously with the quartz-albite-fuchsite association. Thus, the trapping pressure of fluid inclusions could vary from 23 to 114 MPa at temperatures from 200 to 230 °C (Figure 12) in this zone. Gold mineralization at the Slavnaya ore zone was formed later than the quartz-albite-fuchsite association at 105–165 °C, the trapping pressure of fluid inclusions could vary from 5 to 115 MPa (Figure 12).

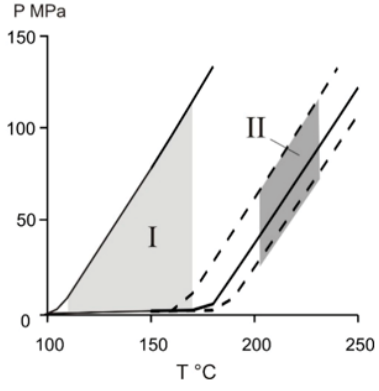

Figure 12. Isochores of fluids from the Slavnaya zone (solid line) and fluids from the Ludnaya zone (dashed line). Isochores were constructed using the "AqSo-NaCl: computer program" for extreme temperatures and homogenization concentrations [21]. The probable trapping PT conditions of fluid inclusions are highlighted in light gray for the Slavnaya zone (I) and in dark gray for Ludnaya zone (II).

Thus, it can be assumed that the PT parameters of formation of Au-Pd mineralization associated with fuchsite, especially in early rhyolites from the Slavnaya zone, are suggested to be higher than those estimated in the fluid inclusion study. The fluids forming Au-Pd mineralization at the Chudnoe deposit are similar in salt composition to the ore-forming fluids of hydrothermal Au-Ag deposits, though the latter are characterized by higher formation temperatures, higher salinity of fluids and frequent presence of dense gases (CO_2, N_2, CH_4) in the composition of fluids [58]. They are similar in temperature, concentration, and composition of salts (Ca-Na-K chlorides, carbonates, and hydrocarbonates) to the ore-forming fluids of Au-Pd deposits (Serra Pelada, Bleida Far West), for which an infiltration model of formation with participation of oxidized basin Na-Ca chloride waters is assumed [59–61]. However, these deposits are characterized by the presence of Se-bearing PGM (Pd–Pt–Se, Pd–Se, Pd–Hg–Se, and Pd–Bi–Se phases, and sudovikovite and palladseite) [62].

Seven metals (Ag, Cu, Pd, Hg, Sn, Tl, Fe), three chalcogenes (Te, S, Se) and three metalloids (As, Sb, Bi) can be indicators of the presence of gold minerals in ores [63]. Four of these metals—Ag, Cu, Pd, and Hg—were detected in the composition of native gold from the Slavnaya ore zone (Chudnoe deposit). Cu also formed intermetallides with Au. As, Sb, and Hg, found in elevated concentrations in the Chudnoe ores, under specific conditions of ore formation were deposited as Pd minerals with these elements—arsenides (atheneite), arsenoantimonides (mertieite-I, mertieite-II, isomertieite), antimonides (stibiopalladinite) [1–3,8].

Zaccarini et al. [64] think that the Pd content in native gold is determined by the evolution of S, Te, As, Sb, Bi, Se concentrations in a fluid, which bind palladium into its own minerals. Many authors [4,64,65] suppose that with a decrease in temperature and change in redox conditions to more oxidizing, the concentrations of sulfide sulfur decrease and those of the palladium binding elements increase. Yanakieva and Spiridonov [36,66] reported that Ag-Au-Pd minerals are typical of telethermal gold deposits formed at low

$f\ S_2$ and elevated $f\ O_2$. They are regarded as the result of deposition of ore components from chloride hydrotherms that have a high oxidation potential. As selenides, tellurides, and bismuthides are not typical of the Chudnoe deposit, the composition of native gold is likely determined by the evolution of Au, Ag, Cu, Pd, Hg, As, Sb concentrations in a fluid, which bind palladium into its own minerals—sulfoantimonides, atheneite, etc.

The data of Borisov from [5] show that the formation of Au-Pd-REE mineralization of ore occurrences is the latest hydrothermal event related to the regressive stage of the Late Hercynian metamorphism. The formation of Au-Pd-REE mineralization of the Chudnoe deposit resulted from the oxidation of ascending reduced metamorphic solutions, which was also accompanied by an increase in their acidity. The part of the oxidation geochemical parameter was played by hematite-rich rocks in the zone of regional unconformity. The conditions of ore deposition at the Chudnoe deposit, according to this author, correspond to $\log f\ O_2 \sim -47$, pH ~ 4.5 at 150 °C. Changes in the set of minerals and their composition are due to the vertical variability of redox conditions and acidity of solutions, which in turn are a result of the different localizations of objects relative to the regional unconformity.

5.3. Genesis of Au-Pd Mineralization, Sources of Ore Components

The genesis of the Chudnoe deposit is still debatable. There are several viewpoints on the origin of complex mineralization of this uncommon type. Tarbaev and coauthors [1] adhered to the hydrothermal genesis of Au-Pd-REE ores at the Chudnoe deposit, while Cr, Pd, Au, and Cu were mobilized from presumably deep-seated mafic and ultramafic rocks, probably, andesite-basalts from the lower series of the Upper Riphean Sablegorskaya formation, and K and lanthanides, from the host porphyry rhyolites. Some researchers of the Chudnoe deposit [5,12,13] suggest a metamorphic-hydrothermal model of formation: ascending metamorphic hydrothermal solutions mobilized metals from underlying rocks and the main factors of ore formation are oxidation and increase in the acidity of ore-bearing solutions. Originally, metamorphic solutions were reduced (field of stability of pyrite and magnetite), weakly-acidic—near-neutral (acidity was controlled by the quartz-K-feldspar-muscovite association). At the later stages of the process, during the formation of Au-Pd mineralization, considerable amounts of meteoric and buried waters participated in the hydrothermal system [12].

On the basis of the results of isotopic and mineralogical study, Galankina [2] shows that Au-Pd-REE mineralization of the Chudnoe deposit should be regarded as hydrothermal, originated in the Riphean after the formation of Sablegor and Maldin rhyolites, occurring in the zone of the deep Maldinskiy fault and represented by pre-ore metasomatites which are the most similar to the berezite-listvenite formation and ore-accompanying near-crack quartz-albite metasomatites and listvenite-like rocks. There are reasons to assume that Cr and Pd mineralization of the Chudnoe deposit is related to the fact that hydrothermal processing of riftogenic complexes localized in the Maldinskiy fault involved ultramafic rocks that are not exposed on the surface. Such complexes of the Riphean age widely occur within the Central-Ural uplift, e.g., Saranovskii massif. Magnetic survey data show the occurrence of a positive magnetic anomaly at the depth, which suggests that the intrusion chamber could be the source of the ore-forming fluid [67].

Co-occurrence of native gold and fuchsite was observed at many gold deposits [68–70]. The associations of fuchsite with native gold can be found in altered ultramafic rocks at Kalgoorlie (Australia), the Kerr-Addison and Dome mines, in the Virginiatown and Porcupine mining districts of northeast Ontario, Canada; the Mother Lode district in California, USA; in the Transvaal district of South Africa (including, confusingly, the Murchison Range); British Columbia and the Yukon, Quebec and Newfoundland; Ireland; Morocco; Egypt; and Saudi Arabia [68]. However, these deposits are characterized by a listvenite or QAM (quartz-ankerite-mariposite) type of hydrothermal alteration formed by the mafic-ultramafic host rocks.

Native gold in listvenites is also typical of many Ural objects [71]. Mechnikovskoe, Altyn-Tash, and Ganeevskoe belong to the listvenite-related gold deposits, which occur

in the large Main Uralian fault zone and some smaller faults within the Magnitogorsk zone (South Urals). Listvenites are developed after serpentinites and composed of quartz, fuchsite (or mariposite), and carbonates (magnesite, dolomite) ± albite. Volcanic and volcanoclastic rocks are altered to beresites, consisting of sericite, carbonates (dolomite, ankerite), quartz, and albite. The process of alteration occurs under the influence of CO_2- and S-rich fluids [72–74]. At the Chudnoe deposit under study, native gold is associated with fuchsite, but in the absence of carbonates and sulfides, which makes it different from other objects with listvenite or QAM (quartz-ankerite-mariposite) type of hydrothermal alteration and suggests the participation of CO_2-free or low-CO_2 fluid.

The formation of native gold I (only with Ag impurity) in rhyolites of the Ludnaya ore zone is, most likely related to the processes of fuchsitization and allanitization of rhyolites with the supply of Cr and REE. The formation of native gold with Ag, Cu, Pd, and Hg impurities (types II–IV), supposedly, took place during the following metasomatic processes: silicification, albitization, and feldspathization in rhyolites. The intersections of quartz-albite metasomatites with fuchsite veinlets support such an assumption. The porous texture of high-fineness gold (type V) is explained by the removal of Cu and Ag. The association of native gold with palladium minerals and presence of Cu and Pd in it, Cr in fuchsite indicate the relationship between ore formation and mafic-ultramafic magmatism.

Author Contributions: Conceptualization, methodology, G.P. and V.M.; investigation, G.P., N.K., and A.B.; writing and editing, G.P., V.M., N.K. and A.B.; visualization G.P., V.M., S.K. and A.B.; supervision G.P. All authors have read and agreed to the published version of the manuscript.

Funding: This research was funded with financial support from the Russian Foundation of Basic Research (project No 20-05-00393) and by within the framework of the state assignment of Sobolev Institute of Geology and Mineralogy, Zavaritsky Institute of Geology and Geochemistry (AAAA-A18-118052590028-9), Institute of Geology, Komi Science Center (Russian Academy of Sciences).

Acknowledgments: We are very grateful to the Reviewers and Academic Editors for their helpful comments that improved our manuscript.

Conflicts of Interest: The authors declare no conflict of interest.

References

1. Tarbaev, M.B.; Kuznetsov, S.K.; Moralev, G.V.; Soboleva, A.A.; Laputina, I.P. New gold-palladium type of mineralization in the Kozhim Region of Circumpolar Ural (Russia). *Geol. Ore Depos.* **1996**, *38*, 11–25.
2. Galankina, O.L.; Gavrilenko, V.V.; Gaydamako, I.M. New data on mineralogy of hydrothermal gold-platinoid mineralization of the Subpolar Urals. *Zapiski RMO* **1998**, *3*, 72–78. (In Russian with English abstract)
3. Shumilov, I.K.; Ostashchenko, B.A. *Mineralogical and Technological Peculiarities of Au-Pd-TR Metallization in the Subpolar Urals*; Geoprint: Syktyvkar, Russia, 2000; p. 104.
4. Anikina, E.V.; Alekseev, A.V. Mineral-geochemical characteristic of gold-palladium mineralization in the Volkov gabbro massif (Platiniferous Urals Belt). *Litosfera* **2010**, *5*, 75–100. (In Russian with English abstract)
5. Borisov, A.V. Geological and Genetic Features of Au-Pd-REE Ore Occurrences in the Maldy-Nyrd Ridge (Subpolar Urals). Ph.D. Thesis, IGEM RAS, Moscow, Russia, 2005; p. 27. (In Russian)
6. Nikulova, N.Y.; Filippov, V.N. Native palladium in gold from conglomerates of the Telpos (O1TP) Formation Muldynyrd Ridge, Subpolar Urals. *J. Proc. Komi Sci. Centre Ural Branch RAS* **2009**, *138*, 69. (In Russian with English abstract)
7. Onishchenko, S.A.; Kuznetsov, S.K. Palladium-gold sulfide mineralization in andesites at the Chudnoe deposit (Subpolar Urals). *J. Proc. Komi Sci. Centre Ural Branch RAS* **2019**, *294*, 20–27. (In Russian with English abstract)
8. Kuznetsov, S.K.; Mayorova, T.P.; Shaibekov, R.I.; Sokerina, N.V.; Filippov, V.N. Mineral composition and conditions of formation of gold-platinum-palladium occurrences in the north of the Urals and Pai-Khoi. *Geol. Miner. Resour.* **2014**, *3*, 81–85. (In Russian with English abstract)
9. Pystin, A.M.; Potapov, I.L.; Pystina, Y.I.; Generalov, V.I.; Onishchenko, S.A.; Filippov, V.N.; Shloma, A.A.; Tereshko, V.V. *Low-Sulfide Platinum-Metal Mineralization in the Polar Urals*; Pystin, A.M., Ed.; Institute of Economics Ural Branch of RAS: Yekaterinburg, Russia, 2011; p. 150. (In Russian with English abstract)
10. Ozerov, V.S. Metamorfogennye rossypi zolota Pripolyarnogo Urala (Metamorphogenic gold placers in the Subpolar Urals). *Ores Metals* **1996**, *4*, 28–37. (In Russian)
11. Galankina, O.L. Peculiarities of Mineralogy of Palladium-Gold Occurrences of the Subpolar Urals. Ph.D. Thesis, St. PMU, Saint Petersburg, Russia, 2001; p. 156. (In Russian)

12. Surenkov, S.V. Formation Conditions and Sources of Ore Matter Au-PGE-REE of Ore Occurrences in Alkesvozhskaya Area (Subpolar Urals). Ph.D. Thesis, IGEM RAS, Moscow, Russia, 2003; p. 23. (In Russian)
13. Moralev, G.V.; Borisov, A.V.; Surenkov, S.V.; Tarbaev, M.B.; Ponomarchuk, V.A. First 39Ar-40Ar datings on micas from the Chudnoe Au-Pd-REE occurrence, Near-Polar Urals. *Dokl. Earth Sci.* **2005**, *400*, 109–112.
14. Kuznetsov, S.K.; Onishchenko, S.A. Gold content of local areas of metasomatic alteration of rhyolites of the Chudnoe deposit (Subpolar Urals). *J. Proc. Komi Sci. Centre Ural Branch RAS* **2018**, *288*, 39–45. (In Russian with English abstract)
15. Kuznetsov, S.; Mayorova, T.; Sokerina, N.; Glukhov, Y. Gold-bearing areas of the western slope of Northern Urals and Timan. *J. Proc. Komi Sci. Centre Ural Branch RAS* **2018**, *4*, 81–94. [CrossRef]
16. Onishchenko, S.A.; Kuznetsov, S.K.; Tropnikov, E.M. Epigenetic alteration of cupreous gold in the Au-Ag-Cu-Pd exsolution texture. *Dokl. Earth Sci.* **2020**, *492*, 418–421. [CrossRef]
17. Lafuente, B.; Downs, R.T.; Yang, H.; Stone, N. The power of databases: The RRUFF project. In *Highlights in Mineralogical Crystallography*; Armbruster, T., Danisi, R.M., Eds.; De Gruyter: Berlin, Germany, 2015; pp. 1–30.
18. Chernova, A.E.; Moralev, G.V.; Tarbaev, M.B.; Kuznetsov, S.K.; Wolfson, A.A. Distribution and forms of occurrence of mercury in the Au-Pd-REE ore occurrence Chudnoye, Kozhimsky region, Subpolar Urals. In *The Main Problems of Teaching About Magmatoid Ore Deposits*; IGEM RAS: Moscow, Russia, 1997; pp. 172–173. (In Russian)
19. Borisenko, A.S. Cryometric analysis of salt composition of solutions of gas-liquid inclusions in minerals. In *Application of Therobarogeochemical Methods in Prospecting and Study of Ore Deposits*; Nedra: Moscow, Russia, 1982; pp. 37–47. (In Russian)
20. Bodnar, R.J.; Vityk, M.O. Interpretation of microthermometric data for NaCl-H_2O fluid inclusions, Fluid Inclusions in Minerals. In *Methods and Applications*; De Vivo, B., Frezzotti, M.L., Eds.; Virginia Polytechnic Institute State University: Blacksburg, VA, USA, 1994; pp. 117–131.
21. Bakker, R.J. AqSo NaCl: Computer program to calculate p-T-V-x properties in the H_2O-NaCl fluid system applied to fluid inclusion research and pore fluid calculation. *Comput. Geosci.* **2018**, *115*, 122–133. [CrossRef]
22. Fisher, N.H. The fineness of gold, with special reference to the Morobe gold field, New Guinea. *Econ. Geol.* **1945**, *40*, 449–495. [CrossRef]
23. Morrison, G.W.; Rose, W.J.; Jaireth, S. Geological and geochemical controls on the silver content (fineness) of gold in gold-silver deposits. *Ore Geol. Rev.* **1991**, *6*, 333–364. [CrossRef]
24. Gammons, C.H.; Williams-Jones, A.E. Hydrothermal geochemistry of electrum; thermodynamic constraints. *Econ. Geol.* **1995**, *90*, 420–432. [CrossRef]
25. Pal'yanova, G. Physicochemical modeling of the coupled behavior of gold and silver in hydrothermal processes: Gold fineness, Au/Ag ratios and their possible implications. *Chem. Geol.* **2008**, *255*, 399–413. [CrossRef]
26. Liang, Y.; Hoshino, K. Thermodynamic calculations of Au_xAg_{1-x}-Fluid equilibria and their applications for ore-forming conditions. *Appl. Geochem.* **2015**, *52*, 109–117. [CrossRef]
27. Palyanova, G.; Zinina, V.; Kokh, K.; Seryotkin, Y.; Zhuravkova, T.; Mikhlin, Y. New gold chalcogenides in the Au-Te-Se-S System. *J. Phys. Chem. Solids* **2020**, *138*, 109276. [CrossRef]
28. Chapman, R.J.; Banks, D.A.; Styles, M.T.; Walshaw, R.D.; Piazolo, S.; Morgan, D.J.; Grimshaw, M.R.; Spence-Jones, C.P.; Matthews, T.J.; Borovinskaya, O. Chemical and physical heterogeneity within native gold: Implications for the design of gold particle studies. *Miner. Deposita* **2021**, 1–26. [CrossRef]
29. Letnikov, F.A. Fluid regime of endogenous processes and problems of ore genesis. *Rus. Geol. Geophys.* **2001**, *47*, 1296.
30. Williams-Jones, A.E.; Bowell, R.J.; Migdisov, A.A. Gold in Solution. *Elements* **2009**, *5*, 281–287. [CrossRef]
31. Murzin, V.V.; Sazonov, V.N. Origin of cupriferous gold mineralization in Alpine-type ultramafic rocks. *Dokl. Earth Sci.* **1999**, *367*, 634–635.
32. Duuring, P.; Hagemann, S.G.; Cassidy, K.F.; Johnson, C.A. Hydrothermal Alteration, Ore Fluid Characteristics, and Gold Depositional Processes along a Trondhjemite-Komatiite Contact at Tarmoola, Western Australia. *Econ. Geol.* **2004**, *99*, 423–451. [CrossRef]
33. Rauchenstein-Martinek, K.; Wagner, T.; Walle, M.; Heinrich, C.A. Gold concentrations in metamorphic fuids: A LA-ICPMS study. *Chem. Geol.* **2014**, *385*, 70–83. [CrossRef]
34. Prokof'ev, V.Y. Main Principles of Hydrothermal Deposit Typification Based on Fluid Inclusion Study: The Case of Gold. Trans. *Rus. Acad. Sci. Earth Sci. Sect.* **2003**, *354*, 2553–2555. (In Russian)
35. Mountain, B.W.; Wood, S.A. Chemical controls on the solubility, transport and deposition of platinum and palladium in hydrothermal solutions: A thermodynamic approach. *Econ. Geol.* **1988**, *83*, 492–510. [CrossRef]
36. Spiridonov, E. Ore-magmatic systems of the Noril'sk ore field. *Russ. Geol. Geophys.* **2010**, *51*, 1059–1077. [CrossRef]
37. Gorbachev, N.S.; Dadze, T.P.; Kashirtseva, G.A.; Kunts, A.F. Fluid transfer of gold, palladium, and rare earth elements and genesis of ore occurrences in the Subpolar Urals. *Geol. Ore Deposits* **2010**, *52*, 215–233. [CrossRef]
38. Olivo, R.; Gauthier, M.; Bardoux, M. Palladian gold from the Caue iron mine, Itabira District, Minas Gerais, Brazil. *Mineral. Mag.* **1994**, *58*, 579–587. [CrossRef]
39. Varajão, C.; Colin, F.; Vieillard, P.; Melfi, A.; Nahon, D. Early weathering of palladium gold under lateritic conditions, Maquiné Mine, Minas Gerais, Brazil. *Appl. Geochem.* **2000**, *15*, 245–263. [CrossRef]
40. Cabral, A.R.; Lehmann, B.; Kwitko, R.; Jones, R.D. Palladian gold and palladium arsenide-antimonide minerals from Gongo Soco iron ore mine, Quadrilátero Ferrífero, Minas Gerais, Brazil. *Appl. Earth Sci.* **2002**, *111*, 74–80. [CrossRef]

41. Chapman, R.J.; Leake, R.C.; Bond, D.P.G.; Stedra, V.; Fairgrieve, B. Chemical and Mineralogical Signatures of Gold Formed in Oxidizing Chloride Hydrothermal Systems and their Significance within Populations of Placer Gold Grains Collected during Reconnaissance. *Econ. Geol.* **2009**, *104*, 563–585. [CrossRef]
42. Chudnenko, K.V.; Palyanova, G.A.; Anisimova, G.S.; Moskvitin, S.G. Ag-Au-Hg solid solutions and physicochemical models of their formation in nature (Kyuchyus deposit as an example). *Appl. Geochem.* **2015**, *55*, 138–151. [CrossRef]
43. Palyanova, G.; Murzin, V.; Zhuravkova, T.; Varlamov, D. Au-Cu-Ag mineralization in rodingites and nephritoids of the Agardag ultramafic massif (southern Tuva, Russia). *Russ. Geol. Geophys.* **2018**, *59*, 238–256. [CrossRef]
44. Nielsen, T.F.D.; Andersen, J.C.O.; Holness, M.; Keiding, J.K.; Rudashevsky, N.S.; Rudashevsky, V.N.; Salmonsen, L.P.; Tegner, C.; Veksler, I.V. The Skaergaard PGE and Gold Deposit: The Result ofin situFractionation, Sulphide Saturation and Magma Chamber-scale Precious Metal Redistribution by Immiscible Ferich Melt. *J. Pet.* **2015**, *56*, 1643–1676. [CrossRef]
45. Rudashevsky, N.S.; Rudashevsky, V.N.; Nielsen, T.F.D.; Shebanov, A.D. Alloys and intermetallic compounds of gold and copper in gold-palladium ores of the Skaergard massif (Greenland). *J. Proc. Komi Sci. Centre Ural Branch RAS* **2014**, *143*, 1–23.
46. Sluzhenikin, S.F.; Mokhov, A.V. Gold and silver in PGE-Cu-Ni and PGE ores of the Noril'sk deposits, Russia. *Miner. Depos.* **2014**, *50*, 465–492. [CrossRef]
47. Palacios, C.; Hérail, G.; Townley, B.; Maksaev, V.; Sepulveda, F.; De Parseval, P.; Rivas, P.; Lahsen, A.; Parada, M.A. The composition of gold in the cerro casale gold-rich porphyry deposit, maricunga belt, Northern Chile. *Can. Miner.* **2001**, *39*, 907–915. [CrossRef]
48. Arif, J.; Baker, T. Gold paragenesis and chemistry at Batu Hijau, Indoneisa: Implications for gold-rich porphyry copper deposits. *Miner. Depos.* **2004**, *39*, 523–535. [CrossRef]
49. Chudnenko, K.; Pal'yanova, G. Thermodynamic properties of solid solutions in the Ag-Au-Cu system. *Russ. Geol. Geophys.* **2014**, *55*, 349–360. [CrossRef]
50. Gas'kov, I.V. Major impurity elements in native gold and their association with gold mineralization settings in deposits of Asian fold belts. *Russ. Geol. Geophys.* **2017**, *58*, 1080–1092. [CrossRef]
51. Murzin, V.V.; Sustavov, S.G. Solid-phase transformation in natural cuprous gold. *Izv. USSR Acad. Sci. Ser. Geol.* **1989**, *11*, 94–104. (In Russian)
52. Okamoto, H.; Charkrabarti, D.J.; Laugylin, D.E.; Massalski, T.B. The Au-Cu (Gold-Copper) System. *Bull. Alloy Ph. Diagr.* **1987**, *8*, 454–473. [CrossRef]
53. Spiridonov, E.M.; Pletnev, P.A. *Zolotaya Gora Cupriferous Gold Deposit "Gold-Rodingite" Formation*; Spiridonov, E.M., Ed.; Nauchnyi Mir: Moscow, Russia, 2002; p. 220. (In Russian)
54. Murzin, V.V.; Chudnenko, K.V.; Palyanova, G.A.; Varlamov, D.A.; Naumov, E.A.; Pirajno, F. Physicochemical model of formation of Cu-Ag-Au-Hg solid solutions and intermetallic alloys in the rodingites of the Zolotaya Gora gold deposit (Urals, Russia). *Ore Geol. Rev.* **2018**, *93*, 81–97. [CrossRef]
55. Knight, J.; Leitch, C.H. Phase relations in the system Au-Cu-Ag at low temperatures, based on natural Assemblages. *Can. Miner.* **2001**, *39*, 889–905. [CrossRef]
56. Surenkov, S.V.; Moralev, G.V.; Borisov, A.V. *Physicochemical Parameters of the Au-PGE-REE Mineralization of the Chudnoe and Nesterovskoe Ore Occurrences (Subpolar Urals)*; VII Student School Metallogeny of Ancient and Modern Oceans-2001; Institute of Mineralogy, Ural Branch of RAS: Miass, Russia, 2001; pp. 195–198. (In Russian with English abstract)
57. Omelyanenko, B.I. *Near-Ore Hydrothermal Alteration of Rocks*; Nedra: Moscow, Russia, 1978; p. 215. (In Russian)
58. Prokofiev, V.Y. *Geochemical Features of Ore-Forming Fluids of Hydrothermal Gold Deposits of Various Genetic Types (According to the Study of Fluid Inclusions)*; Zorina, L.D., Ed.; Siberian Publishing Company "Science": Novosibirsk, Russia, 2000; p. 192.
59. Berni, G.V.; Heinrich, C.A.; Wälle, M.; Wall, V.J. Fluid geochemistry of the Serra Pelada Au-Pd-Pt deposit, Carajás, Brazil: Exceptional metal enrichment caused by deep reaching hydrothermal oxidation. *Ore Geol. Rev.* **2019**, *111*, 102991. [CrossRef]
60. Barakat, A.; Marignac, C.; Boiron, M.-C.; Bouabdelli, M. Caractérisation des paragenèses et des paléocirculations fluides dans l'indice d'or de Bleïda (Anti-Atlas, Maroc). *Comptes Rendus Geosci.* **2002**, *334*, 35–41. [CrossRef]
61. El Ghorfi, M.; Oberthür, T.; Melcher, F.; Lüders, V.; Boukhari, A.; Maacha, L.; Ziadi, R.; Baoutoul, H. Gold–palladium mineralization at Bleïda Far West, Bou Azzer–El Graara Inlier, Anti-Atlas, Morocco. *Miner. Depos.* **2006**, *41*, 549–564. [CrossRef]
62. Berni, G.V.; Heinrich, C.A.; Lobato, L.M.; Wall, V. Ore mineralogy of the Serra Pelada Au-Pd-Pt deposit, Carajás, Brazil and implications for ore-forming processes. *Miner. Deposita* **2016**, *51*, 781–795. [CrossRef]
63. Palyanova, G.A. Gold and Silver Minerals in Sulfide Ore. *Geol. Ore Depos.* **2020**, *62*, 383–406. [CrossRef]
64. Zaccarini, F.; Pushkarev, E.; Fershtater, G.B.; Garuti, G. Composition and mineralogy of PGE-rich chromitites in the nurali lherzolite gabbro complex, Southern Urals, Russia. *Can. Miner.* **2004**, *42*, 545–562. [CrossRef]
65. Anikina, E.V.; Zaccarini, F.; Knauf, V.V.; Rusin, I.A.; Pushkarev, E.V.; Garouti, J. Palladium and gold minerals in the ores of the Baron ore occurrence, Volkovsky gabbro-diorite massif. *Bull. Ural Dep. Rus. Mineral. Soc.* **2005**, *4*, 5–25. (In Russian with English abstract)
66. Spiridonov, E.; Yanakieva, D. Modern mineralogy of gold: Overview and new data. *ArchéoSciences* **2009**, *33*, 67–73. [CrossRef]
67. Kuznetsov, S.K.; Tarbaev, M.B.; Moralev, G.V.; Soboleva, A.A.; Ivanova, T.I. Gold-platinoid mineralization in the Subpolar Urals. In *Mater. Vseros. Conf. "Gold, Platinum and Diamonds of the Komi Republic and Adjacent Regions"*; Institute of Geology, Komi Science Center: Syktyvkar, Russia, 1998; pp. 13–14. (In Russian with English abstract)

68. Buisson, G.; Leblanc, M. Gold bearing listwanites (carbonatized ultramafic rocks) in ophiolite complexes. In *Metallogeny of Basic and Ultrabasic Rocks*; Gallagher, J.M., Iscer, R.A., Neary, C.R., Prichard, H.M., Eds.; Institute of Mining and Metallurgy: London, UK, 1986; pp. 121–132.
69. Halls, C.; Zhao, R. Listvenite and related rocks: Perspectives on terminology and mineralogy with reference to an occurrence at Cregganbaum, Co., Mayo, Republic of Ireland. *Miner. Depos.* **1995**, *30*, 303–313. [CrossRef]
70. Azer, M.K. Evolution and economic significance of listwaenites associated with Neoproterozoic ophiolites in south Eastern Desert, Egypt. *Geol. Acta* **2013**, *11*, 113–128.
71. Belogub, E.V.; Melekestseva, I.Y.; Novoselov, K.A.; Zabotina, M.V.; Tret'Yakov, G.A.; Zaykov, V.V.; Yuminov, A.M. Listvenite-related gold deposits of the South Urals (Russia): A review. *Ore Geol. Rev.* **2017**, *85*, 247–270. [CrossRef]
72. Sazonov, V.N. *Gold-Bearing Metasomatic Associations in Fold Belts*; Institute of Geology and Geochemistry: Yekaterinburg, Russia, 1998; p. 181. (In Russian)
73. Zharikov, V.A.; Rusinov, V.L. *Metasomatism and Metasomatic Rocks*; Scientific World: Moscow, Russia, 1998; p. 492.
74. Harlov, D.E.; Austrheim, H. *Metasomatism and the Chemical Transformation of Rock*; Metzler, J.B., Ed.; Springer: Berlin/Heidelberg, Germany, 2013; p. 806.

minerals

MDPI

Article

Gold in the Oxidized Ores of the Olympiada Deposit (Eastern Siberia, Russia)

Sergey A. Silyanov [1,*], Anatoly M. Sazonov [1], Yelena A. Zvyagina [1], Andrey A. Savichev [2,3] and Boris M. Lobastov [1]

[1] Institute of Mining, Geology and Geotechnology, Siberian Federal University, 79 pr. Svobodny, 660041 Krasnoyarsk, Russia; sazonov_am@mail.ru (A.M.S.); elena_zv@mail.ru (Y.A.Z.); lbm02@ya.ru (B.M.L.)
[2] Department of Mineralogy, Crystallography and Petrography, Saint-Petersburg Mining University, 2 21st Line, 199106 St. Petersburg, Russia; a_savichev@mail.ru
[3] LLC Norilskgeologia, 11 Grazhdanskiy Avenue, 195220 St. Petersburg, Russia
* Correspondence: silyanov-s@mail.ru; Tel.: +7-963-188-9156

Abstract: Native gold and its satellite minerals were studied throughout the 300 m section of oxidized ores of the Olympiada deposit (Eastern Siberia, Russia). Three zones are identified in the studied section: Upper Zone ~60 g/t Au; Middle Zone ~3 g/t Au; Lower Zone ~20 g/t Au. Supergene and hypogene native gold have been found in these zones. Supergene gold crystals (~1 μm), their aggregates and their globules (100 nm to 1 μm) predominate in the Upper and less in Middle Zone. Relic hypogene gold particles (flattened, fracture and irregular morphology) are sporadically distributed throughout the section. Spongiform gold occurs in the Lower Zone at the boundary with the bedrock, as well as in the bedrock. This gold formed in the process of oxidation of aurostibite, leaching of impurities and its further dissolution. Hypogene gold is commonly isolated but for supergene gold typically associated with ferric (hydr)oxides. New formation of gold occurred due to oxidation of sulfide ores and release of "invisible" gold, as well as dissolution, mobilization and re-deposition of metallic hypogene gold. A model for the formation of oxidized ores with the participation of meteoric and low-temperature hydrothermal waters has been proposed.

Keywords: oxide ore; weathering; supergene gold; Olympiada gold deposit; Yenisei Ridge; mineral exploration

Citation: Silyanov, S.A.; Sazonov, A.M.; Zvyagina, Y.A.; Savichev, A.A.; Lobastov, B.M. Gold in the Oxidized Ores of the Olympiada Deposit (Eastern Siberia, Russia). *Minerals* **2021**, *11*, 190. https://doi.org/10.3390/min11020190

Academic Editor: Galina Palyanova

Received: 30 December 2020
Accepted: 9 February 2021
Published: 11 February 2021

1. Introduction

Oxidized ores of gold deposits are important formations for the mining and metallurgical industry, as the weathering process leads to their partial enrichment and increased content of the noble metal. Moreover, oxidized ores do not require complex processing technologies and are profitable even at low grades. Commercially valuable oxidation zones of gold ores are known in Russia, Kazakhstan, Australia, Brazil and other countries [1–5].

In addition to the economic value, the oxidation zones of gold ore deposits are of fundamental interest due to the exogenous geochemistry and metallogeny of gold. Today there is a lot of evidence of gold mobility in supergene conditions in the form of various complexes [1,2,5–14]. Significant attention is also paid to the participation of bacteria in the remobilization and redeposition of gold [15–22]. The mobility of gold has been established in different climatic zones (subtropical, tropical, arid, humid, moderate, subarctic), including the permafrost zone [23–25].

Despite the progress made in understanding the mechanisms of gold behavior in exogenous conditions, some aspects remain controversial, both for specific deposits and in a broader sense. Most of them are about the way gold is transported and its mobility in the supergenesis zone, changes in the morphology and size, and bacterial participation in the remobilization and redeposition of gold. In this connection, there is a need to further study the process of oxidation of gold-sulfide ores. Therefore, the purpose of this research

was to study native gold in oxidized ores of the Olympiada deposit (Russia), as well as mechanisms of formation of supergene gold and its secondary enrichment.

The Olympiada gold deposit is a unique object in terms of the scale of mineralization with accumulated resources of about 80 Moz (about 2500 metric tons) of gold. Since 1985, just under 20 Moz metal has been mined at the deposit. According to PJSC Polyus, the proven and probable reserves as of 2020 comprise 24 Moz, and the estimated and identified resources comprise 39.4 Moz of gold.

The Olympiada deposit is unique also in terms of the scale of the gold-bearing oxidation zone developed within it. In terms of the depth of its distribution (over 400 m from the recent surface), the deposit has no analogs among gold projects of the world. Oxidized ores of the deposit were mined from 1985 to 2007. During this period, about 17 Mt of ore with an average grade of ~11 g/t was mined, which in terms of pure metal was about 193 tons [26].

In our recent work, we provided a general review of geology and primary (hypogene) sulfides ore of the Olympiada gold deposit [26]. However, oxidized ores have not been described since 2003. Therefore, our present work is devoted to the description of gold of the oxidized ores of the deposit.

Studies of oxidized ores of the Olympiada deposit allowed new data to be obtained on the morphology, chemical composition and gold differentiation in the stratum (at a depth of ~300 m) of oxidized ores, as well as proposing a model of supergene redistribution of noble metal and other elements in the oxidation zone.

2. Geological Setting of Olympiada Deposit and Characteristics of Sulfide Ores

2.1. Geological Setting

The Olympiada deposit is located in the center of the Yenisei Ridge (Eastern Siberia, Russia), which is a Neo-Proterozoic (860–800 Ma) collision orogen. The latter has passed to the riftogenic stage of development at the boundary of ~750–680 Ma [27], which coincides with the age of gold-sulfide and gold-antimony mineralization [28].

The deposit is confined to the silicate and carbonate band of the Lower Riphean Kordinskaya suite clastic stratum. Granitoids located 2.5 km away from and above the deposit surround it. The structure of the ore field is an ensemble of conjugated W-shaped folds (Figure 1).

2.2. Primary (Hypogene) Sulfide Ore

The main reserves of the deposit are concentrated in bedrock hypogene ores (average gold grade 4.0–4.6 g/t). When additional exploration of deep horizons of the deposit was carried out, ore intersections with commercial grades at depths of over 1500 m were recorded.

Sulfides (2 to 7%), which gold is associated with, are developed in quartz (30–45%)–mica (20–35%)–carbonate (35–40%) rocks. More than 50 hypogene ore minerals have been found at the deposit, among which arsenopyrite, pyrrhotite, pyrite, stibnite and berthierite prevail. They are present in the form of dissemination of submillimeter and submicron grains in metasomatites and more rarely in pocket-like inclusions in quartz segregations. The earliest ore minerals (Au-As association) are needle-shaped arsenopyrite, pyrite, pyrrhotite and chalcopyrite. The Au-Sb ± (Pb-Ag-Hg-W) association, represented by stibnite, berthierite, mercurous gold, aurostibite, jamesonite, gudmundite, late arsenopyrite and rarely scheelite, has been identified with time lag. Mercury minerals, mainly coloradoite, are also noted here [35]. Gold-arsenic and gold-antimony ores are the main ore components.

On the surface, the Olympiada deposit consists of two spatially separated parts, Western and Eastern Olympiada, which are joined at the depth of the Intermediate part. The deposit is located within the complex Medvezhinskaya anticline complicated by a junction of broadly E–W, NE and NW faults. The core of the fold is composed of quartz-two-mica schists, and the limbs are formed by quartz-mica-carbonate (with layers and

lenticular layers of marbled limestone) and quartz-mica-carbonate schists (Figure 1). Ore bodies of the deposit are confined to the limbs and joint part of this block-folding structure. The result of the different positions of the Western, Intermediate and Eastern sections in it is their abrupt difference in the scale of mineralization, 90% of which (including oxidized ores) falls on the Eastern Olympiada. The geology of the Olympiada deposit is described most fully in the works [26,29–34].

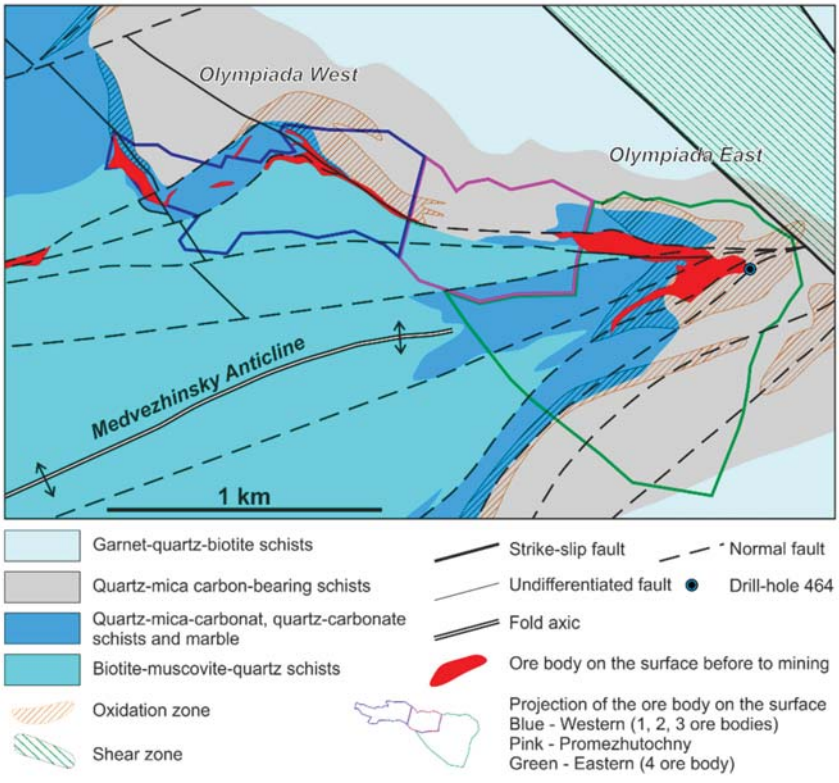

Figure 1. Geological map of the Olympiada gold deposit [26].

Gold in bedrock ores. The gold grade in the ores varies from 0.n to tens of g/t. Gold is mainly fine, pulverized, with a predominant size of about 10 μm (coarse, pocket-like inclusions accompanied by hurricane concentrations reaching kg/t are noted). The form of inclusions is irregular, lamellar, vein-shaped, fracture, droplet-shaped and spongiform. In the ore milled down to −74 μm, about 15% of gold is in a free form, and up to 45% is in a cyanidable form in aggregates with ore minerals [34,36]. The most common gold inclusions in quartz and sulfides are arsenopyrite, pyrite, pyrrhotite and berthierite (Figure 2). Native gold of the early Au-As association is high in fineness (880–1000‰, 970‰ on average); mercury and silver, and less often copper, are present as impurities. In antimony ores, the gold fineness decreases to 647–757‰ due to the increased concentrations of Hg, Cu, Ag, as well as the occurrence of aurostibite, and increases to 1000‰, when spongiform gold replaces aurostibite.

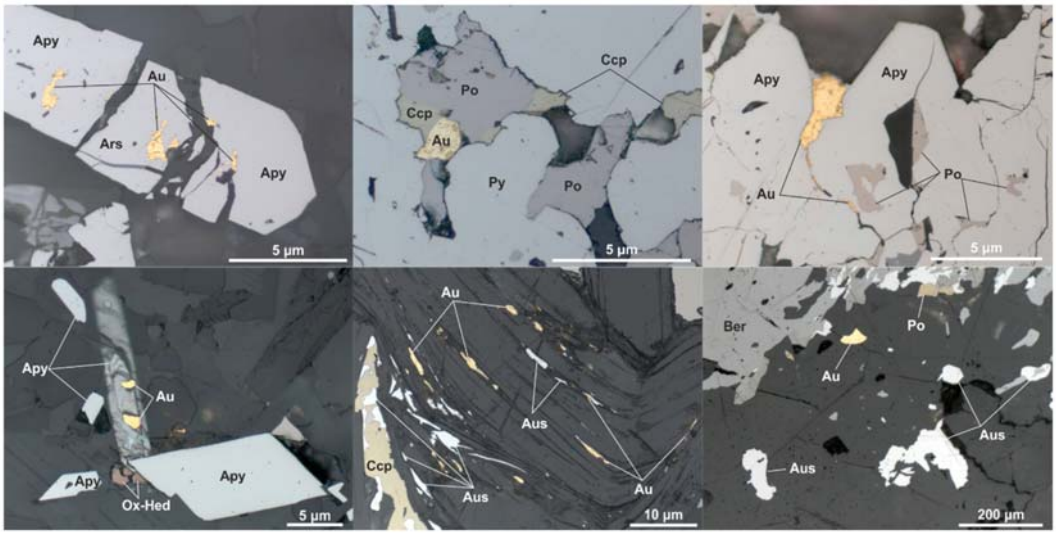

Figure 2. Native gold in primary (hypogene) sulfide ore (optical photo). Apy—arsenopyrite, Au—gold, Aus—aurostibite, Po—pyrrhotite, Py—pyrite, Ccp—chalcopyrite, Ox-Hed—oxidized hedleyite, Ber—berthierite.

In addition to micro- and macroscopic gold, the ores contain "invisible" (refractory) gold, which is not extractable by cyanidation. The share of such gold can reach 40–60%, and its extraction is carried out by JSC Polyus Krasnoyarsk using its own bio-oxidation technology BIONORD® [36]. "Invisible" gold is confined to sulfide minerals of the deposit, first of all, to needle-like arsenopyrite of the early association, in which its concentrations range from 0.0n to 2298 ppm [37,38]. According to modern ideas, "invisible" gold in arsenopyrite is present in the form of nanosized Au^0 inclusions and in a structurally bound form [38–40]. Earlier Mössbauer studies on ^{197}Au atoms for gold-bearing arsenopyrite of the Olympiada deposit showed that the content of structurally bound and nanosized metallic gold varies between 3 and 45% and 55 and 97%, respectively [37].

2.3. Oxide (Supergene) Ore

The oxidation zone of primary sulfide ores within the Eastern Olympiada covered almost the entire area of the ore body (about 45,000 m^2) and reached a depth of more than 400 m from the current surface. In vertical sections, the gold-bearing oxidation zone represented a large column-shaped body (Figure 3), which gradually decreased in size with depth and thinned out in full at horizon +280 m. The gold grade in oxidized ores reached 447.2 g/t. The geochemical spectrum of the Olympiada oxidized ores was characterized by a close correlation of Au with W, Sb, Hg, less often with Ag and Pb, but not with As. Thus, at a horizon +600 m, the average grades (ppm) and concentration coefficients with respect to the primary ores were equal: for Au to 9.9/3.1, for Ag to 0.3/2.8, for Sb to 2228.0/2.5, for Hg to 43.6/4.4, for Pb to 261.0/11.3, for W to 677.0/11.6 and for As to 681.0/0.9.

In the north, in the broadly W–E segment of the ore body of the Eastern Olympiada, the oxidation zone was characterized by lower (up to 130 m) thickness and actually repeated the geochemistry of the primary Au-As-(Sb) ores in terms of the grade and distribution of these and other elements, while not demonstrating noticeable supergene enrichment. In the zone of the Main NE Fault, oxidized ores had the much higher thickness and productivity for gold; subvertical "ore shoots" were distinguished in them [30], containing more than 50 g/t of Au and abruptly enriched the W, Pb, Ag and Sb [31]. Here, oxidized ores were developed mainly after antimony primary ores (Figure 3a). The thickest and highest-grade chimney-shaped body, going down to a depth of 400 m, was characterized by an

abnormally high grade of mercury (up to 0.2 wt.%) and antimony (up to 1.0 wt.%), but a lower grade of As, as well as Ti, Fe, Cr and other siderophiles. Marshallites prevailed in it. These are poorly cemented rocks of gray tints, consisting mainly of quartz (60–85%) and "hydromica", colored by scattered organic matter (up to 1.6%) (Figure 4). Quartz grains, as well as accessory minerals—zircon, tourmaline, and even a number of fine gold grains, often had a spherical shape in marshallites [41].

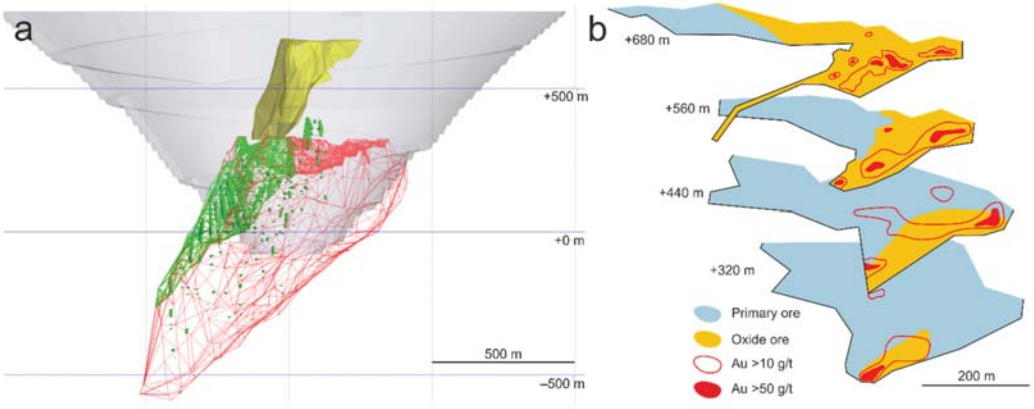

Figure 3. Eastern Olympiada. (**a**)—3D model: yellow—oxidized ores, green—gold-antimony ores, red (frame)—gold-arsenic ores, gray—pit outline; (**b**)—horizon plans of the ore body [30].

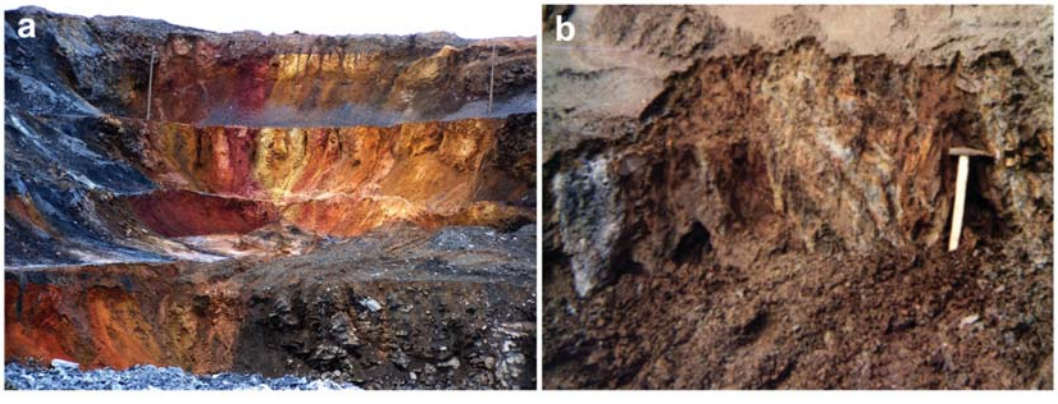

Figure 4. Oxidized ores of the deposit. (**a**)—General view of oxidized ores in the Eastern Olympiada pit (photo by S.A. Kamenev, 2004); (**b**)—outcrop of oxidized ("hydromica") ores with a marshallite body at horizon +580 m (photo by A.A. Savichev, 1999).

Typical "hydromica" oxidized ores of the Olympiada deposit were colored in different tints of brown, red, dark gray, orange, and contrasting isolated rocks [42,43] (Figure 4). In terms of the particle size distribution, the clay fraction prevailed in them (64%), and the smaller part was represented by the debris (10%), sandy (10%) and aleurtic fraction (16%). The mineral composition of oxidized ores had been studied before [41–45]. The main minerals were "hydromica" (40–70%), ferric hydroxides (1–36%), quartz (5–35%), kaolinite (up to 14%) and chlorite (up to 10%). There were relic epidote, calcite, biotite, actinolite, chloritoid, clinozoisite, garnet, plagioclase, staurolite, sillimanite, zircon, rutile, anatase, brookite and titanite.

Oxidized ores contained up to 10% of ore minerals, among which more than 30 species (excluding relic sulfides) were identified. Ferric and manganese oxides (hematite, lepidocrocite) and hydroxides prevailed, while antimony (senarmontite, cervantite, valentinite, "stibiconite") and tungsten (tungstite, hydrotungstite) oxides and hydroxides were rarer. Among manganese minerals, lithiophorite, todorokite and psilomelane with elevated concentrations of Ba (up to 3.0 wt.%), Co, Cu, Ni, Zn (0.*n* wt.%) and REE (0.03–0.04% in lithiophorite) are described. The impurities of As (up to *n*%), P, W and Hg (0.*n* wt.%) were present in the composition of sinter goethite. Scorodite, litharge, cerussite, anglesite, gypsum and baryte were also defined [46,47].

The typical feature of oxides and hydroxides of oxidized ores was wide isomorphism in the cation part between Sb, W, Pb and Hg. Thus, the W grade reached 5–10 wt.% in tripuhyite (up to 23.6 wt.%), and in "stibiconite" it was up to 16.8 wt.%, including 1.2 wt.% of Au. Abnormally high W grades (7.6–8.0 wt.%) were typical for cesàrolite [46]. In spite of the diversity of tungsten concentrator minerals, the main carrier in the oxidation zone was a newly formed scheelite, which differed significantly from scheelite from the primary ores in its REE distribution, and contained fluid inclusions with a homogenization temperature of 197 °C, which is important in genetic terms [47].

Gold from the Olympiada oxidation zone, according to a number of previous studies, is finely dispersed [43–45]. Most of it (63.7–91.8%) is concentrated in class −74 μm, and coarser gold (up to 0.5 mm) makes no more than 4–5% [45,48,49]. According to [45,48,49], a significant portion of gold (78.3–92.1%) is associated with ferric hydroxides, and 0.9–3.1% of Au is in a water-soluble form. In oxidized ores, there is relic primary and newly formed gold [45].

Secondary residual gold is formed in situ during the oxidation and decomposition of gold-containing minerals. It is closely associated with antimony and ferric hydroxides: its micro-particles are present in goethite pseudomorphs after arsenopyrite crystals. Spongiform and veinlet aggregates, lumpy gold grains and filamentous inclusions several μm in size are found in tripuhyite and bindheimite, which replace berthierite. As A.D. Ginkin [45] shows, the etching of such gold grains clearly demonstrates recrystallization structures. Secondary redeposition of gold is rare and associated with local infiltration accumulations of antimony oxides in the upper part of the oxidation zone. Redeposited gold is associated with sinter tripuhyite and "stibiconite", which fill fractures in weathered metasomatites. Gold is present as 0.3–4.0 μm globules scattered on the surface of cryptocrystalline tripuhyite balls. Gold from the oxidation zone is high in fineness (>980‰). The impurities include mercury (0.1–3.7 wt.%) and Ag, Cu, Mn, W and Sb in quantities up to 0.2 wt.% [45]. According to P.V. Bernatonis [43], the average composition of gold from the oxidation zone is (wt.%): Au 94.74, Ag 3.05, Hg 1.63, Fe 0.33, Sb 0.12, and Cu 0.02.

The genesis of the oxidized ores at the deposit is under discussion. According to one model, the oxidized ores belong to supergene products of the linear weathering crust of the Cretaceous–Paleogene age after mineralized carbonate and carbonaceous rocks [42,44]. Another one suggests the occurrence of low-temperature hydrothermal activity up to the Holocene age [41].

3. Samples and Methods

We studied 27 samples of oxidized ores of the Olympiada deposit, collected from Drillhole 464 located in the eastern part of the Eastern section of the deposit (Figure 1). The drillhole was drilled vertically and intersected the entire stratum of oxidized ores, stopping in the structural eluvium of the bedrock. The samples were collected from the depth range of 48–302 m and represent material of clay sizes with different shades of brown, red and gray colors (Figure 4).

Mineralogical studies were performed using SEM Tescan Vega III SBH with EDS Oxford X-Act in the R&D Nornickel SibFU Krasnoyarsk, Russia (analysts S.A.S and L.B.M.). The analytical conditions were the following: accelerating voltage of 20 kV, beam current of 1.2 nA and 60 s measuring time; pure elements (Au, Ag, Cu, Mn, W), as well as FeS_2,

FeAsS, SbS_2, SiO_2, Al_2O_3, $K(AlSi_3O_8)$ and CeO_2, were used as standards; detection limit was 0.05%.

Trace elements (Ag, W, Sb, Ce, Pb, Cu) were determined with the ICP-MS method in the Agilent 7500cx device manufactured by Agilent Technologies. The sample weighted portion was preliminarily transferred by progressive digestion into nitric-acid and aqua regia solutions, which allowed it to be kept in the liquid phase and for analyzing the maximum possible set of elements to be analyzed. The quality of the obtained results was estimated on the basis of rock and ore standards BCR-2, BHWO, SSL-1. The analyses were performed in the common-use Analytical Center of Geochemistry of Natural Systems of the Tomsk State University, Tomsk, Russia.

The gold grade is given according to the data of the fire assay carried out in the laboratory of JSC Polyus Krasnoyarsk, Krasnoyarsk, Russia.

The bulk X-ray analysis was performed using CuKα radiation on polycrystalline X'Pert PRO diffractometer (PANalytical) with a PIXcel detector equipped with graphite monochromator in the Institute of Chemistry, Siberian Branch of the Russian Academy of Sciences, Krasnoyarsk. The dish with the sample was placed in a standard position. The survey was performed for reflection with the sample rotation at 360°/s. The survey range was from 5 to 101° on the 2θ scale, with a 0.026° spacing, Δt = 50 s.

4. Results

4.1. Structure of the Oxidized Ore Section

There are three zones in the studied section of oxidized ores of the deposit. The upper part of the section (Upper Zone) from 0 to ~135 m is characterized by saturated orange, red-orange color, which turns into gray-brown with depth (towards the zone boundary). The middle part of the section (Middle Zone) from a depth of ~135 to ~213 m has a gray-brown color with a yellowish tint in the roof, which changes to light gray-brown and dark raspberry-red towards the bottom. The bottom of the section (Lower Zone) to a depth of ~300 m has the most uniform brown-yellow color, which becomes slightly darker with depth. Below 300 m there are weathered rocks of gray-blue color in the oxidized ore section (Figure 5).

The mineral composition of the oxidized ores is variable in these zones. The Upper Zone is characterized by approximately equal ratios of quartz and "hydromica" in the absence of kaolinite. The Middle Zone contains more layered silicates (about 2/3 by weight), while the amount of kaolinite increases abruptly at the boundary with the Upper Zone and gradually decreases towards the Lower Zone, which is similar in terms of minerals to the Upper Zone. In terms of the structure, the studied oxidation zone differs from the classical one, where the top of the section should contain a hydrolysis zone maximally enriched with kaolinite and "hydromica" [50].

The Au grade in the studied samples varies from 0.2 to 61.1 g/t, and its distribution across the section is not uniform. The upper part of the section (Upper Zone) is the highest-grade, where the amount of Au increases abruptly to ~60 g/t. In the Lower Zone, high (~20 g/t) metal grades are also observed. The Middle Zone is characterized by a variable Au grade from 0.2 to 7.0 g/t. Meanwhile, the boundaries of the identified zones are traced by a sudden change in the metal grade (Figure 5).

The share of Ag does not exceed 1.5 g/t, and the minimum grades have been identified in the bottom of the section and the maximum grades at the top. Antimony and tungsten are characterized by similar distribution throughout the drillhole section. The metal grade in all zones is quite high (250–1750 g/t of Sb and 30–150 g/t of W). However, there is an abrupt decrease in their grade at the zone boundaries (Figure 5).

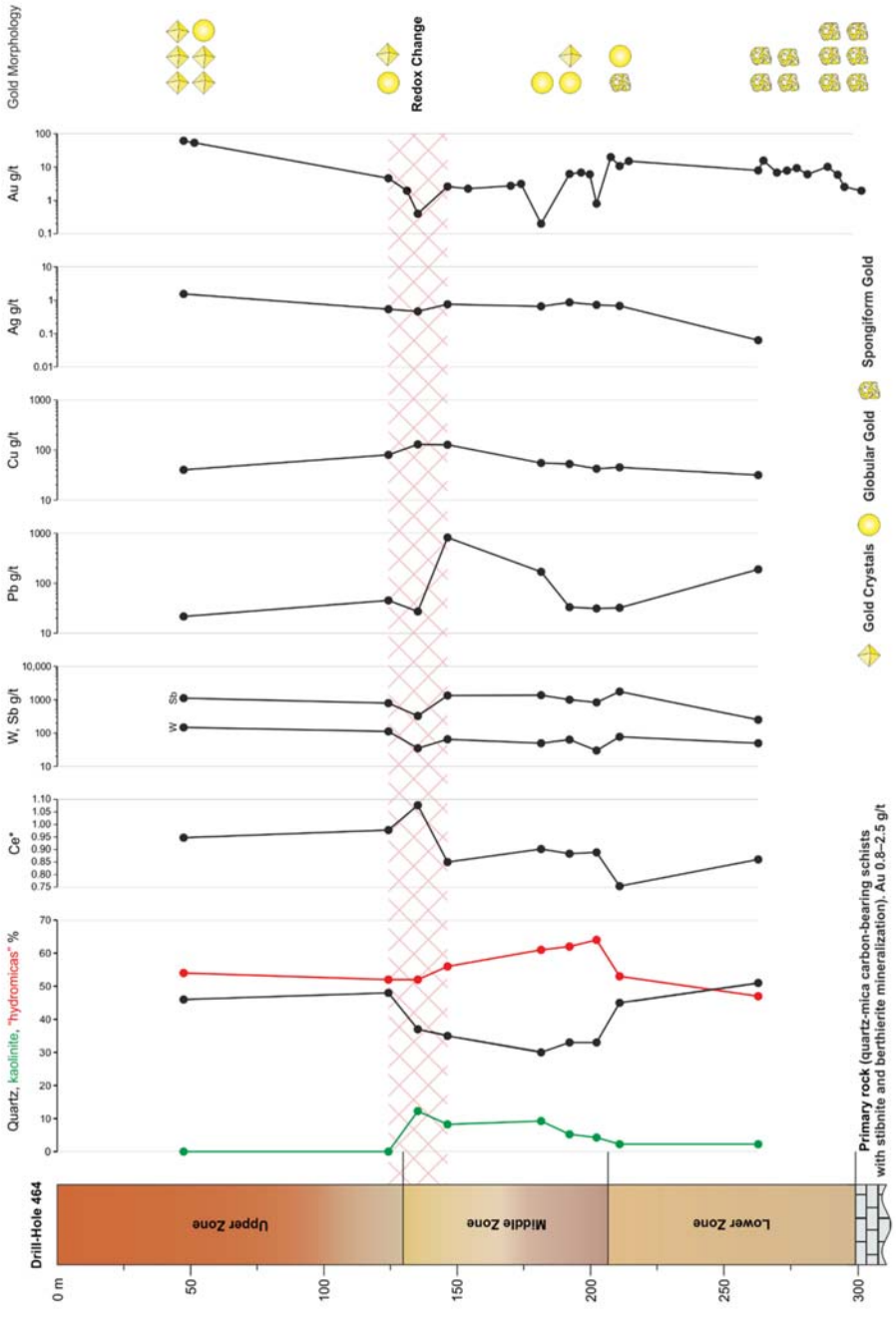

Figure 5. Structure of the oxidized ore section.

4.2. Mineralogy of the Studied Section of Oxidized Ores

The studied samples of oxidized ores consist of quartz, "hydromica", kaolinite and ferric (hydr)oxides. In addition to them, relic chloritoid, chlorite, monazite, rutile, scheelite and tourmaline are present in small quantities. Relics of sulfides oxidized from the surface (pyrite, pyrrhotite, arsenopyrite, stibnite) have been found in single quantities.

Supergene minerals include cervantite ("stibiconite" ?, valentinite ?), tungstibite, tungstite, hydrotungstite, tripuhyite, coronadite, bindheimite, plattnerite, oxyplumboroméite and oxycalcioroméite (Figure 6a–c, Table 1). In several cases, obviously newly formed cerium oxide (cerianite-(Ce)) was found in association with ferric (hydr)oxides and manganese oxides at the Middle and Upper Zone boundary (intervals 125.0–126.5 and 132.0–134.0). The morphology of supergene mineral formations is mainly nodular, sinter and globular; irregularly shaped granular aggregates are observed less frequently (Figure 6d). The size of individual globules and microcrystals of these minerals is usually 1–2 μm or less. Often, the newly formed cerianite-(Ce) forms grains of quartz or other minerals. Samples with numerous findings of cerianite-(Ce) differ in the increasing value of the ceric anomaly up to ~1.08, with its general negative nature in the Middle and Lower Zones (~0.75–0.90).

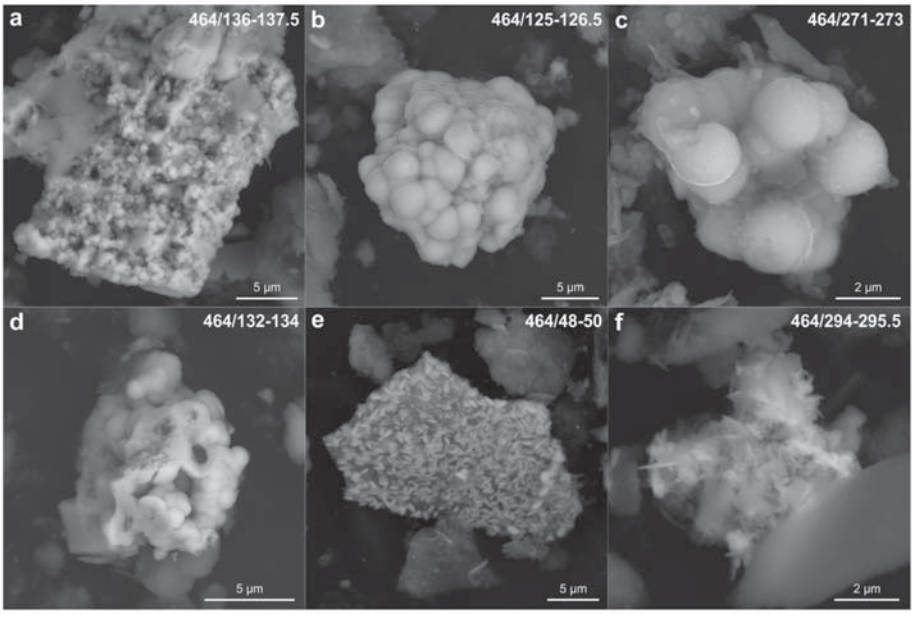

Figure 6. Supergene minerals of oxidized ores. (**a**)—globular tungstibite; (**b**)—nodular cervantite; (**c**)—nodular oxycalcioroméite (?); (**d**)—nodular cerianite (Ce); (**e**)—flakyd lepidocrocite (?) after quartz; (**f**)—needle-like inclusions of montroydite (?).

The predominant supergene ore minerals are ferric (hydr)oxides (lepidocrocite, goethite, hematite, etc.), which almost always contain the As (0.4–3.2 wt.%), S (up to 2.1 wt.%), W (0.2–3.0 wt.%), Sb (0.5–4.9 wt.%) and P (0.2–1.3 wt.%) impurities. In this case, the W impurity and the elevated concentrations of Sb and As are noted mainly in the upper part of the section. The maximum S and P grades are typical for the Middle Zone. The morphology of ferric (hydr)oxide inclusions varies from sinter forms after relic minerals to flaky and scaly inclusions (Figure 6e), as well as split crystals. Most often, secondary ferric minerals grow on the nuclei of relic quartz and mica, but their individual grains and aggregates are also often found. Secondary arsenic minerals (scorodite and phases with similar composition) were founded in the films on the oxidized arsenopyrite grains.

Table 1. Normalized average chemical composition of supergene minerals of oxidized ores (wt.%).

Mineral Name	O	Mg	Al	Si	Ca	Mn	Fe	Co	Ni	Sb	W	Pb	Ce	Sum
Cervantite (n = 2) [1]	20.9	2.4		1.0			0.5			75.2				100
Oxycalcioroméite (n = 2)	25.9		1.0		11.6		4.6			56.9				100
Tripuhyite (n = 3)	25.1		2.2	3.8		0.4	23.0			45.5				100
Tungstite (n = 4)	21.9		2.1				4.3				71.7			100
Hydrotungstite (n = 2)	26.0		3.1				3.3				67.6			100
Tungstibite (n = 2)	20.2									44.1	35.7			100
Plattnerite (n = 2)	15.0						0.5					84.4		100
Bindheimite (n = 2)	17.3									32.3		50.5		100
Oxyplumboroméite (n = 2)	19.2				5.0		3.6			39.2		33.0		100
Coronadite (n = 3)	38.8					31.7	3.6				3.1	22.9		100
Cerianite-(Ce) (n = 4)	17.3						2.6						80.2	100

[1] (n = 2)–number of analyses.

In the lower part of the section of the oxidized ores stratum (Lower Zone), aggregates of crystals of needle-like and near-isometric, tetrahedral morphology (Figure 6f) were observed, in which Hg (52.0 wt.%) and O (23.0 wt.%), as well as S (11.3 wt.%), Cu (7.7 wt.%) and Fe (4.1 wt.%), prevailed. It is assumed that a needle-like mineral is a rhombic mercury oxide montroydite. Its formation is possible during oxidation of coloradoite and/or some minerals of the polymetallic sulfides stage associated with chalcopyrite (probably its relic in Figure 6f in the form of tetrahedral crystals with an even surface of faces) and carrying the isomorphic impurity of mercury—sphalerite, tetrahedrite, berthierite, jamesonite—in which the impurity of Hg up to ~1690 ppm is noted according to LA–ICP–MS. The formation of montroydite may be associated with oxidation of native mercury, the findings of which have been repeatedly observed at the Olympiada deposit [26].

4.3. Native Gold in Oxidized Ores

More than 300 particles of supergene and relic native gold of different morphology ranging in size from ~30 nm to ~5–7 μm, rarely more, were found in the studied samples of oxidized ores of the deposit. The distribution and amount of free gold particles are consistent with its bulk gold grade in the samples.

Obviously newly formed isometric crystals of native gold were often observed (Figure 7a, Figure S1). Their size is uniform, 1.3 μm in diameter on average, with variations from 1.0 to 1.7 μm (sometimes up to 2.5 μm). The cutting of crystals has several simple shapes—usually a combination of a cube {100}, octahedron {111} and rhombodecahedron {110}; facets of a tetragon-trioctahedron {hhl} (?) often supplement them. In a single case (Figure 7b), all shpes possible for the *m3m* symmetry type are observed—tetrahexahedron, trigontrictahedron and hexoctahedron (Figure S1), in addition to the specified ones.

Globular particles may be attributed to the following morphological type of supergene gold (Figure 7c, Figure S2). The diameter of the most representative globules varies from 1.2 to 2.3 μm. The surface of these formations seems to be slightly rough or nanoporous. The same group includes rounded particles of subnanometer size (20 to 50–800 nm), due to which it is difficult to distinguish their true shape. Such nanoformations of native gold are very common. Single disc-shaped particles (Figure 7c, Figure S2) with a diameter of ~1 μm and a visible thickness of about 250 nm were discovered, which can be crystals flattened along one of L_4 and apparently supergene.

Considerably large sizes (~4–5 μm, thickness within 100–200 nm) are typical for rare particles of irregular morphology, which are probably relic gold (Figure 7e, Figure S3). Their peculiar contours suggest that they are fracture inclusions of hypogene gold of primary sulfide ores.

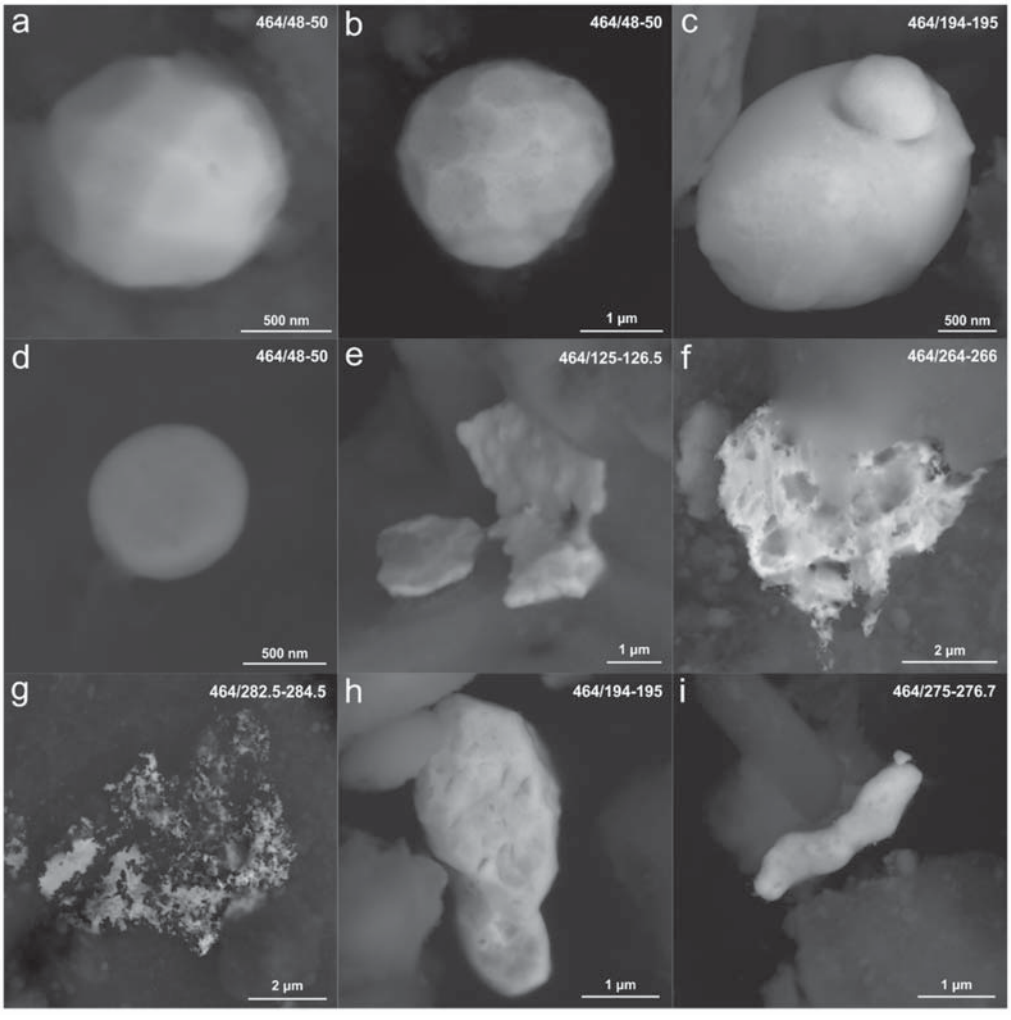

Figure 7. Morphology of native gold in oxidized ores. (**a**,**b**)—crystals; (**c**)—globular gold; (**d**)—disc-shaped gold; (**e**)—relic gold; (**f**,**g**)—spongiform gold; (**h**)—gold of irregular morphology; (**i**)—worm-shaped gold.

One of the most common morphological types is spongiform gold (Figure 7f,g, Figure S4). The size of such gold grains varies within the widest range from ~1 to ~6 µm and above. The contours of the grains are irregular, "torn" and porous. The sizes of branched mineral particles and cavities are within 20–100 nm. This is probably relic gold, which was subjected to the removal of impurities and partial dissolution. One of the mechanisms of its formation can be the replacement of aurostibite, which is common in the primary ore paragenesis, with extremely high-grade gold and stibnite, which was later oxidized to senarmontite, cervantite and valentinite. The latter, while being washed out, left spongiform cavities.

Irregularly shaped gold is found with traces of chipped mineral inclusions (?), with sizes in the range of 1–4 µm (Figure 7h, Figure S5). It may be assumed that this is also relic gold of primary ores, but it may also be crystals with less pronounced cut and induction surfaces. A single worm-shaped gold grain (Figure 7i) with dissolution traces (?) was also noted.

The distribution of the main (most common) morphological types of gold in the section is not homogeneous (Figure 5). Thus, most of the gold crystals are confined to the Upper Zone. In the middle part of the section, single crystals are observed, while there are none in the lower part of the section. In contrast to gold with crystallographic cut, spongiform gold is mostly found in the lower part of the section, closer to the bedrock. Gold with irregular morphology demonstrates the same tendency. Globular gold is found in single quantities in the Upper and Middle Zones and is most often found at the boundaries of geological and geochemical zones. Few relic gold grains are sporadically found throughout the section.

In the sample collected from weathered bedrock underlying the oxidized ores of the deposit, calcite aggregates with inclusions of antimony oxidized minerals and spongiform different fineness gold (Figure 8) were found. Here, spongiform gold with antimony impurity (up to ~38 wt.%) and presumably cervantite are noted in close aggregation. The formation of this association is possible during the decomposition of aurostibite and/or aurostibite and the coexisting antimony (stibnite) minerals. Such formations probably correspond to the initial stage of weathering of gold-antimony ores of the deposit.

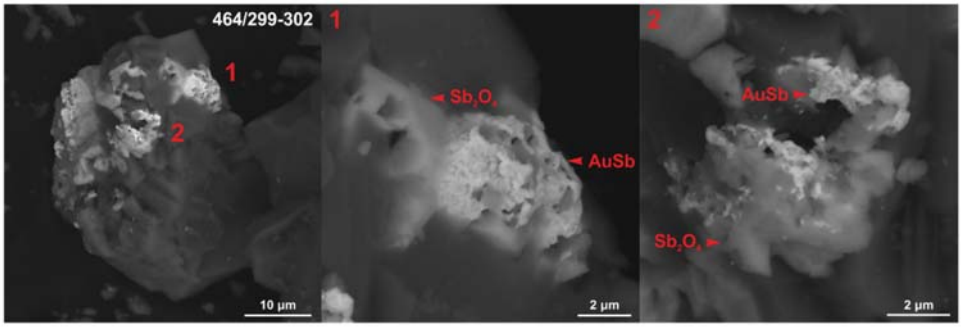

Figure 8. Products of aurostibite decomposition into spongiform gold and cervantite in the carbonate matrix of weathered bedrock of the deposit (the depth is 299–302 m—it is the deepest sample of the studied ones; see Figure 5).

Native gold from the oxidized ore samples is most often isolated in the form of independent particles, but its close aggregations with secondary iron minerals (especially in the upper part of the section) have been repeatedly observed. Figure 9 shows irregular shapes of a ferric (hydr)oxide grain (~10–100 μm) with numerous inclusions of native gold (up to 30 Au grains). The sizes of such inclusions vary widely from several hundreds of nanometers to 3–4 μm. As a rule, gold in such an association has rounded, smooth surfaces, and a single flattened crystal was found (Figure 9b). In addition, a mercurous gold inclusion was noted in tripuhyite.

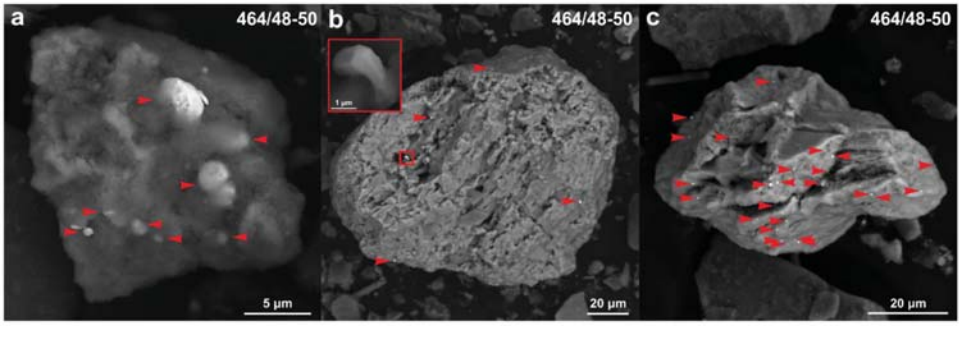

Figure 9. Inclusions of gold (red arrows) in ferric (hydr)oxides (**a**–**c**). The size of gold grains varies from 250 nm to 4 μm.

The SEM-EDS method was used for semi-quantitative (due to small size) determination of the chemical composition of the detected native gold. The overwhelming majority of chemical analyses of native gold in oxidized ores is characterized by the presence of O, Fe, Al, and Si (less often K, Ca, Mg, Mn, and Na). This is due to the presence of oxide and silicate films on gold particles, as well as the parasitic signal of the matrix on which the gold lies. Therefore, the impurities of these elements were not considered.

Among over 300 chemical composition determinations, sixteen analyses showed an impurity of Cu (0.8–10.7 wt.%), seventeen analyses showed Sb (0.5–35.2 wt.%), two showed Ag (3.1–4.2 wt.%) and five showed Hg (1.0–11.6 wt.%). At the same time, gold grains mainly contain only one impurity element. Reduced fineness is typical for spongiform gold and irregularly shaped gold of the lower part of the section. Gold with a mercury impurity has been noted here only. All studied crystals did not contain these impurities, except for one (2.9 wt.% Cu). Listed elements are typical impurities in native gold [51].

5. Discussion of the Oxidized Ores Formation Conditions

The specific geochemistry of the Olympiada oxidation zone is explained by the gold-antimony profile of primary ores (with W, Hg), which mainly served as the primary substrate (Figure 3a). Gold and associated metals were intensively redistributed, migrating from some horizons and accumulating in other horizons, which is controlled primarily by the sulfide content in the hypogene ores and pH and Eh of supergene solutions.

The main mineralogical and geochemical features of the selected horizons are as follows. The Lower Zone is distinguished by a significant accumulation of Au, usually in the form of spongiform gold, which appeared during the destruction of hypogene aurostibite, as well as wide development of supergene antimony and mercury minerals. The antimony concentrations here are maximum for the entire studied section. Oxidized ores of this zone inherit the geochemistry of parental gold-antimony ores to the maximum extent. The Middle Zone, on the contrary, is depleted with gold relative to the primary ores due to the intense removal of metal by oxidized fluids. The result of their activity is the dominance of kaoline and "hydromica" in the oxidized ores. Rare gold grains are represented here by globular shapes. Within the Middle Zone, there are local accumulations of alkali—lead (817 g/t) and copper (130 g/t)—generally not typical for the Olympiada oxidation zone. The Upper Zone has the most enriched ore level and differs in the maximum (up to 61 g/t) gold grade mainly present in the form of microcrystals. The highest concentrations of tungsten, silver and arsenic are also noted here. In the Upper Zone, we observe the maximum (up to several wt.%) sorption level of ore components (W, As, Sb) and metal gold nanoparticles on ferric (hydr)oxides. All of the above indicates a high mobility of supergene fluids in the formation of the oxidation zone, which led to its significant enrichment in the top part of the section [52].

As we have shown earlier [26], sulfide ores of the deposit contain mainly pyrite, pyrrhotite, arsenopyrite, stibnite and berthierite. Under exogenous conditions, these minerals are unstable and exposed to weathering. Oxidation of these sulfides led to the formation of sulfuric acid solutions and increased concentration of sulfate-ion and hydrogen-ion, which determined the reduction in pH and increase in the redox potential.

At the same time, the primary ores of the deposit contain a large amount of carbonates [26]. Dissociation of carbonate lead to neutralization of the acid on a large scale [53]. The combination of these factors led to fluctuations of redox conditions and acidity–alkalinity of the environment within the intensively oxidizing body of sulfide ores. Such a fluctuating area is most probable for the Middle and Upper Zones' boundary.

The existence of a geochemical barrier here is evidenced not only by the appearance of numerous newly formed crystals of native gold but also by the presence of supergene cerianite-(Ce) (Figure 6d). There is also an abrupt increase in Ce* values (up to ~1.1, Figure 5), which is probably caused by oxidation of the element to the low-soluble Ce^{4+} and its removal from aqueous solutions in the form of CeO_2 [54–60].

The kinetics of CeO_2 formation reactions strongly depends on pH and Eh, as well as on the participation of iron-oxidizing bacteria [61,62]. At the same time, it is reported that Ce, in contrast to most REE, has a greater affinity for Mn [63], and lower affinity for Fe [58], which is also noted in the samples studied (cerianite-(Ce) in association with manganese (hydr)oxides was detected). According to the data of the stability diagram of Ce-containing compounds in the Eh–pH coordinates [62], cerianite-(Ce) is stable in weakly reduced to strongly oxidized conditions with pH from 3 to 14. However, the negative Ce-anomaly in the solution (and, as a consequence, positive in the solid phase) is characteristic of the narrower CeO_2 stability field with Eh ~0.1–1.1 and pH ~3–7. On the other hand, there are data confirming that the negative anomaly of Ce occurs only in alkaline waters [64].

Oxidation of primary sulfides (arsenopyrite, pyrite, stibnite, aurostibite, etc., which are common in the primary ore paragenesis) leads to the formation of secondary minerals of Fe, Sb, As, Mn and Pb [5,11,13,65,66]. These minerals were detected in oxidized ore of deposit (see Table 1).

Thiosulphate-ion ($S_2O_3^{2-}$) is effective during dissolution and transportation of Au under near-neutral oxidizing conditions. It is assumed that the complex formation of Au with it is most likely during the oxidation of orogenic deposits [10,11]. The presence of thiosulfate radicals promotes the dissolution, mobilization and re-deposition of both gold, which is released from sulfides during their oxidation, and native Au^0 of bedrock ores. However, these complexes are metastable in the oxidizing environment, which leads to rapid deposition of Au^0 (together with ferric (hydr)oxides) and prevents the long-distance transfer of gold [5,67–70]. Chemical deposition of Au from thiosulfate complexes is possible either by their reduction during migration into not-yet-oxidized sulfide ores or during further oxidation with the formation of Fe hydroxides.

It is also believed that bacteria are capable of restoring the Au nanoparticles from thiosulfate complexes both inside and outside cells [17]. The interaction of $Au(S_2O_3)_2^{3-}$ with bacteria leads to the deposition of its nanoparticles, which are later able to aggregate into octahedral μ-crystals and/or spherical particles [16,71]. P.V. Bernatonis discovered bacteria of the *Thiobacillus ferrooxidans, Thiobacillus thiooxidans, Thiobacillus thiocyanooxidans, Thiobacillus thioparus* and *Thiobacillus denitrificans* species [43] in oxidized ores of the Olympiada deposit, which have contributed to gold redeposition.

Kashefi et al. also demonstrated that hyperthermophilic and mesophilic dissimilatory Fe(III)-reducing Bacteria and Archaea are capable of precipitating gold by reducing Au(III) to Au(0) with hydrogen as the electron donor in subsurface environments [72].

Trivalent complexes of gold Au(III)-OH-Cl-CN can exist in natural surface waters and may be important for the transport and biogeochemical cycling of gold in surface environments [11,73,74]. The possibility of the existence of Au(III)-Cl in the Upper Zone is consistent with the presence of Cl (up to 0.03 wt.%) here. Moreover, it was established earlier that 52% of mercury in the Olympiada oxidation zone exists in the chloride form [43].

In addition, a previous study showed that Au(III)-Cl complexes are adsorbed more readily onto iron oxides than are thio-Au(I) complexes [75]. This may indicate a lesser role of thiosulfate complexes in the deposition of Au in association with iron (hydr)oxides than is shown above. On the other hand, according to Gray and Pirlo, $AuCl_2^-$ is the dominant Au complex in Cl^- rich groundwaters [76]. In this case, the presence of dissolved Fe will reduce $AuCl_2^-$ [76].

Renders and Seward established the presence of $AuHS^0$, $Au(HS)_2^-$ and $Au_2S_2^{2-}$ in aqueous solutions (25 °C, pH 2–12, sulphur concentrations from 0.005 to 0.4 molal) [77]. We assumed that the presence of hydrosulfide gold complexes is most likely in the Lower Zone [5,11]. This complex was dominant form of the gold transport in aqueous-sulfide solutions during formation of primary ores [78].

The occurrence of spongiform gold in the Lower Zone is explained by the process of leaching of impurities (de-alloying), which is experimentally demonstrated in the work [79]. The formation of spongiform gold was also repeatedly observed in nature, as in the supergene zone during oxidation and decomposition of gold tellurides and antimonides,

as well as AuAg alloys [80–83] and under hypogene conditions under the influence of alkaline and neutral fluids with temperatures of 140–200 °C [84,85]. The liberation of gold from impurities in this process is accompanied by an increase in its free surface, which contributes to its further dissolution.

All this allows us to assert that the formation of oxidized ores of the Olympiada deposit took place under comprehensive geochemical conditions, in which Au behaved as a mobile element capable of redistribution and re-deposition on geochemical barriers (zone boundaries).

The formation of oxidized ores at the deposit is associated either with the development of a linear weathering crust or with late low-temperature hydrothermal-metasomatic activity. Apparently, both processes took place at the Olympiada deposit, and it is likely that hydrothermal and gas emanations were repeatedly superimposed on both primary ores and already existing weathering products. In contrast to the Cretaceous–Paleogene estimate of the age of linear weathering crusts at the Yenisei Ridge established in the literature, we tend to believe that the time interval of near-surface mineral formation at the Olympiada deposit may be hundreds of millions of years and primarily initiated by the activation of the Tatar Fault Zone when the Siberian craton collided with the Kazakhstan microcontinent on the border of the Devonian and Carboniferous ages. According to the data [86], the Paleogene-Quaternary spore and pollen spectra were found in the products of oxidized ores of the deposit from a depth of 5–28 m, gradually replaced at a depth of 30–60 m with the Mesozoic spectra and from a depth of 50–110 m with the Paleozoic (Permian, Carboniferous, Upper Devonian) spectra. The Upper Devonian age (368±23 Ma Sm-Nd and 364 ± 7 Ma Rb-Sr based on fluorite) at the Yenisei Ridge has been established for the "telethermal" mineralization (calcite, barite, celestine, anhydrite, fluorite, realgar, smithsonite, cerussite, native silver) superimposed on the Neo-Proterozoic orogenic gold ores of the major Blagodatnoye deposit [87] and is assumed by us to be the beginning of the formation of the oxidation zone at the Olympiada deposit, unique in its composition.

The spatial combination of oxidized ores with the permeable zone of the Main Fault explains to a great extent a significant vertical span of oxidation products' development and does not exclude the influence of late low-temperature hydrotherms during their formation. Thus, methane and carbon dioxide emissions were recorded during drilling within the Eastern open pit in summer 2018, which lasted for two days. According to the geologists of JSC "Polyus Krasnoyarsk", thermal phenomena were repeatedly observed within the fault. This suggests that the Main Fault zone is still active and was able to supply portions of a low-temperature fluid to the near-surface zone of the deposit.

6. Conclusions

Supergene redistribution of gold and other components was detected in the section (to a depth of 300 m) of oxidized ores of the Olympiada deposit. The upper part of the section (Upper Zone) is the highest-grade (up to ~60 g/t of gold). In the Middle Zone, the noble metal content is minimal (~3 g/t). The lower part of the oxidized ores section (Lower Zone) is characterized by an average Au grade (~20 g/t). The boundaries of the identified zones are traced by a sudden change in the metal content.

Supergene and hypogene native gold have been identified. Crystalline individuals and their aggregates, as well as globules that predominate at the top of the section, are classified as supergene. The size of such crystals is quite uniform and averages 1 μm; the size of globular gold varies from several hundred nm to several μm. Flattened (fracture) gold particles of irregular morphology, occurring sporadically throughout the section, are relic hypogene. Spongiform gold is transitional from hypogene to supergene—it is a product of oxidation of aurostibite developed in the lower part of the section at the boundary with the bedrock, as well as in the bedrock, and formed in the process of leaching of impurities and further dissolution. Native gold of oxidized ores is commonly isolated, but close association with secondary iron minerals is typical for the newly formed globular and crystalline gold.

The obtained results suggest that the formation of oxidized ores was accompanied by the mobilization, redistribution and secondary enrichment of gold with the participation of both meteoric waters and low-temperature fluids.

Inflow of low-temperature (up to 200 °C) hydrothermal water, which leached the bedrock and sulfides (with the release of "invisible" gold) in the lower parts of the section, could occur along the permeable zone of the Main Fault upwards. The same fluids led to the removal of impurities from hypogene gold, as well as its partial dissolution and mobilization. It is assumed that stable $AuHS^0$ complex was present here, capable of migrating upwards at long distances together with the rising fluid. Partial destruction of these complexes was possible in the middle part of the section, which led to the formation of rare particles of newly formed globular and crystalline gold. Nanosize Au^0 extracted from sulfide minerals could also migrate upwards as colloids [88,89].

Meteoric waters coming from the day surface led to oxidation of sulfides and inversion of the redox potential in the Upper Zone. Leaching of sulfides was accompanied by local acidifying of the environment, which was neutralized in larger scales by the dissociation of carbonates and the arrival of new portions of meteoric water. The boundary of mixing of meteoric and low-temperature hydrothermal waters was the front of acid leaching and coincided with the boundary of the Middle and Upper Zones. Oxidation of sulfides in this part of the section was accompanied by the formation of thiosulphate complexes with released "invisible" as well as dissolving metal Au. Fluctuating changes in pH and Eh, as well as the influence of bacteria, led to the destruction of gold complexes and release of Au^0 in the form of micro- and nanoparticles, which were intensively sorbed on ferric (hydr)oxides appearing here, and agglomerated into larger crystalline and globular individuals. Ascending low-temperature fluids carrying $AuHS^0$ and probably gold colloids could facilitate secondary enrichment of the top of the section.

Supplementary Materials: The following are available online at https://www.mdpi.com/2075-163X/11/2/190/s1, Figure S1–S5.

Author Contributions: Conceptualization, S.A.S., A.M.S. and A.A.S.; data curation, S.A.S. and B.M.L.; investigation, S.A.S., A.M.S., A.A.S., B.M.L. and Y.A.Z.; writing–original draft, S.A.S., A.M.S. and A.A.S. All authors have read and agreed to the published version of the manuscript.

Funding: The reported study was funded by RFBR, project number 19-35-90017.

Institutional Review Board Statement: Not applicable.

Informed Consent Statement: Not applicable.

Data Availability Statement: Not applicable.

Acknowledgments: We thank to P.A. Tishin, Ye.V. Rabtsevich and Ye.I. Nikitin for ICP-MS study; S.D. Kirik for X-RFA study. We are grateful to G.A. Palyanova, Reviewers and the Editorial Board members, for their comments and improvements.

Conflicts of Interest: The authors declare no conflict of interest.

References

1. Smirnov, S.S. *Oxidation Zone of Sulfide Deposits*; Academy of Sciences USSR: Moscow, Russia, 1955; 232p. (In Russian)
2. Albov, M.N. *Secondary Zoning of the Gold Deposits of the Urals*; Gosgeoltekhizdat: Moscow, Russia, 1960; 215p. (In Russian)
3. Butt, C.R.M.; Smith, R.E. Conceptual models in exploration geochemistry: Australia. *J. Geochem. Explor.* **1980**, *12*, 89–365. [CrossRef]
4. González-Álvarez, I.; Anand, R.R.; Boni, M. Mineral exploration in regolith-dominated terrains. Global considerations and challenges. *Ore Geol. Rev.* **2016**, *73*, 375–379. [CrossRef]
5. Kalinin, Y.A.; Palyanova, G.A.; Naumov, E.A.; Kovalev, K.R.; Pirajnoe, F. Supergene remobilization of Au in Au-bearing regolith related to orogenic deposits: A case study from Kazakhstan. *Ore Geol. Rev.* **2019**, *109*, 358–369. [CrossRef]
6. Petrovskaya, N.V. *Native Gold*; Nauka: Moscow, Russia, 1973; 347p. (In Russian)
7. Greffie, C.; Benedetti, M.F.; Parron, C.; Amouric, M. Gold and iron oxide associations under supergene conditions: An experimental approach. *Geochim. Cosmochim. Acta.* **1996**, *60*, 1531–1542. [CrossRef]

8. Kalinin, Y.A.; Kovalev, K.R.; Naumov, E.A.; Kirillov, M.V. Gold in the weathering crust at the Suzdal' deposit (Kazakhstan). *Russ. Geol. Geophys.* **2009**, *50*, 174–187. [CrossRef]
9. Chapman, R.J.; Leake, R.C.; Bond, D.P.G.; Stedra, V.; Fairgrieve, B. Chemical and mineralogical signatures of gold formed in oxidizing chloride hydrothermal systems and their significance within populations of placer gold grains collected during reconnaissance. *Econ. Geol.* **2009**, *104*, 563–585. [CrossRef]
10. Craw, D.; MacKenzie, D.; Grieve, P. Supergene gold mobility in orogenic gold deposits, Otago Schist, New Zealand. *N. Z. J. Geol. Geophys.* **2015**, *58*, 123–136. [CrossRef]
11. Craw, D.; Kerr, G. Geochemistry and mineralogy of contrasting supergene gold alteration zones, southern New Zealand. *Appl. Geochem.* **2017**, *85*, 19–34. [CrossRef]
12. Horbe, A.M.C.; Martins-Ferreira, M.A.C.; Lima, R.S. Supergene gold characterization by geochemistry, grain morphology and Au-Ag-Cu-Te classification. *J. South Am. Earth Sci.* **2019**, *95*, 102315. [CrossRef]
13. Kalinin, Y.; Pal'yanova, G.; Bortnikov, N.; Naumov, E.; Kovalev, K. Aggregation and differentiation of gold and silver during the formation of the gold bearing regolith (on the example of Kazakhstan deposits). *Dokl. Earth Sci.* **2018**, *482*, 1193–1198. [CrossRef]
14. Khusainova, A.S.; Gaskova, O.L.; Kalinin, Y.A.; Bortnikova, S.B. Physical-chemical model of gold conversion in products of ore processing of silver-polymetallic deposits (Salair Ridge, Russia). *Russ. Geol. Geophys.* **2020**, *61*(9), 964–975. [CrossRef]
15. Amosov, R.A.; Vasin, S.L. Gold microfossils. *Ores Met.* **1993**, *3*, 101–107. (In Russian)
16. Lengke, M.; Southam, G. Bioaccumulation of gold by sulfate-reducing bacteria cultured in the presence of gold(I)-thiosulfate complex. *Geochim. Cosmochim. Acta.* **2006**, *70*, 3646–3661. [CrossRef]
17. Reith, F.; Etschmann, B.; Grosse, C.; Moors, H.; Benotmane, M.A.; Monsieurs, P.; Grass, G.; Doonan, C.; Vogt, S.; Lai, B.; et al. Mechanisms of gold biomineralization in the bacterium Cupriavidus metallidurans. *Proc. Natl. Acad. Sci. USA* **2009**, *106*, 17757–17762. [CrossRef]
18. Zhmodik, S.M.; Kalinin, Y.A.; Roslyakov, N.A.; Belyanin, D.K.; Nemirovskaya, N.A.; Nesterenko, G.V.; Airiyants, E.V.; Moroz, T.N.; Bul'bak, T.A.; Mironov, A.G.; et al. Nanoparticles of noble metals in the supergene zone. *Geol. Ore Depos.* **2012**, *54*, 141–154. [CrossRef]
19. Fairbrother, L.; Brugger, J.; Shapter, J.; Laird, J.S.; Southam, G.; Reith, F. Supergene gold transformation: Biogenic secondary and nano-particulate gold from arid Australia. *Chem. Geol.* **2012**, *320–321*, 17–31. [CrossRef]
20. Reith, F.; Rea, M.A.D.; Sawley, P.; Zammit, C.M.; Nolze, G.; Reith, T.; Rantanen, K.; Bissett, A. Biogeochemical cycling of gold: Transforming gold particles from arctic Finland. *Chem. Geol.* **2018**, *483*, 511–529. [CrossRef]
21. Sanyal, S.K.; Shuster, J.; Reith, F. Cycling of biogenic elements drives biogeochemical gold cycling. *Earth Sci. Rev.* **2019**, *190*, 131–147. [CrossRef]
22. Rea, M.A.; Shuster, J.; Hoffmann, V.E.; Schade, M.; Bissett, A.; Reith, F. Does the primary deposit affect the biogeochemical transformation of placer gold and associated biofilms? *Gondwana Res.* **2019**, *73*, 77–95. [CrossRef]
23. Boyle, R.W. An occurrence of native gold in an ice lens; gaint-Yellowknife gold mines, Yellowknife, Northwest Territories. *Econ. Geol.* **1951**, *46*, 223–227. [CrossRef]
24. Shvartsev, S.L. A possible mechanism for the formation of native gold in ice lenses. *Bull. Tomsk Polytech. Inst.* **1976**, *289*, 107–109. (In Russian)
25. Reith, F.; Brugger, J.; Zammit, C.M.; Nies, D.H.; Southam, G. Geobiological cycling of gold: From fundamental process understanding to exploration solutions. *Minerals* **2013**, *3*, 367–394. [CrossRef]
26. Sazonov, A.M.; Lobanov, K.V.; Zvyagina, E.A.; Leontiev, S.I.; Silyanov, S.A.; Nekrasova, N.A.; Nekrasov, A.Y.; Borodushkin, A.B.; Poperekov, V.A.; Zhuravlev, V.V.; et al. Olympiada gold deposit, Yenisei Ridge, Russia. *Econ. Geol.* **2020**. In press.
27. Kuzmichev, A.B.; Sklyarov, E.V. The precambrian of transangaria, Yenisei Ridge (Siberia): Neoproterozoic microcontinent, Grenville-age orogen, or reworked margin of the Siberian craton? *J. Asian Earth Sci.* **2016**, *115*, 419–441. [CrossRef]
28. Nozhkin, A.D.; Borisenko, A.S.; Nevol'ko, P.A. Stages of Late Proterozoic magmatism and periods of Au mineralization in the Yenisei Ridge. *Russ. Geol. Geophys.* **2011**, *52*, 124–143. [CrossRef]
29. Novozhilov, Y.I.; Gavrilov, A.M. *Gold-Sulfide Deposits in Carbon-Terrigenous Strata*; TsNIGRI: Moscow, Russia, 1999; 175p. (In Russian)
30. Lee, L.V. *Olimpiadinskoe Deposit of Disseminated Gold-Sulfide Ores*; KNIIGiMS: Krasnoyarsk, Russia, 2003; 120p. (In Russian)
31. Savichev, A.A.; Shevchenko, S.S.; Rozinov, M.I.; Lokhov, K.I.; Prasolov, E.M.; Prilepskiy, E.B.; Kapitonov, I.N.; Matukov, D.I.; Berezhnaya, N.G.; Sergeev, S.A. Isotope-geochemical characteristics of the gold-sulfide deposits of the Olympics and its satellites (Yenisei Ridge). *Reg. Geol. Metallog.* **2006**, *26*, 122–143. (In Russian)
32. Gibsher, N.A.; Sazonov, A.M.; Travin, A.V.; Tomilenko, A.A.; Ponomarchuk, A.V.; Sil'yanov, S.A.; Nekrasova, N.A.; Shaparenko, E.O.; Ryabukha, M.A.; Khomenko, M.O. Age and duration of the formation of the Olimpiadinski gold deposit (Yenisei ridge, Russia). *Geochem. Int.* **2019**, *57*, 593–599. [CrossRef]
33. Gibsher, N.A.; Tomilenko, A.A.; Sazonov, A.V.; Bul'bak, T.A.; Ryabukha, M.A.; Sil'yanov, S.A.; Nekrasova, N.A.; Khomenko, M.O.; Shaparenko, E.O. The Olimpiada gold deposit (Yenisei ridge): Temperature, pressure, composition of ore-forming fluids, $\delta^{34}S$ in sulfides, $^{3}He/^{4}He$ of fluids, Ar-Ar age and duration of deposit formation. *Russ. Geol. Geophys.* **2019**, *9*, 1310–1330. [CrossRef]
34. Sazonov, A.M.; Zvyagina Ye, A.; Silyanov, S.A.; Lobanov, K.V.; Leontyev, S.I.; Kalinin Yu, A.; Savichev, A.A.; Tishin, P.A. Ore genesis of the Olimpiada gold deposit (Yenisei Ridge, Russia). *Geosph. Res.* **2019**, 17–43. [CrossRef]

35. Savichev, A.A.; Gavrilenko, V.V. Gold-sulfide mineralization of the North Yenisei region (Siberia) and the conditions for its formation. *Notes All-Russ. Mineral. Soc.* **2003**, *2*, 15–32. (In Russian)
36. Belyi, A.V.; Chernov, D.V.; Solopova, N.V. Development of BIONORD®technology on Olimpiada deposit refractory arsenic-gold ores treatment in conditions of Extreme North. *Hydrometallurgy* **2018**, *179*, 188–191. [CrossRef]
37. Genkin, A.D.; Bortnikov, N.S.; Cabri, L.J.; Wagner, F.E.; Stanley, C.J.; Safonov, Y.G.; McMahon, G.; Friedl, J.; Kerzin, A.L.; Gamyanin, G.N. A multidisciplinary study of invisible gold in arsenopyrite from four mesothermal gold deposits in Siberia, Russian Federation. *Econ. Geol.* **1998**, *93*, 463–487. [CrossRef]
38. Sazonov, A.M.; Silyanov, S.A.; Bayukov, O.A.; Knyazev, Y.V.; Zvyagina, Y.A.; Tishin, P.A. Composition and ligand microstructure of arsenopyrite from gold ore deposits of the Yenisei Ridge (Eastern Siberia, Russia). *Minerals* **2019**, *9*, 737. [CrossRef]
39. Trigub, A.L.; Tagirov, B.R.; Kvashnina, K.O.; Chareev, A.; Nickolsky, M.S.; Shiryaev, A.A.; Baranova, N.N.; Kovalchuk, E.V.; Mokhov, A.V. X-ray spectroscopy study of the chemical state of "invisible" Au in synthetic minerals in the Fe-As-S system. *Am. Miner.* **2017**, *102*, 1057–1065. [CrossRef]
40. Merkulova, M.; Mathon, O.; Glatzel, P.; Rovezzi, M.; Batanova, V.; Marion, P.; Boiron, M.-C.; Manceau, A. Revealing the chemical form of "invisible" gold in natural arsenian pyrite and arsenopyrite with high energy-resolution X-ray absorption spectroscopy. *ACS Earth Space Chem.* **2019**, *3*, 1905–1914. [CrossRef]
41. Peskov, E.G. *Geological Manifestations of Cold Degassing of the Earth*; SVKNII FEB RAS: Magadan, Russia, 2000; 279p. (In Russian)
42. Yablokova, S.V.; Konovalova, M.S.; Sandomirskaya, S.M. Mineralogy of the gold-bearing weathering crust in the deposits of vein-disseminated sulfide ores in terrigenous-carbonate strata of the Precambrian. *Tr. TSNIGRI* **1986**, *208*, 10–19. (In Russian)
43. Bernatonis, P.V. Oxidation Zone of the Olympiadinsky Vein-Disseminated Gold-Sulfide Deposit. Ph.D. Thesis, Tomsk Polytechnic University, Tomsk, Russia, 1999. (In Russian).
44. Sergeev, N.B. Features of the structure and material composition of the gold-bearing weathering crust (Yenisei ridge). *Weather. Crust* **1991**, *20*, 77–90. (In Russian)
45. Genkin, A.D.; Lopatin, V.A.; Saveliev, R.A.; Safonov, Y.G.; Sergeev, N.B.; Kerzin, A.L.; Tsepin, A.I.; Amshutts, H.; Afanasyeva, Z.B.; Wagner, F.; et al. Gold ores of the Olympiada deposit (Yenisei Ridge. Siberia). *Geol. Ore Depos.* **1994**, *3*, 111–136. (In Russian)
46. Sergeev, N.B.; Zvezdinskaya, L.V.; Sergeeva, V.V. Tungsten containing hydromeit—A new mineral variety from Eastern Siberia. *Rep. RAS.* **1993**, *332*, 99–101. (In Russian)
47. Afanas'eva, Z.B.; Ivanova, G.F.; Raimbault, L.; Miklishanskii, A.Z. Rare-earth geochemistry of rocks and minerals from the olimpiada scheelite-bearing Gold Sulfide Deposit, Yenisei Ridge, Russia. *Geochem. Int.* **1997**, *35*, 155–166.
48. Zvyagina, E.A. Metamorphism and Gold Metallogeny of the Upper Enashimo ore Cluster. Ph.D. Thesis, Siberian Federal University, Krasnoyarsk, Russia, 1989. (In Russian).
49. Sazonov, A.M.; Zvyagina, E.A.; Silyanov, S.A.; Babenkov, D.E. Gold in the Olimpiada mine ore and tailings. *Gorn. Zhurnal.* **2019**, *4*, 54–59. [CrossRef]
50. Roslyakov, N.A. *Geochemistry of Gold in Supergene Zone*; Nauka: Novosibirsk, Russia, 1981; 240p. (In Russian)
51. Palyanova, G.A. Gold and silver minerals in sulfide Ore. *Geol. Ore Depos.* **2020**, *62*, 426–449. [CrossRef]
52. Kalinin, Y.A.; Roslyakov, N.A. Geochemistry of noble, rare and radioactive elements in exogenous ore-forming systems. In *The History of the Development of the Institute of Geology and Geophysics SB (USSR Academy of Sciences and RAS) and Its Scientific Directions*; SS RAS: Novosibirsk, Russia, 2010; pp. 503–511.
53. Craw, D. Water–rock interaction and acid neutralization in a large schist debris dam, Otago, New Zealand. *Chem. Geol.* **2000**, *171*, 17–32. [CrossRef]
54. Chudaeva, V.A.; Chudaev, O.V. Accumulation and fractionation of rare earth elements in surface waters of the Russian Far East under the conditions of natural and anthropogenic anomalies. *Geochem. Int.* **2011**, *49*, 498–524. [CrossRef]
55. Radomskaya, V.I.; Radomskii, S.M.; Kulik, E.N.; Rogulina, L.I.; Shumilova, L.P.; Pavlova, L.M. Geochemical features of rare-earth elements in surface and subsurface waters in the field of the Albynskoe Gold-Bearing Placer, Amur oblast. *Water Resour.* **2017**, *44*, 284–296. [CrossRef]
56. Braun, J.J.; Pagel, M.; Muller, J.P.; Bilong, P.; Michaud, A.; Guillet, B. Cerium anomalies in lateritic profiles. *Geochim. Cosmochim. Acta* **1990**, *51*, 597–605. [CrossRef]
57. Koppi, A.J.; Edis, R.; Field, D.J.; Geering, H.R.; Klessa, D.A.; Cockayne, D.J.H. Rare earth trends and cerium-uranium-manganese association in weathered\rock from Koongarra, Northern Territory, Australia. *Geochim. Cosmochim. Acta.* **1996**, *60*, 1695–1707. [CrossRef]
58. Bau, M. Scavenging of dissolved yttrium and rare earths by precipitating iron oxyhydroxide: Experimental evidence for Ce oxidation, Y-Ho fractionation and lanthanide tetrad effect. *Geochim. Cosmochim. Acta.* **1999**, *63*, 67–77. [CrossRef]
59. Ohta, A.; Kawabe, I. REE(III) adsorption onto Mn dioxide (-MnO_2) and Fe oxyhydroxide: Ce(III) oxidation by δ-MnO_2. *Geochim. Cosmochim. Acta* **2001**, *65*, 695–703. [CrossRef]
60. Seto, M.; Akagi, A. Chemical condition for the appearance of a negative Ce anomaly in stream waters and groundwaters. *Geochem. J.* **2008**, *42*, 371–380. [CrossRef]
61. Moffett, J.W. Microbially mediated cerium oxidation in sea water. *Nature* **1990**, *345*, 421–423. [CrossRef]
62. Akagi, T.; Masuda, A. A simple thermodynamic interpretation of Ce anomaly. *Geochem. J.* **1998**, *32*, 301–314. [CrossRef]
63. Kawabe, I.; Ohta, A.; Ishu, S.; Tokumura, M.; Miyauchi, K. REE portioning between precipitates and weakly acid NaCl solutions: Convex tetrad effect and fractionation of Y and Sc from heavy lanthanides. *Geochem. J.* **1999**, *33*, 167–179. [CrossRef]

64. Elderfield, H.; Upstill-Goddard, R.; Sholkovitz, E.R. The rare earth elements in rivers, estuaries, and coastal seas and their significance to the composition of the ocean waters. *Geochim. Cosmchim. Acta* **1990**, *54*, 971–991. [CrossRef]
65. Reith, F.; Lengke, M.F.; Falconer, D.; Craw, D.; Southam, G. The geomicrobiology of gold. *ISME J.* **2007**, *1*, 567–584. [CrossRef] [PubMed]
66. Radkova, A.B.; Jamieson, H.E.; Campbell, K.M. Antimony mobility during the early stages of stibnite weathering in tailings at the Beaver Brook Sb deposit, Newfoundlend. *J. Appl. Geochem.* **2020**, *115*, 104528. [CrossRef]
67. Shabynin, L.L. On the issue of migration of gold in an aqueous medium in thiosulfate form. *Izv. Tomsk Polytech. Inst.* **1967**, *67*, 67–72. (In Russian)
68. Webster, J.G. The solubility of gold and silver in the system Au–Ag–S–O_2–H_2O at 25 °C and 1 atm. *Geochim. Cosmochim. Acta* **1986**, *50*, 1837–1845. [CrossRef]
69. Stezeryanskii, E.; V'yunov, O.; Omelchuk, A. Determination of the stability constants of gold(I) thiosulfate complexes by differential UV spectroscopy. *J. Solut. Chem.* **2015**, *44*, 1749–1755. [CrossRef]
70. Kerr, G.; Craw, D. Mineralogy and geochemistry of biologically-mediated gold mobilisation and redeposition in a semiarid climate, Southern New Zealand. *Minerals* **2017**, *7*, 147. [CrossRef]
71. Reith, F.; Stewart, L.; Wakelin, S.A. Supergene gold transformation: Secondary and nano-particulate gold from southern New Zealand. *Chem. Geol.* **2012**, *320–321*, 32–45. [CrossRef]
72. Kashefi, K.; Tor, J.M.; Nevin, K.P.; Lovley, D.R. Reductive precipitation of gold by dissimilatory Fe(III)-reducing Bacteria and Archaea. *Appl. Environ. Microbiol.* **2001**, *67*, 3275–3279. [CrossRef] [PubMed]
73. Cohen, D.R.; Waite, T.D. Interaction of aqueous Au species with goethite, smectite and kaolinite. *Geochem.-Explor. Env. A* **2004**, *4*, 279–287. [CrossRef]
74. Ta, C.; Reith, F.; Brugger, J.; Pring, A.; Lenehan, C. Analysis of gold(I/III)-complexes by HPLC-ICP-MS demonstrates gold(III) stability in surface waters. *Environ. SciTech.* **2014**, *48*, 5737–5744. [CrossRef]
75. Ran, Y.; Fu, J.; Rate, A.W.; Gilkes, R.J. Adsorption of Au(I, III) complexes on Fe, Mn oxides and humic acid. *Chem. Geol.* **2002**, *1–2*, 33–49. [CrossRef]
76. Gray, D.J.; Pirlo, M.C. *Hydrogeochemistry of the Tunkillia Gold Prospect, South Australia*; CRC LEME Open File Report 194; CRC LEME: Wembley, Australia, 2005; 109p.
77. Renders, P.; Seward, T. The stability of hydrosulphido- and sulphido-complexes of Au(I) and Ag(I) at 25 °C. *Geochim. Cosmochim. Acta* **1989**, *53*, 245–253. [CrossRef]
78. Pal'yanova, G. Physicochemical modeling of the coupled behavior of gold and silver in hydrothermal processes: Gold fineness, Au/Ag ratios and their possible implications. *Chem. Geol.* **2008**, *255*, 399–413. [CrossRef]
79. Schofield, E.J.; Ingham, B.; Turnbull, A.; Toney, M.F.; Ryan, M.P. Strain development in nanoporous metallic foils formed by dealloying. *Appl. Phys. Lett.* **2008**, *92*, 043118. [CrossRef]
80. Makovicky, E.; Chovan, M.; Bakos, F. The stibian mustard gold from the Kriván Au deposit, Tatry Mts., Slovak Republic. *N. Jb. Miner. Abh.* **2007**, *184*, 207–215. [CrossRef]
81. Tolstykh, N.D.; Palyanova, G.A.; Bobrova, O.V.; Sidorov, E.G. Mustard gold of the gaching Ore deposit (Maletoyvayam Ore Field, Kamchatka, Russia). *Minerals* **2019**, *9*, 489. [CrossRef]
82. Kalinin, A.A.; Savchenko, Y.E.; Selivanova, E.A. Mustard gold in the oleninskoe gold deposit, Kolmozero–Voronya Greenstone Belt, Kola Peninsula, Russia. *Minerals* **2019**, *9*, 786. [CrossRef]
83. Anisimova, G.S.; Kondratieva, L.A.; Kardashevskaia, V.N. Characteristics of supergene gold of Karst Cavities of the Khokhoy Gold Ore Field (Aldan Shield, East Russia). *Minerals* **2020**, *10*, 139. [CrossRef]
84. Zhao, J.; Bruger, J.; Gundler, P.V.; Xia, F.; Chen, G.; Pring, A. Mechanism and kinetics of a mineral transformation under hydrothermal conditions: Calaverite to metallic gold. *Am. Miner.* **2009**, *94*, 1541–1555. [CrossRef]
85. Okrugin, V.M.; Andreeva, E.; Etschmann, B.; Pring, A.; Li, K.; Zhao, J.; Gri_ths, G.; Lumpkin, G.R.; Triani, G.; Brugger, J. Microporous gold: Comparison of textures from nature and experiments. *Am. Mineral.* **2014**, *99*, 1171–1174. [CrossRef]
86. Storozhenko, A.A.; Vasiliev, N.F.; Diner, A.E.; Pimanov, A.V.; Trofimov, Y.P.; Gursky, Y.I.; Pimanova, G.P.; Kiseleva, E.A.; Borodushkin, A.B. *State Geological Map of the Russian Federation on a Scale of 1: 200 000*, 2nd ed.; Series Yenisei. Sheet O-46-III. Explanatory Letter; Cartographic Factory VSEGEI: St. Petersburg, Russia, 2002; 125p. (In Russian)
87. Sazonov, A.M.; Gertner, I.F.; Zvyagina, E.A.; Tishin, P.A.; Poleva, T.V.; Leontyev, S.I.; Kolmakov, Y.V.; Krasnova, T.S. Ore-forming conditions of the Blagodat Gold Deposit in the Riphean Metamorphic Rocks of the Yenisey Ridge according to geochemical and isotopic data. *J. Sib. Fed. Univ. Eng. Technol.* **2009**, *2*, 203–220. (In Russian)
88. Goleva, G.A.; Krivenkov, V.A.; Gudz, Z.G. Geochemical regularities of the distribution and forms of migration of gold in natural waters. *Geokhimiya* **1970**, *6*, 744–757. (In Russian)
89. Ong, H.L.; Swanson, V.E. Natural organic acids in the transportation, deposition, and concentration of gold. *Q. Colo. Sch. Mines.* **1969**, *64*, 395–425.

minerals

MDPI

Article

The Features of Native Gold in Ore-Bearing Breccias with Realgar-Orpiment Cement of the Vorontsovskoe Deposit (Northern Urals, Russia)

Sergey Y. Stepanov [1], Roman S. Palamarchuk [2,*], Dmitry A. Varlamov [3], Darya V. Kiseleva [1], Ludmila N. Sharpyonok [4], Radek Škoda [5] and Anatoly V. Kasatkin [6]

[1] The Zavaritsky Institute of Geology and Geochemistry UB RAS, Akademika Vonsovskogo Str. 15, 620016 Ekaterinburg, Russia; Stepanov-1@yandex.ru (S.Y.S.); podarenka@mail.ru (D.V.K.)
[2] South Urals Federal Research Center of Mineralogy and Geoecology UB RAS, Territory of the Ilmeny State Reserve, 456317 Miass, Russia
[3] Institute of Experimental Mineralogy RAS, Academika Osypyana Str. 4, 142432 Chernogolovka, Russia; dima@iem.ac.ru
[4] All-Russian Geological Institute Named after A.P. Karpinsky, Sredny Prospect 74, 199106 Saint Petersburg, Russia; lyudmila_sharpenok@vsegei.ru
[5] Department of Geological Sciences, Faculty of Science, Masaryk University, 602 00 Brno, Czech Republic; rskoda@sci.muni.cz
[6] Fersman Mineralogical Museum of the Russian Academy of Sciences, Leninskiy Prospekt 18/2, 119071 Moscow, Russia; anatoly.kasatkin@gmail.com
* Correspondence: palamarchuk22@yandex.ru; Tel.: +7-(981)-979-9395

Abstract: This paper describes native gold in ore-bearing breccias with realgar-orpiment cement from the Vorontsovskoe gold deposit (Northern Urals, Russia). Particular attention is paid to the morphological features of native gold and its relation to other minerals. The latter include both common (orpiment, barite, pyrite, prehnite, realgar) and rare species (Tl and Hg sulfosalts, such as boscardinite, dalnegroite, écrinsite, gillulyite, parapierrotite, routhierite, sicherite, vrbaite, etc.). The general geological and geochemical patterns of the Turyinsk-Auerbakh metallogenic province, including the presence of small non-economic copper porphyry deposits and general trend in change of the composition of native gold (an increase in the fineness of gold from high-temperature skarns to low-temperature realgar-orpiment breccias) confirm that the Vorontsovskoe deposit is an integral part of a large ore-magmatic system genetically associated with the formation of the Auerbakh intrusion.

Keywords: native gold; fluid-explosive breccia; Vorontsovskoe gold deposit; Northern Urals; Turyinsk-Auerbakh metallogenic province; Vorontsovsko-Peshchanskaya porphyry system; rare Tl and Hg sulfosalts

Citation: Stepanov, S.Y.; Palamarchuk, R.S.; Varlamov, D.A.; Kiseleva, D.V.; Sharpyonok, L.N.; Škoda, R.; Kasatkin, A.V. The Features of Native Gold in Ore-Bearing Breccias with Realgar-Orpiment Cement of the Vorontsovskoe Deposit (Northern Urals, Russia). *Minerals* **2021**, *11*, 541. https://doi.org/10.3390/min11050541

Academic Editors: David Banks and Panagiotis Voudouris

Received: 10 March 2021
Accepted: 13 May 2021
Published: 19 May 2021

1. Introduction

The Vorontsovskoe gold deposit is located in Krasnoturyinskiy district of Sverdlovsk Oblast (Northern Urals, Russia), 13 km south of the town of Krasnoturyinsk and approximately 310 km north of Ekaterinburg. It was discovered in 1985 and is currently operated by the Polymetal International PLC. It is located within the Turyinsk-Auerbakh metallogenic province (Figure 1a), which includes a series of medium-size copper-iron-skarn and small-size gold skarn, medium-size lode and quartz stockwork gold deposits with "berezite" (quartz-sericite-carbonate metasomatites) alteration gold deposits. The ore district combines two magmatic-hydrothermal systems [1]: Vorontsovsko-Peshchanskaya and Turyinskaya (D_{1-2}). Within the Vorontsovsko-Peshchanskaya system, mainly iron-skarn and gold ore deposits are located. The Turyinskaya system includes a number of medium-size copper-skarn deposits [2] and small-size porphyry copper deposits. By 2003, three economic deposits with calculated reserves were discovered within the Turyinsk-Auerbakh

metallogenic province (Figure 1b): Peshchanskoe iron skarn deposit (approximately 80 million tons of iron); Vorontsovskoe gold deposit (approximately 30 tons of gold, including the off-balance reserves); and the small gold and medium copper Vadimo-Aleksandrovskoe deposit (approximately 6 million tons of copper, including the off-balance reserves and approximately 1 ton of gold) [3].

Some researchers [1] consider the Vorontsovskoe gold deposit to be a peripheral zone of the porphyry copper system. Naumov et al. [4] also classifies this deposit as magmatic-hydrothermal type. Numerous authors [5–8] attribute the Vorontsovskoe gold ore deposit to the Carlin type. Despite such a comprehensive study of the Vorontsovskoe gold deposit, it has not yet been possible to unambiguously resolve the issue of its genesis.

Several types of ores associated with various types of alteration have been identified within the Vorontsovskoe deposit, such as calcareous gold-magnetite-sulfide skarns, quartz-sericite, jasperoids and other alteration types [5,6], supergene alterations [6] as well as gold-pyrite-realgar breccias [9]. We also confirm the assessment of the scale of distribution of various types of ores and their gold content within the Vorontsovskoe deposit and show the leading economic value of gold-ore breccias with orpiment-realgar cement [9,10]. In addition, native gold in this breccia ore type associates with thallium and mercury sulfosalts, that distinguishes the gold mineralization of the Vorontsovskoe deposit from all previously known gold ore localities in Russia. The ore-bearing role of breccias in many deposits is very important [11]. Despite such an important role of the gold breccias of the Vorontsovskoe deposit, the morphological features and composition of their gold have not yet been studied. The aim of our work-detailed characterization of gold from breccias with realgar-orpiment cement.

2. Geological Setting

2.1. Regional Geological Setting

The Vorontsovskoe gold deposit is located on the eastern slope of the Northern Urals in the eastern part of the Tagil volcanic megazone (Figure 1a). It is located within the North-striking Devonian volcanic belt [5,6]. The Middle Devonian Auerbakh gabbro-diorite-granodiorite intrusion is located in the southern part of the belt [12], and is associated with the formation of the Turyinsk-Auerbakh metallogenic province [1].

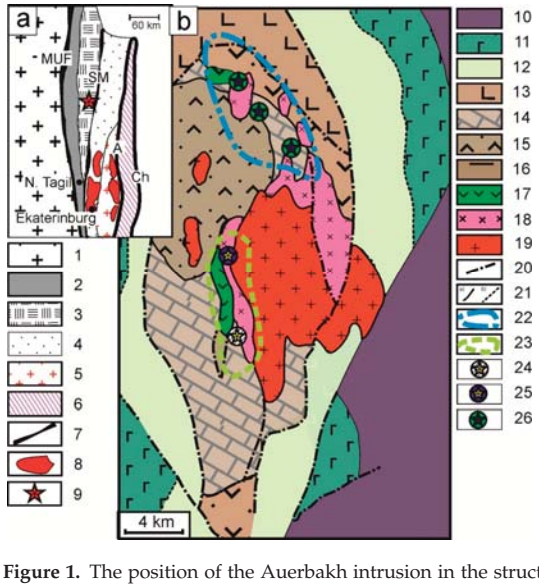

Figure 1. The position of the Auerbakh intrusion in the structures of the Urals (a) and geological scheme of the structure of the Turyinsk-Auerbakh metallogenic province (b). (**a**): 1—the passive margin

of the western slope of the Urals; 2—the platinum belt of Tagil megazone; 3—Tagil volcanic zone; the zones of the active continental margin: 4—Devonian-Carboniferous; 5—continental; 6—northern; 7—tectonic sutures separating large structures of the Urals: the Main Uralian Fault (MUF), Serovsko-Mauksky (SM), Alapaevsky (A), Chelyabinsky (Ch). Plutonic massifs: 8—granite; 9—Auerbakh gabbro-diorite-granite (after [13]). (**b**): 10—Ordovician rocks of ophiolitic association; 11—basalt-rhyolite-plagiogranite association, Ordovician; 12—Silurian trachybasalt-trachyte; Devonian formations: 13—volcanic-sedimentary rocks with intercalations of andesites, andesite-basalts and limestones; 14—reef limestone; 15—volcanomictic rocks with tuff horizons of andesites and andesidacites; 16—andesibasalts; 17—extrusive andesites. Igneous rocks of the Auerbakh Intrusion: 18—porphyritic diorites and gabbro-diorites; 19—quartz diorites, granodiorites and granites; other designations: 20—faults; 21—rock contacts: a) sharp; b) gradual; 22—Turyinskaya ore-magmatic system; 23—Vorontsovsko-Peshchanskaya ore-magmatic system; Deposits: 24—Vorontsovskoe gold ore deposit; 25—Peshchanskoe iron ore deposit; 26—copper-skarn deposit (after [1]).

The Vorontsovsko-Peshchanskaya hydrothermal system is located at the southwestern outer contact of the Auerbakh intrusion [1]. The Vorontsovskoe deposit is located in the southern part of this system, at a distance of 400–500 m from the southwestern exocontact of the Auerbakh massif (Figure 1b) [7]. The volcanic-sedimentary rocks hosting the deposit form a monocline that gently dips to the west [6]. The sedimentary sequence includes limestones and layers of tuffites and siltstones with a thickness of approximately 1 km. Usually, the limestone is metamorphosed to marbles. This sequence is conformably overlain subsequently by volcanic-sedimentary and volcanic rocks, such as tuffaceous siltstone, tuffite and tuff. Coarse clastic breccias with tuffaceous cement are common at the contact of all these rocks with limestones within the entire Turyinsk-Auerbakh metallogenic province [14].

2.2. Local Geological Setting

A quarry in the Vorontsovskoe deposit has exposed a wedge body of volcano-sedimentary rocks with a predominance of tuffs of medium composition and tuffstones (Figure 2a). The western part of this body is bounded by a large tectonic fault (Figure 2b). The bulk of ore-bearing breccia, including realgar-orpiment cement, is located at the contact of the body of volcano-sedimentary rocks with limestones. The gold ore body has the form of a torch that expands outward the top [15]. Within this body, gold mineralization is localized mainly in breccias. Part of the gold mineralization is associated with metasomatically sericite-altered volcanic-sedimentary rocks.

Two stages of ore breccia formation were previously identified earlier [9]. The breccias of the first stage are quite widespread. Limestone fragments predominate in this type of breccias. These fragments are embedded in a matrix consisting of small fragments of volcanic-sedimentary rocks dominated by andesite [16,17]. Pyrite grains with an average size of 0.2 mm are widely distributed in the cement. The breccias of the second stage form a pod-like body of irregular shape (Figure 2c). Limestones, volcanogenic sedimentary rocks and siltstones are found as fragments in breccias of the second stage. First-stage breccias are also found in the wreckage. Realgar and orpiment are widely distributed in breccia cement of the second stage. Barite, quartz and calcite make up a significant part of the cement. Native gold and rare Hg and Tl sulfosalts are common in breccia cement of the second stage. The highest content of realgar and orpiment is typical for the central parts of pod-like bodies of the second stage breccias.

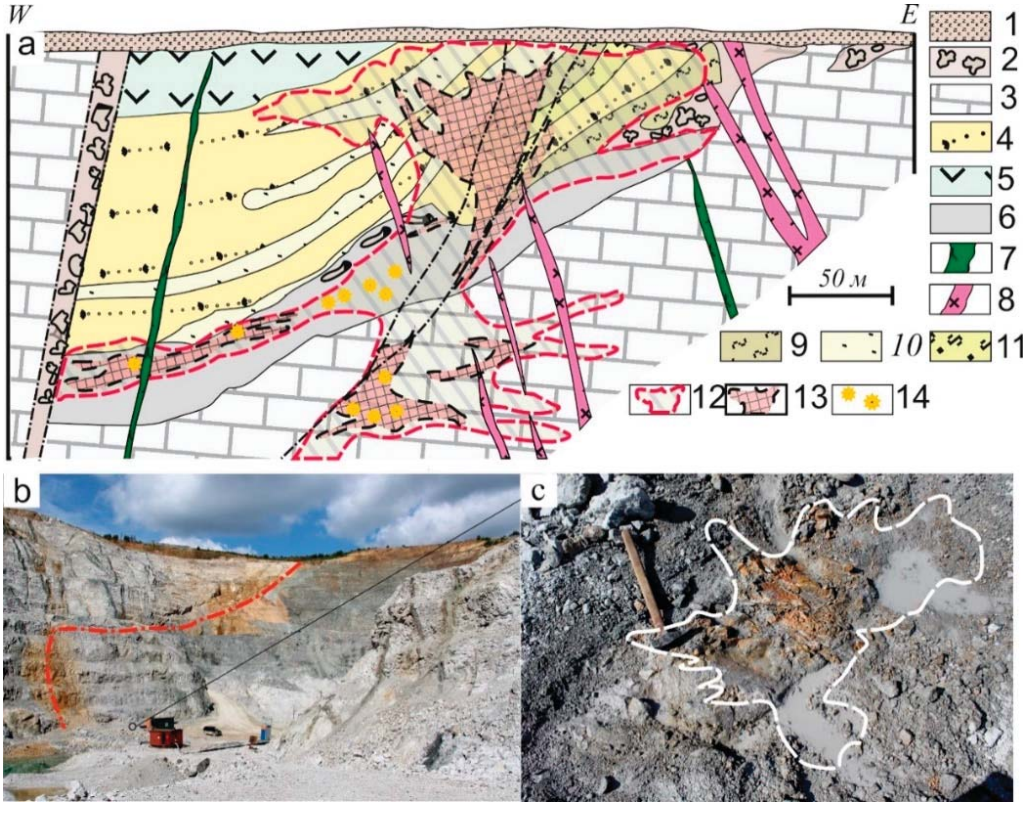

Figure 2. (**a**) Schematic section of the Vorontsovskoe deposit [15–17]; (**b**) the photograph of the northern wall of the quarry with a tectonic contact between marmorized limestone and a layer of volcanic-sedimentary rocks (red dotted line); (**c**) a small body of fluid-explosive breccias with realgar-orpiment cement (sample 2016/2), exposed in one of the quarry layers. The white dotted line shows the boundary of the body. 1—Neogene-Quaternary cover deposits; 2—karst formations; Devonian formations: 3—limestones; 4—tuff aleurolites, tuffstones, tuff-conglomerates; 5—andesites, tuffs and lava breccias; 6—breccia of the 1st stage of breccia formation; 7—lamprophyre dikes; 8—dikes of diorite porphyrites. Metasomatites: 9—quartz-sericite, 10—quartz-sericite-albite, 11—berezite-listvenites, chlorite-sericites. 12—ore bodies with run-of-mine grades of gold content; 13—enriched ore pillars; 14—manifestation areas of realgar-orpiment mineralization.

3. Materials and Methods

3.1. Sample Collection and Preparation

A total of 173 ore samples were taken within the ore body to study the distribution of gold. Of these, 58 specimens were from ore breccias with realgar-orpiment cement. These samples were collected in 2016–2019 at the Northern quarry of the Vorontsovskoe deposit at horizons from –40 to +35 (meters above sea level) from 2016 to 2019 (Figure 3). The weight of ore samples ranged from 0.2 to 0.4 kg.

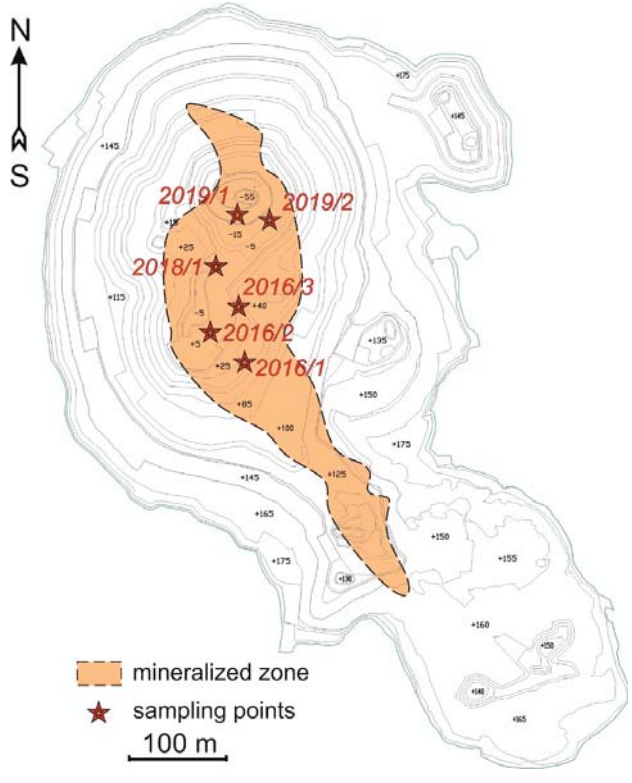

Figure 3. Location of sampling at the Northern quarry of Vorontsovsky deposit. First, digit means the year of collecting, second—the number of sampling point.

To obtain native gold concentrates, two large samples weighing 35 kg were taken from areas richest in realgar and orpiment breccia fragments. The samples were crushed to a fraction of less than 1 mm and enriched with a KR-400 centrifugal concentrator. Grains and crystals of native gold were manually selected using a binocular microscope. Their surface structure details were studied by scanning electron microscopy. Then, the grains of native gold were mounted in polished sections in order to study their internal structure and determine their chemical composition.

3.2. Analytical Methods

Polished and thin sections were made for microscopic examination. After a preliminary description using an optical microscope under transmitted and reflected light, detailed studies of thin sections with native gold using a scanning electron microscope were carried out. The chemical compositions of minerals were identified by an electron microprobe using both energy and wavelength dispersive spectrometers.

A preliminary semi-quantitative analysis of the chemical composition was performed in the Fersman Mineralogical Museum of the Russian Academy of Sciences (Moscow, Russia) using a CamScan 4D scanning electron microscope (CamScan Electron Optics, Ltd, Cambridge, UK) and in the Institute of Experimental Mineralogy RAS (Chernogolovka, Russia) using a CamScan MV2300 scanning electron microscope. In both cases, INCA Energy 350 energy dispersive spectrometers (Tescan, Brno, Czech Republic) were used under the following operational conditions: accelerating voltage—20 kV, probe current—5 nA on metallic cobalt, working distance 25 mm, spectra accumulation time—70 s, spot size 5 μm.

Further study of the mineral chemical composition was carried out in the joint laboratory of electron microscopy and microanalysis of the Department of Geological Sciences of the Masaryk University and the Czech Geological Survey (Brno, Czech Republic) using a Cameca SX 100 wave dispersive electron probe microanalyzer (Cameca, Paris, France) and in the laboratory of the Department of Mineralogy of the Geological Faculty of Moscow State University (Moscow, Russia) using the Camebax SX 50 microanalyzer (Cameca, Paris, France). In the first case, the following operational conditions were applied: accelerating voltage—25 kV, probe current—20 nA, probe diameter—1 μm; reference materials (natural): Fe—FeS_2; Cu—Cu metal; Zn— ZnS; Ag—Ag metal; Hg—HgTe; Tl—Tl (Br, I); Pb and Se—PbSe; As—pararammelsbergite; Sb—Sb; S—chalcopyrite. In the second case, the operational conditions were as follows: accelerating voltage—20 kV, probe current—30 nA, probe diameter—1 μm. The following reference materials were used (natural): Zn—ZnS, As—CoAsS, S, Fe—FeS (troilite), Ag—Ag_2Te, Cu, Sb—$CuSbS_2$, Hg—HgTe, Tl—$TlSbSe_2$, Pb—PbS.

4. Results

4.1. Mineral Composition of the Breccias

The gold-bearing breccias of the second brecciation event consist of marmorized limestone, tuffstones, tuffites and andesite tuffs fragments and contain fragments of individual grains of minerals from these rocks embedded in the hydrothermal cement (manganoan calcite, prehnite, orthoclase and other). Rock fragments have an angular shape (Figure 4) and vary in size from one millimeter to several centimeters. The quantitative ratio of the matrix and lithoclasts in breccias is not constant and varies from 15 to 75%. The breccias are altered to varying degrees. In the breccia matrix, thin (less than 1 mm) fragments of the main rock-forming minerals are widespread: chlorite (clinochlore and chamosite), amphibole (magnesio-ferri-hornblende, tremolite, pargasite), scapolite, quartz, feldspars (orthoclase, microcline, albite) and calcite. However, newly formed minerals predominate, forming the cement of ore breccias.

The most common hydrothermal gangue minerals of breccia cement are manganoan calcite, prehnite, orthoclase var. hyalophane, fluorapatite and barite. Prehnite forms small, idiomorphic prismatic crystals or granular masses cemented by ore minerals—pyrite, realgar, stibnite, aktashite, boscardinite, parapierrotite, routhierite and chabournéite (Figure 5a,b,d,e). Orthoclase var. hyalophane forms intergrowths with prehnite granular aggregates (Figure 5b), or, more rarely, single prismatic crystals. Fluorapatite is found as rare prismatic crystals included in the aggregates of other minerals (Figure 5b). Barite and manganoan calcite form only fine-grained masses (Figure 5c). Gangue minerals are intergrown mainly with realgar (Figure 5b,d,e) and less often with orpiment.

Stibnite (Figure 5d), orpiment, realgar (Figure 5b,d,e) and pyrite (Figure 5a,b,d,e) prevail among the ore minerals in the breccia cement. Pyrite forms idiomorphic pentagonal dodecahedra and often contains up to 4 wt.% As in its structure. Rare Tl- and Hg-bearing sulfosalts, sulfides and tellurides are found among the ore cement minerals and include aktashite, bernardite, boscardinite, weissbergite, vrbaite, gillulyite, dalnegroite, sicherite, imhofite, coloradoite, christite, laffittite, lorándite, parapierrotite, picotpaulite, rebulite, routhierite, philrothite, hutchinsonite, chabournéite, écrinsite, etc. (full list of minerals identified at Vorontsovskoe deposit including rare Tl-Hg-bearing ones is given by [16–18]). These ore minerals were formed later than most gangue minerals. Thus, aktashite and boscardinite cement prehnite crystals (Figure 5a,b), parapierrotite replaces stibnite (Figure 5d), routhierite cements individual prehnite and diopside crystals (Figure 5d) and chabournéite fills veinlets intersecting silicates and realgar (Figure 5c,e). The chemical composition of selected rare Tl and Hg minerals mentioned above is given in Table 1.

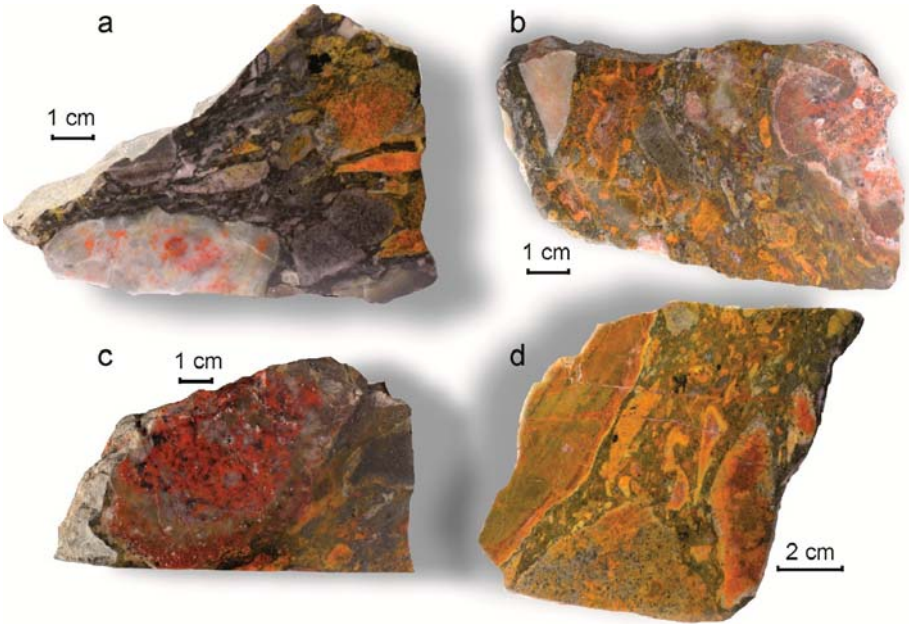

Figure 4. The varieties of gold ore breccias in the Vorontsovskoe deposit: (**a**) with a predominance of tuffstone and a small amount of orpiment-realgar cement in the fragments; (**b**) with a relatively equal amount of fragments of tuffstones (strongly altered) and marmorized limestones with a moderate amount of orpiment-realgar cement; (**c**) with equal amounts of fragments of tuffstones and marmorized limestones and a prevalence of realgar cement (black points are the accumulations of Tl and Hg sulfides and sulfosalts); (**d**) with a prevalence of metasomatically transformed tuffstones with a significant amount of orpiment-realgar cement.

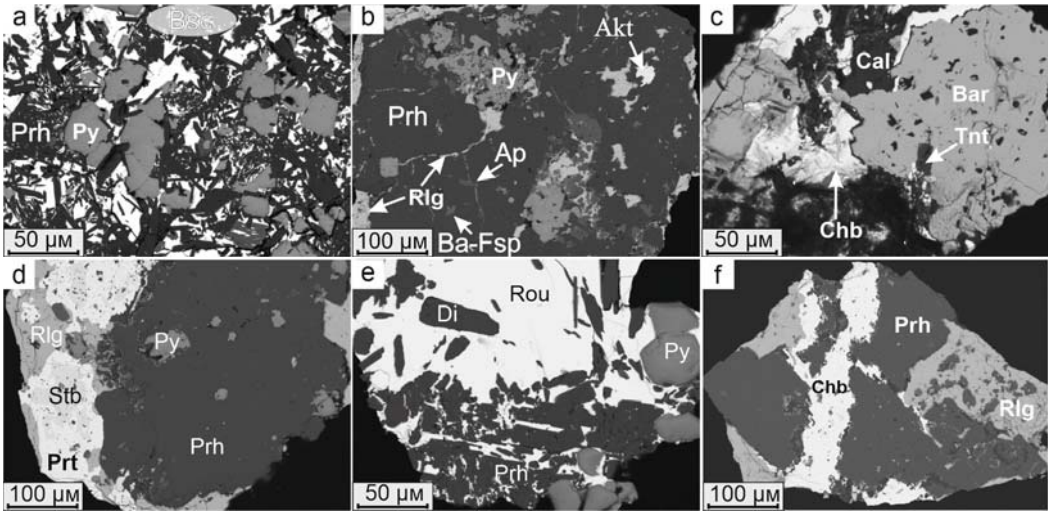

Figure 5. Gangue minerals from gold ore breccia cement. (**a**) The relationship of pyrite (Py) with boscardinite (Bsc) and prehnite (Prh); (**b**) aktashite (Akt) grain in hyalophane (Ba-Fsp); (**c**) the relationship of chabournéite (Chb) with calcite (Cal) and barite (Bar); (**d**) parapierrotite (Prt) and stibnite (Stb) with large prehnite grain; (**e**) routhierite (Rou) cements individual prehnite and diopside (Di) crystals; (**f**) prehnite in realgar-chabournéite cement. Ap—fluorapatite, Tnt—tennantite.

Table 1. The chemical compositions of Tl and Hg sulfosalts from the cement of gold ore breccias, wt. %.

№	Fe	Cu	Ag	Hg	Tl	Pb	As	Sb	S	Total	Mineral
1	1.58	25.48	-	24.29	-	-	19.80	0.49	25.45	99.85	Aktashite
2	-	-	-	-	21.40	0.13	25.32	25.39	27.98	100.22	Bernardite
3	-	-	2.01	-	12.60	17.82	12.19	30.86	24.22	99.70	Boscardinite
4	-	-	-	-	53.46	-	5.17	24.73	16.80	100.16	Weissbergite
5	-	-	-	20.42	28.52	-	20.61	8.57	22.32	100.44	Vrbaite
6	-	-	-	-	29.49	0.19	40.02	1.73	29.52	100.95	Gillulyite
7	-	-	-	-	19.20	9.99	21.04	23.43	25.82	99.48	Dalnegroite
8	0.10	-	23.83	-	22.63	0.22	16.71	13.69	21.61	98.79	Sicherite
9	-	-	-	-	36.30	-	30.02	8.43	25.37	100.12	Imhofite
10	-	-	-	34.50	35.73	-	12.62	-	16.40	99.25	Christite
11	-	-	23.10	40.90	-	-	15.95	-	20.16	100.11	Laffittite
12	-	-	-	-	58.49	0.42	20.57	0.45	19.37	99.30	Lorándite
13	-	-	-	-	20.10	-	8.61	46.08	25.17	99.96	Parapierrotite
14	27.21	-	-	-	49.29	-	-	-	23.86	100.36	Picotpaulite
15	-	-	-	-	34.80	0.36	22.98	16.82	22.23	99.19	Rebulite
16	-	5.92	0.25	38.87	19.21	-	13.97	1.72	19.03	99.48 [1]	Routhierite
17	-	-	-	-	33.17	0.59	34.40	3.94	27.06	99.16	Philrothite
18	-	-	-	-	19.14	18.68	31.25	4.73	26.54	100.34	Hutchinsonite
19	-	-	-	-	17.47	10.96	13.86	32.89	24.85	100.03	Chabournéite
20	0.25	-	1.55	-	8.72	26.04	17.84	20.78	24.28	99.62 [2]	Ecrinsite

№	APFU	Empirical Formulae	Mineral
1	25	$Cu_{6.06}(Hg_{1.83}Zn_{0.64}Fe_{0.43})_{\Sigma 2.90}(As_{3.99}Sb_{0.06})_{\Sigma 4.05}S_{11.99}$	Aktashite
2	14	$Tl_{0.96}Pb_{0.01}(As_{3.10}Sb_{1.92})_{\Sigma 5.02}S_{8.01}$	Bernardite
3	64	$Ag_{0.89}Tl_{2.95}Pb_{4.11}(Sb_{12.12}As_{7.78})_{\Sigma 19.90}S_{36.14}$	Boscardinite
4	4	$Tl_{0.99}(Sb_{0.77}As_{0.26})_{\Sigma 1.03}S_{1.98}$	Weissbergite
5	37	$Hg_{2.94}Tl_{4.02}As_{7.93}Sb_{2.03}S_{20.08}$	Vrbaite
6	22.8	$Tl_{2.04}Pb_{0.01}(As_{7.54}Sb_{0.21})_{\Sigma 7.75}S_{13.00}$	Gillulyite
7	60	$Tl_{3.97}Pb_{2.04}(As_{11.86}Sb_{8.13})_{\Sigma 19.99}S_{34.01}$	Dalnegroite
8	12	$Tl_{0.99}Pb_{0.01}(Ag_{1.97}Fe_{0.02})_{\Sigma 1.99}(As_{1.99}Sb_{1.00})_{\Sigma 2.99}S_{6.02}$	Sicherite
9	47.2	$Tl_{5.83}(As_{13.14}Sb_{2.27})_{\Sigma 15.41}S_{25.96}$	Imhofite
10	6	$Tl_{1.02}Hg_{1.01}As_{0.98}S_{2.99}$	Christite
11	6	$Ag_{1.02}Hg_{0.97}As_{1.01}S_{2.99}$	Laffittite
12	4	$Tl_{0.98}Pb_{0.01}(As_{0.94}Sb_{0.01})_{\Sigma 0.95}S_{2.06}$	Lorándite
13	14	$Tl_{1.00}(Sb_{3.85}As_{1.17})_{\Sigma 5.02}S_{7.98}$	Parapierrotite
14	6	$Tl_{0.98}Fe_{1.99}S_{3.03}$	Picotpaulite
15	40	$Tl_{4.96}Pb_{0.05}(As_{8.94}Sb_{4.03})_{\Sigma 12.97}S_{22.02}$	Rebulite
16	12	$(Cu_{0.94}Ag_{0.02})_{\Sigma 0.96}(Hg_{1.96}Zn_{0.08})_{\Sigma 2.04}Tl_{0.95}(As_{1.89}Sb_{0.14})_{\Sigma 2.03}S_{6.01}$	Routhierite
17	9	$Tl_{0.97}Pb_{0.02}(As_{2.75}Sb_{0.19})_{\Sigma 2.94}S_{5.06}$	Philrothite
18	16	$Tl_{1.02}Pb_{0.98}(As_{4.55}Sb_{0.42})_{\Sigma 4.97}S_{9.03}$	Hutchinsonite
19	60	$Tl_{3.75}Pb_{2.32}(Sb_{11.84}As_{8.11})_{\Sigma 19.95}S_{33.98}$	Chabournéite
20	64	$Ag_{0.68}Fe_{0.21}Tl_{2.01}Pb_{5.93}(As_{11.24}Sb_{8.06})_{\Sigma 19.30}(S_{35.76}Se_{0.10})_{\Sigma 35.86}$	Ecrinsite

Notes: [1] the total includes 0.51 wt.% of Zn; [2] the total includes 0.16 wt.% of Se.

4.2. Morphological Features of Native Gold in Breccias

Native gold in the breccias occurs both in cement (Figure 6a) and in the limestone's fragments. The analysis of ore concentrates obtained during the gravitational concentration of gold breccias with realgar-orpiment cement has made it possible to establish that the grains of 0.1–0.25 mm prevail among the gravitationally enriched aggregate of gold. However, the study of thin sections has revealed the predominance of gold grains less than 0.1 mm in size. Thus, most of the native gold grains (75% of all grains) are 20–80 μm in size. Large grains of native gold (0.2 to 0.8 mm) are quite rare. These grains occur as complex intergrowths of gold with realgar, orpiment and calcite (Figure 6b,c).

The study of thin sections from breccias allowed us to confirm the conclusion that most of the native gold is located directly in the breccias' cement. Gold grains intergrow with orpiment and realgar (Figure 7a,b). Gold grains with prismatic cross-sections are extremely rare and are located directly in the fragments of marmorized limestones

(Figure 7c). Gold crystals are relatively rare among the gold grains from the ore concentrates too (Figure 8a). They are characterized by a complex faceting with a combination of octahedron, pentagonal dodecahedron and cubic faces, which leads to the occurrence of spherical shape of the crystals.

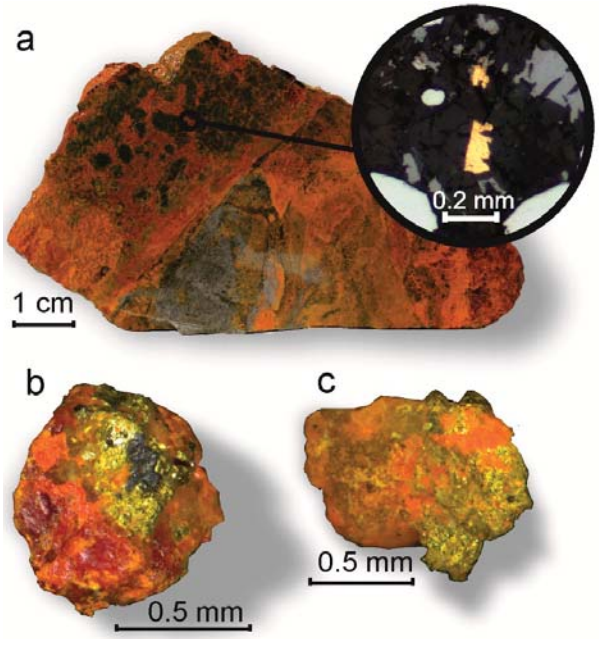

Figure 6. Native gold occurrences in ore breccias: (**a**) gold realgar-orpiment breccia with small pyrite grains and native gold, (**b**) native gold with realgar, (**c**) native gold with orpiment and calcite.

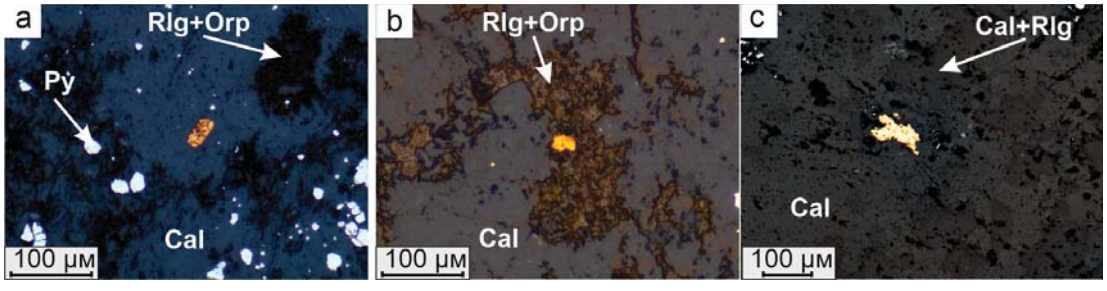

Figure 7. Optical photo of the native gold in realgar-orpiment breccias of the Vorontsovskoe deposit: (**a**) gold grain and pyrite (Py) in calcite; (**b**) the grain of gold in realgar-orpiment (Rlg + Orp) breccia cement; (**c**) gold in brecciated calcite marble; Cal + Rlg—the fine-crystalline calcite and realgar.

Gold grains cementing other minerals are most widely distributed (Figure 8b–e). Often, native gold in such aggregates intergrows with realgar, pyrite and calcite.

Native gold contains numerous mineral inclusions. Small crystals of pyrite, prehnite, quartz and calcite are directly enclosed in the native gold. Polymineral inclusions, consisting of calcite, barite and dalnegroite, are found in gold aggregates as well (Figure 9a). Polymineral inclusions formed by prehnite, barite and routhierite are also detected (Figure 9b). Hyalophane grains are present as inclusions in gold in a very limited quantity. The above-listed minerals can be found not only in the form of inclusions in gold but also as in-

tergrowths with gold. Among the rare minerals intergrown with gold, we also note coloradoite, arsenolite (Figure 9c) and parapierrotite (Figure 9d). Arsenolite is the most recent mineral formed as a result of supergene processes.

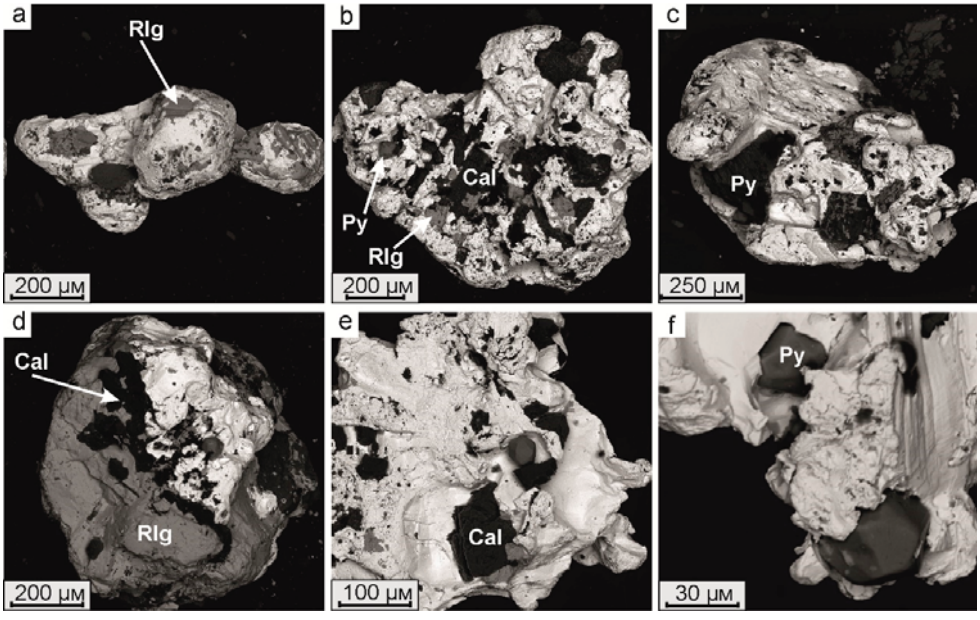

Figure 8. BSE-photo of the morphology of native gold grains and aggregates from breccias with orpiment-realgar cement (explained in the text). (**a**) gold crystal; (**b**) gold with mineral inclusions of calcite (Cal), pyrite (Py) and realgar (Rlg); (**c**) native gold intergrows with pyrite; (**d**) native gold intergrows with realgar; (**e**) native gold intergrows with calcite; (**f**) pyrite crystals in native gold.

Table 2. The chemical composition of minerals intergrown with native gold, wt. %.

№	S	Fe	Cu	As	Sb	Hg	Tl	Pb	Total	Mineral
1	27.41	–	–	31.46	10.15	–	20.87	10.36	100.25	Dalnegroite
2	27.45	–	–	31.50	10.31	–	20.80	10.37	100.43	Dalnegroite
3	27.59	–	–	31.63	10.52	–	20.55	10.45	100.74	Dalnegroite
4 [1]	19.26	0.09	6.18	14.55	0.45	36.88	21.33	–	99.86	Routhierite
5 [2]	19.28	0.12	6.23	14.65	0.53	36.79	21.18	–	99.87	Routhierite
6 [3]	–	–	–	–	–	60.53	–	–	100.48	Coloradoite
7	51.22	43.70	0.10	3.93	–	–	–	–	98.95	Pyrite
8	24.66	–	–	4.13	51.12	–	20.40	–	101.31	Parapierrotite

№	APFU	Empirical Formulae	Mineral
1	60	$Tl_{4.06}Pb_{1.99}(As_{16.68}Sb_{3.31})_{\Sigma 19.99}S_{33.96}$	Dalnegroite
2	60	$Tl_{4.04}Pb_{1.98}(As_{16.67}Sb_{3.36})_{\Sigma 20.03}S_{33.95}$	Dalnegroite
3	60	$Tl_{3.97}Pb_{1.99}(As_{16.66}Sb_{3.41})_{\Sigma 20.07}S_{33.97}$	Dalnegroite
4	12	$Cu_{0.97}(Hg_{1.83}Zn_{0.17}Fe_{0.02})_{\Sigma 2.02}Tl_{1.04}(As_{1.94}Sb_{0.04})_{\Sigma 1.98}S_{5.99}$	Routhierite
5	12	$Cu_{0.98}(Hg_{1.83}Zn_{0.17}Fe_{0.02})_{\Sigma 2.02}Tl_{1.03}(As_{1.95}Sb_{0.04})_{\Sigma 1.99}S_{5.99}$	Routhierite
6	2	$Hg_{0.98}Te_{1.02}$	Coloradoite
7	3	$Fe_{0.96}As_{0.06}S_{1.97}$	Pyrite
8	14	$Tl_{1.04}(Sb_{4.37}As_{0.57})_{\Sigma 4.94}S_{8.01}$	Parapierrotite

Notes: the points of analyses are given in Figure 9, [1] the total includes 1.12 wt.% of Zn; [2] the total includes 1.09 wt.% of Zn; [3] the total includes 39.95 wt.% of Te. Dash is element content below detection limits.

Table 3. The chemical composition of native gold from breccias with realgar-orpiment cement, wt. %. (fineness in ‰).

№	Cu	Ag	Au	Hg	Total	Empirical Formulae	Fineness
1	–	19.55	80.49	–	100.04	$Au_{0.69}Ag_{0.31}$	804.6
2	–	16.30	83.32	–	99.62	$Au_{0.74}Ag_{0.26}$	836.4
3	–	12.38	86.38	0.46	99.22	$Au_{0.79}Ag_{0.21}$	870.6
4	–	11.18	86.84	0.62	98.64	$Au_{0.80}Ag_{0.19}Hg_{0.01}$	880.4
5	–	0.98	99.02	–	100.00	$Au_{0.98}Ag_{0.21}$	990.2
6	–	1.10	99.44	–	100.54	$Au_{0.98}Ag_{0.21}$	989.1
7	–	3.40	97.41	0.13	100.94	$Au_{0.94}Ag_{0.21}$	965.0
8	–	0.16	99.08	–	99.24	$Au_{1.00}$	998.4
9	–	5.43	94.38	1.05	100.86	$Au_{0.90}Ag_{0.09}Hg_{0.01}$	935.8
10	0.13	6.60	92.70	1.16	100.59	$Au_{0.88}Ag_{0.11}Hg_{0.01}$	921.6
11	–	5.71	92.92	0.68	99.31	$Au_{0.89}Ag_{0.10}Hg_{0.01}$	935.7
12	–	2.92	98.72	0.26	101.90	$Au_{0.95}Ag_{0.05}$	968.8
13	0.11	0.24	98.96	0.36	99.67	$Au_{0.99}(Ag,Hg,Cu)_{0.01}$	992.9
14	–	0.26	99.01	0.57	99.84	$Au_{0.99}Hg_{0.01}$	991.7
15	–	–	99.41	–	99.41	$Au_{1.00}$	1000.0
16	0.23	0.20	99.42	0.48	100.33	$Au_{0.99}Cu_{0.01}$	990.9
17	–	–	100.13	0.59	100.72	$Au_{0.99}Hg_{0.01}$	994.1
18	0.11	0.24	98.96	0.36	100.69	$Au_{0.99}Hg_{0.01}$	992.9
19	0.07	7.83	89.66	1.85	99.41	$Au_{0.85}Ag_{0.13}Hg_{0.02}$	901.9
20	0.05	3.73	96.86	–	100.64	$Au_{0.93}Ag_{0.07}$	962.4

Notes: the points of analyses of native gold No. 9–16 are given in Figure 9, No. 1–8, 17–20 are given in Figure 10. Dash is element content below detection limits.

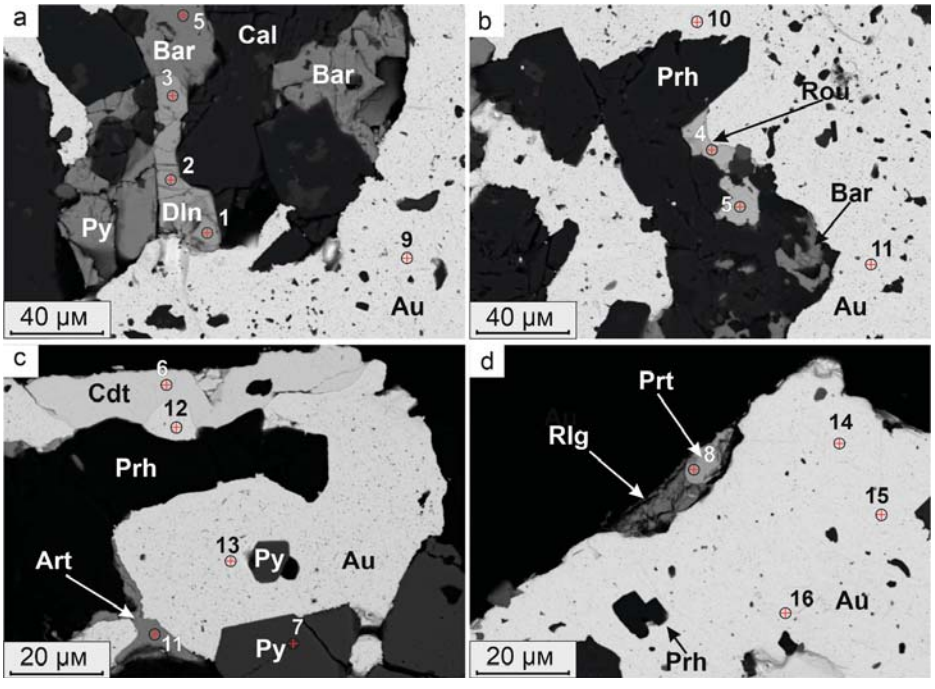

Figure 9. BSE-photo of the minerals intergrown with gold from realgar-orpiment cement breccia. Analyses corresponding to 1–8 point numbers are given in Table 2; the analyses of native gold No. 9–16 are given in Table 3. (**a**) Polymineral inclusions, consisting of calcite (Cal), barite (Bar), pyrite (Py) and dalnegroite (Dln); (**b**) polymineral inclusions formed by prehnite (Prh), barite and routhierite (Rou); (**c**) coloradoite (Cdt) and arsenolite (Art) intergrown with gold; (**d**) parapierrotite (Prt), realgar (Rlg) and prehnite crystals in native gold.

In general, the combination of minerals enclosed by or intergrown with the native gold (Table 2) is similar to the mineral composition of ore-bearing breccia cement. The nature of the relationship of native gold with other minerals indicates that its formation was simultaneous with that of most of the sulfide and sulfosalt grains. The presence of calcite, prehnite, hyalophane and other minerals as inclusions in both gold and sulfides and sulfosalts indicates their earlier formation. Thus, the native gold and most of the sulfides and sulfosalts in the breccias' cement should be attributed to the same assemblage, that has formed at the final stage of the formation of the realgar-orpiment breccia cement.

4.3. Chemical Composition of Native Gold

Native gold from the ore-bearing breccia cement of the Vorontsovskoe deposit is characterized by a homogeneous internal structure (Figure 10). It is divided into two groups by its chemical composition: 1) high-purity gold with Au content from 95 to 100 wt. % and 2) silver-containing gold with Au content from 80 to 95 wt. % (Table 3; Figure 11). Elevated silver concentrations in native gold are accompanied by elevated concentrations of Hg and Cu. The maximum content of mercury in gold reaches 1.85 wt. %. At the same time, copper is most characteristic of the high-purity gold and can reach 0.24 wt. %. However, trace amounts of copper are sometimes found in silver-containing gold as well.

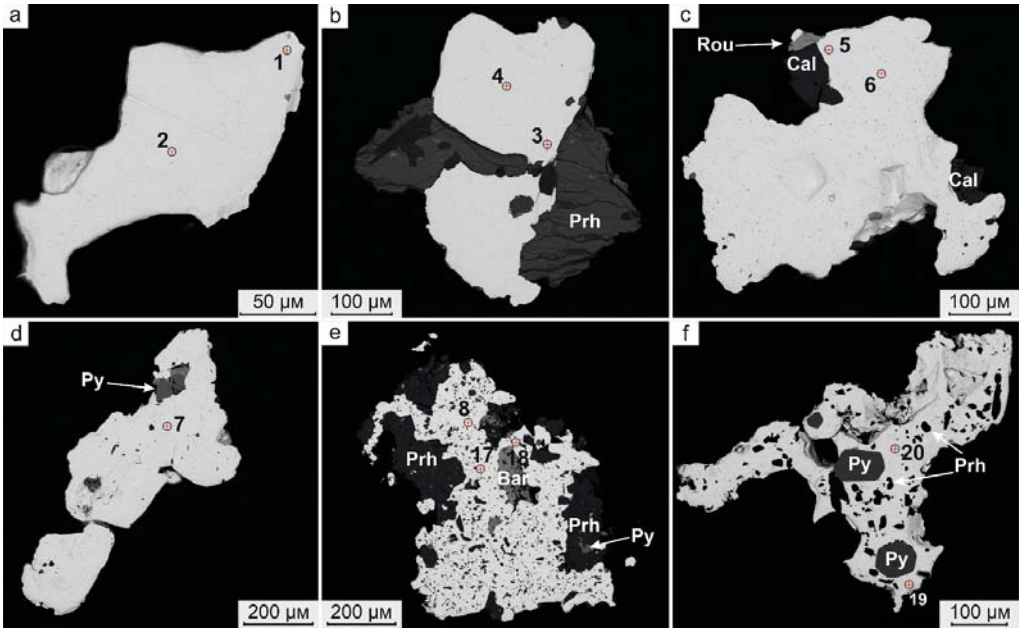

Figure 10. BSE-photo of polished sections of native gold grains. The analyses are given in the Table 3. (**a**) homogeneous gold grain; (**b**) native gold intergrows with prehnite (Prh); (**c**) native gold intergrows with calcite (Cal) and routhierite (Rou); (**d**) pyrite inclusion in native gold; (**e**) native gold with numerous inclusions of barite (Bar), prehnite (Prh) and pyrite; (**f**) euhedral inclusions of pyrite in native gold.

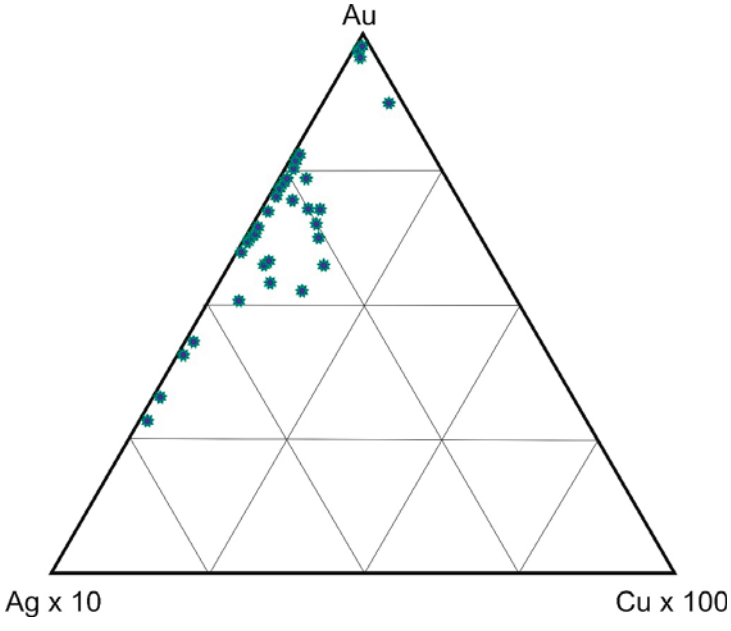

Figure 11. The Au–Ag × 10–Cu × 100 ternary diagram [19] for the native gold composition from ore-bearing breccias of the Vorontsovskoe deposit.

4.4. Chemical Composition of Native Gold–A Comparison

Admixtures of Ag, Cu and Hg are found in native gold from breccias with realgar-orpiment cement. The chemical composition of the native gold is similar to that obtained previously by other researchers [6,20]. Compared to the native gold from other ore types of the Vorontsovskoe deposit [6], the studied gold is featured by its higher fineness (>860) (Figure 12a). This characteristic, along with a uniform internal structure of the grains, distinguishes the native gold in breccias with realgar-orpiment cement from the gold from skarns and other type of gold mineralization found within the Vorontsovskoe deposit (see Figure 12a). The fineness of gold increases in the range from the most high-temperature ore associations (skarns) to the lowest-temperature breccias with realgar-orpiment cement. The last stages of development of the granite-related hydrothermal ore system associated with the Auerbakh intrusion are characterized by the formation of high-purity gold in a single paragenesis with Tl and Hg sulfosalts. It should also be noted that most of the gold compositional data in the classification diagram after [19] fall into the field of epithermal deposits.

High fineness of gold from realgar-orpiment breccias of the Vorontsovskoe deposit is a distinguishing feature in contrast to the native gold from other deposits in the Turyinsk-Auerbakh metallogenic province (Figure 12b), including copper-skarn and iron-skarn sub-economic deposits with low gold concentrations. Thus, the gold in the copper-skarn ores of the Bashmakovskoe and Bogoslovskoe deposits [21], which are located northwest of Auerbakh intrusive, has the lowest fineness due to the significant concentration of silver. A similar composition of native gold is also characteristic of the gold ore skarns in the Dorozhnoe ore occurrence found in 2016 [9], which is located between the Vorontsovskoe deposit and the Auerbakh intrusion. Low-fineness silver-containing gold is also characteristic of sub-economic ore deposits associated with quartz-sericite-altered tuffs within the Turyinsk-Auerbakh metallogenic province. Some similarities in the chemical composition of the studied native gold from the ore breccias of the Vorontsovskoe deposit have been established for a part of the analyses of gold from the iron ore skarns of the Yuzhno-

Peshchanskoe iron-skarn deposit. This similarity is likely a consequence of the unified ore formation process within the Vorontsovsko-Peshchanskaya ore-magmatic system [1].

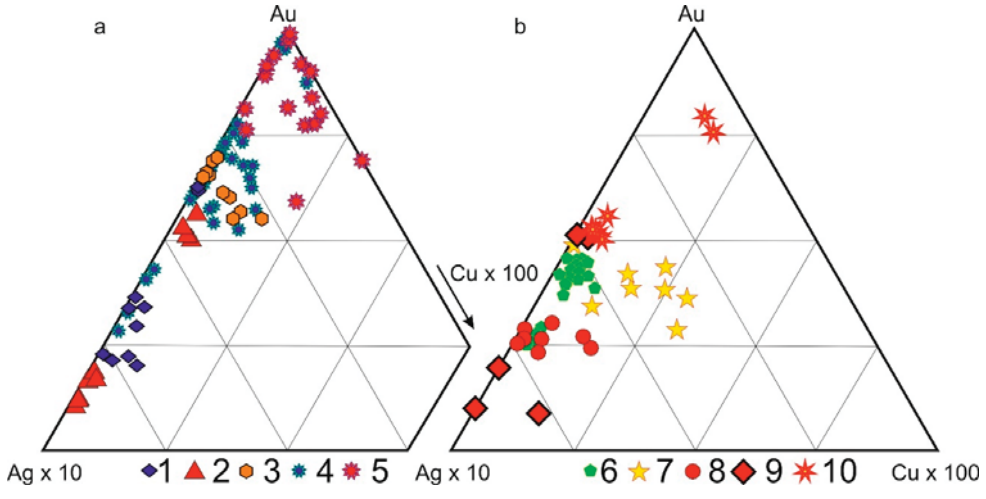

Figure 12. Ternary diagrams [19] for the native gold from different ore types in the Vorontsovskoe deposit (**a**) and other deposits in the Turyinsk-Auerbakh metallogenic province (**b**): 1—jasperoids [6]); 2—skarns [6]; 3—medium-temperature metasomatites developed on tuffs and tuffstones [6]; 4—gold from realgar-orpiment cement of ore breccia (this data); 5—gold from ore breccia [6]; 6—the skarns of the Dorozhnoe ore occurrence [9]; 7—the bornite-chalcopyrite exo- and endoskarns of the Bashmakovskoe deposit (19); 8—medium-temperature gold ore metasomatites on tuffstones (authors' data); 9—the chalcopyrite-pyrrhotite ores of the Bogoslovskoe deposit [21]; 10—the pyrite mineralization of the iron-skarn Yuzhno-Peshchanskoe deposit [21].

5. Discussion

The regular change in the composition of native gold from the most silver-enriched varieties to practically pure native gold in different ore types suggests an evolution of the ore-forming system associated with the Auerbakh polyphase intrusion As a result of the comparative analysis of the gold composition from different rocks of the Vorontsovskoye deposit—trend of changes in the composition of gold has been established. A similar trend with a decrease of silver in native gold depending on the temperature of metasomatite formation, has been established for the ore cluster as a whole [1]. The general geological and geochemical patterns of the Turyinsk-Auerbakh metallogenic province [1], including the presence of small non-economic porphyry copper deposits, suggest that the Vorontsovskoe deposit is an integral part of a large ore-magmatic system genetically associated with the formation of the Auerbakh intrusion. The composition of native gold from the ore-bearing breccias of the Vorontsovskoe deposit corresponds to epithermal deposits [18].

The significant amounts of Tl-containing ore minerals sharing the same paragenesis as native gold from breccias with realgar-orpiment cement in the Vorontsovskoe deposit also indicate a unique mineral gold ore assemblage that has no analogues among the deposits of the Urals. The presence of Tl-As-Hg-Sb-(Te) geochemical signature, including those belonging to the same paragenesis as gold, is also characteristic for Carlin-style gold deposits [22,23]. However, thallium minerals are also widely distributed in deposits associated with the metamorphosed carbonate strata composed of limestone and dolomite [24–26] with the formation of mineralized bodies according to the principle of alpine-type veins. However, in these deposits, the thallium mineralization is not accompanied by gold mineralization. Often, thallium minerals are also found in a distal disseminated Carlin-style deposit, such as the Allchar deposit [27–29] located in southern part of North Macedonia or

in deposits with intermediate position between epithermal deposits and sediment-hosted gold deposits (for example—the Jas Roux deposit, French Alps [30]).

In general, the presence of thallium mineralization in ore bodies of different genetic types can be explained by actively developed models of the magmatic formation of Carlin-style deposits [22–33]. Within these models, thallium mineralization can be localized at a maximum distance from the magmatic source in the zone of intermediate argillic alteration and the distance from the magmatic source can reach more than 5 km.

6. Conclusions

It is important to emphasize that the diversity of thallium minerals, including those first discovered at the Vorontsovskoe deposit—vorontsovite and ferrovorontsovite [34], tsygankoite [35], gladkovskyite [36], luboržákite [37], pokhodyashinite [38], gungerite [39] and auerbakhite [40]—suggest that the Vorontsovskoe deposit is a world-class mineralogical site.

Native gold in the ore breccias of the Vorontsovskoe deposit is concentrated in the form of both small grains ranging in size from 0.05 to 0.15 mm and fairly large grains up to 0.5 mm. In accordance with the technological classification of size [41], the gold of the Vorontsovskoe deposit belongs to the large type. The aggregates of native gold, considering their substantial distribution in the ore breccia cement, represent the bulk of the gold contained in the ores.

The high fineness of native gold from ore breccias distinguishes it from native gold found in other associations of the Vorontsovskoe deposit and other deposits of Turyinsk-Auerbakh metallogenic province. According to the composition, the native gold from the ore breccia cement in the Vorontsovskoe deposit differs from the native gold of other deposit ore types and from the other ore bodies in the Turyinsk-Auerbakh metallogenic province. The formation of gold in breccias occurred during the final stages of the formation of the Vorontsovsko-Peshchanskaya ore-magmatic system, together with barite, pyrite and Tl and Hg sulfosalts.

Author Contributions: Conceptualization, S.Y.S., R.S.P. and A.V.K.; Formal analysis, D.A.V., R.Š. and A.V.K.; Methodology, D.A.V. and R.Š.; Visualization, R.S.P.; Writing—review & editing, S.Y.S., R.S.P., D.V.K., L.N.S. and A.V.K. All authors have read and agreed to the published version of the manuscript.

Funding: This research was funded by the project of Institute Geology and Geochemistry UB RAS, state registration number AAAA-A18-118052590032-6.

Acknowledgments: We are grateful to Olga Plotinskaya for helpful suggestions that improved the manuscript and to Reviewers.

Conflicts of Interest: The authors declare no conflict of interest. The funders had no role in the design of the study; in the collection, analyses, or interpretation of data; in the writing of the manuscript, or in the decision to publish the results.

References

1. Minina, O.V. Auerbakh complex ore-magmatic system in the Middle Urals. *Natl. Geol.* **1994**, *7*, 17–23. (In Russian)
2. Zavaritsky, A.N. Geological outline of copper ore deposits in the Urals. Part 2. In *Materials on General and Applied Geology*; Publishing House of the Geological Committee: St. Petersburg, Russia, 1929; p. 179. (In Russian)
3. Petrov, G.A.; Zhiganov, A.A.; Stefanovsky, V.V.; Shalaginov, V.V.; Petrova, T.E.; Ovchinnikov, R.A.; Gertman, T.A. *State Geological Map of the Russian Federation*; Scale 1: 1,000,000 (Third Generation); Ural Series; Sheet O-41 (Ekaterinburg); Publishing House of VSEGEI: Saint-Petersburg, Russia, 2011; p. 492. (In Russian)
4. Naumov, E.A.; Borovikov, A.A.; Borisenko, A.S.; Zadorozhniy, M.V.; Murzin, V.V. Physicochemical conditions of formation of epithermal gold-mercury deposits. *Geol. Geofiz.* **2002**, *43*, 1003–1013.
5. Sazonov, V.N.; Murzin, V.V.; Grigoriev, N.A. Vorontsovskoe gold deposit—An example of mineralization of the Carlin type in the Urals, Russia. *Geol. Ore Depos.* **1998**, *40*, 157–170. (In Russian)
6. Murzin, V.V.; Naumov, E.A.; Azovskova, O.B.; Varlamov, D.A.; Rovnushkin, M.Y.; Pirajno, F. The Vorontsovskoe Au-Hg-As ore deposit (Northern Urals, Russia): Geological setting, ore mineralogy, geochemistry, geochronology and genetic model. *Ore Geol. Rev.* **2017**, *85*, 271–298. [CrossRef]

7. Vikentiev, I.V.; Tyukova, E.Y.; Murzin, V.V.; Vikentieva, O.V.; Pavlov, L.G. Vorontsovskoe gold deposit. In *Geology Forms of Gold, Genesis*; Fort Dialog-Iset: Ekaterinburg, Russia, 2016; p. 206. (In Russian)
8. Vikentev, I.V.; Tyukova, E.E.; Vikenteva, O.V.; Chugaev, A.V.; Dubinina, E.O.; Prokof'ef, V.Y.; Pavlov, L.G.; Murzin, V.V. Vorontsovka Carlin-style gold deposit in the North Urals: Mineralogy, fluid inclusion and isotope data for genetic model. *Chem. Geol.* **2018**, *408*, 144–166. [CrossRef]
9. Stepanov, S.Y.; Sharpyonok, L.N.; Antonov, A.V. Fluid-explosive breccia of the Vorontsovskoe gold deposit (Northern Urals). *Zapiski RMO* **2017**, *146*, 29–43. (In Russian)
10. Rakhov, E.V. The Ore-Bearing Breccia of Vorontsovskoe Deposit: Structure, Genesis and Role in the Formation of Gold Mineralization. Ph.D. Thesis, The Zavaritsky Institute of Geology and Geochemistry, Ekaterinburg, Russia, 1999. (In Russian).
11. Endogenic Ore-Bearing Breccias. *Methodological Reccomendations on the Identification of Endogenic Breccias of Different Genetic Types and Their Potential Ore-Bearance Evaluating in Relation to the Tasks of State Geological Mapping*; VSEGEI Press: Saint Petersburg, Russia, 2018; p. 104. (In Russian)
12. Krasnobaev, A.A.; Fershtater, G.B.; Bogomolov, E.S.; Larionov, A.N.; Berezhnaya, N.G. *Auerbakch Massif: Zircons, Age, Polychronicity*; Yearbook 2006; IGG UrB RAS: Ekaterinburg, Russia, 2007; pp. 191–196. (In Russian)
13. Fershtater, G.B. *Paleozoic Intrusive Magmatism of the Middle and Southern Urals*; Publishing House of RIO UB RAS: Ekaterinburg, Russia, 2013; p. 368. (In Russian)
14. Korzhinsky, D.S. *Petrology of the Turyinsky Skarn Copper Deposits*; Publishing House of RAS: Moscow, Russia, 1948; p. 148. (In Russian)
15. Cheremisin, A.A.; Zlotnik-Hotkevich, A.G. Vorontsovskoe gold deposit. *Ores Met.* **1997**, *1*, 59–70. (In Russian)
16. Kasatkin, A.V.; Stepanov, S.Y.; Tsyganko, M.V.; Škoda, R.; Nestola, F.; Plášil, J.; Makovicky, E.; Agakhanov, A.A.; Palamarchuk, R.S. Mineralogy of the Vorontsovskoe gold deposit (Northern Urals). Part 1: History of study, mineral assemblages, list of minerals. *Mineralogy* **2020**, *6*, 3–34. (In Russian)
17. Kasatkin, A.V.; Stepanov, S.Y.; Tsyganko, M.V.; Škoda, R.; Nestola, F.; Plášil, J.; Makovicky, E.; Agakhanov, A.A.; Palamarchuk, R.S. Mineralogy of the Vorontsovskoe gold deposit (Northern Urals). Part 2: Native elements, sulfides, arsenides, tellurides. *Mineralogy* **2021**, *7*, 5–22. (In Russian)
18. Townley, B.K.; Herail, G.; Maksaev, V.; Palacios, C.; Parseval, P.; Sepulveda, F.; Jrelana, R.; Rivas, P.; Ulloa, C. Gold grain morphology and composition as an exploration tool: Application to gold exploration in covered areas. *Geochem. Explor. Environ. Anal.* **2003**, *3*, 29–38. [CrossRef]
19. Murzin, V.V.; Sazonov, V.N.; Ronkin, Y.L. Model for the formation of the Vorontsovskoe gold deposit in the Urals (Carlin type): New data and problems. *Lithosphere* **2010**, *6*, 66–73. (In Russian)
20. Murzin, V.V.; Sazonov, V.N. *Mineral Associations and Conditions for the Formation of Sulfide Gold-Bearing Ores of the Turyinsko-Auerbakh Ore Field (the Urals)*; Publishing House of UrB RAS: Ekaterinburg, Russia, 1995; p. 98. (In Russian)
21. Emsbo, P.; Hofstra, A.H.; Lauhna, E.A.; Griffin, C.L.; Hutcinson, R.W. Origin of High-Grade Gold Ore, Source of Ore Fluid Components, and Genesis of the Meikle and Neighboring Carlin-Type Deposits, Northern Carlin Trend, Nevada. *Econ. Geol.* **2003**, *98*, 1069–1105. [CrossRef]
22. Radtke, A. *Geology of the Carlin Gold Deposit, Nevada*; USGS Professional Paper 1267; USGS: Reston, VA, USA, 1985; p. 124.
23. Muntean, J.L.; Cline, J.S. Diversity of carlin-style gold deposit. *Rev. Econ. Geol.* **2018**, *20*, 1–7.
24. Hettmann, K.; Kressig, K.; Rehkamper, M.; Wenzel, T.; Mertz-Kraus, R.; Markl, G. Thallium geochemistry in the metamorphic Lengenbach sulfide deposit, Switzerland: Thallium-isotope fractionation in a sulfide melt. *Am. Mineral.* **2014**, *99*, 793–803. [CrossRef]
25. Raber, T.; Roth, P. The Lengenbach Quarry in Switzerland: Classic Locality for Rare Thallium Sulfosalts. *Minerals* **2018**, *8*, 409. [CrossRef]
26. Hofmann, B.A.; Knill, M.D. Geochemistry and genesis of the Lengenbach Pb-Zn-As-Tl-Ba-mineralization, Binn Valley, Switzerland. *Miner. Depos.* **1996**, *31*, 319–339. [CrossRef]
27. Janković, S.; Jelenković, R. Thallium mineralization in the Allchar Sb–As–Tl–Au deposit. *Neues Jahrb. Fur Mineral.* **1994**, *167*, 283–297.
28. Volkov, A.V.; Serafimovskiy, T.; Kochneva, N.T.; Tomson, I.N.; Tasaev, G. Alshar Au-As-Sb-Tl epithermal deposit (Southern Macedonia). *Geol. Ore Depos.* **2006**, *48*, 205–224. (In Russian) [CrossRef]
29. Palinkaš, S.; Hofstra, A.H.; Percival, T.J.; Borojevic Šoštaric, S.; Palinkaš, L.; Bermanec, V.; Pecskay, Z.; Boev, B. Comparison of the Allchar Au-As-Sb-Tl deposit, Republic of Macedonia, with Carlin-type gold deposits. *Rev. Econ. Geol.* **2018**, *20*, 335–363.
30. Johan, Z.; Mantienne, J. Thallium-rich mineralization at Jas Roux, Hautes-Alpes, France: A complex epithermal, sediment-hosted, ore-forming system. *J. Czech Geol. Soc.* **2000**, *45*, 63–77.
31. Sillitoe, R.H.; Bonham, H.F. Sediment-hosted gold deposits: Distal products of magmatic-hydrothermal systems. *Geology* **1990**, *18*, 157–161. [CrossRef]
32. Cline, J.S.; Stuert, F.M.; Hofstra, A.H.; Premo, W.; Riciputi, L.; Tosda, R.M.; Tretbar, D.R. Multiple sources of ore-fluid components at the Getchell Carlin-type gold deposit, Nevada, USA. In Proceedings of the Mineral Exploration and Sustainable Development, Seventh Biennial SGA Meeting, Athens, Greece, 24–28 August 2003; Volume 2, pp. 965–968.
33. Cline, J.S.; Hofstra, A.H.; Muntean, J.L.; Tosdal, R.M.; Hickey, K. Carlin-type deposits in Nevada: Critical geological characteristics and viable models. *Econ. Geol.* **2005**, *100*, 371–405.

34. Kasatkin, A.V.; Nestola, F.; Agakhanov, A.A.; Skoda, R.; Karpenko, V.Y.; Tsyganko, M.V.; Plasil, J. Vorontsovite, (Hg5Cu)Σ6TlAs4S12, and Ferrovorontsovite, (Fe5Cu)Σ6TlAs4S12: The Tl- and Tl-Fe-Analogues of Galkhaite from the Vorontsovskoe Gold Deposit, Northern Urals, Russia. *Minerals* **2018**, *8*, 185. [CrossRef]
35. Kasatkin, A.V.; Makovicky, E.; Plasil, J.; Skoda, R.; Agakhanov, A.A.; Karpenko, V.Y.; Nestola, F. Tsygankoite, Mn8Tl8Hg2-(Sb21Pb2Tl)Σ24S48, a New Sulfosalt from the Vorontsovskoe Gold Deposit, Northern Urals, Russia. *Minerals* **2018**, *8*, 218. [CrossRef]
36. Kasatkin, A.V.; Makovicky, E.; Plášil, J.; Škoda, R.; Chukanov, N.V.; Stepanov, S.Y.; Agakhanov, A.A.; Nestola, F. Gladkovskyite, MnTlAs3S6, a new thallium sulfosalt from the Vorontsovskoe gold deposit, Northern Urals, Russia. *J. Geosci.* **2019**, *64*, 207–218. [CrossRef]
37. Kasatkin, A.V.; Makovicky, E.; Plasil, J.; Skoda, R.; Agakhanov, A.A.; Stepanov, S.Y.; Palamarchuk, R.S. LuborŽákite, Mn2AsSbS5, a new member of pavonite homologous series from Vorontsovskoe gold deposit, Northern Urals, Russia. *Mineral. Mag.* **2020**, *84*, 738–745. [CrossRef]
38. Kasatkin, A.V.; Makovicky, E.; Plášil, J.; Škoda, R.; Agakhanov, A.A.; Tsyganko, M.V. Pokhodyashinite, IMA 2019–130. CNMNC Newsletter No. 55. *Mineral. Mag.* **2020**, *84*, 485–488. [CrossRef]
39. Kasatkin, A.V.; Plášil, J.; Makovicky, E.; Chukanov, N.V.; Škoda, R.; Agakhanov, A.A.; Tsyganko, M.V. Gungerite, IMA 2020-009. CNMNC Newsletter No. 56. *Eur. J. Mineral.* **2020**, *32*, 443–448. [CrossRef]
40. Kasatkin, A.V.; Plášil, J.; Makovicky, E.; Chukanov, N.V.; Škoda, R.; Agakhanov, A.A.; Stepanov, S.Y.; Palamarchuk, R.S. Auerbakhite, MnTl2As2S5, a new thallium sulfosalt from the Vorontsovskoe gold deposit, Northern Urals, Russia. *J. Geosci.* **2021**, *66*. [CrossRef]
41. Palyanova, G.A. Gold and Silver Minerals in Sulfide ore. *Geol. Ore Depos.* **2020**, *62*, 383–406. [CrossRef]

minerals

MDPI

Article

Criteria for Determining the Genesis of Placers and Their Different Sources Based on the Morphological Features of Placer Gold

Zinaida Nikiforova

Diamond and Precious Metal Geology Institute, Siberian Branch of the Russian Academy of Sciences, 677000 Yakutsk, Russia; znikiforova@yandex.ru; Tel.: +7-41-1233-5872

Abstract: Based on the identified typomorphic features of placer gold, a set of determined morphogenetic criteria is proposed to identify the genesis of placer gold content and different sources in the platform areas, which allow more correctly selecting search methods and improving the efficiency of forecasting ore and placer gold deposits. Gold particles larger than 0.25 mm with signs of wind-worn processing indicate the formation of autochthonous aeolian placers. Gold particles with signs of wind-worn processing with a size of 0.1–0.25 mm, forming an extensive halo of dispersion, indicate the formation of allochthonous placers in Quaternary deposits. Deflationary (autochthonous) placers of native gold can be found by the halo of its distribution of toroidal and spherical hollow forms, which, of course, are the search morphogenetic criterion of aeolian placers. The presence of disc-shaped and lamellar gold particles with ridgelike edges in alluvial placers is typical for placers of heterogeneous origin, formed due to deflation of proluvial placers. The discovery of pseudo-ore gold in alluvial placers indicates the arrival of gold from intermediate gold-bearing sources of different ages and not from primary sources, which is a morphogenetic criterion for determining different sources of the placer. In modern gold placers, the presence of gold of a pseudo-ore appearance can serve as a search criterion for the discovery of gold-bearing conglomerates with high gold content. The developed method for diagnosing the genotype of placer gold by its morphological characteristics (alluvial, aeolian, pseudo-ore) can be successfully used by industrial geological organizations to search and explore ore and placer gold deposits.

Keywords: placer gold; aeolian gold; experiments simulated aeolian environment; morphological and other typomorphic features; morphogenetic criteria ore sources genesis

Citation: Nikiforova, Z. Criteria for Determining the Genesis of Placers and Their Different Sources Based on the Morphological Features of Placer Gold. *Minerals* **2021**, *11*, 381. https://doi.org/10.3390/min11040381

Academic Editors: Panagiotis Voudouris and Galina Palyanova

Received: 26 February 2021
Accepted: 30 March 2021
Published: 2 April 2021

1. Introduction

In the east of the Siberian Platform, unusual toroidal and spherical hollow gold particles were first discovered in Mesozoic–Cenozoic deposits [1–3]. Spherical hollow gold is widely distributed, found in sedimentary rocks from the Riphean to the Cenozoic, and is typical for all platform areas of the earth (Figure 1) [4].

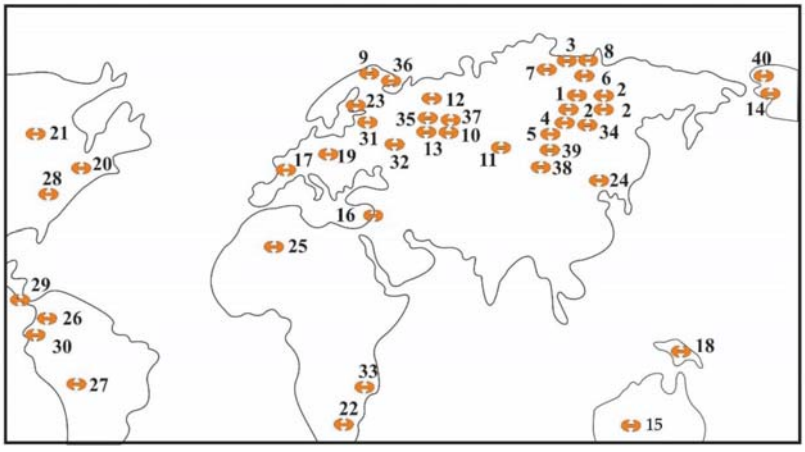

Figure 1. Scheme of distribution of spherical hollow and toroidal gold in different regions of the globe according to researchers: 1 [5]; 2 [2]; 3 [1]; 4 [6]; 5 [7]; 6 [8]; 7 [9]; 8 [10]; 9 [11]; 10 [12]; 11 [13]; 12 [14]; 13 [15]; 14 [16]; 15 [17]; 16 [18]; 17 [19]; 18 [20]; 19 [21]; 20 [22]; 21 [23]; 22 [24,25]; 23 [26]; 24 [27]; 25 [28]; 26–30 [22]; 31 [29]; 32 [30]; 33 [31]; 34 [32]; 35 [33]; 36 [34]; 37 [35]; 38–40 [4,36].

The analysis of the literature sources showed that the description of unusual forms of native gold used various terminology. Shpunt [1] introduced the concept of a tablet-like gold particle with ridgelike edges or a teardrop-shaped gold particle, flattened in the middle on both sides. According to Izbekov [2], scaly gold with ridgelike edges is named "pan-shaped". The term "toroidal" form of gold particles was first proposed by Yablokova [3]. It most successfully reflects the essence of the form. In this case, the toroid is considered as a "bagel", but without a through-hole. This term was later adopted by many researchers who studied similar forms of placer gold. When studying the spherical shape, Izbekov [2] distinguished it as "spherical hollow gold". Shpunt [1] and Yablokova [3] called such gold "teardrop-shaped, globular". Many researchers, when describing similar forms of placer gold, use mainly the term "spherical gold"; some of them distinguish spherical gold with "blebs" [22]. The terms "teardrop-shaped", "globular", "spherical" do not fully reflect the features of the structure of spherical forms. A more accurate name is "spherical hollow" gold; it characterizes not only the appearance but also the internal structure of the gold particle. Later, when studying the considered forms of placer gold, it was proposed to use the terms "toroidal" according to Yablokova [3] and "spherical hollow" gold according to Izbekov [2].

When studying the typomorphic features of spherical gold, it was also revealed that there are two types of them in nature—massive spherical gold or with "blebs", no more than 40 microns in size, clearly of endogenous origin and spherical hollow particles with a partition inside, the size of 0.1–0.16 mm, it is always found together with toroidal gold.

The genesis of toroidal and spherical hollow forms is still one of the controversial issues. Several researchers believe that the origin of such forms of native gold is related to chemogenic processes [1,3,19,20,22,27,28,37]; others explain their genesis by the mechanical transformation of flake gold in hydrodynamic conditions [2,21–23]. Some researchers suggest their possible biogenic [3,38], gas-condensate [39], and even cosmogenic [40] origin.

Chemogenic origin, according to data [1,19,20,22,27,28,37,41,42], there is every reason to accept the assumption of the chemogenic genesis of spherical hollow gold. However, a detailed study of its typomorphic features revealed that there are a number of facts that contradict this assumption. Experimental data indicate the deposition of gold only in the form of massive spherules no larger than 40 μm on activated carbon and sulfide minerals (sphalerite, galena, pyrrhotite and arsenopyrite). Therefore, such gold has nothing in

common with hollow spherical gold, which is widely distributed in many platform areas and has an average size of an order of magnitude larger than the experimentally obtained massive spherules. In addition, in spherical hollow gold with a partition inside the cavities, there are no signs of primary crystallization and the edges of crystal growth; instead, inside the cavities at large (500–1000 times) magnifications, the thinnest (fractions of micrometers) filaments were found, which, as if overlapping each other, form a shell. In the cavities of spherical gold, no "seed" minerals have been found on which gold would be deposited, but inclusions of detrital quartz, zircon, ilmenite, rutile and other minerals have been identified. All of the above does not allow us to consider toroidal and spherical hollow gold as the product of chemical processes occurring in the weathering crust and, therefore, to accept the chemogenic hypothesis to explain their genesis.

The mechanogenic hypothesis, despite all the apparent logical validity of the origin of toroidal and spherical hollow gold in hydrodynamic conditions, has a number of weaknesses that do not allow us to explain all the nuances of the formation of spherical forms. The hypothesis of the formation of spherical gold by mechanical flattening of crystals in an water–alluvial medium [17,21] is not consistent due to the fact that in hydrodynamic conditions, gold particles flatten regardless of their original shape, which is established experimentally [43,44]. The proof of this assumption is provided by natural observations that in any placer, various forms of gold are observed in the "head", and in the "tail", only flattened gold grains are observed.

The hypothesis of the biogenic origin of the discussed morphological type of native gold was first expressed by Yablokova [3]. She believed that the formation of hollow forms is associated with the sorption of gold by the Precambrian organisms. The presence of carbon (up to 0.001%) in native gold and their similarity in shape to the Precambrian organisms confirmed this idea. Other researchers also hypothesized the biogenic origin of spherical gold during the nucleation of gold on bacterial spores with a diameter of 1–2 microns [38]. The direct proof of the validity of this hypothesis for them is a certain similarity of the spherical forms of the mineral with the appearance of Precambrian microorganisms. The main contradiction is that spherical hollow gold is observed not only in the Precambrian deposits but also in the Quaternary deposits. It is found in sedimentary rocks from the Riphean to the Cenozoic inclusive. The second proof in favor of a possible biochemogenic hypothesis for the authors was the presence of carbon in native gold. However, the discovery of carbon in spherical hollow gold does not refute or prove its biogenic origin. During the formation of hollow spherical gold, any particles can be captured, not only quartz, ilmenite, zircon but also fragments of organic origin, primarily vegetable origin. In this regard, the discovery of carbon in the cavities is not an argument for the biogenic origin of spherical hollow gold particles. Finally, the hypothesis under consideration does not explain the mechanism of formation of a large variety of forms of hollow gold.

Gas-condensate (hydrothermal) and meteorite origin. Gladkov et al. [39] suggested that the spherical gold had a gas-condensate origin.They have an almost perfect rounded shape—these are gas microchambers, they do not have dividing partitions, as in spherical hollow gold particles, and they are an order of magnitude smaller in size. The cosmogenic hypothesis is problematic [40] since the possibility of a meteorite falling into gold-bearing formations is unlikely.

It is shown above that each of the proposed hypotheses has weaknesses, and none of them reveals the essence of the process of formation of specific forms of gold particles, constantly observed on ancient platforms.

The mechanical hypothesis of the deformation of flake gold and its transformation into spherical hollow form is beyond doubt, but under what conditions does this happen? Does it occur in stream water? Or does mechanogenic transformation occur in another condition?

We have suggested that the sequence of deformation of flake gold and its gradual transformation into a toroidal and then into a spherical hollow form is more likely in

aeolian conditions than in a hydrodynamic environment. Analysis of the distribution mechanism of toroidal and spherical hollow gold and comparison of its location with the geographical paleoenvironment of the east of the Siberian Platform also allowed us to confirm the hypothesis about the origin of such forms of native gold in aeolian conditions. The proof of this assumption was the fact that the sites of finds of toroidal and spherical hollow gold are well correlated with the deflation deserts mapped by Kolpakov [45].

Transformation of placer gold in ancient gold-bearing sources. In the ancient conglomerates of the Devonian age of the Timan Ridge, along with the typical placer-shaped gold particles, gold particles of the "ore" appearance were found [33], which was the reason for researchers to suggest secondary gold mineralization on the formed ancient placer [14,46].

Gold particles of placer and ore appearance of paleoplacers of the Timan Ridge were studied by us in detail. Along with placer aeolian gold, gold particles of "ore" appearance were found. Gold particles are characterized by a coarse-shagreen surface, with casts of pressing of minerals and a rounded shape, with no growth facet, it often forms pseudo-growths with quartz, ilmenorutile and garnet, which are easily destroyed (Figure 2). The occurrence of gold particles of the "ore" appearance in the placer is usually a small percentage, but sometimes, in some areas, it reaches 80%.

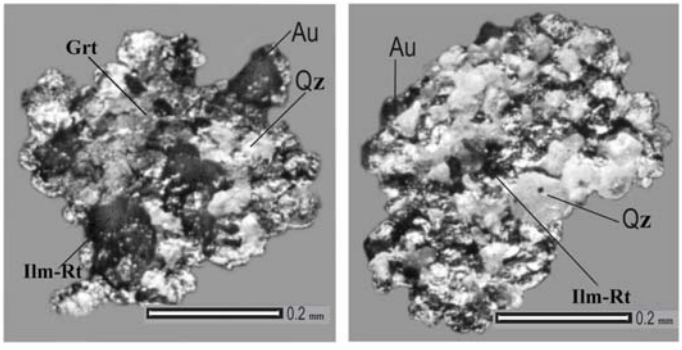

Figure 2. Pseudo-growths of native gold with quartz (Qz), ilmenorutile (Ilm-Rt) and garnet (Grt).

The presence of such native gold allowed previous researchers to assume the proximity of the primary source. However, the above-detailed analysis of individual typomorphic features of this native gold called into question the validity of its distinguishing as gold ore appearance. In this connection, it was suggested that this is placer gold, which took on a pseudo-ore appearance under the influence of the lithostatic pressure of the overlying strata, which was proved experimentally [33,47].

In view of the above, we put forward an assumption about the formation of toroidal and spherical hollow gold with a partition inside as a result of the deformation of flake gold in aeolian conditions and the formation of "pseudo-ore" gold in ancient gold-bearing sources under the influence of lithostatic pressure of the overlying strata. In order to test these assumptions, experiments were conducted that simulate the mechanism of transformation of gold particles of various shapes in aeolian conditions and in ancient gold-bearing conglomerates.

2. Materials and Methods

The article is based on the results of field, experimental and analytical studies on placer gold. The objects of study were placers from the east of the Siberian Platform, Tuva, Mongolia, gold-bearing conglomerates of the Timan Ridge (Ural), as well as the collections of placer gold of the A. E. Fersman Museum, TsNIGRI, MGA, and "VNESHMET" JSC.

In the study, a wide range of well-known mineralogical and geochemical methods for studying the typomorphic features of native gold was used [41,48]. All analytical work

was carried out in the laboratory of physical-chemical methods of analysis, DPMGI SB RAS (Yakutsk). The study of the morphology, surface structures, and internal structure of the gold particles was carried out using a scanning electron microscope "JEOL JSM-6480LV" (Japanese Electron Optics Laboratory, Tokyo, Japan), stereoscopic microscope "LEICA MZ6" (KaVo, Biberach an der Riss, Germany) and an ore microscope "JENAVERT SL 100" (Carl Zeiss AG, Oberkochen, Germany). The trace element composition of native gold was analyzed on an X-ray microanalyzer, "JXA-50A", "JSM-6480LV" (Japanese Electron Optics Laboratory, Tokyo, Japan). The content of impurity elements in it was studied by the atomic emission spectrography. Microinclusions in native gold were identified using a scanning electron microscope "JEOL JSM-6480LV", with an energy-dispersive spectrometer Energy 350 of Oxford Instruments (London, UK). Software Oxford Instruments INCA the microanalysis Suite Issue v.4.17. Quantitative analysis and processing of the results were carried out using the XPP method in the software INCA Energy (Software Oxford Instruments INCA the microanalysis Suite Issue v.4.17). In addition, experimental work was carried out on specially designed equipment by V. E. Filippov, simulating the aeolian process and the lithostatic pressure of the overlying strata.

In the course of experimental studies, the mechanical transformation of gold forms under the influence of sand–air flow under aeolian conditions and the lithostatic pressure of overlying strata on ancient gold-bearing conglomerates, was studied for the first time [47,49].

Experimental studies on the transformation of native gold in a simulated aeolian environment were carried out in several stages.

1. Experiment. First, the transformation of flake gold particles of various configurations in the plan view was studied, then more massive grains of lamellar, tabular and lumpy gold particles were studied.
2. Experiment. In addition, the transformation of endogenic native (further "ore") gold in a simulated aeolian environment was studied. For the study, a large ore gold particle was selected (half of the particle was used in the experiment, and the second part was left for comparison).
3. The experiment was conducted to identify the genesis of the gold film on quartz. For this purpose, the ore gold particle in an intergrowth with quartz was taken and placed in an experimental facility.

Experimental studies of alluvial gold transformation in simulating the influence oflitho static pressure of overlying strata.

The placer gold was covered with sand, imitating the overlying deposits, and was placed under a hydraulic press, where the minerals were pressed in at a certain pressure.

3. Results

3.1. The Results of Experimental Studies Simulated Aeolian Environment

Transformation of flake gold into toroidal and then into spherical hollow shapes. As a result of the experiment, it was possible to obtain spherical hollow forms of gold particles. After a 100 h stay in the imitation conditions of the aeolian process, the gold flakes gradually transformed into typically toroidal and then into hollow spherical formations (Figure 3). The initial stage of transformation is a thin ridge's appearance along the edge of the flake gold particle (Figure 3a). The middle stage—the flake's formation with a well-defined ridge-toroidal shape (Figure 3b). The final stage of transformation is the formation of a hollow ball (Figure 3c).

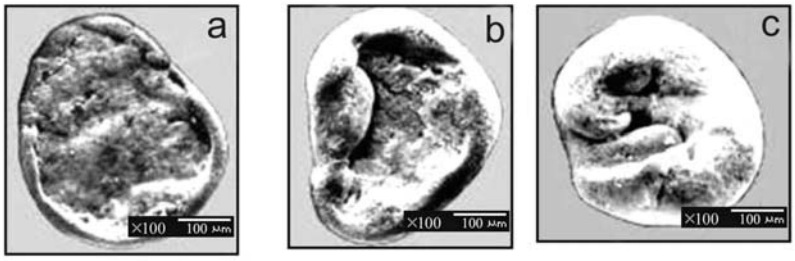

Figure 3. Sequential change of the flaking gold in the course of the experiment: (**a**) the appearance of a thin ridge along the edge of the scaly gold particle; (**b**) the flake's formation with a well-defined ridge toroidal shape; (**c**) forming a hollow ball.

It is established that the change in the shape of the gold grains in the experimental aeolian conditions depends on their initial shape (Figure 4). Toroidal and spherical hollow gold is formed as a result of the transformation of coin-shaped flakes. Scaly gold of other configurations takes on hollow formations of a more complex shape: pear-shaped, canoe-shaped, etc. (Figure 5a,b). Lamellar gold particles are transformed into disc-shaped forms (Figure 5c) and rod-shaped particles—into dumbbell-shaped ones (Figure 4). On the lumpy particles, the protrusions are smoothed out to form a foil, which in the form of the thinnest shell envelops the main core.

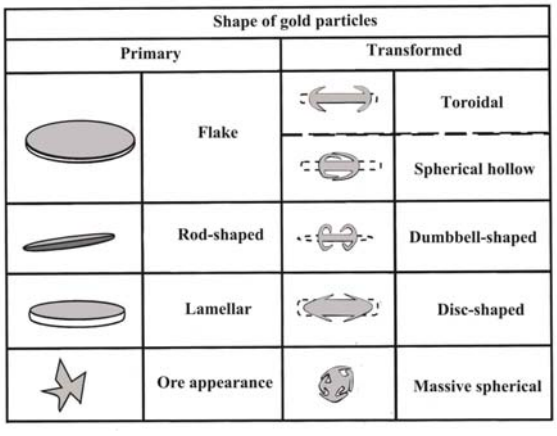

Figure 4. Transformation of gold particles of various shapes in an air–sand flow.

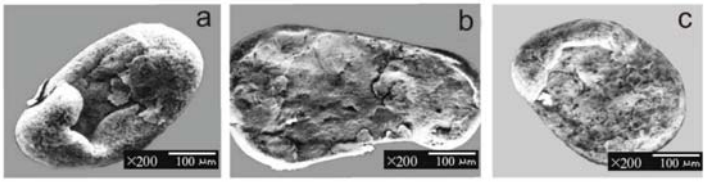

Figure 5. The different nature of the transformation of gold particles, depending on their shape in the course of the experiment: (**a**) canoe-shaped; (**b**) ellipsoid-shaped, lamellar gold particle with ridgelike edges; (**c**) tabular gold particle with a ridge.

Ore gold, after a 100 h stay in the simulated aeolian environment, also changed its shape; its protrusions smoothed out and acquired a rounded shape (Figure 6b).

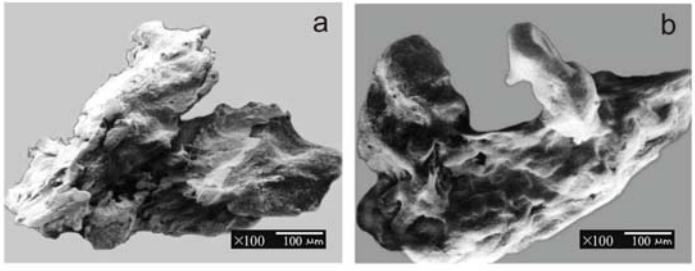

Figure 6. Transformation of a gold particle of ore-appearance in an air–sand flow: (**a**) before the experiment; (**b**) after a 100 h stay in an air–sand flow.

Transformation of "ore" gold in intergrowths with quartz in an air–sand flow. During asimulation of the aeolian process lasting 30 h, protrusions of the gold particles smoothed out, the growth facets and the shiny surface disappeared. After a 100 h stay in the simulated aeolian environment, the gold–quartz intergrowths changed even more, and the surface of the gold acquired a more distinct matte shade, characteristic of wind-worn processes (Figure 7a,b). On these intergrowths, as a result of blows with sand grains, the thinnest films of gold enveloped quartz (Figure 8a). The formed film has a filmy-fibrous surface typical for the transformed gold in aeolian processes (Figure 8b). As a result of the experiment, gold-encrusted quartz was obtained. The mechanism of formation of a filmy-fibrous surface on the intergrowths of gold and quartz is identified.

In the course of the experiments, all the gold particles were compacted, as a result, of which they decreased in size, acquired new various forms. As determined by the control weighting, their weight is practically not changed. According to the structural features, the spherical hollow forms of gold particles obtained during the experiment (Figure 9a–c) are similar to the forms of native gold of natural objects. Inside the hollow chambers, there is a "filamentous" gold (Figures 3 and 9a). In natural gold and in experimental gold, inclusions of quartz, ilmenite, zircon, etc., are observed in "blebs", the capture of grains of quartz and various minerals is recorded.

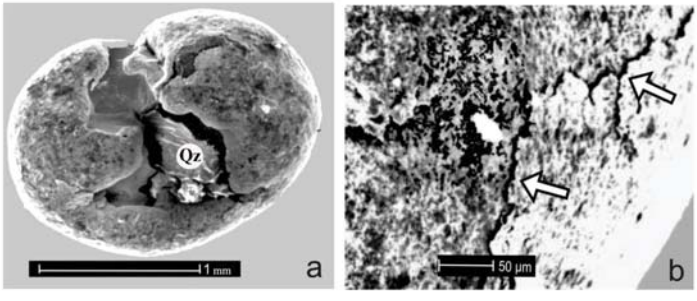

Figure 7. Intergrowth of native gold and quartz (quartz relics in the depth of the cavity, transformed into a lumpy-spherical shape in an experimental facility): (**a**) general view; (**b**) detail, the filmy-fibrous surface of gold (shown by arrows); Qz = quartz.

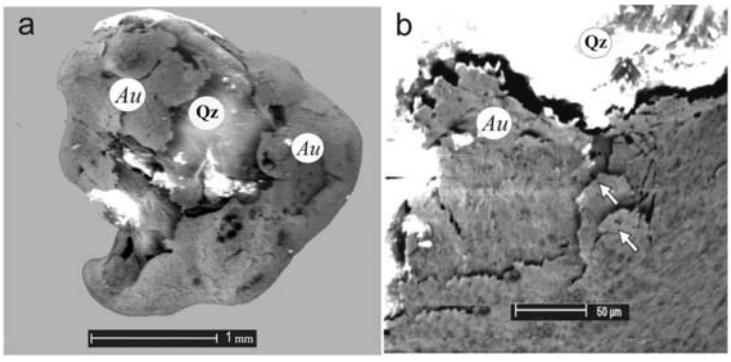

Figure 8. Gold-encrusted quartz obtained as a result of blows with grains of sand and intergrowth of native gold with quartz in an experimental facility: (**a**) general view; (**b**) detail, the filmy-fibrous surface of gold (shown by arrows); Au = gold; Qz = quartz.

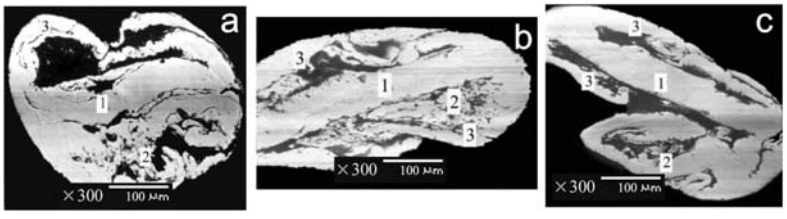

Figure 9. Cross-sections of various forms of hollow gold obtained during the experiment: (**a**) spherical hollow; (**b**) canoe-shaped; (**c**) curved; 1, internal partition; 2, filamentous twisted gold; 3, shell.

3.2. Results of Experimental Studies on the Transformation of Placer Gold in Simulating the Influence of Lithostatic Pressure of Overlying Strata

During the experiment, it was found that under the influence of lithostatic pressure in the simulated environment, gold particles, due to their ductility, are dented by the sand grains depressed into them and acquire a pitted-lumpy surface (Figure 10). Ragged edges and through holes appeared on them, as well as traces of pressing-in of minerals in the host deposits.

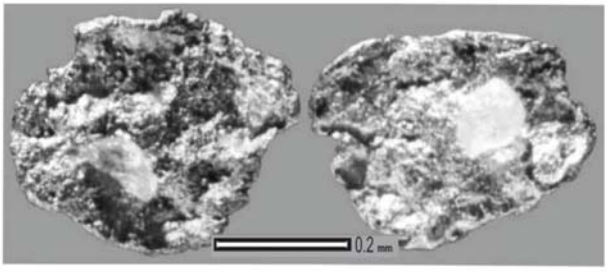

Figure 10. Surface of gold particles with casts of sand grains impressed in them.

Experimental observations of the transformation of native gold in aeolian conditions and in ancient gold-bearing conglomerates allowed us to solve a number of controversial issues that have not been clearly explained for a long time.

1. It turned out to be possible to understand and explain the origin of the filamentous gold and the formation of the shell, which many researchers took for clots of rede-

posited gold. This morphological feature is due to the continuous "bombardment" of the edges of the flakes with grains of sand so that the thinnest threads were stretched from the edges of the flakes, which, overlapping each other, formed a shell;

2. The presence of carbonaceous matter in the cavities of gold particles has led some researchers to associate the genesis of the studied forms with chemogenic processes. However, from the point of view of the conducted experiment, it is quite likely that both fragments of minerals and vegetative detritus can be found in the cavities of spherical gold particles. These inclusions reflect only the possibility of capturing the material that was present in the environment;
3. Obtained experimental data also logically explain the origin of the hollow forms of gold particles of various configurations, depending on the initial variety of morphological features of the gold particles that got into the aeolian conditions. It should be emphasized that hollow spherical forms are formed only from gold flakes. Lamellar and tabular shapes are transformed to disc-shaped forms;
4. The formation of brittle aggregates of growth of native gold with quartz, ilmenite, zircon and other minerals is quite possible under the influence of the lithostatic pressure of the overlying strata;
5. The appearance of scar furrows on the surface and through holes in the native gold occurs when simulating the processes of the effect of lithostatic pressure and tectonic displacements.

3.3. Typomorphic Features of Placer Gold under Various Exogenous Conditions

Native gold, regardless of its original shape, is flattened in hydrodynamic conditions. Identified regularity is proved for the first time by experimental studies Tischenko [43]. Therefore, in the "heads" of all classic placers [50,51], various forms of gold particles are observed, represented euhedral, anhedral, subhedral and other forms [52–54], and in the "tail" of the placer, there are only flattened lamellar forms. The surface of gold particles in hydrodynamic conditions changes from coarse-pitted to fine-shagreen–polished. On the surface of autochthonous placer gold, there are imprints of ore minerals, growth facets typical for the ore gold. Perfectly rounded alluvial placer gold is characterized by a smooth, polished surface, but at high magnifications (500–2000× and more), it has a loose porous structure.The mineralogical–geochemical properties of placer gold in hydrodynamic conditions do not change and depend on the composition of the gold of the destroyed ore source [55,56].

3.3.1. Typomorphic Features of Aeolian Gold

This section presents the results of the study of placer gold with signs of aeolian transformation, its morphological and internal structure and chemical composition on the example of aeolian gold of the east Siberian platform [57]. Depending on the shape of the gold particles and the degree of their transformation under aeolian conditions, they are divided into two groups (Figure 11).

First group—gold particles with signs of wind-worn processing, formed due to the gradual transformation of flakes of different configurations in the plan view into hollow spherical formations. Coin-shaped flakes are transformed into toroidal, and then into spherical hollow ore ellipsoid forms, into canoe-shape or irregular forms, into pear-shaped forms, etc. They are found in aeolian placers, both in the deflation zone and in the transit zone, and sometimes in accumulative aeolian deposits (dunes).

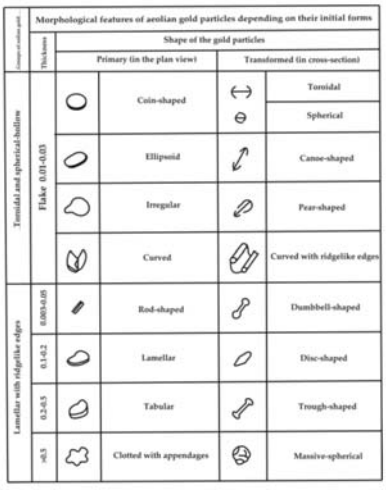

Figure 11. Morphological features of aeolian gold particles depending on their initial forms.

Second group of aeolian gold—this is the result of the transformation in aeolian conditions of massive gold particles with a thickness of more than 0.1 mm, lamellar, tabular, clotted, appendage-like initial forms. In contrast to the first group, the aeolian gold in question is generally more massive and larger, with an average particle thickness of 0.2 mm. Lamellar and tabular forms have a ridgelike edge. Sometimes the ridge is smoothed; consequently, the gold particles become disc-shaped. In the aeolian environment, massive spherical individuals are formed from clotted gold particles with processes. Gold particles of the second group are found in placers only in the deflation zone, at a relatively small distance from the source.

Characteristics of toroidal and spherical hollow gold. As shown experimentally, toroidal and spherical hollow forms are the result of the transformation of flake gold under aeolian conditions. According to the degree of aeolian transformation of the end of flakes, it is advisable to distinguish the stages of this process: initial, middle and final. At the initial stage, a thin ridge appears on the edge of the gold particle, occupying no more than a tenth of the diameter of the original flake. At each subsequent stage of transformation, the ridge increases in size, and at the final stage of transformation, a spherical hollow shape is formed (Figure 12a–c), in which up to half of the conditional diameter of the flake, the gold has passed to the formation of a rounded shell.

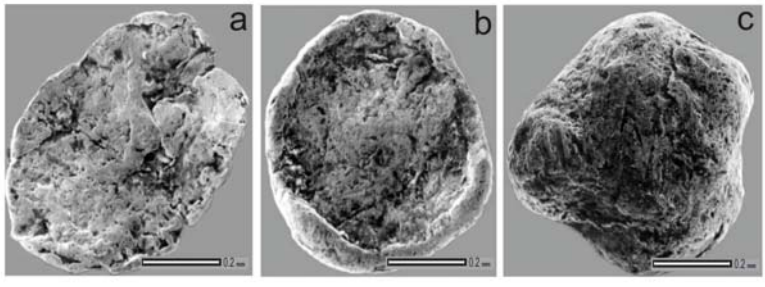

Figure 12. The sequence of the transformation of natural flake gold particles in aeolian conditions (the East Siberian platform, the size is 0.25 mm). Stages of transformation: (**a**) initial (flake with thin, ridgelike edges; (**b**) middle (toroidal shape); (**c**) final (hollow spherical shape).

Depending on the mode of aeolian activity, the process of transformation can stop at any stage or be repeated again and again until the deposits with gold are removed from the zone of influence of aeolian processes. Therefore, in the gold concentrate, all the transitional differences of gold particles are observed from thin flakes with a barely noticeable ridge along the edge to flakes with a well-defined ridge, shaped like a "ring-shaped roll"– toroid and various hollow spherical formations.

Unlike native gold from alluvial deposits, the surface of perfectly rounded aeolian gold is represented, regardless of the magnification scale, by a dense and smooth microrelief. At a magnification of 300×, a specific, film-fibrous surface is observed on this gold. With further magnification (2000–5000×), the surface of aeolian gold remains the same plane, dense and smooth with rare pores. The mechanism of formation of the film-fibrous surface is as follows: in aeolian conditions, as a result of processing with grains of sand, gold is drawn out in the form of the thinnest film, which, superimposed on each other, forms a dense film-fibrous surface.

Spherical hollow gold particles always have a partition that is significantly (2 times or more) greater than the thickness of the shell. In its internal structure, it reveals similarities with the internal structure of the original gold flake. The chambers of hollow spherical gold particles can be symmetrical and asymmetric. At 200–500-fold magnification in the scanning mode of the JEOL microanalyzer JXA-5OA (Japanese Electron Optics Laboratory, Tokyo, Japan), filamentous and weblike gold was found on the inner walls of the chambers (Figure 13a–c). Sometimes mechanical inclusions of quartz, zircon, ilmenite, as well as the remains of vegetative detritus are found in the cavities/chambers of gold particles. When observed in a scanning microscope, no facets of gold crystal growth were found in the internal cavities of spherical hollow gold particles from natural objects. Neither the primary crystallization of gold microindividuals nor the inclusion of any minerals indicating the chemogenic nature of such gold particles was recorded. The morphology of spherical hollow gold, the composition and shape of the inclusions in it clearly indicates the mechanical nature of the studied forms.

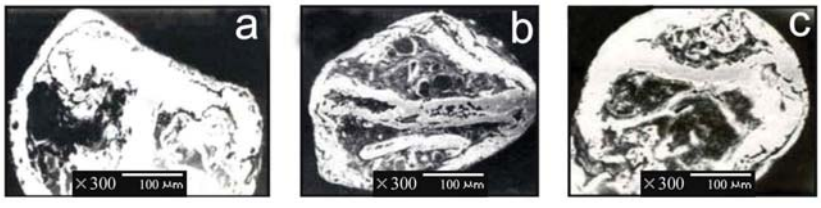

Figure 13. Cross-sections of various forms of hollow gold from natural: (**a**) internal partition; (**b**) filamentous twisted gold; (**c**) shell.

It should be emphasized that sub-spherical gold particles are formed not always in the final stage of the transformation of the flakes. Depending on the primary form of flakes, canoe-shaped and dumbbell-shaped gold particles are also formed from them. When the flake forms are transformed into spherical ones, the surface of the gold particles becomes smooth; the individuals decrease in size, their thickness and their increase (Table 1). Simultaneously with the external morphological transformations, there is a gradual change in the internal structure and fineness of native gold. As a result, each stage of changes from the flake to the hollow ball corresponds to certain typomorphic features of native gold. It is known that the degree of recrystallization and changes in the chemical composition of native gold is determined by the duration of its stay in an exogenous environment. Our studies confirmed the previously revealed fact that recrystallized fine-grained structures predominate in all varieties of modified gold particles with ridgelike edges. However, in the central parts of some relatively large, massive gold particles, areas with primary medium-grained structures and even blocks of monocrystals of the mineral

were identified. High-grade shells of different thicknesses of the fine-grained structures are always developed on these gold particles.

Table 1. Typomorphic features of complex-deformed gold particles of the Lena–Viluy interfluve (east Siberia platform). Number of objects: 300.

Gold Particle Shape	Average Weight of Gold Particles (mg) by Fractions, mm		Average Size, mm	Average Thickness, mm	Average Hydro-Size, m/sec	Degree of the Surface Processing	Average Fineness, ‰ from-to/Average	Trace Elements, %	Degree of the Trans-formation	Main Internal Structures
	0.1	0.25								
Flake	0.009	0.05	0.25–0.5	0.02	5–6	From pitted-lumpy to polished	810–970/890	Pb-0.003 Cu-0.05 Fe-0.1 Mn-0.01 Pd-traces Ni-traces Hg-traces	Initial	Inequigranular Luder'slines, the presence of high-grade fringe, partial recrystallization
Toroidal	0.012	0.05	0.15–0.2	0.05	7–10	Thin-shagreen, polished	920–970/940	Fe-0.1 Cu-0.02 Mn-0.03 Ni-traces Hgtraces	Middle	Fine-,medium-grained, high-grade fringes, Intergranular veinlets, partial and complete recrystallization
Spherical hollow	0.013	0.05	0.1–0.16	0.1	12–17	Thin-shagreen, polished	960–990/970	Fe-0.1 Cu-0.017 Mn-0.001	Final	Fine-grained, complete recrystallization (decompression)

Toroidal gold is mainly characterized by a fine-grained structure with a partially or completely recrystallized shell. Occasionally, gold particles with well-developed fine-grained high-grade shells are observed with preserved relics of an unchanged medium-grained core with a lower fineness. The spherical hollow forms are usually completely recrystallized with the formation of the fine-grained internal structure of native gold.

When the flake forms are transformed into a spherical hollow form, the native gold is ennobled, the fineness is increased, and the trace elements are reduced (Table 1). Permanent trace elements of gold particles of flake forms are iron, lead, nickel, copper, manganese and some others. In spherical gold particles, only such trace elements as iron, copper and manganese are found.

Toroidal and spherical hollow forms of gold particles, regardless of their location, are characterized by surprisingly similar typomorphic features. They have a size of mainly 0.1–0.16 mm, high fineness >900‰ and low content of trace elements. It is found out that, in aeolian conditions, when flake gold transforms into toroidal, and then in a spherical hollow, there is a change not only in the morphology (decrease in size from 0.25 to 0.16 mm), the internal structure (recrystallization–decompression) but also in chemical composition (from 900 to 999‰). It is determined that the long period of transformation of flake gold particles into a spherical hollow form in aeolian conditions contributed to their ennobling. At the same time, there was a decrease in the variety and content of trace elements, an increase in the fineness and the formation of a high-grade shell in spherical hollow gold to 1000‰.

The main signs of deflationary aeolian gold. Native gold transformed in aeolian conditions, in addition to the considered toroidal and spherical hollow forms, is also represented by lamellar and tabular individuals that have thickenings along the periphery and form trough-shaped, canoe-shaped and boomerang-shaped morphological forms, as well as dumbbell-shaped and massively lumpy-shaped gold particles. A specific film-fibrous surface typical for gold transformed under aeolian conditions is observed on all gold grains. The size of gold grains of such forms is from 0.25 to 5.0 mm or more. The average thickness is 0.1–0.8 mm. The average grain weight is 0.5 to 50 mg; the average fineness is from 750 to 900‰. The internal structure can be coarse-grained, medium-grained, or the individual is a mono-grain. The presence of thin shells of high-grade gold is

noted. The granulometric and chemical composition of massive gold with signs of aeolian transformation in other regions may be different since it depends on the type of gold ore sources. In this case, specific values are given for the placer deflationary gold of the Lena–Viluy interfluve (east of the Siberian Platform). In general, the gold in question is less chemically altered. It is characterized by a larger size and is, therefore, non-mobile, occurring only in the basal Aeolian horizon at a relatively short distance from the ore source. Such gold can form high concentrations and be of commercial interest.

According to the published data, lamellar and tabular gold particles with ridge like edges or lumpy-shaped forms with rounded appendages were found in the east of the Siberian Platform in a number of objects of the Viluysyneclise [2], Anabaranteclise [1], as well as in the Urals [12]. Since the aeolian features of deflationary gold are less evident in comparison with the morphological features of toroidal and spherical hollow gold, the halos of its distribution are not so widely found. Apparently, such gold was usually taken by researchers as a native metal of alluvial placers. However, based on the results of mineralogical, experimental and field observations, we have every reason to assert that massive gold with signs of wind-worn processing with toroidal and spherical hollow forms is found together. In a single aeolian deflationary placer, in its main part, more massive gold is mainly concentrated—lamellar and tabular forms with ridgelike edges, and in the tail part of the placer—toroidal and spherical hollow formations. Thus, it is easiest to detect a deflationary gold placer by the halo of its distribution of individuals of toroidal and spherical hollow forms, which can serve as a search mineralogical criterion of the aeolian-type of placer gold content.

In addition, deflationary gold includes rounded quartz grains encrusted with gold (Figure 14a,b), found along with lamellar forms of gold with ridgelike edges, toroidal and spherical hollow. The analysis of the literature data showed that the identified form of gold occurs together with the gold particles of aeolian appearance in placers of the Timan Ridge [33]; the Nindzhi River in Tanzania [31]; the Khuzhir gold-bearing conglomerates of the Vendian [58], in alluvial deposits of the east of the Siberian Platform [59], and in a number of other.

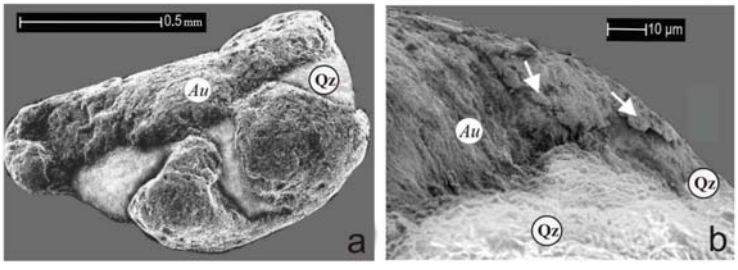

Figure 14. Gold-encrusted well-rounded quartz found in one of the placer occurrences of the Lena–Anabar interfluve: (**a**) general view; (**b**) detail, the film-fibrous surface of gold, characteristic of aeolian transformations (shown by arrows); Au = native gold, Qz = quartz.

The origin of the rounded quartz encrusted with a gold film is still debatable. Researchers who have studied similar-shaped gold particles in the Khuzhir gold-bearing conglomerates have suggested that this is the result of the precipitation of "new" gold formed during the dissolution of gold in the process of epigenesis [7,58]. Some researchers believe that the gold film on the intergrowths of gold with quartz could be formed under hydrodynamic conditions. The formation of gold-encrusted quartz in a hydrodynamic environment is impossible since, in this environment, the quartz intergrowths from ore gold are first destroyed and removed, and then the appendages of gold particles are flattened [44]. In this regard, it was suggested that the transformation of gold–quartz intergrowths resulted from blows by gold grains under the influence of aeolian processes, which was confirmed experimentally (section methodology).

3.3.2. Characteristics of Pseudo-Ore Gold

Pseudo-ore gold includes gold particles in "growth" with quartz, ilmenite, zircon and other minerals of the host deposits, as well as flake gold particles with casts of pressing-in of minerals, traces of scars, scratches and slickensides on the surface, sometimes with ragged edges or with through holes (Figure 15). The surface of such particles is coarse-pitted and fine-cellular. The size of the gold particles is 0.1–0.25 mm; it is mainly of high fineness with recrystallized internal structures.

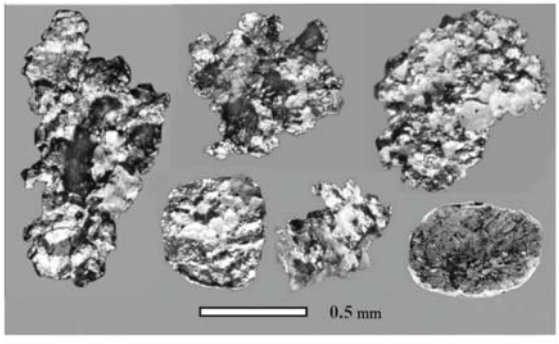

Figure 15. Pseudo-gold appearance.

The genesis of such forms of gold is explained by the influence of the overlying strata's lithostatic pressure on the formed placer, while the minerals of the host deposits are pressed into the particles of gold. Placer gold acquires an ore appearance, which is proved experimentally (see the section methodology).

Three types of placer gold have beenare identified—alluvial, aeolian and pseudo-ore. We first discovered this process when studying native gold from Devonian placers on the Timan Ridge [33], where, as a result of tectonic processes, the formed placer was buried by thick (up to 700 m) deposits. In this regard, the placer's gold-bearing deposits were subjected to both vertical and horizontal micromovements, which led to the deformation of the placer gold particles. Under the influence of vertical lithostatic pressure, the minerals of the host deposits were pressed in, and with horizontal displacement, scratches, furrows, and slickensides appeared on the gold particles up to the rupture of the gold particles. The process of deformation of gold particles under the influence of lithostatic pressure (vertical and horizontal micromovements), as shown above, was proved by us experimentally.

4. Discussion

The results of studying the typomorphism of placer gold and the mechanisms of its distribution in the east of the Siberian Platform are generalized for the first time. Based on the identified typical morphological features, it is pseudo-ore. In this connection, the following genetic types of placers were first identified in the studied area—alluvial modern and ancient (gold-bearing intermediate sources), aeolian (unconventional type).

In hydrodynamic conditions, gold grains, regardless of their shape, flatten, which is proved experimentally [43,44]. In the east of the Siberian Platform, flake and lamellar gold particles are observed in all alluvial bar placers. Slightly processed autochthonous ore gold in modern alluvial deposits was found locally—in the basins of the Eekit, Ebelyakh (Morgogor) rivers, the middle course of the Anabar River, as well as in the southeast in the middle Lena basin at the mouth of the Bolshaya Patom, Kamenka, and the Tokko and Torgo rivers [60,61]. For the first time, native gold of ore appearance ("Anabar" type) was identified by Shpunt [1] in the northeast of the Siberian platform. Identification of "ore" gold along the entire length of the Morgogor River (25 km) indicates the presence of an ore source in the riverbed itself [62]. The presence of gold particles of ore appearance in

alluvial placers in well-rounded flattened gold particles indicates just an additional supply of gold from the ore source.

In gold-bearing deposits, placer gold does not retain its morphological features but acquires a pseudo-ore appearance [47]. It is defined that gold of pseudo-ore appearance and gold particles, which surface records the casts of pressing-in of host strata's minerals, are widely distributed in the Quaternary alluvial deposits in all watercourses of the east of the Siberian Platform (Figure 16a–f). Such native gold is found at the Lena–Viluy interfluve in the river basins of the Viluy and the middle Lena, and in areas of erosion of the Ukukut formation of the Jurassic age, and the Anabar-Olenek interfluve of the basins of the Anabar, Eekitrivers, etc. and draining gold-bearing conglomerates of different ages. Earlier, previous researchers identified this gold as ore—"beligs-khaisky" [2] and "Olenek" [1] types of native gold (intergrowth of gold with quartz, ilmenite and other minerals), which gave them the reason to assume that the ore mineralization was superimposed on the gold-bearing intermediate sources of the Permian and Jurassic age.

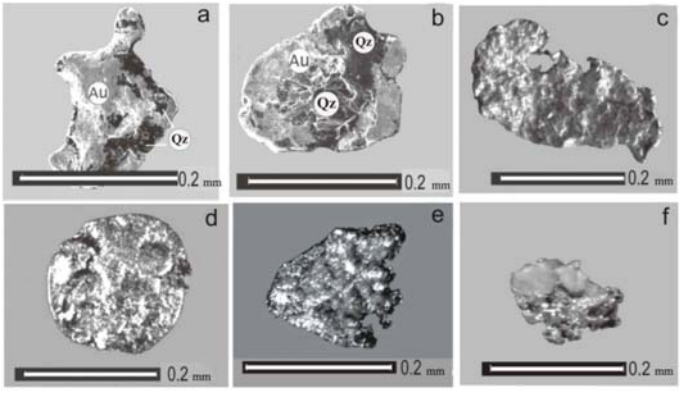

Figure 16. Pseudo-ore gold from deposits of different ages in the east of the Siberian Platform: (**a**,**b**) pseudo-intergrowths of gold (Au) with quartz (Qz), Lena–Anabar interfluve; (**c**,**d**) flake gold particles with casts of pressing-in on the surface of the minerals of the host deposits of the middle Lena basin; (**e**,**f**) flakes with ragged edges and depressed quartz on the surface of the Lena–Viluy interfluves.

Identified morphological features of native gold allowed us to refer to pseudo-ore one. This is due to the fact that native gold in ancient deposits undergoes several changes as a result of the impact of the lithostatic pressure of the overlying strata; in this case, there is a false " intergrowth" of native gold with quartz, ilmenorutile, zircon and other minerals of the host rocks, and in case of horizontal movements—the genesis of interstitial formations, splinters, hooks, needles and other forms. Pseudo-ore gold often forms aggregates, as it were, "intergrowths" of native gold with quartz and other minerals, which are not typical for intergrowths of "ore" gold since they do not have strong contacts of intergrowth of native gold with minerals (Figure 16). The surface of pseudo-ore gold from ancient conglomerates has a coarse-pitted, lumpy, fine-cellular microrelief, with casts of pressing-in of minerals of the host deposits. They differ from the primary casts of ore minerals by rounded shapes with no sharp appendages on the edges of the pits and from corrosion structures of the relief of supergene zones by a wider range of pits from 0.01 to 0.05 microns. Angular, elongated dents in the form of scars, longitudinal furrows, scratches, and areas of a mirror-polished surface are observed on the surface of gold particles.

This native gold is found in all alluvial bar placers and is represented by allochthonous well-rounded particles, mainly flake and lamellar forms with signs of pressing-in on the surface of minerals of the host deposits. They have a size of 0.1–0.25 mm, high fineness, are characterized by a practical absence of trace elements, and by recrystallized internal structure and thick high-grade shells. The presence of flaky gold with signs of pressing-in

on the surface of the host deposits' minerals indicates only the supply of native gold from gold-bearing intermediate sources of various ages.

Pseudo-ore gold, along with aeolian-shaped gold particles, was also first discovered by us in the Devonian conglomerates of the Timan Ridge [33]. Previous researchers explained the presence of "ore" gold by superimposed gold mineralization on the formed ancient placer [14,46]. In this regard, intensive searches were conducted in this area to find ore sources. However, we have revealed that the gold particles of the "ore" appearance are placer gold, and they are characterized by a coarse-pitted, lumpy and fine-cellular relief, the appendages have rounded outlines, and on the edges of some "ore" gold particles, relicts of ridges and a film-fibrous surface acquired in aeolian conditions were found. Sometimes in the "ore" gold, a capture of rounded minerals and pseudo-intergrowth of gold particles with quartz, ilmenorutile, garnet, etc., is observed. The casts of pressing minerals are characterized by a rounded shape and lack of growth facets. Identified morphological features in gold indicate its exogenous nature.

In the analysis of typomorphic features of placer gold in the Lena–Viluy and the Anabar-Olenek interfluves of the East Siberian platform, previously identified by Izbekov [2] —"beligs-khaisky" and by Shpunt [1]—"olenek" types of placer gold of ore, appearance was referred by us to pseudo-ore gold [47]. Gold of pseudo-ore appearance has been found in all watercourses in the east of the Siberian Platform [60]. The presence of gold of a pseudo-ore appearance indicates that the placer occurrences were formed due to the arrival of gold from ancient gold-bearing intermediate sources and not from primary sources. Thus, identifying pseudo-ore gold in alluvial placers is a specific criterion for determining which sources formed a gold-bearing placer (gold ore or gold-bearing intermediate sources).

Based on the identification of "ore" gold, called the "olenek type" by B. R. Shpunt [1], the Yakutskgeologiya conducted prospecting work to find ore sources of native gold in the Permian conglomerates of the Olenek uplift in the Sololi River basin, in the late 80s. However, we found that there are no signs of superimposed mineralization on this object. Recommendations on the inexpediency of searching for ore sources both in the Sololi River basin in the east of the Siberian Platform and in the Devonian conglomerates of the Ichet'yuTimanRidge were given by "Yakutskgeologiya", "Polyarnouralgeologiya", Ukhta Expedition. Thus, the discovery of pseudo-ore gold indicates only the supply of native gold from intermediate sources and not from primary sources, which serves as a morphogenetic criterion for determining the provenance of the gold placer.

The discovery of gold particles with signs of pressing of minerals of the host deposits and pseudo-ore gold in the gold-bearing deposits of the Paleozoic and Mesozoic in the east of the Siberian Platform is typical for all platform areas and served as the basis for the search for gold ore sources. It should be emphasized that the native gold of the ore appearance of the Proterozoic conglomerates of the Witwatersrand has the same shape and origin [24]. The identification of pseudo-ore gold indicates just the presence of gold-bearing conglomerates but not gold deposits. Identified morphological features of pseudo-ore gold can be a criterion for determining which sources formed the placer (ore or gold-bearing intermediate sources).

In aeolian conditions, regardless of the shape, native gold tends to acquire a ball shape. As a result of experimental, mineralogical and field studies, a new morphological type of placer gold—aeolian and a new genetic type of placer—aeolian were identified and proved [63]. The unusual forms are the result of the mechanical transformation of native gold in aeolian conditions. A detailed study of the typomorphic features of aeolian gold showed that it has certain morphological forms, granulometry, chemical composition and internal structure. Aeolian gold is not only of mineralogical interest but also forms high commercial concentrations, for example, the Witwatersrand deposit [25]. It is widely distributed; it occurs in deposits from the Proterozoic to the Cenozoic and is typical for all platform areas [4].

Experimental and mineralogical studies have proved that in the east of the Siberian Platform, the types of gold particles previously identified by Izbekov [2]: "baaginsky"—

toroidal, "chokulsky"—spherical hollow (globular), "kyuellyakhsky"—lamellar and tabular with rounded edges, lumpy, Shpunt [1] "udzhinsky" (toroidal and globular) are of aeolian origin. Formation of "baaginsky","chokulsky", "udzhinsky" types of placer gold is associated with the mechanical transformation of flake gold in aeolian conditions into a toroidal and then into a spherical hollow form [49]. The origin of the gold "kyuellyakhsky" type is explained by transforming the more massive lamellar, tabular, lumpy and rod-like shapes that form trough-shaped, canoe-shaped, disc-shaped, etc., and also massively lumpy and dumbbell-shaped gold particles with a film-fibrous surface, acquired in aeolian conditions.

A detailed study of typomorphic features of aeolian gold and mechanisms of distribution in the East Siberian platform made it possible to determine that aeolian gold of toroidal and spherical hollow form (transit gold) is widely observed in the territory of the Lena–Viluy and Lena–Anabar interfluves. On some objects, there are massive gold particles (deflationary gold), lamellar, tabular with ridgelike edges, and lumpy-spherical forms with signs of aeolian transformation (Figure 17a–i).

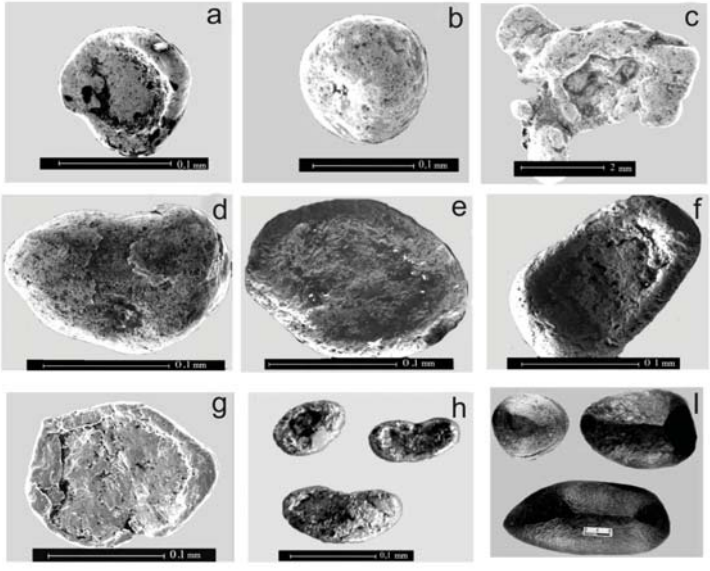

Figure 17. Gold with signs of wind-worn processing and ventifacts from the Quaternary deposits of the East of the Siberian Platform: (**a**–**c**) Lena–Anabar interfluve; (**d**–**f**) Lena–Viluy interfluve; (**g**,**h**) basin of the middle course of the Lena River; (**i**) ventifacts.

Aeolian gold (transit gold) forms high concentrations in the heads of the rivers of the Lena–Anabar and Lena–Viluy interfluves, where the basal aeolian horizons of the Cenozoic deposits formed during the Quaternary glaciation are eroded (sartanskoe, karginskoe, etc.). The producing layer overlaps the deflationary surface in a blanket-like manner and is complicated by jet fans. This layer has a low thickness (no more than 15–30 cm), is represented by pebble-gravel deposits with a low content of clay fraction, where there are gold particle sand associate minerals with signs of wind-worn processing, as well as ventifacts (Figure 17i).

The sites of the finds of aeolian gold are well correlated with the fragmentally developed surfaces of deflationary palaeodeserts, which halo can be reconstructed from the finds of ventifacts [45]. Gold particles with signs of wind-worn processing (flakes with ridgelike edges) with a size of 0.1–0.25 mm have an extensive halo of dispersion (transit) compared to aeolian gold particles larger than 0.25 mm (deflationary) since the latter isnot transported

over long distances due to their massiveness (aero-size). Therefore, it is possible to discover a deflationary gold placer by the halo of the distribution of toroidal and spherical hollow gold particles, which can serve as a search morphogenetic criterion for the aeolian type of placers.

Gold particles of aeolian-type in the natural environment are most likely formed in the zone of aeolian denudation. It is assumed that the grains of sand, drawn by the airflow, bombard the golden particles brought by denudation to the surface of the day. In this regard, there is a gradual deformation of the gold particles and their transformation.

Analysis of the mechanism of distribution of gold particles with signs of wind-worn processing based on the literature data and collections provided by Russian scientists allowed us to determine that toroidal and spherical hollow forms (aeolian gold) are widely distributed on all platforms of the world and are found in sedimentary deposits from the Proterozoic to the Cenozoic (Figures 1 and 18a–i).

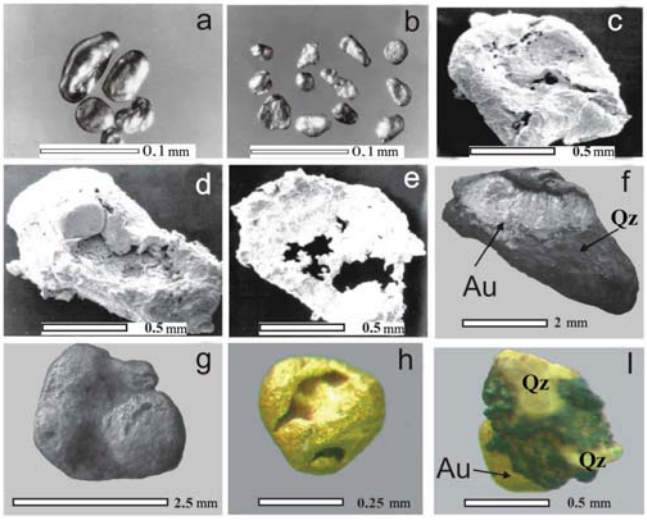

Figure 18. Gold particles with signs of wind-worn processing of platform areas, as well as on the territory of Tuva and Mongolia: (**a**,**b**) Russian [41]; (**c**–**e**) African [37]; (**f**,**g**) Tuva (TIIDNR); (**h**,**i**) Mongolia (IGM SB RAS).

Gold grains of a similar shape have been found on the Siberian, East European, North American, South American, African, and Australian platforms [4]. An extensive halo of dispersion of toroidal and spherical hollow gold was first identified in the Siberian Platform deposits of different ages. Massive gold particles with signs of wind-worn processing were found in the ancient Precambrian metaterrigenous rocks of the Baltic Shield [11] in the Northern Urals [12], in metal-bearing conglomerates of the Devonian age of the Timan Ridge [33], as well as in fluvioglacial deposits of the Cenozoic age of the Kola Peninsula [34] and in the central part of Russia [13,15,29,30,35]. Similar forms of gold particles were also found in deposits of different ages in the Scandinavian countries, France, Czechoslovakia, and Cyprus [18,19,21,26]. On the North American platform, spherical hollow forms of gold are observed in the alluvial deposits of the Alberta deposits in Canada, Abitibi—the province of Ontario and states of Oregon and Alaska—Colorado, Klondike and Nome [16,22,23]. In the south of the American platform, gold particles with signs of wind-worn processing were found in placer deposits of Bolivia, Colombia, Panama, Ecuador, and in the south-eastern part of Africa—in Mozambique, Zimbabwe, and Tanzania [22,58]. On the African platform, aeolian gold particles were found in the Baffing River basin (Republic of Guinea), in the Kangaba (Mali) deposits [28] and in the

Witwatersrand [25,64]. On the Australian platform, spherical hollow forms of native gold were found in alluvial deposits [17]. Native gold of a similar shape is found in the alluvium (Papua New Guinea) [20], in the Yinan deposit (China) [27]. Aeolian gold was discovered in Mongolia (Samar Mine) and Tuva (Tanku-Tuva).

Massive gold particles with signs of wind-worn processing are not so widely found since the alluvial signs of this gold are less evident, in contrast to the morphological features of toroidal and spherical hollow forms. In this regard, it was usually taken for alluvial gold. This gold was found in a number of objects of the Anabaranteclise [1], the Viluysyneclise [2], as well as in the Urals [12] and in Mongolia and Tuva [4,36]. Thus, gold with signs of wind-worn processing is widely distributed on all platforms of the World and adjacent territories in sedimentary deposits from the Proterozoic to the Cenozoic [4] (Figure 1).

Based on the discovery of native gold particles with signs of wind-worn processing, it is determined that aeolian placers of gold can occur both due to the direct destruction of the ore source and due to previously formed proluvial alluvial and coastal-marine placers. In this connection, in the east of the Siberian platform and in other studied territories (the East-European platform, Mongolia, Tuva, etc.), aeolian placers (autochthonous and allochthonous) and placers of heterogeneous origin (aeolian-proluvial, aeolian-alluvial, etc.) are identified. Since gold particles with wind-worn processing are not only of mineralogical interest but also form high concentrations of metal, the conclusion about the prospects of discovering aeolian placers of gold of various ages on all platforms, as well as on the territory of Tuva and Mongolia, is proved.

In general, it is determined that aeolian gold is found in both Proterozoic and Cenozoic sediments and is typical for most epochs of the earth's development, where the aeolian processes intensively occurred. At the same time, it was revealed that aeolian gold has not only a scientific "mineralogical interest" but also forms concentrations on a commercial scale. For example, the famous Witwatersrand deposit—here, the aeolian forms of gold deposits form high metal contents in specific deposits (conglomerates), where ventifacts are noted, and clay material is practically absent [25,64].

The extent of the influence of aeolian processes on the formation of placers is poorly understood. In the existing classifications, only the hydrodynamic factor of the formation of these placers is considered. However, Vernadsky [65] described the aeolian placers of gold found in Western Australia in Kalgoorlie and Kolgurla: "The richest placers lay on the very surface and towards the bottom the placer gold-depleted" (V. II p. 161–162). Shilo [66] believed that the development of the problem of the formation of aeolian gold placers deserves special attention and can serve as a basis for improving the search and exploration work for the discovery of aeolian gold placers and methods for their study. The arid climate is most favorable for the formation of gold-bearing aeolian placers. However, the literature data analysis showed that even during the glaciation, aeolian processes also played an important role in sedimentation, which affected the formation of the landscape [46] and, undoubtedly, the nature of placer formation and transformation of gold particles. We found aeolian landforms (basins) (deflation grooves, etc.) on the modern landscape of the east of the Siberian and East-European platforms, as well as on the territory of Mongolia and Tuva [4]. It is revealed that in the sediments composing these landforms, the presence of aeolian gold particles and minerals with signs of wind-worn processing and ventifacts is reported. Aeolian processes affected the formation of placers in the Quaternary and the ancient epochs of the earth's evolution. This is evidenced by the revealed signs of aeolian activity (the presence of aeolian gold particles and ventifacts, a thin producing horizon, etc.) in the Devonian placers of the Timan Ridge [33] and in the Witwatersrand field with a huge gold content [25].

Based on the discovery of gold particles with signs of wind-worn processing, it is determined that aeolian placers of gold can occur both due to the direct destruction of the primary source and due to previously formed proluvial alluvial and coastal-marine placers. In this connection, in the east of the Siberian Platform and in other studied territories (the East-European Platform, Mongolia, Tuva, etc.), aeolian (autochthonous and allochthonous)

placers and placers of heterogeneous origin (aeolian-proluvial, aeolian-alluvial, etc.) are distinguished.

The presence of massive gold particles with signs of wind-worn processing in the deposits indicates the formation of an autochthonous aeolian placer in this area. Aeolian placer is characterized by a specific structure of the producing horizon, which covers the deflationary surface in a blanket-like manner, is complicated by jet fans, and has a low thickness (10–30 cm). This horizon is represented by a pebble-gravel material with a low content of clay fraction, with the presence of ventifacts and massive gold particles with signs of wind-worn processing. The formation of autochthonous aeolian placers with the presence of aeolian gold particles is possible not only in the platform areas but also in the territories of Mongolia and Tuva. The discovery of toroidal and spherical hollow gold indicates the formation of an allochthonous aeolian placer in this area. These placers are characterized by a high differentiation of aeolian gold, presence of toroidal and flake gold particles with thin ridgelike edges. Gold particles here are a transit metal and are characteristic of both autochthonous and allochthonous aeolian placers. The formation of such placers is possible both in the basins and in the deflation grooves. Gold particles of a very fine fraction less than 0.1 mm can be found in dune deposits, but they are not of commercial interest.

5. Conclusions

Based on the identified typomorphic features of placer gold, a set of determined morphogenetic criteria is proposed to identify the genesis of placers and different sources in the platform areas, which allows more correctly selecting search methods and improving the efficiency of forecasting ore and placer gold deposits. The discovery of native gold with signs of wind-worn processing in Quaternary deposits indicates aeolian placers' formation. Gold particles with signs of wind-worn processing (flakes with ridgelike edges, toroidal and spherical hollow) with a size of 0.1–0.25 mm, forming an extensive halo ofdispersionin the Quaternary deposits (allochthonous placers), were identified by us as transit gold according to sieving. Gold larger than 0.25 mm with signs of wind-worn processing (lumpy with rounded appendages with a film-fibrous surface, etc.) is less common and belongs, in terms of sieving, to a deflationary metal. This gold is not transported over long distances and forms autochthonous placers. The presence of disc-shaped and lamellar gold particles with ridgelike edges in alluvial placers is typical for placers of heterogeneous origin, formed due to deflation of proluvial placer. Deflationary (autochthonous) placers of native gold can be found by the halo of its distribution of toroidal and spherical hollow forms, which, of course, are the search morphogenetic criterion of aeolian placers.

The discovery of pseudo-ore gold in alluvial placers only indicates the arrival of gold from intermediate gold-bearing sources of different ages and not from primary endogenic sources, which is a morphogenetic criterion for determining different sources of the placer. In modern gold placers, the presence of native gold of a pseudo-ore appearance can serve as a search criterion for the discovery of gold-bearing conglomerates with a high gold content, which are ancient buried placers of various ages, for example, the placer of the Devonian age of Ichet-Yu (TimanRidge) or the Permian placer of Sololi (Olenek uplift).

Thus, the determination of the genotype of placer gold by morphological features (alluvial, aeolian) makes it possible to more correctly reconstruct the geological-geomorphological conditions of placer formation and, thereby, increases the reliability of the forecast and the efficiency of the search and mining of placers. The discovery of gold of pseudo-ore and ore appearance in the Quaternary alluvial deposits makes it possible to identify which sources formed the modern placers—ore or intermediate gold-bearing deposits (ancient conglomerates), which contributes to the improvement of the methods of search and exploration of placer and ore deposits of gold. The method developed for diagnosing the genotype of placer gold by its morphological characteristics (alluvial, aeolian, pseudo-ore) can be successfully used by production geological organizations to search and explore ore and placer gold deposits.

Funding: The research was carried out within the framework of the state task of the Diamond and Precious Metals Geology Institute, Siberian Branch, Russian Academy of Sciences, funded by the Ministry of Science and Higher Education of the Russian Federation project No. 0381-2019-0004.

Data Availability Statement: All studies were previously approved and published in the following articles, monographs and doctoral work of the author:

1. Filippov, V.E., Nikiforova, Z.S. Transformation of Native Gold Particles in the Process of Eolian Impact. *Rep. USSR Acad. Sci.* **1988**, *299*, 1229–1232.
2. Nikiforova, Z.S., Filippov, V.E. Gold of Pseudo-ore Appearance in Ancient Conglomerates. *Rep. USSR Acad. Sci.* **1990**, *311*, 455–457.
3. Filippov, V.E., Nikiforova, Z.S. Formation of Gold Placers under the Influence of Eolian Processes. Nauka: Novosibirsk, Russia, 1998; p. 160.
4. Nikiforova, Z.S., Filippov, V.E., Gerasimov, B.B. Influence of Eolian Processes on the Formation of Gold-bearing Placers in Various Epochs of the Earth's Evolution. *Geol. Geophys.* **2005**, *5*, 517–528.
5. Nikiforova, Z.S. Typomorphism of placer gold as an indicator of the genesis of placers and indigenous sources (East of the Siberian Platform). Dissertation of the Doctor of Geological and Mineralogical Sciences. North-Eastern Federal University Publishing House, Yakutsk, Russia, 2014, p. 349.

Conflicts of Interest: The author declares that there is no conflict of interest.

References

1. Shpunt, B.R. Genetic Types of Gold Occurences in the North-eastern Part of the Siberian Platform. *Uch. Zap. NIIGA Reg. Geol.* **1970**, *18*, 5–15.
2. Izbekov, E.D. Features of Placer Gold of the Viluy Syneclise and Adjacent Areas. In *Placers of Gold and Their Connections with Primary Sources in Yakutia*; KnizhnoeIzd-vo: Yakutsk, Russia, 1972; pp. 178–199.
3. Yablokova, S.V. New Morphological Variety of Gold and Its Origin. *Dokl. USSR Acad. Sci.* **1972**, *205*, 936–939.
4. Nikiforova, Z.S.; Filippov, V.E.; Gerasimov, B.B. Influence of Eolian Processes on the Formation of Gold-bearing Placers in Various Epochs of the Earth's Evolution. *Geol. Geophys.* **2005**, *5*, 517–528.
5. Timofeev, V.I. Placer Gold Content of the Viluy River. *Explor. Prot. Miner. Resour.* **1965**, *6*, 1–5.
6. Anisimov, N.I.; Tishchenko, E.I.; Tishchenko, M.D. Migration Distance and Conditions of Gold Accumulation in Alluvial Deposits of the Junction Zone of the Siberian Platform with the Baikal Mountain Region. In *Transportation of Mineral Resources in Placers*; YBAS USSR: Yakutsk, Russia, 1975; pp. 77–78.
7. Mordvin, A.P. Khuzhir Ore Occurrence of Gold-bearing Conglomerates. In *Geology and Gold Content of the Riphean and Vendian Conglomerates of the Southern Rim of the Irkutsk Amphitheater*; Irkutsk East-Siberian Publishing House: Irkutsk, Russia, 1972; pp. 154–189.
8. Shalamov, I.V. Morphological Features of Placer Gold in the North-east of the Siberian Platform. In *Theses of the Report of the VIII Meeting on the Geology of Placers*; Kiev Book Printing House of Scientific Books: Kiev, Russia, 1987; pp. 125–126.
9. Goncharov, I.M.; Izraelev, L.M.; Natapov, L.M.; Nedeshev, V.B.; Biterman, I.M.; Yablokova, S.V. Stages of Placer Formation and Mineralogical Features of Gold from One of the Ancient Protrusions of the Siberian Platform. In *Theses of the Report of the VIII Meeting on the Geology of Placers*; Kiev Book Printing House of Scientific Books: Kiev, Russia, 1987; pp. 107–108.
10. Alexandrov, A.G.; Mendel, V.A. Complex Gold-rare-metal Mineralization of Basal Paleozoic Conglomerates of the Siberian Platform Margin. In *Theses of the Report of the VIII Meeting on the Geology of Placers*; Kiev Book Printing House of Scientific Books: Kiev, Russia, 1987; pp. 118–120.
11. Negrutsa, V.Z. Some Mechanisms of Distribution and Morphological Types of Gold in the Precambrian Metaterrigenous Rocks of the Eastern Part of the Baltic Shield. *Rep. USSR Acad. Sci.* **1973**, *211*, 197–200.
12. Ryzhov, B.V.; Nikolaeva, L.A.; Budilin, Y.S.; Lantsev, I.P. Typomorphic Features of Gold Placers of the Northern Urals. *Geol. Explor.* **1977**, *5*, 72–79.
13. Minyailo, L.A. On the Origin of the Toroidal Form of Placer Gold (the Urals and the West Siberian Plain). In *Geology and Mineral Resources of the West Siberian Plate and Its Folded Framing: Theses of the Department of the All-Union Mineralogical Society*; Nauka Publishing House: Moscow, Russia, 1980; pp. 8–11.
14. Kotov, A.A.; Povonsky, V.V.; Yatskevich, B.A. Metalliferous Conglomerates of One of the Regions of the East-European Platform. In *Abstracts of the Report of the VIII Meeting on the Geology of Placers*; Kiev Book Printing House of Scientific Books: Kiev, Russia, 1987; pp. 176–177.
15. Naumov, V.A.; Goldyrev, V.V. Morphology of Gold from the Modern Alluvium of the Upper Kama Basin. *Mineral. Ural.* **1998**, *11*, 38–40.
16. Bogdanovich, K.I. Gold. *Comm. Study Nat. Product. Forces Russ. Ptg.* **1919**, *4*, 10.
17. Dunn, E.J. *Geology of Gold*; Charles Griffin: London, UK, 1929; p. 303.

18. Tourtelot, N.A. Gold Content of Native Sulfur from Cyprus:U.S. Geol. *Surv. Circ.* **1969**, *622*, 5.
19. Machairas, G. Contribution a L'etudeMineralogiqueMetallogenique de L'or. *Bur. Rech. Geol. Min. Bull.* **1970**, *11*, 72.
20. Lowenstein, P.L. Economic Geology of the Morobe Gold Field, Popua New Guinea. *New Guinea Geol. Surv.* **1982**, *9*, 245.
21. Klominsky, J.; Jiranek, J.; Malec, J.; Novák, F.; Odehnal, L.; Veselovský, F. Gold in the Continental Permo-carboniferous of the Bohemian Massif. *Sbornik Geol. Ved.* **1983**, *25*, 111–186.
22. DiLabio, R.N.W.; Newsome, J.W.; McIvor, D.F.; Lomenstein, P.L. The Spherical Form of Gold: Man-made or Secondary? *Econ. Geol.* **1988**, *83*, 153–162. [CrossRef]
23. Giusti, L. The Morphology, Mineralogy and Behaviour of «Fine-grained» Gold from Placer Deposits of Alberta: Sampling and Implications for Mineral Exploration. *Can. J. Earth Sci.* **1986**, *23*, 1662–1672. [CrossRef]
24. Oberthur, T.; Saagger, R. Silver and Mercury in Gold Particles from the Proterozoic Witwatersrand Placer Deposits of South Africa: Metallogenic and Geochemical Implication. *Econ. Geol.* **1986**, *81*, 20–31. [CrossRef]
25. Minter, W.E.L.; Goedhart, M.; Knight, J.; Frimmel, H.E. Morphology of Witwatersrand Gold Grains from the Basal Reef: Evidence for Their Detrital Origin. *Econ. Geol.* **1993**, *88*, 237–248. [CrossRef]
26. Vuorelainen, Y.; Tornroos, R. Man-made Pt-$PtAs_2$ Spherules after Sperrylite from Alluvial Deposits in Finnish Lapland. *Can. Miner.* **1986**, *24*, 523–528.
27. Zhaoxia, Q. Gold Spheroids Form Oxidation Zone of Yinnan Gold Deposit in Ningxia, China. *KexueTongbao* **1986**, *32*, 576.
28. Freyssinet, P.; Zeegers, H.; Tardy, Y. Morphology and Geochemistry of Gold Grains in Lateritic Profiles of Gold Southern Mali. *J. Geoch. Explor.* **1988**, *32*, 17–31. [CrossRef]
29. Lukyanenok, N.P.; Kolpakov, V.V. Discovery of Placer Gold in Belorussia. *Gold Russ.* **1995**, *1*, 35–40.
30. Kalnichenko, S.S.; Ivanov, N.M.; Karimova, N.A.; Konyayev, M.V.; Filippov, V.P.; Yablokova, S.V. The Main Types of Gold-bearing Deposits of the Sedimentary Cover of the Central Part of the East-European Platform. *Ores Met.* **1995**, *6*, 5–15.
31. Sukhoroslov, V.L.; Yablokova, S.V. Factors of Formation of Allochthonous Placers in South-East Africa. In *Natural and Man-Made Placers and Deposits of Weathering Crust at the Turn of the Millennium, Proceedings of the XII International Meeting on the Geology of Placers and Deposits of Weathering Crusts, Moscow, Russia, 25–29 September*; IGEM RAS Publishing House: Moscow, Russia, 2000; pp. 342–344.
32. Nikiforova, Z.S.; Surnin, A.A. Problem of Alluvial Gold Content of the Middle Lena. *Russ. Geol.* **2001**, *5*, 70–72.
33. Nikiforova, Z.S.; Filippov, V.E.; Tsaplin, A.E. Aeolian Gold of One of the Placer Deposits of the Timan Ridge. *Geol. Ore Depos.* **1991**, *33*, 112–116.
34. Surkov, A.V. *Atlas of the Morphology of Native Gold*; Publishing and Printing Company "StudiA": Moscow, Russia, 2000; Volume 1, p. 60.
35. Voskresensky, K.I. Typomorphic Features of Placer Gold and Platinoids of the Upper Kama Depression. In *Natural and Man-Made Placers and Deposits of Weathering Crust at the Turn of the Millennium, Proceedings of theXII International Meeting on the Geology of Placers and Deposits of Weathering Crusts, Moscow, Russia, 25–29 September*; IGEM RAS Publishing House: Moscow, Russia, 2000; pp. 82–83.
36. Nikiforova, Z.S.; Prudnikov, S.G.; Lebedev, V.I.; Oidup, C.K.; Tulaeva, E.G. The Possibility of Identifying Eolian Gold Placers on the Territory of Tuva. *Lithol. Miner. Resour.* **2007**, *1*, 25–32.
37. Petrovskaya, N.V. *Native Gold*; Nedra: Moscow, Russia, 1973; p. 347.
38. Watterson, J.R. Crystalline Gold in Soil and the Problem of Supergene Nugget Formation: Freezing and Exlusion as Genetic Mechanisms. *Precambrian Res.* **1985**, *30*, 321–335. [CrossRef]
39. Gladkov, V.G.; Tatarinov, A.V.; Tomilov, B.V. Fluidoclastogenic Origin of the Gold-bearing Coarse-clastic Strata of the BaleiGraben. *Geol. Geophys.* **1989**, *5*, 42–49.
40. Kyte, F.T.; Zhou, Z.; Wasson, J.T. High Noble Metal Cjncentration in Late Pliocene Sediment. *Nature* **1981**, *292*, 417–420. [CrossRef]
41. Nikolaeva, L.A.; Ryzhov, B.V.; Yablokova, S.V. Globular-toroidal Gold of Sedimentary Strata of the Platforms. In *Abstracts of the Report of the VIII Meeting on the Geology of Placers*; Kiev Book Printing House of Scientific Books: Kiev, Russia, 1987; pp. 56–58.
42. Webster, J.G. The Solubility of Gold and Silver in the System Au-Ag-S-O_2-H_2O at 25 °C and 1 Atm. *Geochim. Cosmochim. Acta* **1986**, *50*, 1837–1845. [CrossRef]
43. Tishchenko, E.I. Evolution of Gold Flattening in Alluvial Placers. *Geol. Geophys.* **1981**, *10*, 34–40.
44. Filippov, V.E. *Modeling of Conditions for the Formation of Alluvial Placers of Gold*; Yakut Institute of Geological Sciences SB AC USSR: Yakutsk, Russia, 1991; p. 44.
45. Kolpakov, V.V. Fossil Deserts of the Lower Lena River. *Bull. Comm. Study Quat. Period* **1970**, *37*, 76–82.
46. Ovsyannikov, I.I.; Barokha, L.S.; Yatskevich, B.A.; Tsaplin, A.E.; Kotov, A.A. Material Composition and Possible Sources of Fossil Polymineral Placers in One of the Areas of the East-European Platform. In *Abstracts of the Report of the VIII Meeting on the Geology of Placers*; Kiev Book Printing House of Scientific Books: Kiev, Russia, 1987; pp. 187–188.
47. Nikiforova, Z.S.; Filippov, V.E. Gold of Pseudo-ore Appearance in Ancient Conglomerates. *Rep. USSR Acad. Sci.* **1990**, *311*, 455–457.
48. Girard, R.; Tremblay, J.; Néron, A.; Longuépée, H. Automated Gold Grain Counting. Part 1: Why Counts Matter! *Minerals* **2021**, *11*, 337. [CrossRef]
49. Filippov, V.E.; Nikiforova, Z.S. Transformation of Native Gold Particles in the Process of Eolian Impact. *Rep. USSR Acad. Sci.* **1988**, *299*, 1229–1232.

50. Miall, A.D. *The Geology of Fluvial Deposits*; Springer: New York, NY, USA, 1996; p. 582.
51. Robert, A. *River Processes: An Introduction to Fluvial Dynamics*; Rutledge: Abingdon, UK, 2003; p. 238.
52. Dill, H.G. Grain Morphology of Heavy Minerals from Marine and Continental Placer Deposits, with Special Reference to Fe-Ti Oxides. *Sediment. Geol.* **2007**, *198*, 1–27. [CrossRef]
53. Dill, H.G. Geogene and Anthropogenic Controls on the Mineralogy and Geochemistry of Modern Alluvial-(Fluvial) Gold Placer Deposits in Man-made Landscapes in France, Switzerland and Germany. *J. Geochem. Explor.* **2008**, *99*, 29–60. [CrossRef]
54. Dill, H.G. Gems and Placers-A Genetic Relationship Par Excellence. *Minerals* **2018**, *8*, 470.
55. Knight, J.B.; Morison, S.R.; Mortensen, J.K. The Relationship between Placer Gold Particle Shape, Rimming, and Distance of Fluvial Transport as exEPMAlified by Gold from the Klondike District, Yukon Territory, Canada. *Econ. Geol.* **1999**, *94*, 635–648. [CrossRef]
56. Chapman, R.J.; Mortensen, J.K. Application of Microchemical Characterization of Placer Gold Grains to Exploration for Epithermal Gold Mineralization in Regions of Poor Exposure. *J. Geochem. Explor.* **2006**, *91*, 1–26. [CrossRef]
57. Nikiforova, Z.S.; Kalinin, Y.A.; Makarov, V.A. Evolution of Native Gold under Exogenous Conditions. *Russ. Geol. Geophys.* **2020**, *61*, 1244–1259. [CrossRef]
58. Slashcheva, L.I.; Vinichenko, M.N. Gold Content of the Vendian Conglomerates of the South-Eastern Sayans. In *Geology and Gold Content of the Riphean and Vendian Conglomerates of the Southern Rim of the Irkutsk Amphitheater*; Irkutsk East-Siberian Publishing House: Irkutsk, Russia, 1972; pp. 115–154.
59. Gerasimov, B.B.; Filippov, V.E.; Nikiforova, Z.S.; Syromyatnikova, A.S. A New Variety of Eolian Gold. *WMO Brief.* **2002**, *6*, 55–56.
60. Nikiforova, Z.S.; Gerasimov, B.B.; Tulaeva, E.G. Genesis of Gold-bearing Placers and Their Possible Sources (East of the Siberian Platform). *Lithol. Miner. Resour.* **2011**, *1*, 21–35.
61. Nikiforova, Z.S.; Gerasimov, B.B.; Glushkova, E.G.; Kazhenkina, A.G. Gold Content of the East of the Siberian Platform (Placers-primary Sources). *Geol. Ore Depos.* **2013**, *55*, 305–319. [CrossRef]
62. Nikiforova, Z.S.; Bazilevskaya, R.V.; Gerasimov, B.B. The Finds of Ore Gold in the Basin of the Ebelyakh River, North-east of the Siberian Platform. *Russ. Geol.* **2006**, *5*, 48–52.
63. Filippov, V.E.; Nikiforova, Z.S. *Formation of Gold Placers under the Influence of Eolian Processes*; Nauka: Novosibirsk, Russia, 1998; p. 160.
64. Safonov, Y.G.; Bershov, L.V.; Bogatyrev, B.A. The Main Features of the Primary Sedimentary Nature of the Early Proterozoic Gold-uranium Ores of the Witwatersrand Basin (South Africa). In *Natural and Man-Made Placers and Deposits of Weathering Crust at the Turn of the Millennium, Proceedings of the XII International Meeting on the Geology of Placers and Deposits of Weathering Crusts, Moscow, Russia, 25–29 September*; IGEM RAS Publishing House: Moscow, Russia, 2000; pp. 325–328.
65. Vernadsky, V.I. Selected Works. In *6 t*; Publishing House of the USSR Academy of Sciences: Moscow, Russia, 1955; p. 616.
66. Shilo, N.A. *The Doctrine of Placers*; Academy of Mining Sciences: Moscow, Russia, 2000; p. 632.

minerals

MDPI

Article

Experimental Study of Pt Solubility in the CO-CO_2 Fluid at Low f_{O2} and Subsolidus Conditions of the Ultramafic-Mafic Intrusions

Alexander Simakin [1,2,*], Tamara Salova [1], Anastassia Y. Borisova [3,4], Gleb S. Pokrovski [3], Olga Shaposhnikova [1], Oksana Tyutyunnik [5], Galina Bondarenko [1], Alexey Nekrasov [1] and Sergey I. Isaenko [6]

1 Institute of Experimental Mineralogy, Russian Academy of Sciences, 142432 Chernogolovka, Moscow Region, Russia; salova@iem.ac.ru (T.S.); olga_geolog@mail.ru (O.S.); bond@iem.ac.ru (G.B.); alex@iem.ac.ru (A.N.)
2 Institute of the Earth Physics, Russian Academy of Sciences, B. Gruzinskaya Str., 10123242 Moscow, Russia
3 Géosciences Environnement Toulouse, GET-UMR 5563-OMP-CNRS, Université de Toulouse III, IRD, CNES, 14 Avenue E. Belin, 31400 Toulouse, France; anastassia.borisova@get.omp.eu (A.Y.B.); gleb.pokrovski@get.omp.eu (G.S.P.)
4 Geological Department, Lomonosov Moscow State University, Vorobievu Gori, 119991 Moscow, Russia
5 Vernadsky Institute of Geochemistry and Analytical Chemistry, Russian Academy of Sciences, Kosygin Str. 19, 119334 Moscow, Russia; NMlab@geokhi.ru
6 Institute of Geology, Komi Science Centre, Ural Branch of Russian Academy of Sciences, Pervomayskaya, 54, 167982 Syktyvkar, Russia; s.i.isaenko@gmail.com
* Correspondence: simakin@iem.ac.ru; Tel.: +7-910-492-63-62

Citation: Simakin, A.; Salova, T.; Borisova, A.Y.; Pokrovski, G.S.; Shaposhnikova, O.; Tyutyunnik, O.; Bondarenko, G.; Nekrasov, A.; Isaenko, S.I. Experimental Study of Pt Solubility in the CO-CO_2 Fluid at Low f_{O2} and Subsolidus Conditions of the Ultramafic-Mafic Intrusions. *Minerals* **2021**, *11*, 225. https://doi.org/10.3390/min11020225

Academic Editor: Galina Palyanova

Received: 22 December 2020
Accepted: 18 February 2021
Published: 23 February 2021

Abstract: The solubility of Pt in CO-CO_2 fluid was studied experimentally at P = 50–200 MPa and T = 950 °C. A mixture of MgC_2O_4 and $MgCO_3$ was used as a source of the fluid. Upon the reaction of the Pt capsule walls and the fluid, a carbonyl of platinum is formed. The use of the high-temperature quartz ceramics as a fluid trap avoids the effect of mechanical contamination with Pt from the eroded capsule walls. The total content of platinum in the porous fluid traps was measured by the Electrothermal Atomic Absorption (ET-AAS) method. In some experiments, the local analysis of traps was carried out by the Laser Ablation Inductively Coupled Plasma Mass Spectrometry (LA-ICP-MS) method. The composition of fluid in bubbles captured in an albite glass trap was studied by micro-Raman spectroscopy. On the capsule walls and MgO, Pt "whiskers" of submicron diameter were observed, which were formed as a product of carbonyl decomposition during quenching. About 5–15% of carbonyl withstands quenching resulting in 1.5 to 2 ppm Pt soluble in acetone (runs at P = 200 MPa) in a quartz glass trap. The amount of Pt soluble in acetone from the capsule walls corresponds to a concentration of up to 8 ppm in the fluid. A high content of soluble Pt of 2000–3000 ppm was determined in a carbon coated MgO matrix. Our study demonstrated that the solubility of Pt in the CO-CO_2 fluid is 15–150 ppm, presumably in the form of $Pt_3(CO)_6^{2-}$ under conditions corresponding to the conditions of the subsolidus stage of layered ultramafic-mafic and ultramafic-alkaline intrusions formation. Our preliminary data showed that this solubility will increase with the addition of water at low f_{O2}.

Keywords: platinum; mafic-ultramafic intrusion; carbonic fluid; isoferroplatinum; platinum carbonyl

1. Introduction

Platinum group elements (PGE) are both chalcophile and siderophile elements. Their lower contents in the mantle and crust relative to those of chondrite are explained by the strong fractionation into the iron core at the early stage of the Earth's formation. Likewise, sulfide melts concentrate all PGE upon separation from basic magmas. At conditions of high oxygen fugacity (f_{O2}) in the basic magmas of the subduction zones, no sulfides are formed and PGE are disseminated in the intrusive rocks. In the Ural-Alaska concentric

intrusions of subduction origin, PGE are mobilized and concentrated at the post-magmatic stage as a result of the high-temperature fluid-rock interaction [1]. Postmagmatic fluid is also involved in the formation of the low sulphide type PGE deposits of Merensky reef type in the layered ultramafic-mafic intrusions with sulfide mineralization (Bushveld, SA and other) [2]. In the Merensky Reef, zircon and thorite were deposited from high-temperature fluid along with PGE and chromite [3]. The crystallization temperature estimated by the titanium contents in the zircon ranges from 750 to 930 °C.

Fluids that are active agents during the evolution of PGE-bearing basic-ultrabasic intrusions contain carbon, which is confirmed by an occurrence of carbonaceous matter in mineral form and in the form of fluid inclusions. The fluid–rock (melt) interaction continues in the temperature range from magmatic to the (background) temperature of the host rocks. Following the high-temperature stage, the fluid-rock system is quenched, and the fluid equilibrates at lower temperature. In a Stillwater complex (MT, USA), assemblage of graphite-calcite-forsterite-antigorite was equilibrated at the temperature below 510 °C [4]. Association of graphite with quartz and magnetite in the ultramafic pegmatites of the Bushveld complex was described to be equilibrated at T = 500–600 °C [5]. The fluid trapped in the solidified basic-ultrabasic rocks was also equilibrated at the subsolidus temperatures, and therefore contained reduced carbon components mainly in the form of CO_2 and CH_4. Hanley et al. [6] reported the $CO_2 \pm CH_4$ fluid and concentrated brine inclusions in quartz of the late granophyric albite-quartz core of a zoned pegmatite body in the Gabbronorite of Stillwater Complex. Konnikov and Vasyukova [7] observed fluid inclusions in quartz from sulfide-bearing amphibolized pyroxenite (Shanuch Ni-bearing pluton, Kamchatka) containing 79 vol.% of CO_2 and 12 vol.% of CH_4. Bulk-rock analysis of the basic-ultrabasic PGE-bearing Yoko-Dovyren intrusion (Trans-Baikal region, Russia) showed an increased content of CH_4 (up to 15 cm^3/kg) and H_2 (up to 7 cm^3/kg) in the mineralized reefs of the Stillwater type [8]. An appreciable CO content (up to 2 cm^3/kg) was found in the lower dunite-troctolite part of this intrusion. According to fluid inclusion data (from Au–Pt-rich quartz-sulfide-epidote veins, Sudbury Igneous Complex), Hanley et al. [9] concluded that at a late stage, Cu and partially Ag and Bi were fractionated into a gas phase enriched in CH_4, in equilibrium with a coexisting brine enriched with Zn, Pb, Mn.

Graphite deposited from the fluid at the low oxygen fugacity (f_{O2}) near CCO buffer (carbon dioxide-carbon oxide buffer) below quartz-fayalite-magnetite buffer (QFM)). There was a unique observation of ilmenite-titanomagnetite inclusion in the isoferroplatinum crystal in Konder PGE deposit (alkaline-ultramafic concentric intrusion, Russia) which indicates equilibration conditions at T = 700 °C and f_{O2} = QFM-1.6 [10]. High solubility of PGE and Au at high oxygen fugacity in form of chloride complexes is well established [11] and it was attributed to the ore formation in the ultramafic cumulus different from actual redox conditions. At low f_{O2} between QFM and wustite-magnetite (WM) buffers, PGE, Au, Ag, Ni, Co may exist in their native states. Methane is a non-polar compound that weakly interacts with most substances. While in a reduced carbonic fluid, CO can react with metals to form carbonyls Me_xCO_y, which can become important PGE transporting species. Many carbonyls, e.g., carbonyls of Ni, Cr, Mo are stable at low pressures and temperatures up to 150–200 °C and are widely used in metallurgy and chemical industry (e.g., [12]). The stability of carbonyls at high pressure and temperature is poorly studied.

In geological processes, the main prerequisite of carbonyls formation is sufficiently high CO content in the fluid. The main forms of the carbon in C-O-H system at high temperatures are CO_2, CO and CH_4. At high oxygen fugacity, CO_2 prevails while at low f_{O2}, carbon monoxide and CH_4. Maximum CO/CO_2 ratio is controlled by the reaction of CCO buffer:

$$C + CO_2 = 2CO, \quad (1)$$

Reaction (1) is endothermic and has positive volume effect, therefore ratio CO/CO_2 rises with temperature increase and pressure decrease. As mentioned above, methane pre-

dominates in the low-temperature fluid inclusions observed mainly in the quartz of late differentiates of basic-ultrabasic magmas. Ratio CO/CH_4 is controlled by reaction:

$$CO + 3H_2 = CH_4 + H_2O, \quad (2)$$

Reaction (2) is exothermic and has negative volume effect correspondingly ratio CO/CH_4 rises with temperature increase and pressure decrease. When the oxygen fugacity in the fluid is buffered externally, for example, by the reaction with cumulus minerals, the CO/CH_4 ratio is also strongly dependent on the C/H ratio in the fluid and fO_2. It is easy to show that at low concentrations of reduced gases in CO_2-H_2O fluid (that is often the case), the CH_4 concentration reaches a maximum in the fluid with $X_{CO2} = X_{H2O} = 0.5$ and increases in proportion to $1/(f_{O2})^2$. The CO concentration increases in proportion to CO_2 content and to $1/(f_{O2})^{1/2}$. At the crustal conditions at pressures of 10–1000 MPa and magmatic temperatures of 900–1200 °C, mole ratio $CO/(CO + CO_2)$ varies in the range of 0.05–0.99. At P = 200 MPa in a fluid with C/H = 0.5 (initial composition $X_{H2O} = X_{CO2}$), CO prevails over CH_4 at T > 700–800 °C: f_{O2} = QFM/QFM-1 [13]. Taking into account high chlorine content in magmatic fluids (10 atomic % of Cl) at low f_{O2} and high T, it leads to the prediction of the high content of CO, CO_2, HCl and CH_3Cl in expense of CH_4 [4]. Fluid inclusions with a high CO contents were found in plagioclases and pyroxenes from magmatic rocks and in xenoliths quenched at high cooling rates at high temperature (e.g., [14,15]).

Figure 1 depicting the vapor pressure data of some carbonyls of the transitional metals as a function of temperature gives a general idea (educated guess) of the stability of the carbonyls. At the marginal stability of the carbonyl as a phase, its evaporation and decomposition reactions are in equilibrium. For example, we can write for nickel carbonyl $Ni(CO)_4$ based on known thermodynamic properties:

$$Ni(CO)_{4l} = Ni(CO)_{4g}, \quad (3)$$

$$Ni(CO)_{4g} = Ni_s + 4CO_g, \quad (4)$$

It follows from Figure 1 that near decomposition point (P = 1 bar, T = 180 °C) $Ni(CO)_4$ vapor pressure is about 0.1 bar. Based on this pressure, constant of the reaction (4) can be estimated as (ideal gas limit):

$$K_2(180\ ^\circ C) = \frac{X_{Ni(CO)_4}}{(X_{CO})^4} \approx \frac{0.1}{0.9^4} = 0.15, \quad (5)$$

In accordance with our thermodynamic calculations [16], K_2 reaches this value at T = 171 °C. The similarity between the calculated and observed values confirms our predictions of the significant Ni solubility of 100–1000 ppm as a carbonyl in the temperature range of 600–900 °C and pressures above 500–700 MPa.

Simple platinum carbonyl $Pt(CO)_4$ was only synthesized at low temperature (4–10 K) by condensation of platinum one atom vapor in the Ar-CO medium [19]. Anionic Chini complex $[Pt_3(CO)_6]_n^{2-}$ is the most common carbonyl form in the solutions [20]. The number of stacked three member rings $(Pt_3(CO)_6)n$ can reach 15. In each triangle, platinum atoms are bonded through a bridging CO, and the three terminal CO are bonded to single Pt atoms. Rings are connected via Pt-Pt bonds (see e.g., [21]). Stable multinuclear (n = 9–15) carbonyls were synthesized in the zeolite cavities with the method "ship in the bottle" [22]. Platinum carbonyls are unstable in air due to the oxidation [23]. There are no thermodynamic data on the platinum carbonyls, therefore it is impossible to predict theoretically their stability at high pressure–temperature (PT) conditions. We performed experimental study of Pt solubility in the dry CO-CO_2 fluid at PT conditions close to the subsolidus conditions of upper crust ultramafic–mafic intrusions. Raman spectra of quenching Pt phases dissolved in acetone confirm the formation of Pt carbonyls in our experiments.

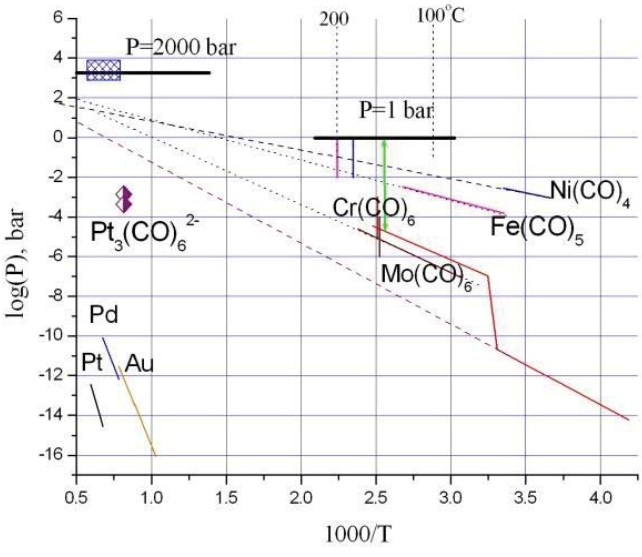

Figure 1. Vapor pressures of carbonyls of the transient metals and PGE according to the experimental data [17,18]. Vertical lines depict decomposition temperature at P = 1 bar. Value of the partial pressure of Pt carbonyl is plotted in accordance to our experimental data. Crossed rectangle corresponds to the typical PT parameters of the cumulus processes in the ultramafic–mafic intrusions.

2. Materials and Methods

For the determination of Pt solubility in the CO-CO_2 fluid, we use analogue of the diamond fluid trap method used for the work with water fluid at the mantle parameters in a rocking multi-anvil apparatus [24]. The reliability of this method is lower than that of in-situ techniques such as probing of fluid and spectral measurements during a run. In our experiments, fluid was generated due to the decomposition of MgC_2O_4 at the temperature above 650 °C in accordance with reaction:

$$MgC_2O_4 = MgO + CO + CO_2, \quad (6)$$

To set higher than 0.5 mole fraction of CO_2 in the fluid $MgCO_3$ was added which is also decomposing at the temperature above 750 °C at P = 200 MPa. In one experiment (cor102) siderite was used which at the thermal decomposition generates fluid with $X_{CO} = 1/3$:

$$3FeCO_3 = Fe_3O_4 + CO + 2CO_2, \quad (7)$$

Solids used as a fluid source were loaded into the small (diameter of 3 mm) open capsule, which was placed in the welded larger capsule (diameter of 5 mm and length of 40 mm) loaded with fluid trap (see Figure 2). Both capsules were made of platinum that was a source of this metal for the dissolution experiment. In our experiments using the Internally Heated Pressure Vessel (IHPV) apparatus, we tried several types of fluid traps.

(1) Albite glass trap (AGT). It is a powder at the beginning of experiment when it is filled with fluid. It is sintered rapidly into the dense material with isolated fluid bubbles. In the loose state, the trap can be mechanically contaminated with platinum particles of the walls. These particles have larger size (up to 10–15 μm) than particles (usually of submicron size) deposited from the fluid. Mechanically produced particles contain less iron than deposited ones. Using of the bulk analysis of albite trap leads to the severely overestimated solubility. After the initial trials, albite traps were used only for probing experimental fluid conserved in the bubbles.

(2) Industrial corundum filter for high temperature gasses (CRT). The advantages of this filter are the high mechanical stability and chemical resistance of the main corundum component. The main disadvantage is the use of alkaline aluminosilicate glass as a binder in the production of ceramics. This glass can react with the fluid and thus affect the platinum solubility. Another drawback of the corundum traps is the impossibility of their analysis by the Laser Ablation Inductively Coupled Plasma Mass Spectrometry (LA-ICP-MS) method.

(3) Trap from the optic silica glass (CGT). These traps were prepared by the high-temperature sintering in the vacuum furnace at T = 1370 °C during an hour. Porosity of this trap measured after experiments at P = 200 MPa is about 40 ± 5%. Traps are not strong enough to clean their surface with mechanical abrasion after experiment, therefore some surface mechanical contamination with platinum is possible. To avoid this effect, trap was split into three pieces analyzed separately with Electrothermal Atomic Absorption (ET-AAS) method.

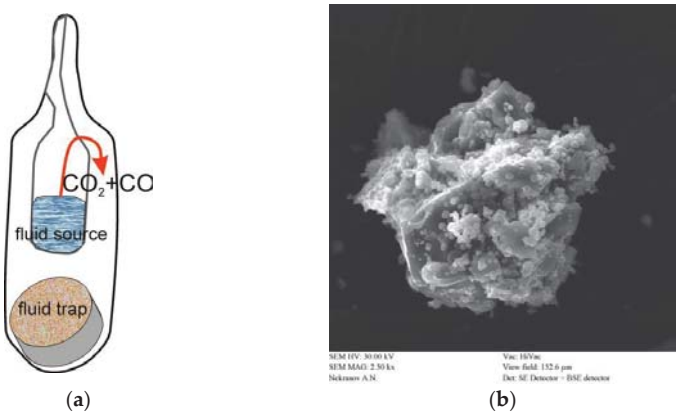

(**a**) (**b**)

Figure 2. The scheme of our experiments (**a**) oxalate or (and) carbonate were placed in the small open capsule within the welded larger one. On the bottom of the large capsule, fluid trap was placed. Fluid trap was a powder of albite or porous ceramics (**b**) SEM image of the piece of the quartz glass ceramics after experiment (qz98).

The procedure for estimating the solubility of Pt from the data on the bulk metal content in the trap is described in details in [25]. Neglecting the quenching effect and assuming an absence of adsorption and deposition during the experiment, the bulk platinum content (C_{bulk}) in the trap is:

$$C_{bulk} = \frac{(1-\varepsilon)C_s\rho_s + \varepsilon\rho_{fl}C_{fl}}{(1-\varepsilon)\rho_s}, \quad (8)$$

where C_s and C_{fl} are metal content in the trap and fluid, ρ_s and ρ_{fl} are densities of the material of the trap and fluid and ε is porosity. Because of negligibly small $C_s \approx 0$, the equation may be written as:

$$C_{bulk} = \frac{\varepsilon\rho_{fl}C_{fl}}{(1-\varepsilon)\rho_s} = \frac{C_{fl}}{\gamma} \; or \; C_{fl} = \gamma C_{bulk}, \quad (9)$$

The porosity of the quartz trap, estimated from BSE images of the slices surface is 0.4 ± 0.05. Quartz glass density is 2.3 g/cm^3. Porosity of the corundum trap at P = 200 MPa is 0.3 ± 0.1, density of corundum is of 4.02 g/cm^3. We estimate fluid density via equation of state for CO_2 [26] correcting average molecular weight for CO mole fraction. Fugacity coefficients of COand CO_2 calculated in accordance with [27] at the experimental conditions differ by no more than 3% justifying this approach. The fluid density in the reference point

at P = 200 MPa and T = 950 °C is ρ_{fl} = 0.589–0.214 X_{CO}. Based on these data, values of conversion factor γ for corundum and quartz traps are in the ranges of γ_{cor} = 14–18 and γ_{qz} = 6–8.5.

Starting materials. We use chemically pure MgC_2O_4 (Onyxmet reagent). By X-ray powder diffraction data it is dihydrate MgC_2O_4 $2H_2O$ (C_{H2O} = 24.3 wt.%). Water content after drying at T = 100 °C for 4 h by KFT analysis becomes 10.4 wt.%. After drying at 260 °C for 4 h, it decreases to less than 2 wt.%. As a source of CO_2, we used natural magnesite (S. Ural). To minimize water contamination, all equipped capsules were additionally heated at 220 °C for 1–1.5 h before experiment, flashed with argon and then welded. Optical quartz (Lytkarino Optical Glass Factory, Lytkarino, Russia) glass was used in the fluid trap and has the concentrations of all impurities below detection limit for microprobe. Dry albite glass was prepared by the melting of the natural albite mineral from pegmatite (Kalba Region, Eastern Kazakhstan).

The experiments were carried out in an apparatus of high gas pressure at the Institute of Experiment Mineralogy, Russian Academy of Sciences (IEM RAS, Chernogolovka). The vessel of stainless steel had a free volume of 262 cm^3, the working medium was Ar. The temperature was measured during the experimental run by a Pt–Rh thermocouple, the gradient-free zone was 40–50 mm. The pressure was measured with piezo sensors accurate to 5%. Temperature was controlled with precision of ±2.5°C, pressure was controlled with precision of ±1%. Quenching was performed by the switching off the furnace at the cooling rate 150 °C/min. The experiments have been performed at a pressure of 100 and 200 MPa and temperature of 950 °C, the duration of the runs was 2 h.

Spectroscopic study of fluid trapped in the albite glass was carried at the Institute of Geology, RAS (Syktyvkar) and at CEMES (Toulouse, France). Raman spectra of quenching platinum phases dissolved in acetone were measured in Institute of Experimental Mineralogy RAS (IEM RAS, Chernogolovka, Russia). Details of spectroscopic measurements are presented in supplementary materials (supplementary text).

Phase compositions of the each run products were studied in IEM RAS (Chernogolovka, Russia). Samples were prepared by mounting the products of the runs in polystyrene and polishing one face of a polystyrene cylinder. The textural and chemical analyses were performed using a CamScan MV2300 and Tescan Vega TS5130MM SEMs with an energy-dispersive spectrometer (INCA Energy 450). The spectrometer was equipped with semi-conductive Si(Li) detector INCA PentaFET X3. All phases were analyzed at an accelerating voltage of 20 kV, the current of the absorbed electrons on the Co sample was 0.1–0.2 nA. The smallest beam diameter was 0.2 μm for point phase analysis; some glasses were analyzed using a rectangle scanning area with a width of up to 50–80 μm. The measurements results were processed by the software package INCA Energy 200.

Water contents in the starting $Mg_2C_2O_4$ were measured by the Karl–Fischer titration (KFT) on an Aqua 40.00 system with a high-temperature HT 1300 unit at IEM RAS (Chernogolovka, Russia). Detectable water weight (m_W) range: 1 μg–100 mg, reproducibility: ± 3 μg at m_W 1–1000 μg, 3% at the m_W > 1 mg.

Platinum analyses were performed using a New Wave Research I3107 system (Fremont, CA, USA). This is a UV femtosecond laser system equipped with a Pharos HE from Light Conversions coupled with a high-resolution ICP-MS Element-XR. A 65 μm spot size was applied with 5 Hz and 3.34 J/cm^2 conditions (laser output 48%). The background was measured during 60 s, ablation for 60 s and wash-out after ablation for 30 s. To quantify the elemental composition of the glasses, average silica concentrations (based on ^{29}Si) measured by electron microprobe were used as an internal standard. For external calibration in bracketing mode, we used NIST SRM 612 reference material [28]. Furthermore, to control the accuracy, we used the MPI-DING mafic and ultramafic glasses (NIST SRM 610, GOR132-G, GOR128-G) [28,29] as secondary standards. The detection limit for major elements varied between 1 and 20 ppm, whereas it was 0.2 ppm for ^{195}Pt. The distribution of platinum in the samples was uneven on a scale of 65 μm, therefore measurements are

characterized by a large relative standard deviation of 60–80% of the measured values (see Supplementary text, Table S2, Figure S5).

To prepare for analysis by Electrothermal Atomic Absorption (ET-AAS) method, the samples were decomposed by heating to 120 °C in a mixture of strong HF + HNO_3 in Savillex screw vessels, and then dried to wet salt. Then the sample was treated with Aqua Regia (HCl:HNO_3 = 3:1) to obtain wet salts, and then it was treated with concentrated HCl to convert the salts into chlorides. After complete dissolution of the salts, the solution was cooled and filtered in a 5–10 mL flask. Determination of the nanograms quantities of Pt was carried out using a Solaar MQZ (Thermo Electron Corp. UK) ETAA spectrometer with a Zeeman background correction [30]. The measurements were conducted on the most sensitive line of λ = 265.9 using pyrolytically coated graphite furnaces. The sample was introduced automatically or manually with a micropipette with disposable plastic tips (5 to 20 μL). The signal was measured using the height of the peak and its area. The metrological performance of the methods was assayed using standard reference materials of known composition: SARM-7B, SOP-3-SR and others and samples available under the international GeoPT Proficiency Testing Programme (peridotite OPY-1, harzburgite HARZ-01, and iron–manganese nodules FeMn-1). The analytical inaccuracy of ET-AAS analysis within the concentration range of 1–100 ng/mL is no higher than 4 relative %. Detection limit is 2.5 ppb for Pt. To analyze the forms of platinum dissolved in acetone and chloroform, an organic phase was introduced directly into the ET-AAS graphite furnaces. The measurement was performed using water calibration solutions.

3. Results

3.1. Qualitative Observations of the Reduced Carbonic Fluid Activity

In our experiments, the reduced carbonic fluid reacts not only with the walls of the platinum capsule, but also with the material of the trap. In earlier publication [25] interaction of such fluid with iron oxides matrix formed at siderite (used as a fluid source) decomposition was described. Figure 3a shows the SEM image of aliminosilicate glass ellipsoids deposited from the reduced carbonic fluid in the experiment ab84 (see Supplementary text, Table S3 for details) with albite trap. Small axes of the ellipsoids are in several microns range while maximum axes are up to 10 microns. SEM-EDS gives composition of the glass close to the albite with Na/Al ratio less than unity. This probably reflects the tendency of sodium to fractionate into the fluid. Tiny platinum particles were co-precipitated with albite. In Figure 3b, SEM image of the surface of the silica glass trap may be seen. Small deposited silica balls along with Pt particles are on the surface of the glass shreds. In the presence of water, silica glass began to actively crystallize from the surface at the parameters of our runs. Upon contact with a dry fluid, only the sharp silica glass edges were smoothed out due to dissolution. Thus, SEM observations indicate high dissolution ability of carbonic fluid at relatively low pressure of 200 MPa. The composition of the fluid and the solubility of Pt were quantitatively characterized by various instrumental methods and described below.

3.2. Fluid Composition

3.2.1. Raman Data Interpretation

The composition of the fluid in the first series of experiments was characterized by micro-Raman measurements of fluid inclusions in the albite glass trap. In Figure 4, Raman spectra of a fluid bubble from run ab108 recorded in Syktyvkar and Toulouse are displayed. They are similar and demonstrate strong CO band at $k = 2141$ cm^{-1}. Quantitative estimation of the fluid composition can be made in accordance with the following relation (e.g., [31]).

$$X_i = \frac{A_i/(\sigma_i \zeta_i)}{\sum_{k=1..n} A_k/(\sigma_k \zeta_k)}, \quad (10)$$

where A_i area of the peak, σ_i–Raman cross-section, a ζ_i–device efficiency coefficient for component *i*. The efficiency coefficients of devices are unknown. We use the products

$z_i = \sigma_i \zeta_i$ as in [15] $z_{CO} = 0.95$, $z_{CO2} = 1.25$ for bands CO with $k = 2140$ cm^{-1} and CO_2 with $k = 1388$ cm^{-1}, correspondingly.

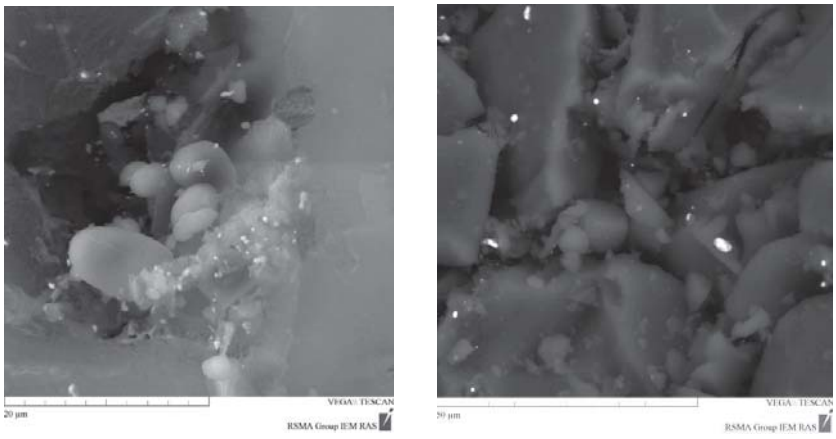

(**a**) (**b**)

Figure 3. Products of experiments with reduced carbonic fluid at P = 200 MPa and T = 950 °C (**a**) SEM micro-image of quenching glass balls with Pt, run ab84 on the bottom of the capsule; (**b**) SEM micro-image of Pt microparticles on the surface of quartz glass shreds of the fluid trap from experiment qz98.

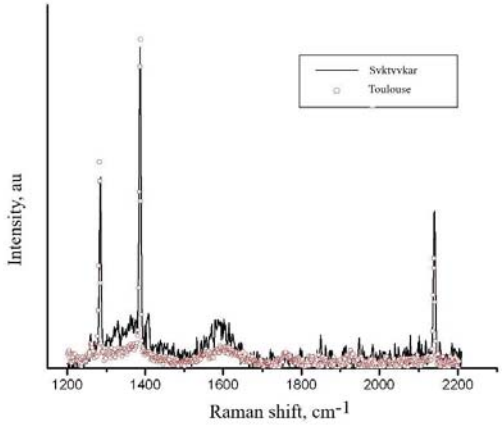

Figure 4. Raman spectrum of the same fluid bubble from AGT of the run ab108 recorded in two laboratories. CO band is near k = 2140 cm^{-1} and CO_2 bands are at k = 1388 cm^{-1} and 1286 cm^{-1}.

Results of Micro-Raman Study

The initial CO_2/CO ratio in the fluid was determined by the composition of the fluid source. When the CO content exceeds the level constrained by CCO buffer, it decomposes into carbon and CO_2 at some finite rate. The equilibration of fluid can continue after trapping. The walls of the bubbles in the albite trap from experiment ab86 (P = 200 MPa) were covered with an opaque carbon layer formed in-situ, which hampers to carry out Raman measurements of the fluid composition.

In experiment ab108 (P = 100 MPa) pure MgC_2O_4 was used and an initial mole ratio (r = CO/CO_2 + CO) was 0.5. The equilibrium value constrained by CCO buffer reaction at P = 100 MPa T = 950 °C is 0.23. For the trapped fluid, we estimated r = 0.40 (Syktyvkar)

and 0.39 ± 0.03 (Toulouse); the smallest value was obtained for the smallest bubble. All r values are between the initial and equilibrium values, reflecting incomplete equilibration in 2 h.

The fluid composition formed at P = 50 MPa (run ab107) measured in Toulouse corresponds to r = 0.54 ± 0.03. This value is close to the initial value of 0.5 for pure MgC_2O_4. From these data, it follows that the used values of coefficients z_i are in good agreement with the values given in [15]. No carbon was detected in the products of the experiment, despite the fact that the equilibrium $X_{CO} = 0.31$ is lower than the initial mole fraction. At this pressure, the CO disproportionation rate was negligible. More information is presented in supplementary information (Supplementary text, Figures S1–S4, Table S1).

3.3. Platinum Dissolution in the Fluid

3.3.1. Pt Content in the Traps

The viscosity of the fluid under the PT conditions of our experiments is not more than 1.0×10^{-5} Pas. Due to the efficient diffusion in such a low viscosity fluid, the quenching phases can become significant in size, which they do. The supplementary information files (capsule_walls_I.xls, capsule_walls_II.xls) contain images of quenching Pt whiskers several tens of microns in length. Platinum is deposited from the fluid mainly as the particles (nuggets). Obviously, the "nugget" picks up metal in a significant volume of the fluid, forming a wide bare zone around itself, which leads to a greater uneven distribution of Pt. Similar nuggets were encountered in experimental studies of the solubility of noble metals in silicate melts (e.g., [32]). However, the possibility of a quenching mechanism of the nugget's formation is excluded due to the low diffusivity of these metals in silicate melts, the contribution of nuggets is excluded from the analytical data.

Thus, the distribution of platinum particles in fluid traps is inherently irregular. First, the particles were initially located on the surface of the glass shards. When using the local LA-ICP-MS method, the analyzed volume is an ablation pit, the shape of which can be approximated by a hemisphere with a diameter equal to the spot width of 65 μm. The maximum width of fragments of quartz glass was 100–200 μm, albite glass—up to 1000 μm. When the analytical volume avoids the former grain boundaries, the analysis will give a blank result.

The next factor is particles size distribution. The largest particles were formed as a result of mechanical abrasion of the capsule walls. They are rare and there is a small chance of being captured by the ablation pit. The next set of relatively large particles can be attributed to a slow change in the intensive parameters during the experiment, causing a drop in solubility. These particles are larger than the particles formed during the several minutes of the quenching process. 3D distribution of large particles in the albite trap from the experiment ab86 was characterized by microX-Ray computer tomography (x-Ray CMT) with resolution 1.8 mkm (see supplementary information x-Ray_CMTab86.avi). For MCT, the SkyScan 1172 apparatus (MSU, Moscow) was used. Due to the large density contrast (21.45 g/cm^3 Pt versus 2.2 g/cm^3 glass) strong reflections appear in the recordings of transmission images of sample slices. The actual particles sizes were distorted and x-Ray CMT data cannot be used for a quantitative analysis. As a result, these factors lead to a large scatter in the results of local analysis using the LA-ICP-MS (see supplementary_text, Table S2). The bulk ET-AAS method gives a concentration averaged over the entire volume of the trap (or part of it) that is approximately 3.5 orders of magnitude greater than the sampling volume for LA-ICP-MS. However, in this case, all possible large particles are taken into account that are not related to deposition from the fluid during quenching and, therefore, to solubility.

The most reliable data was obtained for the reference point P = 200 MPa and T = 950 °C with different traps and different analysis methods. For initial CO/CO_2 ratio of 0.5 (pure oxalate source) and quartz trap (run qz98), bulk C_{Pt} = 57.7 ppm (ET-AAS). The local concentration obtained with LA-ICP-MS is 22.1 ± 15.6 ppm. This difference can be attributed to the irregular in space Pt deposition during CO decomposition. The laser ablation spots

transmit the sparsely distributed large Pt particles, resulting in a lower concentrations obtained by the LA-ICP-MS. In run qz118 with an initial r = $CO/(CO + CO_2)$ = 0.15 close to the equilibrium ratio r = 0.14, averaged over three parts C_{Pt} = 22.9 ± 7 ppm (ET-AAS). Corundum ceramics is the strongest trap, guaranteeing the absence of mechanical contamination. However, it appeared to have an irregular structure with the locally isolated pore space and sometime gives low C_{Pt}. As mentioned above, even at the highest laser power, corundum does not evaporate that makes it impossible to use LA-ICP-MS for analysis. The highest bulk concentration (run cor99) obtained by the ET-AAS method for an initial $CO/CO + CO_2$ = 0.5 is 27.5 ppm. The density of corundum is high and the solubility corresponding to this value is practically the same as for qz98 by ET-AAS method (see Table 1). With the fluid generated by the decomposition of $FeCO_3$ (run cor102) the bulk C_{Pt} is 11.5 ppm. In terms of solubility, it is close to the value obtained using a quartz glass trap and an equilibrium initial CO/CO_2 ratio (183 and 133 ppm for cor102 and qz118, respectively, see Table 1). To assess the dynamics of equilibration of the fluid trap, experiment qz97 was quenched shortly after the decomposition of oxalate at T = 800 °C and P = 200 MPa (holding for 5 min at these parameters). The local concentration of platinum found by LA-ICP-MS is 15.3 ± 11.8 ppm, which is only slightly lower than the value adopted above for 2 h runs at T = 950 °C. Experiments at low pressure 100 and 50 MPa gave generally lower platinum content. Especially low values of 2.5 and 0.22 ppm were obtained using LA-ICP-MS analysis of albite traps from experiments ab108 (P = 100 MPa) and ab107 (50 MPa), respectively (see Table 1). However, from the single piece ET-AAS analysis of CRT from run cor105 and SGT from run qz120 (P = 100 MPa) we get larger values of 5 and 10 ppm with corresponding solubility of 75.3, 70.5 ppm, respectively. And at P = 50 MPa, the results are similar: the bulk ET-AAS concentrations of SGT (run qz119) and CRT (run cor104) are 11.6 and 5 ppm, which corresponds to solubility of 119 and 93 ppm, which is significantly higher than the solubility of 5.2 ppm from LA-ICP-MS analysis data of AGT (run ab107). In other words, we do not find a large difference between the solubility at 200, 100 and 50 MPa estimated from the bulk analysis of SGT and CRT by the ET-AAS method. However, AGTs analyzed by local LA-ICP-MS have demonstrated a strongly decreasing solubility at lower pressures.

3.3.2. Influence of Pressure and CO Concentration on Pt Solubility

All our estimates of Pt solubility at T = 950 °C are presented in Table 1 and plotted in Figure 5. Variations in solubility caused by the different CO concentrations and pressures are comparable by magnitude. CO concentration in equilibrium with carbon decreases approximately as $1/P^{1/2}$, while stability of carbonyl increases with rise of X_{CO} in accordance with reaction scheme:

$$mPt + nCO = Pt_mCO_n, \quad (11)$$

as defined by the equilibrium condition

$$\frac{\gamma_{CO}^n X_{CO}^n P^{n-1}}{\gamma_{crb} X_{Pt_m(CO)_n}} = K(T), \quad (12)$$

where X_{CO}-mole fraction of CO and γ_i are fugacity coefficients of CO and Pt carbonyl. Using the reference pressure $P_{0,}$ the variation in solubility can be expressed as

$$\frac{C(P)}{C(P_0)} = \left(\frac{X_{CO}\gamma_{CO}(P)}{X_{CO}\gamma_{CO}(P_0)}\right)^n \left(\frac{P_0}{P}\right)^{n-1} \frac{\gamma_{crb}(P_0)}{\gamma_{crb}(P)} \quad (13)$$

In our case, reference pressure is P_0 = 200 MPa (T = 950 °C). To estimate the activity coefficient γ for CO, we use the ideal solution model of the non-ideal components and take the fugacity coefficient of pure CO from [27]. The fugacity coefficient for carbonyl is unknown. As a first proxy, we take it equal to γ_{co}. We also assume that the speciation of Pt in fluid does not depend on the pressure in the studied interval and its weight

concentration is proportional to the carbonyl molar fraction used in Equations (12) and (13). The dependence of Pt solubility as a function of pressure was calculated under these assumptions with the reaction coefficient n in the range 2–5.5 and is shown in Figure 5. Plots calculated for n = 4 and 5.5 are in the concentration interval for the pressure range 50–200 MPa. Two groups of experimental points below and above the reference point (P = 200 MPa) arose due to the influence of CO concentration on solubility. The low point corresponds to the published estimate [25] obtained with siderite as a source of fluid and albite fluid trap. The average CO concentration characterized by micro-Raman is 12 mol.%. The best fit with the reported concentration of Pt in the fluid of 15 ppm is obtained for n = 5.1. Upper group of points correspond to the effective solubility in the experiment with MgC_2O_4 as fluid source. In the course of experiment, mole fraction of CO dropped from 0.5 to some lower value. In experiment ab108 (P = 100 MPa), the molar fraction of CO in the fluid from the albite trap, determined using micro-Raman, is X_{CO} = 0.39, which is between the initial and equilibrium values of 0.5 and 0.21. In experiment ab86 (P = 200 MPa), the walls of the fluid bubbles in the albite trap are coated with carbon, which makes it impossible to analyze the fluid composition using micro-Raman. Reducing of CO content towards CCO buffer limit resulted in the deposition of carbon, carbonyl decomposition and growth of the relatively large Pt particles. By discarding the LA-ICP-MS data points affected by mechanical contamination of trap and large particles, we get an estimate of the solubility in fluid of about 500 ppm. The increase in solubility from 130 to 500 ppm at X_{CO} = 0.18–0.19 can be explained by the effective value of n = 5 in Equation (13). For low pressure experiments with an albite glass trap analyzed by LA-ICP-MS, n = 5.5 is the best fit. The only value for 300 MPa was obtained with a corundum trap, the use of which often underestimates the results. However, this solubility is at least 100 ppm and is expected to be higher (see Figure 2).

Table 1. Results of fluid traps analyses and Pt concentration in the fluid.

Run	T/P (°C/Kbar)	X_{CO}/X_{COeq}	LA-ICP-MS (ppm)	ET-AAS (ppm)	Porosity	C_{fl}/C_{CO2} [2]
ab86	950/2	0.5/0.14	109.5 ± 129.8	335.5	0.35 [1]	mechanical contamination
ab86	950/2	0.5/0.14	55.3 ± 53.0 [3]	-	0.35 [1]	489.6/418.5
cor99	950/2	0.5/0.14	-	27.5	0.4	512.4/437.9
qz98	950/2	0.5/0.14	-	57.7	0.35 [1]	490.0/418.4
ab86	950/2	0.5/0.14	32.7 ± 33.7 [4]	n.d.	0.4 [1]	289.5/247.5
qz98	950/2	0.5/0.14	22.1 ± 15.1	n.d.	0.30	136.3/129.3
cor102	950/2	0.33/0.14	-	11.5	0.4 [1]	192.9/183.1
qz118	950/2	0.15/0.14	-	22.9 ± 7.1	0.5	141.0/133.8
ab108	950/1	0.5/0.22	2.5 ± 2.0	n.d.	0.45	20.5/18.0
cor105	950/1	0.5/0.22	-	5.1	0.5	85.5/75.3
qz120	950/1	0.21/0.22	-	10.2	0.60	80.1/70.5
cor104	950/0.5	0.5/0.31	-	1.4	0.60	24.1/19.7
ab107	950/0.5	0.5/0.31	0.22 ± 0.17	n.d.	0.6 [1]	6.3/5.16
qz119	950/0.5	0.5/0.31	-	11.6/32.4	0.21	114/93.6
cor106	9500/3	0.5/0.10	-	5.0	0.4 [1]	145.8/119.3
qz117	950/2;1000/1	0.2/0.29	-	1.3/6.4	0.4 [1]	44.0/40.8

[1] estimate of porosity; [2] solubility recalculated on pure CO_2 fluid, [3] excluding largest particle, [4] excluding large particles.

3.4. Solubility of the Pt Quenching Phases in Organic Solvents

Additionally, we study platinum quenching phases soluble in organic solvents chlorophorm and acetone, providing an estimate of the decomposition degree of carbonyl during quenching (Table 2). Platinum deposited from fluid on the walls of capsule, trap, and periclase matrix has the morphology of whiskers and wires with a submicron width and up to tens of microns in length (see Figure 6 and supplementary files capsule_walls_I.xls and capsule_walls_II.xls). This morphology is indicative of high supersaturation and fast

growth. Due to decomposition of carbonyl, the concentration of the soluble form of Pt is less than the bulk content determined both by ET-AAS and LA-ICP-MS methods.

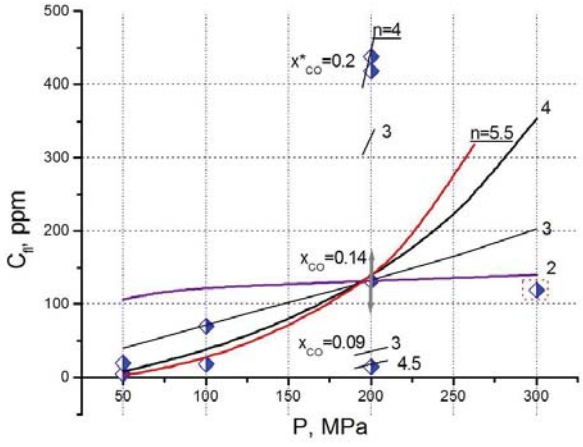

Figure 5. Interpretation of the experimental data on the Pt solubility in CO-CO_2 fluid at T = 950 °C. Circles are experimental points from Table 1. Curves plotted through the most reliable point P = 200 MPa and x_{CO} = 0.14 (equilibrium CCO) are results of extrapolation for different formula of carbonyl complex $Pt_m(CO)_n$: n = 2; 3; 4; 5.5. Points beyond curves at P = 200 MPa are for different CO concentrations. Upper group (x_{CO} = 0.19) short lines are calculated at n = 3 and 4.0 (best fit) and for the lower point (x_{CO} = 0.09) at n = 3 and 4.5 (best fit). Point at P = 300 MPa is out of sequence.

Table 2. Content of acetone-soluble Pt form in fluid traps and in washes from capsule walls.

Run	Time, Hours	Dissol. Time, h	X_{CO}/X_{COeq}	Pt in MgO ppm	Comments	Pt in Flush ppm [1]
qz121	21	0.5	0.5/0.14	1469	MgO + acetone stirred	8.8 [2]
qz122	2	0.5	0.5/0.14	2393	stirred	48.2 [2]
qz123	2	0.25	0.5/0.14	17.4	not stirred	4.3
O56	21	0.25	0.16/0.14	1.4	no carbon	21.5
O57	21	0.25	0.16/0.14	3.4	no carbon	0.1
qz114	2	12	0.5/-	21.8	fluid with X_{H2O} = 0.046	-

[1] recalculated for C_{fl} assuming half fluid was out of the trap; [2] walls were scrabbled at washing; all experiments were carried out at P = 200 MPa and T = 950 °C.

3.4.1. Pt in Carbon-Periclase Matrix

As mentioned above, in experiments with MgC_2O_4 as a fluid source, the periclase matrix was coated with carbon adsorbing carbonyl from the fluid. At the initial stage of the research, the capsule is opened immediately after experiment, some days before being dissolved in acetone. Carbonyl is oxidized in air, and the content of the soluble Pt in the matrix was only 21.8 ppm and 32.4 ppm in experiments 114qz (acetone) and 91qz (chloroform), respectively. The total content of Pt in the periclase matrix was 87.1 and 32,403 ppm (high due to the mechanical contamination) in experiments 114qz and 91qz, respectively. The content of Pt soluble in acetone in experiments 98qz (silica glass trap) and 99cor (corundum trap) was even lower—1.5 and 6.0 ppm, respectively.

When the matrix was placed in acetone immediately after opening of the capsule, the Pt content in the solution was significantly higher. The matrix from runs qz121 and qz122 was thoroughly mixed with acetone, and the Pt concentrations in the solution were 1469 and 2393 ppm, respectively. The duration of these experiments was 21 and 2 h, and

the difference in concentration may reflect the gradual decomposition of excess CO and carbonyl over time during approaching the C-CO-CO_2 (CCO) buffer equilibrium. The matrix from run 123 was dissolved without stirring, and the concentration of soluble Pt was 17.4 ppm, which is close to the bulk content of quenching Pt in fluid traps treated at P = 200 MPa and T = 950 °C.

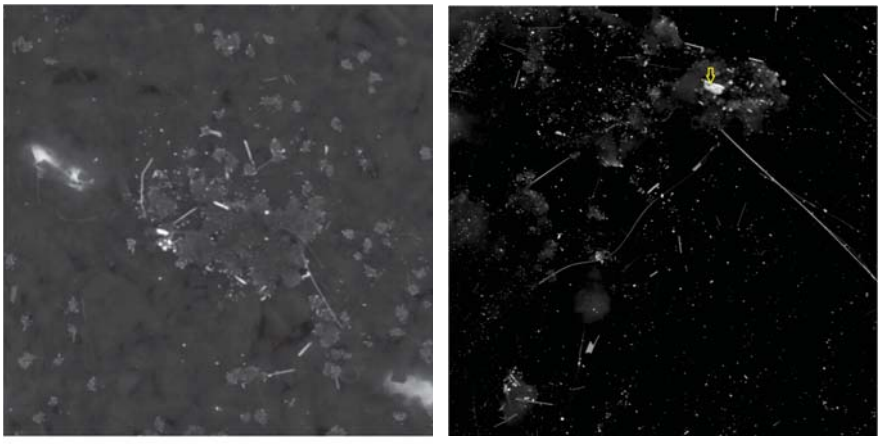

(**a**) (**b**)

Figure 6. Platinum alloys in experimental samples (**a**) BSE micro-image of carbon and MgO coated platinum capsule wall from experiment qz121; Pt/Fe atomic ratio is 4.2 ± 0.6; different morphology of Pt particles from dot to hair-like can be seen (image width 76 μm) (**b**) BSE micro-image of carbon and MgO coated platinum capsule wall from experiment qz122 (image width 76 μm); platinum particle from the wall is labeled with an arrow.

3.4.2. Pt in Pure Periclase Matrix

The pure periclase matrix, formed in experiments with $MgCO_3$ + MgC_2O_4 mixture providing an equilibrium CO/CO_2 ratio, was also investigated. Acetone soluble Pt concentrations in the runs O56 and O57 (immediate dissolution) were 1.4 and 3.4 ppm, respectively. Comparison of the data on the periclase matrix with and without carbon indicated that the carbonyl adsorbed on the carbon is almost completely retained during quenching. While in the carbon free matrix only about 13–15% of the carbonyl is conserved.

We also analyze solutions of quenching phases taken by flushing with acetone from the surface of the capsule walls. The total mass of soluble Pt in the flushing liquid was recalculated to the concentration in the fluid, assuming that half of the fluid was in the trap. Residual concentrations in the fluid were estimated at 2–24 ppm, which is 1.5–18% of our estimate of the equilibrium concentration of 130 ppm at the reference point. No systematic difference in Pt concentrations in the flush from runs with and without excess CO was observed.

3.5. Surface-Enhanced Raman Scattering (SERS) Spectra of the Quenching Phase Solution

The concentration of platinum in acetone solution determined with ET-AAS method is in the range 0.01–1 ppm, which is usually below the detection limit of Raman spectroscopy. It was discovered in 1977 that the Raman spectra of compounds adsorbed on the Ag surface are strongly amplified [33]. Currently, this effect known as Surface-Enhanced Raman scattering (SERS) is widely used in practice. For example, nano-sized supercrystals of gold (built of micro-spheres) with amplification factor up to 10^5 times are applied in medicine and forensic investigations to determine organic compounds [34,35].

In our acetone solutions, native platinum is formed during carbonyls oxidation, which allows spectroscopic investigation of the quenching phase in solution.

3.5.1. Excitation of Raman Spectrum with Infrared Laser

In the first series of measurements, fresh periclase and periclase-carbon matrices were kept in acetone for a day before measurements. In the second series, measurements were made after 10 min of dissolution. In both cases, acetone bands dominate in the spectra.

When using infrared laser light (1064 nm), a broad fluorescence band in the range 1000–3000 cm^{-1} was obtained after subtracting the acetone spectrum. This band was modulated with several peaks. In the series with a long dissolution time (Figure 7), a peak with a maximum of around 1946 cm^{-1} is clearly recognized, which corresponds to the main band of the terminal CO in $Pt_3(CO)_6^{2-}$ complex [20]. A bridging CO peak of about 1740 cm^{-1} can be anticipated from the shoulder of the fluorescence band. In the solution with a small dissolution time (runs O59 and O63), a peak with a maximum of 1954 cm^{-1} is clearly recognized and can be associated with a polynuclear Pt carbonyl. In addition, two bands with wave numbers k = 210 cm^{-1} and 420 cm^{-1} are well expressed. These lines can be attributed to bonds Pt-Pt in metallic nanoparticles. The theoretical Raman spectrum of three atoms cluster has two lines 147 and 228 cm^{-1} [36]. Pt-Pt stretching mode in the crystalline Pt_3Fe is prescribed k = 253 cm^{-1} [37]. Au micro-particles have a strong Raman band at k = 412 cm^{-1} [34].

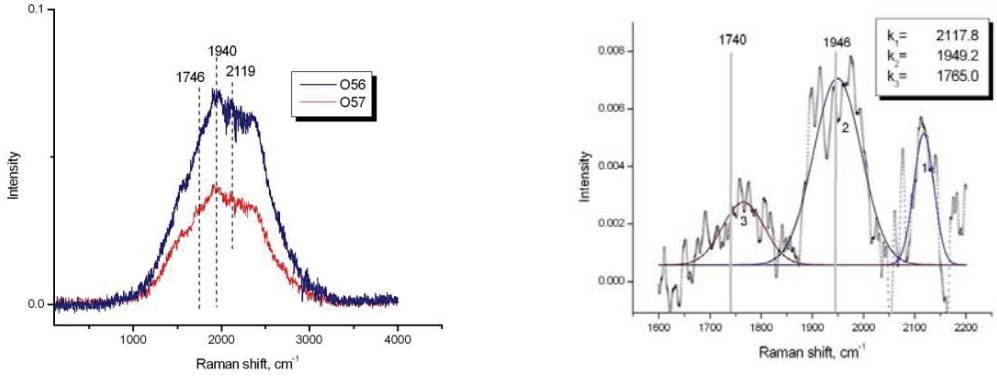

Figure 7. Spectra of the solution in acetone of quenched phases in periclase-carbon matrix from the runs O56 and O57 measured with red laser (spectrum of pure acetone is subtracted), dissolution time of a day; (**a**) fluorescence band with peaks, peaks of Pt carbonyl are labeled with vertical dashed lines; (**b**) peaks assignment for the O56 spectrum (broad fluorescence band is subtracted).

3.5.2. Excitation of Raman Spectrum with Green Laser

When using green laser (λ = 532 nm), the low frequency edge of the fluorescence band is shifted to k_{left} = 100 cm^{-1} (Far Infrared), and the maximum—to k_{max} = 800 cm^{-1}—compared to k_{left} = 1000 cm^{-1} and k_{max} = 2000 cm^{-1} for an infrared laser (λ = 1064 nm). In the spectrum of the O59 sample (Figure 8), the local maximum on the shoulder of the fluorescence band is located in the region of CO vibrations of about 2100 cm^{-1}. The spectrum obtained when subtracting the smooth fluorescence band is deconvoluted in four Gaussians, two of which with k = 1931 cm^{-1} and 2119.7 cm^{-1} are close to the platinum carbonyl lines. Thus, spectroscopic observations are direct evidence of the formation of Pt carbonyls at high PT parameters.

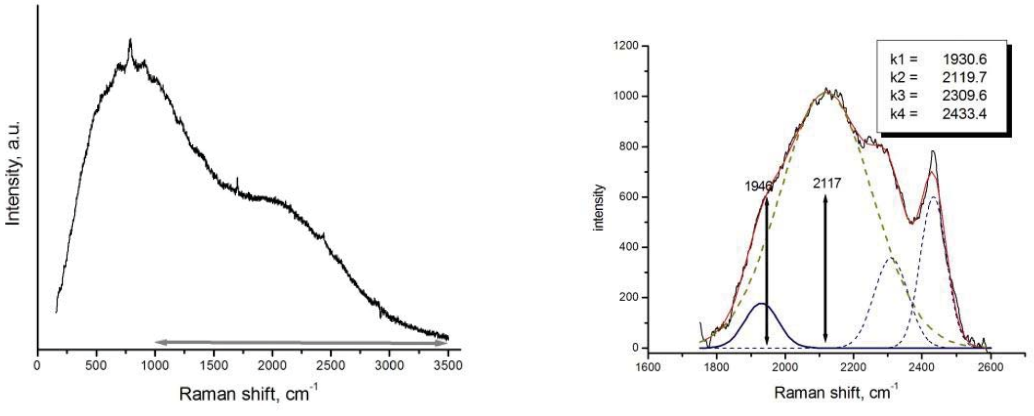

Figure 8. Spectrum of the solution in acetone of quenched phases in periclase matrix from the runs O59 measured with green laser (spectrum of pure acetone is subtracted), dissolution time 15 min: (**a**) fluorescence band with acetone spectrum subtracted; small sharp peaks and negative peak around 2800 cm^{-1} are from not completely compensated acetone; (**b**) deconvolution of O59 spectrum minus fluorescence band; positions of peaks related to Pt carbonyls from Figure 7b are labeled by arrows.

4. Discussion

It is generally accepted that in the post-magmatic processes, platinum is dissolved in a hydrous fluid in the form of chloride, bisulphide, polysulphide, thiosulphate, depending on pH, f_{O2}, temperature and ligand concentration [38–40]. The calculated maximum solubility of PtS at f_{O2} near QFM-1 at T = 300 °C as $Pt(HS)_2$ is 3 ppb in an acidic fluid and 0.01 ppb in an oxidized conditions at pH = 2 as $PtCl_4^{2-}$ [41]. Our results demonstrated that at P = 200 MPa and T = 950 °C platinum solubility in the carbonic fluid in the form of carbonyl at the low CO content is about 15 ppm and increases to 130 ppm in the equilibrium with graphite. This value approaches the highest solubility level of Au in the hydrous fluid under close pressure–temperature (PT) conditions and high f_{O2} [11]. This means that the formation of carbonyl itself can be an important mechanism for the transport of Pt by fluid at the post-magmatic stage of evolution of layered ultramafic-mafic intrusions. There are numerous observations that the chlorine content in such fluids is high, which makes it possible to associate the transfer of Pt with chlorine [42]. Mixed chlorine/carbonyl complexes of Pt are known under ambient conditions and their study at elevated PT parameters deserves attention.

Our preliminary data indicate that low concentration of H_2O in $CO\text{-}CO_2$ fluid increases the solubility of Pt (see supplementary text, Table S3). As described in details in [25], we are limited in our attempts to quantitatively constrain the solubility of Pt using a dry $CO\text{-}CO_2$ fluid due to the use of Pt capsules in the IHPV apparatus. During the experiment, the fluid is oxidized via the loss of H_2 through the capsule walls, and it is not clear to what extent the high contents of Pt in the traps in hydrous carbonic fluid is caused by the re-deposition of Pt under conditions of the fO_2 gradient. In the presence of water, organic compounds may form, which are potential ligands for complexation with Pt. However, it is expected that at P = 200 MPa and T above c.a. 700 °C (close to subsolidus conditions of mafic intrusions) CO predominates as a form of reduced carbon [13], and complexation with organic ligands can become significant at lower temperatures. As it follows from our experiments, carbon (graphite) will adsorb Pt carbonyl and may contribute to the concentration of the diluted relative PGE natural fluids. The origin of graphitized rocks enriched in PGE and Au [43] may be related to this process.

Carbonyl speciation may explain origin of isoferroplatinum (Pt_3Fe), the most abundant nonsulfide platinum mineral. It is the main mineral of placer PGE deposits related to the origin of ring alkaline-ultrabasic (Konder) and ring ultrabasic-basic (Alaska type) intrusions. Pt alloys are also quite common in the Bushveld intrusion, where the main forms of platinum are sulfides, arsenides, tellurides [44]. Some investigators attributed the formation of Pt-Fe alloys to the magmatic stage of evolution of gabbro-pyroxenite-dunite massifs (e.g., [45,46]). Karpinsky in 1926 (see in [1]) proposed metasomatic mechanism of formation of chromitite-Pt association as a result of interaction of dunite with fluid containing Cr and Pt. Some modern researchers are developing similar models of the interaction cumulus-fluid as a mechanism of PGE localization [1,47].

Assuming crystallization of Pt_3Fe from fluid, it should be noted that oxygen fugacity in ultramafic-mafic intrusions is close to CCO (near QFM-2) and much exceeds the IW buffer. Consequently, iron is present in the fluid as the Fe^{2+} ion and is reduced to native metal during the deposition of Pt_3Fe. The specific mechanism of Pt_3Fe crystallization can be associated with the nature of platinum carbonyl. The most probable form is the multinuclear anion $Pt_3(CO)_6{}^{2-}$. The origin of the negative charge can be explained with redox reactions:

$$Pt_3(CO)_6 + O^{2-} + CO = Pt_3(CO)_6{}^{2-} + CO_2, \quad (14)$$

$$Pt_3(CO)_6 + 2Fe^{2+} = Pt_3(CO)_6{}^{2-} + 2Fe^{3+} \quad (15)$$

If the anionic form of the carbonyl does prevail, a neutral complex with Fe^{2+} will naturally form in the fluid:

$$Pt_3(CO)_6{}^{2-} + Fe^{2+} = FePt_3(CO)_6 \quad (16)$$

At the decomposition of this complex during quenching in experiment or in due to a decrease in the CO fugacity in nature, isoferroplatinum crystallizes:

$$FePt_3(CO)_6 = Pt_3Fe + 6CO, \quad (17)$$

The formation of a Fe-Pt alloy with a higher Fe content (tetraferroplatinum PtFe) can be explained by the secondary leaching of Pt from isoferroplatinum. The less common Pt_2FeCu and Pt_3Cu are also thought to be formed from lower temperature fluid leaching [48].

Supplementary Materials: The following are available online at https://www.mdpi.com/2075-163X/11/2/225/s1, word file S1: suppl. text, excel sheet S2: capsule wall I, excel sheet S3: capsule wall II. Figure S1: Optic images of the bubbles, run ab108, Figure S2: Raman spectra of fluid, run ab108, Figure S3: Optic images of the bubbles, run ab107, Figure S4: Raman spectra of fluid, run ab107, Figure S5: Examples of representative LA-ICP-MS transient signals, Table S1: Measurements of CO concentration in fluid, Table S2: Measurements of Pt concentration by LA-ICP-MS method, Video S1:. x-Ray_CMTab86.avi.

Author Contributions: Conceptualization, project administration and writing were carried out by A.S.; experimental work was done by T.S. and O.S.; Raman measurements were performed by G.B., S.I.I., G.S.P.; interpretation of Raman data by A.S., LA-ICP-MS analysis was done by A.S., G.S.P. and A.Y.B.; microprobe analysis and SEM observations were done by A.N.; ET-AAS analyses were performed by O.T. All authors have read and agreed to the published version of the manuscript.

Funding: This study was supported by Russian Foundation for Basic Research, project no. 18-05-00597, visit of AS to Toulouse was funded by Metchnikov program-2018 grant.

Institutional Review Board Statement: Not applicable.

Informed Consent Statement: Not applicable.

Data Availability Statement: The data presented in this study are available on request from the corresponding author.

Acknowledgments: Authors thank Dmitriy Korost (MSU, Moscow) for MCT study of our run products. Two anonymous reviewers appreciably improve the final version of MS.

Conflicts of Interest: The authors declare no conflict of interest.

References

1. Mochalov, A.G. A genetic model of PGM in cumulative gabbro-pyroxenite-dunite complexes of Koryak Highland, Russia. *Geol. Ore Depos.* **2013**, *66*, 145–161. [CrossRef]
2. Kanitpanyacharoen, W.; Boudreau, A.E. Sulfide-associated mineral assemblages in the Bushveld Complex, South Africa: Platinum-group element enrichment by vapor refining by chloride–carbonate fluids. *Miner Depos.* **2013**, *48*, 193–210. [CrossRef]
3. Yudovskaya, M.; Kinnaird, J.; Naldrett, A.J.; Rodionov, N.; Antonov, A.; Simakin, S.; Kuzmin, D. Trace-element study and age dating of zircon from chromitites of the Bushveld Complex (South Africa). *Miner. Petrol.* **2013**, *107*, 915–942. [CrossRef]
4. Mathez, E.A.; Dietrich, V.J.; Holloway, J.R.; Boudreau, E. Carbon Distribution in the Stillwater Complex and Evolution of Vapor during Crystallization of Stillwater and Bushveld Magmas. *J. Petrol.* **1989**, *30*, 153–173. [CrossRef]
5. Ballhaus, C.G.; Stumpfl, E.F. Occurrence and petrological significance of graphite in the Upper Critical Zone, Western Bushveld Complex, South Africa. *Earth Planet. Sci. Lett.* **1985**, *74*, 58–68. [CrossRef]
6. Hanley, J.J.; Mungall, J.E.; Pettke, T.; Spooner, E.T.C.; Bray, C.J. Fluid and Halide Melt Inclusions of Magmatic Origin in the Ultramafic and Lower Banded Series, Stillwater Complex, Montana, USA. *J. Petrol.* **2008**, *49*, 1133–1160. [CrossRef]
7. Konnikov, E.G.; Vasyukova, O.N. Composition of Fluid Inclusions from Intrusive Rocks of the Norite–Cortlandite Complex, Kamchatka. *Geol. Ore Depos.* **2007**, *49*, 227–237. [CrossRef]
8. Konnikov, E.G.; Meuer, W.P.; Neruchev, S.S.; Prasolov, E.M.; Kislov, E.V.; Orsoev, D.A. Fluid regime of platinum group elemens (PGE) and gold-bearing reef formation in the Dovyren mafic-ultramafic layered complex, eastern Siberia, Russia. *Miner. Depos.* **2000**, *35*, 526–532. [CrossRef]
9. Hanley, J.J.; Mungall, J.E.; Pettke, T.; Spooner, E.T.C.; Bray, C.J. Ore metal redistribution by hydrocarbon–brine and hydrocarbon–halide melt phases, North Range footwall of the Sudbury Igneous Complex, Ontario, Canada. *Miner. Depos.* **2005**, *40*, 237–256. [CrossRef]
10. Shcheka, G.G.; Lehmann, B.; Gierth, E.; Gömann, K.; Wallianos, A. Macrocrystals of Pt–Fe alloy from the Kondyor PGE placer deposit, Khabarovskiy Kray, Russia: Trace-element content, mineral inclusions and reaction assemblages. *Can. Miner.* **2004**, *42*, 601–617. [CrossRef]
11. Pokrovski, G.S.; Borisova, A.Y.; Harrichoury, J.C. The effect of sulfur on vapor-liquid fractionation of metals in hydrothermal systems. *Earth Planet Sci. Lett.* **2008**, *266*, 345–362. [CrossRef]
12. Uel'skiy, A.A.; Grebennikov, A.V.; Storozhenko, P.A. Carbonyl Materials: Preparation, Properties, and Application. *Polym. Sci. Ser. D Glues Seal. Mater.* **2011**, *4*, 228–235. [CrossRef]
13. Simakin, A.G.; Kislov, E.V.; Salova, T.P.; Shaposhnikova, O.Y.; Nekrasov, A.N. Reduced CO_2 Fluid as an Agent of Ore-Forming Processes: A Case Study of Dolomite-Replacement Skarns at the Yoko-Dovyren Massif. *Petrology* **2019**, *27*, 1–16. [CrossRef]
14. Torok, K.; Degi, J.; Szep, A.; Marosi, G. Reduced carbonic fluids in mafic granulite xenoliths from the Bakony–Balaton Highland Volcanic Field, W-Hungary. *Chem. Geol.* **2005**, *223*, 93–108. [CrossRef]
15. Bergman, S.C.; Dubessy, J. CO_2–CO fluid inclusions in a composite peridotite xenolith: Implications for upper mantle oxygen fugacity. *Contrib. Miner. Petrol.* **1984**, *85*, 1–13. [CrossRef]
16. Simakin, A.; Salova, T.; Devyatova, V.; Zelensky, M. Reduced carbonic fluid and possible nature of high K magmas of Tolbachik. *J. Volcanol. Geotherm. Res.* **2015**, *307*, 210–221. [CrossRef]
17. Gamer, M. Vapor Pressures and Thermodynamic Properties of Tungsten, Chromium, Cobalt and Rhodium Carbonyls. Ph.D. Thesis, University of Nevada, Reno, NV, USA, 1994; p. 80.
18. Moskvin, A.B. (Ed.) *New Handbook of Chemist and Technologist. v.12. General Information: Structure of Matter*; World and Family: Saint Petersburg, Russia, 2006; p. 1464. (In Russian)
19. Kundig, E.P.; McIntosh, D.; Moskovits, M.; Ozin, G.A. Binary Carbonyls of Platinum, Pt(CO)n, (Where n = 1–4). A Comparative Study of the Chemical and Physical Properties of M(CO)n, (Where M = Ni, Pd, or Pt; n = 1–4). *J. Am. Chem. Soc.* **1973**, *95*, 7234–7241. [CrossRef]
20. Longoni, G.; Chini, P. Synthesis and Chemical Characterization of Platinum Carbonyl Dianions [Pt3(C0)6]n2- (n = −10, 6, 5, 4, 3, 2, 1). A New Series of Inorganic Oligomers. *J. Am. Chem. Soc.* **1976**, *98*, 7225–7231. [CrossRef]
21. Torigoe, K.; Remita, H.; Picq, G.; Belloni, J.; Bazin, D. Structural Characterization of Supported Platinum Carbonyl Clusters by X-ray Absorption Spectroscopy. *J. Phys. Chem. B* **2000**, *104*, 7050–7056. [CrossRef]
22. Li, G.J.; Fujimoto, T.; Fukuoka, A.; Ichikawa, M. Ship-in-Bottle synthesis of Pt9-Pt15 carbonyl clusters inside NaY and NaX zeolites, in-situ FTIR and EXAFS characterization and the catalytic behaviors in 13CO exchange reaction and NO reduction by CO. *Catal. Lett.* **1992**, *12*, 171–186. [CrossRef]
23. Bradford, C.W. The Carbonyls of the Platinum Group Metals. *Platin. Metals Rev.* **1972**, *16*, 50–55.
24. Kessel, R.; Schmidt, M.W.; Ulmer, P.; Pettke, T. Trace element signature of subduction-zone fluids, melts and supercritical liquids at 120–180 km depth. *Nature* **2005**, *437*, 724–727. [CrossRef]
25. Simakin, A.G.; Salova, T.P.; Gabitov, R.I.; Isaenko, S.I. Dry CO_2–CO fluid as an important potential deep Earth solvent. *Geofluids* **2016**, *16*, 1043–1057. [CrossRef]
26. Kerrick, D.M.; Jacobs, G.K. A modified redlich-kwong equation of state for H_2O, CO_2, and H_2O–CO_2 mixtures at elevated pressures and temperatures. *Am. J. Sci.* **1981**, *281*, 735–767.
27. Shi, P.; Saxena, S.K. Thermodynamic modeling of the C–H–O–S fluid system. *Am. Miner.* **1992**, *77*, 1038–1049.

28. Borisova, A.Y.; Toutain, J.-P.; Stefansson, A.; Gouy, S.; de Parseval, P. Processes controlling the 2010 Eyjafjallajökull explosive eruption. *J. Geophys. Res.* **2012**, *117*, B05202. [CrossRef]
29. Jochum, K.P.; Weis, U.; Stoll, B.; Kuzmin, D.; Yang, Q.; Raczek, I.; Jacob, D.E.; Stracke, A.; Birbaum, K.; Frick, D.A.; et al. Determination of Reference Values for NIST SRM 610–617 Glasses Following ISO Guidelines. *Geostand. Geoanal. Res.* **2011**, *35*, 397–429. [CrossRef]
30. Kubrakova, I.V.; Nabiullina, S.N.; Tyutyunnik, O.A. Au and PGE Determination in Geochemical Materials: Experience in Applying Spectrometric Techniques. *Geochem. Int.* **2020**, *58*, 377–390. [CrossRef]
31. Burke, E.A.J. Raman microspectrometry of fluid inclusions. *Lithos* **2001**, *55*, 139–158. [CrossRef]
32. Jégo, S.; Pichavant, M. Gold solubility in arc magmas: Experimental determination of the effect of sulfur at 1000 °C and 0.4 GPa. *Geochim. Cosmochim. Acta* **2012**, *84*, 560–592. [CrossRef]
33. Albrecht, M.G.; Creighton, J.A. Anomalously Intense Raman Spectra of Pyridine at a Silver Electrode. *J. Am. Chem. Soc.* **1977**, *99*, 5215–5217. [CrossRef]
34. Radzol, A.R.M.; Lee, K.Y.; Mansor, W.; Yahaya, S.R. Nano-Scale Characterization of Surface Enhanced Raman Spectroscopic Substrates. *Procedia Eng.* **2012**, *41*, 867–873. [CrossRef]
35. Matricardi, C.; Hanske, C.; Garcia-Pomar, J.L.; Langer, J.; Mihi, A.; Liz-Marzán, L.M. Gold Nanoparticle Plasmonic Superlattices as Surface Enhanced Raman Spectroscopy Substrates. *ACS Nano* **2018**, *12*, 8531–8539. [CrossRef]
36. Singh, N.B.; Sarkar, U. Structure, vibrational, and optical properties of platinum cluster: A density functional theory approach. *J. Mol. Model* **2014**, *20*, 2537. [CrossRef]
37. Kloprogge, J.T.; Wood, B.J. X-ray photoelectron spectroscopy and Raman microscopy of ferroan platinum crystal from the Kondyor Massif, Russian Far East. *Spectrosc. Lett.* **2018**, *52*, 43–48. [CrossRef]
38. Mountain, B.W.; Wood, S.A. Solubility and Transport of Platinum-Group Elements in Hydrothermal Solutions: Thermodynamic and Physical Chemical Constraints. In *Geo-Platinum 87*; Prichard, H.M., Potts, P.J., Bowles, J.F.W., Cribb, S.J., Eds.; Springer: Dordrecht, The Netherlands, 1988; pp. 57–82. [CrossRef]
39. Sassani, D.C.; Shock, E.L. Solubility and transport of platinum-group elements in supercritical fluids: Summary and estimates of thermodynamic properties for ruthenium, rhodium, palladium, and platinum solids, aqueous ions, and complexes to 1000 °C and 5 kbar. *Geochim. Cosmochim. Acta* **1998**, *62*, 2643–2671. [CrossRef]
40. Kubrakova, I.V.; Tyutyunnik, O.A.; Silantyev, S.A. Mobility of Dissolved Palladium and Platinum Species during the Water–Rock Interaction in a Chloride Environment: Modeling of PGE Behavior during Interaction between Oceanic Serpentinites and Seawater Derivatives. *Geochem. Int.* **2019**, *57*, 282–289. [CrossRef]
41. Barnes, S.J.; Liu, W. Pt and Pd mobility in hydrothermal fluids: Evidence from komatiites and from thermodynamic modeling. *Ore Geol. Rev.* **2012**, *44*, 49–58. [CrossRef]
42. Barnes, S.J.; Campbell, I.H. Role of late magmatic fluids in Merensky-type platinum deposits: A discussion. *Geology* **1988**, *16*, 488–491. [CrossRef]
43. Khanchuk, A.I.; Plyusnina, L.P.; Ruslan, A.V.; Likhoidov, G.G.; Barinov, N.N. Nature of Graphitization and Noble Metal Mineralization in Metamorphic Rocks of the Northern Khanka Terrane, Primorye. *Geol. Ore Depos.* **2013**, *55*, 225–244. [CrossRef]
44. Schouwstra, R.P.; Kinloch, E.D.; Lee, C.A. A Short Geological Review of the Bushveld Complex. *Platin. Met. Rev.* **2000**, *44*, 33–39.
45. Johan, Z.; Ohnenstetter, M.; Slansky, E.; Barron, L.M.; Suppel, D. Platinum mineralization in the Alaskan-type intrusive complex near Fifield, New South Wales, Australia: Part 1. platinum group minerals in clinopyroxenites of the Kelvin Grove Prospect, Owendale Intrusion. *Miner. Petrol.* **1989**, *40*, 289–309. [CrossRef]
46. Johan, Z.; Slansky, E.; Kelly, D.A. Platinum nuggets from the Kompiam area, Enga Province, Papua New Guinea: Evidence for an Alaskan-type complex. *Miner. Petrol.* **2000**, *68*, 159–176. [CrossRef]
47. Ivanov, O.K. *Concentrically Zoned Pyroxenite–Dunite Massifs of the Urals: Mineralogy, Petrology, and Genesis*; UrGU: Yekaterinburg, Russia, 1997; 32p, ISBN 5-7525-0507-0. (In Russian)
48. Tolstykh, N.; Krivenko, A.; Sidorov, E.; Laajoki, K.; Podlipsky, M. Ore mineralogy of PGM placers in Siberia and the Russian Far East. *Ore Geol. Rev.* **2002**, *20*, 1–25. [CrossRef]

MDPI
St. Alban-Anlage 66
4052 Basel
Switzerland
Tel. +41 61 683 77 34
Fax +41 61 302 89 18
www.mdpi.com

Minerals Editorial Office
E-mail: minerals@mdpi.com
www.mdpi.com/journal/minerals

MDPI
St. Alban-Anlage 66
4052 Basel
Switzerland

Tel: +41 61 683 77 34
Fax: +41 61 302 89 18

www.mdpi.com

ISBN 978-3-0365-2527-3